



# Single atoms supported on carbon materials for hydrogenation reactions

Camila Rivera-cárcamo

## ► To cite this version:

Camila Rivera-cárcamo. Single atoms supported on carbon materials for hydrogenation reactions. Coordination chemistry. Université Paul Sabatier - Toulouse III, 2020. English. NNT : 2020TOU30174 . tel-03170789

**HAL Id: tel-03170789**

**<https://theses.hal.science/tel-03170789>**

Submitted on 16 Mar 2021

**HAL** is a multi-disciplinary open access archive for the deposit and dissemination of scientific research documents, whether they are published or not. The documents may come from teaching and research institutions in France or abroad, or from public or private research centers.

L'archive ouverte pluridisciplinaire **HAL**, est destinée au dépôt et à la diffusion de documents scientifiques de niveau recherche, publiés ou non, émanant des établissements d'enseignement et de recherche français ou étrangers, des laboratoires publics ou privés.



# THÈSE

## En vue de l'obtention du DOCTORAT DE L'UNIVERSITÉ DE TOULOUSE

Délivré par l'Université Toulouse 3 - Paul Sabatier

---

Présentée et soutenue par  
**Camila RIVERA CARCAMO**

Le 30 octobre 2020

**Atomes isolés supportés sur des matériaux carbonés pour la  
catalyse de réactions d'hydrogénation**

---

Ecole doctorale : **SDM - SCIENCES DE LA MATIERE - Toulouse**

Spécialité : **Chimie Organométallique et de Coordination**

Unité de recherche :

**LCC - Laboratoire de Chimie de Coordination**

Thèse dirigée par  
**Philippe SERP**

Jury

**Mme Sophie HERMANS**, Rapporteuse

**M. Antonio LEYVA PEREZ**, Rapporteur

**Mme Katerina SOULANTIKA**, Examinatrice

**M. Cyril GODARD**, Examineur

**M. Bruno CHAUDRET**, Examineur

**Mme Montserrat GOMEZ**, Examinatrice

**M. Peter WITTE**, Examineur

**M. Philippe SERP**, Directeur de thèse

## Acknowledgements

I would like to express my most sincere acknowledgments to my supervisor Professor Philippe Serp. You have been the best mentor and scientific guide that I could ever have. Thank you for your trust, for pushing me and for making me a better professional.

Thanks to my jury members, Professor Sophie Hermans and Dr. Antonio Leyva, reviewers of my thesis, for your kind comments in the report, and Professor Montserrat Gomez, Professor Cyril Godard, Dr. Bruno Chaudret, Dr. Katerina Soulantika and Dr. Peter Witte for the interesting questions and discussion during my defense.

To the collaborators of the project, Dr. Iann Gerber, Dr. Iker del Rosal and Professor Romuald Poteau from Laboratoire de Physique et Chimie des Nano-objets INSA Toulouse, who performed invaluable contributions to this thesis, specifically DFT calculations and Dr. Regis Philippe and Dr. Boris Guicheret from Laboratoire de Génie des Procédés Catalytiques Lyon who carried out the experiments of myrcene hydrogenation and mass transfer studies.

This thesis could not have been accomplished without the assistance of many other persons, whose contribution I gratefully acknowledge. Special thanks to Vincent Colliere, for TEM measurements but also for his friendship and patience, for the long hours of STEM and for having always been available to answer last minute calls. I am very much thankful to Dr. Pierre Lecante for WAXS analysis, Professor Anna Corrias for EXAFS analysis, Professor Hervé Martinez and Dr. Yann Tison for the XPS analysis.

I want also recognize the members of LCC-Team C, who I shared almost the past 4 years of my life, who made this journey sweeter.

Carole, thank you so much for looking after me when it was necessary, for being an inspiration as woman and professional, for your support and of course for the words of encouragement these last hard few months that helped me finish my PhD.

Idaline Romana, Nora Imlyhen and Laurent Ropiquet, not only for their technical assistance on all my experimental work but also for their kindness, infinite patience and invaluable personal conversations. Thank you Laurent for the Qi Gong!!

Toky Rasaminirina thank you for your helpfulness, your morning smiles and your always so accurate words of reassurance.

## Acknowledgements

---

Martine, Maryse, Odile, the Jeromes and Philippe K, for your cordiality during all these years, I will keep in my memory all our Christmas lunches, summer picnics and all the moments that we shared together.

Thanks to my dear friends, who became an important support and relief from the stress and pressure of doing a doctorate: Mario, Elias, Mayra, Angelica, Ayman, Eren, Pedro, Alejandro, Yann, Perla, Catalina and all those who gave me their friendship. I will treasure all our moments forever!

To my fellow colleagues with whom I lived these wonderful years as a student. Thanks, Nicolás, my fav pisces, for driving me home even when you did not want to, YuanYuan for keeping my secrets safe, Joel for the Pica Fresas, Jeremy for teaching me French and Canio for all the guanciale, salsiccia and pecorino that you have shared with me.

Thank you, Cristopher, for your unconditional love and company.

To my beloved family, Papi, Mami, Yimi, Benja and of course all my aunties, and cousins, that supported me from thousands of kilometers away in Chile, that cheered me up so many times with everlasting video calls, messages, pictures, emojis and all the love demonstrations that they sent me daily. I love you all <3

And finally, to the life, to the nature... for allowing me to live this wonderful experience,

Camila RIVERA-CÁRCAMO



## Table of contents

Résumé .....	1
Abstract.....	3
General Introduction and objectives.....	5
 <b>Chapter 1. Single atom catalysts on carbon-based materials</b> .....	<b>9</b>
1. Single atom catalysts on carbon-based materials .....	11
1.1. Introduction .....	11
1.2. Types of carbon materials for single atom deposition and nature of the adsorption sites .....	16
1.2.1. Graphitic carbon nitride and related structures.....	16
1.2.2. Graphene and carbon nanotubes.....	20
1.2.3. Graphene oxide.....	31
1.2.4. Fullerenes .....	33
1.2.5. Graphyne and graphdiyne.....	36
1.2.6. Material perspectives .....	37
1.3. Single atom catalyst characterization .....	40
1.4. Preparation of single atom catalysts .....	43
1.4.1. Low loading SAC (<1% w/w).....	44
1.4.2. High loading SAC (>1 % w/w) .....	51
1.5. Catalysis with single atom catalysts on carbon-based materials .....	61
1.5.1. Oxygen reduction reaction.....	61
1.5.2. Hydrogen and oxygen evolution reactions .....	65
1.5.3. Photocatalysis .....	67
1.5.4. CO oxidation .....	72
1.5.5. Hydrogenation reactions.....	75
1.5.6. CO <sub>2</sub> reduction .....	80
1.5.7. Other reactions.....	83
1.6. Conclusion.....	86
 <b>Chapter 2. High loading single atom catalysts</b> .....	<b>89</b>
2. High loading single atom catalysts.....	91
2.1. Introduction .....	91
2.2. Results .....	94
2.2.1 Ru@C <sub>60</sub> hetero-structure synthesis and TEM characterization.....	94

2.2.2 Raman, XPS, WAXS and EXAFS characterizations .....	105
2.2.3 Catalytic activity of the Ru@C <sub>60</sub> nanostructures .....	113
2.3. Conclusions .....	119
2.4. Experimental.....	120
2.4.1. General methods .....	120
2.4.2. Synthesis of Ru@C <sub>60</sub> nanostructures .....	120
2.4.3. Hydrogenation of nitrobenzene .....	120
2.4.4. Hydrogenation of 2,3-dimethyl-2-butene .....	122
2.4.5. Catalyst characterization.....	122
2.4.6. Density Functional Theory (DFT) calculations.....	124
 <b>Chapter 3. Preparation of low loading carbon supported metal single atoms .....</b>	<b>125</b>
3. Preparation of low loading carbon supported metal single atom .....	127
3.1. Introduction .....	127
3.2. Vacancies.....	130
3.2.1. Thermogravimetric analyses.....	134
3.2.2. Temperature-programmed desorption analyses.....	135
3.2.3. Raman analyses .....	138
3.2.4. X-ray photoelectron spectroscopy analyses .....	140
3.3. Detection of vacancy .....	143
3.3.1. Nuclear magnetic resonance analyses .....	145
3.3.2. Magnetization measurement analyses .....	146
3.3.3. Electron paramagnetic resonance analyses.....	149
3.4. Synthesis of supported single atom catalysts (SAC) .....	153
3.5 Mixture of single atoms and nanoparticles.....	165
3.6 Conclusion.....	173
3.7 Experimental section .....	173
3.6.1 Catalysts preparation .....	173
3.6.2 Catalysts Characterization .....	174
 <b>Chapter 4. Hydrogenation of alkenes with single atom catalysts .....</b>	<b>177</b>
4. Hydrogenation of alkenes with single atom catalysts .....	179
4.1. Introduction .....	179
4.2. Hydrogenation and isomerization of alkenes .....	181
4.3. Mechanistic insights from DFT calculations.....	190

4.4.	Control of the single atom/nanoparticle ratio .....	198
4.5.	Catalyst stability .....	203
4.6.	Conclusion.....	207
4.7.	Experimental part .....	207
4.7.1.	Palladium catalyst synthesis .....	207
4.7.2.	DFT periodic calculations (LPCNO, Dr. Iann Gerber, Dr. Iker del Rosal and Prof. Romuald Poteau).....	209
4.7.3.	DFT Gaussian calculations (LPCNO, Dr. Iann Gerber, Dr. Iker del Rosal and Prof. Romuald Poteau).....	210
4.7.4.	Catalytic experiments (LGPC, Dr. Boris Guicheret, Dr. Laurent Vanoye, Dr. Alain Favre-Réguillon, Prof. Claude de Bellefon and Dr. Régis Philippe) ...	211
<b>Chapter 5. Hydrogenation of carbon dioxide over SA catalysts .....</b>		<b>223</b>
5.	Hydrogenation of carbon dioxide over SA catalysts .....	225
5.1.	Introduction .....	225
5.2.	Results and discussion .....	229
5.3.	Conclusion.....	239
5.4.	Experimental part .....	240
5.4.1.	Catalysts preparation .....	240
5.4.2.	Catalysts characterization .....	241
5.4.3.	Catalytic tests.....	241
General conclusions and perspectives .....		243
<b>Chapter 6. Résumé .....</b>		<b>247</b>
6.	Résumé .....	249
6.1.	Catalyseurs à base d'atomes métalliques isolés sur matériaux carboné.....	249
6.2.	Catalyseurs à base d'atomes métalliques isolés à fort chargement en métal	251
6.3.	Catalyseurs à base d'atomes métalliques isolés à faible chargement en métal	257
6.4.	Hydrogénation d'alcènes sur des catalyseurs à atomes métalliques isolés ...	261
6.5.	Hydrogénation du dioxyde de carbone sur des catalyseurs à atomes isolés.	265



## Résumé

Ce travail de recherche se concentre sur la préparation de catalyseurs de site unique supportés sur matériaux carbonés et leur applicabilité aux réactions d'hydrogénation. Le chapitre 1 correspond à une revue complète des études expérimentales et théoriques visant à: i) préparer le SAC sur les matériaux carbonés, ii) comprendre les interactions métal-support dans le SAC, et iii) étudier comment cela est lié aux performances catalytiques. Dans le chapitre 2, nous avons pu comprendre la possibilité de produire différentes nanostructures Ru@fullerène qui peuvent être modulées nanométriquement en faisant varier les conditions lors de leur synthèse, solvant et rapport Ru/C<sub>60</sub>, à travers des nanoparticules (NP) bien définies à de très petits clusters et même des atomes simples (SA) avec une charge métallique élevée (~ 6-20% en poids). Nous avons appliqué ces nanostructures comme catalyseurs dans l'hydrogénation du nitrobenzène, constatant que Ru SA est moins efficace que Ru NP, performance qui a également été étudiée par des calculs DFT. Le chapitre 3 détaille un nouveau protocole simple pour la création de lacunes sur des supports carbonés. Nous proposons qu'il soit possible de créer des défauts/lacunes sur les supports par un processus contrôlé en deux étapes, qui comprend la subséquent création et décomposition de groupes oxygène sur la surface. La caractérisation magnétique a reflété la présence d'espèce réactive avec un comportement paramagnétique soulevant d'éventuels radicaux en surface. Par la suite, nous avons montré qu'il était possible d'utiliser de tels défauts comme point d'ancrage pour stabiliser avec succès des atomes métalliques (Ru, Pd, Pt, Ni, Cu, Co, Ir) avec une charge allant jusqu'à ~ 1,6% en poids. Aussi, en améliorant cette méthode, nous sommes arrivés à être capables de contrôler le rapport SA/NP pour un chargement métallique donné allant de 10 à 200. Chapitre 4, à travers une étude expérimentale-théorique combinée, nous fournissons une explication de l'influence de la structure caractéristiques des catalyseurs Pd/C pour l'hydrogénation d'alcène. Des nanoparticules de Pd hautement dispersées (Pd<sub>NP</sub>) sont nécessaires pour activer le dihydrogène. Une concentration élevée de défauts de surface sur le support de carbone est nécessaire pour stabiliser les atomes simples de Pd (Pd<sub>SA</sub>), qui coexistent avec le Pd<sub>NP</sub> sur les catalyseurs Pd / C. Une concentration élevée de groupes de surface oxygénés est également nécessaire sur le support de carbone pour permettre le débordement d'hydrogène. Nous démontrons qu'une telle combinaison permet à une catalyse coopérative d'opérer entre Pd<sub>NP</sub> et Pd<sub>SA</sub> qui impliquent la formation

d'espèces  $\text{Pd}_{\text{SA}}\text{-H}$ , qui sont beaucoup plus actives que  $\text{Pd}_{\text{NP}}\text{-H}$  pour l'hydrogénation d'alcène mais aussi l'isomérisation. En effet, pour l'activité d'hydrogénation du myrcène, des variations de plusieurs ordres de grandeur ont été mesurées en fonction de la valeur de ce rapport SA / NP. Nous montrons que la maîtrise de ce ratio permet le développement d'une nouvelle génération de catalyseurs hautement actifs intégrant l'utilisation ultra-rationnelle des métaux précieux en pénurie. Enfin, le chapitre 5 se concentre sur les performances catalytiques des catalyseurs SA dans l'hydrogénation du dioxyde de carbone. Les résultats montrent une activité la plus élevée pour le Pt ainsi qu'une sélectivité de 99% pour le CO. Par ailleurs, les catalyseurs Ru avaient la plus haute sélectivité pour le  $\text{CH}_4$ .

## Abstract

This research work focuses on the preparation of carbon-based single atom (SA) catalysts and their applicability on hydrogenation reactions. Chapter 1 correspond to a comprehensive review over experimental and computational studies aiming at: i) preparing SAC on carbon materials, ii) understanding the metal-support interactions in SAC, and iii) studying how this relates to catalytic performances. In Chapter 2 we were able to understand the possibility of producing different Ru@fullerene nanostructures that can be nanometrically modulated by varying the conditions during their synthesis, solvent and Ru/C<sub>60</sub> ratio, through well-defined nanoparticles (NP) to very small clusters and even single atoms (SA) with a high metallic loading (~ 6-20wt%). We applied these nanostructures as catalysts in the hydrogenation of nitrobenzene, finding that Ru SA is less efficient than Ru NP, performance that was also studied by DFT calculations. Chapter 3, details a new and straightforward protocol for the creation of vacancies over carbonaceous supports. We propose that is possible to create defects/vacancies over the supports by a controlled subsequent two-steps process, which comprises the subsequent creation and composition of surface oxygen groups. Magnetic characterization reflexed the presence of this reactive species with a paramagnetic behavior raising form possible radicals species on the surface. Afterwards, we showed that was possible to use such defects as anchoring point to successfully stabilize single metallic atoms (Ru, Pd, Pt, Ni, Cu, Co, Ir) with a loading up to ~ 1.6wt%. Also, by improving this method, we arrived to be capable to control the ratio SA/NP for a given metallic loading ranging from 10 to 200. Chapter 4, through a combined experimental-theoretical study, we provide an explanation of the influence of structural characteristics of Pd/C catalysts for alkene hydrogenation. Highly dispersed Pd nanoparticles (Pd<sub>NP</sub>) are necessary to activate dihydrogen. A high concentration of surface defects on the carbon support is necessary to stabilize Pd single atoms (Pd<sub>SA</sub>), which coexist with Pd<sub>NP</sub> on Pd/C catalysts. A high concentration of oxygenated surface groups is also necessary on the carbon support to allow hydrogen spillover. We demonstrate that such combination allows a cooperative catalysis to operate between Pd<sub>NP</sub> and Pd<sub>SA</sub> that involve the formation of Pd<sub>SA</sub>-H species, which are much more active than Pd<sub>NP</sub>-H for alkene hydrogenation but also isomerization. Indeed, for myrcene hydrogenation activity variations of several orders of magnitude were measured as a function of the value of this ratio SA/NP. We show that the control of this ratio allows the development of a new generation of highly active catalysts integrating the ultra-rational use of precious metals in short supply.

Finally, Chapter 5, focuses on the catalytic performance of SA catalysts in carbon dioxide hydrogenation. The results show highest activity for Pt as well as 99% selectivity to CO. On the other hand, Ru catalysts had highest selectivity to CH<sub>4</sub>.



## General Introduction and objectives

Size reduction of the active phase in supported catalysts induces: i) the increase in the proportion of catalytically active surface species or in highly uncoordinated atoms, and ii) quantum size effect (for particle size close to the nanometer). This may result in enhanced catalytic performances (Figure 1).<sup>1</sup> Indeed, as the catalyst size is reduced, the surface atomic structure, electronic structure, and defects will change significantly. Therefore, the catalytic activity or selectivity of the catalyst is often improved. The smallest size that can be reached for this type of object is of course the isolated atom deposited on a support. Discoveries of breakthroughs in the catalytic performance of supported isolated atom compared to traditional catalysts demonstrate the strong potential of these materials in various applications.

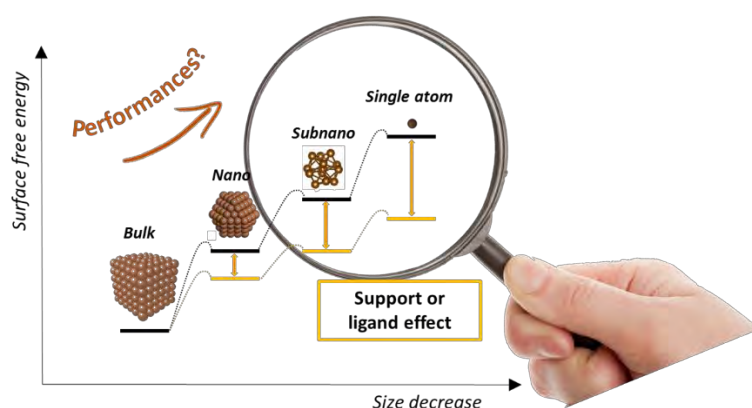


Figure 1. Particle size effects in heterogeneous catalysis.

Catalysts based on supported isolated atom have long existed in different forms (Figure 2). However, the possibility to visualize their presence in previously unknown systems has sparked enormous renewed interest in the past decade.<sup>2</sup> Metallic species with different size (nanoparticles (NP), clusters and single atoms (SA)) usually show different catalytic performances for various reactions, and many factors (particle size, shape, chemical composition, metal-support interaction, and metal-reactant interaction) can have significant influences on the catalytic properties. The electronic and geometric structures

<sup>1</sup> V. Polshettiwar. In *Nanomaterials in Catalysis* edited by P. Serp, *et al.*: Wiley-VCH, Weinheim Germany (2013), p. 11199.

<sup>2</sup> S. Mitchell, *et al.* *Nature Communications* **2020**, *11*, 4302.

of isolated supported atoms, clusters, and nanoparticles have been recently reviewed by A. Corma *et al.*<sup>3</sup>

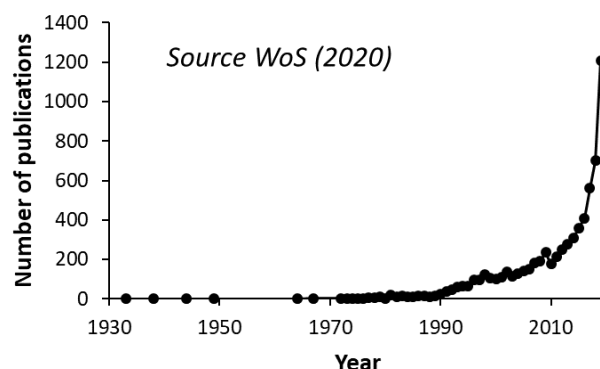


Figure 2. Number of publications dealing with supported isolated atoms for catalytic applications.

The number of variables that can have an effect on the catalytic behavior is obviously quite high. Among them, A. Corma *et al.* highlight different important aspects linked to the origins of particle size effects in heterogeneous catalysis:

- ✓ The intrinsic electronic difference and binding capacities when going from SA to clusters and to NP.
- ✓ The dynamic characteristics of the catalytic process, which is directed by the metal-reactant interaction.
- ✓ The fact that these changes can be for the good or for the bad from a catalytic point of view.
- ✓ In the extreme case of supported SA, the real active site will be the “single metal atom”, but the “ligand” atoms of the support will play an important role.

Concerning the last item, it is important to stress that, as in homogeneous catalysis, the direct environment of the SA will have a pivotal role on its catalytic performances. Consequently, further advances in both the controlled synthesis and the characterization of supported SA catalysts are definitively required to move forward in the design. Another challenge for single atom catalysts (SAC) for industrial applications is to increase the active site density. In addition, the difficulty in experimentally verifying the structures of

<sup>3</sup> L. Liu, et al. *Chemical Reviews* **2018**, 118, 4981-5079.

this type of catalysts has generated a growing reliance on computational methods to support hypotheses for the observed reactivity.

Single atoms undoubtedly have a different reactivity than metal NP conventionally used in catalysis, and today, the very large majority of catalytic studies addressing the subject are limited to a comparison of the reactivity of isolated atoms with that of metallic particles; even though these two types of species must coexist in many catalysts. Few studies have been reported up to day concerning a possible synergy between metal NP and SA,<sup>456789</sup> and in most of them very few efforts have been devoted to explain the origin of this synergy.

In that context, the objectives of this thesis were to explore new routes for the preparation of carbon-supported low and high loading SAC, and to investigate possible synergy between SA and NP for hydrogenation reactions. This thesis was carried out at the Laboratory of Coordination Chemistry (UPR 8241 CNRS) and involved active collaborations with the Laboratoire de Physique et Chimie des Nano-Objets (LPCNO – UMR 5215) in Toulouse and the Laboratoire de Génie des Procédés Catalytiques (LGPC – UMR 5285) in Lyon.

In chapter 1, we present a comprehensive bibliographic analysis of experimental and theoretical studies on SAC supported on carbon-based materials. Fundamental aspects dealing with the type of carbon materials used for SA deposition are discussed, together with the characterization of the resulting materials. Furthermore, an in-depth analysis was made on the use of carbon-supported SAC in a wide range of reactions, including thermal, photo- and electro-catalysis, trying to elucidate the metal-support interactions in SAC, and how it impacts the catalytic performances.

Chapter 2 describes an efficient method to produce high loading SAC. The main objective was to produce Ru fullerides consisting in a polymeric structure interspersing Ru atoms and fullerenes (C<sub>60</sub>) as monomers. We have also evaluated the possibility to introduce in a controlled way more metal, so as to produce novel architectures combining Ru clusters and C<sub>60</sub>. We studied the influence of solvent, temperature and Ru/C<sub>60</sub> ratio on the

---

<sup>4</sup> L. Kuai, et al. *Nature Communications* **2020**, *11*, 48.

<sup>5</sup> Y. Ma, et al. *Advanced Materials* **2020**, *32*, 2002177.

<sup>6</sup> Y. Fu, et al. *ACS Sustainable Chemistry & Engineering* **2020**, *8*, 8338-8347.

<sup>7</sup> J. N. Tiwari, et al. *Nano Energy* **2020**, *78*, 105166.

<sup>8</sup> B. Yuan, et al. *Journal of Energy Chemistry* **2020**, *51*, 312-322.

<sup>9</sup> J. Peng, et al. *International Journal of Hydrogen Energy* **2020**, *45*, 18840-18849.

morphology of the resulting products. These compounds were exhaustively characterized by WAXS, EXAFS, or XPS which, in combination with theoretical calculations such as DFT, allow the nature of the structures to be more precisely elucidated. In an innovative way, catalysis was used as a tool to discriminate the nature of the metallic species present in these structures.

In Chapter 3 a simple and reproducible method for preparing low loading SAC on carbon supports was proposed. First, we try to create and identify by magnetic measurements and EPR analyses the adsorption sites necessary to stabilize supported SA. Then, the dispersion of the active phase on the modified support was carried out. Trying to evaluate the scope of the method, different parameters were evaluated such as: solvent, impregnation time, precursor type, activation temperature, type of support and nature of the metal. Atomic resolution microscopy was used to characterize the resulting materials. Finally, we attempted to develop a protocol for depositing both NP and SA on the carbon support, and for controlling the NP/SA ratio.

In chapter 4, we assessed the catalytic performances of the above-mentioned catalysts for the hydrogenation of different alkenes (terpenes such as myrcene, squalene and farnesene). Besides, exhaustive theoretical studies over a simpler model molecule were carried out in order to understand the catalytic hydrogenation and isomerization mechanisms. Factors such metal dispersion, concentration of oxygen surface groups and defects on the support were taken into account to evaluate the possibility of hydrogen spillover in these systems. We attempted to understand the cooperative effect between SA and NP, and how the control of the ratio between these two species allows optimizing the catalytic system design to produce ultra-active catalysts.

Chapter 5 provides a general insight of the performance of SAC for the thermocatalytic hydrogenation of carbon dioxide under methanation conditions. Six different metals were tested (Ru, Pt, Pd, Ni, Co, Cu), and a comparison of different catalysts was made, including samples containing only SA and other series with mixtures of SA and NP. Furthermore, SAC doping with alkali was investigated in order to evaluate its effect on the catalytic performances.

Finally, prospects for further studies and obtaining optimized catalysts with better performances will be suggested.

## Chapter 1. Single atom catalysts on carbon-based materials





## 1. Single atom catalysts on carbon-based materials

### 1.1. Introduction

Heterogeneous catalysis on supported metals consists in multi-step surface reactions, in which most of the time, the underlying atoms of the active phase play no direct role in the reaction. The presence of SA with higher reactivity at the surface of this active phase has been proposed in 1925 by H.S. Taylor, in the case of Ni hydrogenation catalysts (Figure 1.1).<sup>1</sup> Somorjai and others have shown that surface defects such as steps and kinks on many metals may dramatically influence the reaction by ‘poisoning’ it or by acting as the catalytically active centers.<sup>2</sup> As the active phase is often made up of noble metals, expensive and for the most part identified as critical elements, a logical step in heterogeneous catalysis is to try to optimize their dispersion on the support. The maximum dispersion that can be achieved involves the use of isolated atoms on the support; however, their stability is usually not sufficient and therefore their more stable particle aggregation cannot be avoided, except if stabilization is accomplished by an environment not prone to their surface migration.<sup>3</sup>

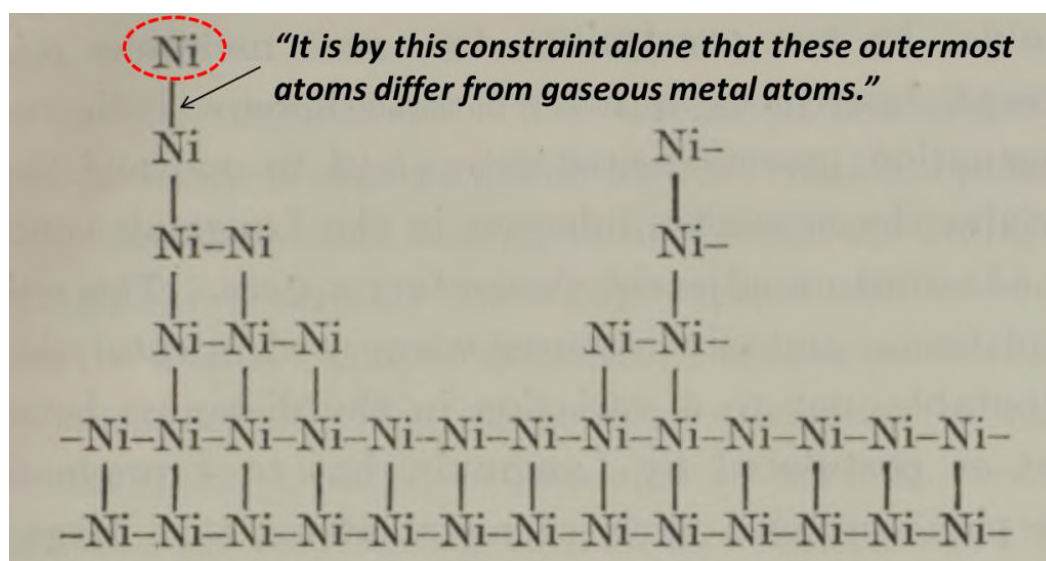


Figure 1.1. Schematic representation of a portion of a Ni granule surface in cross-section. From ref. [1].

<sup>1</sup> H. S. Taylor, et al. In *Proceedings of the Royal Society of London. Series A, Containing Papers of a Mathematical and Physical Character*: Royal Society (1925), pp. 105-111.

<sup>2</sup> G. A. Somorjai, et al. In: Willey (2010).

<sup>3</sup> G. M. Veith, et al. In *Scientific Bases for the Preparation of Heterogeneous Catalysts, Proceedings of the 9th International Symposium*, edited by E. M. Gaigneaux, et al. (2006), pp. 71-78.

In 1947, V. Haensel and co-workers at Universal Oil Products followed such a strategy for the development of a reforming Pt/Al<sub>2</sub>O<sub>3</sub> catalyst.<sup>4</sup> In order to make such a process, involving inexpensive reagents and products and an active phase such as platinum, economically viable, it was imperative to minimize the amount of metal by maximizing its dispersion on the alumina support. The Pt content of this catalyst was 0.1 % w/w. The first commercial unit, at the Old Dutch Refinery in Muskegon Michigan, started to operate in November 1949.<sup>5</sup> This may be the first example of an industrial application of a bifunctional SAC, combining both isolated metal atoms and acidic functions. Seventy years later, the group of G. Hutchings and researchers from Johnson Matthey followed a similar strategy to replace the conventional Hg/C acetylene hydrochlorination catalyst by a Au/C catalyst.<sup>6</sup> They set as a target a Au loading < 0.25 % w/w, since loadings higher than this were considered not to be economically viable. In situ X-ray absorption fine structure spectroscopy experiments (EXAFS) have definitively shown that the active catalyst predominantly comprises Au(I) isolated cationic species.<sup>7</sup> In these two industrial catalysts, a strong metal-support interaction plays an essential role in preventing aggregation, creating stable and finely dispersed SAC. These two examples show that the concept of single atom catalysis, patented by an US company in 2010,<sup>8</sup> is attractive, particularly in the context of sustainable technologies that will make use of critical metals, which are expensive and of limited abundance. In this context, the use of SAC is particularly attractive because it limits the use of precious metals; but it is of course also necessary that it achieves optimum performance in terms of stability, activity and selectivity. Figure 1.2 shows that different types of heterogeneous catalysts can meet the definition of SAC: i) a supported single metal-atom catalyst containing only isolated single atoms embedded on a support, in this chapter we will call SAC this type of catalyst; ii) site-isolated atoms incorporated in the framework of a material (*i. e.* in zeolite, metal-organic frameworks (MOF), or aluminum phosphate molecular sieves (ALPOs)); and iii) a supported homogeneous catalyst or site-isolated heterogeneous catalyst<sup>9</sup> that contains a coordination complex (that may contain one or several metallic atoms) anchored on a support. A generic term to name this set of catalysts was introduced by J.M. Thomas in

---

<sup>4</sup> V. Haensel. Universal Oil Products Company (US 2623861) **1952**.

<sup>5</sup> V. Haensel, et al. *Acs Symposium Series* **1989**, 411, 2-11.

<sup>6</sup> P. Johnston, et al. *Journal of the American Chemical Society* **2015**, 137, 14548-14557.

<sup>7</sup> G. Malta, et al. *Science* **2017**, 355, 1399-1402.

<sup>8</sup> Xin Xiao, et al. Savannah River Nuclear Solutions, LCC (US2012/0004098A1) **2012**.

<sup>9</sup> J. Liu *Acs Catalysis* **2017b**, 7, 34-59.



2005, “single site heterogeneous catalysts”.<sup>10</sup> In this chapter, we will concentrate only on SAC dispersed on carbon materials. The readers interested by supported homogeneous catalysts on carbon materials are invited to refer to literature reviews.<sup>11,12</sup> The borderline between SAC and supported homogeneous catalysts is tenuous. Indeed, during catalysis, a SAC may become a supported homogeneous catalyst, due to chemisorption of reactants that will become ligands during the reaction; this phenomenon can be accompanied by a partial detachment of the metal from the support.

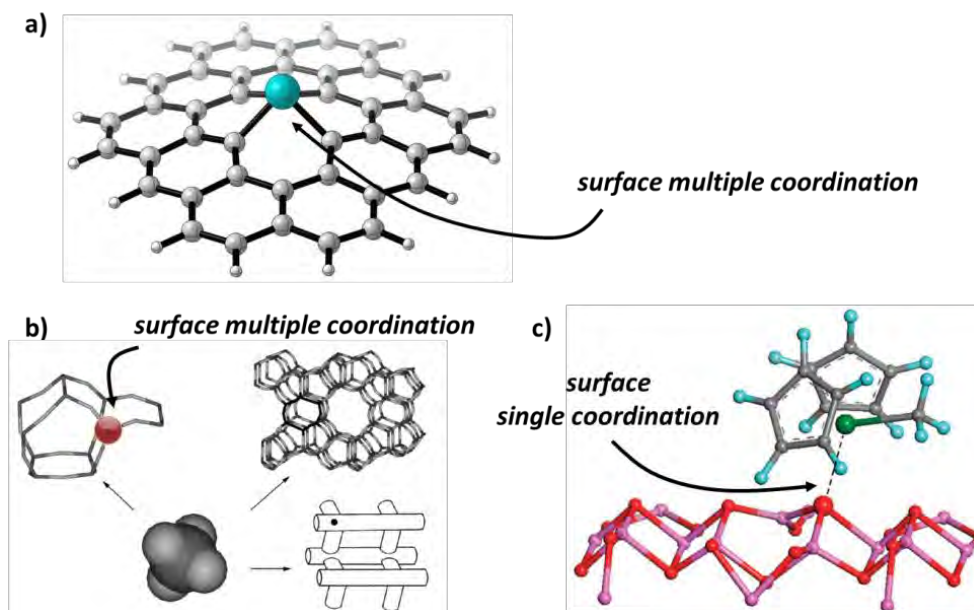


Figure 1.2. Schematic illustrations of: a) a supported single Pd atom on carbon catalyst (SAC), the Pd atom is located in a carbon vacancy; (b) a site-isolated Al atom incorporated in the framework of a T site, zeolite ring, and zeolite channel system. (From ref. [13]); and (c) a supported homogeneous catalyst, oxo-bridged zirconocenium coordination on a  $\mu^3$ -O alumina surface site. From ref. [14].

On the other side, Samantaray *et al.* have shown many years ago that a supported homogeneous catalyst can lead, after ligand removal, to SAC;<sup>15</sup> and the definition of single-site heterogeneous catalyst given by Zecchina *et al.* is the following: “The usual definition of single-site heterogeneous catalyst is a catalyst constituted by a metal atom, ion, or small cluster of atoms, held by surface ligands to a rigid framework”.<sup>16</sup> It is thus

<sup>10</sup> J. M. Thomas, *et al.* *Angewandte Chemie-International Edition* **2005**, 44, 6456-6482.

<sup>11</sup> M. R. Axet, *et al.* *Coordination Chemistry Reviews* **2016**, 308, 236-345.

<sup>12</sup> C. Freire, *et al.* In *Carbon Materials for Catalysis*: John Wiley & Sons (**2008**), pp. 267-307.

<sup>13</sup> J. Dedeczek, *et al.* *Catalysis Reviews-Science and Engineering* **2012**, 54, 135-223.

<sup>14</sup> A. Motta, *et al.* *Journal of the American Chemical Society* **2008**, 130, 16533-16546.

<sup>15</sup> M. K. Samantaray, *et al.* *Chemical Reviews* **2020**, 120, 734-813.

<sup>16</sup> A. B. Zecchina, S.; Groppo, E. In: Wiley-VCH Verlag GmbH & Co. KGaA (**2011**), pp. 1-27.

interesting to notice that there is now more than forty years that the community of homogeneous catalysis and coordination chemistry, which strongly contribute to supported homogeneous catalyst, and heterogeneous catalysis, currently involved in SAC, try to meet;<sup>17</sup> and the day they do it, do not realize it!

Up to now, supported homogeneous catalysts have been limited to few industrial applications, for example oligo- and polymerization or oxidation reactions.<sup>18</sup> This is mainly due to the fact that the synthetic approach used to prepare them was by molecular chemistry involving the use of coordination complexes, and the main goal, most of the times, is to maintain a coordination sphere around the metal as close as possible to the homogeneous catalyst. The result is that the linkage between the active phase and the support can be weak (often a single coordination, as shown on Figure 1.2c). SAC, on the other side can be very robust: Nie *et al.* have shown that a thermally stable catalyst, atomically dispersed Pt<sup>2+</sup> on CeO<sub>2</sub>, can become active for CO oxidation at 150 °C after steam treatment at 750 °C.<sup>19</sup> This is linked to the fact that chemists from solid state chemistry used a different synthetic approach, in which the catalyst precursor should be completely decomposed to create an as strong as possible interface with the support (multi-coordination, as shown in Figure 1.2a,b). We will see in this chapter that carbon materials can provide such an environment for SAC.

Since the beginning of the century, SAC have attracted a great deal of research interest, and many reviews have already been devoted to this subject.<sup>20,21,22,23,24</sup> The recent developments of characterization techniques, modelling tools, and the progresses in surface coordination chemistry have allowed significant advances in that field. It is plausible that SAC are operating in many catalytic reactions; however, in the past, the lack of powerful characterization tools such as aberration-corrected transmission electron microscopy, was detrimental to their identification.<sup>25</sup> Thus, relatively few studies dealing with SAC have been published in the last century.<sup>26</sup> They often rely on EXAFS studies; for example Sachtler and co-workers have investigated in 1982 the structure of cobalt-

---

<sup>17</sup> K. Philippot, et al. In *Nanomaterials in Catalysis*: Wiley-VCH Verlag GmbH & Co. (2013), pp. 1-54.

<sup>18</sup> B. C. Gates, et al. *Catalysis Science & Technology* **2017**, 7, 4259-4275.

<sup>19</sup> L. Nie, et al. *Science* **2017**, 358, 1419-1423.

<sup>20</sup> C. Rivera-Cárcamo, et al. *ChemCatChem* **2018**, 10, 5058-5091.

<sup>21</sup> A. Wang, et al. *Nature Reviews Chemistry* **2018c**, 2, 65-81.

<sup>22</sup> M. Li, et al. *Advanced Materials* **2020b**, 32, 2001848.

<sup>23</sup> S. Mitchell, et al. *Angewandte Chemie-International Edition* **2018**, 57, 15316-15329.

<sup>24</sup> R. Gusmao, et al. *Acs Catalysis* **2020**, 10, 9634-9648.

<sup>25</sup> J. C. Matsubu, et al. *Journal of the American Chemical Society* **2015**, 137, 3076-3084.

<sup>26</sup> R. Linke, et al. *Surface Science* **1994**, 307, 407-411.

porphyrin catalysts supported on active carbon, an active oxygen-reduction electrocatalysts.<sup>27</sup> Their works show that, after a heat treatment (700 °C under nitrogen), the carbon atoms originally present in the supported homogeneous catalyst have been displaced, although the CoN<sub>4</sub> group is retained in the heat-treated material. It is also interesting to note that the first report on the visibility of SA by high-resolution scanning electron microscopy dated from 1970: it was about uranium atoms on a thin carbon film.<sup>28</sup> Carbon, due to its low atomic weight, is indeed an interesting element for visualizing metallic atoms by electron microscopy observations. Ten years later, direct observation of the behavior of heavy SA (U, Pt, Au, In, Cd, Ag, and Pd) on amorphous carbon substrates was reported.<sup>29</sup> In this study it was stated that “*the motion of heavy atoms on amorphous carbon substrates is found to depend on the atom species and the local substrate structure*”. DFT calculations performed more than twenty five years later have shown that transition metals (TM) such as V, Cr, Mn, Fe, Co, Mo and Ru have strong adsorption energy and strong migration barrier energy on graphene (G), whereas for Cu, Ag, and Au binding energies are very small and the diffusion barrier energies are also expected to be very small.<sup>30</sup> Electron microscopy as well as DFT calculations have also shown that these mobile atoms can be trapped by mono- and di-vacancies in graphene.<sup>31</sup> Additionally, the first report, in 1991, on single atom detection by EELS was also about uranium atoms on carbon.<sup>32</sup> In 2015, the visualization of reacting Pt<sub>SA</sub> deposited on carbon support in chemical reactions was reported.<sup>33</sup> All these progresses in surface science and modelling allow today an easier characterization of SA on carbon materials. We have organized this chapter to have a complete overview of SAC on carbon materials. We will first discuss the types of carbon materials for single atom deposition and the structure of the adsorption sites. Then, we will briefly present the main SAC characterization techniques, and present the preparation of these catalysts. Finally, we will discuss the performances of these catalysts.

---

<sup>27</sup> R. W. Joyner, et al. *Journal of the Chemical Society-Faraday Transactions I* **1982**, 78, 1021-1028.

<sup>28</sup> A. V. Crewe, et al. *Science* **1970**, 168, 1338-&.

<sup>29</sup> M. Utlaut *Physical Review B* **1980**, 22, 4650-4660.

<sup>30</sup> A. Ishii, et al. *Journal of Physics Conference Series* **2008**, 100.

<sup>31</sup> A. W. Robertson, et al. *Nano Letters* **2013**, 13, 1468-1475.

<sup>32</sup> O. L. Krivanek, et al. *Microscopy Microanalysis Microstructures* **1991**, 2, 257-267.

<sup>33</sup> E. D. Boyes, et al. *Mrs Bulletin* **2015**, 40, 600-605.

## 1.2. Types of carbon materials for single atom deposition and nature of the adsorption sites

As stated in the introduction, the preparation of a SAC requires specific sites on the support that will act as traps for the metallic atoms. In that context, a perfect  $sp^2$  carbon surface do not appear convenient to obtain stable SAC, even if for some metals on graphene, DFT calculations have shown strong adsorption energy, high diffusion barrier and significant charge transfer.<sup>34</sup> Most of the time however, the adsorption energy of metal adatoms on defect-free graphitic-like materials (0.2 to 1.55 eV)<sup>35</sup> are lower than the metal-metal bonding energies in supported NP ( $> 1.55$  eV);<sup>36</sup> consequently, the formation of metal NP is favored over SAC. The presence of defects in the carbon material, such as vacancies will significantly increase the adsorption energy of metal adatoms.<sup>37</sup> The creation of defects is therefore a key step in the preparation of SAC. It can be achieved by physical or chemical methods, and will allow the anchoring of isolated atoms because of the potential existing around these centers.<sup>38</sup> The use of  $sp^{2+\delta}$  materials presenting curved surface allows significantly higher binding energies, particularly with fullerenes, for which binding energy ranging between 1.25 and 3.1 eV have been reported for TM adatoms.<sup>39</sup> Consequently, the production of metal fullerenes, in which single metallic atoms are bonded to  $C_{60}$  is possible, even if, in some cases, they constitute the kinetic product of the reaction.<sup>40</sup> Nitrogen or boron incorporation in carbon materials can efficiently enhance the binding energy of TM metal adatoms.<sup>41</sup> Two-dimensional porous carbon nitride sheet have attracted research interest because CN monolayers naturally come with regular pattern defect sites, which make it suitable for easy trapping of various atoms in a well-defined environment.<sup>42</sup>

### 1.2.1. Graphitic carbon nitride and related structures

Graphitic carbon nitride (g- $C_3N_4$ ) is a N-doped carbon material that exists both in 2D and 3D structures. It can be produced by polymerization of cyanamide, dicyandiamide or melamine precursors. The choice of the operating conditions of the reaction makes it possible to obtain, in a controlled manner, materials having different levels of

---

<sup>34</sup> H. Valencia, et al. *Journal of Physical Chemistry C* **2010**, *114*, 14141-14153.

<sup>35</sup> X. Liu, et al. *Crystals* **2013**, *3*, 79-111.

<sup>36</sup> C. T. Campbell *Accounts of Chemical Research* **2013**, *46*, 1712-1719.

<sup>37</sup> A. V. Krasheninnikov, et al. *Physical Review Letters* **2009**, *102*, 126807.

<sup>38</sup> O. Cretu, et al. *Physical Review Letters* **2010**, *105*.

<sup>39</sup> M. Robledo, et al. *Rsc Advances* **2014**, *4*, 53010-53020.

<sup>40</sup> F. Leng, et al. *Rsc Advances* **2016**, *6*, 69135-69148.

<sup>41</sup> H. Feng, et al. *Journal of Materials Chemistry* **2010**, *20*, 1702-1708.

<sup>42</sup> J. Wen, et al. *Applied Surface Science* **2017**, *391*, 72-123.

condensation and, *in fine*, different properties.<sup>43</sup> According to this work, cyanamide-based precursors can polycondense into dicyandiamide, melamine, melam, dimelem, melon, melon sheet and g-C<sub>3</sub>N<sub>4</sub>. Polymeric g-C<sub>3</sub>N<sub>4</sub> becomes unstable at above 600 °C. The first highly organized polymeric structure (melon) of composition C<sub>3</sub>N<sub>4</sub> that is formed has pendant groups of amine type. Condensation continuing, less defective structures based on triazine or heptazine (2,5,8-triaminotri-s-triazine, or melem) elementary units are obtained. Although g-C<sub>3</sub>N<sub>4</sub> is a promising material, its structure, which is believed to possess graphite like layered structure, is still under investigation. The two architectural units triazine and heptazine serve as a basis for obtaining allotropes of g-C<sub>3</sub>N<sub>4</sub>, which present different properties, particularly in terms of stability, because of the different environment of the nitrogen atom in these materials (Figure 1.3a-b). DFT calculations have shown that the polyheptazine-based material is 30 kJ.mol<sup>-1</sup> more stable than the triazine one.<sup>44</sup>

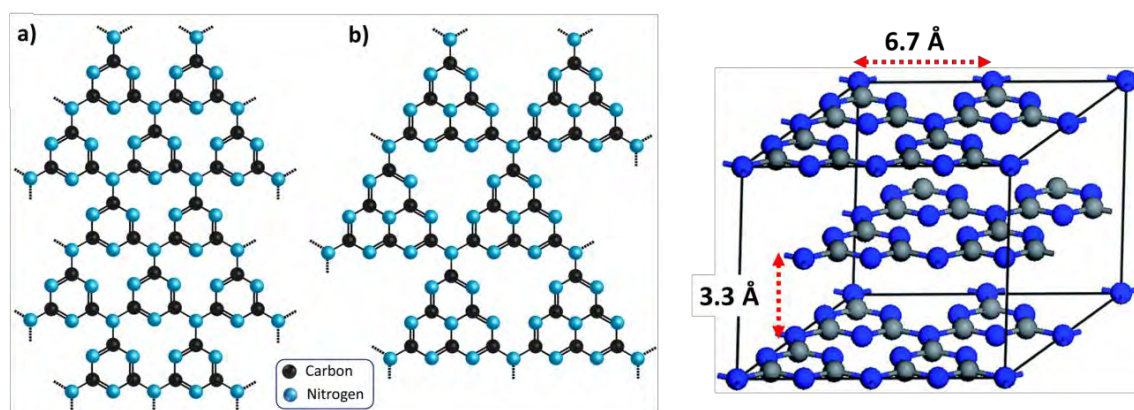


Figure 1.3. a) Triazine and b) polyheptazine-based g-C<sub>3</sub>N<sub>4</sub> allotropes; and c) structural parameters (from XRD) of polyheptazine-based g-C<sub>3</sub>N<sub>4</sub>.

Therefore, it is recognized as the building block for graphitic carbon nitride in many recent works.<sup>45</sup> Structural information can be obtained through crystallographic methods; XRD peaks at  $2\theta = 12.8^\circ$  to  $13.6^\circ$  and the main peak at  $26.8\text{--}27.6^\circ$  are typical of this material. They correspond to the (100) and (002) planes, respectively; with intra-layer and inter-layer d-spacing of 0.680 and of 0.326 nm, respectively (Figure 1.3c).<sup>46</sup> Carbon and nitrogen atoms are *sp*<sup>2</sup> hybridized. The most reactive atoms in these materials are the nitrogen atoms connected to two carbon atoms. Efficient syntheses of: monolayer g-C<sub>3</sub>N<sub>4</sub>

<sup>43</sup> A. Thomas, et al. *Journal of Materials Chemistry* **2008**, 18, 4893-4908.

<sup>44</sup> E. Kroke, et al. *New Journal of Chemistry* **2002**, 26, 508-512.

<sup>45</sup> J. Wang, et al. *Chemistry of Materials* **2017a**, 29, 2694-2707.

<sup>46</sup> F. Fina, et al. *Chemistry of Materials* **2015**, 27, 2612-2618.

2D nanosheet,<sup>47</sup> sub-microspheres of g-C<sub>3</sub>N<sub>4</sub> (surface area of 89 m<sup>2</sup> g<sup>-1</sup>),<sup>48</sup> g-C<sub>3</sub>N<sub>4</sub> mesoporous spheres (surface area of 550 m<sup>2</sup> g<sup>-1</sup>),<sup>49</sup> micro-rods (surface area of 15-60 m<sup>2</sup> g<sup>-1</sup>),<sup>50</sup> mesoporous g-C<sub>3</sub>N<sub>4</sub> (surface area > 150 m<sup>2</sup> g<sup>-1</sup>),<sup>51</sup> have been reported, highlighting the versatility of this material.

Interestingly, Antonietti *et al.*, have reported that in the case of metallic NP on g-C<sub>3</sub>N<sub>4</sub> charge transfer occurs between the metal NP and the semiconductor, altering the electronic properties of both the metal and the semiconductor and in fine the catalytic performances.<sup>52</sup> Thus, the equilibration of the Fermi-levels makes in many cases the metal more electron rich and reductive, while the semiconductor become electron deficient. The possibility to tune the band gap of this material to extend visible light absorption through the introduction of point defects has been investigated. For example, through thermal heating, cyano groups as well as nitrogen vacancies could be introduced into the framework of g-C<sub>3</sub>N<sub>4</sub>.<sup>53</sup> Foreign element atoms in g-C<sub>3</sub>N<sub>4</sub> can occupy either substitutional or interstitial sites. Eleven adsorption sites are possible in the heptazine-based structure: i) five substitutional atomic sites labeled N'<sub>1</sub>, N'<sub>2</sub>, N'<sub>3</sub>, C'<sub>1</sub> and C'<sub>2</sub>; ii) two interstitial sites I<sub>1-2</sub> at the centers of the 6-membered ring and heptazine unit, respectively; and iii) four bonding sites marked as B<sub>1-4</sub> bridging the N<sub>1</sub>-C<sub>1</sub>, C<sub>1</sub>-N<sub>2</sub>, N<sub>2</sub>-C<sub>2</sub> and C<sub>2</sub>-N<sub>3</sub> bonds (Figure 1.4).<sup>54</sup> The site I<sub>2</sub> has the largest binding energy for metal atoms. Other forms of graphitic carbon nitride, although not so in-depth characterized, have been reported. Graphene-like carbon nitride (g-CN) nanotubes have been produced from C<sub>3</sub>N<sub>3</sub>Cl<sub>3</sub> and Na by a simple solvothermal method.<sup>55</sup> This material shows, as graphene, a honeycomb-like structure but with six-membered carbon-nitrogen rings (see Figure 1.5a).<sup>56</sup> The size of the cavities is significantly different for triazine-based g-C<sub>3</sub>N<sub>4</sub> (C<sub>6</sub>N<sub>6</sub> cavity), heptazine-based g-C<sub>3</sub>N<sub>4</sub> (C<sub>9</sub>N<sub>9</sub> cavity) and g-CN (C<sub>12</sub>N<sub>6</sub> cavity). This could have an effect on the adsorption of TM. The adsorption of 3d TM on g-CN (C<sub>12</sub>N<sub>6</sub> cavity), g-C<sub>3</sub>N<sub>4</sub> (C<sub>6</sub>N<sub>6</sub> cavity) and g-C<sub>3</sub>N<sub>4</sub> (C<sub>9</sub>N<sub>9</sub> cavity) has been investigated by DFT.<sup>57</sup> It was found that 3d

<sup>47</sup> Q. Lin, et al. *Applied Catalysis B-Environmental* **2015**, 163, 135-142.

<sup>48</sup> H. Dai, et al. *Diamond and Related Materials* **2013**, 38, 109-117.

<sup>49</sup> Q. Li, et al. *Nano Research* **2010a**, 3, 632-642.

<sup>50</sup> R. C. Pawar, et al. *Scientific Reports* **2016**, 6.

<sup>51</sup> M. Peer, et al. *Chemistry of Materials* **2017**, 29, 1496-1506.

<sup>52</sup> X.-H. Li, et al. *Chemical Society Reviews* **2013**, 42, 6593-6604.

<sup>53</sup> P. Niu, et al. *Nano Energy* **2018**, 44, 73-81.

<sup>54</sup> B. Zhu, et al. *Applied Catalysis B-Environmental* **2018**, 224, 983-999.

<sup>55</sup> H. Li, et al. *Diamond and Related Materials* **2006**, 15, 1593-1600.

<sup>56</sup> K. Srinivasu, et al. *Journal of Physical Chemistry C* **2014**, 118, 26479-26484.

<sup>57</sup> S. Zhang, et al. *Physics Letters A* **2016b**, 380, 1373-1377.



TM stand in the cavities of g-CN sheet while keeping the planar structure of the material (Figure 1.5b and 1.5c, for vanadium and iron atoms).

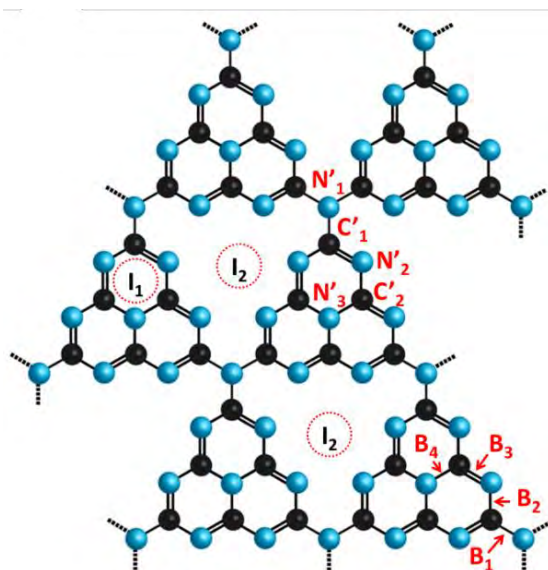


Figure 1.4. Different adsorption sites on heptazine-based  $g\text{-C}_3\text{N}_4$ .

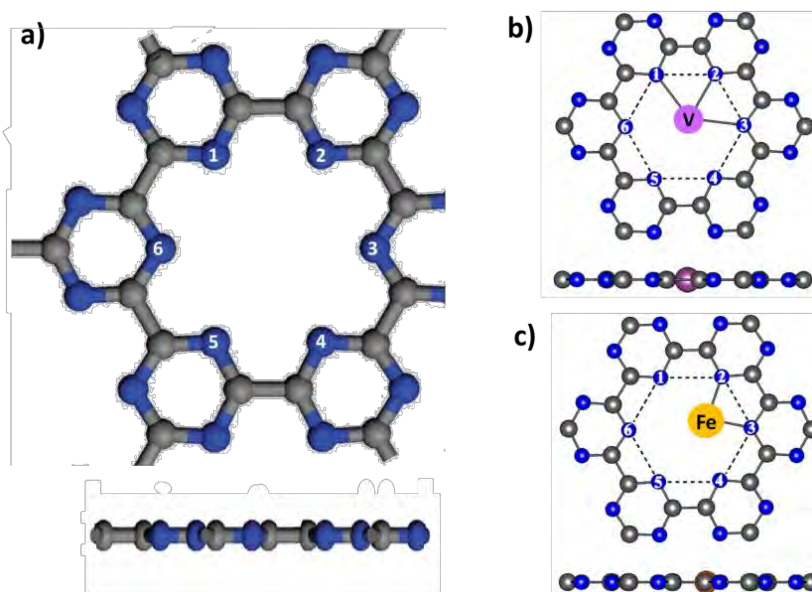


Figure 1.5. a) Structure of graphene-like carbon nitride ( $g\text{-CN}$ ); and b) top and side views of two types of  $\text{TM}@g\text{-CN}$  structures, taking V and Fe for examples, respectively. Color code: nitrogen blue; carbon grey; vanadium violet; and iron orange. From ref. [57].

For  $\text{C}_9\text{N}_9$  and  $\text{C}_6\text{N}_6$  cavities, the planarity increases with the decrease in the metal's atomic number.<sup>58</sup> The calculated metal binding energies for selected 3d TM atoms to triazine-, heptazine-based  $g\text{-C}_3\text{N}_4$  and  $g\text{-CN}$  are reported in Figure 1.6.

<sup>58</sup> D. Ghosh, et al. *Journal of Materials Chemistry C* **2014**, 2, 7943-7951.

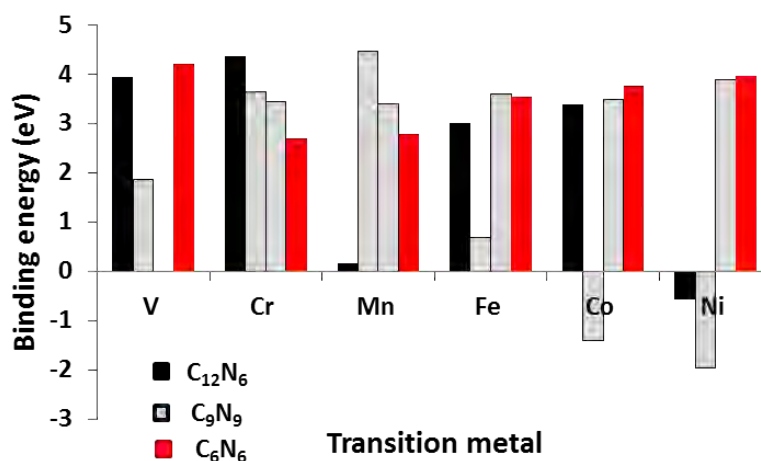


Figure 1.6. The binding energies (eV) of TM atoms adsorbed onto triazine-, heptazine-based  $g\text{-C}_3\text{N}_4$ , and  $g\text{-CN}$ .

From the energetics, it can be observed that in most cases, the binding energies are relatively strong, but some of them are smaller than the corresponding metal cohesive energies. For similar metal atoms, the corresponding binding energies to  $\text{N}_4$  type cavities were reported to be relatively higher (see next section, Figure 1.16b).<sup>59</sup> This can be attributed to the larger size of the  $\text{N}_6$  or  $\text{N}_9$  cavities, where the metal is bonding strongly to the closest nitrogen atoms, with remaining nitrogen atoms located somewhat far from it. Charge transfer from metal  $d$ -states to the  $\pi^*$  states of the support have been evidenced using Bader charge density. As a result of this charge transfer, the occupied anti-bonding states are found to be stabilized and shifted to lower energies. This result highlights the different behavior of SA related to metal NP, for which the charge transfer occurs from the support to the metal.<sup>52</sup>

### 1.2.2. Graphene and carbon nanotubes

These two materials can be composed of a single graphene layer or of few to multilayers. Single layer graphene and single-walled carbon nanotubes (SWCNT) have a strong tendency to stack due to high surface energy, and constitute relatively expensive materials. Consequently, few layer graphene (FLG) and multi-walled carbon nanotubes (MWCNT) are generally preferred as supports for SAC synthesis. These two materials can be produced by catalytic chemical vapor deposition in high yield, and present relatively large surface area.<sup>60</sup> One considering adsorption on defect free pure  $sp^2$  carbon materials (like FLG), the adsorption may basically occur on two types of surfaces:

<sup>59</sup> M. Yang, et al. *Aip Advances* **2015b**, 5, 067136.

<sup>60</sup> R. Philippe, et al. *Chemical Vapor Deposition* **2007**, 13, 447-457.



prismatic (edge), and basal plane surfaces (Figure 1.7a). The graphene edges (if not H-terminated) are the most reactive sites of defect-free materials thanks to the presence of C atoms with unpaired electrons. Two types of sites exist: zigzag sites (carbene-like), and armchair sites (carbyne-like).

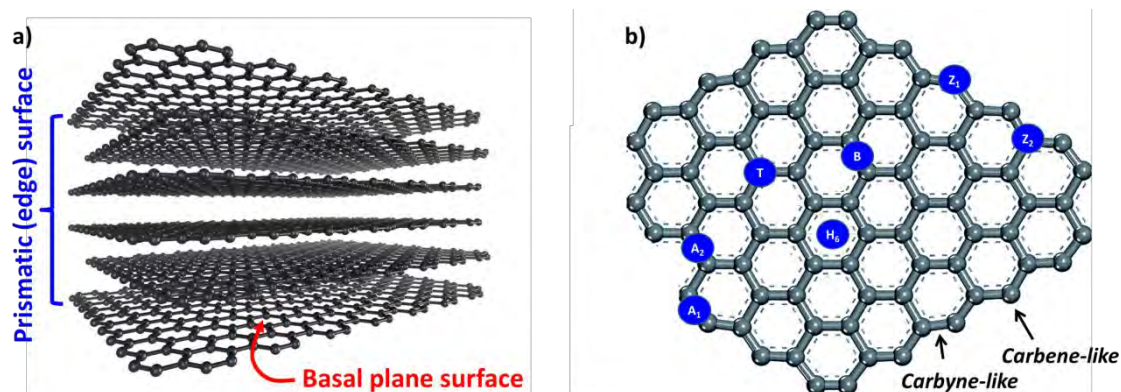


Figure 1.7. a) Basal plane and prismatic surfaces on  $sp^2$  carbon materials; and b) adsorption sites on  $sp^2$  carbon materials: hollow  $H_6$ , bridge B, top T,  $A_1$  and  $A_2$  high symmetry armchair sites, and  $Z_1$  and  $Z_2$  high symmetry zigzag sites.

Even though this correspondence with organic chemistry species (carbene and carbyne) is not very rigorous, the carbon community generally accepts it. The basal plane surface of graphene or CNT is homogeneous and consists in  $sp^2$  C atoms. Except for very small diameter CNT, the curvature of the tubes does not significantly affect the hybridization of these carbon atoms. On the contrary, the edges (prismatic surface) are very heterogeneous and may contain many surface groups, often oxygenated, and here also similarities with organic chemistry can be made: carbonyl, carboxylic acid, phenol... It is important to note that the reactivity of a surface group, even if it approaches that of organic species, is often different due to the presence of the surface, or to the porosity of the material. The ratio basal surface/prismatic surface is an important parameter when we consider adsorption; it can be estimated from NMR<sup>61</sup> or gas adsorption data.<sup>62</sup> The possible adsorption sites on graphene basal plane are top, T-(on top of a carbon atom); bridge, B-(bridging a C–C bond); and hollow,  $H_6$ - (at the center of hexagons) sites (Figure 1.7b).<sup>63</sup> The nature and strength of the adsorption is correlated to carbon hybridization. For small diameter CNT, strain is characterized by pyramidalization and misalignment of

<sup>61</sup> V. A. Likholobov. In *Catalysis by Unique Metal Ion Structures in Solid Matrices: From Science to Application*, edited by G. Centi, et al. (2001), pp. 295-306.

<sup>62</sup> J. P. Olivier, et al. *Journal of Power Sources* 2001, 97-8, 151-155.

<sup>63</sup> K. Nakada, et al. In *Graphene Simulation: InTech*. Rijeka (2011), pp. 3-20.

the  $\pi$ -orbital.<sup>64</sup> Adsorption of an atom or a functional group onto the CNT external surface will release the strain. For classical MWCNT (external diameter around 10 nm) this phenomenon is negligible (very low pyramidalization angle and  $\pi$ -orbital misalignment), and the chemical reactivity approach that of planar graphite.

The convex outer surface of small diameter CNT is chemically more reactive than the concave (inner) surface, since pyramidalized carbon atom arrangement is optimum to form chemical bonds with reactants. Distortions of CNT will accentuate this phenomenon, suggesting that local reactivity can be significantly enhanced. Thus, tube diameter, but also CNT helicity,<sup>65</sup> another parameter that dictated the CNT electronic properties, are expected to affect the adsorption properties of carbon nanotubes. The CNT tips can be open or closed, according to chemical treatments. Although this surface is low compared to the total surface area of the material if CNT have not been cut, it is expected that it will react differently with single atoms, due the presence of reactive pentagons, and edges. Durgun and co-workers carried out a DFT study on the adsorption of 3d TM atoms onto zigzag and armchair SWCNT.<sup>66</sup> The  $H_6$  site was the more reactive for all 3d TM atoms, except nickel and copper atoms, which preferred the B adsorption site. Frapper and co-workers used DFT and molecular orbital analysis to investigate the trends in the adsorption of 3d TM atoms onto graphene and CNT surfaces (Figure 1.8).<sup>34</sup> It is obvious from this figure that the reactivity of the two surfaces for metal atom adsorption is very similar, despite the curvature of SWCNT. On both graphene and SWCNT it is the  $H_6$  sites the most reactive for metal adsorption.

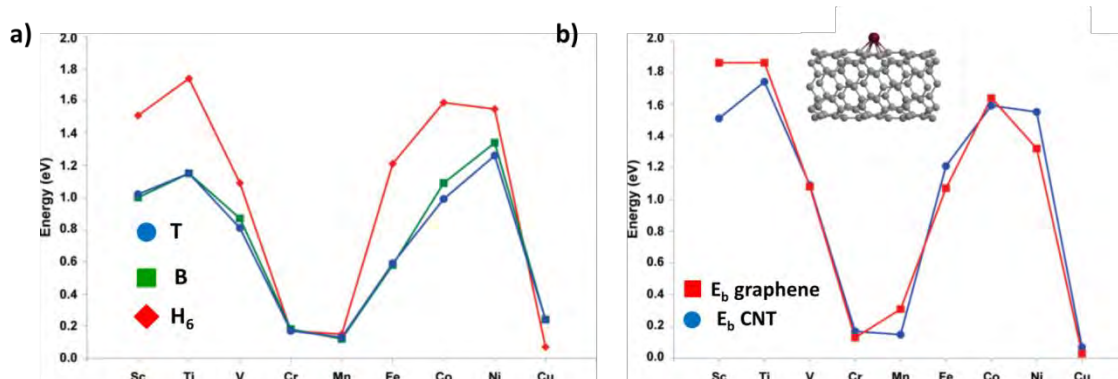


Figure 1.8. a) Binding energies (eV) of 3d TM atom adsorbed onto graphene, considering different possible adsorption sites; and b) binding energies (eV) corresponding to each 3d TM atom adsorbed onto graphene and SWCNT on the  $H_6$  site. From ref. [34].

<sup>64</sup> S. Banerjee, et al. *Advanced Materials* **2005**, 17, 17-29.

<sup>65</sup> O. Gulseren, et al. *Physical Review Letters* **2001**, 87.

<sup>66</sup> E. Durgun, et al. *Physical Review B* **2003**, 67.

The metallic atoms bound mainly covalently, and as expected, the ionicity degrees varied with the electronegativity of the metal atom, with a charge transfer from the metal to the support. With the exception of Cr, Mn, and Cu, the other 3d TM atoms were chemisorbed with an  $\eta^6$  hollow geometry ( $E_b = 1.09$ -1.74 eV). It is the strong hybridization between the  $d_{x^2-y^2}$  and  $d_{yz}$  orbitals of the 3d-TM atoms and the  $p_z$  orbitals of the carbon atoms that constitutes the main contribution to the covalent bonds.<sup>67</sup> Cr and Mn with half-filled atomic orbitals and Cu with its completely filled atomic orbital are only physisorbed on these surfaces. The adsorption binding energy increased as one moved in either direction away from the copper-manganese couple of the series. Sc, Ti, Fe, Co and nickel could be relatively stable as single-atoms on these carbon surfaces. For the other metals an easy surface diffusion and aggregation into particles can be anticipated. We can see however that, as expected, the metal adsorption binding energy on these defect-free surfaces are significantly lower than the ones calculated for graphitic carbon nitride. Systematic DFT studies performed for 3d, 4d, and 5d TM atom adsorption onto the graphene surface has confirmed that TM prefer to stand on the  $H_6$  sites when they are chemisorbed, but on B or T sites when they are physisorbed; which is the case of atoms with half-filled atomic orbitals ( $d^5$ ) and filled atomic orbitals ( $d^{10}$ ).<sup>68</sup> The trends for diffusion energy barriers follow the adsorption energy trends as shown on Figure 1.9.<sup>69</sup> Interestingly, in the case of platinum or aluminum atom adsorption on CNT, a significant curvature effect was reported. For Pt,<sup>70</sup> the adsorption energy was stronger on the outer wall than on the inner ones, and this adsorption energy increases when the tube diameter decreases.

---

<sup>67</sup> X. Liu, et al. *Physical Review B* **2011**, 83.

<sup>68</sup> M. Manadé, et al. *Carbon* **2015**, 95, 525-534.

<sup>69</sup> M. Manadé, et al. *Physical Chemistry Chemical Physics* **2018**, 20, 3819-3830.

<sup>70</sup> G. Chen, et al. *Physical Review B* **2006**, 73.

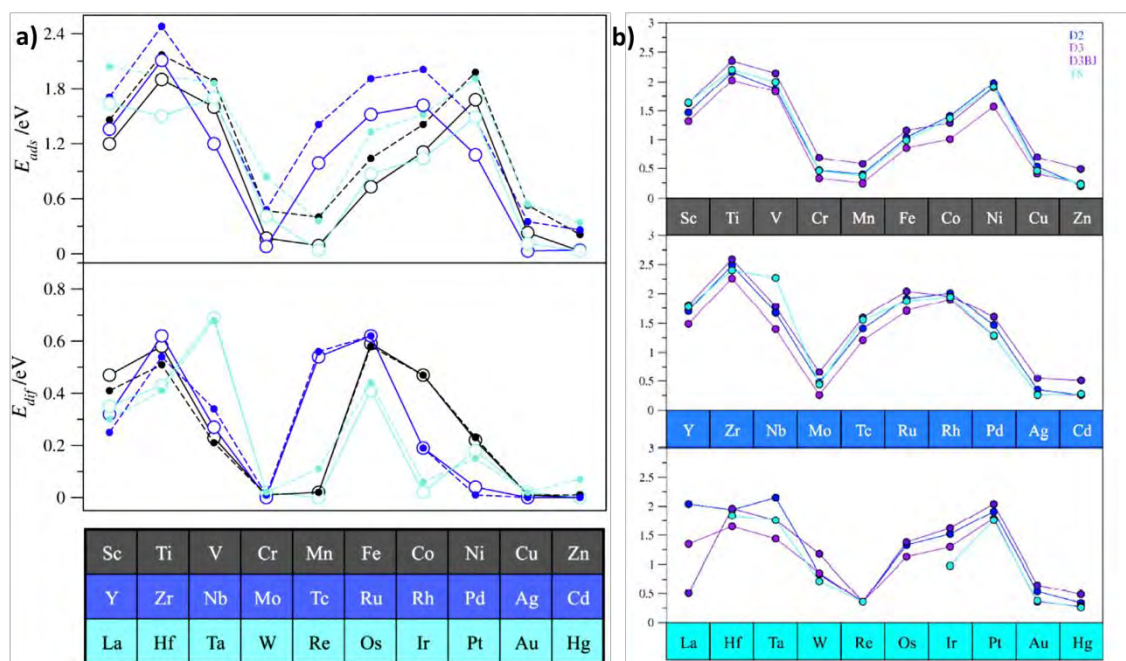


Figure 1.9. a) Adsorption energy ( $E_{ads}$ ) of 3d, 4d, and 5d TM atoms on graphene, as well diffusion energies,  $E_{diff}$ , both in eV. Results obtained with two different functionals: Perdew-Burke-Ernzerhof (PBE) functional (open circles and solid lines) and PBE-D2 dispersion correction (filled circles and dashed lines) DF results. b) Trends along the 3d (upper curve), 4d (middle curve), and 5d (bottom curve) series for the adsorption of TM adatoms on graphene on most stable sites plotted as calculated at PBE level using D2, D3, D3BJ, or TS methods to describe vdW forces. From ref. [69].

The contribution of the edge sites ( $A_1$ ,  $A_2$ ,  $Z_1$  and  $Z_2$ , Figure 1.7b) to TM atom stabilization has been much less studied, although it is an important aspect of SAC stability. The reactivity of the edge sites of graphene and FLG towards 3d TM atom adsorption (Au, Cr, and Al) has been investigated.<sup>71</sup> The contribution of graphene sublayers to the total binding energy was predicted to be significant, although the edge binding energies were found to be substantially higher for all atoms in all cases (Figure 1.10a), and the defect-free regions of the lattice were completely free of single atoms (Figure 1.10b). The activation barriers of adatom migration have been calculated and were found to be small for all adatoms studied, implying high surface mobility. This suggests that these metal adatoms will migrate rapidly onto the graphene surface until they find a stable site, such as the  $A_{1-2}$  and particularly  $Z_{1-2}$  sites, for their binding to the support. The authors confirmed this hypothesis in the case of gold deposition on graphene. Scanning transmission electron microscopy micrographs (Figure 1.10a) showed that Au

<sup>71</sup> T. P. Hardcastle, et al. *Physical Review B* **2013**, 87.

atoms are located exclusively at edge sites, but also in some places contaminated by hydrocarbons, whereas the defect-free regions do not present any metal adatoms.

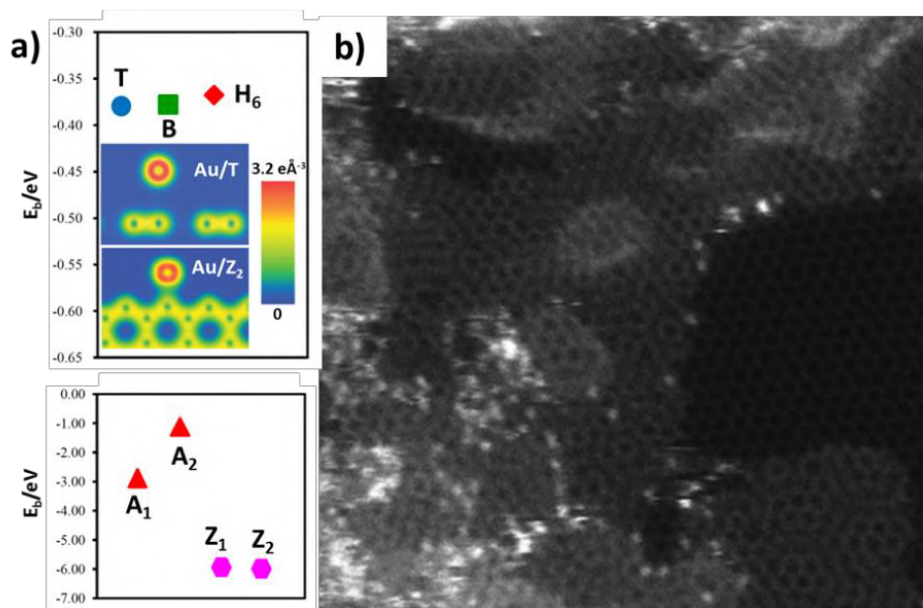


Figure 1.10. a) The calculated binding energy for Au atoms adsorbed on pristine graphene (T, B, and  $H_6$  sites) and bound at monolayer edge sites ( $A_{1-2}$  and  $Z_{1-2}$  sites). The insets are the electron density images showing the difference in bonding character between adsorption and edge sites for Au. b) STEM HAADF images showing monolayer graphene sheet with bilayer and trilayer regions onto which a 5 Å layer of Au was evaporated. Individual Au atoms clearly bind preferentially to edge sites. From ref. [71].

It is thus obvious that the preparation of SAC with these elements on pristine graphene (or CNT) will be limited to very low loading (considering the basal plane/prismatic surface ratio), and that the SA will concentrate on edges. A similar tendency, *i. e.*; a preferred adsorption on edges than on pristine graphene, but also than on vacancies has been reported for iron.<sup>31</sup> Anomalous diffusion at graphene edges was reported both experimentally and theoretically.<sup>72</sup> It is finally worth mentioning that graphene edges in nanostructured carbon materials produced by chemical vapor deposition (often in the presence of dihydrogen either added in the gas phase or arising from hydrocarbon decomposition) should be H-terminated. In that case, the adsorption energy of the TM atom to a H-terminated site will decrease significantly. Thus, for an Fe atom, the binding energy to graphene was measured at 0.96 eV, and at 1.35 eV on a H-terminated zigzag

<sup>72</sup> J. Zhao, et al. *Proceedings of the National Academy of Sciences of the United States of America* **2014**, *111*, 15641-15646.



edge site.<sup>73</sup> This latter value has to be compared to the binding energy of an iron atom to graphene zigzag edge site (5.77 eV).<sup>72</sup>

In order to modify the chemical reactivity of graphene, defects or doping element can be introduced either during its synthesis or by post-treatment. In many materials as in graphene, crystalline defects constitute a very common type of defects.<sup>74</sup> Point defects such as Stone-Wales defect (SW), single vacancy (SV) and multiple vacancies, as well as 1D defects or grain boundaries (that could lead to nanolines of transition metals)<sup>75</sup> are the most common reactive sites (Figure 1.11 and 1.12). These 0D or 1D defects can strongly modify the local electronic structure of the  $sp^2$  carbon materials, and thus significantly change their adsorption properties.

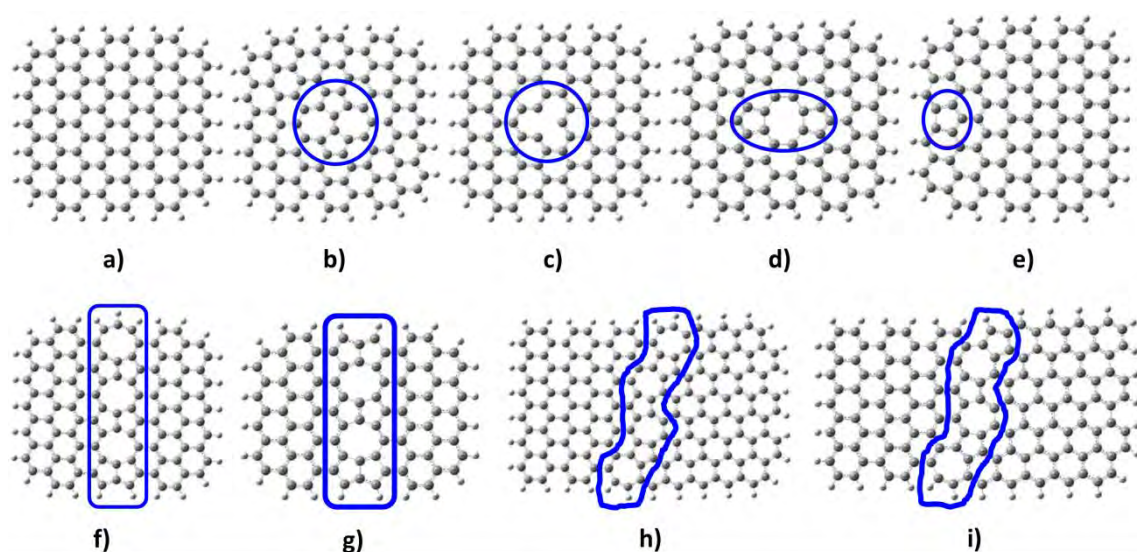


Figure 1.11. Perfect and defective graphene clusters. (a) Perfect graphene cluster, (b) Stone–Wales defect (SW), (c) single vacancy (SV), (d) double vacancies (DV), (e) edge defect with pentagon ring at zigzag edge, octagon and fused pentagon carbon rings line defect with (f) odd number of octagon rings (GLD-558-01) and (g) even number of octagon rings (GLD-558-02), and pentagon-heptagon pairs line defects with (h) odd number of heptagon rings (GLD-57-01) and (i) even number of heptagon rings (GLD-57-02); The larger grey and smaller white balls denote carbon and hydrogen atoms, respectively. From ref. [74].

Among the 0D defects, double vacancy (DV), produced for example by coalescence of two SV are suitable for metal adatom adsorptions. Indeed, adatom adsorption on these sites leads to thermodynamically more favorable situations. In addition, these 0D defects are stable up to relatively high temperatures. The DV (Figure 1.12b) can reorganize upon

<sup>73</sup> Y.-E. Yang, et al. *Chinese Physics B* **2015a**, 24, 117204.

<sup>74</sup> L. Zhang, et al. *Physical Chemistry Chemical Physics* **2015**, 17, 16733-16743.

<sup>75</sup> F. D. C. de Lima, et al. *Materials Chemistry and Physics* **2017**, 194, 118-127.

heating to produce three different configurations: i) a DV(5-8-5) that contains two pentagons and one octagon (Figure 1.12d); ii) a DV(555-777) that contains three pentagons and three heptagons (Figure 1.12e); and iii) a DV(5555-6-7777) that contains four pentagons, one hexagon and four heptagons (Figure 1.12f). Among these configurations, the DV(555-777) is the most stable structure.<sup>76</sup>

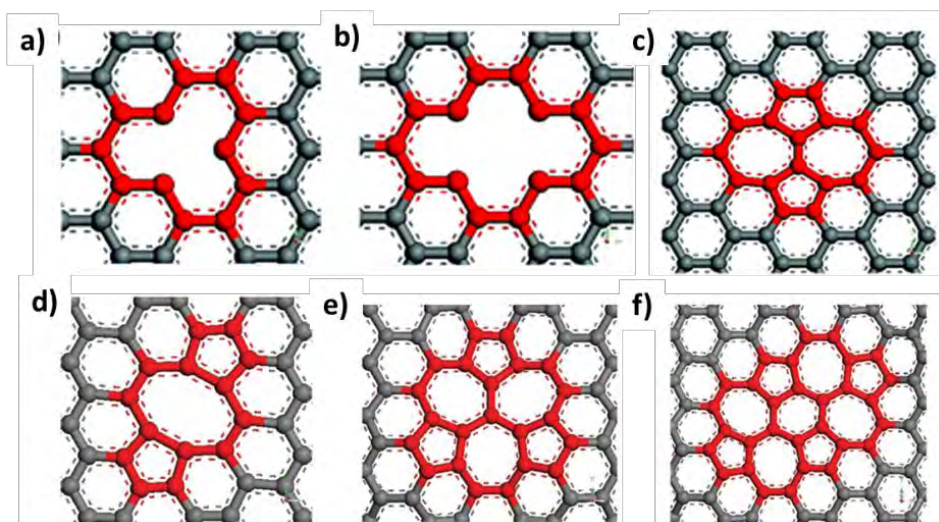


Figure 1.12. Schematic defects in graphene sheets: (a) single vacancy defect; (b) double vacancy defect; (c) Stone–Wales defect SW (55–77); (d) double vacancy DV(5-8-5); (e) DV(555-777); and (f) DV(5555-6-7777). From ref. [77].

Modelling studies based on DFT of TM atoms adsorbed on graphene vacancies have demonstrated that metal atoms show a high affinity to these adsorption sites compared to defect-free graphene surface.<sup>78</sup> The typical atomic configurations of TM-SV/DV complexes are shown in Figure 1.13, together with the example for an iron atom.<sup>79</sup> As the atomic radii of TM are larger than that of carbon, the metal adatoms are usually located above the graphene plane; this phenomenon is more pronounced on SV (Figure 1.13a) than on DV (Figure 1.13b). The binding energies for such complexes ranged between 2 and 8 eV, according to the systems, showing a strong bonding and pointing to the possible use of such species as SAC. The effect of vacancy on metal binding is, in fact, very similar to that observed for pyridine-like nitrogen doped graphene consisting in one carbon vacancy with three neighboring carbon atoms replaced by nitrogen.<sup>80</sup>

<sup>76</sup> F. Banhart, et al. *Acs Nano* **2011**, 5, 26-41.

<sup>77</sup> N. Jing, et al. *Rsc Advances* **2012**, 2, 9124-9129.

<sup>78</sup> A. Bhattacharya, et al. *Journal of Physical Chemistry C* **2010**, 114, 10297-10301.

<sup>79</sup> Z. He, et al. *Nano Letters* **2014b**, 14, 3766-3772.

<sup>80</sup> G. Kim, et al. *Applied Physics Letters* **2009a**, 94.

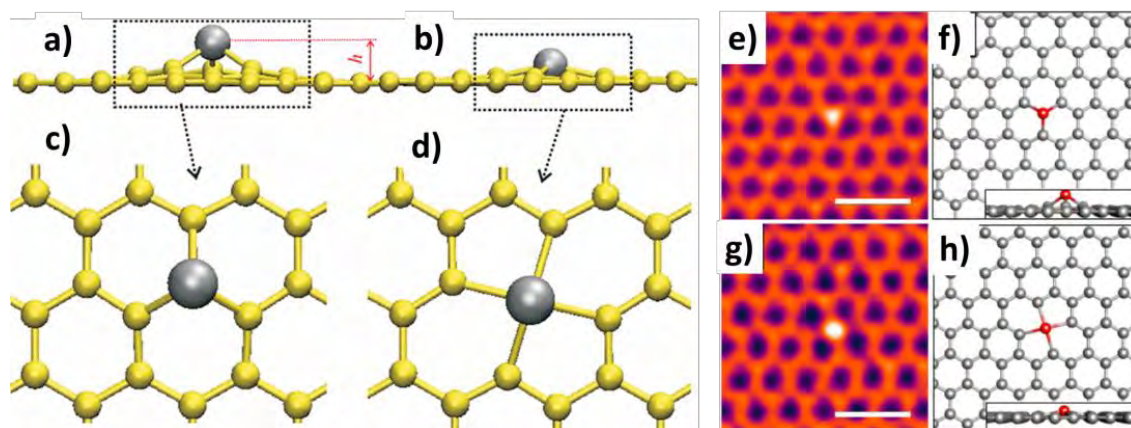


Figure 1.13. Typical atomic configurations of TM atoms adsorbed on SV and DV in a graphene sheet. Metal atom on a SV: Side view (a), top view (c). Note that the metal atom is above the surface, with an elevation  $h$  of up to 2 Å. Metal atom on a DV: Side view (b) and top view (d). The grey balls are metal atoms, the yellow balls carbon atoms. e)–h) Single Fe atoms in graphene vacancies. (e) Smoothed ACTEM images of single Fe atoms in (e) monovacancy and (g) divacancy sites shown in false colour. (f,h) DFT optimized atomic models corresponding to (e,g). From ref. [79].

Binding energies of selected 3d TM adsorbed on defect-free graphene as well as on SV are shown on Figure 1.14. The binding energies of 3d TM adatoms placed on the  $H_6$  site of a defect-free graphene sheet ranged between 1 and 1.4 eV, which is much lower than the corresponding cohesive energies of the 3d TM atoms: this should favor clustering. The much higher binding energies obtained in the case of a SV should allow SAC stabilization and limit the clustering on the surface. Finally, the adsorption of all of the elements of the periodic table up to an atomic number of 86 at the SV of a graphene sheet has also been analyzed by DFT.<sup>81</sup> For the large majority of the elements, strong binding energies (2–13 eV) with the SV site were found. Physisorptions were seen only and as expected for the elements of groups with filled atomic orbitals ( $d^{10}$  and  $p^6$ ) such as the noble gases. A correlation between the cohesive energies of the pure elements and their adsorption energies on the SV was observed. Indeed, these two values can be correlated to the tendency of these atoms to dissolve from the graphene SV.

<sup>81</sup> I. A. Pasti, et al. *Physical Chemistry Chemical Physics* **2018**, 20, 858–865.



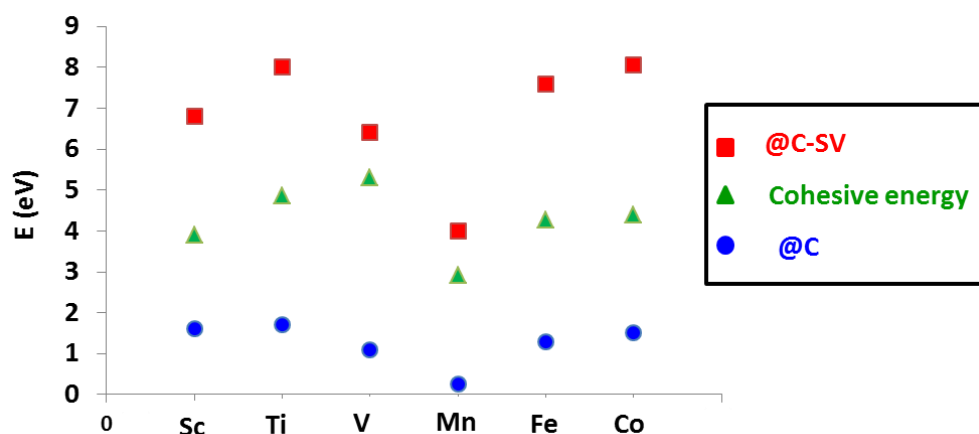


Figure 1.14. Binding energies of 3d TM atoms located: (i) at a  $H_6$  site of a graphene sheet (blue diamond); and (ii) on SV of a defected graphene sheet (red square). The cohesive energies of the respective 3d TM atoms are also shown (green triangle).

Beside these intrinsic structural defects, substitutional defects, such as heteroatoms introduced by doping are also attractive for TM immobilization on graphene or CNT surfaces.

For SAC preparation, nitrogen doping has been particularly studied due to the availability of a wide range of nitrogen-doped carbons, and to both Brønsted and Lewis basicity of these materials caused by nitrogen-doping.<sup>82</sup> As shown in Figure 1.15, it exists three different ways to bond a nitrogen atom in a graphene layer: pyridinic N, graphitic N, or pyrrolic N. Thermodynamically, the N pyrrolic doping is less stable compared to the doping of N graphitic and N pyridinic. The bonding orbitals in the graphitic N, and pyrrolic N groups have higher  $p$  orbital contributions than the pyridinic N groups. Two-fold coordinated pyridinic N atoms can be present either in vacancies ( $N_0$  type) or at the edges ( $N_1$  type) of graphene layers. In such structures, the C–N bond length is between 1.35–1.38 Å, and it has been shown that these groups, and particularly the  $N_0$  type, show strong Brønsted and Lewis basicity.<sup>83</sup> N pyrrolic atoms are incorporated into 5-membered heterocyclic rings; the C–N bond length is between 1.42–1.44 Å. Three-fold coordinated graphitic nitrogen (or quaternary nitrogen) refers to N atom that substitute a carbon atom in the graphene layer. In these structures, the nitrogen has the lowest basicity.

<sup>82</sup> S. Zhou, et al. *Accounts of Chemical Research* **2014**, 47, 3331–3339.

<sup>83</sup> B. Li, et al. *Physical Chemistry Chemical Physics* **2015**, 17, 6691–6694.

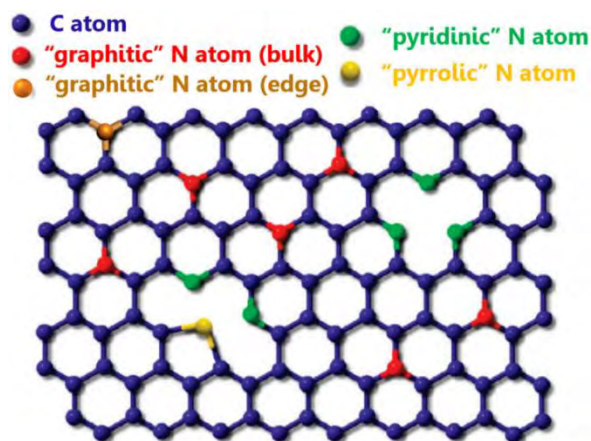


Figure 1.15. Schematic representation of different types of N atoms (graphitic, pyridinic and pyrrolic N) in nitrogen-doped FLG and CNT. Reproduced with permission from ref. [84].

Thus, the N-doping contribute to the tuning of the local density of state around the Fermi level of the material. This may play a pivotal role in tuning the electronic and adsorption properties. In fact, DFT calculations have clearly demonstrate that CNT or FLG N-doping not only allows a strong interaction between metal adatoms and the support, but also impact the electronic structures of the immobilized atoms, which provide a promising approach for optimizing SAC.<sup>85</sup> The structural stability of 3d TM adatoms embedded in N-doped graphene with N graphitic, N pyridinic and N pyrrolic atoms, has been investigated by DFT calculations.<sup>86,87</sup> The TM adatoms forming a 4 N-centered structure (TM-N<sub>4</sub>V<sub>2</sub>, Figure 1.16a) shows the strongest binding, with binding energies of more than 7 eV (Figure 1.16b).

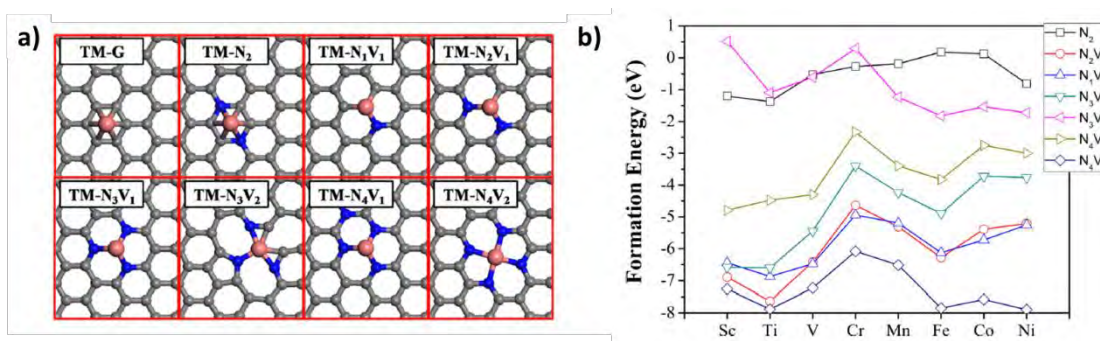


Figure 1.16. (a) Optimized configurations and (b) formation energies for TM atoms embedded into different types of N-doped graphene. From ref. [59].

<sup>84</sup> Q. Wei, et al. *Catalysts* **2015**, 5, 1574-1602.

<sup>85</sup> T. Granzier-Nakajima, et al. *Nanomaterials* **2019**, 9, 425.

<sup>86</sup> G. Q. Zhu, et al. *Physical Chemistry Chemical Physics* **2019**, 21, 12826-12836.

<sup>87</sup> M. D. Esrafil, et al. *Applied Surface Science* **2019**, 475, 363-371.

### 1.2.3. Graphene oxide

Graphene oxide (GO) is a complex material, and elucidating its structure is crucial to achieve control over its use as SA support. GO is a nonstoichiometric material with a lamellar structure, and its physico-chemical properties depend critically on synthesis procedures and post-synthesis treatments. GO is usually prepared by exfoliation of graphite with strong oxidants under acidic conditions. This highly exothermic (and potentially dangerous) reaction results in the formation of functional groups such as alcohols, epoxides, and carboxylic acids (Figure 1.17a).

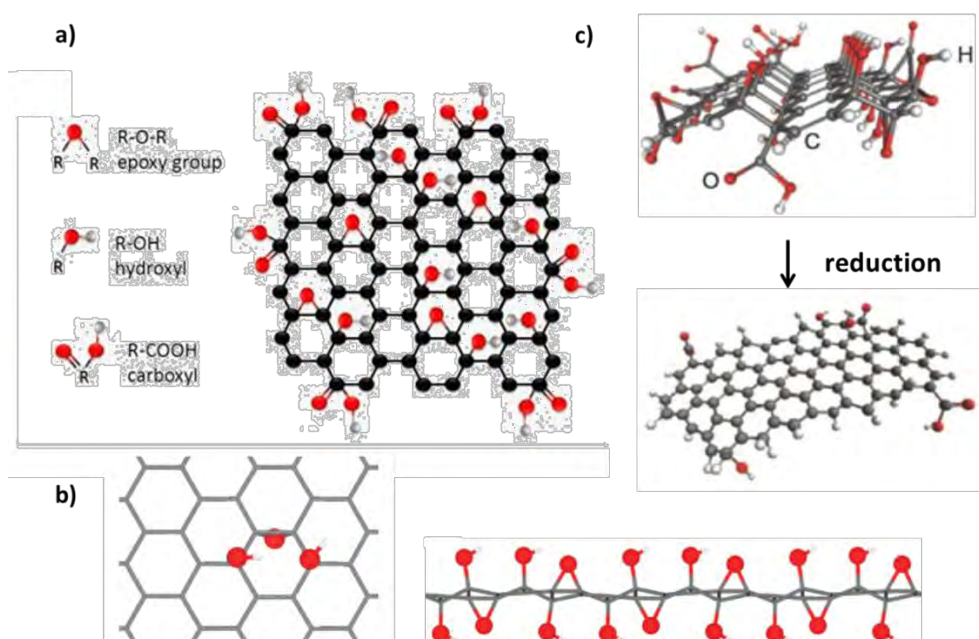


Figure 1.17. (a) Representation of GO structure; (b) one of the most stable structure computed for GO and GO model side view along the armchair direction; and (c) 3D molecular models of GO and r-GO. From ref. [91].

The oxidation level varied with the method of preparation, graphite precursor and reaction conditions. Different GO structural models have been proposed in the literature.<sup>88</sup> A common point of these models is the presence hydroxyl (-OH) and 1,2-ethers (epoxy) groups as basic functional groups on both sides of the GO sheet (Figure 1.17b). Even if the O/C ratio depends much on the oxidation processes, a C/O ratio of 1.5 fits well with many commercial products.<sup>89</sup> It has been found that the epoxide groups stay close to the -OH, but on the opposite sides of the graphene layer.

<sup>88</sup> M. Yang, et al. *Journal of Physical Chemistry C* **2012**, 116, 22336-22340.

<sup>89</sup> H. Luo, et al. *Journal of Applied Physics* **2017**, 122.

The reduction of GO is particularly studied since it can contribute to the restoration of graphene structure and properties. Different reduction procedures exist, resulting in different reduced GO (r-GO) presenting different properties, which in turn affect the final performance of r-GO.<sup>90</sup> 3D molecular models of GO and r-GO and DFT calculations have shown that the removal of the -OH and -COOH groups by a reductive treatment restores a planar structure (Figure 1.17c).<sup>91</sup>

There are relatively few theoretical studies dealing with adsorption of metals (or other elements) on GO or r-GO.<sup>92</sup> On GO supports the binding energy reported are higher than the one obtained on defect-free graphene. For example, for a single titanium atom, the binding energy are: 1.38 eV for Ti on graphene, 2.65 eV for Ti on a Stone Wales defect, 3.53 eV for Ti on a 555–777 defective graphene, 7.95 eV for Ti on a 585 defective structure,<sup>93</sup> and 4.98 eV for Ti on GO.<sup>94</sup> The adsorption of iron atom on GO has been studied by DFT.<sup>95</sup> Four adsorption sites have been investigated (Figure 1.18a), among them site **1** gives the more stable situation (7.07 eV, Figure 1.18b). The process for iron anchoring on **1** requires the removal of a dihydrogen molecule. The entire process of hydrogen formation was investigated, and it was found to be barrierless. The relatively high energy barrier (3.27 eV) for the Fe atom migration from **1** to the neighboring “O–O bridge” suggests the absence of metal clustering issues, and evidences the remarkable stability of such system. This high bonding energy can be compared to the ones of Fe atom on defect-free graphene ( $\approx 0.8$  eV),<sup>96</sup> or on graphene SV (7.4 eV) or DV (6.2 eV).<sup>37</sup>

---

<sup>90</sup> S. Pei, et al. *Carbon* **2012**, 50, 3210-3228.

<sup>91</sup> V. C. Tung, et al. *Nature Nanotechnology* **2009**, 4, 25-29.

<sup>92</sup> A. S. Dobrota, et al. *Electrochimica Acta* **2015**, 176, 1092-1099.

<sup>93</sup> R. Lotfi, et al. *Physica E-Low-Dimensional Systems & Nanostructures* **2014**, 60, 104-111.

<sup>94</sup> L. Wang, et al. *Acs Nano* **2009a**, 3, 2995-3000.

<sup>95</sup> F. Li, et al. *Journal of Physical Chemistry C* **2012**, 116, 2507-2514.

<sup>96</sup> N. Dimakis, et al. *Applied Surface Science* **2015**, 334, 2-6.

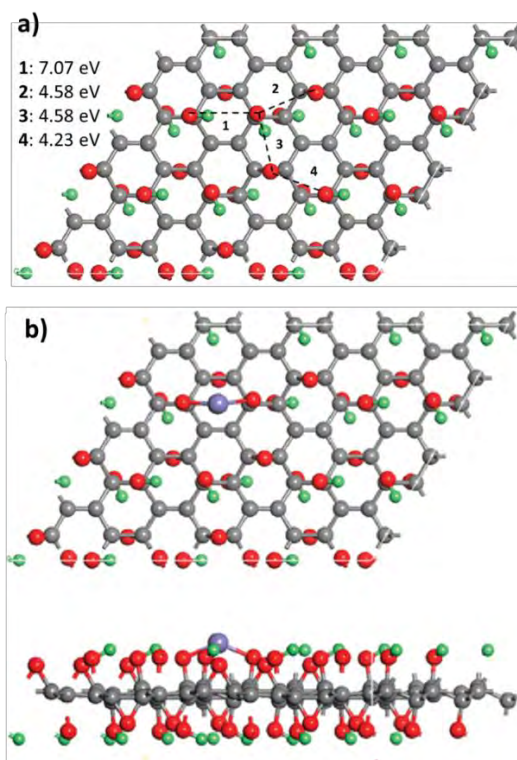


Figure 1.18. (a) Four possible sites depicted by the dashed lines for anchoring Fe atom on GO, where the Fe atom is bonded to the oxygen atoms; and (b) top (upper) and side (lower) views of the most stable Fe–GO structure. Color scheme: Fe, purple; C, grey; H, green; O, red. From ref. [95].

#### 1.2.4. Fullerenes

In metallofullerenes the metallic atoms can be either trapped inside (endohedral metallofullerenes)<sup>97</sup> or bound outside (exohedral metallofullerenes)<sup>98</sup> the fullerene cage, without destruction of the cage. The introduction of the metal atom changes the electronic properties of C<sub>60</sub> fullerene, with the work function of the material being higher than that of the pure C<sub>60</sub>. These metallofullerenes show a high chemical reactivity because of their much smaller HOMO-LUMO gaps. Stable substitutionally doped fullerenes or heterofullerenes constitute another type of compounds, in which one of the carbon atoms from the cage has been replaced by a doping atom.<sup>99</sup> These kinds of compounds can be seen as SAC, and have already found potential applications in catalysis.<sup>100</sup> In spite of a high symmetry, C<sub>60</sub> fullerene presents different adsorption sites for single atom adsorption (Figure 1.19).<sup>101</sup>

<sup>97</sup> H. Cong, et al. *Coordination Chemistry Reviews* **2013**, 257, 2880-2898.

<sup>98</sup> H. Shinohara *Reports on Progress in Physics* **2000**, 63, 843-892.

<sup>99</sup> C. G. Ding, et al. *Journal of Chemical Physics* **1999**, 111, 8481-8485.

<sup>100</sup> T. He, et al. *Journal of Catalysis* **2017**, 354, 231-235.

<sup>101</sup> D. Soto, et al. *Molecules* **2012**, 17, 7151-7168.



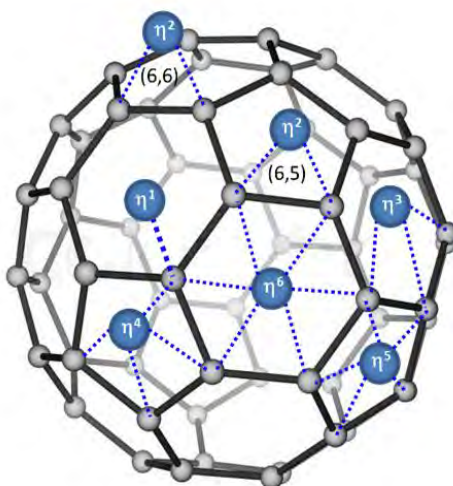


Figure 1.19. Most common adsorption sites on  $C_{60}$  fullerenes.

Six different coordination modes have been reported:

- the  $\eta^1$  hapticity with suspected  $\sigma$  bond, in which the metal atom is directly bounded above any carbon atom;
- the  $\eta^2$  hapticity; involving either two 6-membered rings (6,6) or one 6-membered ring and one 5-membered ring (6,5), the  $\eta^2$  (6,5) being not common;
- the  $\eta^3$  hapticity, in which the metal linked to three carbon atoms on either a 6- or 5-membered rings;
- the  $\eta^4$  hapticity, for which the metal atom linked to four carbon atoms;
- the  $\eta^5$  hapticity, in which the metal is directly bounded to a 5-membered ring; and
- the  $\eta^6$  hapticity, in which the metal is directly bounded to a 6-membered ring.

Even if some examples of other hapticities exist, the great majority of exohedral metallofullerenes generally present  $\eta^2$ ,  $\eta^5$  or  $\eta^6$  hapticities. The fullerene family can be classified in the group of the non-planar conjugated systems. In  $C_{60}$ , and due to the curvature, the hybridization at each carbon atom is not pure  $sp^2$  but  $sp^{2.3}$ . As hybridization depends on curvature, the hybridization in fullerene is not fixed but changes depending on the fullerene diameter, and thus on the number of carbon atoms in the molecule. Few data are available on the adsorption energies of TM on  $C_{60}$ , and some of them differ largely for a single metal (see the case of Ni on Figure 1.20, which shows the adsorption energy of various TM on  $C_{60}$ ).<sup>102</sup> For  $Mn_1@C_{60}$   $\eta^6$  hapticity leads to the most stable situation, whereas for  $Co_{SA}@C_{60}$  both  $\eta^6$  and  $\eta^5$  hapticity coexist. For  $Pd_{SA}@C_{60}$  the  $\eta^2$  hapticity was preferred. The structural and electronic properties of exohedral

<sup>102</sup> R. E. Estrada-Salas, et al. *Journal of Molecular Structure-Theochem* **2008**, 869, 1-5.

metallofullerenes with TM of group 9 and 10 have been investigated by DFT.<sup>103</sup> Adsorption of metal atom on C<sub>60</sub> results in elongated C–C bonds at the coordination. The electron-rich metals lower the electron affinity of C<sub>60</sub>, and the electron excess is mainly located on the carbon atoms engaged in the bonding with the metal.

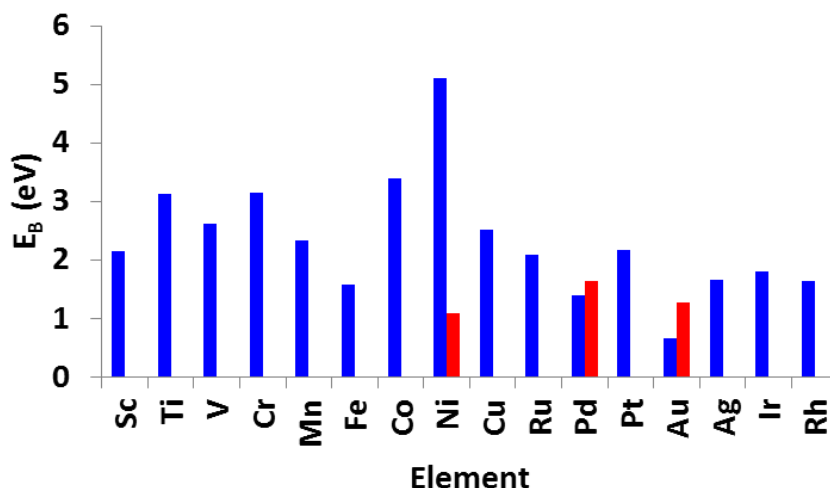


Figure 1.20. Adsorption energies for TM atoms adsorbed on C<sub>60</sub>.

DFT was used to study the adsorption of 3d TM on C<sub>60</sub> fullerene.<sup>104</sup> For Sc, Ti, Co, Ni, Cu and Zn the  $\eta^2$  (6,6) hapticity lead to the more stable structure; while the  $\eta^6$  hapticity was preferred for V, Cr, Mn, and Fe. The stronger adsorption energy was for Ni (5.11 eV), followed by Co (3.40 eV), Cr (3.15 eV). For the other elements, the order is: Ti (3.12 eV) > V (2.61 eV) > Cu (2.52 eV) > Mn (2.34 eV) > Sc (2.15 eV) > Fe (1.58 eV) > Zn (1.53 eV). In these structures, the positive charges on the transition metal atoms and the negative charges on the C atoms engaged in the TM–C bond ensure charge transfer from the TM to the C<sub>60</sub> fullerene. For Ti, it was shown that if two atoms are present, they will prefer to cluster than to stay isolated on the C<sub>60</sub> cage.<sup>105</sup> DFT was also used to study the adsorption of 3d TM (Ti, Cr, Fe, Ni, and Zn) on a N<sub>4</sub> cavity doped C<sub>60</sub> fullerene (C<sub>54</sub>N<sub>4</sub>).<sup>106</sup> All the adsorption energies are very large as compared to the corresponding TM metal cohesive energies so that the problem of TM aggregation is expected to be overcome, and the TM@C<sub>54</sub>N<sub>4</sub> should result in stable SAC.

<sup>103</sup> O. Loboda *Fullerenes Nanotubes and Carbon Nanostructures* **2009**, 17, 457-475.

<sup>104</sup> A. M. El Mahdy *Applied Surface Science* **2016**, 383, 353-366.

<sup>105</sup> Q. Sun, et al. *Journal of the American Chemical Society* **2005**, 127, 14582-14583.

<sup>106</sup> A. Hosseini, et al. *Physica E: Low-dimensional Systems and Nanostructures* **2019**, 110, 5-9.

## 1.2.5. Graphyne and graphdiyne

The honeycomb structures of graphyne (GY) and graphdiyne (GDY), two 2D carbon allotropes of graphene, is shown in Figures 1.21a-b.

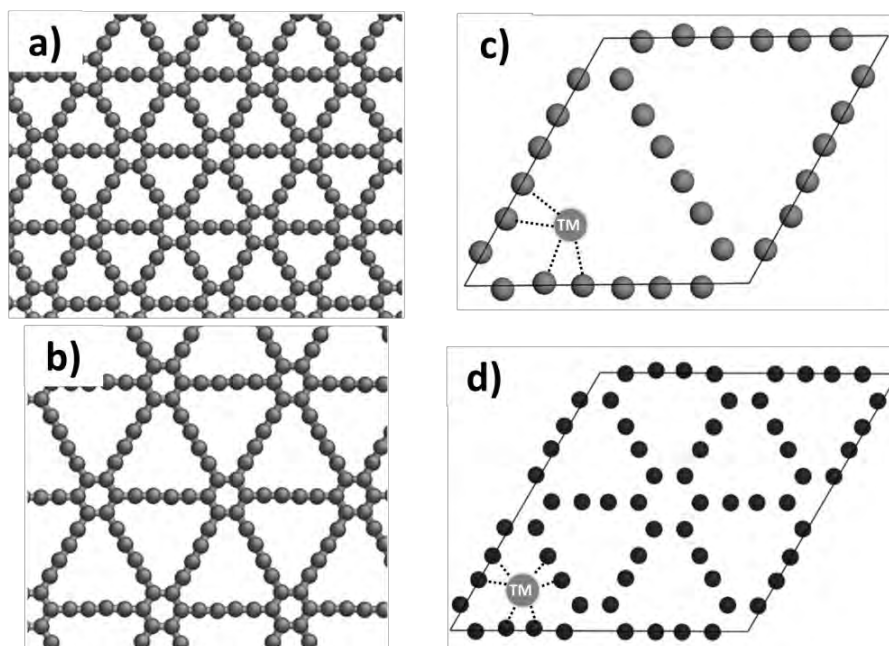


Figure 1.21. Structure of: (a) graphyne and (b) graphdiyne; and (c) and (d) most favorable adsorption site for 3d TM on GY and GDY. From ref. [112].

The carbon bonds that connected aromatic  $C_6$  rings in graphdiyne are triple and single bonds that form an acetylene link. Thus, GY is made up of  $C_6$  rings and acetylene bridges, and GDY consists of  $C_6$  rings and butadiyne bridges.<sup>107</sup> The potential application of such material (particularly GDY) in catalysis has already been reported.<sup>108</sup> Their use as support for SAC could be of interest because of their structure presenting cavities and a well-defined environment that can host metal SA. Some theoretical works have reported the interaction of single TM atoms absorbed on GY or GDY.<sup>109,110,111</sup> Figures 1.21c,d display the most favorable adsorption site for six 3d TM (V, Cr, Mn, Fe, Co and Ni) on both GY and GDY.<sup>112</sup> In the case of iron, the adsorption energy was calculated to be  $-4.52$  eV, whereas it was  $-5.26$  eV in the case of Co and Ni decorated systems.<sup>113</sup> These binding energies are significantly higher than the one obtained on graphene, and higher than the cohesive energies of the corresponding metals.

<sup>107</sup> Q. Peng, et al. *Nanotechnology Science and Applications* **2014**, 7, 1-29.

<sup>108</sup> R. Liu, et al. *Nanoscale* **2014**, 6, 11336-11343.

<sup>109</sup> P. Wu, et al. *Physical Chemistry Chemical Physics* **2015a**, 17, 1441-1449.

<sup>110</sup> Z.-Z. Lin *Carbon* **2016**, 108, 343-350.

<sup>111</sup> A. Seif, et al. *Physical Chemistry Chemical Physics* **2017**, 19, 19094-19102.

<sup>112</sup> J. He, et al. *Journal of Physical Chemistry C* **2012**, 116, 26313-26321.

<sup>113</sup> K. Srinivasu, et al. *Journal of Physical Chemistry C* **2013**, 117, 26021-26028.



### 1.2.6. Material perspectives

It is important to note that most of the results presented in the previous sections are relying on DFT calculations. Standard functionals in DFT poorly capture dispersive interactions, which participate in long-range interactions and can influence the bonding character. Additionally, many studies are dealing with single layer materials (for example graphene), and few studies are available for multi-layered materials. In the case of graphene, few-layer graphene and highly oriented pyrolytic graphite, some differences may exist in the adsorption energy values of TM.<sup>114</sup> It is thus important to take the given data as a guideline of TM adsorption. This overview of the different carbon (nano)materials that can be used for SA stabilization allows us to draw some conclusions concerning the rational choice of a carbon support for SA stabilization.

The use of defect free  $sp^2$  carbon materials do not allow to stabilize SA sufficiently, since the TM-carbon interactions are weak compared to the cohesive energy of the bulk metal or of metal NP. The use of  $C_{60}$ -fullerene, thanks to pyramidalization and  $\pi$ -orbital misalignment, allows reaching higher adsorption energy for single metal atoms. The presence of crystalline defects or heteroatoms in  $sp^2$  carbon materials allows reaching high adsorption energy for metal adatoms. In order to have a more precise view of TM adsorption on carbon materials, we have concentrated our analysis on three elements presenting low, medium and high adsorption energy on defect free graphene: Au, Fe, and Pt, respectively. The Figure 1.22 shows the adsorption energy of these three elements on the different types of adsorption sites potentially present in these materials. This figure has been drawn from data collected in more than 50 scientific publications. In the case of defect-free graphene, the variations in adsorption energy observed for a given metal are linked to the use of different functionals or to the size of the models. The mean adsorption energy is 0.45 eV for gold, 1.75 eV for platinum, and 1.05 eV for iron. If we compare this value to the cohesive energy of the metal for a nanoparticle of 5 nm (dotted lines in the figures), it is obvious that SAC should not be obtained on this surface, particularly if we considered the low diffusion energy of these metals on defect-free graphene (0.028 eV for Au,<sup>115</sup> 0.14 eV for Pt,<sup>116</sup> and 0.8 eV for Fe<sup>35</sup>). The presence of defects or edges on the carbon surface allows to significantly increase the adsorption energy for single TM atoms. Vacancies, either SV, DV or even triple vacancies (TV) are particularly reactive. Indeed,

---

<sup>114</sup> V. Sessi, et al. *New Journal of Physics* **2014**, 16.

<sup>115</sup> W. H. Brito, et al. *Physical Review B* **2010**, 82.

<sup>116</sup> K. J. Kong, et al. *Materials Science & Engineering C-Biomimetic and Supramolecular Systems* **2006**, 26, 1207-1210.

when one or multiple carbon atoms are removed from the graphene network, the created dangling bonds represent areas of greater chemical reactivity. For the three metals investigated, the presence of SV and/or DV is enough to stabilize SA, since the adsorption energy for single TM atoms is significantly higher than the cohesive energy<sup>117</sup> of the TM in NP of 5 nm.

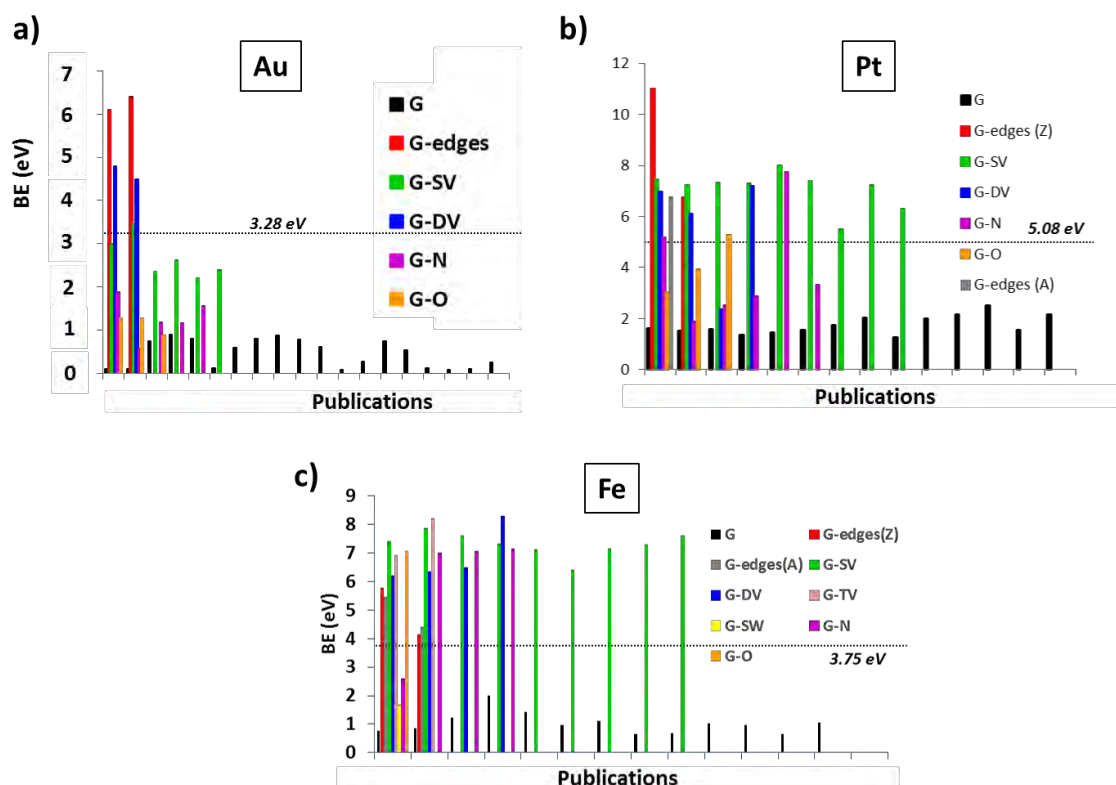


Figure 1.22. Adsorption energy of (a) gold; (b) platinum; and (c) iron on various sites of a graphene layer (black: defect free graphene surface; green: single vacancy; blue: double vacancy; pink: triple vacancy; red: graphene edges (zigzag type); grey: graphene edges (armchair type); yellow: Stone Wales defect; magenta: nitrogen doped graphene; orange: graphene oxide). The dotted line corresponds to the cohesive energy of the metal for a particle of 5 nm.

However, the presence of such vacancies in the carbon materials is questionable. Indeed, they have most of the time been prepared in the presence of hydrogen, which should lead to H-terminated vacancies of much lower (if any) reactivity.<sup>118</sup> A dissociation barrier of 1.1 eV has been reported for H<sub>2</sub> on the SV of graphite.<sup>119</sup> A similar reactivity is expected to occur at graphene/graphite edges, since a dissociation barrier of 0.5 eV has been

<sup>117</sup> S. S. Batsanov, et al. *Materials Chemistry and Physics* **2017**, 196, 245-248.

<sup>118</sup> R. Nieman, et al. *Chemical Physics* **2017**, 482, 346-354.

<sup>119</sup> A. Allouche, et al. *Carbon* **2006**, 44, 3320-3327.

reported for H<sub>2</sub> on armchair type edges of graphite,<sup>120</sup> and the reaction on zigzag type edges is barrierless.<sup>121</sup> The atomic hydrogen adsorption energies are larger on the vacancy than on the edges. Production process of non-functionalized graphene edges have been reported, but they involved specific growth condition, such as sputtering in vacuum.<sup>122</sup> If produced, these highly reactive sites will allow the preparation of stable SAC. A competition between SA and hydrogen to saturate graphene vacancies can also occur during post-synthesis treatments, like reduction or during catalysis in the presence of H<sub>2</sub>.<sup>123</sup> If produced, these highly reactive sites are also able to easily react with small atmospheric molecules such as water or oxygen; in that case the vacancies (or edges) will be O-terminated.<sup>124</sup> Water and oxygen dissociate on SV with respective barriers of 1.6 and 0.2 eV, respectively.<sup>119</sup> The interaction of SA with O-terminated edges or vacancies could be relatively high, depending on the metal and on the type of oxygen functional groups created. Nevertheless, the force of the TM–O bond created is lower than the M–C bond in a vacancy.<sup>125</sup>

As the incorporation of heteroelement such as oxygen, nitrogen, boron,<sup>126</sup> sulphur<sup>127</sup> or phosphorous<sup>128</sup> in the graphitic network can potentially improve single TM atom adsorption, the use of doped materials has been particularly studied; in particular with nitrogen containing materials such as g-C<sub>3</sub>N<sub>4</sub>. In the case of nitrogen doped carbon materials, different adsorption sites are available, which present significantly different affinity for SA.<sup>129</sup> This explain the differences in binding energy observed in Figure 1.22 for G–N samples. Similarly, oxidized carbon materials presented a large variety of surface oxygenated groups that will present different reactivity towards SA. The works of G. Hutchings and researchers from Johnson Matthey have shown that stable Au/C SAC can be prepared on activated carbons, a support that usually present sounds amount of oxygenated groups.<sup>6</sup> As one of the potential advantages of SAC is the possibility to create a well-defined chemical environment in a robust heterogeneous catalyst, the use of a support presenting different anchoring sites could be detrimental. That's why the use of

---

<sup>120</sup> W. A. Dino, et al. *Solid State Communications* **2004**, 132, 713-718.

<sup>121</sup> W. A. Diño, et al. *e-Journal of Surface Science and Nanotechnology* **2004**, 2, 77-80.

<sup>122</sup> K. He, et al. *Nature Communications* **2014a**, 5.

<sup>123</sup> A. Granja-DelRio, et al. *Journal of Physical Chemistry C* **2017**, 121, 10843-10850.

<sup>124</sup> X. Qi, et al. *Applied Surface Science* **2012**, 259, 195-200.

<sup>125</sup> J. C. Charlier, et al. *Nanotechnology* **2009**, 20.

<sup>126</sup> M. N. Groves, et al. *Journal of Physical Chemistry C* **2012**, 116, 10548-10556.

<sup>127</sup> D. Higgins, et al. *Advanced Functional Materials* **2014**, 24, 4325-4336.

<sup>128</sup> L. Feng, et al. *Science of The Total Environment* **2020**, 698, 134239.

<sup>129</sup> N. Cheng, et al. *Nature Communications* **2016**, 7.

carbon materials with a better-defined surface chemistry, as in g-C<sub>3</sub>N<sub>4</sub> or graphdiyne is particularly attractive. For the other materials, we have to rely on the fact that the more reactive sites will be the ones that will stabilize SA preferentially. This poses the problem of the quantification of these sites. The use of high surface area support, with a high degree of functionalization should be preferred to reach high metal loadings in SAC.

Finally, it is important to note that in SAC the electronic metal-support interaction is of fundamental importance to establish correlations between the electronic properties of catalytic sites and catalytic activity.<sup>130</sup> In that context, the possibility to tune the electronic properties of carbon materials *via* doping is particularly appealing.

### 1.3. Single atom catalyst characterization

By definition, SAC only contain isolated single atoms dispersed on a support. Their characterization should ideally combine modeling studies and physico-chemical/structural characterizations. From the modelling side, the reduction of the number of atoms is interesting from the practical point of view, since modelling will become less time consuming and simpler than with metallic nanoparticles. On the other side, the experimental confirmation of the existence of only isolated single metal atoms on a carbon support, and the determination of their chemical environment and spatial distribution is critical to develop SAC.

The most convincing and intuitive strategy is to directly visualize the SAC immobilized on supports. For this purpose, the use of scanning tunneling electron microscopy (STEM)<sup>131</sup> and aberration-corrected high-angle annular dark field scanning transmission electron microscopy (HAADF-STEM) in combination with single-atom X-ray spectroscopy (atomic-resolution energy dispersive X-Ray spectroscopy (EDX) mapping)<sup>132</sup> provide a direct approach to precisely locate the isolated metal atoms in SAC. This can provide direct local structural information about the metallic species present on the support. Carbon materials are particularly interesting for these analyses since carbon is a light element, and the metal atoms are easily visualized. On the other side, carbon poorly scatters high energy electrons, and this limits the resolution obtained for carbon materials. Additionally, the electron beam may destroy the structure of the carbon support. A chemical analysis of individual metal atoms on high-surface-area supports is

---

<sup>130</sup> P. Hu, et al. *Angewandte Chemie-International Edition* **2014a**, 53, 3418-3421.

<sup>131</sup> S. J. Pennycook, et al. *Philosophical Transactions of the Royal Society a-Mathematical Physical and Engineering Sciences* **2009**, 367, 3709-3733.

<sup>132</sup> J. Liu *Chinese Journal of Catalysis* **2017a**, 38, 1460-1472.

not easily accessible by EDX or electron energy loss spectroscopy (EELS).<sup>133</sup> Obtaining high resolution elemental mapping depends on the progress of the highly focused electron probe in a specific frame, on the collection of a significant number of characteristic X-rays over time, and on the absence of damage to the sample. However, EDX analyses can be used to address the nature of groups of individual atoms, as shown on Figure 1.23 that shows the STEM-HAADF image and the EDX analysis of a 15 %Co/CNT Fischer-Tropsch catalyst that has been doped with 0.1 % w/w of Pt<sub>SA</sub>. A finer characterization to determine the environment close to the isolated atom, the number and type of bonds as well as the degree of oxidation of the metal atom can be performed through X-Ray absorption near-edge spectroscopy (XANES) and EXAFS in combination with modelling.<sup>134</sup> Such an approach has been followed for the characterization of Ru<sub>SA</sub>@C<sub>60</sub> SAC.<sup>40</sup>

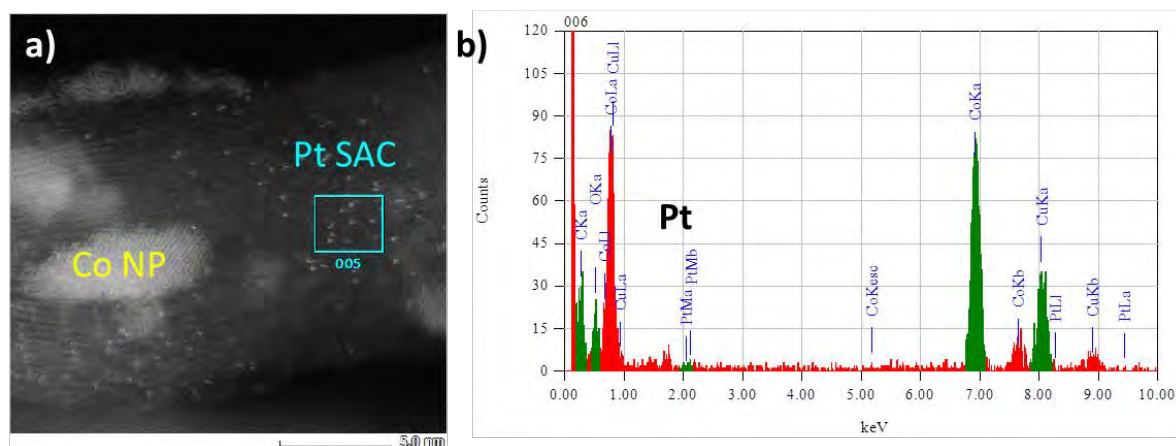


Figure 1.23. Characterization of a 15 %Co–0.1 %Pt/CNT catalyst: (a) STEM-HAADF micrographs; and (b) EDX analysis.

Figure 1.24 shows the STEM-HAADF, EXAFS, and DFT characterization of this SAC. EXAFS and DFT have shown that in this material, the Ru<sub>SA</sub> show a  $\eta^2$ - $\eta^6$  coordination to the C<sub>60</sub>. Other methods, such as solid-state magic-angle spinning NMR (SS-NMR),<sup>135</sup> infrared spectroscopy with probe molecule such as carbon monoxide<sup>136</sup> and X-Ray photoelectron spectroscopy,<sup>137</sup> can also be used to obtain structural information of SAC. SS-NMR can provide atomic-level characterization with high sensitivity.

<sup>133</sup> K. Suenaga, et al. *Nature Photonics* **2012**, 6, 545-548.

<sup>134</sup> D. Koningsberger, et al. In *Handbook of Heterogeneous Catalysis*: Wiley-VCH (2008), pp. 774-803.

<sup>135</sup> J. H. Kwak, et al. *Science* **2009**, 325, 1670-1673.

<sup>136</sup> B. Qiao, et al. *Nature Chemistry* **2011**, 3, 634-641.

<sup>137</sup> F. Dvořák, et al. *Nature Communications* **2016**, 7, 10801.

New hyperpolarization techniques such as dynamic nuclear polarization allows improving SS-NMR sensitivity, and performing one and two dimension SS-NMR experiments, in order to get fine information on the structures of SAC.<sup>138</sup>

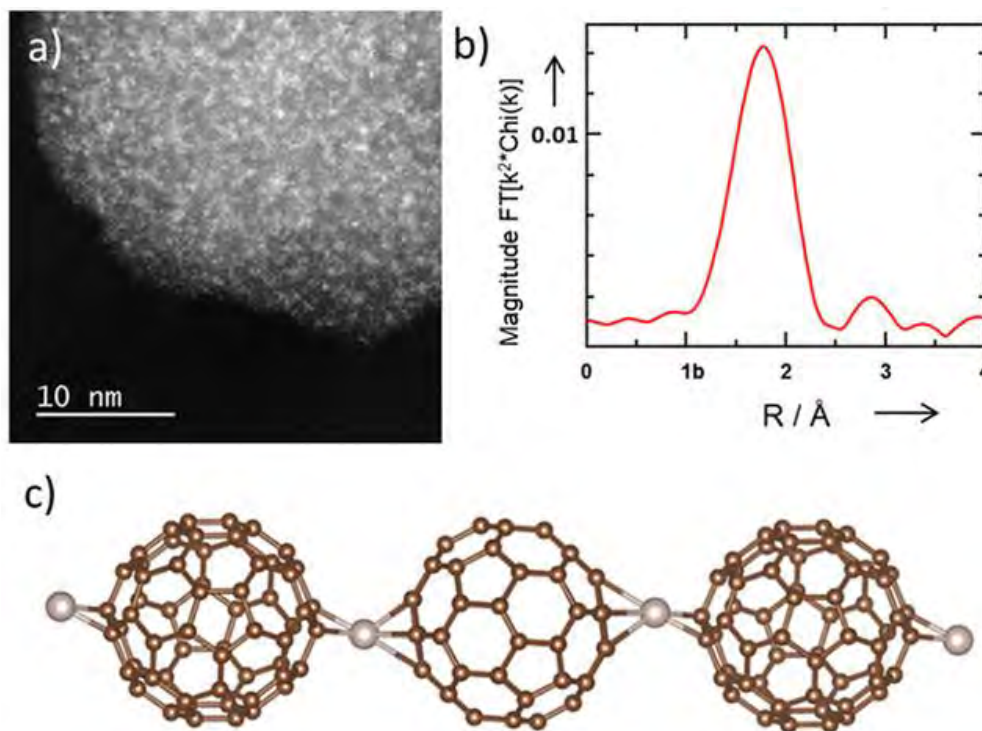


Figure 1.24. Characterization of a  $Ru_{SA}@C_{60}$  SAC: (a) STEM-HAADF micrographs of  $Ru_{SA}@C_{60}$ ; (b) magnitude of the Fourier Transform of  $k^2$ -weighted Ru EXAFS; and (c) side view of an ideal 1D chain for  $Ru@C_{60}$  ratio in the  $\eta^2$ - $\eta^6$  state. Ru atoms are in grey, carbon atoms in brown. From ref. [139]

This technique however can be difficult to apply for some carbon materials that contain magnetic impurities from their synthesis.<sup>140</sup>  $^{13}C$  SS-NMR studies of carbon materials involves the use of cross polarization, to enhance the polarization of the un abundant  $^{13}C$  nuclei through their interaction with  $^1H$  nuclei, combined to magic angle spinning to limit peak broadening due to the chemical shift anisotropy.<sup>141,142</sup> Infrared spectroscopy represents one of the most important characterization technique in catalysis research that

<sup>138</sup> C. Coperet, et al. *Journal of the American Chemical Society* **2017**, 139, 10588-10596.

<sup>139</sup> C. Rivera-Cárcamo, et al. *Catalysis Science & Technology* **2020**, 10, 4673-4683.

<sup>140</sup> J. C. C. Freitas, et al. In *Chemistry and Physics of Carbon*, edited by L. R. Radovic (**2012**), pp. 85-170.

<sup>141</sup> J. C. C. Freitas, et al. *Journal of Spectroscopy* **2016**, 1543273.

<sup>142</sup> H. Darmstadt, et al. *Carbon* **2000**, 38, 1279-1287.



allows the direct monitoring of the interaction between probe molecules and the surfaces of the catalyst.<sup>143</sup>

There also, the use of this technique with carbon materials is not trivial.<sup>144</sup> Indeed, spectra of carbon materials are difficult to obtain, mainly because of poor transmission, and uneven light scattering related to large particle size.<sup>145</sup> In principle, X-ray photoelectron spectroscopy (XPS)<sup>146</sup> analyses could provide valuable interaction on charge transfer in SAC.<sup>147</sup> These characterization methods, if performed *in situ* (EXAFS, IR)<sup>148</sup> or under environment conditions (STEM) are also extremely useful to obtain insight into the nature of the catalysis with SAC. Figure 1.25 shows an overview of the complementary characterization methods (including DFT studies) required to assess structure and composition of SA on carbon materials.

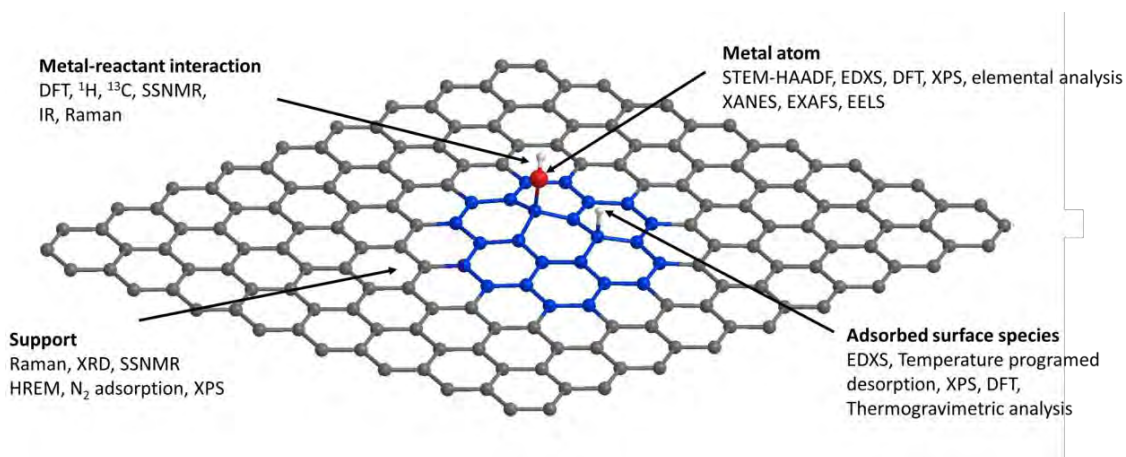


Figure 1.25. Overview of the complementary characterization methods and studies required to assess structure and composition of SAC on carbon materials.

#### 1.4. Preparation of single atom catalysts

It is accepted that the application of all new materials is limited by the capability of their reproducible and large-scale production. In the case of SAC, the difficulties are obvious, and the inability to produce isolated atoms on carbon materials on a large scale is a problem yet. It is therefore essential to develop methods that allow the systematic

<sup>143</sup> J. Ryczkowski *Catalysis Today* **2001**, 68, 263-381.

<sup>144</sup> V. Tucureanu, et al. *Critical Reviews in Analytical Chemistry* **2016**, 46, 502-520.

<sup>145</sup> E. Fuente, et al. *Journal of Physical Chemistry B* **2003**, 107, 6350-6359.

<sup>146</sup> E. D. Boyes, et al. *Annalen Der Physik* **2013**, 525, 423-429.

<sup>147</sup> S. Liu, et al. *Angewandte Chemie-International Edition* **2020b**, 59, 798-803.

<sup>148</sup> X. Li, et al. T. Zhang, et al. *iScience* **2019a**, 22, 97.

preparation of heterogeneous catalysts containing isolated and well characterized active sites. This still remains a challenge, due to process low production efficiency (high cost precursors, high cost preparation devices, particle formation, etc.). As we previously mentioned, this section will be especially focused on the preparation of single catalytic active-sites over carbon materials. In order to have a broader view on the choice of catalytic supports (oxide, alloy or carbons), the reader is encouraged to refer to literature dealing with chemical methods for the preparation of SAC.<sup>149</sup>

#### 1.4.1. Low loading SAC (<1% w/w)

Without any doubt, low loading metallic SA supported on carbon materials has far the advantage over the number of articles, owing almost 90 % of the total references to date. There are plenty of methods to synthesize SAC, however all of them have a common characteristic: maximizing the metal-support interactions in order to generate single atoms as stable as possible, along with fighting against the natural tendency of the atoms to aggregate either during the synthesis processes or during the subsequent treatments. From a general point of view, we have seen certain tendencies relative to the methods of insertion of SA into the carbon material.

Low loading catalysts have been typically prepared through “post-synthetic methods” *i. e.*, the addition of the active phase is carried out on synthesized supports, and not during the synthesis of the support. As will be seen later, another approach is also possible, where the metallic atoms are integrated at the same time than the production of the carbon network. This latter method is preferred for obtaining higher metallic loadings (>1%). We will discuss below methods that have been regularly used to produce low loading carbon based-SAC.

##### 1.4.1.1. Atomic layer deposition

Atomic layer deposition (ALD) is a deposition technique based on the sequential use of a gas phase chemical reaction. Generally, the ALD process includes four steps, as shown in Figure 1.26: i) exposure to the metal precursor; ii) purge of the ALD reactor; iii) exposure to a reactive gas to eliminate remaining ligands on the metal; and iv) a further purge of the ALD reactor. ALD has been used to produce single atoms in a controlled manner over 2D carbon materials, as graphene and graphitic carbon nitride. Sun's group has reported a practical ALD synthesis of isolated Pt<sub>SA</sub> anchored to graphene

---

<sup>149</sup> Z. Li, et al. *National Science Review* **2018c**, 5, 673-689.



nanosheets<sup>150</sup> and N-doped graphene nanosheets<sup>151</sup> using the precursor (methylcyclopenta-dienyl) trimethylplatinum [MeCpPtMe<sub>3</sub>] and O<sub>2</sub> as reactive gas.

After 50 cycles SA were obtained but also sub-nanometer clusters with a 1.52 wt% Pt. Figure 1.27 shows the evolution of Ru deposition on the triple boundary of a graphene particle with an increasing number of ALD cycles.<sup>152</sup>

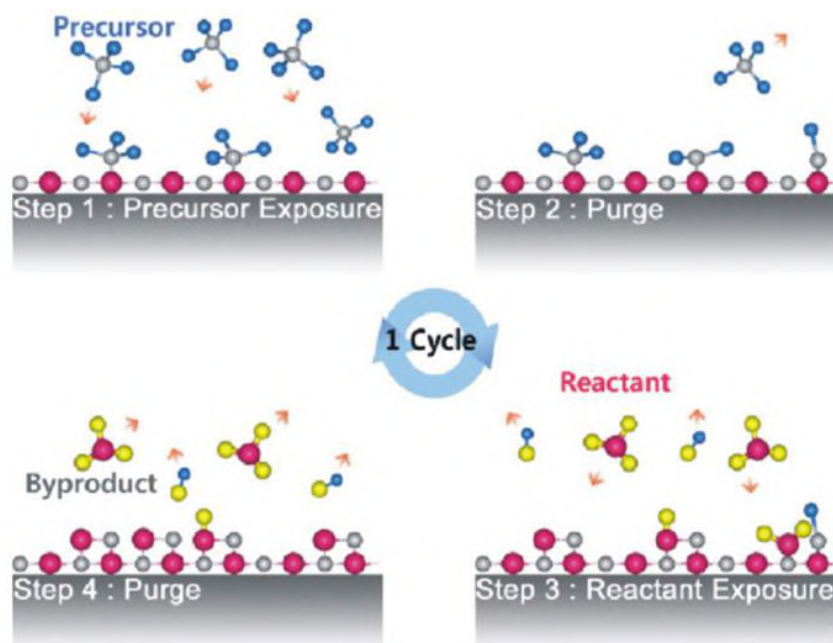


Figure 1.26. Different steps of the ALD process for SAC preparation. From ref. [153].

The line defects are considered to be either wrinkles or grain boundaries, points that act as nucleation sites for nanoparticle formation. These results suggest that a controlled number of cycles should be performed to obtain exclusively SA sites. Thus, after just one [Pd(hfac)<sub>2</sub>]-formalin ALD cycle on g-C<sub>3</sub>N<sub>4</sub> (Pd<sub>1</sub>/g-C<sub>3</sub>N<sub>4</sub>), a Pd loading of 0.5 wt% is obtained. Aberration-corrected HAADF-STEM observations have shown that a high density of atomically dispersed Pd atoms was obtained on this support;<sup>154</sup> neither Pd<sub>NP</sub> nor subnanometer clusters were observed at low or high magnifications. The six-fold cavities on g-C<sub>3</sub>N<sub>4</sub> are likely the anchoring sites for Pd atoms. When ten cycles are performed, 6.0 ± 1.2 nm Pd<sub>NP</sub> are formed. In this case, the contribution of impurities, such as the oxygen-functional groups introduced during g-C<sub>3</sub>N<sub>4</sub> synthesis can also promote the nucleation of these nanoparticles.

<sup>150</sup> S. Sun, et al. *Scientific Reports* **2013**, 3.

<sup>151</sup> N. Cheng, et al. *Nature Communications* **2016**, 7, 13638.

<sup>152</sup> M. Kim, et al. *Acs Applied Materials & Interfaces* **2017**, 9, 701-709.

<sup>153</sup> H. Kim, et al. *Thin Solid Films* **2009b**, 517, 2563-2580.

<sup>154</sup> X. Huang, et al. *Nano Research* **2017**, 10, 1302-1312.

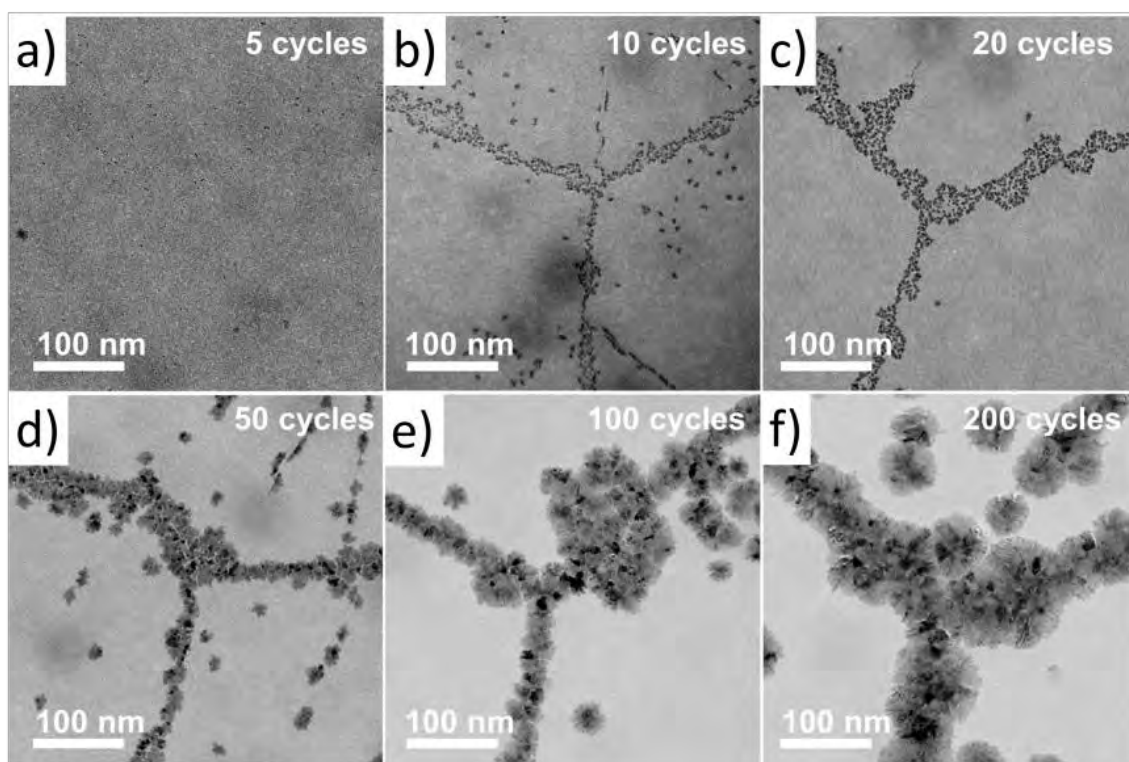


Figure 1.27. Evolution of Ru growth on graphene triple grain boundaries shown through magnified bright-field TEM images taken after: (a) 5, (b) 10, (c) 20, (d) 50, (e) 100, and (f) 200 ALD cycles, respectively. From ref. [152].

Another approach is to use those functional groups to carefully control the formation of Pd species during ALD.<sup>155</sup> Graphene oxide powder was precisely heated to control the type and concentration of oxygenated surface functional groups. After annealing under helium at 1050 °C for 2 min, XPS analyses revealed that the dominant remnants groups on the graphene support were the phenolic groups. Next, Pd ALD was performed to reach a 0.25 wt% Pd loading, and to form exclusively randomly dispersed Pd atoms. If prolonged annealing is performed (10 min), a large decrease in the amount of phenolic groups is observed, so the Pd loading turned negligible (0.01 %). Additionally, when GO was annealed at lower temperatures (700 °C), the Pd loading became higher (1.7 %), and a considerable fraction of Pd<sub>NP</sub> was produced. Comparable techniques, such as chemical or physical vapor deposition, cannot always provide such a level of uniformity, conformality and thickness control at the Angstrom level. It seems that ALD should be an efficient technique to achieve atomically dispersed catalysts. However, in some cases nucleation delay or island growth during the beginning of the film deposition are

<sup>155</sup> H. Yan, et al. *Journal of Catalysis* **2018b**, 366, 70-79.

observed, inducing severe deviations from an ideal germination. Additionally, this method has some disadvantages such as: i) the lack of industrial reactors, ii) the relatively high price of the metal precursors as well as their reactivity/availability, iii) the high cost of the operation, and iv) the fact that traditionally, the process of ALD is very slow and this is known to be its major limitation.

#### *1.4.1.2. Wet chemistry methods*

In wet-chemistry also, since the precursor materials already contain single metal atom, the goal is to anchor those atoms onto the supports and to obtain a tough anchoring. A classical wet chemistry technique implies: i) introduction of the metal precursor on the support by different methods such as impregnation/ion-exchange, co-precipitation, or deposition-precipitation, ii) a drying step, and iii) a calcination and/or reduction step. It is important to stress that every step should be finely controlled to obtain reproducible procedures, and to avoid the production of metallic NP together with SA. An important factor to consider for this method as for the others is that carbon supports have a chemically inert surface in comparison with other supports such as oxides; so as already stated in the previous section, the odds to lead NP are much higher. Hence, a strong metal-support interaction should be obtained in order to avoid aggregation of SA on the surface. In practice, it is relatively easy to produce SAC by reducing the metal loading to an extremely low level, since the concentration of efficient anchoring sites should be extremely low in most of the carbon materials. Considering this principle, usually these wet chemistry methods are associated with a low metal loading to maintain high dispersion. Even with the simplest protocol it has been possible to prepare SAC.<sup>156</sup> In that case, the chosen support is firstly simply dispersed in deionized water together with an ionic metallic precursor. When the impregnation step is finished, the solvent is evaporated to proceed with a soft reduction under H<sub>2</sub>. Pd/CNF<sup>157</sup> was synthesized with a 0.04-0.5 wt% metal loading using this approach. The analyses indicate that the palladium was found to exist as SA just in the samples with concentration of 0.2 wt% or less. Other works have shown that SA can coexists with metallic NP even at low loading, as shown in Table 1.1.

---

<sup>156</sup> V. V. Chesnokov, et al. *Diamond and Related Materials* **2018**, 89, 67-73.

<sup>157</sup> D. I. Kochubey, et al. *Carbon* **2012**, 50, 2782-2787.

Table 1.1. List of low loading (&lt;1 % w/w) SAC reported in the literature.

Sample	Preparation	Metal loading <sup>[a]</sup> [wt%]	Ref
Fe-P-C <sub>3</sub> N <sub>4</sub>	Wet impregnation in water from Fe(NO <sub>3</sub> ) <sub>3</sub> ·9H <sub>2</sub> O	0.2–0.5–1.0 (not informed)	153
Pd/CNF	Wet impregnation in water from PdCl <sub>2</sub>	0.04–0.1–0.2–0.5 (from 0.2 % particles)	152
Pt/C <sub>3</sub> N <sub>4</sub>	Wet impregnation in water from H <sub>2</sub> PtCl <sub>6</sub>	0.075, 0.11, 0.16, and 0.38 (Pt clusters at 0.38 %)	158
Au/g-C <sub>3</sub> N <sub>4</sub>	Wet impregnation in water from HAuCl <sub>4</sub>	0.1, 0.3, 0.5, 1, 3, and 5 (Au particles from 0.3 %)	159
Au/AC	Wet impregnation in water from HAuCl <sub>4</sub> ·xH <sub>2</sub> O	1 % (Au particles)	7
Au/MWCNT	Wet impregnation in water from HAuCl <sub>4</sub> + sodium citrate	0.1	160
Pt/MWCNT	Reduction of H <sub>2</sub> PtCl <sub>6</sub> ·xH <sub>2</sub> O by NaBH <sub>4</sub> on thiol-functionalized MWCNT	0.17	161
Ru or Pd/CNF Ru, Pt or Pd/N-CNF	Incipient wetness impregnation from (Ru(NO)(NO <sub>3</sub> ) <sub>3</sub> or Pd acetate in acetone) and coprecipitation from H <sub>2</sub> PtCl <sub>6</sub> with NaOH in water	1 (with particles) 0.3 –1.0	162
Pt or Ir/g-C <sub>3</sub> N <sub>4</sub>	Wet impregnation in water from H <sub>2</sub> PtCl <sub>6</sub> ·xH <sub>2</sub> O or K <sub>2</sub> IrCl <sub>6</sub> ·6 H <sub>2</sub> O reduction with NaBH <sub>4</sub>	0.5 (with particles)	163
Pd/g-C <sub>3</sub> N <sub>4</sub>	Wet impregnation aqueous from PdCl <sub>2</sub> +NaCl reduced NaBH <sub>4</sub>	0.5 (no particles)	164
Pt/TiC	Wet impregnation from H <sub>2</sub> PtCl <sub>6</sub> ·6H <sub>2</sub> O	0.2 (no particles)	165
Ni-NCNT/AC	Wet impregnation on water of NiCl <sub>2</sub> ·6H <sub>2</sub> O	0.35 – 0.88 at. %	166

[a] In parenthesis is indicated the presence or not of metal clusters or NP.

In order to increase the amount of supported metal, functionalization of carbon materials with different heteroatoms such as O, N, P or S can be performed. Thus, Fe/P-doped-gC<sub>3</sub>N<sub>4</sub> have been synthesized using the same process as above mentioned but obtaining loadings up to 1 wt%.<sup>167</sup> Occasionally, techniques such as incipient wetness impregnation<sup>168</sup> have also been used to generate atomically dispersed metallic species containing almost 1 wt% of active phase on functionalized carbons. Other examples of low loading SAC prepared by wet impregnation are given in Table 1.1. This approach

<sup>158</sup> X. Li, et al. *Advanced Materials* **2016a**, 28, 2427-2431.

<sup>159</sup> Z. Chen, et al. *Advanced Materials* **2018a**, 30, 1704720.

<sup>160</sup> A. Corma, et al. *Chemistry-a European Journal* **2015**, 21, 7012-7015.

<sup>161</sup> Y.-T. Kim, et al. *Angewandte Chemie International Edition* **2006**, 45, 407-411.

<sup>162</sup> D. A. Bulushev, et al. *Acs Catalysis* **2016**, 6, 3442-3451.

<sup>163</sup> Z. Chen, et al. *Advanced Functional Materials* **2017a**, 27, 1605785.

<sup>164</sup> G. Vile, et al. *Angewandte Chemie-International Edition* **2015**, 54, 11265-11269.

<sup>165</sup> S. Yang, et al. *Acs Catalysis* **2017**, 7, 1301-1307.

<sup>166</sup> C. Jin, et al. *Communications Chemistry* **2019**, 2, 135.

<sup>167</sup> S. Hu, et al. *Applied Surface Science* **2014b**, 311, 164-171.

<sup>168</sup> B. Zugic, et al. *Applied Catalysis B-Environmental* **2014**, 144, 243-251.

can be considered part of the wet-impregnation classification because it comprises as a first step an impregnation but requires an extra step at high-temperature ( $>500\text{ }^{\circ}\text{C}$ ) or pyrolysis treatment to obtain the final catalyst. The objective of the high-temperature treatment is the anchoring of the metal and the introduction of the dopant (usually nitrogen) within the graphitic network. The doping is achieved by the incorporation of a nitrogen source as a solid such as urea<sup>169</sup> or as a gas like  $\text{NH}_3$ <sup>170</sup> over the metal impregnated support during the annealing. For this preparation,  $\text{GO}$ <sup>171,172</sup> has been recurrently selected as a support (see Figure 1.28 for a Co catalyst prepared on nitrogen-doped  $\text{GO}$ ).<sup>173</sup>

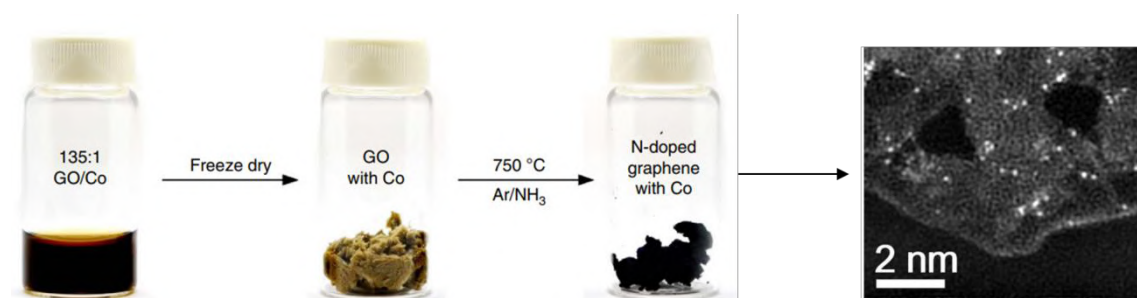


Figure 1.28. Schematic illustration of the synthesis of Co@N-doped graphene catalyst (0.57 %Co w/w). From ref. [173].

The high density of defects in GO and the large surface area of this negatively charged support, provide optimum characteristics for N-doping and uniform adsorption of a monolayer of metal cations for SA deposition. In that case, the density of the active sites could be maximized on the 2D surface for higher catalytic activity. Noble and non-noble single metal atoms have been embedded into porous carbon supports and stabilized by strong binding to nitrogen with this procedure. Liu and co-workers<sup>174</sup> studied the effect of N-doping on carbon black for the formation of platinum species. While the examination by STEM of multiple regions of the sample reveals that only individual Pt atoms were present in  $\text{Pt}_1\text{@N-CB}$ ; in the absence of nitrogen,  $\text{Pt}_{\text{NP}}$  were observed at the same Pt loading (0.4 wt %). It was shown that the nitrogen doping can enhance the interaction between the metallic atom and the carbon support, but also that it can promote metal-support electron transfer. Atomically dispersed  $\text{Fe-N}_x$  species anchored on

<sup>169</sup> J. Zhao, et al. *Applied Catalysis B: Environmental* **2019**, 256, 117778.

<sup>170</sup> X. Zhang, et al. *Advanced Materials* **2020b**, n/a, 1906905.

<sup>171</sup> Y. Xu, et al. *Journal of Energy Chemistry* **2020**, 43, 52-57.

<sup>172</sup> K. Jiang, et al. *Energy & Environmental Science* **2018b**, 11, 893-903.

<sup>173</sup> H. Fei, et al. *Nature Communications* **2015**, 6, 8668.

<sup>174</sup> J. Liu, et al. *Nature Communications* **2017a**, 8, 15938.



nitrogen and sulfur co-doped carbon layers were obtained by coating CNT with 2,2-bipyridine, potassium isothiocyanate, and an Fe precursor, followed by pyrolysis at 900 °C under N<sub>2</sub>, and acid leaching to dissolve undesired iron sulfide particles (Figure 1.29).<sup>175</sup> TEM images of S,N-Fe/N/C-CNT show a 3D organization comprising a great number of carbon layers grown on entangled CNT.

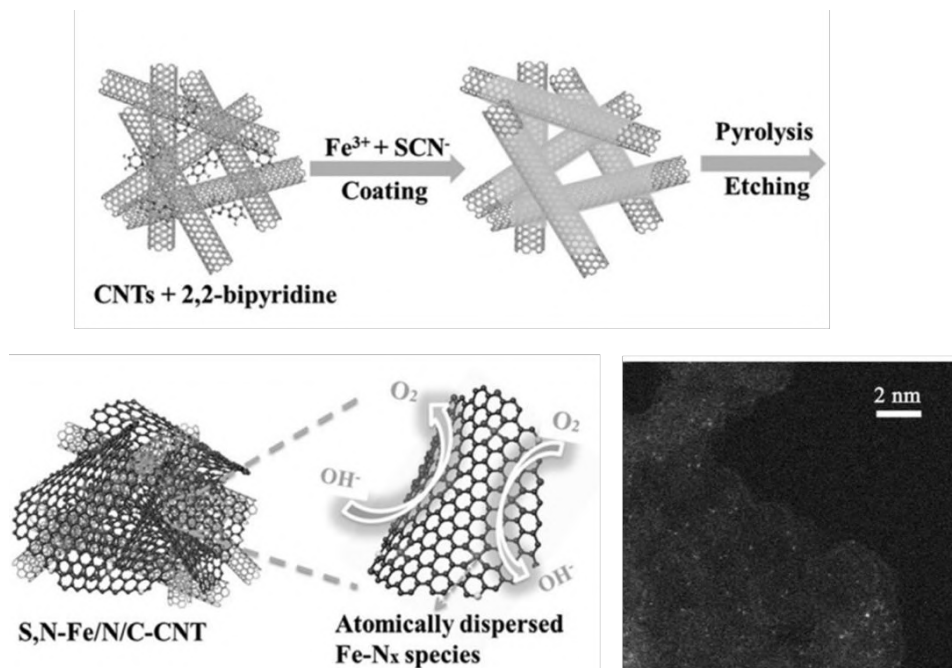


Figure 1.29. Synthetic process for S,N-Fe/N/C-CNT synthesis. From ref. [175].

Notably, no NP can be found, showing a 0.8 % Fe atomic content, but in samples prepared without addition of SCN<sup>−</sup> salts (denoted N-Fe/N/C-CNT) few crystalline phases appear associated with Fe-based carbides.

#### 1.4.1.3. Other methods

After impregnation, deposition of Ni and Fe over GDY was conducted by a facile electrochemical reduction method (Ni 0.28 wt%; Fe 0.68 wt%).<sup>176</sup> The presence of stable atoms over GDY surface was explained in terms of electronic interaction. GDY exists with strong electronegative *sp*-hybridized orbitals that, in the presence of a positively charged metal, allow the C(*sp*)-M(*d*) orbital overlapping. A three-step method based on pyrrole polymerization on oxidized CNT has been used to immobilize single Fe atoms and to produce a Fe<sub>SA</sub>-N-PC/CNT SAC (Figure 1.30).<sup>177</sup> During this process and thanks

<sup>175</sup> P. Chen, et al. *Angewandte Chemie-International Edition* **2017c**, 56, 610-614.

<sup>176</sup> Y. Xue, et al. *Nature Communications* **2018**, 9.

<sup>177</sup> J.-C. Li, et al. *Npg Asia Materials* **2018b**, 10, e461.

to the spatial isolation effect of zinc, many pores were generated and a high concentration of Fe–N<sub>x</sub> species was obtained instead of iron NP. Quantitative elemental analysis performed by XPS gives 0.3 at % of Fe, providing an outstanding activity, selectivity but also stability in the oxygen reduction reaction.

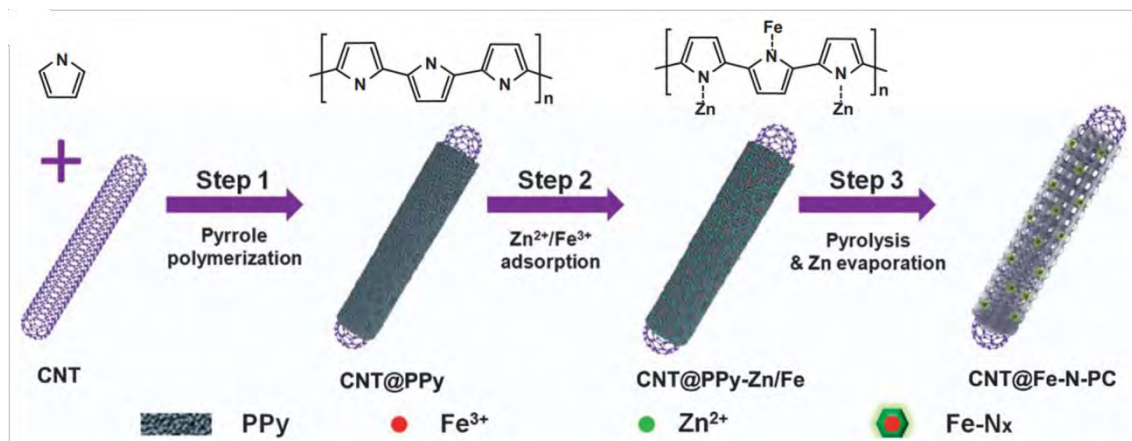


Figure 1.30. Preparation of a Fe<sub>SA</sub>-N-PC/CNT SAC. From ref. [177].

Finally, an unexpected method of obtaining SA comprises the redispersion of noble metal nanoparticles (Pd, Pt, Au) deposited over ZIF-8 composites. Through in-situ environmental TEM was evidenced a dynamic process where sintering and atomization are competing at 900 °C under inert atmosphere achieving 0.16, 0.51 and 0.18 wt% for Pd, Pt and Au, respectively.<sup>178</sup> Molecular dynamic simulations reveal the mechanism associated with the transformation of a metal NP into an array of stable SAs on a carbon surface. This study shows the pivotal role of defects in the carbon surface in trapping and stabilizing SA.<sup>179</sup> NP should perform Brownian-like random walk on the surface (above 1200 °C) and when there are no defects, isolated atoms can collide and remain as NP. Contrarily, on a defective support free SA gets immobilized into the defect avoiding to merge back to NP. From these findings, it appears that methods involving high temperature thermal post-treatments would be promising for the synthesis of low loading SAC.

#### 1.4.2. High loading SAC (>1 % w/w)

Until now, the requirement of practical synthesis of metal SA on carbon materials with high loading (>1 wt% metal) has been challenging to satisfy. Indeed, it is easy to find examples where, despite the efforts to increase the metallic loading, the resulting catalyst contains a significant portion of metallic NP. A practical solution to achieve the exclusive

<sup>178</sup> S. J. Wei, et al. *Nature Nanotechnology* **2018**, 13, 856.

<sup>179</sup> L. Wu, et al. *npj Computational Materials* **2020**, 6, 23.



presence of isolated atoms on the supports is the subsequent treatments of the catalyst in strong mineral acids, which are able of dissolving metal particles without removing the metallic atoms present on the support. It is worth mentioning that the reaction of these strong acids with SAC has not been yet investigated in detail. This is regrettable since it can affect the chemical state of the SA. Zhou *et al.*<sup>180</sup> prepared through the pyrolysis of cobalt phthalocyanine-silica colloid composites a cobalt-nitrogen/carbon catalyst (Co-N<sub>x</sub>@C), which contained a total of 12.3 wt% of Co, present as single atoms as well as NP. After being washed off with 10 wt% HF, only 0.25 % w/w of Co remained. This means that about 98 wt% of cobalt was present in the form of metallic Co NP.<sup>181</sup> For this reason, it is necessary to specify that we will consider as “high loading catalysts” those catalysts that contains a percentage greater than 1 % of metal exclusively in the form of SA. Table 1.2 summarizes the reports published to date claiming to contain more than 1 wt% metal loading in the form of SA dispersed all over the carbon support. Although the methods of preparation changed, with a couple of exceptions (entries 15–19), it can be asserted that there is a certain preference in the preparation methods: the use of one-pot or direct approaches such as pyrolysis, template-sacrificial approach, and copolymerization. In these methods, the deposition of the active phase is carried out during the synthesis of the support, the final inclusion of the metal happens in the same process of formation of the graphitic network, which is generally achieved by pyrolysis of the carbon source. Although the manufacture of catalysts by this technique has been quite profitable for lab-scale preparation, it must be considered that the small control in the final metal loading and the fact that a large amount of metal is lost during the acid etching represent major disadvantages for upscaling. Additionally, the proportion of atoms on the surface and embedded in the carbon structure is difficult to control, and it is difficult to claim that all the atoms are located on the surface of the support, and therefore active in catalysis.

---

<sup>180</sup> P. Zhou, et al. *Science Advances* **2017**, 3, e1601945.

<sup>181</sup> P. Yin, et al. *Angewandte Chemie-International Edition* **2016**, 55, 10800-10805.

Table 1.2. Selected examples of high loading (&gt;1 % w/w) SAC reported in the literature.

Entry	Sample	Preparation	Loading (wt%)	Ref
1	Co-N/C	pyrolysis of bimetallic MOF	1.5–4.3	174
2	Ni-N/C	pyrolysis of MOF	1.5 <sup>[a]</sup>	182
3	Fe-N/C	pyrolysis of MOF	1.76	183
4	Co-N/C	pyrolysis of ZIF	0.34	184
5	Pt-S/C	pyrolysis MOF	5.0	185
6	Co-N/C	pyrolysis of MOF	3.5	186
7	Ni and Co/N-CNT	pyrolysis of organometallic precursor	20.0	187
8	Co-N/C	template-sacrificial approach	3.6	188
9	Fe-N/C	template-sacrificial approach	2.9	189
10	Co and Fe/N-C	template-sacrificial approach	1.3 – 1.4 <sup>[b]</sup>	190
11	Mo-N/C	template-sacrificial approach	1.32	191
12	Ni and Fe-N/C	template-sacrificial approach	1.2	192
13	Fe-N/C	template-sacrificial approach	1-2	193
14	Ag/g-C <sub>3</sub> N <sub>4</sub>	copolymerization	1-10	194
15	Ag/g-C <sub>3</sub> N <sub>4</sub>	copolymerization	1-10	195
16	Co(OH) <sub>x</sub> -N-CNT	wet impregnation and annealing	17	196
17	Pt/S-MWCNT	wet impregnation, NaBH <sub>4</sub> reduction	20	197
18	Fe-N/G	ball milling	1.5	198
19	Ru/C <sub>60</sub>	decomposition of organic precursor	10.0	40
20	Ni-porous graphene	wet impregnation and annealing	6.9	199
21	Co-N-nanosheets	salt-template method	15.3	200

[a] only 78 % SAC; [b] atomic %.

<sup>182</sup> L. Fan, et al. *Nature Communications* **2016**, 7.<sup>183</sup> L. Jiao, et al. *Angewandte Chemie-International Edition* **2018**, 57, 8525-8529.<sup>184</sup> X. X. Wang, et al. *Advanced Materials* **2018b**, 30.<sup>185</sup> C. H. Choi, et al. *Nature Communications* **2016**, 7.<sup>186</sup> X. Sun, et al. *Journal of Catalysis* **2018b**, 357, 20-28.<sup>187</sup> Y. Cheng, et al. *Advanced Materials* **2018**, 30, 1706287.<sup>188</sup> W. Liu, et al. *Chemical Science* **2016b**, 7, 5758-5764.<sup>189</sup> Y. J. Sa, et al. *Journal of the American Chemical Society* **2016**, 138, 15046-15056.<sup>190</sup> H.-W. Liang, et al. *Journal of the American Chemical Society* **2013**, 135, 16002-16005.<sup>191</sup> W. Chen, et al. *Angewandte Chemie-International Edition* **2017b**, 56, 16086-16090.<sup>192</sup> J. Xie, et al. *ChemSuschem* **2017**, 10, 359-362.<sup>193</sup> B. Wang, et al. *Nano Letters* **2017b**, 17, 2003-2009.<sup>194</sup> Y. Wang, et al. *Applied Catalysis B-Environmental* **2017c**, 211, 79-88.<sup>195</sup> Z. Chen, et al. *Acs Nano* **2016a**, 10, 3166-3175.<sup>196</sup> J. E. Kim, et al. *Acs Applied Materials & Interfaces* **2016**, 8, 1571-1577.<sup>197</sup> E.-K. Lee, et al. *Journal of Catalysis* **2017**, 352, 388-393.<sup>198</sup> D. Deng, et al. *Science Advances* **2015**, 1, e1500462.<sup>199</sup> Y. Cheng, et al. *Applied Catalysis B: Environmental* **2019**, 243, 294-303.<sup>200</sup> Y. Li, et al. *Energy Storage Materials* **2020d**, 30, 250-259.

#### 1.4.2.1. Pyrolysis of MOFs or carbon-metal sources.

MOFs (metallic organic frameworks) or ZIFs (zeolitic imidazolate frameworks) have been used in an innovative route to prepare metal supported N-doped carbon materials. The pyrolysis of the MOF containing the target metal is carried out, and the organic linker is carbonized providing the formation of a porous carbon support.<sup>201</sup> The potential advantages of this technique for SAC preparation and uses have been recently summarized by Xu *et al.*:<sup>202</sup> i) the MOF-derived carbon can inherit the tunable surface area and porosity of the precursors, ii) various metals can be easily and uniformly introduced in the metal nodes, ligands, or pores of the precursors; and iii) the large amounts of nitrogen in precursors built from nitrogen-containing ligands contribute to a strong stabilization of SAC. A type of Zn/Co bimetallic MOF<sup>181</sup> with a homogeneous distribution of Zn and Co can be systematically designed due to the same coordination of  $\text{Co}^{2+}$  and  $\text{Zn}^{2+}$  with 2-methylimidazole. Due to the low melting point (m.p. 420 °C - b.p. 907 °C) of zinc, Zn atoms can be evaporated during the pyrolysis step at 800 °C under nitrogen that also contributes to cobalt reduction (Figure 1.31). The leaving  $\text{Zn}^{2+}$  generates free N sites during pyrolysis, which are beneficial for the stabilization of  $\text{Co}_{\text{SA}}$ . The intentional addition of  $\text{Zn}^{2+}$  replacing certain proportion of  $\text{Co}^{2+}$  sites serves as a “fence” to further expand the adjacent distances between Co atoms. To support this analysis, a sample without the presence of Zn was prepared and the results consistently show the abundant formation of crystalline cobalt NP. Fe dispersed on N-doped carbons nanosheet ( $\text{Fe}_{\text{SA}}/\text{NCS}$ )<sup>203</sup> were produced by direct pyrolysis of hemin-doped polyaniline (PANI) in which the carboxyl groups of the hemin were doped into PANI main chains by electrostatic interaction (Fig 1.32).

---

<sup>201</sup> Y.-N. Gong, et al. *Angewandte Chemie International Edition* **2020**, 59, 2705-2709.

<sup>202</sup> Z. Liang, et al. *Angewandte Chemie-International Edition* **2018**, 57, 9604-9633.

<sup>203</sup> Y. Zhu, et al. *ChemistrySelect* **2020**, 5, 1282-1287.

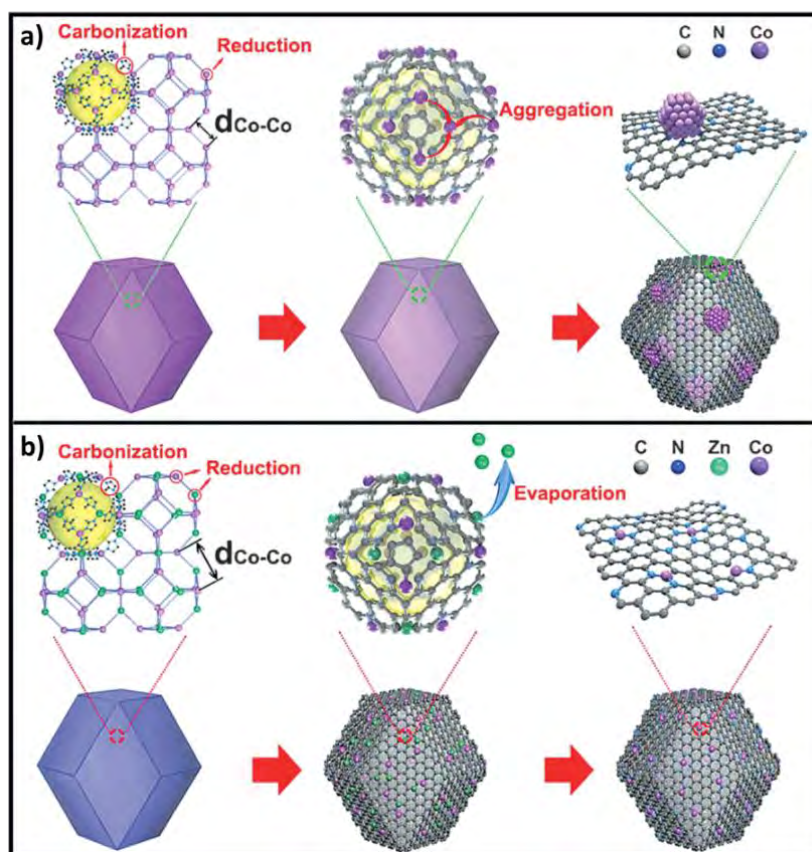


Figure 1.31. Formation of (a)  $\text{Co}_{\text{NP}}@\text{N}-\text{C}$  (no zinc in the precursor); and (b)  $\text{Co}_{\text{SA}}@\text{N}-\text{C}$  (presence of zinc in the precursor). From ref. [202].

PANI provided a rich nitrogen source to introduce the N-dopant into carbon matrix and to anchor an individual iron atom for the formation of a Fe-N<sub>4</sub> site. In accordance with the data the pyrolyzation temperature is a fundamental parameter to control during the synthesis. The content of N and Fe is changed as well as the number of defects when temperature is increased from 700 to 800 and 900 °C. The optimal results were found on Fe<sub>SA</sub>/NCS-700 had 0.89 at % metal loading and highest total N content (8.54 at %) relating pyridinic N-species with Fe content. Based on DFT calculations the presence of these nitrogen groups can have synergistically enhanced the catalytic activity. A similar approach was used for the formation of atomically dispersed TM (Ni, Co, NiCo, CoFe, and NiPt) on N-doped CNT.<sup>187</sup> The N-doped CNT were produced through the catalytic decomposition of a dicyandiamide metal (Ni, Co) complex.

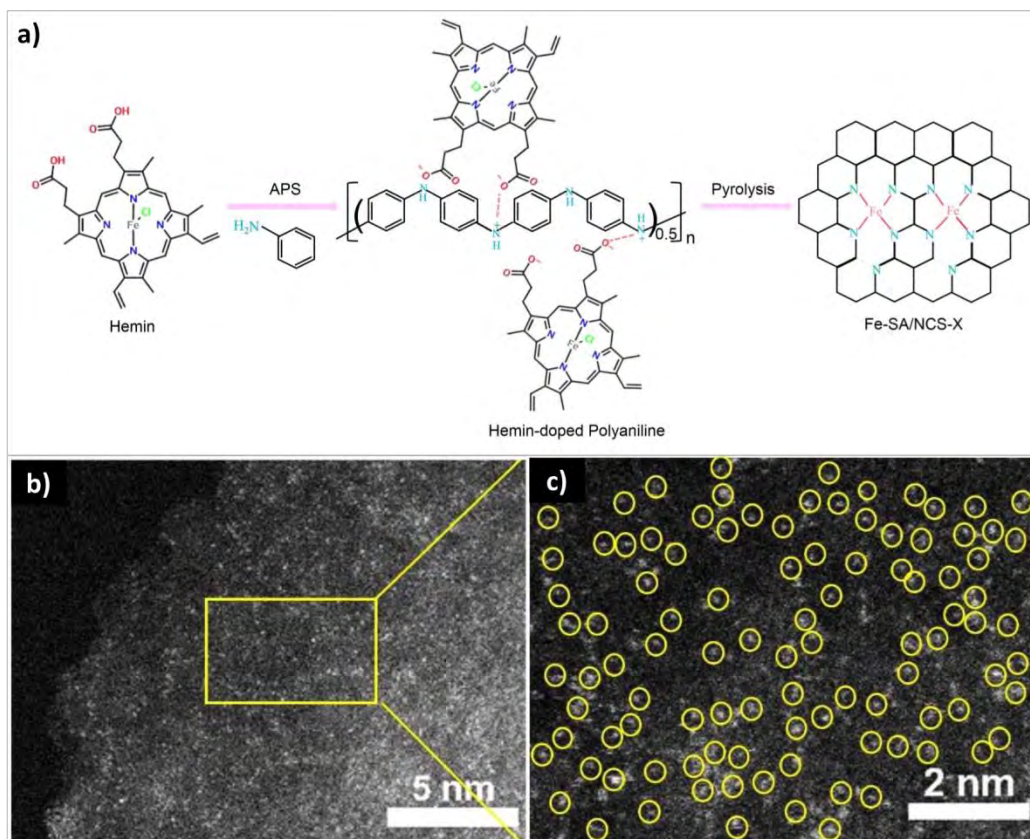


Figure 1.32. (a) Synthesis route of the Fe-SA/NCS catalysts. (b, c) HAADF-STEM and magnified images of Fe-SA/NCS. From ref. [203].

XANES analyses performed on the nickel SAC have shown a NiN<sub>4</sub> environment for nickel. Progressive heating under argon at 350 °C (formation of Ni-O-C on the melem skeleton), 650 °C (formation Ni-g-C<sub>3</sub>N<sub>4</sub>) and 700-900 °C (formation of the tube) leads directly and without acid etching to Ni- or Co-doped N-CNT with ultrahigh loading of 20 wt%, which is the highest value reported to date. Based on XRD analyses, the authors proposed that the individual atoms are incorporated in the carbon layers rather than confined between the carbon layers.

#### 1.4.2.2. Template-sacrificial method.

By using a template, it is also possible to modulate the textural characteristics of the desired catalyst. The template-sacrificial approach involves the addition of a textural agent or “template” that confers greater surface and porosity, which is thereafter eliminated by an etching process using acids or bases. Figure 1.33<sup>190</sup> shows three different template materials (SiO<sub>2</sub> particles, ordered mesoporous silica SBA-15, and montmorillonite clay (MMT)) that have been used for the synthesis of Co<sub>SA</sub>@N-C and Fe<sub>SA</sub>@N-C SAC. Vitamin B12 (VB12) and polyaniline-Fe (PANI-Fe) were selected as



cobalt and iron precursors, respectively. The high nitrogen/carbon atomic ratios of these precursors allow, after pyrolysis, the production of N-doped carbon materials with high nitrogen content (9.3-9.5 at% N from XPS for the Co SAC). As shown on Figure 1.33, different microstructures were obtained according to the geometric characteristics of the original templates. For example, a lamellar structure was produced after pyrolysis with MMT. Although these samples contain a relatively high cobalt loading (1.3-1.4 at%), TEM observation did not show the presence of any metal NP after the etching step with HF that dissolves both the inorganic templates and the metal or metal oxide NP. There are other examples of works using silica NP as template, from which worm-like porous materials were produced;<sup>204</sup> but under appropriated conditions it was also possible to keep the spherical structure after template removal.<sup>205,206</sup> Iron oxide nanocubes self-assembled in cubic superlattices and stabilized by oleic acid ligands were also used as sacrificial template (Figure 1.34).

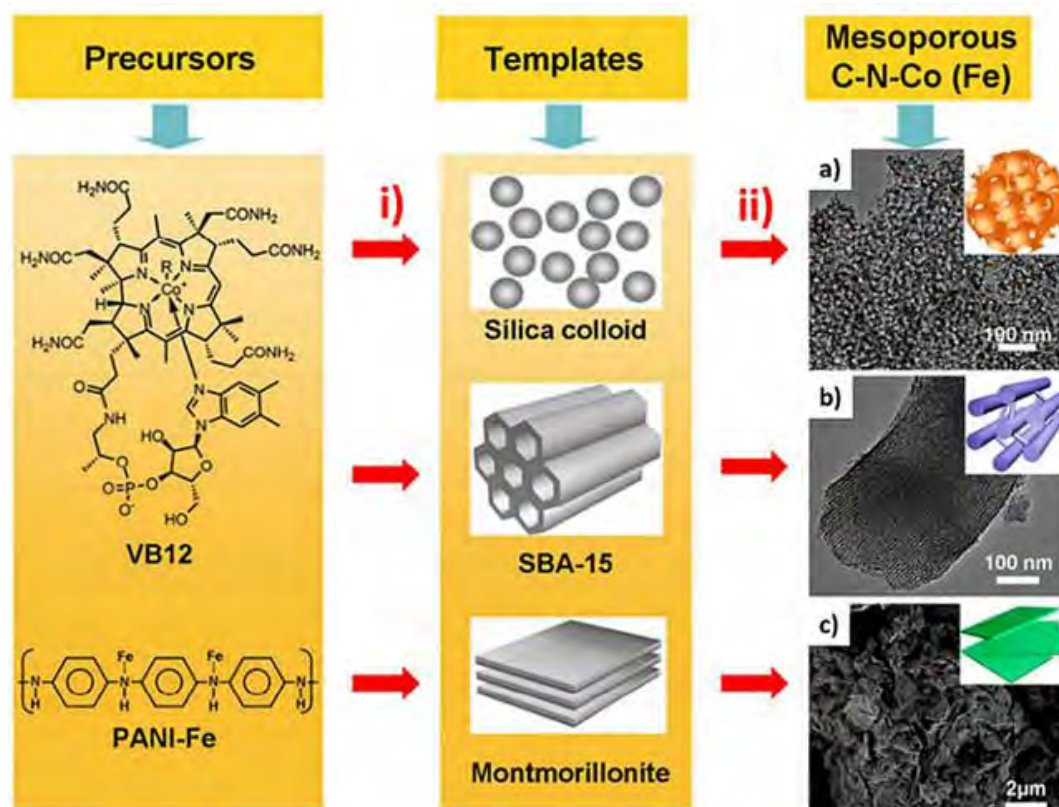


Figure 1.33. Template synthesis of mesoporous C–N–Co (Fe) catalysts; i) impregnation; and ii) pyrolysis and etching: (a) interconnected vesicle-like frameworks; (b) well-defined linear array of mesoporous structures; and (c) nanosheet-like structures. From ref. [190].

<sup>204</sup> J. Yuan, et al. *Chemical Communications* **2018**, 54, 2284-2287.

<sup>205</sup> J. Xi, et al. *Applied Catalysis B-Environmental* **2018**, 225, 291-297.

<sup>206</sup> Y. Wang, et al. *Acs Catalysis* **2015**, 5, 3887-3893.

In that process, the superlattices were obtained by a drying-mediated assembly of  $\text{Fe}_3\text{O}_4$  nanocubes. After a calcination step at 500 °C under argon, the carbonized sample was treated 3–5 times with HCl until no iron was detected by ICP in the supernatant. In a final step, N-doping was realized by a heat treatment under ammonia at 900 °C.

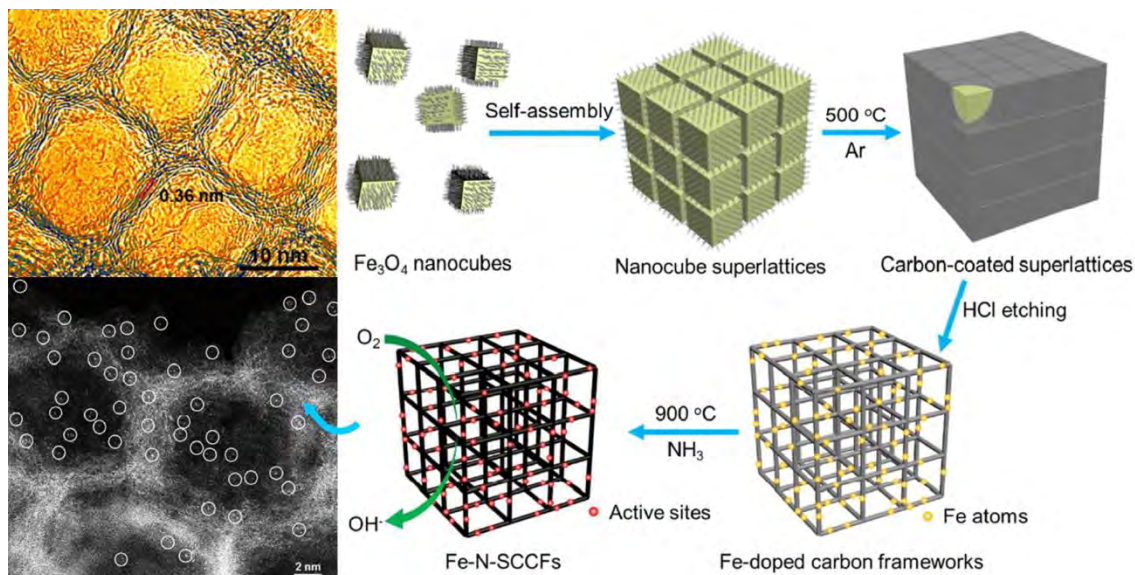


Figure 1.34. Schematic illustration of the fabrication of Fe-N-SCCFs. From ref. [193].

This latter treatment also contributes to the graphitization of the material, and to the partial reduction of  $\text{Fe}^{3+}$  into  $\text{Fe}^{2+}$  species. XANES analyses have shown that the coordination of iron was also affected by this treatment, from Fe–C coordination before  $\text{NH}_3$  treatment to Fe–N coordination after treatment. Although it is difficult to control the iron loading with this method,  $\text{Fe}_{\text{SA}}$  were systematically observed by STEM-HAADF (Figure 1.34) for samples showing a 1–2 wt % iron loading.

#### 1.4.2.3. Polymerization method

This method consists in a one-step reaction for network-doping during the  $\text{g-C}_3\text{N}_4$  synthesis involving the use of a metallic precursor as a monomer. Silver tricyanomethanide with cyanamide (Figure 1.35)<sup>194</sup> were used as starting molecules to produce  $\text{Ag}_{\text{SA}}/\text{g-C}_3\text{N}_4$  ranging from 1 to 10 wt% of silver. After the polymerization, carried out at 550 °C no Ag NP were observed. If silica nanosphere template was used during the synthesis, a reverse replication of the template was obtained after etching. This is an encouraging strategy to produce well-organized and dispersed SAC. Furthermore, the introduction of negative charges in the structure of carbon nitrides can be beneficial since it contributes to a change in the bandgap of this material.<sup>195</sup> Alternatively, thermal polymerization at 550 °C of melamine–Cu complex and cyanuric acid produces porous



hollow g-C<sub>3</sub>N<sub>4</sub> spheres (HCNS) inlaid with single Cu atoms. HR-TEM images indicates that no NP or clusters are present on Cu<sub>SA</sub>/HCNS.<sup>207</sup>

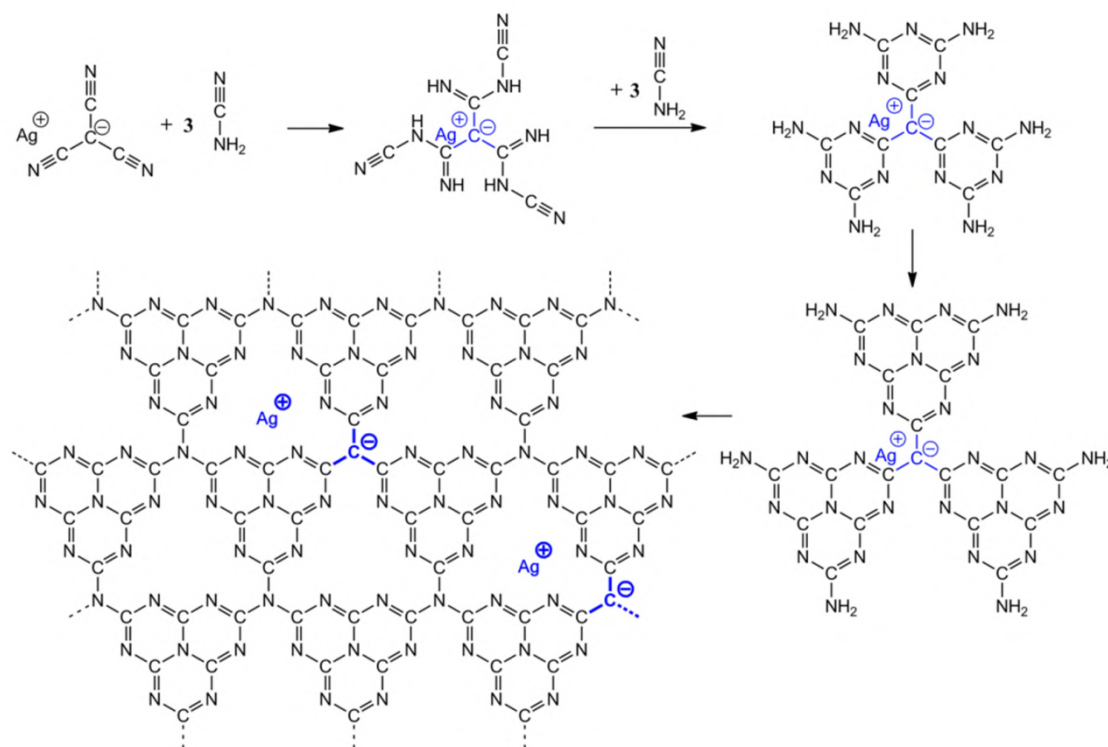


Figure 1.35. Modification of a carbon nitride network with silver tricyanomethanide. From ref. [195].

Another report using this method indicates the use of inorganic metal salts ( $\text{NiCl}_2 \cdot 6\text{H}_2\text{O}$ ,  $\text{FeCl}_3 \cdot 6\text{H}_2\text{O}$ ) and dicyandiamide (DCDA) to produce the corresponding complexes for later growing Ni and Fe-doped g-C<sub>3</sub>N<sub>4</sub> nano-patches around CNT skeletons, where isolated Ni and Fe atoms were embedded into the tri-*s*-triazine units of g-C<sub>3</sub>N<sub>4</sub> (Fig. 1.36).<sup>208</sup> The metal contents in this sample were found to be 2.0 wt% Ni and 2.6 wt% Fe. The reason to use CNT as a carbon-based skeleton is that: i) g-C<sub>3</sub>N<sub>4</sub> can be immobilized *in situ*; ii) it benefits from charge transfer, iii) there is the suppression of the stacking between g-C<sub>3</sub>N<sub>4</sub> layers, and iv) there is an improvement of the surface area.

<sup>207</sup> T. Zhang, et al. *Journal of the American Chemical Society* **2018a**, 140, 16936-16940.

<sup>208</sup> D. Liu, et al. *Journal of Materials Chemistry A* **2018a**, 6, 6840-6846.

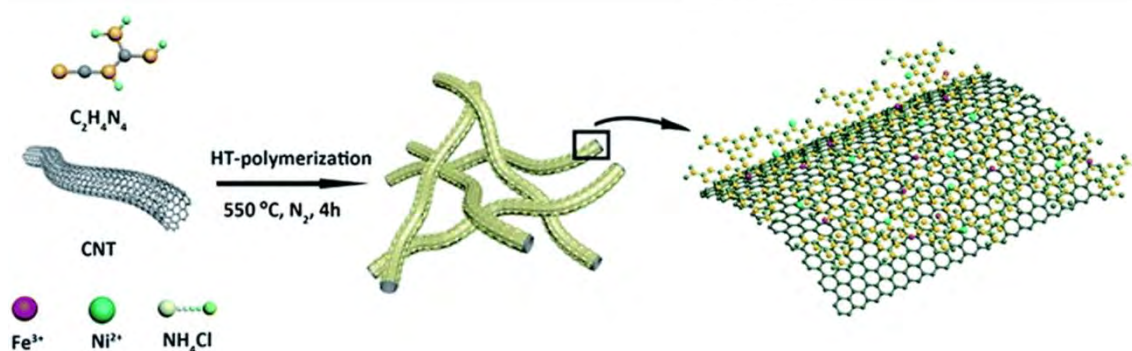


Figure 1.36. Schematic illustration of the fabrication of the rationally designed NiFe@g-C<sub>3</sub>N<sub>4</sub>/CNT. From ref. [208].

#### 1.4.2.4. Other methods.

There are a couple of isolated cases, where other pathways are used to successfully achieve the deposition of high quantities of single atoms. Among them, we can find surface grafting. For example, the functionalization of the support with thiol groups, which are known for their high affinity for precious metals, allows the production of Pt<sub>SA</sub> on thiolated CNT.<sup>197,209</sup> A fine control of the deposition rate by controlling temperature and pH has allowed the deposition of subnanometer patches of amorphous Co hydroxides on N-doped CNT.<sup>196</sup> Transition metal fullerides, in which each metallic atom acts as a binder between C<sub>60</sub> fullerenes were produced by decomposition of coordination complexes of Co, Ru and Rh in the presence of C<sub>60</sub>.<sup>210,211</sup> This method is interesting because it is simple and allows obtaining high metal loading. High-energy ball milling was used to obtain in large quantity Fe-doped graphene nanosheets by reacting a nitrogen-containing iron precursor and graphene during 20 hours with steel balls.<sup>294</sup> The evaporation of niobium atoms from bulk phase by arc-discharge during the simultaneous decomposition of methane has also been used.<sup>212</sup> The formed black smoke that was deposited on the cool walls of the reactor was mainly composed of onion-like structures, containing 13.7 % w/w of Nb and 86.3 % of carbon. However, annular dark-field images unambiguously indicate that the single niobium atoms are prone to migrate from the carbon matrix and aggregated into niobium carbide clusters, reducing the dispersion. Nanoporous graphene with nickel single-atoms was prepared by dealloying Ni<sub>30</sub>Mn<sub>70</sub> alloy sheets with (NH<sub>4</sub>)<sub>2</sub>SO<sub>4</sub> and further chemical vapor deposition using benzene for

<sup>209</sup> L. Wang, et al. *Science Advances* **2019a**, 5, 8.

<sup>210</sup> Z. Luo, et al. *Catalysis Science & Technology* **2019**, 9, 6884-6898.

<sup>211</sup> V. Lavrentiev, et al. *Chemical Physics Letters* **2006**, 424, 101-104.

<sup>212</sup> X. Zhang, et al. *Nature Communications* **2013**, 4.

graphene growth.<sup>213</sup> The content of Ni (4-8 at. % by EDX) as dopants was controlled by the dissolution time of the alloy.

### 1.5. Catalysis with single atom catalysts on carbon-based materials

Without doubt, catalysis on isolated atoms has become one of the most promising areas for new discoveries in heterogeneous catalysis.<sup>18,214</sup> Indeed, in addition to saving metal, these isolated atoms often have a specific reactivity different from that obtained on metal surfaces. This can lead to an acceleration of the reaction rate and therefore to new reactivities, both in terms of activity and selectivity. In addition, as we saw in the previous section, their modes of preparation sometimes lead to entities anchored very firmly on the support, which gives them a great stability, which, too, can be exploited in catalysis. This last point distinguishes them particularly from supported homogeneous catalyst, which often lead to leaching, greatly limiting their industrial use. Finally, the fact that theoretical studies can be carried out easily should lead to a good understanding of these systems, and their optimization be simplified compared to supported catalysts based on metal particles. This set of advantages makes that SAC deposited on carbon materials have already been used in a large number of catalytic reactions in thermal-, electro- or photo-catalysis.<sup>215,216,217</sup>

#### 1.5.1. Oxygen reduction reaction

A fuel cell generally converts directly chemical combustion energy (oxidoreduction) into electrical energy, heat and water. Fuel cells are differentiated first by the nature of their electrolyte, acidic electrolytes leading protons from the anode to the cathode, or basic in the opposite direction. The charge transfer rate (ions or electrons) mainly determines the electrochemical activity of the electrodes. For an H<sub>2</sub>/O<sub>2</sub> fuel cell, the oxidation reaction of hydrogen is extremely rapid while the oxygen reduction reaction (ORR) is comparatively extremely slow. The ORR being limiting for this reconversion of energy, it requires large quantities of a powerful catalyst.<sup>218</sup>

Today, the catalysts used are essentially composed of quasi-spherical Pt<sub>NP</sub> supported on carbon black mixed with an ionomer. The metal loading is typically of the order of 400 µg/cm<sup>2</sup> at the cathode and 100 µg/cm<sup>2</sup> at the anode, requiring about 0.5 g<sub>Pt</sub>/kW (*i. e.* 10

---

<sup>213</sup> H. J. Qiu, et al. *Angewandte Chemie-International Edition* **2015**, *54*, 14031-14035.

<sup>214</sup> X. Cui, et al. *Nature Catalysis* **2018**, *1*, 385-397.

<sup>215</sup> M. Dhiman, et al. *Chemcatchem* **2018**, *10*, 881-906.

<sup>216</sup> L. Wang, et al. *Chinese Journal of Catalysis* **2017e**, *38*, 1528-1539.

<sup>217</sup> Y. L. Guo, et al. *Catalysts* **2019**, *9*, 135.

<sup>218</sup> J. Kim, et al. *Chemsuschem* **2018**, *11*, 104-113.

times more Pt metals than in a catalytic converter vehicle equipped with an internal combustion engine). Cost reduction can be achieved by two approaches, either reducing the amounts of Pt or eliminating its use completely. In relation to the first measure, it becomes obvious to deepen the use of SAC for ORR, considering its original precept, which considers the maximum and ideal dispersion of the metal on the support. Nevertheless, a recent article indicates that pure carbon-supported single Pt atoms are electron deficient, and as such are almost inert to ORR process.<sup>174</sup> By contrast, it has been demonstrated in multiple recent reports the effectiveness of metal-nitrogen-doped carbon systems, mostly using Fe<sup>219</sup> and Co<sup>220</sup> but also Pt,<sup>221</sup> Ru<sup>222</sup> and Zn.<sup>223</sup> DFT calculations have also predicted that SAC of Au, Co, and Ag on graphene could be used as ORR catalysts.<sup>224</sup> Due to their low cost, high surface area, stability and electronic conductivity, doped carbon materials, particularly nitrogen-doped carbon materials, are particularly attractive as electrodes. It has been shown that in basic medium, these free-metal materials present an intrinsic activity close to that of Pt.<sup>225</sup> In that context, the combination of these nitrogen-sites with metal single atoms can boost the catalytic activity. Indeed, it has been shown that Co<sub>1</sub>-N<sub>x</sub>/C or Fe<sub>1</sub>-N<sub>x</sub>/C catalysts exhibit an electrochemical activity greater than the nitrogen-doped supports alone.<sup>226</sup> Theoretical evaluations validate those results confirming that the high electrochemical activity originates from the precise M-N coordination environment.<sup>227</sup> Even more, a report affirms that ORR does take place at a faster rate on a single atom than over NP. To prove that, a catalyst containing NP and SA, Co-NP/HNCS (HNCS=hollow N-doped carbon sphere) with 2.2 % w/w Co was evaluated in ORR in acidic 0.5 M H<sub>2</sub>SO<sub>4</sub> media.<sup>228</sup> With the passage of time the catalytic activity E<sub>1/2</sub> increased significantly by 32 mV due to the dissolution of Co<sub>NP</sub> in the acidic medium, suggesting that now, the exposed dispersed cobalt atoms (Figure 1.37) were responsible for the improved activity. After 5000 and 10000 cycles, the ORR activity of the catalyst remains constant, outlining the remarkable stability of this catalyst. The electrochemical performances of this system (E<sub>1/2</sub> = 0.773 V vs reversible hydrogen

<sup>219</sup> H. Shen, et al. *Nano Energy* **2017**, 35, 9-16.

<sup>220</sup> Q. Cheng, et al. *Acs Catalysis* **2017**, 7, 6864-6871.

<sup>221</sup> X. Zeng, et al. *Advanced Energy Materials* **2018**, 8, 1701345.

<sup>222</sup> C. Zhang, et al. *Acs Nano* **2017c**, 11, 6930-6941.

<sup>223</sup> J. Li, et al. *Angewandte Chemie International Edition* **2019c**, 58, 7035-7039.

<sup>224</sup> X. Chen, et al. *Applied Surface Science* **2016b**, 379, 291-295.

<sup>225</sup> A. Ferre-Vilaplana, et al. *Electrochimica Acta* **2016**, 204, 245-254.

<sup>226</sup> H. T. Chung, et al. *Science* **2017**, 357, 479-483.

<sup>227</sup> Y. Zheng, et al. *Journal of the American Chemical Society* **2017**, 139, 3336-3339.

<sup>228</sup> Y. Han, et al. *Journal of the American Chemical Society* **2017**, 139, 17269-17272.

electrode (RHE)), approaches the one of a commercial Pt/C catalyst (0.790 V). Additionally, to have more evidence of the role of the SA the authors decide to use poisoning agents to block the metallic atom and thus limit their reactivity.

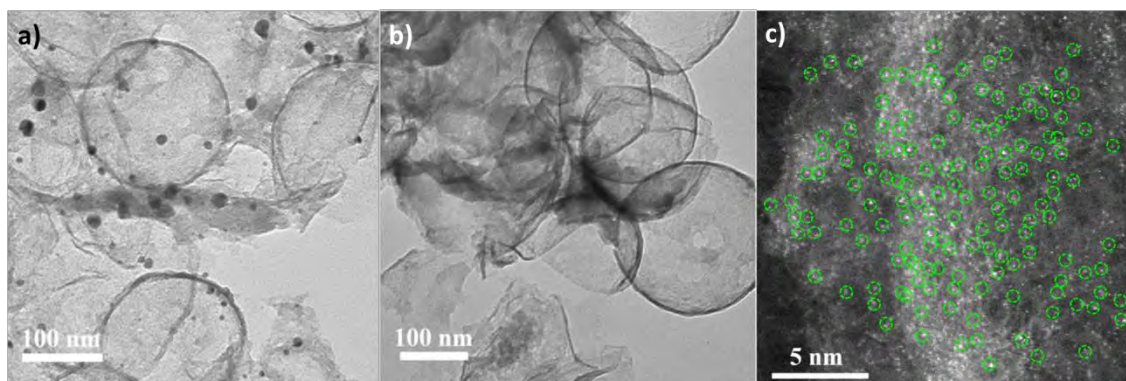


Figure 1.37. TEM images of  $Co_{NP}/HNCS$ : (a) before reaction; (b) after reaction; and (c) HAADF-STEM image of  $Co_{NP}/HNCS$  after CVs of 1000 cycles. From ref. [228].

Indeed, it is known that cyanate and thiocyanate anions coordinate strongly to metals, and consequently can passivate active sites. Following this principle, it has been shown that the introduction of  $CN^-$  ions on  $Fe_{SA}/N$ -doped C or  $Co_{SA}/N$ -doped C catalysts was detrimental to their performances in ORR, demonstrating the activity of these SAC.<sup>193,220</sup> Theoretical calculations have confirmed that  $FeN_4$  sites present in nitrogen-doped carbon materials can act as very efficient sites for oxygen adsorption and O=O bond cleavage, with performances reaching the ones of platinum.<sup>229,230</sup> Important achievements have also been obtained in terms of selectivity. Taking into account the mechanism of the reduction of oxygen, the reaction can proceed involving either four-electron reduction ( $4e^-$ ) from  $O_2$  to  $H_2O$  ( $O_2 + 4H^+ + 4e^- \rightarrow 2H_2O$ ) or two-electron reduction ( $2e^-$ ) of  $O_2$  to  $H_2O_2$  ( $O_2 + 2H^+ + 2e^- \rightarrow H_2O_2$ ).<sup>231</sup> A direct  $4e^-$  pathway is highly preferred in order to get high efficiency in fuel cell operations. ORR polarization curves at different rotation rates can be measured to determine whether the reaction occurs by a 4- or 2-electron pathway. By using the Koutecky-Levich equation, the electron-transfer number ( $\eta$ ) can be calculated. SAC have demonstrated an excellent selectivity, obtaining values of  $\eta > 3.5$ , pointing to the preferential path of  $4e^-$  and production of  $H_2O$ . To validate this result, it is also possible to perform measurements to detect the generation of reactive intermediate

<sup>229</sup> L. Yang, et al. *Proceedings of the National Academy of Sciences* **2018c**, 115, 6626.

<sup>230</sup> H. Zhang, et al. *Journal of the American Chemical Society* **2017d**, 139, 14143-14149.

<sup>231</sup> S. Kattel, et al. *Physical Chemistry Chemical Physics* **2013**, 15, 148-153.

species or hydrogen peroxide.<sup>232</sup> For SA supported on carbon, values below 5 % of conversion toward H<sub>2</sub>O<sub>2</sub> were systematically reported.<sup>233,234,235</sup> In contrast, we can find examples of catalyst based on other carbon supports, particularly carbides, which are able to change the selectivity towards the formation of hydrogen peroxide, as for Pt/TiC<sup>236</sup> or Pt/S-doped-C.<sup>185</sup>

The long-term stability of these systems, which is essential for commercial application of these catalysts, was often assessed during the amperometric measurements on ORR. SAC display a remarkable resistance and stability, and in the majority of the cases better than the benchmark Pt/C catalyst. The resistance of SAC to methanol crossover in a direct methanol fuel cell (DMFC) was also evidenced for Ru<sup>222</sup> and Fe<sup>237</sup> SAC. It is worth noting that when the mass activity is normalized by the metal loading, in 100 % of the cases the SAC show a better result in comparison with commercial Pt/C, which contains usually between 10 and 20 wt% of Pt, indicating that the SAC could notably increase the utilization of metal, provided higher metal loadings are achieved.<sup>238</sup>

Besides the above-mentioned application SA bifunctional catalysts, capable of assist ORR and oxygen evolution reaction (OER), play a major role in the construction of zinc-air batteries.<sup>239</sup> Exploring efficient (and low cost) materials is of a paramount importance to promote the practical applications. To this effect, SAC over graphitic carbon-based porous materials have shown great potential due to their high specific surface area and good electroconductivity. Several publications have shown high catalytical performance of M-N-C sites for ORR and OER. For instance, Co-N-C,<sup>240,241</sup> Cu-N-C,<sup>242</sup> Mn-N-C<sup>243</sup> and Mo-N-C<sup>244</sup> deliver a charging–discharging gap of above 0.86 V, which is superior to that of a benchmark Pt-Ir/C catalyst (0.775 V) and 20 wt % Pt/C (0.83 V).

<sup>232</sup> Z. Jia, et al. In *Rotating Electrode Methods and Oxygen Reduction Electrocatalysts*, edited by W. Xing, et al.; Elsevier. Amsterdam (2014a), pp. 199-229.

<sup>233</sup> P. Song, et al. *Advanced Functional Materials* **2017**, 27, 1700802.

<sup>234</sup> A. Zitolo, et al. *Nature Materials* **2015**, 14, 937.

<sup>235</sup> A. Zitolo, et al. *Nature Communications* **2017**, 8.

<sup>236</sup> S. Shin, et al. *Chemical Communications* **2019**, 55, 6389-6392.

<sup>237</sup> Y. Chen, et al. *Angewandte Chemie-International Edition* **2017d**, 56, 6937-6941.

<sup>238</sup> X. Wan, et al. *Journal of Power Sources* **2017**, 346, 80-88.

<sup>239</sup> W. M. Zhang, et al. *Nanomaterials* **2019c**, 9, 1402.

<sup>240</sup> B. Q. Li, et al. *Advanced Materials* **2019a**, 31, 1900592.

<sup>241</sup> W. Xie, et al. *Advanced Functional Materials* **2019**, 29, 1906477.

<sup>242</sup> Y. Wang, et al. *ACS Applied Energy Materials* **2019c**, 2, 8659-8666.

<sup>243</sup> Z. Lin, et al. *ACS Sustainable Chemistry & Engineering* **2020**, 8, 427-434.

<sup>244</sup> Z. Kou, et al. *Nano Energy* **2020**, 67, 104288.



### 1.5.2. Hydrogen and oxygen evolution reactions

Hydrogen (HER) and oxygen (OER) evolution reactions are key reactions in various electrochemical systems.<sup>245</sup> For these reactions, as for ORR, it has been evidenced that the catalytic activity of SAC is highly correlated with the local environment of the metal center, namely its coordination number and electronegativity of the nearest neighbor atoms.<sup>246</sup> This result points the necessity to precisely control the synthesis of SAC. The HER is important in electrocatalysis as well as for the concept of a “hydrogen economy”. Indeed, hydrogen evolution from water electrolysis is one of the efficient ways to obtain clean hydrogen energy in the future.<sup>247</sup> Among the many electrocatalysts, multiple investigations<sup>248</sup> have demonstrated the effectiveness of isolated Pt sites, coordinated either directly by carbon atoms but mainly by nitrogen, as responsible for the catalytic performances, allowing reaching the best activity.

As example, platinum atoms can be immobilized on GDY by coordination with the alkynyl carbon atoms of the support (Figure 1.38).<sup>249</sup> These SAC show exceptionally high catalytic activity for HER, with a mass activity up to 26.9 higher than a state-of-the-art commercial Pt/C catalyst. This excellent behavior in HER was related to the optimal Gibbs free energy for hydrogen adsorption  $\Delta G_{H^*}^{Pt}$  (0.092 eV) over an individual Pt active site anchored on GDY with a C<sub>2</sub>-Pt-Cl<sub>2</sub> coordination environment (Figure 1.38), which is close to that on the surface of Pt metal ( $\Delta G_{H^*}^{Pt} \approx -0.09$  eV). A novel approach for stabilization of Pt atoms (0.53 % w/w) was carried out using the pyrolysis of Pt-impregnated mesostructured polydopamine particles to produce porous carbon matrix.<sup>250</sup>

---

<sup>245</sup> L. Zhang, et al. *Acs Catalysis* **2017a**, 7, 7855-7865.

<sup>246</sup> H. Xu, et al. *Nature Catalysis* **2018b**, 1, 339-348.

<sup>247</sup> P. C. K. Vesborg, et al. *Journal of Physical Chemistry Letters* **2015**, 6, 951-957.

<sup>248</sup> C. Zhu, et al. *Angewandte Chemie-International Edition* **2017**, 56, 13944-13960.

<sup>249</sup> X.-P. Yin, et al. *Angewandte Chemie International Edition* **2018**, 57, 9382-9386.

<sup>250</sup> H. Zhang, et al. *Science Advances* **2018b**, 4, eaao6657.



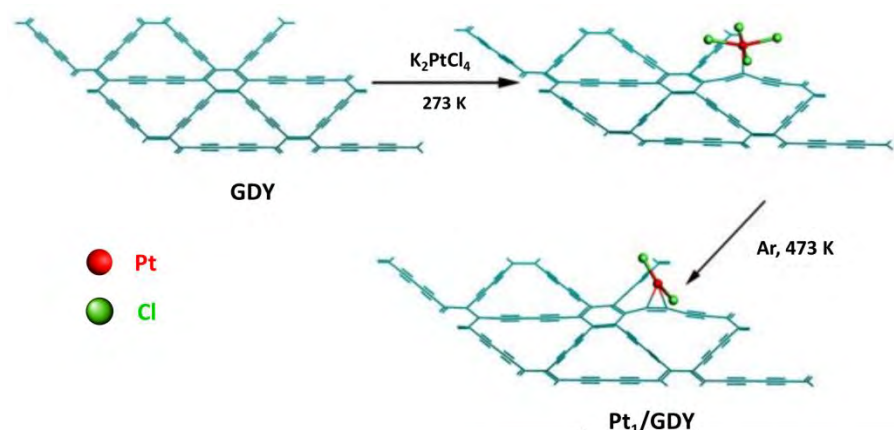


Figure 1.38. Schematic illustration for the synthesis of Pt<sub>SA</sub>-GDY catalyst. From ref. [249].

Based on experiments and DFT calculation, it was proposed that the isolated Pt centers can activate the adjacent C/N atoms, making these non-metal atoms electrocatalytically active for HER. Another study proposed that due to the strong electron transfer from the Pt to the adjacent coordinated N, the unoccupied Pt 5d orbitals can interact with H 1s orbitals to form an hydride.<sup>251</sup> This allows not only to increase the number of chemically bonded H atoms, but also to decrease the adsorption energy of H<sub>2</sub>.

Other studies have proposed that atomic clusters (dimers, trimers, etc.) exist in many SAC, exhibiting superb electrocatalytic activity. Such atomic clusters deposited on defective graphene (Pt<sub>n</sub>-DG)<sup>252</sup> and N-doped graphene/g-C<sub>3</sub>N<sub>4</sub> (Pt<sub>n</sub>-NG/C)<sup>253</sup> showed excellent HER performances. These catalyst with metal loading of 2 wt% show an activity 2.5 times higher than Pt/C at a overpotential of 50 mV (36.9 and 14.8 mA/cm<sup>2</sup>, respectively when current is normalized with the geometric surface area of the electrode) and 21 times higher than that of a 20 wt% Pt/C reference catalyst when normalization is made with the Pt loading.

In spite of these results, the high cost and scarcity of platinum largely limit its wide application. Therefore, it is significant to develop non-precious metal catalysts with high activity, good retention, low cost and environmental benignancy to replace Pt in both ORR and HER. In an effort to produce cheap, efficient and durable alternatives, mainly Co, Ni and Fe SAC have been investigated. Fei *et al.* reported a low cost and direct approach for distributing cobalt atoms onto nitrogen-doped graphene (Co<sub>SA</sub>/NG) for

<sup>251</sup> T. Li, et al. *Acs Catalysis* **2018a**, 8, 8450-8458.

<sup>252</sup> Q. Cheng, et al. *Journal of the American Chemical Society* **2020**, 142, 5594-5601.

<sup>253</sup> M. Sun, et al. *ACS Catalysis* **2019b**, 9, 8213-8223.

HER.<sup>173</sup> This catalyst is robust and highly active in aqueous media with very low overpotentials (30 mV). Deep investigation and electrochemical testing confirm that the catalytically active centers are isolated cobalt atoms coordinated to nitrogen ( $\text{MN}_4\text{C}_4$  species). These  $\text{MN}_4\text{C}_4$  species were also predicted by DFT to be efficient catalysts for the OER with activities following the trend  $\text{Ni} > \text{Co} > \text{Fe}$ , which was confirmed by electrochemical measurements.<sup>254</sup>

DFT calculations have also shown that single-atom transition metal (Pt, Pd, Co, Ni, Cu) supported on g- $\text{C}_3\text{N}_4$  should be high-performance OER catalysts.<sup>255</sup> Cobalt on N-doped graphene (0.7 wt%) requires an ultra-low onset overpotential of approximately 210 mV on a glassy carbon electrode in both 1.0 M KOH and 0.1 M KOH solutions for OER.<sup>256</sup> Although the most studied active sites for this reaction correspond to metal-nitrogen sites, it has been evidenced cases in which oxygen-coordinated metal promotes performance at OER. Atomically dispersed Ni-oxygen species on graphene-like carbon (Ni-O-G) show overpotential of 224 mV, two times lower than  $\text{NiO}_{\text{NP}}$  anchored on graphene (450 mV).<sup>257</sup> XPS, EXAFS and DFT reveal that nickel has a valence state higher than +2 (+ 2.34) due to the coordination with six oxygen atoms in the configuration  $\text{Ni-O}_4(\text{OH})_2$ . These sites allow a lower energy barrier (the formation of  $\text{O}^*$  is the rate-determining step) compared with NiO and even Ni/N-G SAC.

Finally, it is important to note that the overall water splitting reaction involves anodic OER and cathodic HER. Therefore, the ultimate goal for SAC would be to generate a unique bifunctional electrocatalyst capable to simultaneously promote both HER and OER.<sup>258,259,260</sup>

### 1.5.3. Photocatalysis

Searching for highly efficient photocatalysts has become a strategic domain all over the world, due to their promising applications for energy conversion (particularly HER) and environment (photo-oxidation reactions). However, an important issue is that some of these catalysts are seriously mismatched with the solar spectrum. Their large band gap restricts their use to the UV-light. To face this this problem, g- $\text{C}_3\text{N}_4$  is particularly

<sup>254</sup> H. Fei, et al. *Nature Catalysis* **2018**, 1, 63-72.

<sup>255</sup> X. Li, et al. *Chemical Communications* **2016b**, 52, 13233-13236.

<sup>256</sup> Q. Q. Zhang, et al. *Chemical Communications* **2020a**, 56, 794-797.

<sup>257</sup> Y. Li, et al. *Advanced Science* **2020c**, 7, 1903089.

<sup>258</sup> W. H. Lai, et al. *Angewandte Chemie-International Edition* **2019**, 58, 11868-11873.

<sup>259</sup> G. Gao, et al. *Catalysis Science & Technology* **2018b**, 8, 996-1001.

<sup>260</sup> X. S. Lv, et al. *Applied Catalysis B-Environmental* **2020**, 264, 118521.

attractive, due to its moderate band gap (2.7 eV) that allows absorbing light up to 450 nm. In spite of that, g-C<sub>3</sub>N<sub>4</sub> suffers from a low quantum efficiency originated from its slow charge mobility and high recombination rate of photo-generated electron-hole pairs. The introduction of single-atom noble metals in the cavities of g-C<sub>3</sub>N<sub>4</sub> provides an interesting strategy to modulate the electronic structure. Indeed, metal and non-metal atom doping are one of the most effective and convenient ways to improve the separation rate of photo-generated electrons and holes. Au,<sup>261</sup> Fe<sup>262</sup> and Pt<sup>263</sup> single-atoms were embedded in g-C<sub>3</sub>N<sub>4</sub> and used as a co-catalyst in photocatalytic HER. It was recently shown that N vacancies in g-C<sub>3</sub>N<sub>4</sub> are efficient for the reactive metal-support interaction (RMSI). This allows not only improving the stability of supported Pt<sub>SA</sub> thanks to strong Pt–C bonds, but also enhancing the performances of Pt SAC for capturing electron and evolving H<sub>2</sub> thanks to electronic and geometric effects.<sup>264</sup> Pt SAC largely enhanced the hydrogen production with performances 9 times higher than that of Pt<sub>NP</sub>, and 50 times higher than that of the bare support. Theoretical as well as experimental works have shown that Pt and Pd atoms trapped between g-C<sub>3</sub>N<sub>4</sub> layers act as bridges that facilitate the charge carrier transfer between the layers (interlayer charge transfer),<sup>265</sup> exhibiting superior optical absorption.<sup>266</sup> In general, the participation of metallic impurities imposes additional binding functions, which lowers the band gap to enhance the absorption of visible light.<sup>267</sup> Figure 1.39<sup>268</sup> displays the absorbance of the metal-containing samples in the visible region. In all cases the absorption of light was higher than that of pure g-C<sub>3</sub>N<sub>4</sub>. Environmental remediation, through the degradation of organic pollutants such as dyes, hormones and medicines from the water have been studied over single atom photocatalyst. Co-N<sub>4</sub>/carbon quantum dots<sup>269</sup> was used for the degradation of organic dyes and Cu/C<sub>3</sub>N<sub>4</sub><sup>270</sup> for degradation of norfloxacin antibiotic. Chen *et al.* prepared a set of different catalysts using Fe, Cu, Ti, Ni and Zn, getting the best results in the photo-oxidation of benzene to phenol with Fe/g-C<sub>3</sub>N<sub>4</sub>.<sup>267</sup>

<sup>261</sup> L. Zeng, et al. *Journal of Materials Chemistry A* **2019**, 7, 24217-24221.

<sup>262</sup> W. Y. Zhang, et al. *Small* **2019b**, 1905166.

<sup>263</sup> M. Ou, et al. *International Journal of Hydrogen Energy* **2017**, 42, 27043-27054.

<sup>264</sup> P. Zhou, et al. *Nano Energy* **2019b**, 56, 127-137.

<sup>265</sup> S. Cao, et al. *Advanced Functional Materials* **2018**, 28, 1802169.

<sup>266</sup> T. Tong, et al. *Applied Surface Science* **2018**, 433, 1175-1183.

<sup>267</sup> G. Dong, et al. *Journal of Photochemistry and Photobiology C-Photochemistry Reviews* **2014**, 20, 33-50.

<sup>268</sup> Z. Ding, et al. *ChemSusChem* **2011**, 4, 274-281.

<sup>269</sup> Q. Wang, et al. *Chemistry of Materials* **2020**, 32, 734-743.

<sup>270</sup> Y. H. Dai, et al. *Applied Surface Science* **2020**, 500.

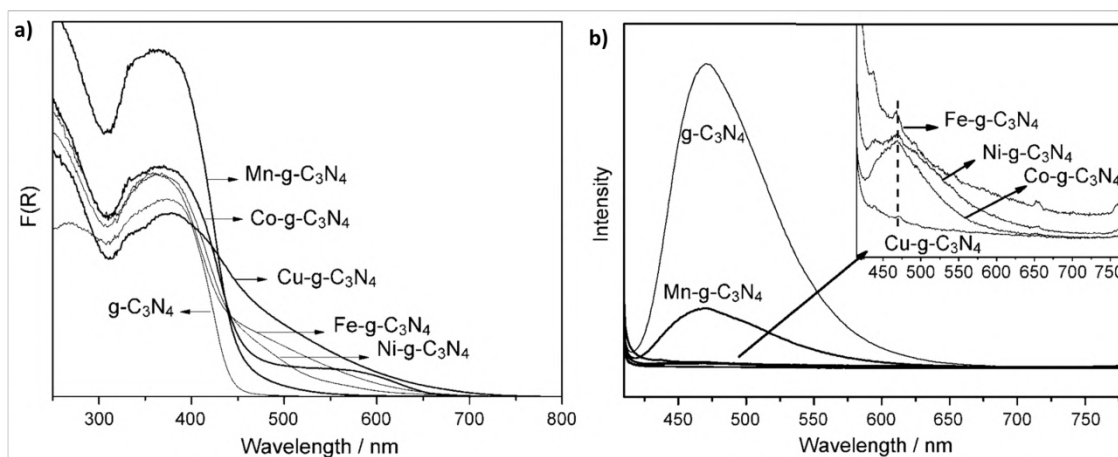


Figure 1.39. (a) UV/vis spectra of g-C<sub>3</sub>N<sub>4</sub> and M/g-C<sub>3</sub>N<sub>4</sub> (M = Mn, Fe, Co, Ni, Cu); (b) PL spectra of M/g-C<sub>3</sub>N<sub>4</sub> (M = Mn, Fe, Co, Ni, Cu) at 400 nm excitation at 298 K. From ref. [267].

Another drawback of g-C<sub>3</sub>N<sub>4</sub> is its low specific surface area, usually around 10 m<sup>2</sup>/g.<sup>271</sup> To overcome this inconvenient, the same research group expanded the surface area of the catalyst by coating mesoporous silica (SBA-15) with nanometer thin Fe/g-C<sub>3</sub>N<sub>4</sub> layers.<sup>272</sup> Table 1.3 shows the results obtained for phenol production from benzene oxidation using H<sub>2</sub>O<sub>2</sub> and visible light. The TOF are markedly increased in the systems 0.2 % Fe/g-C<sub>3</sub>N<sub>4</sub>/SBA-15 compared with the system without SBA-15, either after exposition to radiation or not. This improvement is associated to the obtained high exposed structure of Fe/g-C<sub>3</sub>N<sub>4</sub>, and also to the homogeneous atomic Fe-coating achieved. It should be noted that Fe loadings higher than 0.1 % w/w lead to a decrease of the specific surface area, and consequently to lower reaction TOF. Finally, it can be seen that in the absence of g-C<sub>3</sub>N<sub>4</sub>, the Fe/SAB-15 SAC is practically inactive; this demonstrating the synergic effect between the metal and the carbon support. Among plenty of variables, the photooxidation activity can also be enhanced by the choice of the oxidants, such as H<sub>2</sub>O<sub>2</sub>, persulfate (PS) and peroxymonosulfate (PMS). The activation of the oxidant to produce highly reactive species occurs thanks to the electrons photogenerated on the catalyst surface. In this context, Ag<sub>SA</sub> immobilized on a mesoporous g-C<sub>3</sub>N<sub>4</sub> were produced and used as catalyst to degrade bisphenol A in the presence of PMS.<sup>194</sup> A positive effect of Ag content increment on the band gap energies was measured. The band gap decreases from 2.50 to 2.09 eV from 1 % to 10 % w/w Ag<sub>1</sub>/g-C<sub>3</sub>N<sub>4</sub>, respectively.

<sup>271</sup> D. Feng, et al. *Carbon* **2017**, 125, 454-463.

<sup>272</sup> X. Chen, et al. *Journal of the American Chemical Society* **2009**, 131, 11658-11659.

Table 1.3. Catalytic activities for phenol production from benzene oxidation by g-C<sub>3</sub>N<sub>4</sub> based catalysts with (+) or without(–) visible light ( $\lambda > 420$  nm). From ref. [272].

Catalyst	$S_{BET}$ [m <sup>2</sup> /g]	$h\nu$	C <sub>6</sub> H <sub>6</sub> conv. (%)	TOF ×100 <sup>[a]</sup> [h <sup>−1</sup> ]
g-C <sub>3</sub> N <sub>4</sub>	–	–	0	–
g-C <sub>3</sub> N <sub>4</sub>	–	+	0	–
10 % Fe/g-C <sub>3</sub> N <sub>4</sub>	8	–	1.8	16
10 % Fe/g-C <sub>3</sub> N <sub>4</sub>	8	+	4.8	43
0.1 % Fe/g-C <sub>3</sub> N <sub>4</sub> /SBA-15	506	–	6.1	1257
0.2 % Fe/g-C <sub>3</sub> N <sub>4</sub> /SBA-15	451	–	6.7	836
0.2 % Fe/g-C <sub>3</sub> N <sub>4</sub> /SBA-15	451	+	11.9	1484
2.0 % Fe/g-C <sub>3</sub> N <sub>4</sub> /SBA-15	34	–	1.5	25
Fe/SBA-15	556	+	1.0	–

[a] Turnover frequency: n (phenol) per n (melem units) per hour.

This represents an improvement in the absorption of visible light. At the same time, the removal efficiency of bisphenol A increases from 88 % to 99.4 % with Ag contents from 1 % to 10 %. This improvement, directly associated with the increase of absorption in the visible region, is of course correlated to an increase in PMS activation, and thus to a greater concentration of reactive (SO<sub>4</sub><sup>−</sup>) species generated due to the higher concentration of photogenerated electrons. Silver single-atoms serve as electron traps to capture those electrons from the of g-C<sub>3</sub>N<sub>4</sub> conduction band, which results in a limited charge-recombination process, and further promote the photocatalytic efficiency of the Ag<sub>SA</sub>/g-C<sub>3</sub>N<sub>4</sub> SAC. Ag<sub>SA</sub>/g-C<sub>3</sub>N<sub>4</sub> SAC were also reported to be active for Naproxen photocatalytic degradation.<sup>273</sup> On the other hand, photocatalytic degradation of the Rhodamine B by H<sub>2</sub>O<sub>2</sub> activated with Fe<sub>SA</sub>/g-C<sub>3</sub>N<sub>4</sub> SAC under visible-light ( $\lambda > 420$  nm) irradiation has also been studied.<sup>274</sup> Although atomic Fe embedded in the g-C<sub>3</sub>N<sub>4</sub> is capable to perform the oxidation of Rhodamine B by itself, the light absorption properties of g-C<sub>3</sub>N<sub>4</sub> can be also manipulated due to the presence of non-metal doping (as phosphorous atoms), and therefore enhance even more the yields of the reaction. Figure 1.40a displays the semiconductor UV-Vis light absorption (originated by the charge transfer from the valence band populated by nitrogen 2*p* orbital to the conduction band formed by the carbon 2*p* orbital) of phosphorus doped carbon nitride (P-CN), which is compared to g-C<sub>3</sub>N<sub>4</sub>.<sup>167</sup>

<sup>273</sup> F. Wang, et al. *Applied Catalysis B-Environmental* **2018a**, 221, 510-520.

<sup>274</sup> X. Wang, et al. *Advanced Materials* **2009b**, 21, 1609.

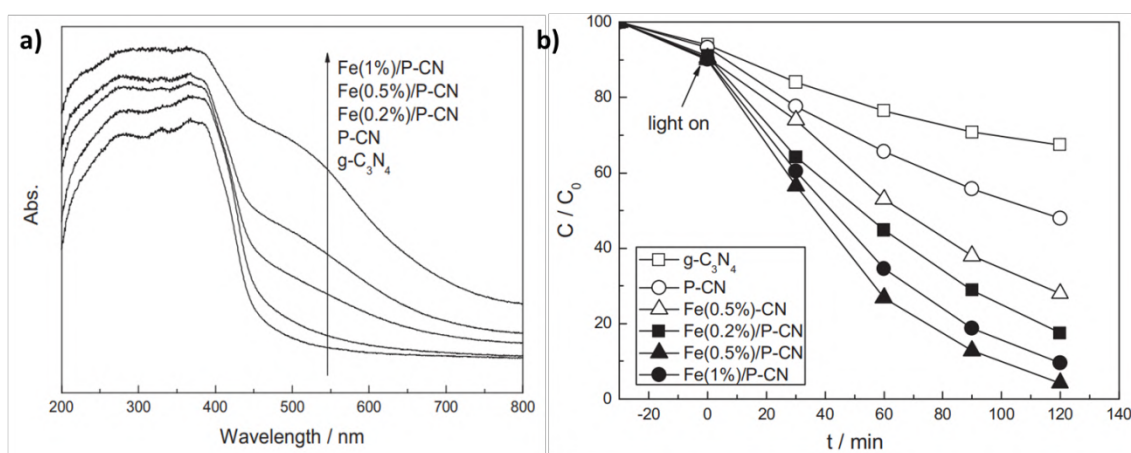


Figure 1.40. (a) UV-vis diffuse reflectance spectra of  $g\text{-C}_3\text{N}_4$  based catalysts. (b) Rhodamine B degradation rate over  $g\text{-C}_3\text{N}_4$  based catalysts under visible light. From ref. [167].

A clear red shift of the absorption band can be observed for the P-CN sample, indicating a decrease of the band gap energy. Theoretical calculations have confirmed that the band gap energy dropped rapidly when nitrogen was gradually replaced by phosphorous to form  $\text{C}_3\text{N}_{4-n}\text{P}_n$  compounds.<sup>275</sup> As a consequence, P-CN showed a higher activity than  $g\text{-C}_3\text{N}_4$  for Rhodamine B photooxidation (Figure 1.40b). Additionally, the increase of the absorption intensity for iron loaded P-CN samples in visible light region, when increasing the Fe loading, points to a strong interaction between the support and the metal. For 0.5 %Fe/P-CN catalysts, the activities were further improved in relation to 0.5 %Fe/ $g\text{-C}_3\text{N}_4$ . This Fe doping, in addition to the cooperative effect of P-doping, which also improved the  $S_{\text{BET}}$ , contribute to a further decrease of the band gap energy and to the limitation of the recombination of photo-generated electron-hole pairs. Another work reports loadings as high as 50 % w/w for Fe on  $g\text{-C}_3\text{N}_4$ , with the total absence of XRD peaks from iron species, such as Fe-Fe, Fe-O, Fe-Cl, and Fe-C.<sup>274</sup> These results suggest that iron species should be chemically coordinated to the support, most likely in the form of Fe-N bonds. These catalysts are able to activate  $\text{H}_2\text{O}_2$  for the direct oxidation of benzene to phenol, and for the oxidative degradation of various organic dyes using  $\text{H}_2\text{O}_2$  (e. g., Rhodamine B, methylene blue, methyl orange, and p-hydroxyazobenzene).

Finally, DFT calculations were used to elucidate the role of  $\text{Au}_{\text{SA}}$  in the enhancement of the photocatalytic activity of  $\text{Au}_{\text{SA}}/\text{GO}$ .<sup>276</sup> It was found that the work function of the gold single atom anchored on GO is lower than the one of GO due to the charge transfer from

<sup>275</sup> F. Ding, et al. *Computational Materials Science* **2004**, 30, 364-370.

<sup>276</sup> L. Ju, et al. *Surface Science* **2018**, 669, 71-78.



Au to GO, suggesting an enhancement of surface activity. In this system, the gold atoms act as electron traps and play a mediating role in electron transfer to the GO conduction band. In addition, the photogenerated electron-hole pairs are easily separated, and the lower band gap of the Au<sub>SA</sub>/GO SAC compared to bare GO will facilitate the light absorption.

#### 1.5.4. CO oxidation

The spectrum of study of CO oxidation has been dominated by metal oxides supports such as CeO<sub>2</sub>,<sup>19</sup> Al<sub>2</sub>O<sub>3</sub>,<sup>277</sup> and CuO,<sup>278</sup> among others; in the field of carbon materials there is not major development. There are only few examples of the use of carbon-supported SAC in the CO oxidation reaction.<sup>279</sup> P. Zhou *et al.*,<sup>280</sup> report the use of neighboring Pt and Ru (Pt–Ru) monomers on N-vacancy-rich g-C<sub>3</sub>N<sub>4</sub> (Figure 1.41). The catalytic tests were carried out at atmospheric pressure with reactant feedstocks of 1 vol% CO and 20 vol% O<sub>2</sub>. At 150 °C, PtRu/C<sub>3</sub>N<sub>4</sub> shows a lowest conversion temperature (T<sub>100%</sub>) compared with samples having each metal independently, suggesting the synergistic promotion effect of Pt–Ru monomers. A stability test was carried out by continuous reaction during 50 hours showing 100% CO conversion all over the course of the essay.

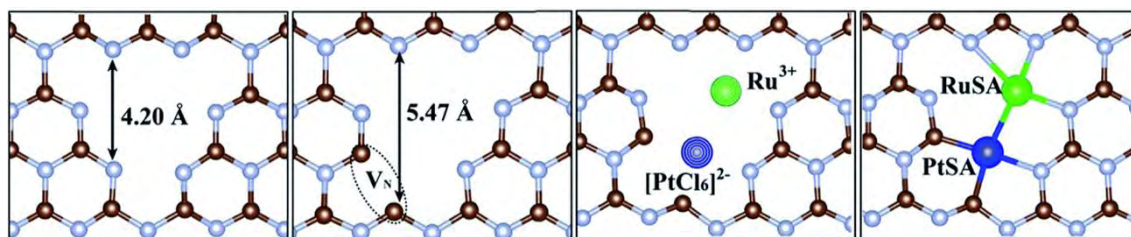


Figure 1.41. Schematic illustration of PtRu/C<sub>3</sub>N<sub>4</sub> catalyst. From ref. [280].

In recent studies, theoreticians have taken CO oxidation as a prototype reaction, delivering interesting results about the possible utilization as effective catalysts of atomically dispersed species over different carbon matrices. Langmuir-Hinshelwood (LH), Eley-Rideal (ER) and termolecular Eley-Rideal (TER) mechanisms can operate in this reaction. As shown on Figure 1.42a,<sup>281</sup> in ER mechanism, gaseous CO directly reacts with preadsorbed O<sub>2</sub>, and CO<sub>2</sub> is produced by the subsequent dissociation of the carbonate-like species.

<sup>277</sup> Z. Zhang, et al. *Nature Communications* **2017b**, 8.

<sup>278</sup> X. Zhou, et al. *Journal of the American Chemical Society* **2018**, 140, 554-557.

<sup>279</sup> Y. Zhao, et al. *RSC Advances* **2018**, 8, 1583-1592.

<sup>280</sup> P. Zhou, et al. *Chemical Science* **2019a**, 10, 5898-5905.

<sup>281</sup> Y. C. Rao, et al. *Physical Chemistry Chemical Physics* **2019**, 21, 25743-25748.

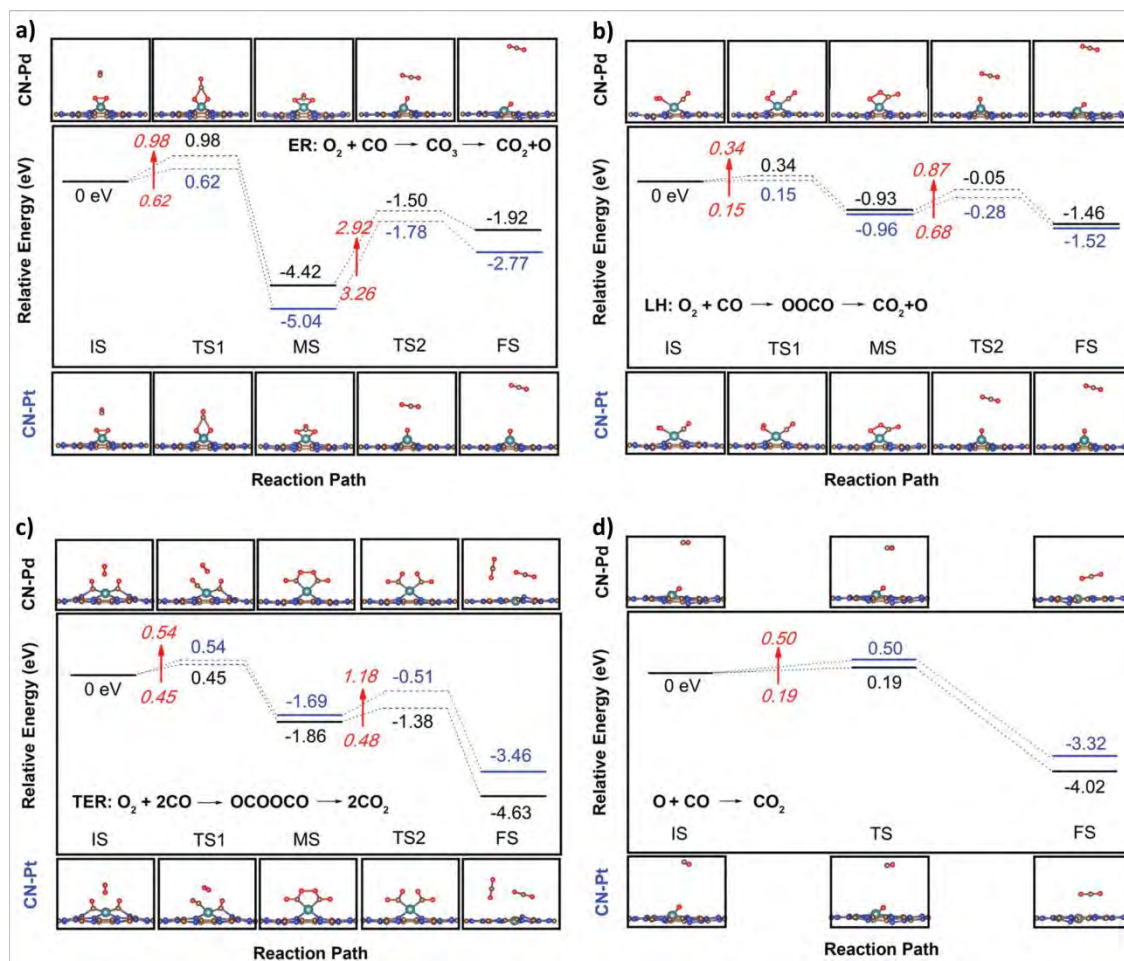


Figure 1.42. Schematic energy profiles of the (a) ER, (b) LH, (c) TER mechanisms, and (d) CO oxidation by atomic O along the minimum-energy pathway. All energies are given with respect to the reference energy (eV) of IS. From ref. [281].

Some systems such as Al/GO<sup>282</sup> and Co-N<sub>3</sub>/G,<sup>283</sup> proposed the ER mechanism, as be the most favorable. The LH mechanism involves in a first step the co-adsorption of CO and O<sub>2</sub> molecules, which is followed by the formation of a M-OOCO peroxy intermediate in which 2 oxygen and 1 carbon atoms are bound to the metallic center. Finally, the formation and desorption of CO<sub>2</sub> proceeds *via* the dissociation of the peroxy intermediate, leaving an adsorbed O (O<sub>ads</sub>) atom on the metal. Pt@CN (Figure 1.42b) is inclined to promote the CO oxidation through the LH mechanism, with a relatively small energy barrier of 0.68 eV. Other works have also reported prefer LH mechanism in the case of

<sup>282</sup> M. D. Esrafil, et al. *Journal of Molecular Graphics & Modelling* **2016**, 69, 8-16.

<sup>283</sup> Y. N. Tang, et al. *Journal of Physical Chemistry C* **2019b**, 123, 10926-10939.

Cr/G,<sup>284</sup> Fe/G,<sup>285</sup> Au/g-C<sub>3</sub>N<sub>4</sub>,<sup>286</sup> Mn/G,<sup>287</sup> Co/G,<sup>288</sup> Ni-N<sub>3</sub>/G,<sup>289</sup> Pt/penta-graphene<sup>290</sup> or Pd/G<sup>291</sup>. Contrarily to Pt, in Pd@CN (Figure 1.42c) the TER mechanism is more preferable. It is worth noting that the termolecular Eley-Rideal mechanism was also proposed for Mn-N<sub>4</sub>/CNT<sup>292</sup> and Pd/G.<sup>293</sup> In this mechanism, the dioxygen is activated in the presence of two CO molecules adsorbed on the Pd center, and the as-produced OOC–Pd–COO intermediate further dissociates to produce two carbon dioxide molecules synchronously. Au, Pd, Pt, Cu, Co, Mn, Ni and Al doped graphene are theoretically predicted to be potential catalysts for CO oxidation following a LH mechanism. Table 1.4 enlists diffusion barriers, binding energies and energy barriers of the determinant step of the reaction. It is shown that the reaction could process readily with activation energy lower of 0.8 eV<sup>294</sup>. It is thus possible to anticipate a high catalytic activity with such SAC. Diffusion energy barriers are large enough to suppose that metal clustering issues will be absent, with the exception of Fe, for which an easy agglomeration of atoms over the graphene could be observed. Of course, the location of the single atom in the graphene layer (H<sub>6</sub> site, N-doped site, SV or DV) will impact the course of the reaction, since strong electronic effects are anticipated, as shown in the first part of this review. Another way to predict clustering issues is the comparison between metal binding energy and its cohesive energy.

The binding energy of the atoms on graphene needs to be stronger than the cohesive energy. For instance, for Al–G (Table 1.4, entry 1) cohesive energy of Al–Al (3.39 eV) is inferior to the binding Al–C<sub>graph</sub> (5.60 eV), in that way the dopant can disperse on graphene quite stably without formation of nanoparticles. The good predicted catalytic performances of this type of SAC can be correlated to the partially occupied *d* orbital of the metal that is localized close to the Fermi level, due to the metal-support interaction.

<sup>284</sup> G. Dai, et al. *Journal of Materials Science* **2019**, 54, 1395-1408.

<sup>285</sup> Y. Tang, et al. *RSC Advances* **2016**, 6, 93985-93996.

<sup>286</sup> A. Kandala, et al. *Journal of the Indian Chemical Society* **2019**, 96, 1011-1017.

<sup>287</sup> L. Xu, et al. *Theoretical Chemistry Accounts* **2018a**, 137, 98.

<sup>288</sup> S. Ali, et al. *Journal of Materials Chemistry A* **2017**, 5, 16653-16662.

<sup>289</sup> M. Wang, et al. *RSC Advances* **2017d**, 7, 48819-48824.

<sup>290</sup> R. Krishnan, et al. *Physical Chemistry Chemical Physics* **2019**, 21, 12201-12208.

<sup>291</sup> X. Liu, et al. *ACS Catalysis* **2020a**, 10, 3084-3093.

<sup>292</sup> Z. Lu, et al. *Applied Surface Science* **2017**, 426, 1232-1240.

<sup>293</sup> G. Xu, et al. *Carbon* **2017**, 118, 35-42.

<sup>294</sup> Q. Deng, et al. *Small* **2013**, 9, 3506-3513.

Table 1.4. DFT calculated parameters for the reaction of oxidation of CO.

Entry	Metal	Support	Diffusion barrier [eV]	Energy barrier [eV]	M-C <sub>graph</sub> Binding energy [eV]	Cohesive energy eV/atom	E <sub>ads</sub> CO [eV]	E <sub>ads</sub> O <sub>2</sub> [eV]	E <sub>ads</sub> CO <sub>2</sub> [eV]	Ref.
1	Al	Graphene	2.98	0.32	5.60	3.39	0.83	1.57	0.16	<sup>295</sup>
2	Au	Graphene	n.i. <sup>[c]</sup>	0.31	n.i.	3.81	1.53	1.34	0.13	<sup>296</sup>
3	Fe	Graphene	0.66	0.57	n.i.	4.28	1.38	1.65	0.23	<sup>297</sup>
4	Cu	Graphene	2.34	0.54	n.i.	3.49	1.71	2.67	0.49	<sup>298</sup>
5	Pt	Graphene	5.62	0.58	7.23	5.84	0.86	1.49	0.03	<sup>299</sup>
6	Pd	Graphene	1.55	0.57	5.63	3.89	1.07	1.13	0.36	<sup>300</sup>
7	Ni	Graphene	3.41	0.58	7.57	4.44	1.25	1.65	0.33	<sup>301</sup>
8	Mn	Graphene	5.91	0.41	6.81	2.92	1.70	1.96	0.20	<sup>302</sup>
9	Co	PVG <sup>[d]</sup>	n.i.	0.86	n.i.	4.39	1.21	3.36	0.83	<sup>303</sup>
10	Fe	PVG <sup>[d]</sup>	n.i.	0.13	7.77	4.28	1.19	0.95	0.12	<sup>304</sup>

[a] Diffusion energy of the metal on the support. [b] Binding energy of the single atom to the support. [c] n.i. = no informed. [d] PVG = pyridinic vacancy in N-doped graphene.

Additionally, the low adsorption energy of the product, and the large exothermicity of the reaction strongly contribute to an easy CO<sub>2</sub> desorption and to the regeneration of the activated centers for subsequent CO oxidation. Considering the possibility to produce SAC on graphene and this literature on modelling studies, it is surprising that up today there is no abundant experimental reports on the use of SAC on carbon materials for this important reaction.

#### 1.5.5. Hydrogenation reactions

Selective hydrogenation is an important catalytic industrial process that until a few years ago only had thought possible to carry out on metallic NP. Nevertheless, it has been shown that SAC are capable of adsorbing the hydrogen molecule, and generate needed species to lead the hydrogenation of the reactants. For instance, Pt<sub>SA</sub>/N-C (Figure 1.43) showed an excellent chemoselectivity in the semi-hydrogenation of terminal alkynes to

<sup>295</sup> Q. G. Jiang, et al. *Rsc Advances* **2014**, *4*, 20290-20296.

<sup>296</sup> Y.-H. Lu, et al. *Journal of Physical Chemistry C* **2009**, *113*, 20156-20160.

<sup>297</sup> Y. Li, et al. *Journal of Physical Chemistry C* **2010b**, *114*, 6250-6254.

<sup>298</sup> E. H. Song, et al. *Journal of Physical Chemistry C* **2011**, *115*, 3678-3683.

<sup>299</sup> Y. Tang, et al. *Physical Chemistry Chemical Physics* **2012**, *14*, 16566-16572.

<sup>300</sup> T.-T. Jia, et al. *Journal of Nanoparticle Research* **2014b**, *16*.

<sup>301</sup> X.-Y. Xu, et al. *New Journal of Chemistry* **2016**, *40*, 9361-9369.

<sup>302</sup> Q. Jiang, et al. *Frontiers in Chemistry* **2018a**, *6*.

<sup>303</sup> X. Zhang, et al. *Journal of Molecular Catalysis a-Chemical* **2016a**, *417*, 28-35.

<sup>304</sup> Z. Liu, et al. *Rsc Advances* **2017b**, *7*, 7920-7928.

alkenes ( $\text{Pt}_{\text{SA}}/\text{N-C}$ , with 0.43 wt% Pt loading).<sup>305</sup> At 10 bar of  $\text{H}_2$ , 50 °C (Figure 1.43a,b)/80 °C (Figure 1.43c,d) and ratio Pt:substrate = 1:1200, SAC allows obtaining 99 % selectivity at 20 % conversion for all four molecules tested. In contrast, similar catalysis on  $\text{Pt}_{\text{NP}}/\text{N-C}$  induced the formation of multiple products, resulting from the co-hydrogenation of the secondary functional group. Additionally, other groups have reported good activity for SAC in the hydrogenation of triple bonds. For the reduction of phenylacetylene, Cu atoms anchored over the surface-defective nanodiamond–graphene ( $\text{Cu}/\text{ND@G}$ )<sup>306</sup> and  $\text{Pd}_{\text{SA}}$  fully embedded in the inner walls of mesoporous nitrogen-doped carbon foam nanospheres ( $\text{Pd}/\text{MPNC}$ )<sup>307</sup> show a higher activity compared with  $\text{Cu}_1/\text{nanodiamond}$ , and their Pd NP counterparts, respectively.<sup>308</sup> Interestingly, comparing (Pd, Pt, Au)  $\text{M}_{\text{NP}}@\text{ZIF-8}$  composites with their SA counterparts,  $\text{Pd}_{\text{SA}}$  exhibit significantly better activity and selectivity than metal  $\text{Pd}_{\text{NP}}$  for semi hydrogenation acetylene.<sup>178</sup> According to DFT calculations, the performance of this SAC was rationalized considering that hydrogenation of ethylene to ethane on  $\text{Pd}_{\text{SA}}$  requires two barriers of 0.93 and 1.22 eV to be overcome (only 0.62 and 0.35 eV on  $\text{Pd}_{\text{NP}}$ ). Furthermore, in the case of  $\text{Pd}_{\text{SA}}\text{-N}_4$  site these barriers lie above the ethylene level, which is not the case for  $\text{Pd}_{\text{NP}}$ . Also, coking resistance on  $\text{Pd}_{\text{SA}}$  is due to a geometric effect, since the multiple adjacent adsorption sites required for polymerization of acetylene or ethylene to form green oil (or coke) are not available, rendering fewer opportunities for coke formation than on an extended  $\text{Pd}_{\text{NP}}$  surface. Finally, HAADF-STEM images and EXAFS of Pd SAC showed the Pd remained atomically dispersed after catalysis and reducing treatment. Ni was also investigated for this reaction.

---

<sup>305</sup> X. H. He, et al. *Nature Communications* **2019**, *10*, 3663.

<sup>306</sup> F. Huang, et al. *Nature Communications* **2019**, *10*, 4431.

<sup>307</sup> Q. C. Feng, et al. *Advanced Materials* **2019**, *31*, 1901024.

<sup>308</sup> Y. J. Sun, et al. *Chemical Physics Letters* **2019a**, *723*, 39-43.

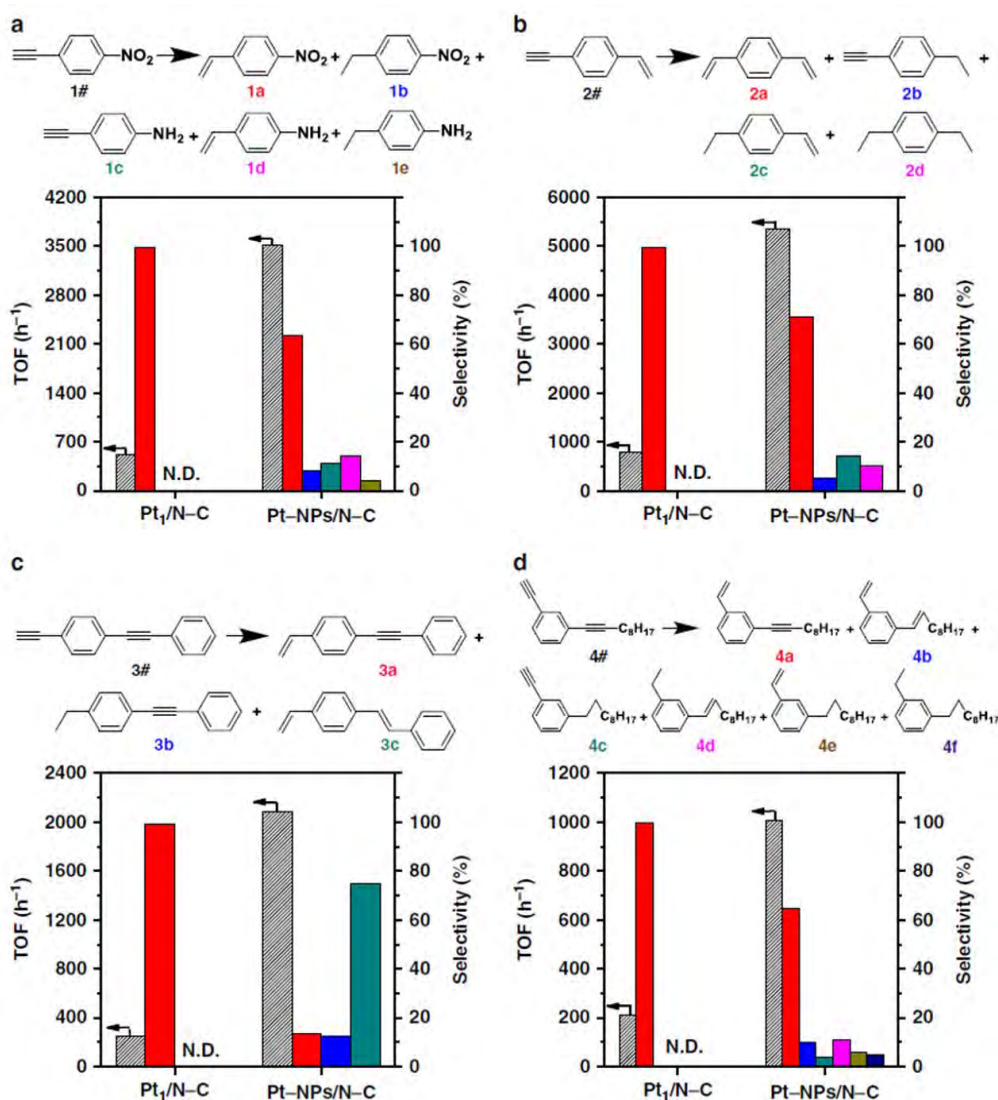


Figure 1.43. Catalytic performance of  $\text{Pt}_{\text{SA}}/\text{N-C}$  and  $\text{Pt}_{\text{NP}}/\text{N-C}$ . Reaction results for the hydrogenation of (a) 1-nitro-4-ethynylbenzene; (b) 1-ethynyl-4-vinylbenzene; (c) 1-ethynyl-4-(phenylethynyl)benzene; and (d) 1-(dec-1-yn-1-yl)-3-ethynylbenzene on  $\text{Pt}_{\text{SA}}/\text{N-C}$  and  $\text{Pt}_{\text{NP}}/\text{N-C}$ . From ref. [305].

A Ni SAC ( $\text{Ni}_{\text{SA}}$  embedded in an N-doped carbon) showed a conversion of acetylene and a selectivity for ethylene both over 90 %, whereas the selectivity shown by Ni NP on was less than 55 % at all tested temperatures.<sup>309</sup> The excellent selectivity of the Ni SAC for ethylene may have been due to the uniform coordination of N atoms around the Ni centers, allowing modifying the electronic density on the Ni atoms. DFT calculations and XANES analyses have shown that on N-doped carbon, the active center structure is  $\text{Ni-N}_4$ , and that an unusual heterolytic dihydrogen activation mode on a frustrated Lewis pair

<sup>309</sup> X. Dai, et al. *Chemical Communications* **2017**, 53, 11568-11571.



occurs.<sup>310</sup> Indeed, when H<sub>2</sub> approaches the Ni-N<sub>4</sub> center, it is activated *via* an interaction with Ni and the adjacent pyridinic N atoms.

The chemoselective hydrogenation of nitroarenes is a great challenge for SAC essentially because the relatively harsh conditions in which the reaction is carried out (T, H<sub>2</sub> pressure) promote to the agglomeration of the active phase or the destruction of the nanostructure. For instance, hydrogenation of 4-chloronitrobenzene (4-ClNB) has been investigated over 4.4 wt% Ni<sub>SA</sub>/N-C catalyst.<sup>311</sup> The maximal conversion (0.25 mmol) was reached after 8 hours of reaction at 120 °C, 30 bar of hydrogen, 5 mg of catalyst (4-ClNB/Ni  $\approx$  70) and 5 mL of ethanol as solvent. Nevertheless, deactivation process was evidenced in the recycling tests. The decreasing of catalytic activity can be related to the leaching of the active phase in the solution. The amount of nickel after 5 cycles was almost an half of the original quantity, proof of the poor stability of the catalyst. However, other reports have shown the effectiveness of SAC for the hydrogenation of nitroarenes.<sup>312,313</sup> Pt<sub>SA</sub> trapped in carbon onion graphitic shells (Pt<sub>SA</sub>@C), with an ultra-low Pt loading of 0.298 wt% showed an outstanding performance.<sup>314</sup> At 1 bar H<sub>2</sub>, 40 °C, 60 min, 0.5 mmol of 4-ClNB, > 99 % activity and 99 % selectivity were obtained (4-ClNB/Pt = 820). A cobalt SAC on a N-doped porous carbon support presenting Co-N<sub>x</sub> sites has shown high activity and selectivity (> 99 %) for the selective hydrogenation of nitrobenzene to aniline under relatively mild conditions (1-2 MPa, 70-100 °C).<sup>315</sup> This system also allows the selective production (> 99 %) of substituted anilines from functionalized nitroarenes. High performances of Co SAC on N-doped carbon supports were also reported by Zhou *et al.*<sup>180</sup> The Co<sub>SA</sub>/N-C SAC showed good performances in terms of activity, selectivity, and stability for the reduction under dihydrogen (3.5 bar) at 110 °C of various nitro compounds. Selectivity higher than 97 % were obtained at complete substrate conversion in water after 1.5 hours of reaction. This reaction can also be performed under milder conditions with nitrobenzene (40 °C, 1 bar H<sub>2</sub>) with an aniline yield of 98.7 % and a complete conversion. For comparison, a Pd/C catalyst under the same conditions allows also complete conversion but the selectivity to aniline was only 68 %. Pd SAC on r-GO were also reported to be extremely active for nitrophenol hydrogenation.<sup>205</sup> This result,

<sup>310</sup> W. Liu, et al. *Angewandte Chemie-International Edition* **2018b**, 57, 7071-7075.

<sup>311</sup> F. Yang, et al. *Green Chemistry* **2019**, 21, 704-711.

<sup>312</sup> H. N. Li, et al. *Science China-Materials* **2019b**, 62, 1306-1314.

<sup>313</sup> W. C. Cheong, et al. *Acs Applied Materials & Interfaces* **2019**, 11, 33819-33824.

<sup>314</sup> X. L. Yan, et al. *Carbon* **2019**, 143, 378-384.

<sup>315</sup> A. Hu, et al. *Molecular Catalysis* **2019**, 472, 27-36.

once again highlight the specific reactivity of SA compared to metallic NP. Moreover, this SAC was also active for the transfer hydrogenation reaction of nitrobenzene into aniline.

The performances of a single Pd atom catalyst on graphene were evaluated for the selective hydrogenation of 1,3-butadiene into butenes, and compared to those of different Pd<sub>NP</sub> catalysts.<sup>316</sup> Under mild reaction condition (50 °C), the distribution of butenes (100 % selectivity) at 95 % conversion was 71 % 1-butene (the most desirable product), 22 % *trans*-2-butene and 6 % *cis*-2-butene. In order to largely reduce the contributions from the isolated Pd atoms, Pd<sub>SA</sub>/graphene was annealed at 500 °C under Ar for 1 h to form Pd<sub>NP</sub> with an average size of 5.5 nm. As expected, the new catalyst shows a pronounced decrease of the butane selectivity ( $\approx 75\%$ ) and a different product distribution with 40 % 1-butene, 40 % *trans*-2-butene and 14 % *cis*-2-butene. The author proposed that, contrarily to Pd<sub>NP</sub>, on which butadiene adsorbed *via* the two double bonds (di- $\pi$ -adsorption), Pd<sub>SA</sub> favors the adsorption of the substrate *via* the mono- $\pi$ -adsorption mode, since the di- $\pi$ -adsorption usually requires a large ensemble of Pd atoms on the surface. The adsorption mode on SAC avoids complete hydrogenation of butadiene to butane and favors 1-butene production.

The performances of SAC were evaluated in the semi-hydrogenation of 2-methyl-3-butyn-2-ol.<sup>317</sup> Pd SAC was produced on g-C<sub>3</sub>N<sub>4</sub> supports presenting different crystallinity and different environment for the Pd atoms. The obtained results revealed an inverse correlation between the activity and the Pd oxidation degree. These findings further demonstrate the impact of tuning metal-support interaction in SAC by tailoring the electronic properties of the carbon support, where the least oxidized surface Pd<sup>2+</sup> species seems to be more active than the Pd<sup>4+</sup> species.

The valorization of biomass through the hydrogenation of model molecules such as furfural<sup>318</sup> (Ir<sub>SA</sub>/g-C<sub>3</sub>N<sub>4</sub>), benzaldehyde<sup>319</sup> (Co-N<sub>x</sub>-C) or vanillin<sup>320</sup> (Ru<sub>SA</sub>/g-C<sub>3</sub>N<sub>4</sub>) have been evaluated over SAC obtaining good results especially on selectivity. Finally, hydrogenation of quinoline into 1,2,3,4-tetrahydroquinoline was investigated on Co<sub>SA</sub>/N-

---

<sup>316</sup> H. Yan, et al. *Journal of the American Chemical Society* **2015**, *137*, 10484-10487.

<sup>317</sup> Z. Chen, et al. *National Science Review* **2018b**, *5*, 642-652.

<sup>318</sup> S. B. Tian, et al. *Acs Catalysis* **2019**, *9*, 5223-5230.

<sup>319</sup> W. Gong, et al. *Advanced Materials* **2019b**, *31*, 1808341.

<sup>320</sup> S. B. Tian, et al. *Journal of the American Chemical Society* **2018**, *140*, 11161-11164.

CNT,<sup>321</sup> Ru<sub>SA</sub>/N-C<sup>322</sup> and Ir<sub>SA</sub>/S-C<sup>323</sup> catalysts. On Co<sub>SA</sub>/N-CNT catalyst, the authors proposed that the vast majority of Co<sub>SA</sub> resides inside of N-CNT being inaccessible to the reactant. After the liberation of the confined Co through laser irradiation in liquid, TOF (100 °C, 20 bar, substrate/Co = 400) goes from 13 to 128 h<sup>-1</sup> proving the importance of the active site to be accessible. In contrast, the selectivity toward 1,2,3,4-tetrahydroquinoline ( $\approx$  99%) is found to be independent of this treatment. The Ru<sub>SA</sub>/N-C catalyst was more selective (99%) than Ru<sub>NP</sub> deposited on carbon (79%), and the Ir<sub>SA</sub>/S-C shown very high selectivity ( $>$  99%) and activity with a TOF of 1200 h<sup>-1</sup> (100 °C, 20 bar, substrate/Ir = 10) to be compared to 1200 h<sup>-1</sup> for a commercial Ir/C catalyst.

#### 1.5.6. CO<sub>2</sub> reduction

Catalytic CO<sub>2</sub> reduction using SAC has been investigated in thermal,<sup>324</sup> electro-<sup>325</sup> and photo-catalysis.<sup>326</sup> Only few examples of this reaction in gas phase has been reported using SA. Kwak *et al.*<sup>327</sup> showed that Pd<sub>SA</sub>/CNT was completely inactive for CO<sub>2</sub> reduction. The addition of lanthanum oxide to the inactive Pd<sub>SA</sub>/CNT system, allows to reach good conversion and very high selectivity towards CO, pointing to the importance of the support for this reaction, since it can contribute to CO<sub>2</sub> activation. In this sense, SAC over oxides such as TiO<sub>2</sub>,<sup>328,329</sup> MgO<sup>330</sup> and CeO<sub>2</sub><sup>331</sup> have been studied for CO<sub>2</sub> hydrogenation.

For the electrochemical CO<sub>2</sub> reduction reaction (CO<sub>2</sub>RR), carbon-supported SAC have attracted enormous attention. Indeed, the vast majority of studies associated to carbon-based single atoms are linked to electrochemical reactions.<sup>332</sup> Transition metal atoms N-coordinated are the major active center for CO<sub>2</sub> electroreduction due to the optimum binding energy with the intermediate species involved. EXAFS/XANES studies have allowed reaching some conclusions regarding the adsorption and activation of CO<sub>2</sub> on this SAC. Ni<sub>SA</sub> (2.8 to 4.6 % w/w) supported on g-C<sub>3</sub>N<sub>4</sub> were studied.<sup>333,334</sup> In these SAC,

<sup>321</sup> W. B. Gong, et al. *Advanced Materials* **2019a**, 31, 1906051.

<sup>322</sup> X. Wang, et al. S. B. Tian, et al. *Journal of the American Chemical Society* **2017**, 139, 9419-9422.

<sup>323</sup> L. Wang, et al. *Science Advances* **2019**, 5, eaax6322.

<sup>324</sup> J. D. Jimenez, et al. *ChemCatChem* **2020**, 12, 846-854.

<sup>325</sup> T. Zheng, et al. *Joule* **2019**, 3, 265-278.

<sup>326</sup> C. Gao, et al. *Advanced Materials* **2018a**, 30.

<sup>327</sup> J. H. Kwak, et al. *Acs Catalysis* **2013**, 3, 2094-2100.

<sup>328</sup> X. Su, et al. *Accounts of Chemical Research* **2019**, 52, 656-664.

<sup>329</sup> Y. Tang, et al. *Nature Communications* **2019a**, 10, 10.

<sup>330</sup> M. M. Millet, et al. *Journal of the American Chemical Society* **2019**, 141, 2451-2461.

<sup>331</sup> Y. Guo, et al. *Acs Catalysis* **2018**, 8, 6203-6215.

<sup>332</sup> Y. N. Chen, et al. *Small Methods* **2019**, 3, 1900523.

<sup>333</sup> J. G. Chen *Joule* **2018**, 2, 587-589.

<sup>334</sup> H. B. Yang, et al. *Nature Energy* **2018b**, 3, 140-147.

the Ni atoms have a NiN<sub>4</sub> environment (XANES and DFT analyses), and the oxidation state of Ni is +1. A charge transfer from Ni<sub>SA</sub> to the carbon 2 $\pi$  orbital of CO<sub>2</sub> allows the formation of Ni-CO<sub>2</sub> <sup>$\delta^-$</sup>  species, which could reduce the activation energy needed for CO<sub>2</sub> electroreduction. Among others, Ni-N<sub>4</sub><sup>335</sup> results to be the more cited active site for CO<sub>2</sub>RR, although Rong and co-workers<sup>336</sup> indicate that the vacancies in the support are also of paramount importance. Ni-N<sub>3</sub>-V displays extremely high electrocatalytic activity for CO<sub>2</sub> reduction, achieving a current density of 65 mA cm<sup>-2</sup> at -0.9 V *vs.* RHE, with a slow scan rate of 1 mV s<sup>-1</sup>. This value is much larger than those of Ni-N<sub>4</sub> (19 mA cm<sup>-2</sup>) and carbon matrix (12 mA cm<sup>-2</sup>), and also larger than those of most reported CO<sub>2</sub> reduction electrocatalysts. Active sites with a resulting porphyrin-like structure such as Zn-N<sub>4</sub>,<sup>337</sup> Fe-N<sub>4</sub>,<sup>338</sup> have been persistently identified as responsible for good faradic efficiencies to CO up to 80%, while in the case of Co there are some inconsistencies. All Co-N<sub>2</sub>,<sup>339</sup> Co-N<sub>4</sub><sup>340</sup> and Co-N<sub>5</sub><sup>341</sup> were reported to be the best coordination environment for the production of CO.

The possibility to use SA supported on graphene as CO<sub>2</sub> electroreduction catalysts was investigated using DFT calculations.<sup>342</sup> Complete energy profiles allow to predict the formation of methanol on Ni<sub>SA</sub>/G (limiting potential U<sub>L</sub> = -0.41 V), and particularly on Pt<sub>SA</sub>/G (-0.27 V), and the production of methane on Os<sub>SA</sub>/G (-0.52 V) and Ru<sub>1</sub>/G (-0.52 V). For Pt<sub>SA</sub>/G with the Pt atom located in a DV, the energy profile of the reaction is drastically different from on a Pt (211) surface, where energy barriers are much higher, and the product of the reaction is methane. Interestingly, it was shown that with SAC, the conventional linear relation between CO\* binding energy and the binding energy of the CHO intermediate, which is well respected for metallic surfaces, strongly deviates from linearity (Figure 1.44).

<sup>335</sup> C. Yan, et al. *Energy & Environmental Science* **2018a**, 11, 1204-1210.

<sup>336</sup> X. Rong, et al. *Angewandte Chemie International Edition* **2020**, 59, 1961-1965.

<sup>337</sup> F. Yang, et al. *Angewandte Chemie International Edition* **2018a**, 57, 12303-12307.

<sup>338</sup> F. Pan, et al. *ACS Catalysis* **2018b**, 8, 3116-3122.

<sup>339</sup> X. Q. Wang, et al. *Angewandte Chemie-International Edition* **2018d**, 57, 1944-1948.

<sup>340</sup> Z. Geng, et al. *Applied Catalysis B: Environmental* **2019**, 240, 234-240.

<sup>341</sup> Y. Pan, et al. *Journal of the American Chemical Society* **2018a**, 140, 4218-4221.

<sup>342</sup> S. Back, et al. *Chemical Science* **2017**, 8, 1090-1096.

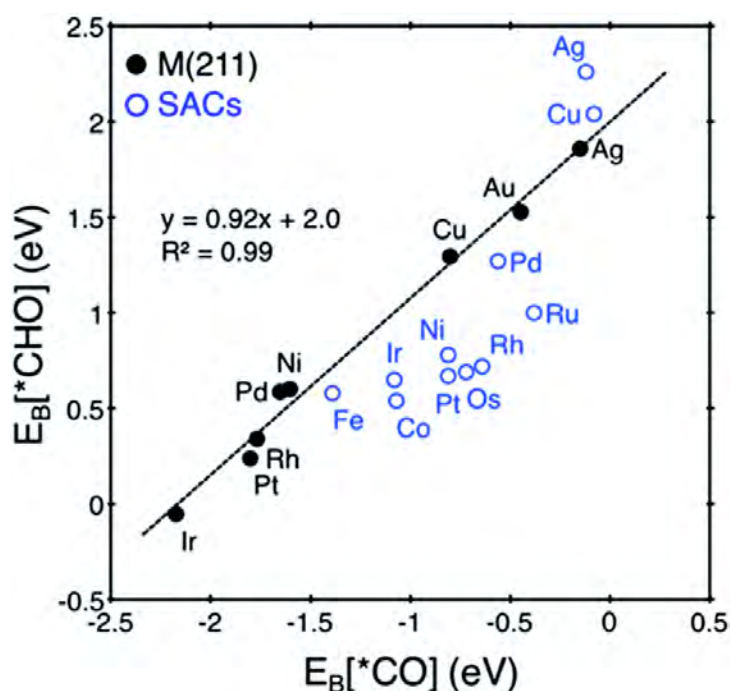


Figure 1.44 Correlation between  $EB[*CO]$  and  $EB[*CHO]$  for transition metal (211) surfaces (black) vs. SAC (blue). The conventional scaling relation for  $M$  (211) is broken in the case of SAC. From ref. [342].

Charge transfer between the metal and the support, as well as the lack of atomic ensemble are reasonable reasons that can explain these differences of reactivity. According to DFT calculations, it would also be possible to perform this reaction toward the selective formation of formic acid over embedded Ru,<sup>343</sup> Cu<sup>344</sup> and Ti<sup>345</sup> on graphene defects, pointing once again that tuning the coordination environment of single atoms is a fundamental aspect to take into account for the final application of the catalysts. In general, results are promising in CO<sub>2</sub> reduction to C<sub>1</sub> products. Production of C<sub>2+</sub> compounds requires further exploration.

Finally, in an effort to mimic the process of natural photosynthesis, the aqueous CO<sub>2</sub> reduction to CO over solar light was investigated on Ni<sub>SA</sub>/G SAC. High FE over 90 % under significant currents up to 60 mA/mg have been obtained with this catalyst.<sup>346</sup>

<sup>343</sup> D. N. Sredojević, et al. *ChemistrySelect* **2018**, 3, 2631-2637.

<sup>344</sup> J. Sirijaraensre, et al. *Applied Surface Science* **2016**, 364, 241-248.

<sup>345</sup> M. D. Esrafil, et al. *Chemical Physics Letters* **2017**, 682, 49-54.

<sup>346</sup> K. Jiang, et al. *Chem* **2017**, 3, 950-960.

## 1.5.7. Other reactions

Other reactions as varied as acetylene dehydrogenation of N-heterocycles,<sup>347,348</sup> hydrochlorination,<sup>349</sup> N-formylation of nitroarenes<sup>350</sup> coupling reaction,<sup>351,352,353</sup>  $\alpha,\beta$ -unsaturated aldehyde hydrogenolysis,<sup>354</sup> oxidation of ethylbenzene,<sup>355</sup> oxidation of alcohols,<sup>356</sup> cycloaddition of epoxides,<sup>357</sup> Fenton-like reaction<sup>358</sup> or N<sub>2</sub> reduction<sup>359</sup> have been also catalyzed by carbon-supported SAC, demonstrating encouraging results, which could lead to further industrial applications. A summary of the most interesting results are summarized in Table 1.5. Additionally, theoretical works have also highlighted the potential of SAC for other reactions. For example, the methane C–H bond activation, the first step in the mechanism of methane conversion into several desired products has been investigated.<sup>360</sup> The reaction has been studied over a set of single TM atoms such as Cr, Mn, Fe, Co and Cu adsorbed (H<sub>6</sub> site adsorption) and embedded (substitution of one C by the TM) in graphene. According to the results, the activation energy for the C–H activation for Cr-, Mn-, Fe-, Co-, and Cu-methane systems are 1.67 eV, 1.94 eV, 1.08 eV, 1.32 eV and 1.72 eV, respectively. These results suggest that the C–H bond can be activated on Fe or Co systems. Additionally, cobalt showed the highest binding energies onto the support for the adsorbed and embedded cases, suggesting that a Co<sub>SA</sub>/G SAC could be an efficient catalyst for methane activation. Thus, employing first principles calculations, a two-step reaction mechanism was evidenced for direct CH<sub>4</sub> oxidation to CH<sub>3</sub>OH over a Co<sub>SA</sub>/G SAC, with N<sub>2</sub>O as the O-donor molecule.<sup>361</sup> C–H activation was the rate-limiting step. In the case of Fe<sub>SA</sub>/G SAC it was shown by DFT that Fe<sub>SA</sub>/G@SV has lower energy barrier than that on Fe<sub>SA</sub>/G@DV for the cleavage of the first CH bond of methane.<sup>362</sup> Another group has investigated the transformation of methane to methanol

<sup>347</sup> S. Wei, et al. *Chemical Science*, **2020**, 11, 786-790

<sup>348</sup> Y. Han, et al. *Angewandte Chemie-International Edition* **2018**, 57, 11262-11266.

<sup>349</sup> Z. Chen, et al. *Acs Catalysis* **2020**, 10, 1865-1870.

<sup>350</sup> J. L. Li, et al. *Chemcatchem* **2020a**, doi:10.1002/cctc.201902109.

<sup>351</sup> A. Beltzung, et al. *Apl Materials* **2018**, 6, 100704.

<sup>352</sup> Z. Chen, et al. *Nature Nanotechnol* **2018**, 13, 702-707.

<sup>353</sup> E.-K. Lee, et al. *Journal of Catalysis* **2017**, 352, 388-393

<sup>354</sup> L. M. Ning, et al. *Carbon* **2019**, 154, 48-57.

<sup>355</sup> S. S. Jie, et al. *Molecular Catalysis* **2018**, 458, 1-8.

<sup>356</sup> Y. M. Lin, et al. *Acs Nano* **2019**, 13, 13995-14004.

<sup>357</sup> X. J. Cui, et al. *Chinese Journal of Catalysis* **2019**, 40, 1679-1685.

<sup>358</sup> W. Miao, et al. *Carbon* **2020**, 159, 461-470.

<sup>359</sup> B. Yu, et al. *Advanced Functional Materials* **2020**, 30, 1905665.

<sup>360</sup> S. Sahoo, et al. *ChemCatChem* **2018**, 10, 3229-3235.

<sup>361</sup> J. Yuan, et al. *Chemical Communications* **2018**, 54, 2284-2287

<sup>362</sup> C. Wu, et al. *Molecular Catalysis* **2019**, 469, 40-47.



not over one but two Pt atoms deposited on GO.<sup>363</sup> Apparently the presence of dimers allows the separate adsorption of CH<sub>4</sub> on Pt(1) and O<sub>2</sub> on Pt(2), which can favor the conversion. In a deeper insight of the behavior of SAC, the electro-oxidation of methanol has been used to analyze the influence of defects.<sup>364</sup> The calculations revealed that a SV allows stabilization of Pt, and that the Pt<sub>SA</sub>/G@SV shows good tolerance towards CO, compared to Pt<sub>SA</sub>/G or Pt<sub>SA</sub>/G@SW. However, it was also shown that the C–H/O–H cleavage activation energy was also significantly increases on Pt<sub>SA</sub>/G@SV, which should limit the catalytic activity. DFT calculations have also shown that the doping of CNT with nitrogen allows modulating the adsorption of several species involved in the methanol oxidation reaction, such as CH<sub>3</sub>OH, HCHO and HCOOH, which could be useful to modulate the catalytic performances. Besides, the direct dehydrogenation of propane to produce propylene has been investigated over Pt<sub>SA</sub> supported on N- and B-doped graphene.<sup>365</sup> The use of a N-doped support allows to reach higher reactivity for C–H bond activation than the B-doped graphene. The N-doped support renders the Pt center more electrodeficient (+0.45 from Bader charge analysis), while the B-doped support gives electrons to the metal (−0.85). The shift of the Pt *d*-band center, which impact the C–H activation step, explain the differences of activity, and a linear relation was established between C–H dissociation energy barrier, the complete reaction activation energy, and the charge on the Pt<sub>SA</sub>. Additionally, the calculated activation energy on Pt<sub>SA</sub>/N-G SAC is comparable or even lower than the calculated barriers on Pt(111) or Pt(211) surfaces, and Pt clusters, suggesting a higher activity of SA over NP. Ethylene epoxidation to produce ethylene oxide has been investigated on Au<sup>366</sup> and Ti<sup>367</sup> atoms dispersed on graphene. In the case of Au, the reaction would go through the formation of an intermediate species with a peroxametallacycle structure by the co-adsorption of C<sub>2</sub>H<sub>4</sub> and O<sub>2</sub>. The dissociation of this species is the rate determining step (*E*<sub>a</sub> = 0.84 eV) that produces ethylene oxide molecule and an adsorbed O atom. Further reaction of ethylene with the adsorbed O atom leads to the formation of a second ethylene oxide molecule. There also, the calculations have shown that it is the strong interaction between Au and a SV of graphene that tunes the energy level of Au *d* states, and finally the reactivity.

---

<sup>363</sup> S. Y. Wu, et al. *Physical Chemistry Chemical Physics* **2015b**, 17, 26191-26197.

<sup>364</sup> Q.-Y. Wang, et al. *Electrochimica Acta* **2016**, 216, 140-146.

<sup>365</sup> X. Sun, et al. *Journal of Physical Chemistry C* **2018a**, 122, 1570-1576.

<sup>366</sup> X. Liu, et al. *Catalysis Science & Technology* **2016a**, 6, 1632-1641.

<sup>367</sup> J. Sirijaraensre, et al. *Structural Chemistry* **2018**, 29, 159-170.

Table 1.5. Catalytic reactions performed on carbon-supported SAC.

Reaction	Catalyst	Performances	Ref.
Hydrogenative coupling of nitroarenes	3.6 %Co <sub>SA</sub> /N-doped-C	<p>Co-N-C (0.7 mol%) 80 °C, 3 MPa H<sub>2</sub> NaOH (0.2 equiv) t-BuOH (2 mL)</p> <p>isolated yield</p> <p>Yield ranging between 63 and 99 % according to the substrate</p>	188
Suzuki coupling	0.6 wt% Pd <sub>SA</sub> /C <sub>3</sub> N <sub>4</sub>	<p>PPh<sub>3</sub>, K<sub>2</sub>CO<sub>3</sub> DME:H<sub>2</sub>O (1.5:4.5) T = 393 K, P = 8 bar W<sub>cat</sub> = 0.1 g, <math>\tau</math> = 10 min</p> <p>Conv = 63%, Selec = 90% TOF = 549h<sup>-1</sup>, outperformed all of the investigated homogeneous catalysts</p>	352
Reductive coupling of nitrobenzene	Co <sub>SA</sub> /N-doped-C	<p>180 °C 12 hours 20 bar N<sub>2</sub> Benzyl alcohol</p> <p>Co<sub>SA</sub>/N-C (conv. 100% - S = 91.4%) &gt; homogeneous Ir Pd catalyst (yield = 76%)</p>	205
N <sub>2</sub> reduction reaction	1.1% Fe-N-C	The electrochemical N <sub>2</sub> RR was tested in N <sub>2</sub> -saturated 0.1 M KOH (30 mL in each cell compartment) at ambient T and P. Selectivity 100% to formation of ammonia Faradaic efficiency of 56.55%	368
Selective aerobic oxidation of alcohols	M <sub>SA</sub> /N-doped-C (M=Fe, Cu, Cr, Ni, Co)	<p>HMF HDO GLYCEROL ETHANOL</p> <p>HMF (80 °C - 8h - 10 bar O<sub>2</sub>): conv. = 49 % - S<sub>aldehyde</sub> = 78 % Ethanol (80 °C-8h-10 bar O<sub>2</sub>): conv. = 4 % - S<sub>aldehyde</sub> = 98 %</p>	192
Hydroalkoxylation of 3-buten-1-ol	Pt <sub>SA</sub> /CNT	<p>Catalyst, PPh<sub>3</sub> dioxane, 8 h, 80 °C</p> <p>Pt<sub>SA</sub>/CNT (conv. = 70 %) &gt; [Pt(COD)Cl<sub>2</sub>] (conv. = 10 %) &gt; Pt<sub>NP</sub>/CNT (conv. = &lt;&lt; 10 %)</p>	369
Dehydrogenation and transfer hydrogenation of N-heterocycles	Co-N-Carbon	<p>Ar 120 °C BHT</p> <p>Conv = 99%, 8h</p> <p>HCOOH Toluene 100 °C 4h</p> <p>Conv = 99%, selec = 99%</p>	370
Fenton-like reaction	Co-N-graphene	oxidation of bisphenol A via activation of peroxymonosulfate TOF=12.51 min <sup>-1</sup> at room T°, pH=6.0	371

<sup>368</sup> M. F. Wang, et al. *Nature Communications* **2019b**, 10, 341.<sup>369</sup> H. Woo, et al. *Bulletin of the Korean Chemical Society* **2017**, 38, 1221-1225.<sup>370</sup> Y. H. Han, et al. *Angewandte Chemie-International Edition* **2018**, 57, 11262-11266.<sup>371</sup> X. Li, et al. *Journal of the American Chemical Society* **2018d**, 140, 12469-12475.

In contrast, over  $\text{Ti}_{\text{SA}}/\text{G@SV}$ ,  $\text{C}_2\text{H}_4$  ethylene reacts directly with a peroxo ligand previously produced by the  $\text{O}_2$  adsorption, which lead to ethylene epoxidation. The computational results reveal that the highly electron deficient Ti centers significantly enhance the activation of the adsorbed  $\text{O}_2$ . Without the defective graphene support, Ti atoms are not active for this reaction. SAC have been proposed to be very selective electrocatalysts for the electrochemical reduction of dinitrogen to produce  $\text{NH}_3$ , in that sense that their use should limit very significantly the HER.<sup>372</sup> Various TM were investigated (Mo, Nb, V, Mn, Ti, Sc) both on graphene SV and in the  $\text{MN}_4$  environment of a N-doped graphene. It was proposed that the main reason of the selectivity was the formation on these SAC of very unstable  $\text{M}_{\text{SA}}\text{-H}$  and  $\text{M}_{\text{SA}}\text{-NH}_2$  species due to the absence of ensemble effect. The high potential activity of these catalysts originates from a charge transfer from the metal to the support ( $1.8\text{ e}^-$  in the case of titanium) that makes Ti atoms very electrodeficient, which can favor nitrogen activation. Mo atoms supported on N-doped carbon support have also been predicted to be potential catalysts for this reaction.<sup>373</sup>

## 1.6. Conclusion

The rapidly emerging field of single-atom catalysis aims at reducing precious metal loading in supported catalysts, and at tuning catalytic reactivity in numerous reactions. As such, and provided there are stable, SAC present great potential for industrial catalysis in the future. The stabilization of SA on carbon supports is possible if there are sites allowing a strong interaction with the support. These sites may be vacancies, or heteroatoms introduced by doping. Some carbon supports such as g- $\text{C}_3\text{N}_4$  or graphyne and graphdiyne are particularly interesting because they allow a well-controlled environment of SA. Such an environment induces a strong stabilization of the SA, since multi-coordination occurs, as well as marked electronic effects that can significantly affect their reactivity. The use of carbon supports presents the advantage of being able to modulate these electronic interactions, for example by doping the support with specific heteroelements, such as nitrogen, oxygen, boron or sulfur. If some carbon supports have a relatively well-defined surface, which allows a fine control of the environment of the SA, it should be noted that the majority of carbon supports present a very heterogeneous surface. Substantial efforts are therefore necessary in the synthesis and characterization

---

<sup>372</sup> C. Choi, et al. *Acs Catalysis* **2018**, 8, 7517-7525.

<sup>373</sup> C. Ling, et al. *Journal of Physical Chemistry C* **2018**, 122, 16842-16847.

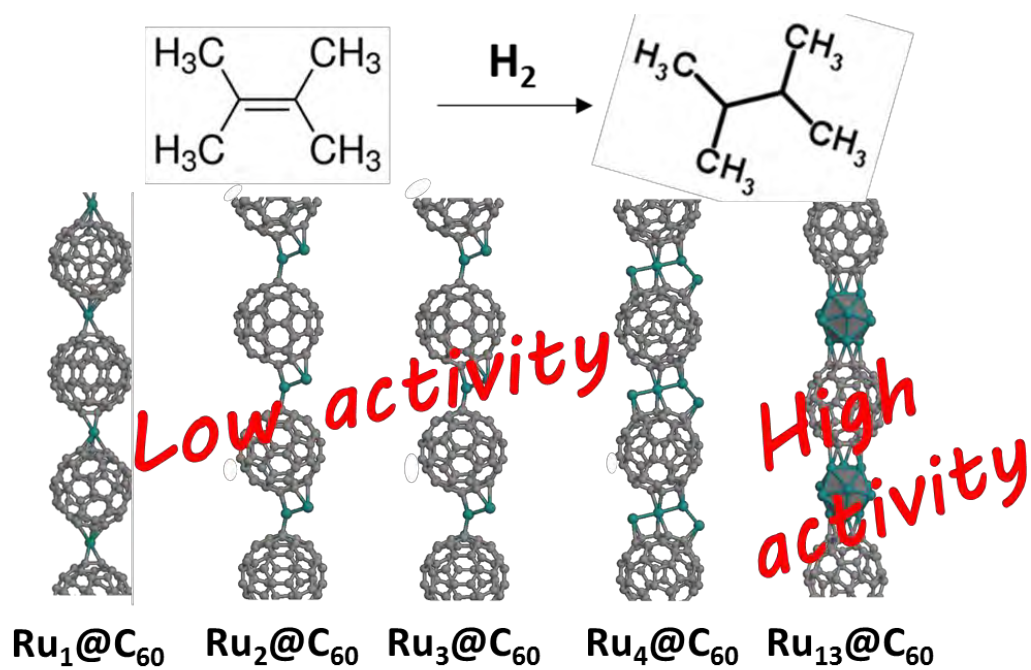
of these supports, to better control the type and amount of surface defects, in order to produce SAC with a control environment. With regard to the preparation of SAC on carbon supports, it appears quite simple to prepare catalysts with low metal loading on most supports using conventional methods of catalyst preparation. Methods that are more efficient are still needed to be developed to obtain SAC with high metal loadings ( $>1\%$  w/w). Indeed, the methods used so far suffer either not to guarantee a localization of the SA on the surface of the support (atoms may be present in the bulk material); or to use washes with strong acids that are not compatible with the stated desire to reduce the amount of metal precursors in the preparation of these catalysts. Advanced characterization techniques, such as STEM, EXAFS, XANES, DRIFTS, and NMR, along with DFT studies allow most of the time verifying the atomic nature of the catalysts and preferred binding sites. However, unravelling the mechanisms of a SAC under reaction conditions requires a level of resolution that is yet to be demonstrated. The number of catalytic reactions for which SAC on carbon supports are used is rapidly expanding. The absence of atomic ensemble effects and the existence of electronic effects from the support that strongly modifies the electronic structure of a metal atom in SAC significantly affect the adsorption, and definitively induce a different reactivity compared to metallic nanoparticles.<sup>374</sup> Of course, depending on the reaction studied, these marked effects can be either positive or negative, and as for any catalyzed reactions, a reaction/catalyst adequacy must be found.

---

<sup>374</sup> I. C. Gerber, et al. *Chemical Reviews* **2020**, 120, 1250-1349.



## Chapter 2. High loading single atom catalysts







## 2. High loading single atom catalysts

### 2.1. Introduction

As reviewed in the previous chapter, extensive research is currently devoted to the reproducible synthesis of supported SA.<sup>1,2,3,4</sup> This is due to the specific physicochemical properties of these species compared to bulk metal but also to nanometric particles,<sup>5</sup> which open the route through applications in many fields such as quantum technologies, sensors, energy, environment, biology or catalysis.<sup>6,7,8</sup> In the last few years, various strategies for dispersing metal SA on supports have emerged.<sup>9</sup>

Both of the most used method of preparation of high loading SAC (> 1%), pyrolysis of MOF and template-sacrificial approach, comprises sophisticated synthesis and high-temperature annealing steps,<sup>10,11,12</sup> producing porous carbons with embedded SA species, in which there is no control of the final metal loading, and the proportion of surface metallic atoms is hard to modulate, making very challenging to guarantee practical applications. On the other hand, taking advantage of solution chemistry, it is also possible to prepare atomically precise metal clusters, but mainly with few metals such as gold or silver.<sup>13,14,15,16,17,18,19</sup> The formation of these SA (or atomic clusters) necessarily requires stabilization to prevent aggregation, which would eradicate most of their desirable properties compared with bulk materials of identical composition. Additionally, for many applications these objects have to be integrated into a system, so the preparation of assemblies of subnanometric metal particles linked by strong covalent bonds could solve

<sup>1</sup> J. Calvo Fuentes, et al. In *Encyclopedia of Nanotechnology*, edited by B. Bhushan: Springer Netherlands. Dordrecht (2014), pp. 1-15.

<sup>2</sup> C. Rivera-Cárcamo, et al. *ChemCatChem* **2018**, 10, 5058-5091.

<sup>3</sup> A. Wang, et al. *Nature Reviews Chemistry* **2018b**, 2, 65-81.

<sup>4</sup> J. Liu *ACS Catalysis* **2017**, 7, 34-59.

<sup>5</sup> X.-F. Yang, et al. *Accounts of Chemical Research* **2013**, 46, 1740-1748.

<sup>6</sup> A. Mathew, et al. *Particle & Particle Systems Characterization* **2014**, 31, 1017-1053.

<sup>7</sup> X. Yuan, et al. *Particle & Particle Systems Characterization* **2015**, 32, 613-629.

<sup>8</sup> J. M. Thomas, et al. *Angewandte Chemie International Edition* **2005**, 44, 6456-6482.

<sup>9</sup> H. Zhang, et al. *Advanced Energy Materials* **2018**, 8, 1701343.

<sup>10</sup> Y.-B. Huang, et al. *Chemical Society Reviews* **2017**, 46, 126-157.

<sup>11</sup> H.-C. Zhou, et al. *Chemical Reviews* **2012**, 112, 673-674.

<sup>12</sup> L. Jiao, et al. *Chem* **2019**, 5, 786-804.

<sup>13</sup> G. Li, et al. *Accounts of Chemical Research* **2013**, 46, 1749-1758.

<sup>14</sup> K. S. Krishna, et al. In *Atomically-Precise Methods for Synthesis of Solid Catalysts*: The Royal Society of Chemistry (2015), pp. 87-122.

<sup>15</sup> A. Ghosh, et al. *European Journal of Inorganic Chemistry* **2014**, 2014, 5271-5275.

<sup>16</sup> Z. Wu, et al. *J Am Chem Soc* **2011**, 133, 9670-9673.

<sup>17</sup> Y. Zhu, et al. *Journal of Materials Chemistry* **2011**, 21, 6793-6799.

<sup>18</sup> I. Chakraborty, et al. *Chemical Reviews* **2017**, 117, 8208-8271.

<sup>19</sup> R. Jin *Nanoscale* **2015**, 7, 1549-1565.

this problem. Very few strategies have been proposed to prepare such assemblies. One example is Pd-polymer micelles containing 0.7 nm Pd clusters, which have been prepared by ligand exchange from  $[\text{Pd}(\text{PPh}_3)_4]$ .<sup>20</sup> From these observations, it appears that the development of simple synthetic strategies to produce nanoarchitectures with SA and/or subnanometric particles, with significant metal loading, is particularly appealing and challenging.

Fullerene  $\text{C}_{60}$  is an interesting building block to stabilize single metal atoms or NP. Indeed, the high degree of symmetry, the strong tendency toward polymerization of this molecule, and its coordinating geometries make it an ideal candidate for the construction of well-defined nanostructures.<sup>21</sup> In transition metal fullerides, depending on the amount of metal, the suggested structure could be polymeric with a chain-like  $-(\text{M}_1@C_{60})_n-$  arrangement of metal SA, or with two- or three-dimensional coordination.<sup>22,23</sup> Palladium,<sup>24,25,26</sup> and more recently ruthenium<sup>27</sup> spherical nanostructures containing SA have been produced. For Pd, it has been proposed that the synthesis of Pd fullerides can produce polymeric structures containing isolated Pd atoms with a stoichiometry between  $\text{Pd}_1\text{C}_{60}$  and  $\text{Pd}_{4.9}\text{C}_{60}$ .<sup>24,28</sup>

DFT calculations were used to predict the structure of different types of Pd fullerides.<sup>22</sup> The structures of one- (1-D), two- (2-D), and three-dimensional (3-D) polymers were examined. It was found that the most stable polymer is that represented by bonding via the [6,6] position of the  $\text{C}_{60}$  molecules with Pd in a distorted tetrahedral coordination (Figure 2.1).

However, a closer inspection of the literature data for the Pd- $\text{C}_{60}$  system shows that these syntheses are sensitive to the experimental conditions and not selective. In the cases in which HRTEM was used to characterize the reaction products, metallic  $\text{Pd}_{\text{NP}}$  were also observed, even at low Pd/ $\text{C}_{60}$  ratio (Figure 2.2).<sup>26,29</sup>

<sup>20</sup> K. Okamoto, et al. *J Am Chem Soc* **2005**, 127, 2125-2135.

<sup>21</sup> E.-Y. Zhang, et al. *Current Opinion in Colloid & Interface Science* **2009**, 14, 148-156.

<sup>22</sup> J. Goclon, et al. *RSC Advances* **2017**, 7, 2202-2210.

<sup>23</sup> A. L. Balch, et al. *Chemical Reviews* **2016**, 116, 3812-3882.

<sup>24</sup> H. Nagashima, et al. *Journal of the Chemical Society, Chemical Communications* **1992**, 377-379.

<sup>25</sup> A. V. Talyzin, et al. *Carbon* **2007**, 45, 2564-2569.

<sup>26</sup> J. M. Cowley, et al. *Carbon* **1994**, 32, 746-748.

<sup>27</sup> F. Leng, et al. *RSC Advances* **2016b**, 6, 69135-69148.

<sup>28</sup> A. S. Lobach, et al. *Russian Chemical Bulletin* **1996**, 45, 464-465.

<sup>29</sup> E. Brancewicz, et al. *Electrochimica Acta* **2014**, 128, 91-101.

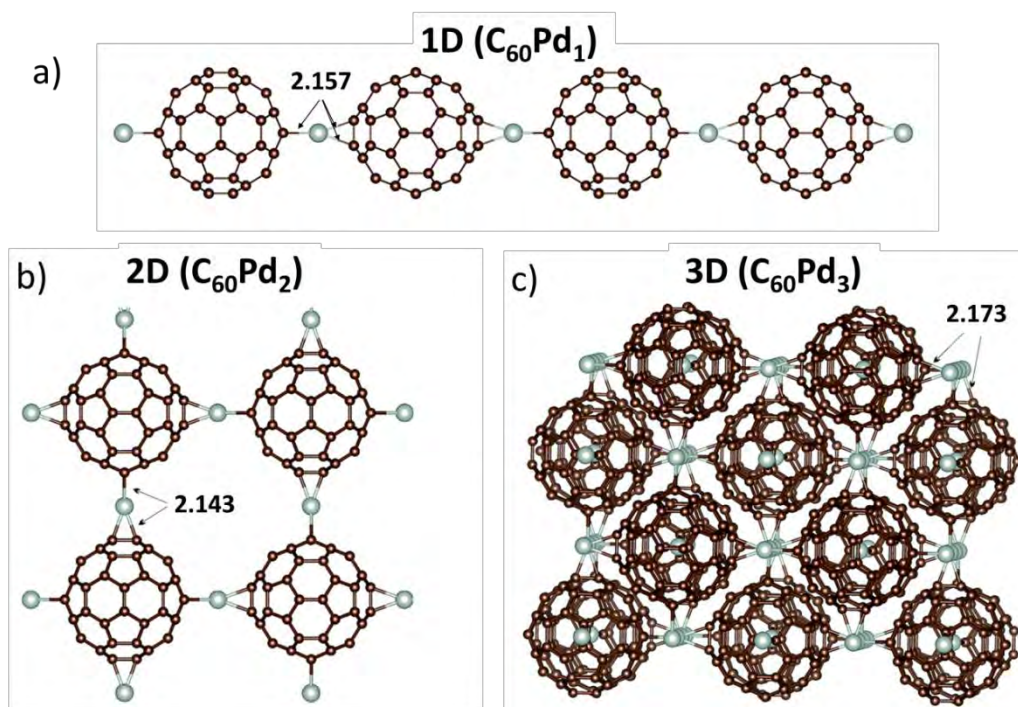


Figure 2.1. Optimized structures of the most stable configurations of the palladium–fullerene polymers: a) 1-D ( $C_{60}Pd_1$ ); b) 2-D ( $C_{60}Pd_2$ ); and c) 3-D ( $C_{60}Pd_3$ ). The bonds of interest are displayed (in Å).

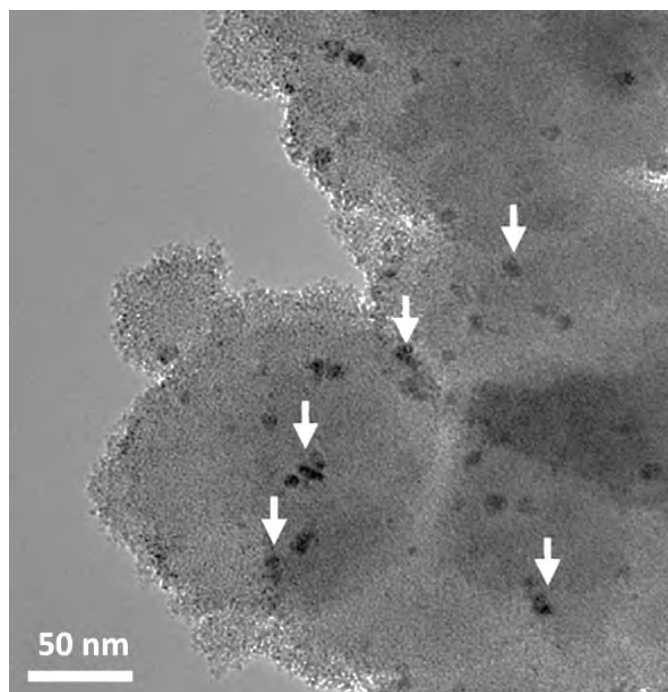


Figure 2.2 TEM image of the Pd- $C_{60}$  system prepared from 0.48 mM  $C_{60}$  and 0.73 mM  $Pd_2(dba)_3 \cdot CHCl_3$ . Arrows indicate palladium metallic NP. From ref. [29]

If a  $\text{Pd}_3\text{C}_{60}$  fulleride has indeed been produced and characterized,<sup>25,26</sup> when a  $\text{Pd}/\text{C}_{60}$  ratio of 3 was used, it was not the only product of the reaction, and also significant amount of NP (5-20 nm) were observed. DFT calculations have suggested that both isolated atoms and weakly bonded metal aggregates may exist in equilibrium.<sup>30</sup> EXAFS analyses have allowed to propose the presence of Pd clusters in  $\text{Pd}_3\text{C}_{60}$ ,<sup>31</sup> and XRD analyses have shown the presence of metallic Pd, starting from composition  $\text{Pd}_2\text{C}_{60}$  and higher.<sup>25</sup> From these results, it seems that if the kinetic product of the reaction, the  $-(\text{Pd}_1\text{C}_{60})-$  polymer, is rapidly formed, the incorporation of additional Pd in the structure is not straightforward. We suspect that diffusional limitations should prevail, which may lead to Pd clusters or NP formation on the surface of the  $-(\text{Pd}_1\text{C}_{60})-$  polymer.

From a previous report of our group, in which similar results were obtained in the case of ruthenium,<sup>27</sup> it appears difficult to produce fulleride metal-clusters, and this must be linked to the fact that once the kinetic product of the reaction is formed (the polymeric structures containing SA), the additional metal is deposited on the external surface of the spheres because it cannot diffuse in their porosity. Thus, if  $\text{C}_{60}$  fullerene-metal cluster complexes are well known for many years,<sup>32</sup> up to now,  $\text{C}_{60}$  metal-cluster fullerides are essentially hypothetical.<sup>33</sup>

The work described in this chapter was conducted to try to overcome this difficulty in the case of  $\text{Ru}@\text{C}_{60}$  hetero-structures by using mixtures of solvents during the synthesis to favor the deposition of ruthenium in the porosity of the  $-(\text{Ru}_1@\text{C}_{60})-n$  materials so as to obtain  $-(\text{Ru}_n@\text{C}_{60})n-$  metal-cluster fullerides. Thus, we report the straightforward self-assembly synthesis of  $\text{Ru}_{\text{SA}}$  and Ru subnanometric particles with  $\text{C}_{60}$ .

## 2.2. Results

### 2.2.1 $\text{Ru}@\text{C}_{60}$ hetero-structure synthesis and TEM characterization

The  $\text{Ru}@\text{C}_{60}$  hetero-structures were synthesized by decomposing  $[\text{Ru}(\text{COD})(\text{COT})]$  in the presence of  $\text{C}_{60}$ , varying the ratio  $\text{Ru}/\text{C}_{60}$ , under  $\text{H}_2$  (3 bar) using dichloromethane (D), toluene (T) and methanol (M). The reaction conditions for each sample, the resulting metal loading, and the  $\text{Ru}_{\text{NP}}$  size are summarized in Table 2.1. From previous experiences,

<sup>30</sup> O. Loboda, et al. *Fullerenes, Nanotubes and Carbon Nanostructures* **2006**, 14, 365-371.

<sup>31</sup> V. A. Chernov, et al. *Nuclear Instruments and Methods in Physics Research Section A: Accelerators, Spectrometers, Detectors and Associated Equipment* **1995**, 359, 250-253.

<sup>32</sup> K. Lee, et al. *Accounts of Chemical Research* **2003**, 36, 78-86.

<sup>33</sup> N. Goldberg, et al. *Inorganic Chemistry* **1996**, 35, 4369-4377.

we observed well-defined spherical objects (30-40 nm, Figure 2.3a) when using pure  $\text{CH}_2\text{Cl}_2$  for the synthesis (entry 1, Table 2.1, D-Ru<sub>1</sub>@C<sub>60</sub>).

Table 2.1. Loading and mean particle size of the Ru@C<sub>60</sub> samples.

Entry	Ru@C <sub>60</sub> samples	Solvent	Temperature (°C)	Ru loading (%) <sup>a</sup>	Ru NP size (nm)
1	D-Ru <sub>1</sub> @C <sub>60</sub> 1/1 <sup>27</sup>	CH <sub>2</sub> Cl <sub>2</sub>	25	10.6 (12.3)	n. d. <sup>b</sup>
2	D-Ru@C <sub>60</sub> 2/1 <sup>27</sup>	CH <sub>2</sub> Cl <sub>2</sub>	25	16.7 (21.9)	1.2 ± 0.1
3	D-Ru@C <sub>60</sub> 5/1 <sup>27</sup>	CH <sub>2</sub> Cl <sub>2</sub>	25	35.6 (41.2)	1.3 ± 0.1
4	T-Ru <sub>1</sub> @C <sub>60</sub> 1/1 <sup>27</sup>	Toluene	25	9.1 (12.3)	n. d.
5	T-Ru@C <sub>60</sub> 5/1	Toluene	25	11.0 (41.2)	n. d.
6	T-Ru@C <sub>60</sub> 10/1	Toluene	25	16.6 (58.3)	n. d.
7	T-Ru@C <sub>60</sub> 20/1	Toluene	25	20.0 (73.7)	n. d.
8	T-Ru@C <sub>60</sub> 40/1	Toluene	25	19.2 (84.8)	n. d.
9	T-Ru@C <sub>60</sub> 20/1	Toluene	50	19.6 (73.7)	n. d.
10	T-Ru@C <sub>60</sub> 20/1	Toluene	100	20.5 (73.7)	n. d.
11	T <sub>95</sub> D <sub>5</sub> -Ru@C <sub>60</sub> 20/1	Toluene (95%)/CH <sub>2</sub> Cl <sub>2</sub> (5%)	25	24.4 (73.7)	n. d.
12	T <sub>75</sub> D <sub>25</sub> -Ru@C <sub>60</sub> 20/1	Toluene (75%)/CH <sub>2</sub> Cl <sub>2</sub> (25%)	25	35.8 (73.7)	n. d.
13	T <sub>50</sub> D <sub>50</sub> -Ru@C <sub>60</sub> 20/1	Toluene (50%)/CH <sub>2</sub> Cl <sub>2</sub> (50%)	25	36.0 (73.7)	suspected
14	T <sub>95</sub> M <sub>5</sub> -Ru@C <sub>60</sub> 20/1	Toluene (95%)/MeOH (5%)	25	34.7 (73.7)	suspected
15	T <sub>75</sub> M <sub>25</sub> -Ru@C <sub>60</sub> 20/1	Toluene (75%)/MeOH (25%)	25	41.6 (73.7)	suspected
16	T <sub>50</sub> M <sub>50</sub> -Ru@C <sub>60</sub> 20/1	Toluene (50%)/MeOH (5 %)	25	47.1 (73.7)	suspected

a) From ICP analyses. The value between parentheses is the aimed Ru loading considering the initial amount of metallic precursor used. b) n. d. = not detected



On the other hand, nanostructures of undefined shape were produced using pure toluene (entry 4, Table 2.1, T-Ru<sub>1</sub>@C<sub>60</sub>, Figure 2.3c).<sup>27</sup> This indicates the pronounced influence of the solvent on the shape of the structures produced. Nonetheless, regardless the solvent, no nanoparticles were detected in materials synthesized with a 1/1 Ru/C<sub>60</sub> ratio. We proposed that these structures constitute the kinetic product of the reaction and contain only Ru single atoms Ru<sub>1</sub>@C<sub>60</sub> (Figure 2.3b,d) connected by C<sub>60</sub> with a  $\eta^2$ - $\eta^6$  coordination as previously reported by our group for similar structures produced in dichloromethane.<sup>27</sup>

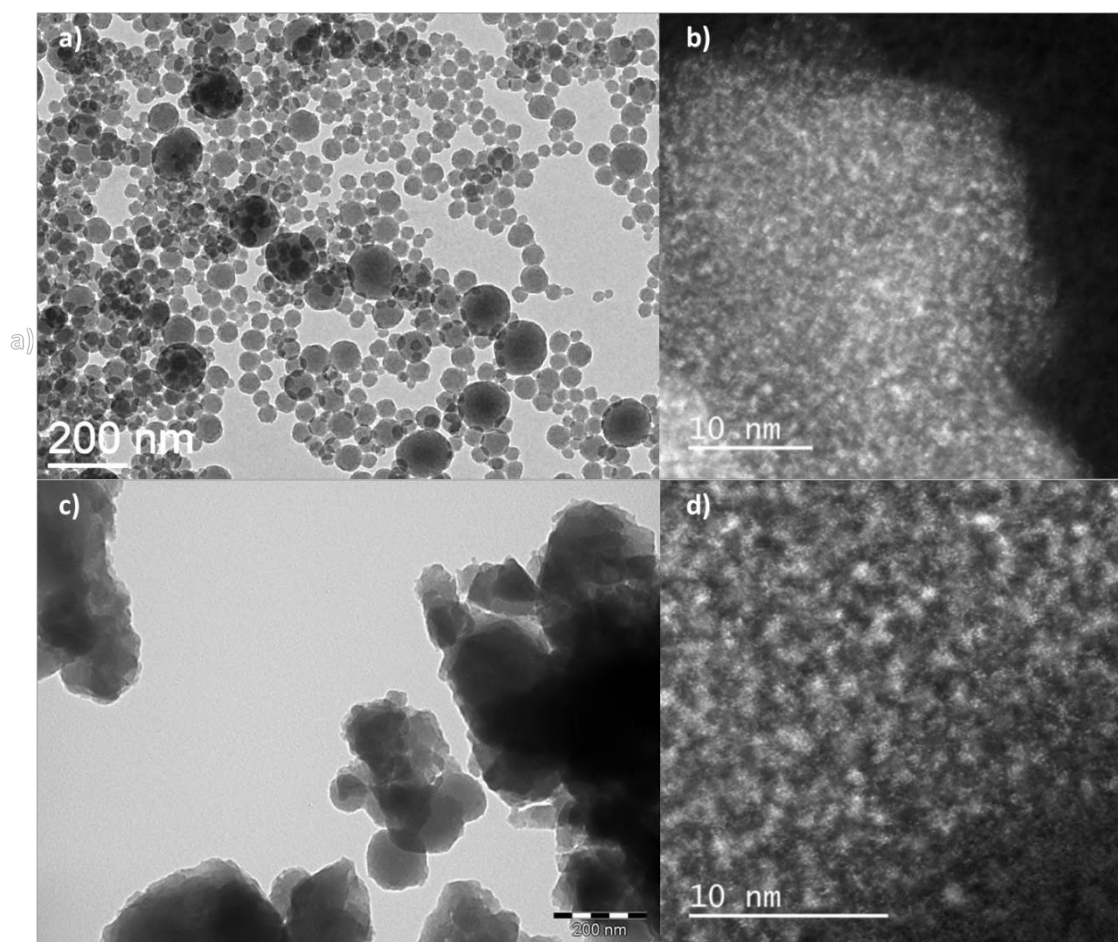


Figure 2.3. a) TEM of D-Ru@C<sub>60</sub> 1/1; b) STEM-HAADF of D-Ru@C<sub>60</sub> 1/1; c) TEM of T-Ru@C<sub>60</sub> 1/1; and d) STEM-HAADF of T-Ru@C<sub>60</sub> 1/1.

We have attributed this morphology difference to the fact that C<sub>60</sub> are much more soluble in toluene (2.80 mg/mL) than in CH<sub>2</sub>Cl<sub>2</sub> (0.26 mg/mL). Indeed, it is known that self-assembly mainly based on specific amphiphilicity in a surrounding medium, may result in a selection of morphologies.<sup>34</sup>

<sup>34</sup> M. Sathish, et al. *J Am Chem Soc* **2009**, 131, 6372-6373.

When we increased the Ru/C<sub>60</sub> ratio to 2/1 in CH<sub>2</sub>Cl<sub>2</sub> (entry 2, Table 2.1), the polymeric spheres are already covered by a shell of 1.2 nm size Ru<sub>NP</sub> (Figure 2.4a,b), whose thickness increases with the increase of the Ru/C<sub>60</sub> ratio.<sup>27</sup>

Theoretically, based on thermodynamics arguments, the formation of Ru clusters and Ru<sub>NP</sub> is favored over the increase of number of single atoms. Coordination energy between one Ru atom and two C<sub>60</sub> is -84 kcal/mol, the cohesive energy per Ru atom in naked Ru<sub>13</sub> is -96 kcal/mol or -90 kcal/mol in the -(Ru<sub>2</sub>@C<sub>60</sub>)<sub>n</sub>- model shown in Figure 2.5. Despite the fact that we cannot completely exclude the formation of complex 2D or 3D structures (such as in Figure 2.1) since they appear to be stable when increasing the metal/carbon ratio,<sup>22</sup> it seems that the electronic structures of various transition metals embedded in more structured systems remain very similar to the 1D case. Therefore, in our models we will retain only the wire configuration.<sup>35</sup> This result is consistent with the idea of “polymer swelling”, where the solvent has the capability to penetrate through the cross-linked polymer network. In this case, -(D-Ru<sub>1</sub>@C<sub>60</sub>)<sub>n</sub>- polymer does not swell in CH<sub>2</sub>Cl<sub>2</sub>, so the additional Ru atoms on solution cannot be incorporated in the structure due to diffusional limitations, and nucleation of Ru<sub>NP</sub> occurs on the surface of the nanospheres (Figure 2.4f). Using pure toluene as solvent -(T-Ru<sub>1</sub>@C<sub>60</sub>)<sub>n</sub>- swelling favors the incorporation of Ru into the structure avoiding NP deposition as seen from HRTEM and STEM-HAADF images even for a 5/1 Ru/C<sub>60</sub> ratio (entry 5, Table 2.1, and Figure 2.4c-e). Indeed, experimental evidence has shown the importance of polymer swelling by controlling the diffusion rate.<sup>36</sup> Interestingly, we noticed that the final Ru loading is lower in toluene than in dichloromethane at the same Ru/C<sub>60</sub> ratio (Table 2.1). In order to increase the Ru loading we firstly increased the Ru/C<sub>60</sub> ratio (entries 4-8, Table 2.1). By increasing the Ru/C<sub>60</sub> ratio from 1/1 to 40/1, only a moderate increase in Ru loading was obtained, and a plateau is reached at 20 % w/w Ru. We also investigated the effect of the temperature (entries 7, 9 and 10, Table 2.1). An increase of the temperature of reaction from 25 to 100 °C for a Ru/C<sub>60</sub> ratio of 20/1 does not allow increasing the Ru loading above 20% w/w.

---

<sup>35</sup> X. Zhang, et al. *The Journal of Physical Chemistry C* **2019**, 123, 30571-30577.

<sup>36</sup> M. Zhu, et al. *European Polymer Journal* **2007**, 43, 4503-4515.

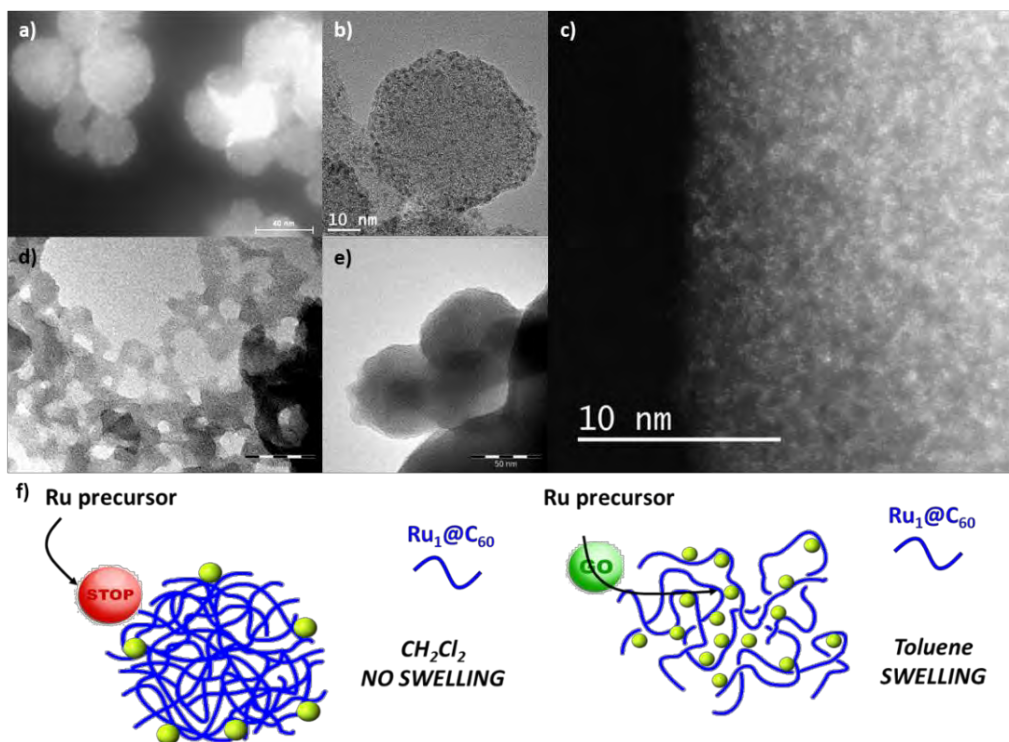


Figure 2.4. a) STEM-HAADF of D-Ru@C<sub>60</sub> 2/1; b) TEM of D-Ru@C<sub>60</sub> 2/1; c) STEM-HAADF of T-Ru@C<sub>60</sub> 1/1; d) and e) TEM of T-Ru@C<sub>60</sub> 5/1; and f) scheme showing the incorporation of Ru on/in Ru<sub>1</sub>@C<sub>60</sub> according to the nature of the solvent.

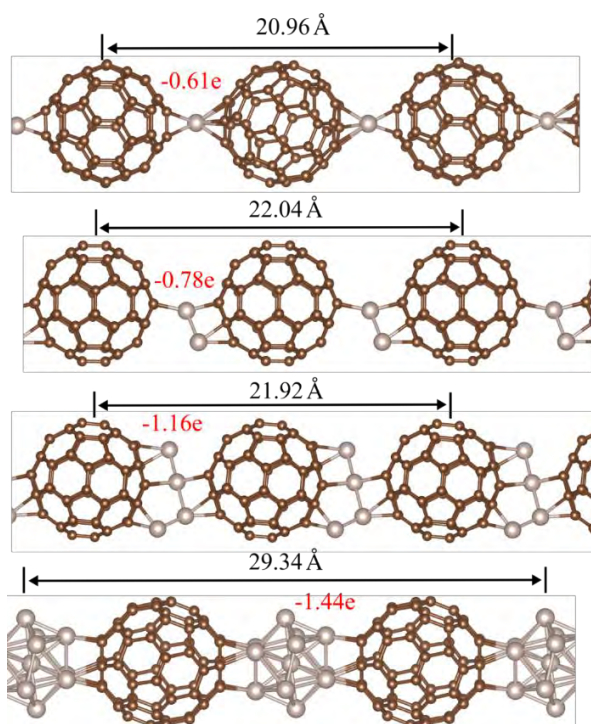


Figure 2.5. Models of polymeric phases for Ru<sub>1</sub>-C<sub>60</sub>, Ru<sub>2</sub>-C<sub>60</sub>, Ru<sub>4</sub>-C<sub>60</sub>, Ru<sub>13</sub>-C<sub>60</sub> building blocks used for the evaluation of charge transfer and the simulated Pair Distribution Function (PDF), and total charge loss for the corresponding Ru<sub>n</sub> cluster.

It is important to notice that, contrarily to the sample D-Ru@C<sub>60</sub> 2/1 (16.7% Ru w/w),<sup>27</sup> at 20 % w/w Ru loading, the sample produced in toluene does not contain any Ru<sub>NP</sub> from HRTEM and STEM-HAADF observations (Figure 2.6).

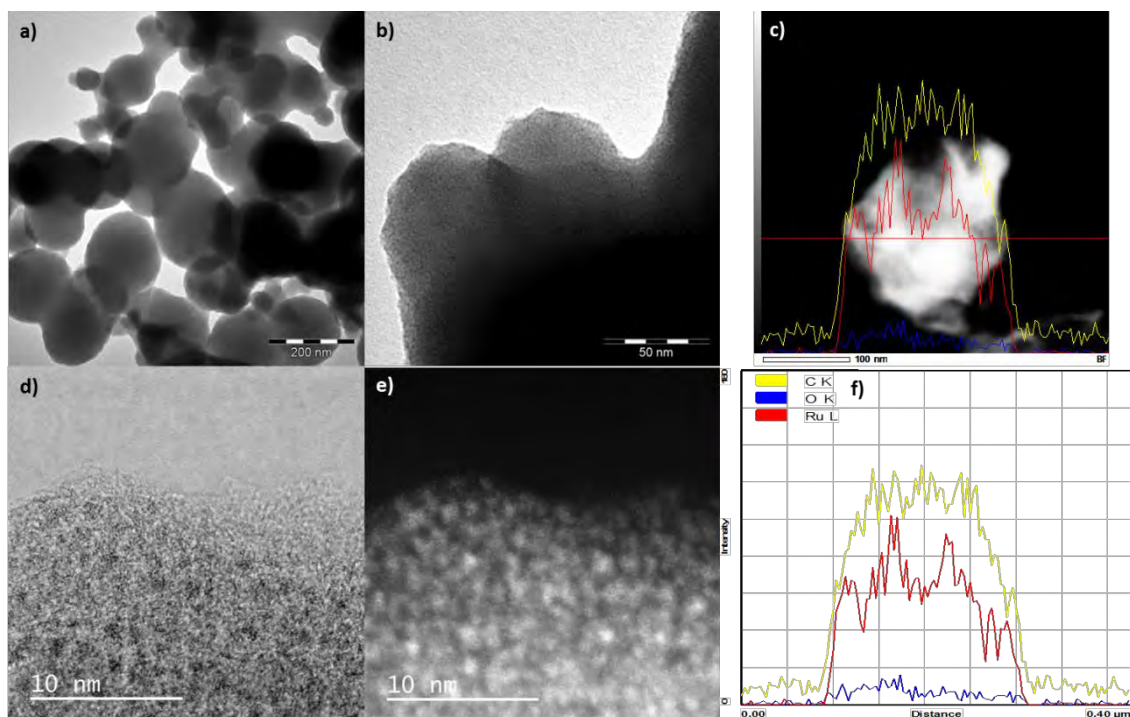


Figure 2.6. a), b) TEM, d) STEM, c), d) STEM-HAADF micrographs and f) EDX mapping of the T-Ru@C<sub>60</sub> 20/1 sample.

This result is again consistent with swelling of the T-Ru<sub>1</sub>@C<sub>60</sub> structure, allowing incorporation of Ru atoms in the polymeric matrix. We evidenced toluene retention due to swelling in -(T-Ru<sub>1</sub>@C<sub>60</sub>)<sub>n</sub>- detected by TGA analyses (Figure 2.7a). It has already been reported that the Pd fulleride C<sub>60</sub>Pd<sub>n</sub> showed good adsorptivity toward toluene.<sup>37</sup> We performed DFT calculations including van der Waals interactions in LPCNO (Toulouse) to measure the stabilization energy of toluene molecules on -(Ru<sub>1</sub>@C<sub>60</sub>)<sub>n</sub>- (Figure 2. 7b). For one toluene molecule the stabilization energy was 12 kcal/mol, and it was 22 and 49 kcal.mol<sup>-1</sup> for two and four toluene molecules, respectively.

<sup>37</sup> A. Hayashi, et al. *Journal of Materials Chemistry* **2004**, 14, 2633-2637.



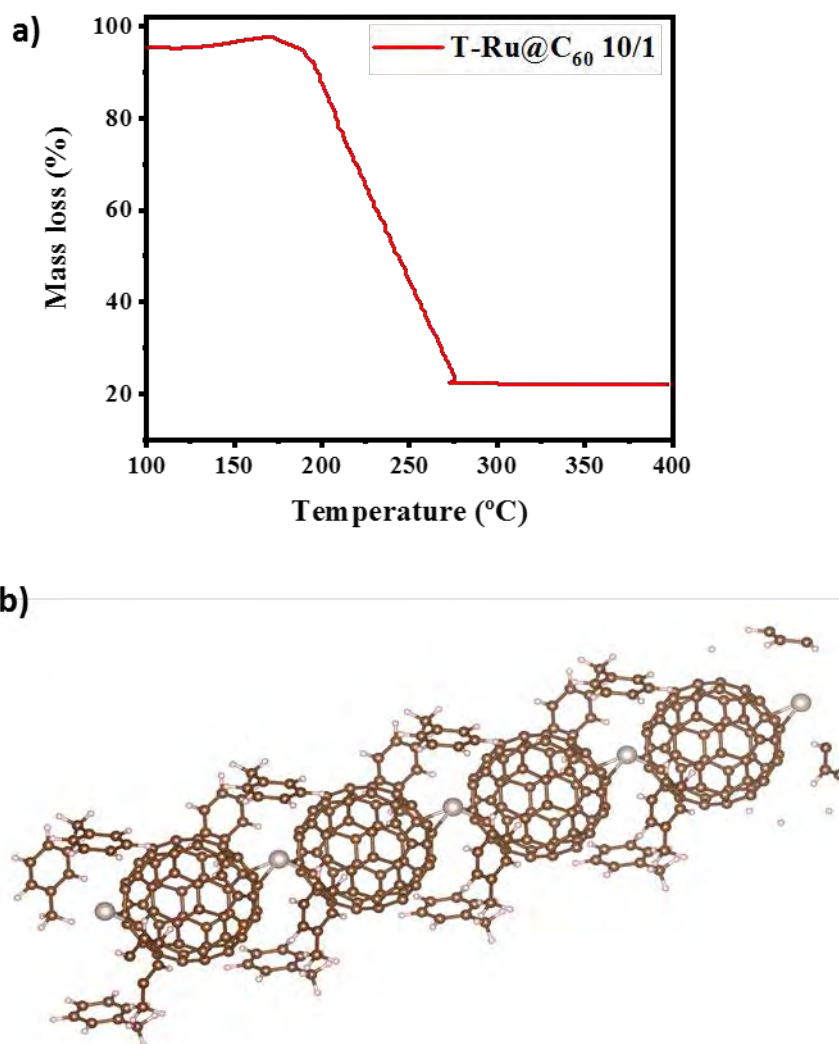


Figure 2.7. a) Mass loss of T-Ru@C<sub>60</sub> 10/1 swelled in pure toluene (24 h and then dried at room temperature during 3 days), TG curve measured under nitrogen flow 40 cm<sup>3</sup>/min; and b) Interaction of four toluene molecules with the -(Ru<sub>1</sub>@C<sub>60</sub>)<sub>n</sub>- structure.

We discovered that the existence of the plateau is connected to the rapid formation of a stable complex [(1,5-cyclooctadiene)(toluene)Ru(0)] in solution by the reaction of the solvent with the ruthenium precursor. The formation of this product has been confirmed by <sup>1</sup>H-NMR, and this complex was isolated from the yellow filtrates obtained at the end of the reactions (Figure 2.8).

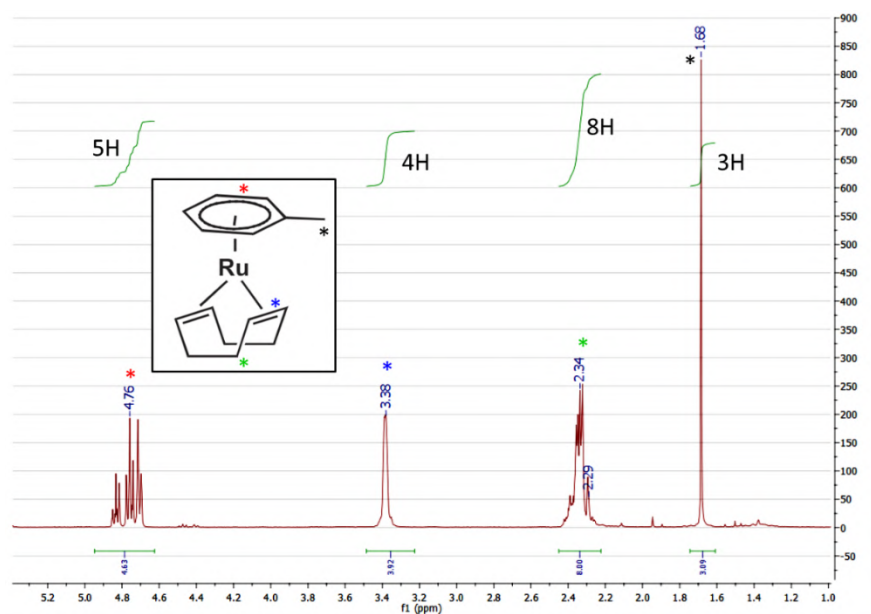


Figure 2.8.  $^1\text{H}$ -NMR spectrum of  $[\text{Ru}(0)(1,5\text{-cyclooctadiene})(\text{toluene})]$  isolated from the yellow filtrates obtained at the end of the reaction of entry 7, Table 2.1.

Trying to assess the reactivity of this molecule, separately, we synthesized this complex by mixing  $[\text{Ru}(\text{COD})(\text{COT})]$  and toluene in the presence of dihydrogen.<sup>38</sup> Using this compound as precursor in our synthesis, we confirmed that it hardly reacts in the presence of  $\text{C}_{60}$  under the reaction conditions. After 24 h reaction, a black solid is obtained in low yield (16%) that contains only 6% Ru w/w. In order to limit the formation of  $[\text{Ru}(\text{COD})(\text{toluene})]$  and to increase the Ru loading we investigated the use of solvent mixtures with toluene. Two solvents have been investigated,  $\text{CH}_2\text{Cl}_2$  (entries 11-13, Table 2.1) and methanol (entries 14-16, Table 2.1), which can act as coordinating solvents to the Ru atoms to limit the formation of the stable Ru complex with toluene.<sup>39,40</sup> The use of toluene/ $\text{CH}_2\text{Cl}_2$  mixtures (50/50) allows increasing the Ru loading (for a Ru/ $\text{C}_{60}$  ratio = 20) from 20 to 36%. The Ru reaches 34.7 wt.% for a toluene/methanol mixture (95/5), and 47.1 wt.% for a toluene/methanol mixture (50/50). The sample  $\text{T}_{95}\text{D}_5\text{-Ru@C}_{60}$  20/1 was analyzed by STEM-HAADF (Figure 2.9).

<sup>38</sup> P. Pertici, et al. *Journal of the Chemical Society, Dalton Transactions* **1982**, 1019-1022.

<sup>39</sup> M. Bown, et al. *J Am Chem Soc* **1990**, 112, 2442-2443.

<sup>40</sup> M. Kawai, et al. *Acta Crystallographica Section C* **2002**, 58, m581-m582.



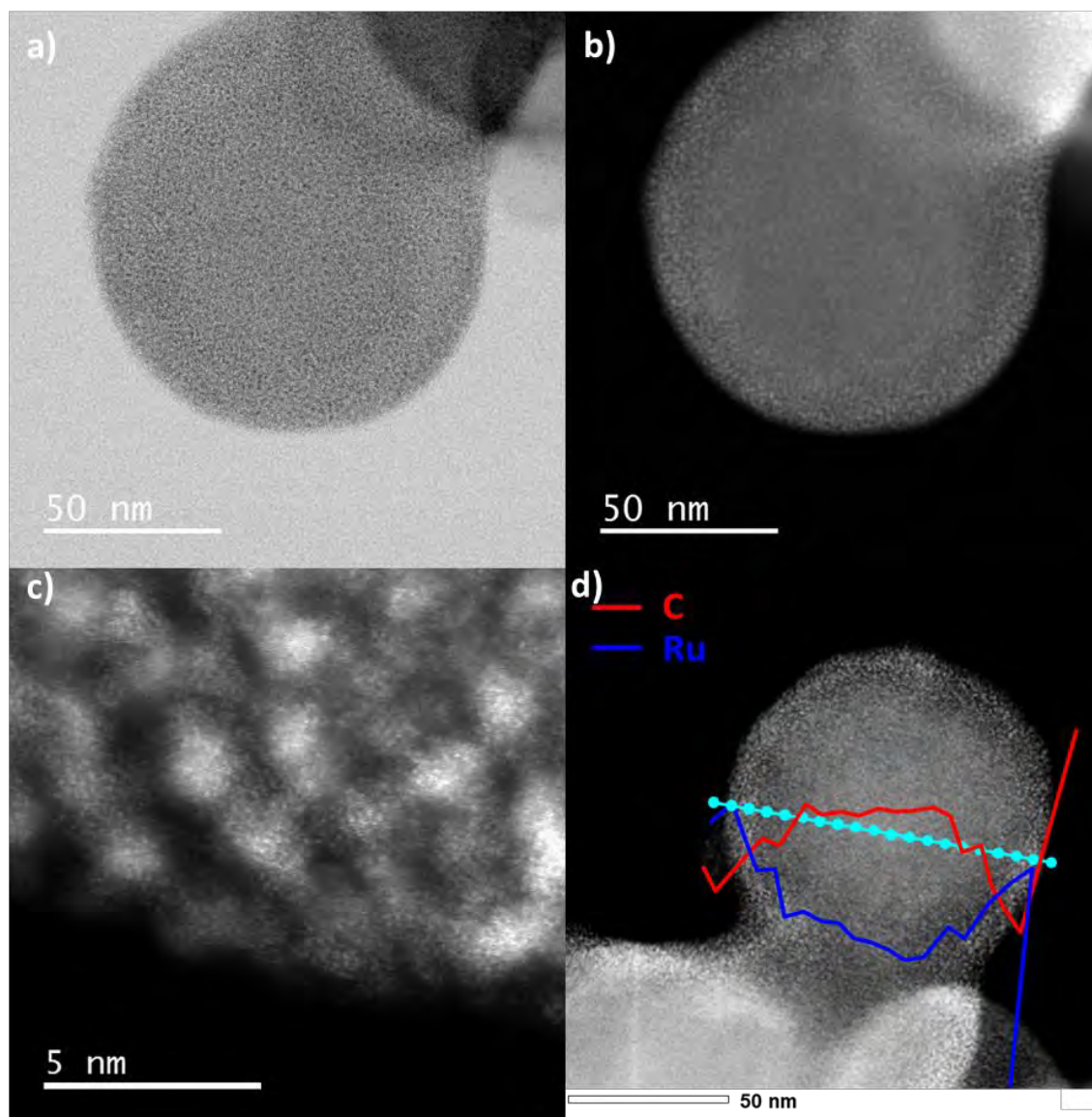


Figure 2.9. a) STEM; and b-d) STEM-HAADF micrographs of the  $T_{95}D_5\text{-Ru}@C_{60}$  20/1 sample.

The EDX profiles of this specific sample show a higher content of Ru on the nanostructure surface indicating that a core-shell structure starts to develop, with a Ru rich shell (Figure 2.9d). However, at this high Ru loading, the detection of  $\text{Ru}_{\text{NP}}$  was not straightforward. The sample  $T_{95}M_5\text{-Ru}@C_{60}$  20/1 was also observed by STEM-HAADF and no Ru NP was clearly observed (Fig. 2.10), but no core-shell structure was formed. So, we can propose that for the samples prepared in toluene/methanol mixture, the extra Ru atoms are incorporated into the hetero-structure to provide more Ru atoms or subnanometric Ru clusters.

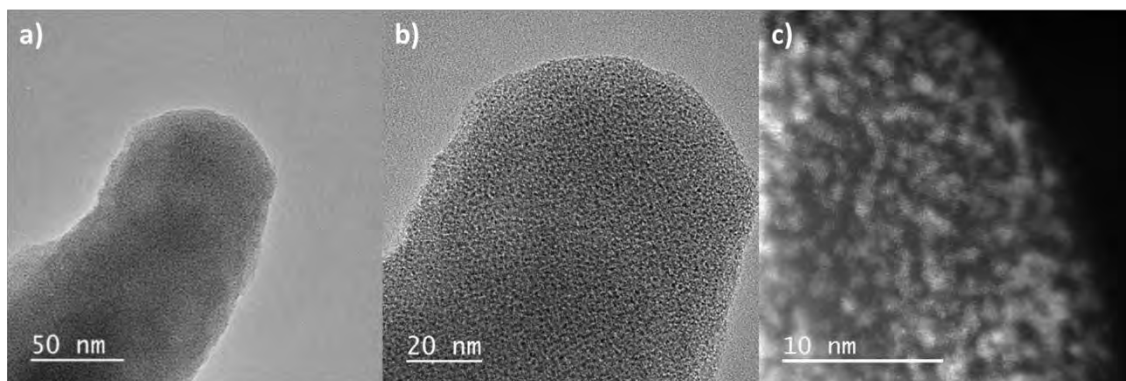


Figure 2.10. a) and b) STEM; and c) STEM-HAADF micrographs of the  $T_{95}M_5\text{-Ru}@C_{60}$  20/1 sample.

The  $T_{50}D_{50}\text{-Ru}@C_{60}$  sample presented a similar metal loading as  $T_{95}M_5\text{-Ru}@C_{60}$  (Table 2.1, entries 13 and 14), and the formation of core-shell spherical particles is clearly observed (Figure 2.11a,b), on which the extra Ru atoms have the tendency to deposit on the external surface of the spheres (see Figure 2.11a for EDX mapping). There also, the structuration of Ru as metallic NP was not clear (Figure. 2.11b).

Finally, for the  $T_{50}M_{50}\text{-Ru}@C_{60}$  20/1 sample, no core shell structure was produced (Figure 2.11c-d), and once again the detection of metallic NP was not easy due to the extremely high Ru loading (47 % w/w, which corresponds to 6 Ru atoms for 1  $C_{60}$ ). From these results, it appears that the use of solvent mixtures during the synthesis impacts the fate of the reaction. First, the use of toluene/ $CH_2Cl_2$ , and particularly of toluene/ $CH_3OH$  mixtures allows to significantly increase the Ru loading, which reaches almost 50 % w/w in the  $T_{50}M_{50}\text{-Ru}@C_{60}$  sample. This could be attributed to a competition between the solvents for coordination to Ru, and to the generation of Ru intermediate species that are more easily decomposed than the stable  $[Ru(COD)(\text{toluene})]$  complex. An easier coordination of methanol compared to dichloromethane is not surprising. Second, the choice of the second solvent ( $CH_2Cl_2$  or  $CH_3OH$ ) has also an impact on Ru location. The use of  $CH_2Cl_2$  does not allow depositing the extra Ru inside the hetero-structure and a shell of Ru species are deposited around the  $-(Ru_1@C_{60})_n\text{-}$  core.

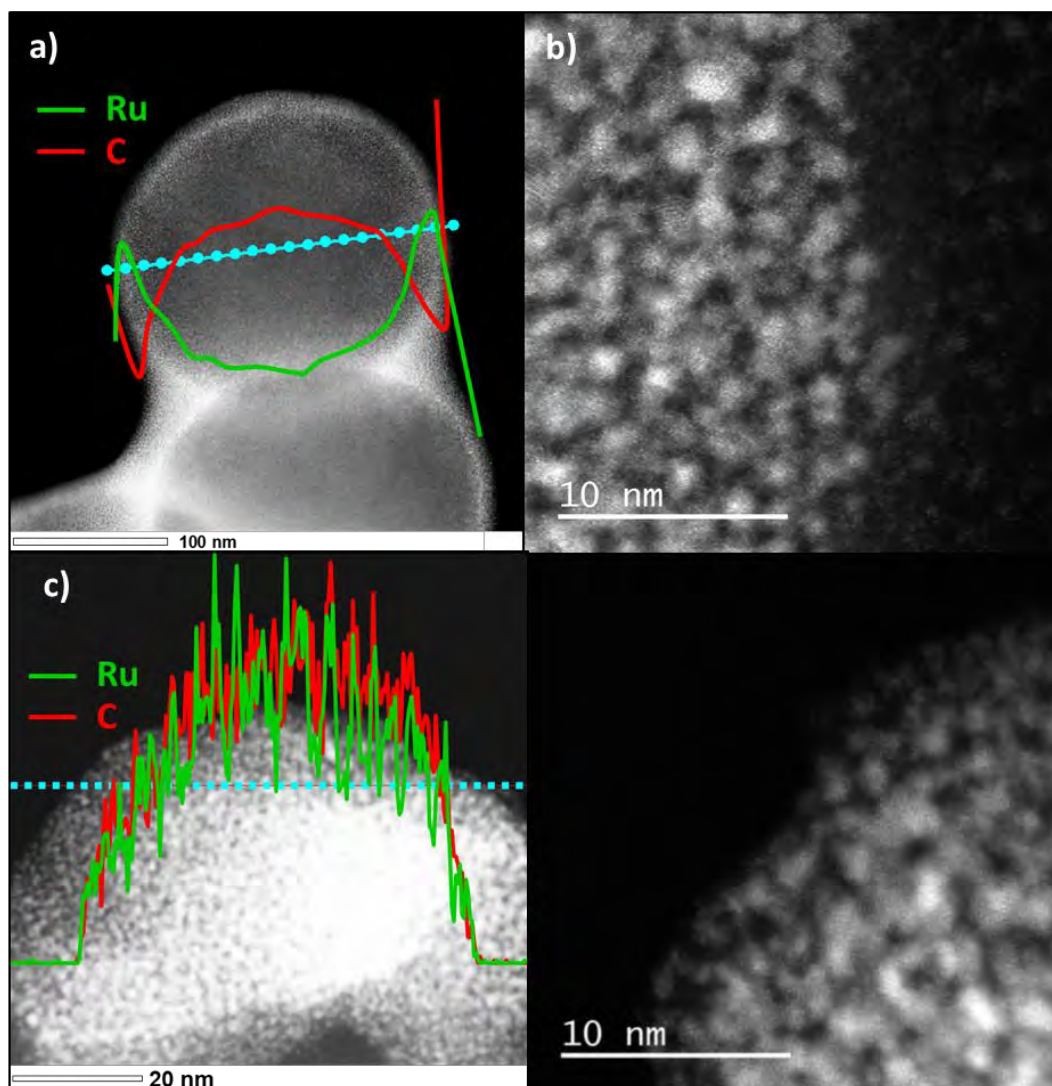


Figure 2.11. a), b) STEM-HAADF micrographs and EDX mapping of the  $T_{50}D_{50}\text{-Ru@C}_{60}$  sample; and c), d) STEM-HAADF micrographs and EDX mapping of the  $T_{50}M_{50}\text{-Ru@C}_{60}$  sample.

When  $\text{CH}_3\text{OH}$  is used, the extra Ru atoms are incorporated inside the hetero-structure. We propose that it is the swelling of the  $-(\text{Ru}_1\text{@C}_{60})_n-$  product that allows the incorporation of extra Ru atoms inside the hetero-structure. Methanol should act as a porogen (pore generating solvent) for the  $-(\text{Ru}_1\text{@C}_{60})_n-$  structure. In polymer chemistry, the porogen is the most influencing parameter to the surface area, porosity, and morphology of the polymer.<sup>41</sup> Finally, it is worth mentioning that if the presence of Ru subnanometric particles could be suspected in samples prepared using mixtures of solvents (up to 6 Ru atoms for 1  $\text{C}_{60}$ ), the high metal loadings makes their identification by STEM-HAADF complex.

<sup>41</sup> S. Mane *Canadian Chemical Transactions* **2016**, 4, 210-255.

## 2.2.2 Raman, XPS, WAXS and EXAFS characterizations

Since fullerene  $C_{60}$  is a powerful electron acceptor,<sup>42</sup> we investigated by Raman spectroscopy the possibility of electron transfer in the materials synthesized in toluene. Figure 2.12a shows Raman spectra (532 nm) of T-Ru@ $C_{60}$  at different Ru/ $C_{60}$  ratio. The spectral range is mainly focused on the pentagonal pinch mode  $A_g(2)$ , because it has been proven that it is a reliable probe of metal fulleride polymer states. It is known that the energy of the  $A_g(2)$  mode ( $1460\text{ cm}^{-1}$  for pure  $C_{60}$ ) is sensitive to charge transfer in transition metal fullerenes.<sup>43</sup>

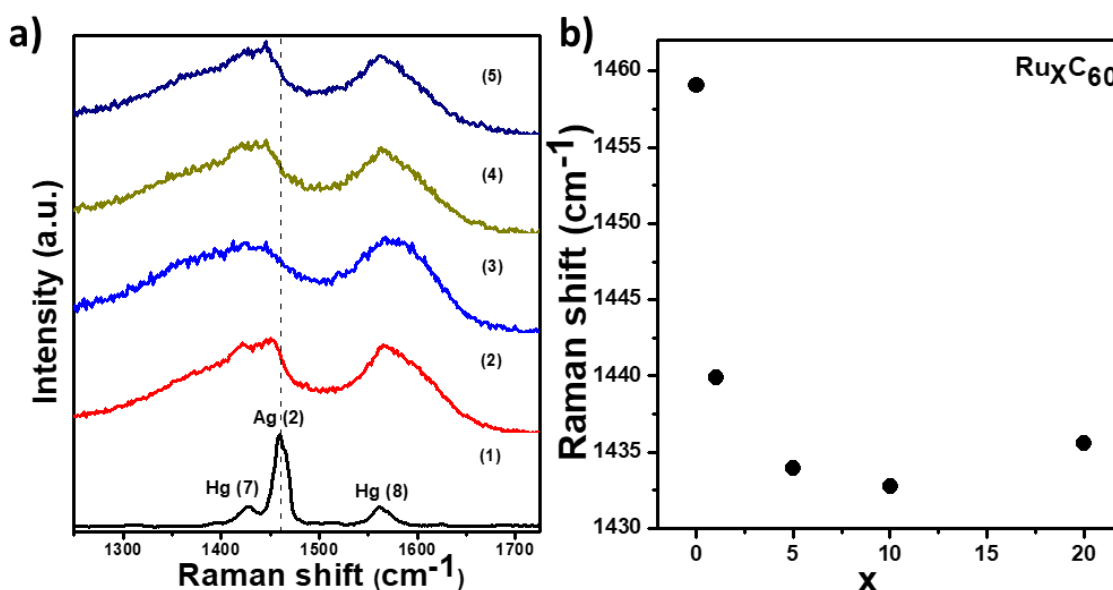


Figure 2.12. a) Raman spectra of (1)  $C_{60}$ , (2) T-Ru@ $C_{60}$  1/1, (3) T-Ru@ $C_{60}$  5/1, (4) T-Ru@ $C_{60}$  10/1 and (5) T-Ru@ $C_{60}$  20/1; and b) Raman shift vs. Ru composition in  $C_{60}$  illustrates the broadening and down shift of  $A_g(2)$  peak with respect to increase in Ru content.

We observe a spectral shift as large as  $-16.2\text{ cm}^{-1}$  for the T-Ru@ $C_{60}$  20/1 sample, and a significant broadening with increasing the amount of Ru, caused by strong electron-phonon interaction. Thus, a clear tendency can be observed where the displacement increases as the Ru content increases (Figure 2.12b). It is commonly accepted that the  $A_g(2)$  mode is downshifted by approximately  $6\text{ cm}^{-1}$  transferred to  $C_{60}$  in alkali metal fulleride compounds.<sup>44</sup> The downshift of alkali metal fullerenes depends on the number of metal atoms and each metal atom donates one electron to  $C_{60}$ , because there are only

<sup>42</sup> R. C. Haddon, et al. *Philosophical Transactions: Physical Sciences and Engineering* **1993**, 343, 53-62.

<sup>43</sup> S. J. Chase, et al. *Physical Review B* **1992**, 46, 7873-7877.

<sup>44</sup> K.-A. Wang, et al. *Physical Review B* **1992**, 45, 1955-1958.



ionic bonds between  $C_{60}$  and alkali atoms. For transition metal fullerides, the relationship between shift and composition is more complex since these compounds exhibit a large proportion of covalent bonding between metal and  $C_{60}$ . However, a significant charge transfer is observed for our samples, suggesting the presence of electron deficient Ru species in the T-Ru@ $C_{60}$  series, as we had already shown for the D-Ru@ $C_{60}$  series.<sup>27</sup> The charge transfer from Ru to  $C_{60}$  was also evidenced by XPS (Figure 2.13), by comparing the binding energy of Ru $_{3p_{3/2}}$  (462.2 eV) with that of Ru $^0$  (461.2 eV). Raman<sup>45</sup> and XPS<sup>46</sup> signatures for charge transfer were already reported for Pd@ $C_{60}$  fullerides. DFT estimates of the charge transfer for various Ru $_n$ @ $C_{60}$  models ( $n = 1, 2, 4, 13$ ) confirm this general trend, with values from 0.1 (Ru $_{13}$ @ $C_{60}$ ) to 0.6 e $^-$  (Ru $_1$ @ $C_{60}$ ) per Ru center from Ru $_{SA}$ /clusters to neighboring  $C_{60}$  (Figure 2.5).

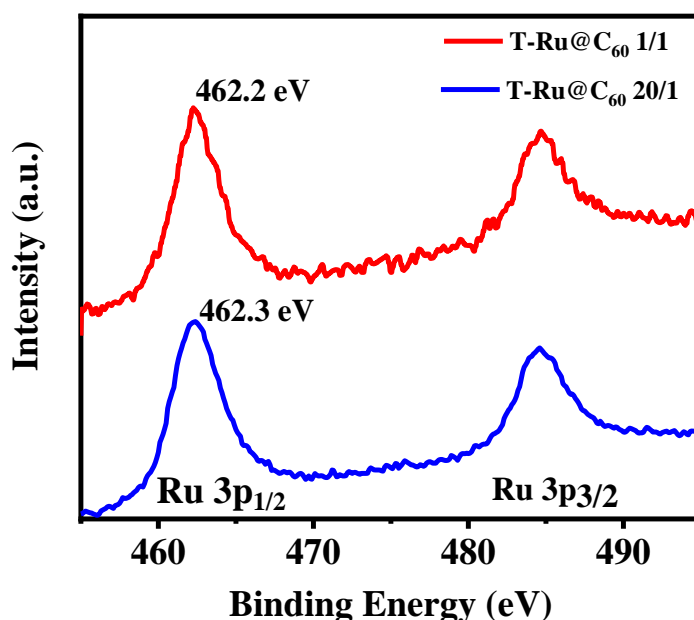


Figure 2.13. Ru 3p XPS spectra of a) T-Ru@ $C_{60}$  1/1; and b) T-Ru@ $C_{60}$  20/1 samples.

Further analyses were performed in CEMES (Toulouse) by WAXS in order to shed some light on the possible presence of metallic Ru clusters in the Ru@ $C_{60}$  hetero-structures. We first compared the T $_{50}$ D $_{50}$ -Ru@ $C_{60}$  and T $_{50}$ M $_{50}$ -Ru@ $C_{60}$  samples with the T-Ru@ $C_{60}$  sample at a similar Ru/ $C_{60}$  ratio of 20/1 (Fig. 2.14). For T $_{50}$ D $_{50}$ -Ru@ $C_{60}$ , a strong contribution can be observed at 0.267 nm in very good agreement with Ru-Ru metallic bond length (0.265 nm); confirming the presence of Ru clusters in this sample showing a

<sup>45</sup> A. V. Talyzin, et al. *Thin Solid Films* **2003**, 429, 96-101.

<sup>46</sup> K. Winkler, et al. *Journal of Materials Chemistry* **2003**, 13, 518-525.

core-shell structure (Figure 2.11a). In the two other compounds, this distance could not be observed; however, they share a strong contribution close to 0.360 nm, likely also related to Ru-Ru distances but clearly non-bonding ones. A contribution in the 0.20-0.23 nm range is also observed for these two samples, which could be related to bonding of Ru with a light element (likely C, since Ru-C is close to 0.2 nm).

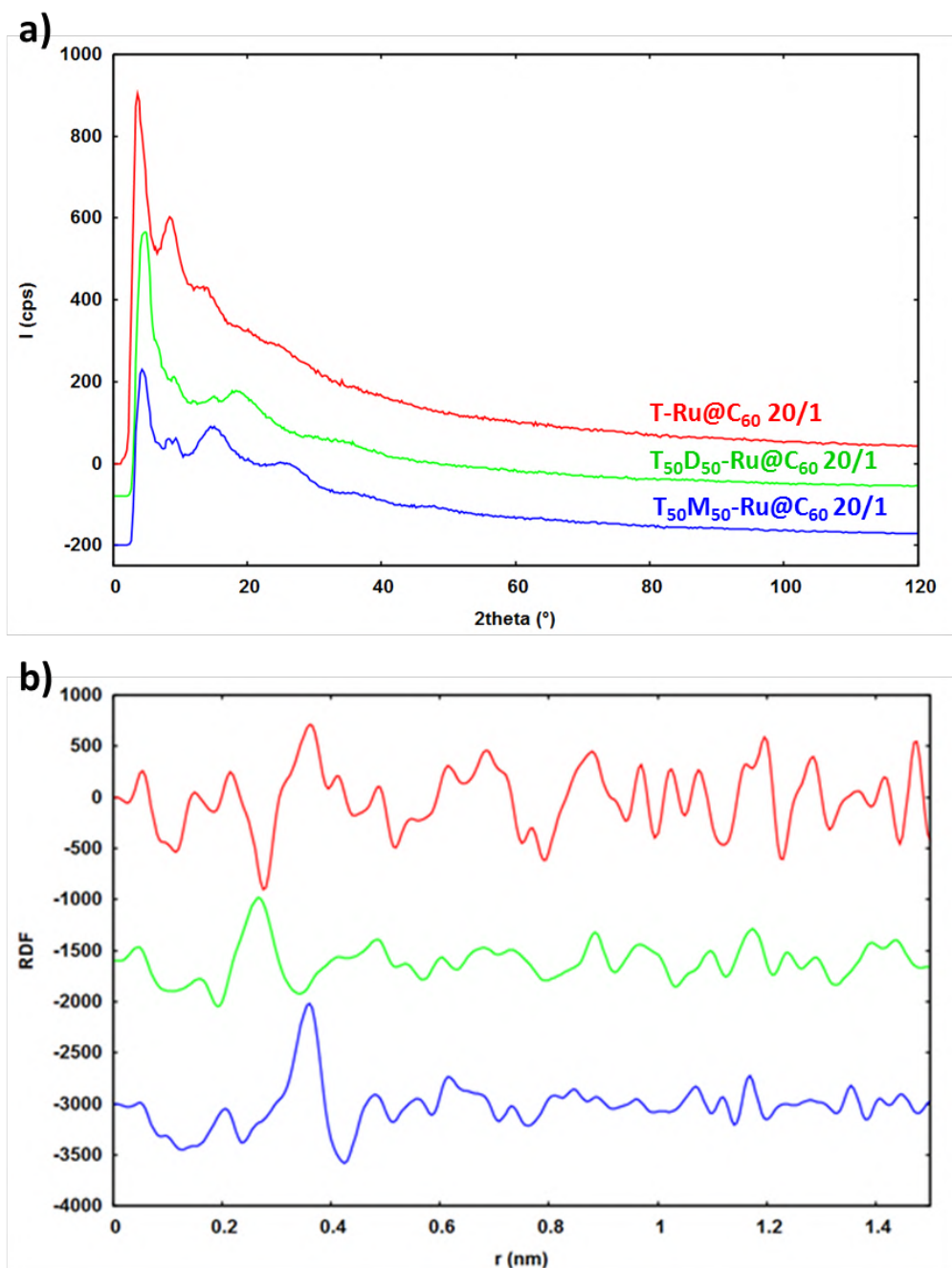


Figure 2.14. a) WAXS Diffractograms of  $T_{95}D_5\text{-Ru@C}_{60}$ ,  $T_{95}M_5\text{-Ru@C}_{60}$  and  $T\text{-Ru@C}_{60}$  samples ( $\text{Ru/C}_{60} = 20/1$ ); and b) related PDF.



We also analyzed the samples prepared in pure toluene at different Ru/C<sub>60</sub> ratio (Figure 2.13). As expected, for all ratios, it was impossible to detect a metallic Ru-Ru distance but a contribution in the 0.20-0.23 nm range could also systematically be observed.

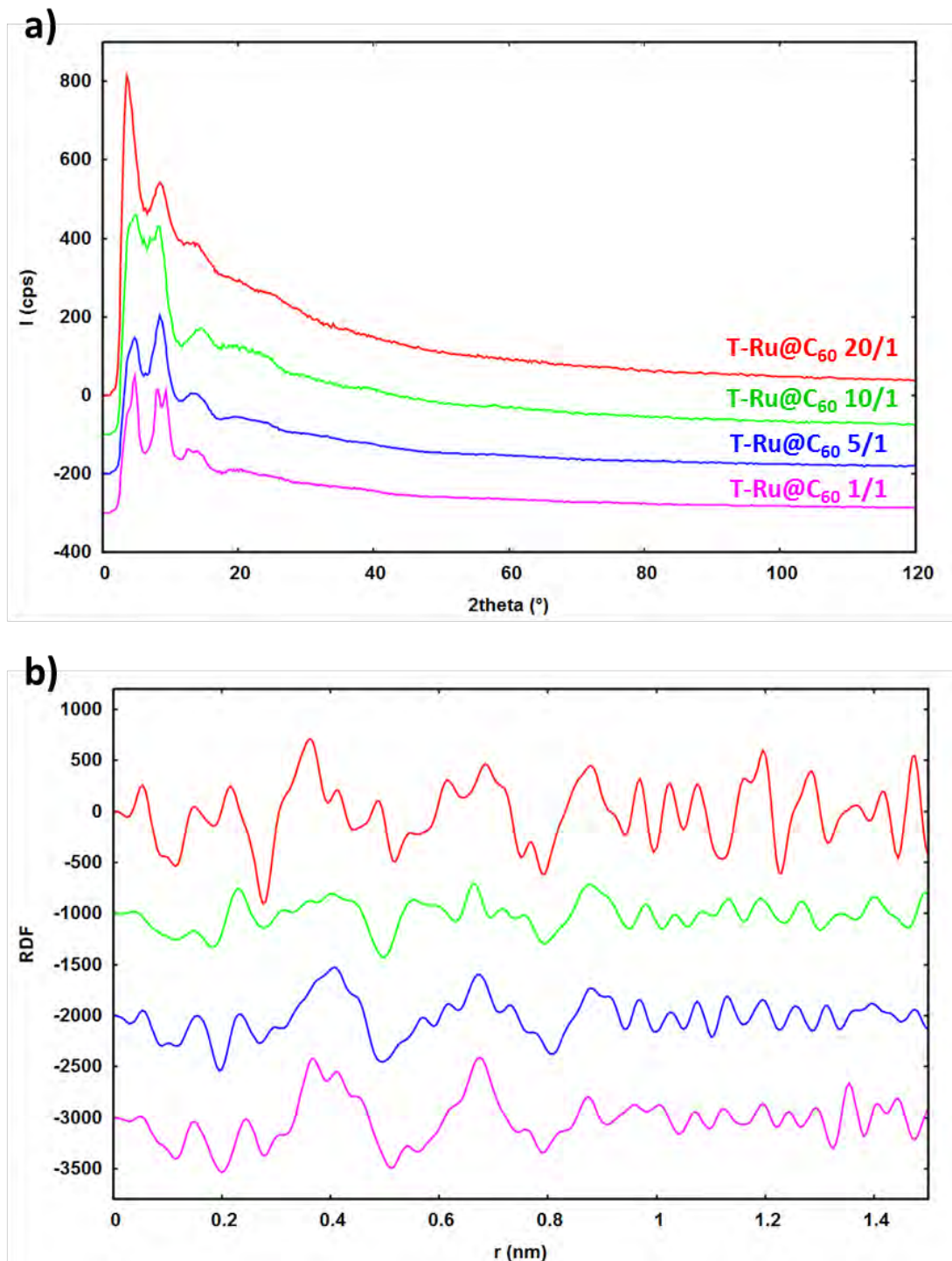


Figure 2.15. a) WAXS Diffractograms for T-Ru@C<sub>60</sub> compounds at different Ru/C<sub>60</sub> ratio; and b) related PDF.

Finally, we compared the  $T_{95}D_5\text{-Ru@C}_{60}$  and  $T_{95}M_5\text{-Ru@C}_{60}$  samples with the  $T\text{-Ru@C}_{60}$  sample at a theoretical  $\text{Ru/C}_{60}$  ratio of 20/1 (Figure 2.16). Differences could be observed between the different samples but poorly defined RDFs and extreme complexity make any analysis irrelevant beyond the observation of a similar distance in the 0.20-0.23 nm range strongly pointing to Ru-C bonding.

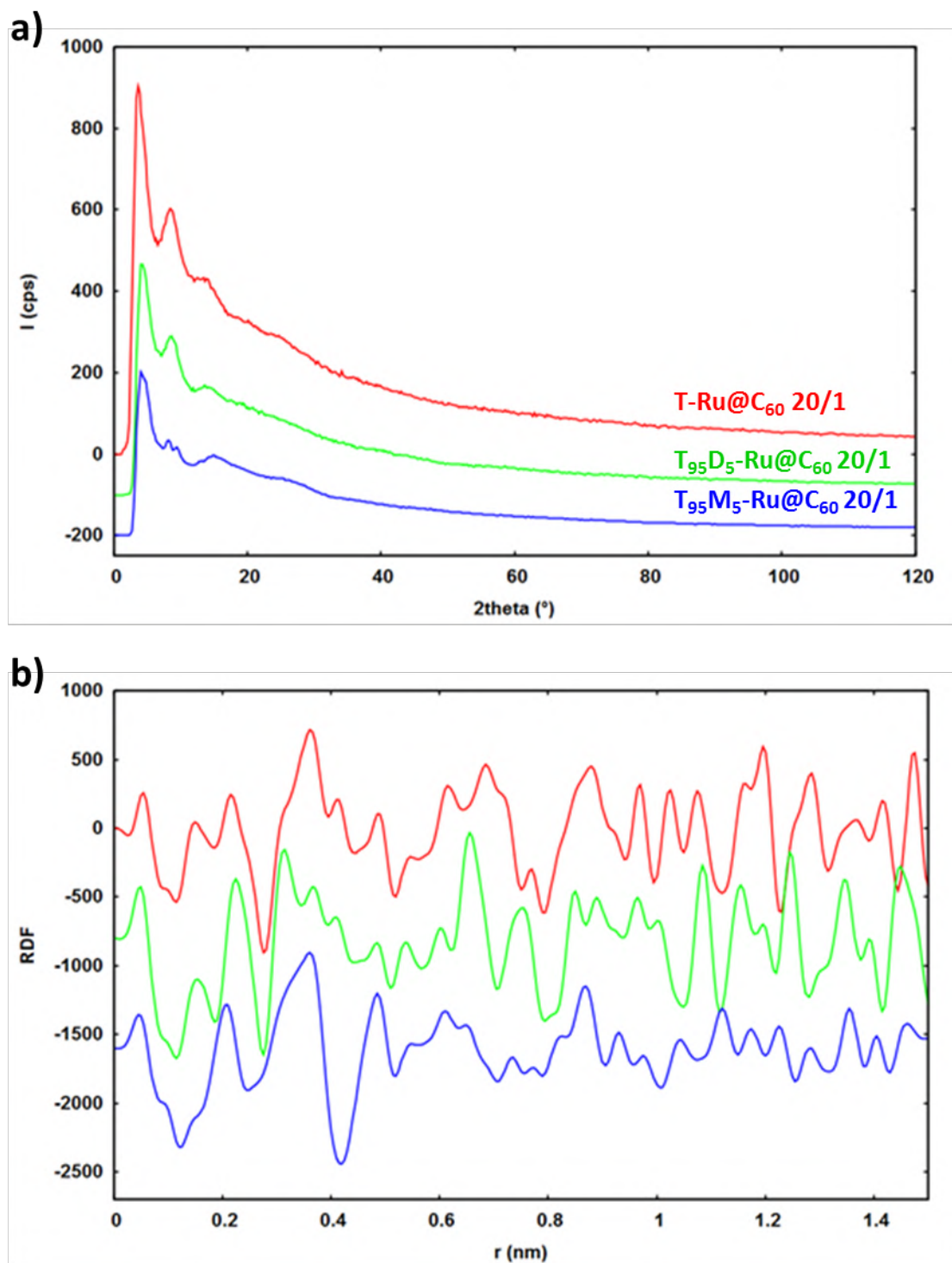


Figure 2.16. a) WAXS Diffractograms of  $T_{95}D_5\text{-Ru@C}_{60}$ ,  $T_{95}M_5\text{-Ru@C}_{60}$  and  $T\text{-Ru@C}_{60}$  samples ( $\text{Ru/C}_{60} = 20/1$ ); and b) related PDF.

Despite the difficulty to apply WAXS to these complex systems, in which both SA and few atom clusters may be present, it was possible from this technique to detect metallic Ru in T<sub>50</sub>D<sub>50</sub>-Ru@C<sub>60</sub>.

This complexity is confirmed by the simulated PDF profiles (Figure 2.17) derived from the DFT models previously used to evaluate the charge transfer, which are poorly comparable to the experimental profiles. It is however interesting to notice that no contribution at *ca.* 0.270 nm is observed for small clusters with a limited number of metallic Ru-Ru bonds on the simulated PDF profiles.

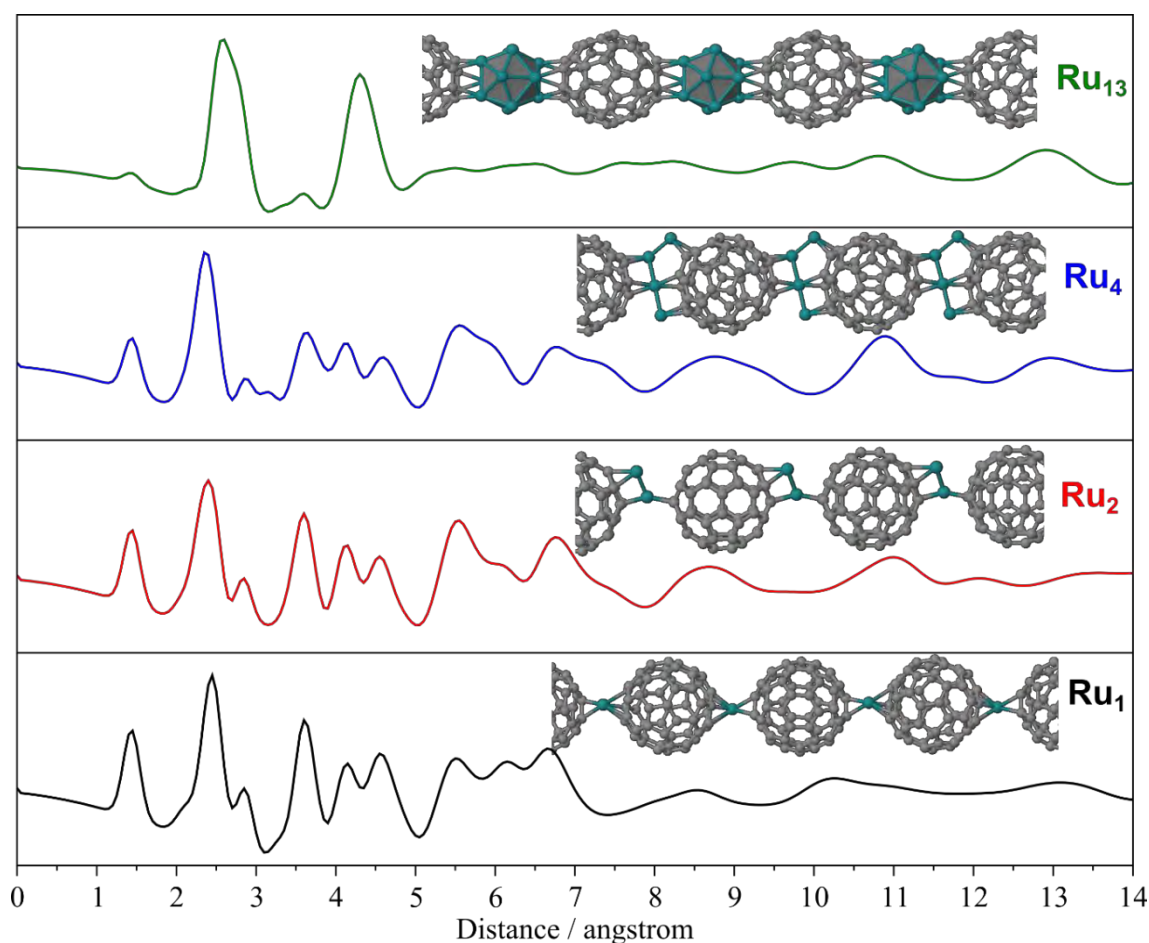


Figure 2.17. Simulated PDF profiles derived from the models optimized at the DFT-PBE level of theory that are shown in Figure 2.3. DFT details regarding such simulations can be found in Ref. 47,48,49,50.

<sup>47</sup> R. L. McGreevy, et al. *Molecular Simulation* **1988**, *1*, 359-367.

<sup>48</sup> T. Proffen, et al. *Journal of Applied Crystallography* **1999**, *32*, 572-575.

<sup>49</sup> L. Cusinato, et al. *Dalton Transactions* **2017**, *46*, 378-395.

<sup>50</sup> J. A. Vargas, et al. *ACS Nano* **2018**, *12*, 9521-9531.

EXAFS analyses were also performed on the sample series prepared in pure toluene at different Ru/C<sub>60</sub> ratio and on the T<sub>95</sub>M<sub>5</sub>-Ru@C<sub>60</sub> sample. The  $k^2\chi(k)$  and the corresponding Fourier Transforms (FTs) are reported in Figure 2.18. A qualitative inspection of the FTs of the samples indicates that samples prepared in pure toluene show a single peak whose intensity increases with the Ru/C<sub>60</sub> ratio.

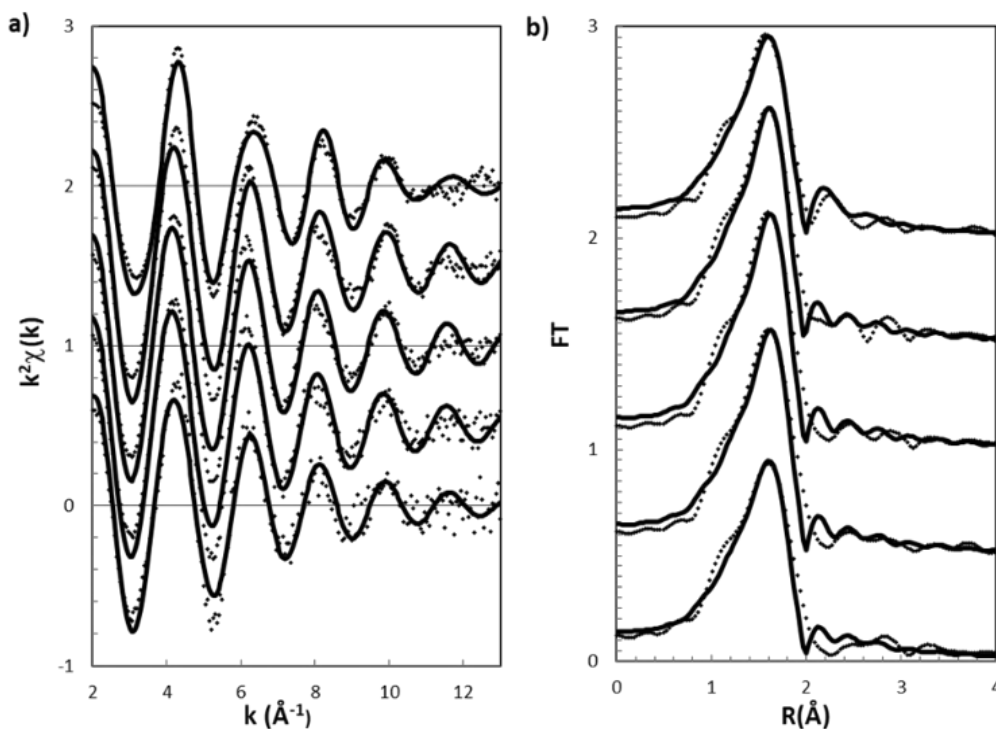


Figure 2.18. a) Fit of the EXAFS region;  $k^2\chi(k)$ ; and b) corresponding FTs for T-Ru@C<sub>60</sub> 1/1, T-Ru@C<sub>60</sub> 5/1, T-Ru@C<sub>60</sub> 10/1, T-Ru@C<sub>60</sub> 20/1, and T<sub>95</sub>M<sub>5</sub>-Ru@C<sub>60</sub> 20/1 using toluene/methanol (from bottom to top). Dots: experiment; Fit: full line.

The sample prepared using toluene/methanol does show some differences, in that a hint of a second shell is detectable and the intensity of the peak is much lower than that of a sample produced using toluene with a comparable Ru/C<sub>60</sub> ratio. There is an additional difference in the position of the maximum that is slightly shifted to shorter distances, as also evidenced by the shift in the oscillations in the  $k^2\chi(k)$ . Data for all the samples were initially fitted with a single shell and a good fit was obtained with a Ru-C shell for all the samples. Ru-C coordination numbers are close to 8 for all samples (consistent with  $\eta^2$ - $\eta^6$  coordination), with the main difference for the sample made using toluene/methanol being a larger Debye-Waller factor. For this sample, the fit did improve by adding a second Ru-Ru shell. In Fig. 2.18 the fitting results are shown and the fitting parameters are reported in Table 2.2. It should be pointed out that, due to the small weight of the

second Ru-Ru shell in the sample  $T_{95}M_5\text{-Ru@C}_{60}$  and the strong correlation between coordination number and Debye-Waller factor, the values of the parameters reported in Table 2.2 can be considered as purely indicative. Notwithstanding, the fit improvement provides a suggestion that Ru clusters could be incorporated in the  $T_{95}M_5\text{-Ru@C}_{60}$  sample containing 34.7 % w/w of Ru. It is also worth mentioning that the EXAFS data reported for reduced  $\text{Pt}_8$  clusters deposited on carbon black do have common features with our results (Fig. 2.19).<sup>51</sup> The very small coordination number ( $\text{CN} = 2.7 \pm 0.2$ ) in the  $T_{95}M_5\text{-Ru@C}_{60}$  sample supports the formation of tiny clusters.

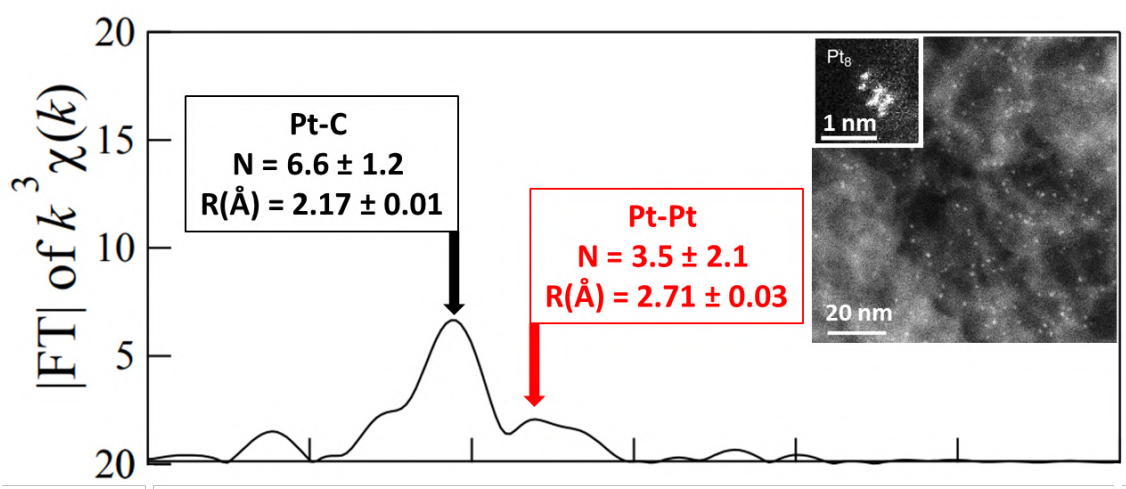


Figure 2.19. Fourier-transformed  $k^3$ -weighted Pt L3-edge EXAFS spectra of  $\text{Pt}_8/\text{CB}$ . Inset dark-field STEM image. From ref. [51]

For the sample prepared in pure toluene, the fact that only  $\text{Ru}_{\text{SA}}$  are produced with a well-defined environment ( $\eta^2\text{-}\eta^6$  coordination) for Ru loading between 10 and 20% w/w is a remarkable result. Indeed, the challenges for SA catalysis for industrial applications are currently to achieve an accurate control over the local structure of metal SA and to increase the active site density.<sup>52</sup> Currently the maximum loadings obtained for SA type catalysts are around 10% w/w.<sup>53,54,55</sup>

<sup>51</sup> T. Imaoka, et al. *Nature Communications* **2017**, 8, 688.

<sup>52</sup> J. Wang, et al. *Advanced Materials* **2018a**, 30, 1801649.

<sup>53</sup> L. Zhao, et al. *Nature Communications* **2019**, 10, 1278.

<sup>54</sup> J. Li, et al. *Angewandte Chemie International Edition* **2019**, 58, 7035-7039.

<sup>55</sup> J. Wu, et al. *Small Methods* **2020**, 4, 1900540.



Table 2.2. Best fit parameters obtained by fitting the experimental EXAFS of samples. Coordination numbers ( $N$ ), interatomic distances ( $R$ ), Debye-Waller factors,  $\Delta E_0$  and  $R$ -factors are shown.

Sample		$N$	$R(\text{\AA})$	$\sigma^2(\text{\AA}^2)$	$\Delta E_0$	$R$ -factor
T-Ru@C <sub>60</sub> 1/1	Ru-C	7.7±0.2	2.17 ± 0.02	0.006 ± 0.003	3±2	0.037
T-Ru@C <sub>60</sub> 5/1	Ru-C	7.9±0.1	2.18 ± 0.01	0.005 ± 0.002	4±1	0.040
T-Ru@C <sub>60</sub> 10/1	Ru-C	8.1±0.2	2.17 ± 0.02	0.005 ± 0.002	4±2	0.039
T-Ru@C <sub>60</sub> 20/1	Ru-C	8.0±0.2	2.16 ± 0.02	0.005 ± 0.003	4±2	0.039
T <sub>95</sub> M <sub>5</sub> -Ru@C <sub>60</sub>	Ru-C	8.0±0.2	2.16 ± 0.02	0.007 ± 0.002	3±2	0.013
20/1	Ru-Ru	2.7±0.2	2.67 ± 0.03	0.015 ± 0.004	-	-

### 2.2.3 Catalytic activity of the Ru@C<sub>60</sub> nanostructures

Since STEM-HAADF observations and WAXS and EXAFS analyses were not decisive concerning the presence or not of Ru subnanometric particles in all the samples obtained with a mixture of solvents, we decided to use catalysis to probe their presence. Indeed, in hydrogenation reactions, the electron deficient Ru<sub>SA</sub> should be less efficient than Ru<sub>NP</sub>/clusters for hydrogen dissociative chemisorption, which is often rate limiting.<sup>56</sup> The electro-deficiency in Ru SAC results in a lower d-band center that offers less electron back-donation to the antibonding orbital of H<sub>2</sub> molecules, resulting in relatively high activation energy for H<sub>2</sub> dissociation.<sup>57,58</sup> On the other side, it was reported that subnanometer Ru clusters can be very active hydrogenation catalysts.<sup>59</sup> It was also reported that among Pd<sub>n</sub>C<sub>60</sub> fullerides, active hydrogenation compounds are those with  $n > 3$ ,<sup>60</sup> that is the samples suspected to contain Pd<sub>NP</sub>.<sup>30</sup>

We chose as first probe reaction the hydrogenation of nitrobenzene (NB) (Figure 2.20) to aniline (AN), since Ru<sub>NP</sub> are known to be active for this reaction.<sup>61,62,63,64</sup> The reaction was studied at 30 bar H<sub>2</sub> and 80 °C in ethanol with a Ru concentration of 0.025 mmol. The activity of the catalysts expressed in moles of NB consumed per mole of Ru

<sup>56</sup> M. D. Rossell, et al. *Catalysis Science & Technology* **2016**, 6, 4081-4085.

<sup>57</sup> J.-Z. Qiu, et al. *Chemistry of Materials* **2019**, 31, 9413-9421.

<sup>58</sup> D. N. Sredojević, et al. *ChemistrySelect* **2018**, 3, 2631-2637.

<sup>59</sup> Y. Qian, et al. *Green Chemistry* **2020**, 22, 850-859.

<sup>60</sup> N. F. Goldshleger *Fullerene Science and Technology* **2001**, 9, 255-280.

<sup>61</sup> F. Leng, et al. *ACS Catalysis* **2016a**, 6, 6018-6024.

<sup>62</sup> M. R. Axet, et al. *ACS Applied Nano Materials* **2018**, 1, 5885-5894.

<sup>63</sup> F. Leng, et al. *Chemistry – A European Journal* **2017**, 23, 13379-13386.

<sup>64</sup> C. S. Srikanth, et al. *Journal of Nanoscience and Nanotechnology* **2015**, 15, 5403-5409.



(determined by ICP) and per second, and being equivalent to an instantaneous Site Time Yield (“STY” in the following).

We independently checked that the C<sub>60</sub> fullerene has no activity for this reaction under these experimental conditions. Table 2.3 shows the results obtained with the Ru@C<sub>60</sub> samples prepared in different solvents and at different Ru/C<sub>60</sub> ratio.

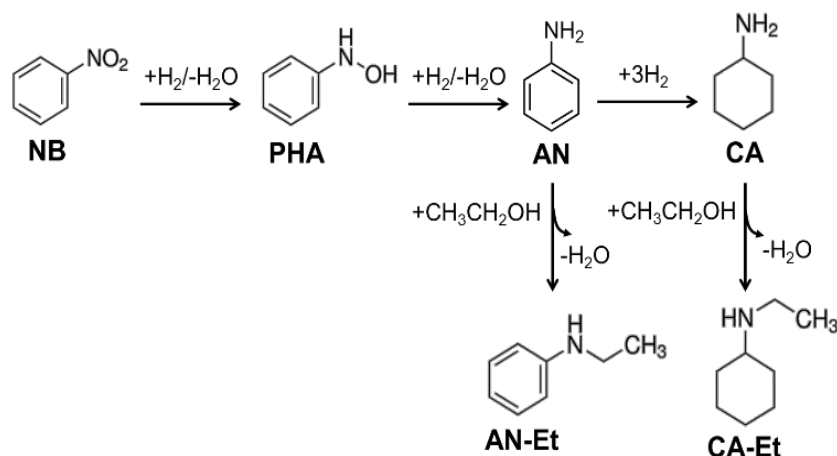


Figure 2.20. Pathways for products and by products formed during NB hydrogenation to aniline.

Table 2.3. Results of hydrogenation of nitrobenzene in ethanol with different Ru@C<sub>60</sub> catalysts.

Ru/C <sub>60</sub>	Nitro- group		Selectivity [%] <sup>a</sup>				
	STY (h <sup>-1</sup> ) <sup>b</sup>	Time (h) <sup>c</sup>	AN	AN-Et	CA	CA-Et	PHA
T-Ru@C <sub>60</sub> 1/1	14.5	2.3	82.4	8.5	7.1	2.0	-
T-Ru@C <sub>60</sub> 5/1	15.0	2.2	85.3	4.6	-	-	10.1
T-Ru@C <sub>60</sub> 10/1	13.4	2.5	78.4	6.4	5.5	3.6	2.9
T-Ru@C <sub>60</sub> 20/1	12.5	3.0 <sup>d</sup>	86.7	5.4	3.1	-	4.9
T <sub>95</sub> M <sub>5</sub> -Ru@C <sub>60</sub> 20/1	49.9	0.64	100.0	-	-	-	-
T <sub>75</sub> M <sub>25</sub> -Ru@C <sub>60</sub> 20/1	107.36	0.34	83.5	-	-	2.9	13.6
T <sub>50</sub> M <sub>50</sub> -Ru@C <sub>60</sub> 20/1	135.5	0.30	79.9	-	0.4	-	19.0
T <sub>75</sub> D <sub>25</sub> -Ru@C <sub>60</sub> 20/1	12.6	2.5	75.9	14.3	-	-	8.8
T <sub>50</sub> D <sub>50</sub> -Ru@C <sub>60</sub> 20/1	18.2	2.6	66.6	30.8	-	-	2.6

Reaction conditions: 0.025 mmol Ru, 500 mg (4.06 mmol) nitrobenzene, 200mg (1.1 mmol) dodecane (internal standard), 30 bar H<sub>2</sub>, 80 °C, 30 mL EtOH. <sup>a</sup> determined by GC-FID using internal standard technique at  $\approx$  20% of conversion. <sup>b</sup> STY (mol<sub>NBconverted</sub>/mol<sub>Ru</sub>·t) calculated at  $\approx$  20% of conversion. <sup>c</sup> Time to reach 20% of conversion. <sup>d</sup> Time to reach 16% of conversion, which is de maximal obtained with this sample.

The main products of the reaction were AN and cyclohexylamine (CA). N-phenylhydroxylamine (PHA), and N-ethylaniline (AN-Et) and N-ethylcyclohexylamine (CA-Et) both formed by N-alkylation from ethanol, were the only detected by-products. All catalysts were found active for NB hydrogenation. The evolution of the NB conversion over the time is shown in Figure 2.21a for the Ru@C<sub>60</sub> series prepared in toluene at different Ru/C<sub>60</sub> ratio, and for the series prepared in toluene/methanol mixtures.

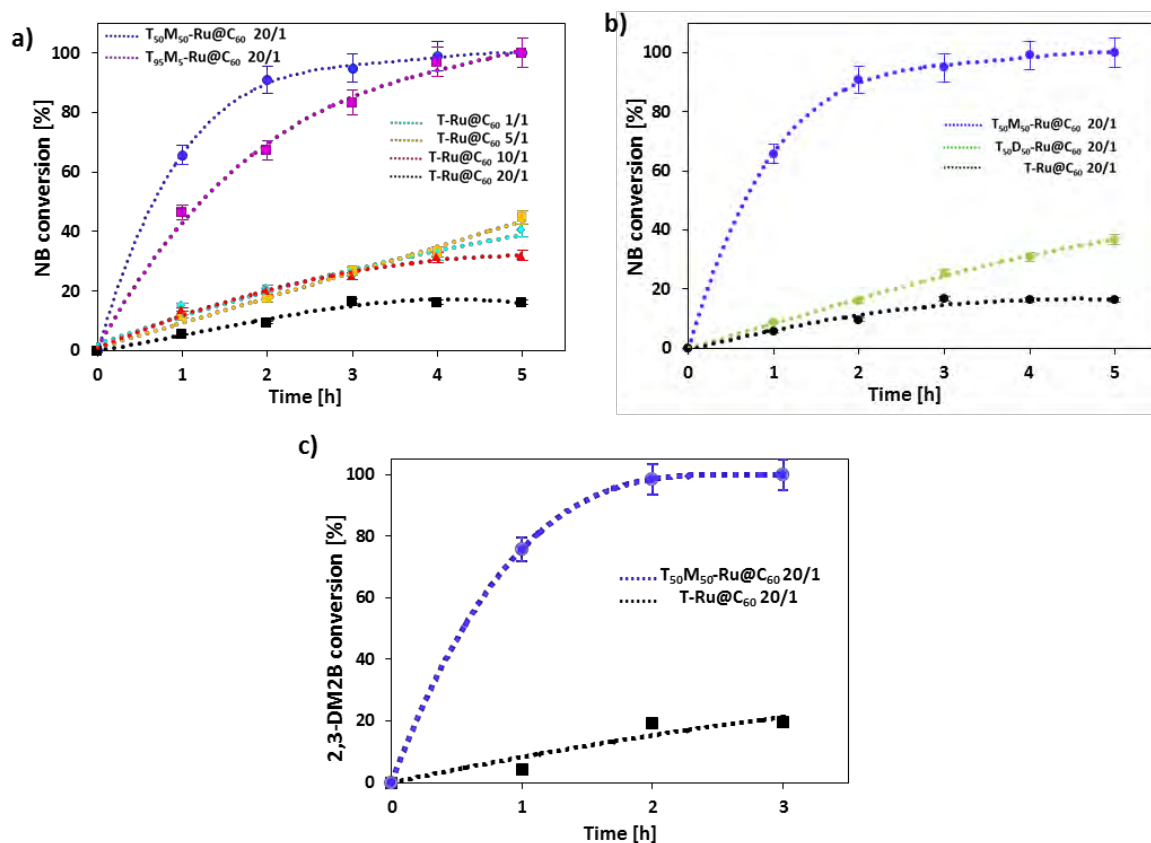


Figure 2.21. Time-conversion curve for a) NB hydrogenation with T-Ru@C<sub>60</sub> and TM-Ru@C<sub>60</sub> materials; and b) T-Ru@C<sub>60</sub> 20/1, T<sub>50</sub>M<sub>50</sub>-Ru@C<sub>60</sub> and T<sub>50</sub>D<sub>50</sub>-Ru@C<sub>60</sub>; and c) for 2,3-dimethyl-2-butene hydrogenation with T-Ru@C<sub>60</sub> and T<sub>50</sub>M<sub>50</sub>-Ru@C<sub>60</sub>.

For all the samples prepared in pure toluene (Ru/C<sub>60</sub> ratio 1/1 to 20/1), for which only SA are present, the conversion of NB is low compared to the ones prepared in toluene/methanol mixtures. For these latter series, the activity increase is already observable for the T<sub>95</sub>M<sub>5</sub>-Ru@C<sub>60</sub> sample, for which the presence of Ru clusters has been suggested from EXAFS analyses. The T<sub>50</sub>M<sub>50</sub>-Ru@C<sub>60</sub> sample is by far the most active catalyst with a STY of 135.5 h<sup>-1</sup>. Comparison between samples prepared in pure toluene and in solvent mixtures are shown in Fig. 2.21b. The T<sub>50</sub>D<sub>50</sub>-Ru@C<sub>60</sub> sample, for which metallic Ru has been evidenced by WAXS is much less efficient (STY of 18.2 h<sup>-1</sup>) than

the  $T_{50}M_{50}\text{-Ru@C}_{60}$  sample (STY of  $135.5\text{ h}^{-1}$ ). This result should be related to the core-shell structure of the  $T_{50}D_{50}\text{-Ru@C}_{60}$  catalyst, for which the active ruthenium is limited to the external surface of the spheres (Figure 2.11a,b). In order to investigate the ability of various  $-(\text{C}_{60}\text{-Ru}_n\text{-C}_{60})_n$ - hetero-structures to chemisorb  $\text{H}_2$  molecules, and thus get an idea on the activity of such metallic centers for further substrate hydrogenation, we have performed a series of calculations for naked  $\text{Ru}_1$ , and  $\text{Ru}_2$ ,  $\text{Ru}_4$  and  $\text{Ru}_{13}$  clusters embedded in a 1D- $\text{C}_{60}$  polymeric phase. Dissociative adsorption energies per H with respect to the  $\text{H}_2$  molecule number in interaction with a  $\text{Ru}_n$  cluster are shown in Figure 2.22, as well as final geometry representations.

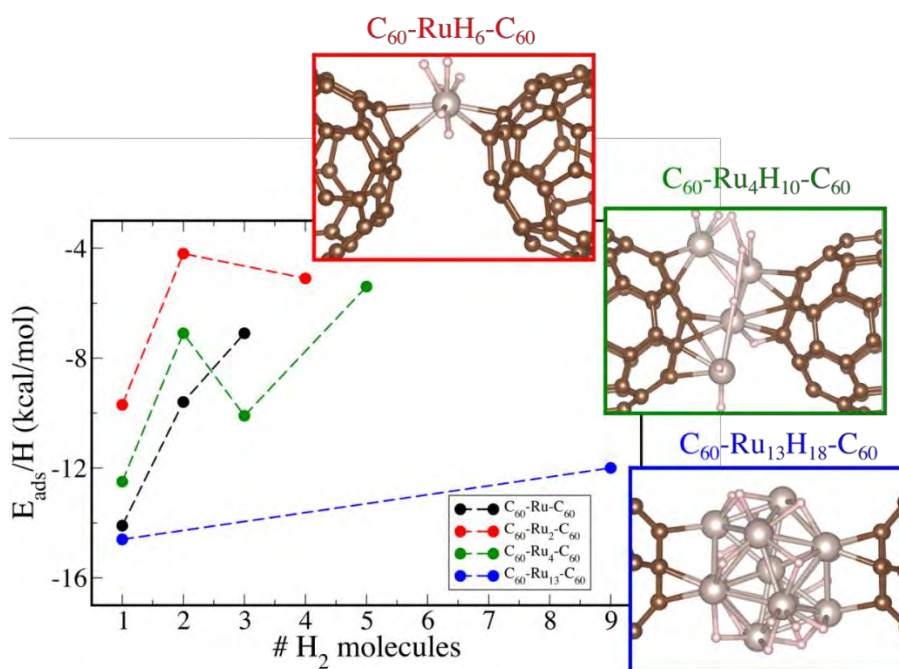


Figure 2.22. Dissociative adsorption energy (in kcal/mol) per adsorbed H on various  $-(\text{C}_{60}\text{-Ru}_n\text{-C}_{60})_n$ - hetero-structures.

Since for a  $\text{Ru}_{\text{SA}}$ , the 18-electron rule is satisfied upon the adsorption of 3  $\text{H}_2$  molecules, the adsorption energy drops and no further  $\text{H}_2$  can be adsorbed. Interestingly, the Ru center coordination mode, changes from  $\eta^2\text{-}\eta^6$  to  $\eta^2\text{-}\eta^2$  with 3 partially activated  $\text{H}_2$  presenting elongated H-H bonds, around  $0.9\text{ \AA}$  ( $0.74\text{ \AA}$  in  $\text{H}_2$ ). With larger clusters, more  $\text{H}_2$  can be adsorbed and dissociated, but adsorption energy values always reach a plateau (around  $-5\text{ kcal/mol}$ ) for clusters smaller than  $\text{Ru}_{13}$ , experiencing a surface saturation effect. However, in the case of  $\text{Ru}_{13}$ , for a value of  $1.5\text{ H/per surface Ru}$ , a ratio usually

reported experimentally,<sup>65,66</sup> the energy per adsorbed H is still large and agrees well with previous reports.<sup>67</sup> Those results strongly suggest that very electro-deficient Ru SA and few atom aggregates are not performing for H<sub>2</sub> activation compared to larger clusters.

We have also evaluated the catalytic activity of the most active T<sub>50</sub>M<sub>50</sub>-Ru@C<sub>60</sub> catalyst for the hydrogenation of toluene to methylcyclohexane. Ruthenium has been widely used for this reaction since toluene is more strongly adsorbed on this metal than other metallic surfaces such as Pd or Pt.<sup>68,69</sup> The results are depicted in Table 2.4. Although the results reported in this table show very contrasting catalytic activity for various Ru catalysts, a modest activity for the T<sub>50</sub>M<sub>50</sub>-Ru@C<sub>60</sub> catalyst is measured compared to the best ruthenium catalysts. An explanation of this result could come from differences in the adsorption energy of toluene on the various catalysts. Indeed, when the size of a reactant molecule is comparable to that of a nanometer catalyst (such as toluene and the Ru clusters in T<sub>50</sub>M<sub>50</sub>-Ru@C<sub>60</sub>), the adsorption configuration of the molecule on the catalyst becomes different from that on their larger counterparts. Consequently, distinct catalytic performances can be observed for catalysts of different sizes. Thus, size-dependent adsorption of styrene was demonstrated on Pd clusters.<sup>70</sup> When the surface of the Pd cluster becomes too small (clusters between Pd<sub>7</sub> and Pd<sub>16</sub>), the styrene molecule cannot fully bond with the cluster. Typical adsorption energy of toluene on Ru(0001) surface ranged from 48 to 54 kcal/mol.<sup>71</sup> DFT calculations should be performed in the future to determine the adsorption energy of toluene on a -(C<sub>60</sub>-Ru<sub>n</sub>-C<sub>60</sub>)<sub>n</sub>- structure to confirm this hypothesis.

Finally, the high TOF obtained in NB hydrogenation compared to previous studies,<sup>72,73</sup> incite us to evaluate the catalytic activity of the T<sub>50</sub>M<sub>50</sub>-Ru@C<sub>60</sub> sample in the difficult hydrogenation of the tetra-substituted olefin 2,3-dimethyl-2-butene. This reaction can be performed with cationic iridium complexes under mild conditions (room temperature, 1-

<sup>65</sup> J. García-Antón, et al. *Angewandte Chemie International Edition* **2008**, 47, 2074-2078.

<sup>66</sup> R. Berthoud, et al. *Journal of Catalysis* **2008**, 260, 387-391.

<sup>67</sup> L. Cusinato, et al. *Nanoscale* **2016**, 8, 10974-10992.

<sup>68</sup> Q. Tan, et al. *ACS Catalysis* **2015**, 5, 6271-6283.

<sup>69</sup> S. Furukawa, et al. *ACS Catalysis* **2018**, 8, 8177-8181.

<sup>70</sup> Z. Xia, et al. *The Journal of Physical Chemistry C* **2019**, 123, 2182-2188.

<sup>71</sup> S. Furukawa, et al. *ACS Catalysis* **2018**, 8, 8177-8181.

<sup>72</sup> J. Wu, et al. *Small Methods* **2020**, 4, 1900540.

<sup>73</sup> F. Leng, et al. *ACS Catalysis* **2016a**, 6, 6018-6024.

5 bar, TOF = 4000 h<sup>-1</sup>).<sup>74,75,76</sup> However, with some complexes irreversible deactivation process occurs, preventing reaction completion.<sup>75</sup>

Table 2.4. Results toluene hydrogenation over ruthenium catalysts.

Sample	Conditions	Time (hours)	Conversion (%)	TOF (mol conv./mol <sub>Metal</sub> *h)	Ref
20/1 Ru@C <sub>60</sub> - T <sub>50</sub> M <sub>50</sub>	70 °C, 30 bar H <sub>2</sub> , Tol/Ru ~ 900	2	>99	704 <sup>a)</sup>	<sup>b)</sup>
Ru/CNF-P	100°C, 30 bar H <sub>2</sub> Tol/Ru ~ 11200	2.5	>99	35800	77
Ru/C-silica	110°C, 40 bar H <sub>2</sub> , Tol/Ru ~ 10000	1.02	>99	0.0098	78
Ru/NHPC	100°C, 14 bar H <sub>2</sub> , Tol/Ru ~ 12700	1	72	9160	79
Ru/hectorite	50°C, 50 bar H <sub>2</sub> , Tol/Ru ~ 3000	0.25	-	3550	80
Ru/MgO	120°C, 10 bar H <sub>2</sub> , Tol/Ru ~ 4000	1.5	100	1000	81

<sup>a)</sup> At 1h of reaction. <sup>b)</sup> This study

Colloidal metallic NP (Rh, Ru, Pt), although less active (TOF = 160-320 h<sup>-1</sup>) are also efficient catalysts for this reaction under relatively mild conditions (room temperature to 75°C, 1-10 bar of H<sub>2</sub>).<sup>82,83</sup> As far as supported catalysts are concerned (Rh, Co), much lower activities were reported (TOF = 2-10 h<sup>-1</sup>) under slightly harsher operating conditions (25 to 150°C, 5-40 bar).<sup>84,85</sup> At 50 °C and under 20 bar of H<sub>2</sub>, the reaction with the T<sub>50</sub>M<sub>50</sub>-Ru@C<sub>60</sub> catalyst is completed within 2 h. The calculated STY at 20% conversion 470 h<sup>-1</sup> is to the best of our knowledge the higher ever reported for supported metallic NP. For this reaction also, the catalysts prepared in pure toluene containing only SA are much less active (Fig. 2.21c), pointing their low hydrogenation activity. Finally,

<sup>74</sup> R. H. Crabtree, et al. *Journal of Organometallic Chemistry* **1977**, 141, 205-215.

<sup>75</sup> R. Crabtree *Accounts of Chemical Research* **1979**, 12, 331-337.

<sup>76</sup> L. D. Vázquez-Serrano, et al. *Chemical Communications* **2002**, 2518-2519.

<sup>77</sup> M. Takasaki, et al. *Chemistry – An Asian Journal* **2007**, 2, 1524-1533.

<sup>78</sup> F. Su, et al. *J Am Chem Soc* **2007**, 129, 14213-14223.

<sup>79</sup> M. Tang, et al. *Green Chemistry* **2016**, 18, 6082-6090.

<sup>80</sup> G. Süss-Fink, et al. *Journal of Cluster Science* **2007**, 18, 87-95.

<sup>81</sup> M. Fang, et al. *Journal of Catalysis* **2014**, 311, 357-368.

<sup>82</sup> L. Gao, et al. *Tetrahedron* **2015**, 71, 6414-6423.

<sup>83</sup> E. T. Silveira, et al. *Chemistry – A European Journal* **2004**, 10, 3734-3740.

<sup>84</sup> F. K. Scharnagl, et al. *Science Advances* **2018**, 4, eaau1248.

<sup>85</sup> A. Sánchez, et al. *Applied Catalysis A: General* **2014**, 477, 117-124.

we have performed a series of calculations to propose the mechanism of tetra-substituted olefin 2,3-dimethyl-2-butene hydrogenation.

Interestingly due to the high steric hindrance induced by the small C<sub>60</sub>-C<sub>60</sub> distance, the hydrogenation is not possible on Ru<sub>SA</sub>. On Ru<sub>13</sub>H<sub>18</sub>, the hydrogenation reaction appears thermodynamically favorable, as it can be seen in Fig. 2.23, with a negative balance of 26 kcal/mol with respect to the separated reactants. The regeneration of the catalyst leading to the release of the 2,3-dimethylbutane molecule and the coordination of a H<sub>2</sub> and 2,3-dimethyl-2-butene molecules is also favorable by -12 kcal/mol with respect to the final product (-38 kcal/mol with respect to the entrance channel). The first hydrogenation step leading to an alkyl intermediate is kinetically easily accessible with an activation barrier of 11 kcal/mol with respect to the  $\pi$ -coordinated adduct.

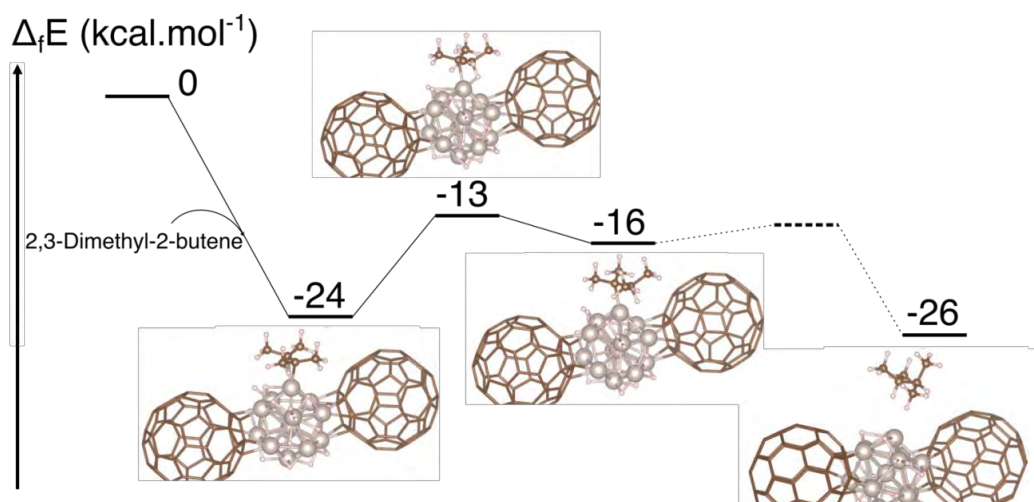


Figure 2.23 Possible reaction path of 2,3-dimethyl-2-butene hydrogenation.

On this intermediate, it is interesting to note the presence of a  $\beta$ -agostic C-H interaction as evidenced by the H-Ru and H-C distances of 1.86 and 2.44 Å, respectively. The second step is a barrierless process with an energy barrier of less 2 kcal/mol leading to the formation of the 2,3-dimethylbutane product.

### 2.3. Conclusions

In conclusion, we have highlighted the crucial role of the solvent for the growth of subnanometric ruthenium NP in Ru@C<sub>60</sub> hetero-structures. While Ru<sub>SA</sub> are selectively obtained in pure toluene (Ru@C<sub>60</sub> hetero-structures with very high Ru loading = 9-20% w/w), the use of a toluene/methanol solvent mixture makes it possible to increase the metal loading up to 50% w/w and to obtain ruthenium clusters uniformly distributed in



the materials. These novel catalysts are extremely active for the hydrogenation reactions of nitrobenzene and tetra-substituted 2,3-dimethyl-2-butene. For this latter reaction a STY of  $485 \text{ h}^{-1}$  was calculated, which is the higher ever reported for supported metallic NP. This work provides a general strategy for producing high loading and ultra-dispersed supported catalyst for enhanced catalytic performance.

## 2.4. Experimental

### 2.4.1. General methods

All operations were carried out under argon atmosphere using standard Schlenk techniques or in an MBraun glovebox. Solvents were purified by standard methods or by an MBraun SPS-800 solvent purification system.  $[\text{Ru}(\text{COD})(\text{COT})]$  (COD= 1,5 cyclooctadiene, COT= 1,3,5-cyclooctatriene) was purchased from Nanomeps Toulouse, fullerene  $\text{C}_{60}$  from Sigma-Aldrich, Ar and  $\text{H}_2$  from Air Liquid. All these reactants were used as received. The ruthenium content was established by inductively coupled plasma optical emission spectroscopy (ICP-OES) with a Thermo Scientific ICAP 6300 instrument on samples dried 2 h at  $200^\circ\text{C}$ .

### 2.4.2. Synthesis of $\text{Ru}@\text{C}_{60}$ nanostructures

In a typical experiment the  $[\text{Ru}(\text{COD})(\text{COT})]$  complex was introduced in a Fisher-Porter bottle with a solution of fullerene  $\text{C}_{60}$  in the desired solvent. The resulting purple solution was stirred for 30 min at room temperature, after which the bottle was pressurized with 3 bar of  $\text{H}_2$ . The solution, which turned black after few minutes of reaction, was kept under stirring overnight at room temperature. After this period, excess of  $\text{H}_2$  was eliminated and the volume of solvent was reduced under vacuum. Pentane was then added to precipitate the colloidal suspension. After filtration under argon with a cannula, the black solid was washed twice with pentane and filtrated again before drying under vacuum. The quantities of reactant used for each  $\text{Ru}/\text{C}_{60}$  ratio studied are detailed in Table 2.5.

### 2.4.3. Hydrogenation of nitrobenzene

Hydrogenation reactions were performed in Top Industry high pressure and temperature Stainless steel autoclave with a controlling system. In a typical experiment, the autoclave was purged by three vacuum/argon cycles. The mixture of  $\text{Ru}@\text{C}_{60}$  catalysts (0.025 mmol Ru), dodecane (as internal standard, 1.1 mmol) and nitrobenzene (4.06 mmol) in 30 mL of ethanol was prepared in a glovebox, ultrasonicated for 5 min and then transferred into

a high-pressure autoclave under argon atmosphere. The autoclave was heated to 80 °C and pressurized with 30 bar of H<sub>2</sub>; the stirring rate was fixed at 1000 rpm. Samples of the reaction mixture were taken periodically and then analysed by GC-FID. Quantitative analysis of reaction mixtures was performed via GC-MS using calibration solutions of commercially available products.

*Table 2.5. Reactant and solvent quantities of the prepared Ru@C<sub>60</sub> samples.*

Ru@C <sub>60</sub> samples	Solvent (mL)	Fullerene (mg)	Ru(COD) (COT) (mg)	Yield (mg)	Ru loading (%) <sup>a</sup>
D-Ru <sub>1</sub> @C <sub>60</sub> 1/1 <sup>27</sup>	CH <sub>2</sub> Cl <sub>2</sub> (300)	68.5	30	68.1	10.6
D-Ru@C <sub>60</sub> 2/1 <sup>27</sup>	CH <sub>2</sub> Cl <sub>2</sub> (400)	91.3	80	100	16.7
D-Ru@C <sub>60</sub> 5/1 <sup>27</sup>	CH <sub>2</sub> Cl <sub>2</sub> (400)	91.3	200	129	35.6
T-Ru <sub>1</sub> @C <sub>60</sub> 1/1 <sup>27</sup>	Toluene (50)	91.3	62.5	116	9.1
T-Ru@C <sub>60</sub> 5/1	Toluene (50)	114.2	250	136.8	11.0
T-Ru@C <sub>60</sub> 10/1	Toluene (50)	57.2	250	88.9	16.6
T-Ru@C <sub>60</sub> 20/1	Toluene (50)	28.6	250	58.3	20.0
T-Ru@C <sub>60</sub> 40/1	Toluene (50)	14.3	250	18	19.2
T-Ru@C <sub>60</sub> 20/1 (50 °C)	Toluene (50)	22.9	200	31.7	19.6
T-Ru@C <sub>60</sub> 20/1(100 °C)	Toluene (50)	17.1	150	24.7	20.5
T <sub>95</sub> D <sub>5</sub> -Ru@C <sub>60</sub> 20/1	Toluene (47.5)/ CH <sub>2</sub> Cl <sub>2</sub> (2.5)	28.6	250	56.7	24.4
T <sub>75</sub> D <sub>25</sub> -Ru@C <sub>60</sub> 20/1	Toluene (37.5)/ CH <sub>2</sub> Cl <sub>2</sub> (12.5)	28.6	250	73.0	35.8
T <sub>50</sub> D <sub>50</sub> -Ru@C <sub>60</sub> 20/1	Toluene (25)/ CH <sub>2</sub> Cl <sub>2</sub> (25)	28.6	250	80.6	36.0
T <sub>95</sub> M <sub>5</sub> -Ru@C <sub>60</sub> 20/1	Toluene (47.5)/ MeOH (2.5)	24.1	200	50.0	34.7
T <sub>75</sub> M <sub>25</sub> -Ru@C <sub>60</sub> 20/1	Toluene (37.5)/ MeOH (12.5)	28.6	250	70.0	41.6
T <sub>50</sub> M <sub>50</sub> -Ru@C <sub>60</sub> 20/1	Toluene (25)/ MeOH (25)	28.6	250	103.8	47.1

a) Determined by ICP-OES

#### 2.4.4. Hydrogenation of 2,3-dimethyl-2-butene

In a typical experiment, the Top Industry autoclave was purged by three vacuum/argon cycles. The mixture of Ru@C<sub>60</sub> catalysts (5 mg), dodecane (as internal standard, 1.1 mmol) and 2,3-dimethyl-2-butene (10.0 mmol) in 30 mL of cyclohexane was prepared in a glovebox, ultra-sonicated for 5 min and then transferred into a high-pressure autoclave under argon atmosphere. The autoclave was heated to 50 °C and pressurized with 20 bar of H<sub>2</sub>; the stirring rate was fixed at 1000 rpm. Samples of the reaction mixture were taken periodically and then analysed by GC-MS. Quantitative analysis of reaction mixtures was performed via GC-FID using calibration solutions of commercially available products.

#### 2.4.5. Catalyst characterization

**TEM analyses.** TEM and HRTEM analyses were performed at the “Centre de microcaracterisation Raimond Castaing, UMS 3623, Toulouse”. Low resolution TEM was performed by using a JEOL JEM 1011 CX-T electron microscope operating at 100 kV with a point resolution of 4.5 Å, and a JEOL JEM 1400 electron microscope operating at 120 kV. The high-resolution analyses were conducted using a JEOL JEM 2100F equipped with a Field Emission Gun (FEG) operating at 200 kV with a point resolution of 2.3 Å and a JEOL JEM-ARM200F Cold FEG operating at 200 kV with a point resolution of > 1.9 Å. The approximation of the particles mean size was made through a manual analysis of enlarged micrographs by measuring at least 200 particles on a given grid. Other TEM micrographs were acquired with a JEOL 2100F S/TEM microscope equipped with a FEG operating at 200 kV, a spherical aberration probe corrector and a GATAN Tridiem energy filter. The resolutions attained are 2 Å and 1.1 Å under parallel TEM mode and scanning STEM modes, respectively. For STEM-HAADF analyses the spot size was of 0.13 nm, a current density of 140 pA, the camera focal length was 10 cm, corresponding to inner and outer detection angle of the annular detector of about 60 mrad and 160 mrad.

**WAXS, EXAFS, Raman and XPS analyses.** Wide Angle X-ray Scattering measurements were performed at CEMES (Dr. Pierre Lecante) on a diffractometer dedicated to Pair Distribution Function (PDF) analysis: graphite-monochromatized Molybdenum radiation (0.07169 nm), solid-state detection and low background setup. Samples were sealed in Lindemann glass capillaries (diameter 1.5mm) to avoid any

oxidation after filling in a glove box. For all samples data were collected on an extended angular range (129 degrees in 2 theta) with counting times of typically 150s for each of the 457 data points, thus allowing for PDF analysis. Classic corrections (polarization and absorption in cylindrical geometry) were applied before reduction and Fourier transform. The X-ray absorption spectra were recorded on the B18 beamline at the DIAMOND synchrotron (Oxfordshire, UK, Dr. Anna Corrias). Extended X-ray Absorption Fine Structure (EXAFS) spectra at the Ru (22117 eV) K-edge were collected at room temperature in transmission mode using a Si(311) monochromator. The monochromator energy scale was calibrated *via* a third ion chamber with a reference foil. The samples, in form of powder, were diluted with polyvinylpyrrolidone (PVP) in an appropriate concentration inside a glove box and pressed to form a pellet, which was then sealed in an aluminum pouch to avoid any oxidation. The data analysis was performed using the ATHENA and ARTEMIS software.<sup>86</sup> With ATHENA, the absorption edge, E<sub>0</sub>, is determined, and the absorption due to the isolated atom is subtracted, by fitting the pre-edge and post-edge regions to obtain  $\chi(k)$ . The software ARTEMIS is used to perform the fit of the EXAFS region to scattering models in R-space obtained by FEFF, validated on standard compounds. The number of fitted parameters was always lower than the number of independent points. Raman measurements were carried out with a Horiba XPLORA-MV2000 spectrometer in CEMES (Prof. Wolfgang Bacsá). For the measurements, an excitation wavelength of 532 nm and laser power of 0.084 mW was used. The samples were kept under vacuum and exposed to atmospheric air shortly before measurements. The samples were analyzed by X-ray photoelectron spectroscopy (XPS) using a VG Escalab MKII spectrophotometer operating with a non-monochromatized Mg K source (1253.6 eV).

---

<sup>86</sup> B. Ravel, et al. *Journal of Synchrotron Radiation* **2005**, 12, 537-541.

#### 2.4.6. Density Functional Theory (DFT) calculations

Calculations were performed in LPCNO (Dr. Iann Gerber and Prof. Romuald Poteau) using the Vienna *ab initio* simulation package VASP,<sup>87,88,89,90,91</sup> which employs the full-potential projector augmented waves (PAW) framework.<sup>91,92</sup> Exchange-correlation effects were approximated using the PBE functional and applied in spin-polarized calculations.<sup>93</sup> A kinetic energy cutoff of 400 eV was found to be sufficient to achieve a total energy convergence within several meV, in conjunction with a k-point sampling grid of (1x1x4), by applying a 0.05 eV-width Gaussian smearing, on the various Ru<sub>n</sub>-C<sub>60</sub> polymer phase models, based on the models already proposed in a previous work, that satisfy Ru/C<sub>60</sub> ratio and may represent only an idealized view of the real system.<sup>27</sup> All atoms were fully relaxed in order to have forces smaller than 0.01 eV/Å<sup>-1</sup>. The calculation cell parameters were at least equal to 21 Å on the (*Ox*, *Oy*) directions when on (*Oz*) it was dependent on the Ru cluster sizes. See Figure 2.5 for more details.

Bader charge analysis was used to estimate charge transfer.<sup>94,95</sup> Transition state searches were performed using the Nudge Elastic Band method, as implemented by Henkelman et al.,<sup>96,97</sup> on a molecular model made of a fully hydrogenated Ru<sub>13</sub> decorated by two C<sub>60</sub> ligands.

---

<sup>87</sup> G. Kresse, et al. *Physical Review B* **1993**, 47, 558-561.

<sup>88</sup> G. Kresse, et al. *Physical Review B* **1996b**, 54, 11169-11186.

<sup>89</sup> G. Kresse, et al. *Computational Materials Science* **1996a**, 6, 15-50.

<sup>90</sup> G. Kresse, et al. *Physical Review B* **1994**, 49, 14251-14269.

<sup>91</sup> P. E. Blöchl *Physical Review B* **1994**, 50, 17953-17979.

<sup>92</sup> G. Kresse, et al. *Physical Review B* **1999**, 59, 1758-1775.

<sup>93</sup> J. P. Perdew, et al. *Physical Review Letters* **1996**, 77, 3865-3868.

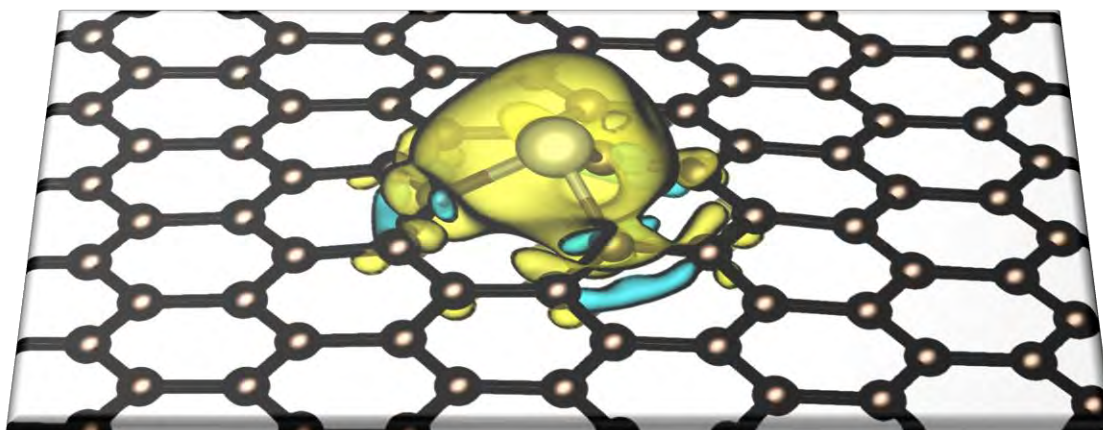
<sup>94</sup> G. Henkelman, et al. *Computational Materials Science* **2006**, 36, 354-360.

<sup>95</sup> W. Tang, et al. *Journal of Physics: Condensed Matter* **2009**, 21, 084204.

<sup>96</sup> G. Henkelman, et al. *The Journal of Chemical Physics* **2000a**, 113, 9901-9904.

<sup>97</sup> G. Henkelman, et al. *The Journal of Chemical Physics* **2000b**, 113, 9978-9985.

## Chapter 3. Preparation of low loading carbon supported metal single atoms







### 3. Preparation of low loading carbon supported metal single atom

#### 3.1. Introduction

As we saw in the previous chapter, effective SAC production relies on the ability to produce strong metal-support interactions. This leads us to meditate on the need to find susceptible sites to be used as traps to host metallic atoms. In this sense, when visualizing a perfect and smooth graphenic lattice (Fig. 1.11a), the obvious assumption would be that, except on the edges and if they are not decorated, there is not chance to anchor a metallic atom at least this lattice contains *vacancies or defects* within the stable hexagonal network of  $sp^2$  carbons.

In general, defects in graphene can be categorized into two different groups: the first group, called intrinsic defects are those of non- $sp^2$  carbons in graphene. These defects are usually caused by the existence of non-hexagonal rings surrounded by hexagonal rings. The second group consists in extrinsic defects where the crystalline order is perturbed with non-carbon atoms. The intrinsic defects of graphene can be divided into four categories: single vacancy defects, multiple vacancy defects, line defects and Stone-Wales defects (Fig. 1.11b-i).<sup>1</sup> We have shown in the bibliographic chapter that the stability of SA depends not only on the nature of the defects, but also of the metal (Fig. 1.22). The general tendency being that carbon edges and single vacancy (SV), double vacancies (DV) and even triple vacancies (TV) are particularly efficient to trap metallic single atoms.

A SV is the simplest defect in graphene, which is formed by removing one atom from the lattice. According to DFT calculations, the energy needed to form a SV ranged between 7.2 and 8.58 eV,<sup>2</sup> values that are in good agreement with experimental measurements of  $7.0 \pm 0.5$  eV.<sup>3</sup> This vacancy can diffuse through the network to be stabilized with estimated energies ranging between 0.87-1.70 eV,<sup>4,5,6,7</sup> suggesting that they could be observed even at 200 °C on CNT.<sup>8</sup> Tight-binding molecular dynamics simulations and

---

<sup>1</sup> M. S. Shafeeyan, et al. *Journal of Analytical and Applied Pyrolysis* **2010**, 89, 143-151.

<sup>2</sup> S. T. Skowron, et al. *Chemical Society Reviews* **2015**, 44, 3143-3176.

<sup>3</sup> P. A. Thrower, et al. *Physica Status Solidi (a)* **1978**, 47, 11-37.

<sup>4</sup> J. D. Wadey, et al. *Chemical Physics Letters* **2016**, 648, 161-165.

<sup>5</sup> H. Shi, et al. *Physical Chemistry Chemical Physics* **2013**, 15, 4897-4905.

<sup>6</sup> G.-D. Lee, et al. *Physical Review Letters* **2005**, 95, 205501.

<sup>7</sup> A. A. El-Barbary, et al. *Physical Review B* **2003**, 68, 144107.

<sup>8</sup> A. V. Krashennnikov, et al. *Chemical Physics Letters* **2006**, 418, 132-136.

first principles total energy calculations have shown that two SV can coalesce into a 5-8-5 DV (energy barrier for this process is 1.5-1.6 eV), which is further reconstructed at higher temperatures into a new defect structure, the 555-777 defect, by the Stone-Wales type transformation.<sup>6</sup> The energy barrier for the 5-8-5 to 555-777 transformation is high (5.2-5.7 eV) and therefore this state is considered to be inaccessible from thermal activation alone. Once formed, the immobile 5-8-5 DV will act as a nucleation site for further coalescence of additional mobile SV to form higher order multi-vacancy structures. DFT calculations have also shown that graphene layers with SV at the edge are energetically more stable than the layers with SV in the middle.<sup>9</sup> For graphite, it is suggested that the hexavacancy, is the most stable defect. This stability was explained by the dangling bond counting model, where the number of dangling bonds of the system decreased as the vacancy became more stable,<sup>10</sup> although the stability of the defect also depends on pentagons formed upon reconstruction of the system (Figure 3.1).<sup>11</sup> Other modeling studies have suggested that the thermally activated coalescence of SV will not result in ‘holes’ in the graphene structure, but in lines which will create 5–7 dislocation pairs and/or stacking faults (Figure 3.1c).<sup>12</sup>

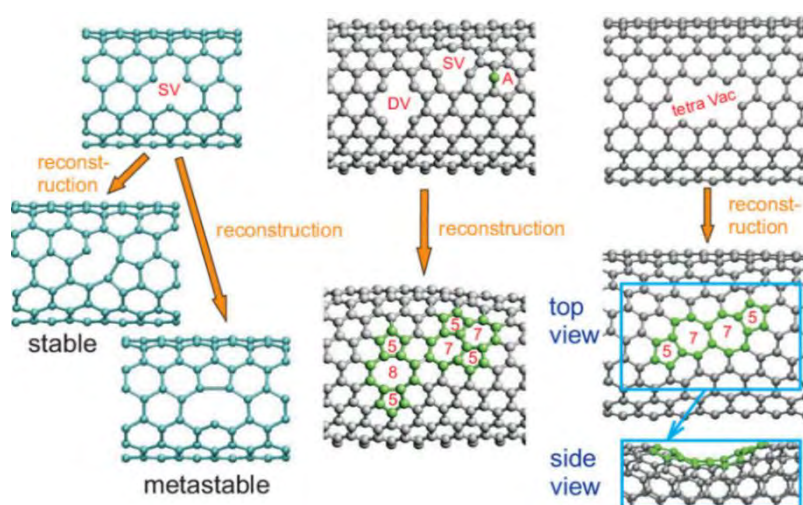


Figure 3.1. Reconstructions of the atomic network near vacancies in single-walled carbon nanotubes. Only front walls of the nanotubes are shown. From ref. [13].

As mentioned before, the presence of vacancies is highly desired; dangling bonds around the vacancies can serve as bridges for the chemical connection or provide active sites for

<sup>9</sup> A. Santana, et al. *Chemical Physics Letters* **2013**, 557, 80-87.

<sup>10</sup> Z. Tang, et al. *Physical Review Letters* **1999**, 82, 2532-2535.

<sup>11</sup> M. Saito, et al. *Japanese Journal of Applied Physics* **2007**, 46, L1185-L1187.

<sup>12</sup> T. Trevethan, et al. *Nanoscale* **2014**, 6, 2978-2986.

<sup>13</sup> A. V. Krashennnikov, et al. *Journal of Applied Physics* **2010**, 107, 071301.

atom adsorption.<sup>14</sup> Even though some vacancies are created in the process of carbon material synthesis, important technologies have been developed to induce such defects later on.<sup>15</sup> During decades scientist have used high energy beams (ions or electrons) using sophisticated equipment such as scanning tunneling/atomic force microscopes to produce irradiation-induced vacancies.<sup>16</sup> These techniques possess high degree of control, being capable to remove even atom by atom to form monovacancy to multivacancy, by manipulating exposure time, size and energy of the focused beam (Figure 3.2).<sup>17</sup> Clearly, these modifications cannot be achieved with conventional macroscopic tools hence the limitations for mass production or scale-up are obvious.

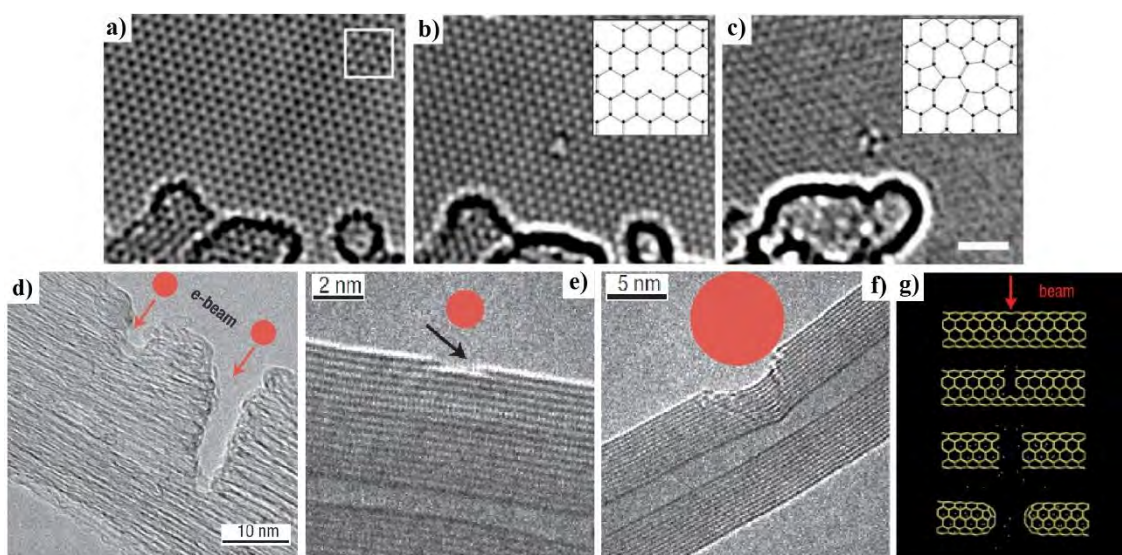


Figure 3.2. First line: HRTEM images of proton-irradiated layer graphene. a) before irradiation, b) monovacancy after irradiation, c) 555-777 rearranged divacancy. Adapted from ref. [18]. Second line: TEM images electron-beam irradiated CNT d) SWCNT, e), f) irradiated MWCNT with different beam size, g) model of electron-beam-irradiated CNT. Adapted from ref. [19].

Despite the progress in the area, there is still a lack of efficient processes to scale up the creation of vacancies in the carbon matrix. In this context we decided to study the

<sup>14</sup> H. L. Zhuang, et al. *Computational Materials Science* **2008**, 43, 823-828.

<sup>15</sup> *Carbon Nanomaterials Sourcebook Volume II: Nanoparticles, Nanocapsules, Nanofibers, Nanoporous Structures, and Nanocomposites*. In, edited by K. Sattler: CRC Press (**2016**).

<sup>16</sup> A. V. Krashennnikov, et al. *Journal of Vacuum Science & Technology B: Microelectronics and Nanometer Structures Processing, Measurement, and Phenomena* **2002**, 20, 728-733.

<sup>17</sup> A. W. Robertson, et al. *Nature Communications* **2012**, 3, 1144.

<sup>18</sup> O. Lehtinen, et al. *Nanoscale* **2014**, 6, 6569-6576.

<sup>19</sup> F. Banhart, et al. *Small* **2005**, 1, 953-956.

possibility of creating carbon vacancies in the surface of our materials by the decomposition of surface oxygen groups. In this chapter, we describe a simple procedure to incorporate defects in the graphitic network as well as characterization and their utilization as anchoring point to produce single atom catalysts.

### 3.2. Vacancies

We decided to resort to a common procedure such as functionalization through oxidation with nitric acid for subsequent defunctionalization in order to achieve a defective material. In a typical experiment, the 2 steps (functionalization and defunctionalization) were carried out as described in the experimental section and summarized in Figure 3.3.

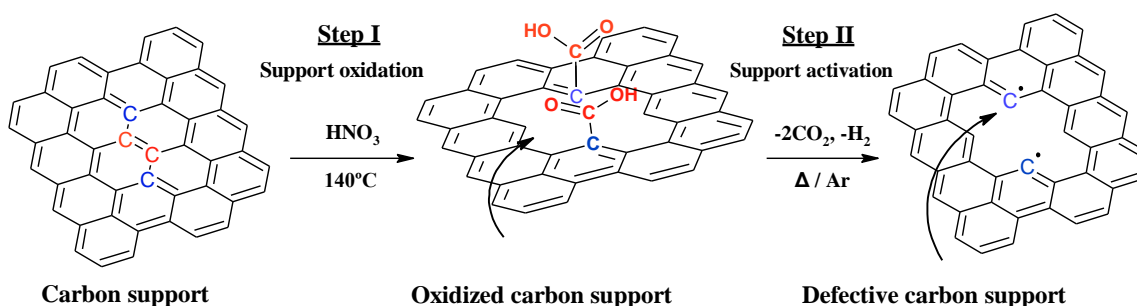


Figure 3.3. Schematic representation of activation method on carbon materials.

Conceptually, **step I** involve the addition of different oxygen surface functional groups over the carbon support as seen in Figure 3.3. The oxidation of CNT with concentrated nitric acid leads to the formation of various functional groups, among them carbonyl, phenol or carboxylic groups,<sup>20,21</sup> which are mainly located on the edges but also in the frame of the aromatic planes.<sup>22</sup> Mapping at the nanometer scale by EELS/STEM analyses of the functional groups on oxidized multi-walled CNT, has shown that these groups are inhomogeneously distributed across the entire length of the nanotubes.<sup>23</sup>

**Step II** attempts the removal of the previously formed oxygen-groups through thermal decomposition under an inert atmosphere. Each one of these groups decomposes at

<sup>20</sup> I. Gerber, et al. *Chemistry – A European Journal* **2011**, 17, 11467-11477.

<sup>21</sup> V. Datsyuk, et al. *Carbon* **2008**, 46, 833-840.

<sup>22</sup> S. Biniak, et al. *Carbon* **1997**, 35, 1799-1810.

<sup>23</sup> A. E. Goode, et al. *Chemical Communications* **2014**, 50, 6744-6747.

specific temperatures to form CO<sub>2</sub> and/or CO (Table 3.2) and water. These decomposition temperatures are well-established, and can be determined by Temperature Programmed Decomposition (TPD) profiles.<sup>24,25</sup> The control of the presence of these surface groups in a given material could *a priori* be achieved by heating at a desired temperature to remove selectively specific groups.

Table 3.1 Decomposition temperatures of different functional groups on carbon surfaces. From ref. [26].

Group	Temperature of decomposition (°C)	Pyrolysis gas
Carboxylic acid (strong acids)	245	CO <sub>2</sub>
Carboxylic acid (weak acids)	325	CO <sub>2</sub>
Carboxylic anhydride	480-500	CO <sub>2</sub> + CO
Lactones	616-755	CO <sub>2</sub>
Phenols	635	CO
Carbonyls + quinones	700-950	CO

It is important to mention that the majority of these investigations primordially focus on the identification and quantification of the outgoing species, but do not provide further inquiries regarding the surface chemistry on the carbon. There are few reports dealing with the mechanism of thermal decomposition and the resulting species. In 1996, Menéndez *et al.*<sup>27</sup> proposed that thermal treatment under N<sub>2</sub> atmosphere removes oxygen in the form of CO<sub>2</sub> (predominantly at lower temperatures) and CO (predominantly at higher temperatures), leaving unsaturated carbon atoms (also called defective sites) at the edges, as shown in Figure 3.4. In conjunction with different characterizations and early theoretical work from Coulson,<sup>28</sup> the authors propose three types of defective sites, *type I*: isolated unpaired-electron (free-radical), *type II*: edge sites formed from the dangling carbon atoms by acquiring a triple-bond character; and *type III*: edge sites forming an in-plane  $\sigma$  pair, with  $s^2p^2$  hybridization. Clearly, the resultant surface should be very

<sup>24</sup> J. L. Figueiredo, et al. *Carbon* **1999**, 37, 1379-1389.

<sup>25</sup> T. J. Bandosz. In *Carbon Materials for Catalysis*, edited by P. Serp, *et al.* (2009), pp. 45-92.

<sup>26</sup> S. Wenzhong, et al. *Recent Patents for Chemical Engineering* **2008**, 1, 27-40.

<sup>27</sup> J. A. Menéndez, et al. *Langmuir* **1997**, 13, 3414-3421.

<sup>28</sup> C. A. Coulson (1960). *Fourth Conference on Carbon* p. 215. University of Buffalo: Pergamon Press.



(re)active due to the Lewis basicity,<sup>29</sup> especially from sites *I* and *II*. Eventually, this highly unstable structure would be stabilized by the adsorption of different atoms either O from the air or H from water.

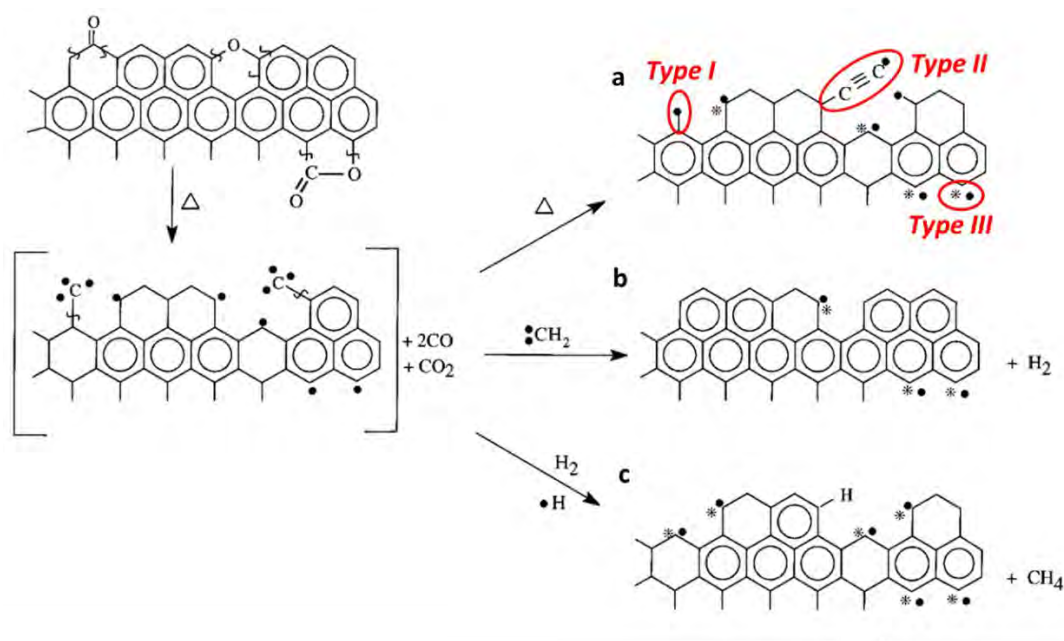


Figure 3.4. Proposed model for the stabilization of carbon surfaces upon heat treatment ( $\Delta$ ) under a,b)  $N_2$ , and b,c)  $H_2$ . For simplicity and illustrative purposes, only two types of oxygen surface groups (pyrone and lactone) and three types of carbon active sites are shown. Type I, isolated unpaired-electron sites  $Ar-\bullet$  (where  $Ar$  represents the aromatic (graphene) layer); type II,  $Ar-C\equiv C\bullet$  (see text); and type III, divalent in-plane  $\sigma$  pairs,  $Ar-\bullet^*$  (where  $*$  represents a localized  $\pi$  electron). Adapted from ref. [30].

A later publication in 2012 reports that the desorption of oxygen-bonded carbons generates large number of topological defects and vacancies in the graphene lattice.<sup>31</sup> The authors propose a five steps defunctionalization mechanism: a) the physically adsorbed and intercalated water is evaporated (physical water), b) the intermolecular dehydration takes place between neighboring carboxylic and/or hydroxyl (chemical water), c) the anhydrides decompose to evolve both  $CO_2$  and  $CO$ , d) the most stable carbonyls and quinones will decompose to evolve  $CO$  (Figure 3.5).

<sup>29</sup> M. Montes-Moran, et al. In *Novel Carbon Adsorbents*, edited by J. M. D. Tascón: Elsevier Ltd (2012), pp. 173-203.

<sup>30</sup> J. A. Menéndez, et al. *Langmuir* **1996**, 12, 4404-4410.

<sup>31</sup> C.-M. Chen, et al. *Carbon* **2012**, 50, 3572-3584.

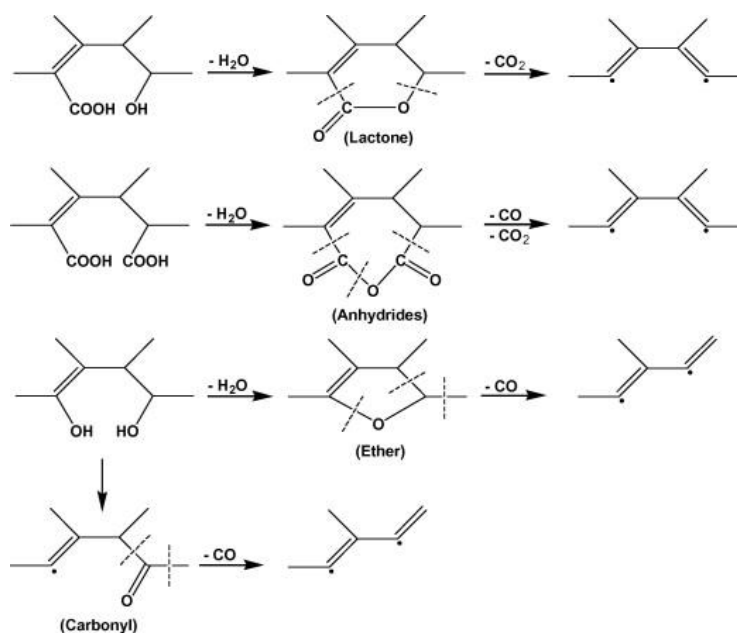


Figure 3.5. Proposed pathway for transformation and evolution of oxygen containing functional groups during thermal treatment. From ref. [34].

Finally, Chernyak *et al.*<sup>32</sup> proposed a mechanism of thermal defunctionalization of multiwalled CNT proposing the formation of zwitterionic species after heterolytic cleavage of lactones and anhydrides, based on the mechanism of thermal decomposition in organic carboxylic acids.<sup>33</sup> From this analysis of the literature, it seems reasonable to propose that, after heat treatment the support will contain high density of reactive sites/defects (either radical or ionic species), which could be used for stabilization of metal single atoms. The fact that some active sites remain at room temperature, represents a great opportunity for the formation of new chemical bonds between carbon boundary atoms and atoms/molecules, as it has already been shown for NO molecule reactivity on freshly cleft graphite.<sup>34</sup> Shaffer and co-workers have used such an approach for the thermochemical organic functionalization of CNT.<sup>35</sup> In this work, the key step of the treatment is the activation of CNT at high temperatures (1000 °C) under inert atmosphere or in a vacuum, which results in the desorption of almost all oxygen containing functional groups at pre-existing defect sites and the generation of surface radicals. The reactive sites were used to initiate radical polymerisation of functional monomers leading to the

<sup>32</sup> S. A. Chernyak, et al. *The Journal of Physical Chemistry C* **2016**, 120, 17465-17474.

<sup>33</sup> B. R. Brown *Quarterly Reviews, Chemical Society* **1951**, 5, 131-146.

<sup>34</sup> Y. A. Zarifyanz, et al. *Carbon* **1967**, 5, 127-135.

<sup>35</sup> R. Menzel, et al. *Chemical Science* **2010**, 1, 603-608.

grafting of oligomers (Figure 3.6). Such thermochemical activation was used for various organic functionalization of CNT,<sup>36</sup> carbon black<sup>37</sup> or graphene.<sup>38</sup>

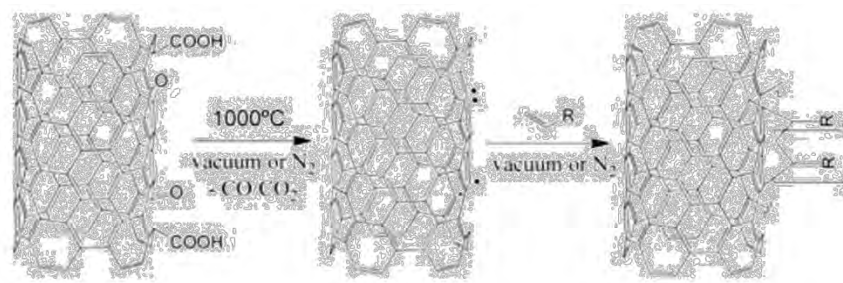


Figure 3.6. Proposed mechanism for the thermochemical activation and grafting of CNT. From ref. [39].

### 3.2.1. Thermogravimetric analyses

To begin our study, it was essential to monitor oxidation degree and thermal stability of the carbon support (CNT).<sup>39</sup> To do so, we have performed thermogravimetric analyses (TGA) under nitrogen atmosphere on our supports. Figure 3.7 shows the TGA and differential TG (DTG) profiles of oxidized CNT after step I. As can be seen in Figure 3.7a, three weight loss areas located at 100 °C, 200-300 °C and 600-800 °C are found in the DTG curve. The first signal corresponds to desorbed water and the second and third may be related with decomposition of carboxylic acids and phenols-lactones-carbonyl, respectively. From this data we decided to use 400 °C as annealing temperature, which is in good agreement with previous reports in literature showing that below this point the labile oxygenated groups, weak and strong carboxylic acids, would have effectively decomposed. We also tested two other samples with different oxidation time (1, 3 and 5 h) for comparative purposes. After the activation process at 400 °C during 1 hour (step II), the samples **O1h-CNT**, **O3h-CNT** and **O5h-CNT** have lost a percentage of mass of 3.4, 7.9 and 10.4%, respectively (Figure 3.7b). Although **O5h-CNT** was the material that contained the highest percentage of functional groups, and therefore potentially the largest number of active sites after defunctionalization, we decided to continue this study using the **O3h-CNT** support, since the process of washing and especially filtering

<sup>36</sup> S. Chen, et al. *Biomaterials* **2014**, 35, 4729-4738.

<sup>37</sup> S. Hu, et al. *Faraday Discussions* **2014**, 173, 273-285.

<sup>38</sup> S. Hu, et al. *Chemical Science* **2017**, 8, 6149-6154.

<sup>39</sup> A. G. Bannov, et al. *Journal of Thermal Analysis and Calorimetry* **2020**, 10.1007/s10973-020-09647-2.

required several day to be executed for the **O5h-CNT** sample, which could limit the progress of this investigation.

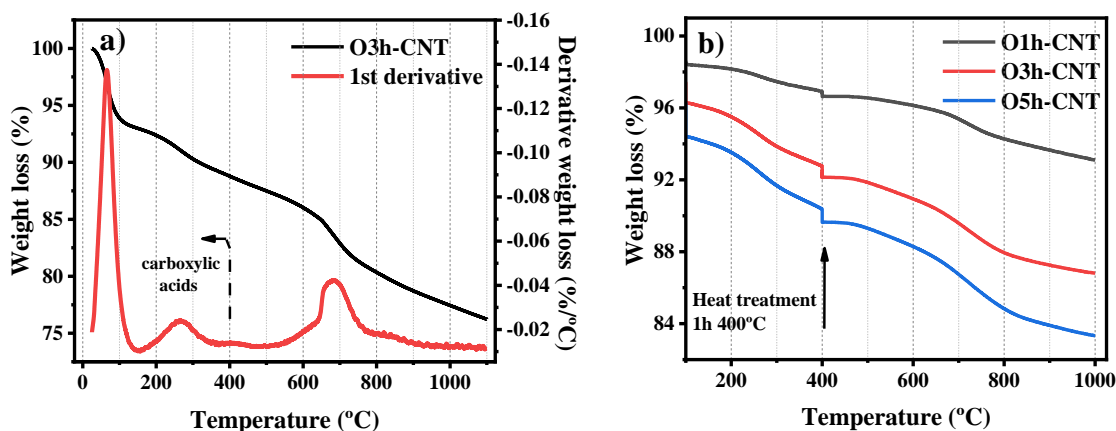


Figure 3.7. TGA profiles of: a) O3h-CNT support; and b) CNT with different oxidation time. The analysis was carried out with the following program: ramp from 25 °C to 100 °C, isotherm at 100 °C during 10 minutes, ramp from 100 °C to 400 °C, isotherm 400 °C during 1 hour, finally a ramp from 400 °C to 1000 °C, all stages heated with rate of 5 °C/min under 20 mL/min of N<sub>2</sub>.

### 3.2.2. Temperature-programmed desorption analyses

Temperature-programmed desorption (TPD) was also used to evaluate the amount and types of oxygen-containing surface groups in these carbon materials. The key principle is to heat the material in an inert atmosphere and record spectra of outlet gases by mass spectrometry.<sup>40</sup> The amounts of CO and CO<sub>2</sub> released during the thermal analysis were quantified at the end of each analysis.

In Figure 3.8 it can be observed the evolution of CO<sub>2</sub>, CO, H<sub>2</sub>O, CH<sub>4</sub> and H<sub>2</sub> ( $m/z$  =44, 28, 18, 16, 2, respectively) along the temperature range 25-1100 °C for **O3h-CNT** and **O3h-CNT400** samples. Figure 3.8a displays the three main CO<sub>2</sub> desorption peaks with maximal temperature at around 250, 420 and 610 °C. These results indicate the presence on the surface of chemical species with different thermal stability. We are aware that different carbon fractions could possibility present a co-decomposition but we identify the nature of the different species based on the most commonly accepted values in

<sup>40</sup> I. V. Krasnikova, et al. In *Carbon-Based Nanofillers and Their Rubber Nanocomposites*, edited by S. Yaragalla, et al.: Elsevier (2019), pp. 75-137.

literature (Table 3.1), which correspond to desorption of carboxylic acid (250 °C), carboxylic anhydrides (420 °C) and lactone groups (610 °C). After the subsequent thermal treatment at 400 °C, the carboxylic acid signal is practically inexistent; prove of the strong decarboxylation of the surface.

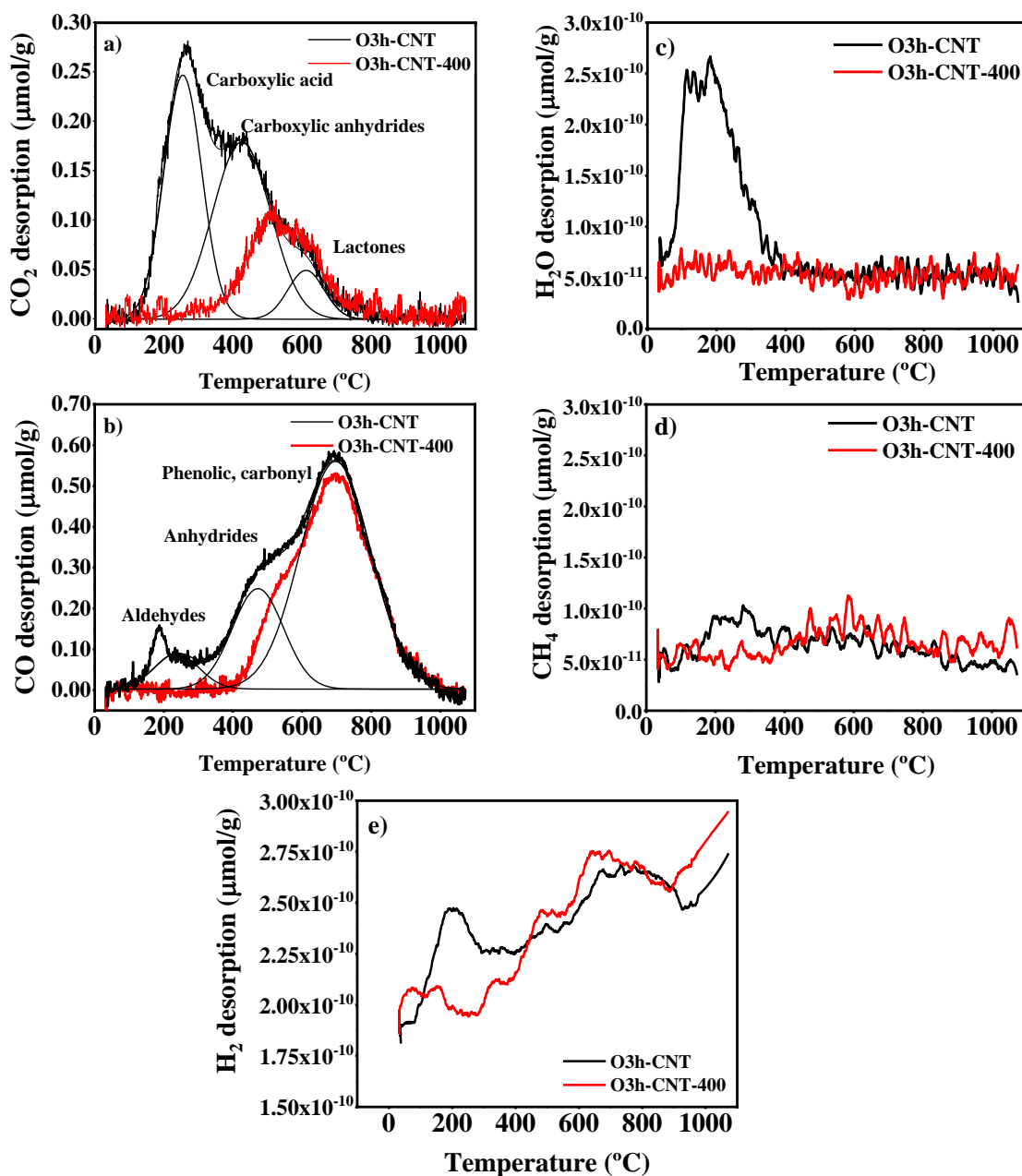


Figure 3.8. TPD profiles: a)  $\text{CO}_2$ ; b) CO; c)  $\text{H}_2\text{O}$ ; d)  $\text{CH}_4$  and e)  $\text{H}_2$  obtained for O3h-CNT and O3h-CNT400.

The CO profile of **O3h-CNT** in Figure. 3.8b presents a weak peak at 200 °C that can be ascribed to the decomposition of aldehyde groups,<sup>41</sup> or may be originated from the decomposition of oxygenated groups linked to nitrogen (from the HNO<sub>3</sub> treatment), leading to CO evolution at temperatures below those usually observed.<sup>42</sup> The second peak, observed in the range of 380-530 °C, can be associated to the decomposition of anhydride groups, known to produce both CO and CO<sub>2</sub> during their decomposition. The larger peak at higher temperatures with maximum at 700 °C, is expected for phenolic and carbonyl/quinone groups.

Considering the specific surface area of the sample (220 m<sup>2</sup>/g measured by the BET method), surface density calculation of each group can be made to have an idea of the population of surface species, before and after step II. Also, considering the hexagonal unit cell of the graphitic planes containing two carbon atoms each 0.052nm<sup>2</sup> *i.e.*, 38.5 C atoms per nm<sup>2</sup>, it was possible to estimate the number of functional groups per carbon atom (Table 3.2).

Table 3.2 Quantification of different surface oxygen groups from TPD analysis.

Group	Percentage releasing group (%)		Desorbed amount (μmol/g)		Oxygen group surface density	
	% CO	% CO <sub>2</sub>	CO	CO <sub>2</sub>	Per nm <sup>2</sup>	Per C
<b>O3h-CNT</b>						
Carboxylic acid	-	43.5	-	419.7	1.15	0.030
Lactone	-	8.3	-	79.9	0.22	0.006
Carboxylic anhydride	22.6	48.2	597.1	465.5	1.63(CO) 1.27(CO <sub>2</sub> )	0.042 (CO) 0.033 (CO <sub>2</sub> )
Aldehyde	6.9	-	181.7	-	0.5	0.013
Phenol, carbonyl, quinone	70.5	-	1858.2	-	5.09	0.132
Total			<b>2637</b>	<b>965</b>	<b>8.23</b>	<b>0.214</b>
<b>O3h-CNT-400</b>						
Carboxylic acid	-	-	-	-	-	-
Lactone	-	50.7	-	168.0	0.46	0.012
Carboxylic anhydride	1.9	49.3	35.5	163.0	0.09 (CO) 0.45(CO <sub>2</sub> )	0.002 (CO) 0.012 (CO <sub>2</sub> )
Aldehyde	-	-	-	-	-	-
Phenol, carbonyl, quinone	98.1	-	1766.5	-	4.84	0.13
Total			<b>1801</b>	<b>331</b>	<b>5.80</b>	<b>0.037</b>

<sup>41</sup> S. Kundu, et al. *The Journal of Physical Chemistry C* **2008**, 112, 16869-16878.

<sup>42</sup> H. F. Gorgulho, et al. *Carbon* **2008**, 46, 1544-1555.



As can be seen, after heating at 400 °C during one hour the total density of groups was reduced by 30%, but only due to the selective elimination of the groups decomposing at low temperatures. Moreover, after heating the amount of lactones increased substantially, product of the intermolecular dehydration between neighboring carboxylic and hydroxyl groups, to generate thermally stable lactones (Figure 3.5).<sup>31,32</sup>

The TPD profiles for water ( $m/z = 18$ ), methane ( $m/z = 16$ ) and hydrogen ( $m/z = 2$ ) have also been recorded but not quantified. The profile of water (Figure 3.8c) shows an asymmetric peak with center at 100-200 °C, which can be attributed to: i) the desorption of surface H<sub>2</sub>O, but also ii) the dehydration by combination of two adjacent carboxyl groups towards formation of carboxylic anhydrides (Figure 3.5) related to the shoulder at higher temperature (~300 °C),<sup>43</sup> or the co-decomposition of a carboxylic group and a phenolic group giving rise to a lactone (Figure. 3.5). The methane signal (Figure. 3.8d) as well as the H<sub>2</sub> signal (Figure. 3.8e) are relatively flat.

### 3.2.3. Raman analyses

Raman spectroscopy is a very valuable tool in the characterization of carbon materials since it is possible by this technique to discern even slight changes in the structure of the material. The Raman spectrum of **O3h-CNT** and **O3h-CNT-400** (Figure 3.9) is characterized by the presence of two sets of peaks. The first, the G band at 1582 cm<sup>-1</sup> comes from the in-plane stretching of the C-C *sp*<sup>2</sup> bonds referring to honeycomb-like domains on graphitic materials. The other peaks that appear at 1345 cm<sup>-1</sup>, 1614 cm<sup>-1</sup>, 1692 cm<sup>-1</sup> and 2938 cm<sup>-1</sup>, are assigned to D, D', 2D, D+D (D for defect or disorder) bands, respectively. Those are associated to out of plane vibrations from all non-regular portions. The intensity of this peak is proportional to the amount of disorder randomly distributed, impurities or surface charges.<sup>44</sup> The ratio between the intensities of the D and G bands, I<sub>D</sub>/I<sub>G</sub>, provides a parameter that can be used for quantifying disorder.<sup>45</sup> We notice a slight increase of the intensity of the I<sub>D</sub>/I<sub>G</sub> after heat treatment, reflecting an increase of the amount of defects on **O3h-CNT-400** compared to the unheated **O3h-CNT**. It should be

---

<sup>43</sup> T. G. Ros, et al. *Chemistry – A European Journal* **2002**, 8, 1151-1162.

<sup>44</sup> A. Jorio, et al. In *2D Materials: Properties and Devices*, edited by P. Avouris, et al.: Cambridge University Press. Cambridge (**2017**), pp. 71-89.

<sup>45</sup> M. M. Lucchese, et al. *Carbon* **2010**, 48, 1592-1597.

noted that after the oxidation treatment, normally D and G signals suffer an upshift due to the "electron extraction" from the  $sp^2$  structure.<sup>46</sup>

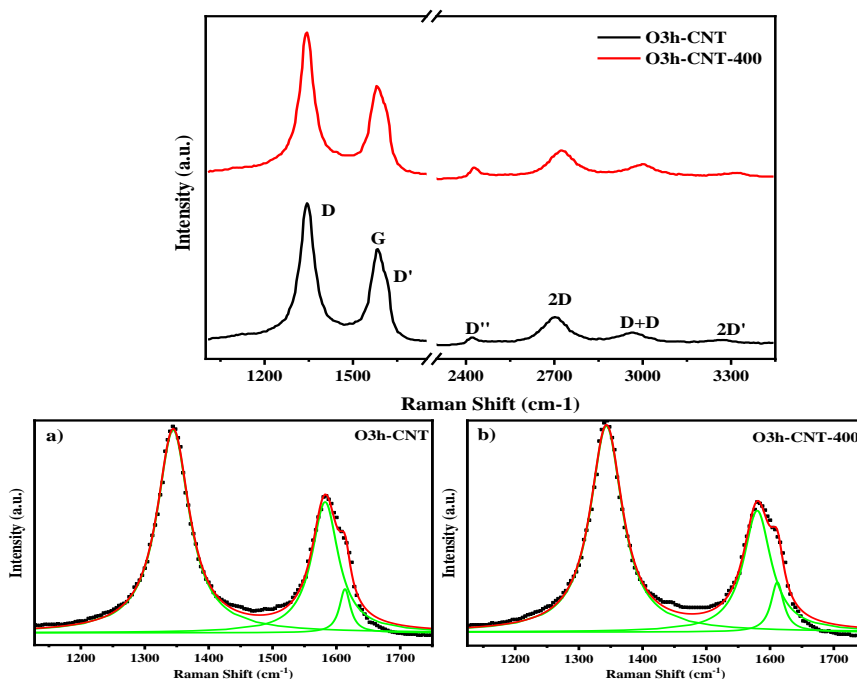


Figure 3.9. Raman spectra of oxidized CNT and annealed oxidized CNT at 400 °C. Lorentzian fitted D, G and D' bands of a) O3h-CNT and b) O3h-CNT-400.

In our case, all signals (Table 3.3) display a downshift after heating, which is a possible indicator of the recovery of electronic density.

Table 3.3 Lorentzian fitted parameters of treated CNT from Raman analysis.

Peak	O3h-CNT		O3h-CNT-400	
	Shift (cm <sup>-1</sup> )	Intensity (a.u.)	Shift (cm <sup>-1</sup> )	Intensity (a.u.)
D	1345.1	0.7797	1343.8	0.7910
G	1582.6	0.5030	1580.5	0.4665
D'	1614.2	0.1682	1612.7	0.1912
2D	2692.1	0.1497	2691.9	0.16921
$I_D/I_G$	1.54		1.68	
$I_G/I_{2D}$	3.33		2.78	
$I_D/I_{D'}$	4.64		4.14	

<sup>46</sup> H. Murphy, et al. *Journal of Vacuum Science & Technology B: Microelectronics and Nanometer Structures Processing, Measurement, and Phenomena* **2006**, 24, 715-720.

It is interesting to note that the  $I_G/I_{2D}$  value has been related to the thickness of graphitic material. with a  $I_G/I_{2D}$  increase with the increase in the number of layers. Therefore, the reduction of this value after annealing could indicate an average reduction of the number of walls on the CNT (see Figure 3.10 for TEM analyses), although the exact quantification of these have been reserved for materials up to 8 layers, which here is not the case.<sup>47</sup>

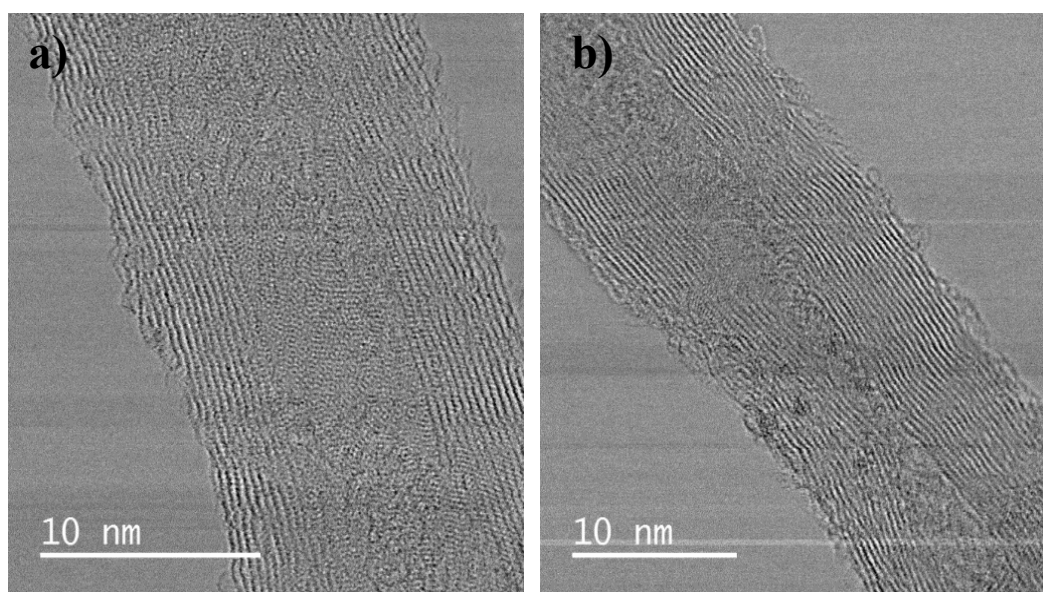


Figure 3.10 a,b) HRTEM micrographs of the MWCNT used in this study with a number of layers superior to 10.

The intensity ratio between the D and D' peak is able to probe the nature of the defects for moderate amount of disorder.<sup>48</sup> According to the obtained value ( $I_D/I_{D'} = 4.14$ ), it is more likely related to vacancy-like and boundary-like defects rather than to  $sp^3$  hybridization defects. Furthermore, Casiraghi and co-workers noticed that defective graphene samples produced by ion-bombardment (vacancy-like defects) show a smaller  $I_D/I_{D'}$  value than the  $sp^3$ -type defective graphene (partially hydrogenated).<sup>35</sup> The decrease of the  $I_D/I_{D'}$  value from 4.64 to 4.14 could thus be associated to a decrease of  $sp^3$ -type defects and/or an increase of vacancy-like defects.

#### 3.2.4. X-ray photoelectron spectroscopy analyses

<sup>47</sup> A. Das, et al. *Bulletin of Materials Science* **2008**, 31, 579-584.

<sup>48</sup> A. Eckmann, et al. *Nano Letters* **2012**, 12, 3925-3930.

An X-ray photoelectron spectroscopy (XPS) study was also performed in order to further investigate the surface chemistry of the carbon supports. The assignment of peaks was performed based on different reports found in the literature.<sup>49,50</sup> It has been possible to identify seven contributions in the C 1s profile (Figure 3.11a) as seen in Table 3.4.

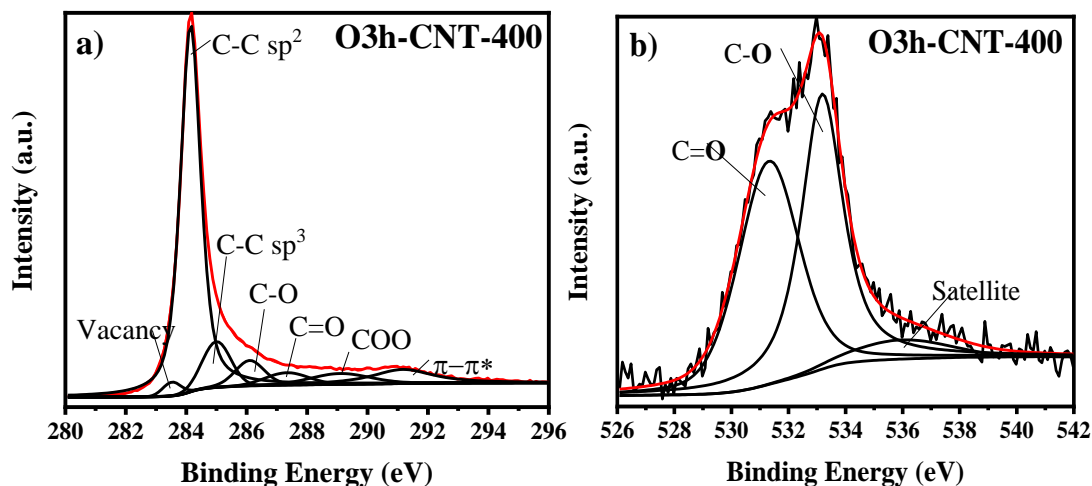


Figure 3.11. High-resolution a) C 1s and b) O 1s XPS spectra of sample O3h-CNT-400: deconvoluted peaks using Shirley background.

Interesting differences can be seen comparing both samples heated and not heated (Table 3.4). In spite of the evidences by TPD (performed under helium), where there can be observed a great loss of oxygen, the XPS C/O ratio did not change significantly. We relate this to the fact that due to the impossibility of carrying out the analyses under an inert atmosphere, the samples were exposed to air where they can re-adsorb oxygen to stabilize reactive surface species.<sup>27</sup> Indeed, vacancies in graphene are very reactive towards O<sub>2</sub> and are quickly saturated by ether and carbonyl groups *via* a two-step barrierless mechanism.<sup>51</sup> The *sp*<sup>2</sup> signal at 284.1 eV increased after heating, confirming the recovery of aromatic structure; and consistently, the *sp*<sup>3</sup> signal at 285.0 eV was reduced.<sup>52</sup> More importantly, the peak associated to defects at 283.5 eV grows in the heated sample, as we aim with the proposed method. This signal could arise from C vacancies, pentagon and

<sup>49</sup> T. I. T. Okpalugo, et al. *Carbon* **2005**, 43, 153-161.

<sup>50</sup> I. Kvande, et al. *The Journal of Physical Chemistry C* **2010**, 114, 1752-1762.

<sup>51</sup> J. M. Carlsson, et al. *Physical Review Letters* **2009**, 102, 166104.

<sup>52</sup> H. S. Vieira, et al. *Journal of Nanoscience and Nanotechnology* **2007**, 7, 3421-3430.

heptagon rings, the formation of fullerene like structures and also with functional groups attached to the graphitic lattice.<sup>53,54,55</sup>

Table 3.4. XPS C 1s and O 1s peak deconvolution assignments and relative content of species.

Species	Binding Energy (eV)	O3h-CNT (at%)	O3h-CNT-400 (at%)
<b>C 1s</b>			
vacancies	283.5	1.34	1.78
C=C ( $sp^2$ )	284.1	41.91	66.41
C-C ( $sp^3$ )	285.0	25.84	9.15
C-OH, C-O	286.1	5.62	5.69
C=O	287.3	8.13	3.73
COOH, ester	289.1	6.87	4.86
$\pi$ - $\pi^*$ shake up	291.2	10.30	8.39
<b>O 1s</b>			
C=O	531.3	59.63	53.61
C-O	533.2	40.36	46.38
Satellite (H <sub>2</sub> O)	536.0	0.01	<0.01
<b>C/O</b>		<b>94.3/5.7 (16.5)</b>	<b>94.8/5.2 (18.2)</b>

Another parameter of graphitic structure can be inferred from a shake-up (ShU) peak at the end of the C1s spectrum (291.2 eV). The ShU belongs to the  $\pi$ -electrons, which rapidly respond to the photo-excitation. The relative magnitude of this ShU signal can be correlated with the conjugation strength in the hexagonal lattice.<sup>56</sup> After heating, this contribution slightly decreased suggesting that despite the increase of the  $sp^2$  character, the general conjugation of the material may be perturbed, more likely by the created defects. In the case of oxygen, Figure 3.11b, the C=O signal decreased in agreement with the TPD results, confirming the decrease in carboxylic groups as well as the permanence of -OH groups or the formation of ether groups evidenced by the relative increase of C-O signal.<sup>57</sup> The third component is probably related to the satellite structure of the spectrum or to adsorbed oxygen containing molecules such as water.<sup>58</sup>

<sup>53</sup> K. Ganesan, et al. *Physical Chemistry Chemical Physics* **2016**, 18, 22160-22167.

<sup>54</sup> A. Barinov, et al. *The Journal of Physical Chemistry C* **2009**, 113, 9009-9013.

<sup>55</sup> Y. Yamada, et al. *Journal of Materials Science* **2013**, 48, 8171-8198.

<sup>56</sup> S. R. Kelemen, et al. *Applied Surface Science* **1993**, 64, 167-174.

<sup>57</sup> J.-H. Zhou, et al. *Carbon* **2007**, 45, 785-796.

<sup>58</sup> T. M. Ivanova, et al. *Russian Chemical Bulletin* **2013**, 62, 640-645.

### 3.3. Detection of vacancy

The above characterization provides general insight about the graphitization degree and relative composition of our carbon support. Nevertheless, there is still need for a proper characterization of the chemical surface of the treated support. The detection of the defective species on carbons became a great challenge mainly due to their intrinsic heterogeneity. Several experimental and theoretical techniques have been used to detect different types of defects, and to understand how they locally change the material's properties.<sup>59,60</sup> For example, the direct observation of vacancies under the microscope has been successfully achieved for graphene<sup>61</sup> and SWCNT,<sup>62</sup> but the direct extrapolation of these studies on multi-layer materials, that is, graphite and MWCNT, becomes harder because the experimental signals became much more complex. For this reason, we have opted for the study of the magnetic properties of the material, which represents a powerful tool for characterization of electronic surface due to its extreme sensitivity to any magnetic "defect".

An important aspect that must be considered is that through traditional carbon nanomaterial production, such as chemical vapor deposition, a variety of ferromagnetic catalyst particles such Fe, FeNi or FeCo are involved, which usually end up encapsulated within the nanostructure even after purification protocols, what will influence the magnetic response of the samples.<sup>63</sup> In order to remove such impurities and obtain highly pure nanotubes we performed a high temperature annealing on the purified CNT sample, process that has been proven to remove all remaining metallic nanoparticles from the synthesis.<sup>64</sup> The treatment performed by Ana B. García (INCAR-CSIC, Oviedo, Spain) consisted in heating 5 g of purified MWCNT at 2800 °C for 1 hour in argon flow using a Xerion-Graphite electrical furnace. Figure 3.12 shows the TEM images of the samples before and after annealing (CNT\*). As can be seen on Figure 3.12a (purified CNT), catalyst particles remain indeed inside the tubes. Energy dispersive X-ray spectroscopy (Figure 3.12b) reveals that the composition of these particles corresponds to 44.62 wt.% of Fe and 55.38 wt.% of Co. A weight loss of 0.36 % was calculated by TGA after heating.

---

<sup>59</sup> P. T. Araujo, et al. *Materials Today* **2012**, 15, 98-109.

<sup>60</sup> M. S. Dresselhaus, et al. *Philosophical Transactions of the Royal Society A: Mathematical, Physical and Engineering Sciences* **2010**, 368, 5355-5377.

<sup>61</sup> A. Hashimoto, et al. *Nature* **2004**, 430, 870-873.

<sup>62</sup> K. Suenaga, et al. *Nature Nanotechnology* **2007**, 2, 358-360.

<sup>63</sup> J. Zhang, et al. *Chinese Physics B* **2018**, 27, 128101.

<sup>64</sup> D. Bom, et al. *Nano Letters* **2002**, 2, 615-619.



The elimination of the catalyst at high temperatures is due to sublimation of FeCo nanoparticles that are swept from the oven by the vacuum pump. Most of the tips of the MWCNT were opened, and the catalyst particles embedded in the tips and the bodies of MWCNT were totally removed (Figure 3.12c,d). Afterwards CNT\* was used as mentioned above in step I and step II to produce O3h-CNT\* and O3h-CNT\*-400, respectively.

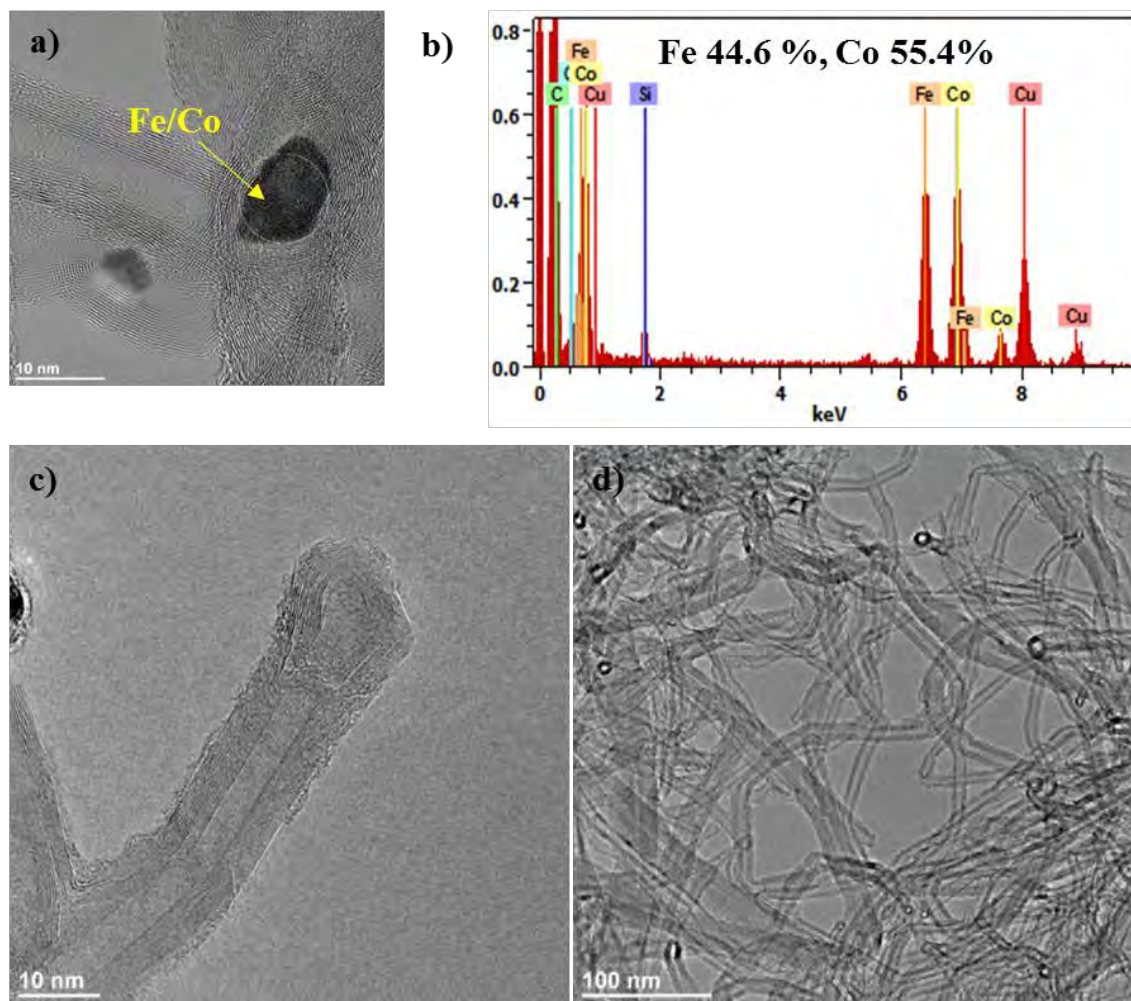


Figure 3.12. a) HRTEM micrographs of the as produced CNT highlighting a metallic nanoparticle, b) EDX analysis of the nanoparticle; and c,d) CNT annealed at 2800 °C (CNT\*).

### 3.3.1. Nuclear magnetic resonance analyses

Carbon-13 high-resolution solid-state nuclear magnetic resonance using magic angle spinning (MAS SS  $^{13}\text{C}$ NMR) has been used as a primary method to characterize CNT. Only a few groups have reported on the properties of carbon nanotubes using nuclear magnetic resonance.<sup>65</sup> The main difficulty concerns the large magnetic inhomogeneity induced by the catalyst used for the growth process, which prevents any magnetic measurements. Anyway, there is consensus that in CNT, the  $sp^2$  signal is located around 100-125 ppm, according to the tube diameter  $D$  in nm ( $\delta = 18.3/D + 102.5$ ).<sup>66</sup> The sample CNT\* exhibits a poorly resolved peak that can be seen in Figure 3.13. This line shape has been related to a mixture of CNT of different types and diameters.<sup>66</sup>

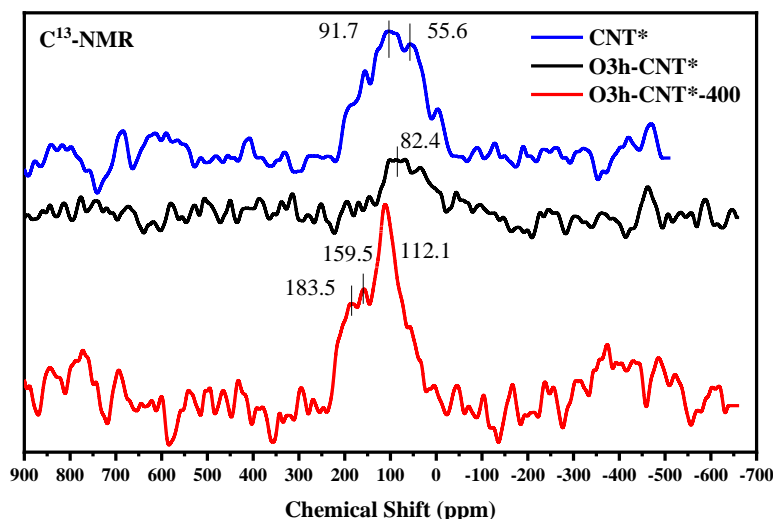


Figure 3.13.  $^{13}\text{C}$  MAS SS-NMR of purified CNT\*, O3h-CNT\* and O3h-CNT\*-400.

$^{13}\text{C}$  NMR studies of various preparations of graphene oxides in the literature show the common feature of  $^{13}\text{C}$  signals at 60 ppm (epoxy groups) and 70 ppm (hydroxyl groups), so we assumed that those signals can also contribute to the broad peak obtained. Additionally, a paramagnetic effect comes from the interaction between nuclei and unpaired electrons. As electrons have a magnetic dipole moment over 1000 times stronger than those of nuclear spins, it can dramatically alter the NMR signals nearby.<sup>67</sup> Although the quality of the spectrum is not adequate to accurately identify different species, some conjectures can be made based on the two peaks that can be distinguished at 183 and 159

<sup>65</sup> A. S. Mazur, et al. *Fullerenes, Nanotubes and Carbon Nanostructures* **2020**, 28, 202-213.

<sup>66</sup> E. Abou-Hamad, et al. *Physical Review B* **2011**, 84, 165417.

<sup>67</sup> A. Marchetti, et al. *Advanced Materials* **2017**, 29, 1605895.

ppm on **O3h-CNT\*-400** sample, which have been ascribed to carbon species at defects or edges.<sup>68</sup>

### 3.3.2. Magnetization measurement analyses

An ideal graphene should be nonmagnetic itself due to  $\pi$ -symmetry electronic states formed by the unhybridized  $p_z$  atomic orbital of  $sp^2$  carbon atoms. Therefore, low magnetic susceptibility by the application of an external magnetic field is achieved on pure graphitic materials. Nonetheless, DFT studies have predicted that carbon atoms with unsaturated bonds play the role of magnetic impurities. For instance, reconstructed mono- and trivacancies with unsaturated carbon bonds were predicted to contribute in magnetic signals.<sup>69</sup> Experimentally, it has been found that defects stated such as the carbon atom adsorbed on the bridge site, the single or multi-vacancies and the complex of carbon vacancies, can introduce a localized magnetic moment.<sup>70,71,72</sup> Ferromagnetism of graphene-based materials at room temperature has already been reported and saturation magnetization ( $M_s$ ) of 0.004-0.020 emu/g<sup>73</sup> were measured for rGO heat-treated at different temperatures. Figure 3.14a shows a typical ferromagnetic hysteresis loop associated to the magnetic catalysts (FeCo NP) used during the synthesis of the nanotubes.

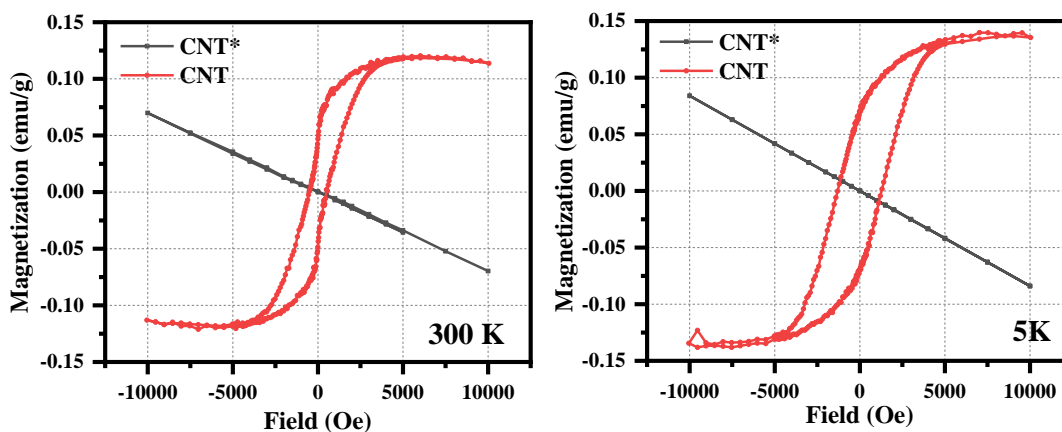


Figure 3.14 a) Hysteresis loop of as prepared CNT at 5 and 300K b) Diamagnetic behavior of CNT after annealing the sample in argon atmosphere at 2800 °C.

<sup>68</sup> S. Hayashi, et al. *Carbon* **2003**, 41, 3047-3056.

<sup>69</sup> Z. Zanolli, et al. *Physical Review B* **2010**, 81, 165406.

<sup>70</sup> M. Aliofkhazraei, et al. In *Graphene Science Handbook: Electrical and Optical Properties* (2016), p. 178.

<sup>71</sup> X. Yang, et al. *Carbon* **2009**, 47, 1399-1406.

<sup>72</sup> J. Červenka, et al. *Nature Physics* **2009**, 5, 840-844.

<sup>73</sup> Y. Wang, et al. *Nano Letters* **2009**, 9, 220-224.

This points out that the acid treatments are not efficient to completely remove such impurities, and the encapsulated FeCo nanoparticles in the tips are hermetically sealed. This result is in accordance with magnetic measurement reported in the literature (Table 3.5). The treatment at 2800 °C (CNT\*) allows a complete removal of these impurities that correspond to 0.17 wt% (determined by ICP-OES analysis), resulting in non-magnetic CNTs. Figure 3.14 highlights the drastic change in the magnetic properties on CNT\*.

Table 3.5. Comparison of the magnetic properties of different CNT.

Sample	T° (K)	Saturation of magnetization M <sub>S</sub> (emu/g)	Remanent magnetization M <sub>R</sub> (emu/g)	Coercivity field H <sub>c</sub> (Oe)	Ref.
O-CNT (FeCo)	5	0.14	0.07	1300	This work
	300	0.12	0.05	500	
O-CNT (Fe)	5	1.89	-	1700	74
	77	2.57	-	1950	
O-CNT (Fe)	4.5	0.22	0.03	1500	75
CNT(Co)	130	0.17	0.07	600	76
CNT (Fe)	4.2	8.5	2.9	1120	77
CNT(FeCo)	300	0.87	-	842	78
CNT-2500°C	300	-	-	-	

The CNT free of magnetic impurities were oxidized 1, 3 and 5 hours in order to observe the influence of the oxygen surface groups on the magnetization (Figure 3.15a,b). The negative slope indicates a decrease in the value of the magnetic moments with increase in applied magnetic field, characteristic of diamagnetic material, showing that the oxygen functional groups do not induce paramagnetic response at room temperature. Nonetheless at 5 K a paramagnetic behavior was evidenced. A similar trend was noticed for graphene oxide quantum dots,<sup>79</sup> where the authors explain this contribution in terms of Pauli's and Curie's paramagnetism. In other words, this phenomenon can be present on materials with highly delocalized electrons in the space, and its magnetization would be directly proportional to the imposed magnetic field but inversely proportional to the temperature. The additional energy per electron comes from the interaction between the electron spin

<sup>74</sup> A. V. Ellis, et al. *Journal of Magnetism and Magnetic Materials* **2006**, 302, 378-381.

<sup>75</sup> I. Kuryliszyn-Kudelska, et al. *Acta Physica Polonica A* **2011**, 119, 597-599.

<sup>76</sup> U. Ritter, et al. *Carbon* **2011**, 49, 4443-4448.

<sup>77</sup> G. E. Grechnev, et al. *Low Temperature Physics* **2010**, 36, 1086-1090.

<sup>78</sup> K. Lipert, et al. *Journal of Physics: Conference Series* **2010**, 200, 072061.

<sup>79</sup> K. Tadyszak, et al. *Nanomaterials (Basel)* **2020**, 10, 10.3390/nano10040798.

and the magnetic field. Also, Tadyszak and co-workers,<sup>80</sup> observed a small paramagnetic signal at 5 K on graphene nanoflakes.

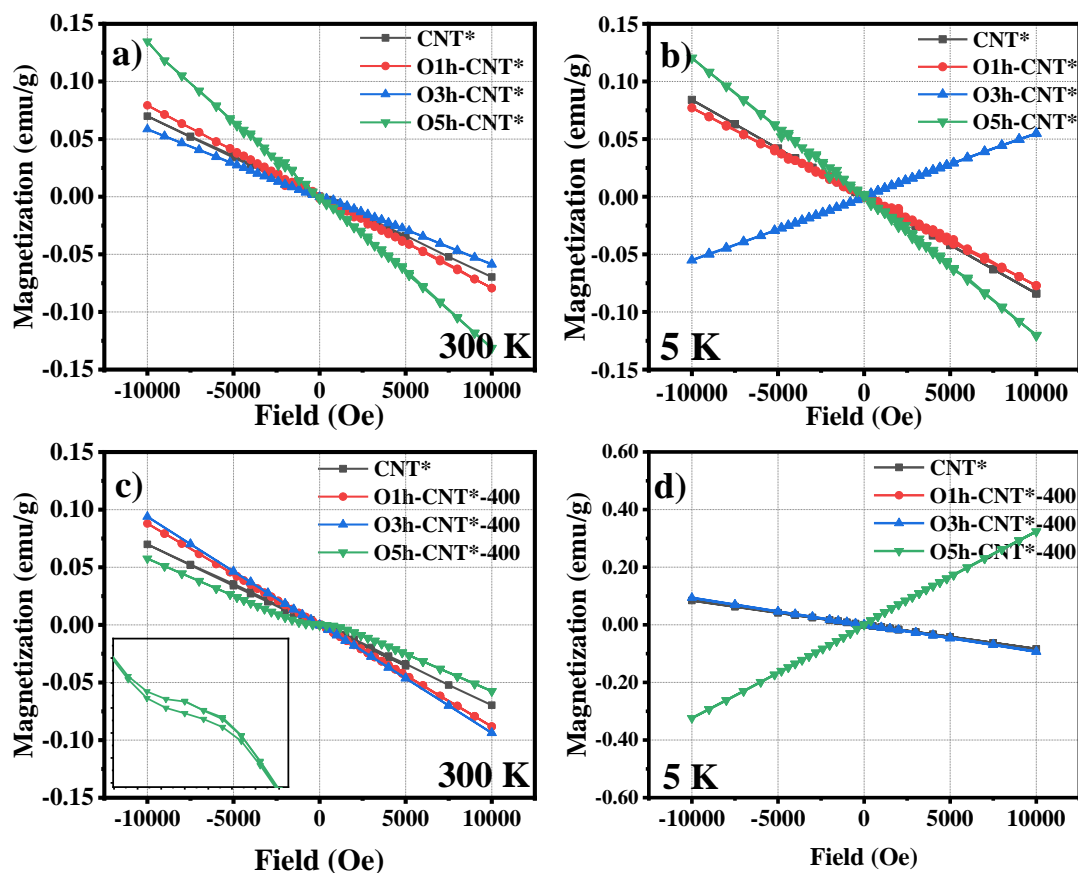


Figure 3.15. Magnetization curves obtained for CNT\*, oxidized CNT\* with different time of oxidation, and oxidized CNT\* with different time of oxidation heat-treated at 400 °C. a) CNT\* and oxidized CNT\* with different time of oxidation (300 K); b) CNT\* and oxidized CNT\* with different time of oxidation (5 K); c) CNT\* and oxidized CNT\* with different time of oxidation heat-treated at 400 °C (300K); and d) CNT\* and oxidized CNT\* with different time of oxidation heat-treated at 400 °C (5K).

They relate the origin of this paramagnetism with contributions from the nonbonding  $p$ -electron states localized at the graphene layer edges (carbon dangling bonds at the edge planes). In the case of heated samples **OXh-CNT\*-400** (Figure 3.15c,d), again at 5 K one of our samples present paramagnetism but more importantly, at 300 K, the specimen **O5h-CNT\*-400** present a weak ferromagnetic signal in a s-shape curve loop (zoomed on Figure 3.15c). After subtracting the diamagnetic background (Figure 3.16), the magnetization was saturated at 2000 Oe with a value of 0.004 emu/g.

<sup>80</sup> A. Ney, et al. *Applied Physics Letters* **2011**, 99, 102504.

Similar behavior has been previously reported on annealed graphitic oxide at 400 °C, showing similar values of ferromagnetism at room temperature.<sup>73</sup>

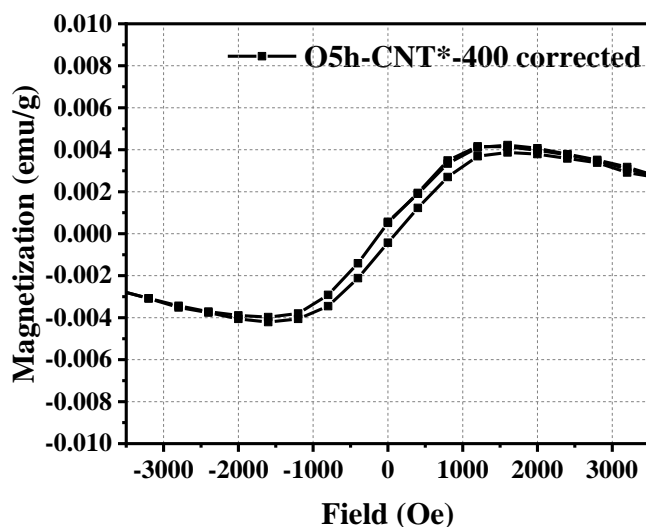


Figure 3.16. Corrected SQUID-VSM magnetization isotherm (300 K) for O5h-CNT\*-400.

Theoretical studies propose that the large  $\pi$ -conjugation structure of graphitic materials offers the required stability for unpaired electrons from radicals to generate net spin units.<sup>81</sup> Several reports have been published regarding magnetic signals on graphitic materials after high energy irradiations, relating those signals to the creation of different types of point defects with unpaired electrons such as vacancies or unsaturated edges.<sup>82,83,71</sup>

### 3.3.3. Electron paramagnetic resonance analyses

Electron paramagnetic resonance (EPR) is also an effective method for studying the defect structure of nanostructured carbon materials. EPR signals are induced by itinerant electrons and unpaired electrons caused by dangling bonds. The energy differences studied in EPR spectroscopy are predominately due to the interaction of unpaired electrons in the sample with an imposed magnetic field.<sup>84</sup> The g-factor is the

<sup>81</sup> M. E. Itkis, et al. *Science* **2002**, 296, 1443–1445.

<sup>82</sup> O. V. Yazyev *Reports on Progress in Physics* **2010**, 73, 056501.

<sup>83</sup> A. V. Krasheninnikov, et al. *Nature Materials* **2007**, 6, 723-733.

<sup>84</sup> J.-M. Spaeth, et al. In *Structural Analysis of Point Defects in Solids: An Introduction to Multiple Magnetic Resonance Spectroscopy*; Springer Berlin Heidelberg. Berlin, Heidelberg (**1992**), pp. 11-33.



spectroscopic factor of free electron that can be calculated from equation (1), where  $h$  is the Planck constant,  $\beta$  is the Bohr magneton,  $\nu$  is the frequency of the radiation, and  $B_0$  the intensity of the magnetic field.<sup>85</sup>

$$(1) \quad g_e = \frac{h\nu}{\beta B_0} = \frac{6.626 \times 10^{-34} [J \cdot s] \nu}{9.274 \times 10^{-28} [J/G] B_0} = 0.7145 \left( \frac{\nu [MHz]}{B_0 [Gauss]} \right) \approx 2.00232$$

A free electron in vacuum has a  $g$  value  $g_e = 2.00232$ . The experimental differences with this value give chemical information that lies in the interaction between the electron and the electronic structure of the molecule/material. For instance, in organic radicals, the  $g$  value is very close to  $g_e$  ranging from 1.99 to 2.01. For transition metal complexes, the  $g$  value varies a lot because of the spin-orbit coupling and zero-field splitting. Usually it ranges from 1.4 to 3.0, depending on the geometry of the complex.

EPR spectrum of single-layer graphene obtained by the scotch-tape method has been reported, giving a Lorentzian line with  $g$ -value varying from 2.0040 at liquid helium temperature to 2.0045 at room temperature. The linewidth diminishes from 9 to  $\sim 6.5$  G with temperature from 4 to 300 K.<sup>86</sup> For the case of graphene the precise values of the components of the  $g$  tensor in graphite are:  $g_{\perp} = 2.00314$  and  $g_{\parallel} = 2.05006$ .<sup>87</sup>

Pure and perfect CNT are inactive to EPR, the experimental data often shows a very narrow signal with a Lorentzian line shape at  $g \approx 2.002$ .<sup>88</sup> As we have mentioned before, the magnetic properties of nano-sized graphenes and graphites are significantly perturbed by the presence of interruptions of the crystal structure.<sup>89</sup> It has been proposed that when localized defects in the  $sp^2$  network or edge-structures are introduced, a broad line appears ( $g = 2.0035$ ). Some researchers have deconvoluted this signal in different contributions. For example, Ćirić *et al.*<sup>90</sup> deconvolute the experimental response of graphene oxide sample into two components (Figure 3.17a), relating the broader one with the presence of defects. In the same way, Tadyszak *et al.*<sup>91</sup> analyzed anthracite powder, being capable to fit two Lorentzian lines in the spectrum (Figure 3.17b). The authors claim that the first

<sup>85</sup> M. D. E. Forbes, *et al.* In *Advances in Physical Organic Chemistry*, edited by I. H. Williams, *et al.*: Academic Press (2013), pp. 1-83.

<sup>86</sup> L. Ćirić, *et al.* *physica status solidi (b)* **2009**, 246, 2558-2561.

<sup>87</sup> J. Stankowski, *et al.* *Fullerene Science and Technology* **1997**, 5, 1203-1217.

<sup>88</sup> M. Zaka, *et al.* *Physical Review B* **2010**, 81, 075424.

<sup>89</sup> A. Barbon. In *Electron Paramagnetic Resonance: Volume 26: The Royal Society of Chemistry* (2019), pp. 38-65.

<sup>90</sup> L. Ćirić, *et al.* *physica status solidi (b)* **2010**, 247, 2958-2961.

<sup>91</sup> K. Tadyszak, *et al.* *Carbon* **2015**, 94, 53-59.

constituent of the signal (representing the 80% of the total), can be related to the intrinsic conduction electrons of the carbon and the second correspond to the localized states due to lattice defects. Thus, this EPR response can be associated to the presence of unpaired electrons mainly found in fragments with an odd-number of electrons, or with unpaired electrons in structures with a peculiar topology, such the edges, dangling bonds and vacancies.

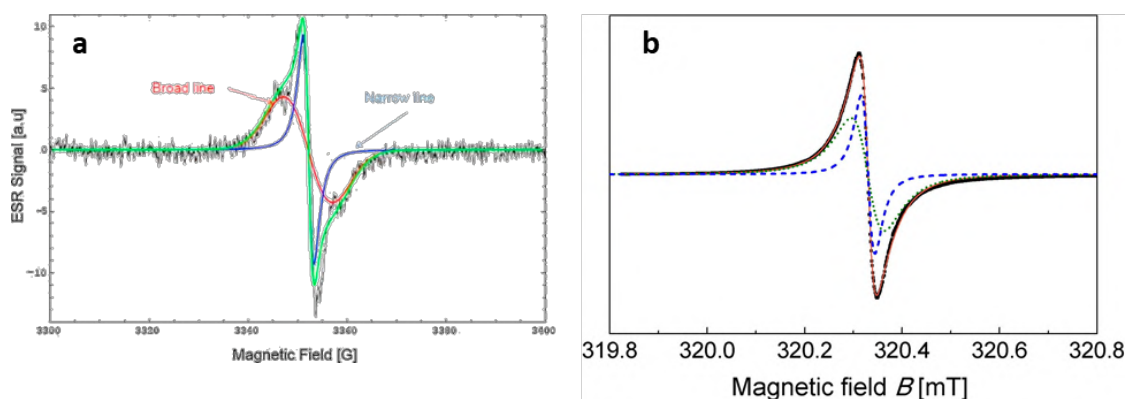


Figure 3.17. a) Two components GO EPR spectra recorded at 6 K, fitted by Gaussian and Lorentzian functions. The narrow Lorentzian line ( $\Delta H = 3.4$  G) is associated with conduction electrons, while the broad one ( $\Delta H = 11$  G) corresponds to defects. From ref. [102]. b) EPR powder spectrum of anthracite, recorded at 10 K. Deconvolution into two Lorentzian lines. From ref. [103].

The EPR measurements performed in this study are presented in Figure 3.18. **O3h-CNT\*** does not show any signal at room temperature, but well resolved band was detected at  $-263$  °C (10 K). A weak peak centered at 3383 G with a peak-to-peak linewidth of 3.13 G was detected. The spectrum was homogeneous, did not exhibit hyperfine coupling or distribution of the  $g$  value (2.003).<sup>92</sup> Magnetic field scanning over a broader field range did not reveal any additional resonances that would belong to frequently observed transition-metal impurities confirming the purity of the samples. **O3h-CNT\*-400** displayed a more intense signal with 13.9 G linewidth. Additionally, the  $g$ -factor was strongly anisotropic. When the magnetic field was parallel to the graphitic planes the  $g$ -factor had a minimum of  $g^{\parallel} = 2.0002$ . A strong  $g$  shift was measured when the field is perpendicular to the planes ( $g^{\perp} = 2.0033$ ). It is worth mentioning that  $g$  values close to

<sup>92</sup> C. V. Pham, et al. *Applied Physics Letters* **2014**, 104, 132102.

2.0029 were predicted by Ishii *et al.* for dangling bonds in amorphous carbon.<sup>93</sup> Similar values were also obtained for point defects in electron irradiated CNT (2.0026),<sup>94</sup> or neutron-irradiated graphite (2.0023).<sup>95</sup>

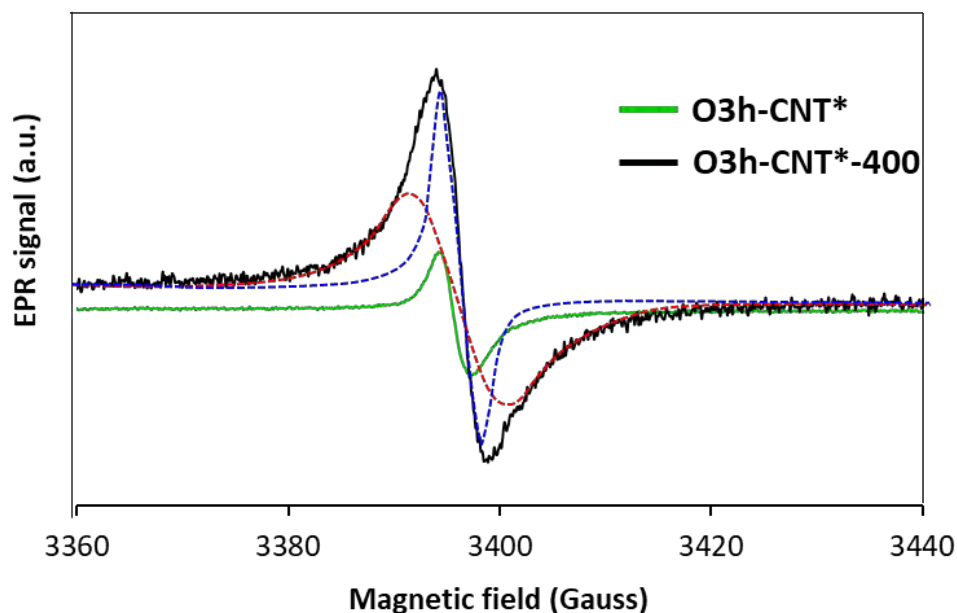


Figure 3.18. EPR spectra of O3h-CNT\* and O3h-CNT\*-400 measured at -263 °C (10K) and X-band at ~ 9.52 GHz.

Our defective material presented a broader signal that can be deconvoluted in two Lorentzian lines with different linewidths. The narrow line (Figure 3.18, blue line) has been associated to interacting conduction electrons, while the broad one (Figure 3.18, red line) corresponds to spin-polarized localized electronic states.<sup>90,91</sup> It is important to mention that the sample was managed avoiding any contact with air so we can exclude the EPR line broadening being due to molecular oxygen.

With this combination of techniques, we can claim the effective creation of defects on the graphitic surface, although the specific nature of those defects needs further clarification. At the same time, we propose that they can be used as trapping centers for metal atoms, thus leading to chemisorption with the formation of strong bonds.<sup>96</sup>

<sup>93</sup> N. Ishii, et al. *Japanese Journal of Applied Physics* **1981**, 20, L673-L676.

<sup>94</sup> F. Beuneu, et al. *Physical Review B* **1999**, 59, 5945-5949.

<sup>95</sup> K. A. Müller *Physical Review* **1961**, 123, 1550-1552.

<sup>96</sup> J. A. Rodríguez-Manzo, et al. *ACS Nano* **2010**, 4, 3422-3428.

### 3.4. Synthesis of supported single atom catalysts (SAC)

The optimization of heterogenous catalytic systems has been of permanent interest in the last century, even more in the last decades, because theoretical and experimental results demonstrated that only surface active-site atoms are involved in the reaction mechanism. Under this premise, in 2011 Zhang's group published an innovative study on the exceptional catalytic performance in CO oxidation over isolated Pt atoms supported on iron oxide.<sup>97</sup> There is consensus that this publication first coined the term "single atom catalysts" referring to heterogeneous catalysts with active phases comprised of a single metallic atom. Since then, hundreds of publications have focused on this topic.<sup>98,99</sup> In the particular case of carbon materials, significant efforts have been devoted in the development of carbon-based SAC due to their remarkable properties such as high specific surface area, tunable porosity, good electrical and mechanical conductivity, easy handling and low production cost, among others. These systems have been employed for promising sustainable energy and technology-related catalytic applications.<sup>100,101,102</sup>

We thought that it could be possible to take advantage of the previously described defective support to introduce effectively metallic single atoms over the defective carbon support in order to produce carbon-based SAC.

We started this study with the preparation of ruthenium supported single atom catalysts on defective CNT (**OXh-CNT-T**). As discussed in the previous sections, this support should contain significant amounts of defects such as carbon vacancies. DFT studies of the spin coupling around a carbon atom vacancy in graphene have shown that the triplet state (spin-unpaired electrons) is slightly more stable (0.2 eV) than the singlet state (spin-paired electrons).<sup>20,103,104</sup> This singlet-triplet quasi-degeneracy shares similarities with the chemistry of carbenes in organic chemistry.<sup>105,106</sup>

The two first steps (I and II described in the previous section) of the synthesis were followed by two subsequent steps (III and IV) that involve wet impregnation of

<sup>97</sup> B. Qiao, et al. *Nature Chemistry* **2011**, 3, 634-641.

<sup>98</sup> X. Li, et al. *Nano Research* **2020**, <https://doi.org/10.1007/s12274-020-2755-3>.

<sup>99</sup> S. Ji, et al. *Chemical Reviews* **2020**, <https://doi.org/10.1021/acs.chemrev.9b00818>.

<sup>100</sup> C. Rivera-Cárcamo, et al. *ChemCatChem* **2018**, 10, 5058-5091.

<sup>101</sup> J. Zhu, et al. *Advanced Functional Materials* **2020**, <https://doi.org/10.1002/adfm.202001097>.

<sup>102</sup> M. B. Gawande, et al. *ACS Catalysis* **2020**, 10, 2231-2259.

<sup>103</sup> G. Ghigo, et al. *The Journal of Physical Chemistry B* **2004**, 108, 3215-3223.

<sup>104</sup> M. Casartelli, et al. *Physical Review B* **2013**, 88, 195424.

<sup>105</sup> D. Bourissou, et al. *Chemical Reviews* **2000**, 100, 39-92.

<sup>106</sup> P. de Frémont, et al. *Coordination Chemistry Reviews* **2009**, 253, 862-892.

[Ru(COD)(COT)] (COD = 1,5 cyclooctadiene, COT = 1,3,5-cyclooctatriene) and the elimination of the remaining ligand. For details, see the experimental section at the end of this chapter. The full procedure is summarized on Figure 3.19 consisting on heating **O3h-CNT** during 1 hour at 400 °C. In a first set of experiments, a higher heat treatment temperature (1000 °C, to produce **O3h-CNT-1000**) was used to ensure the removal of a large fraction of oxygen functional groups trying to obtain maximal formation of reactive sites, such as described in ref.<sup>35</sup> The aimed Ru loading was 0.4 wt.% Ru.

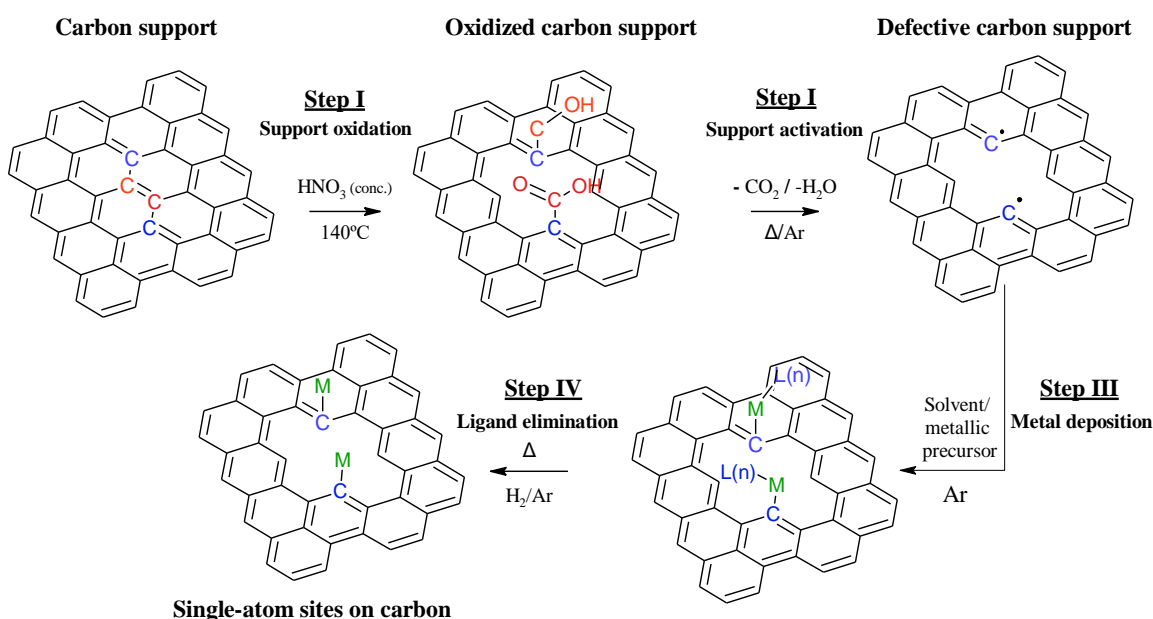


Figure 3.19. Procedure for the synthesis of single atom catalysts on graphitic materials.

The most concise technique for confirming the successful insertion of metal atoms onto a support is high-resolution microscopy. Recent advances in microscopy allow for direct proving of the presence of single surface metal atoms in a sample. For this purpose, we resort to using high-angle annular dark-field scanning transmission electron microscopy (HAADF-STEM) to characterize our samples.

In Figure 3.20 we can clearly identify plenty of bright dots on **Ru/O3h-CNT-1000** thanks to the much higher atomic number of ruthenium compared to carbon atoms. It is worth to indicate the selective production of single atoms, since we were not able to visualize any cluster or  $\text{Ru}_{\text{NP}}$  throughout the entire microscopy grid. The visualization of the SA was easier on thinner tubes rather than on the thicker one. DFT calculations claim that Ru atoms can be trapped on defective graphene surfaces in the order  $\text{Ru/SV} > \text{Ru/DV} >$

Ru/SW.<sup>107</sup> The calculated binding energy of Ru on a 555-777 defective graphene (7.2 eV) is relatively high, therefore, the aggregation of these embedded metal atoms can be efficiently prevented.<sup>108</sup>

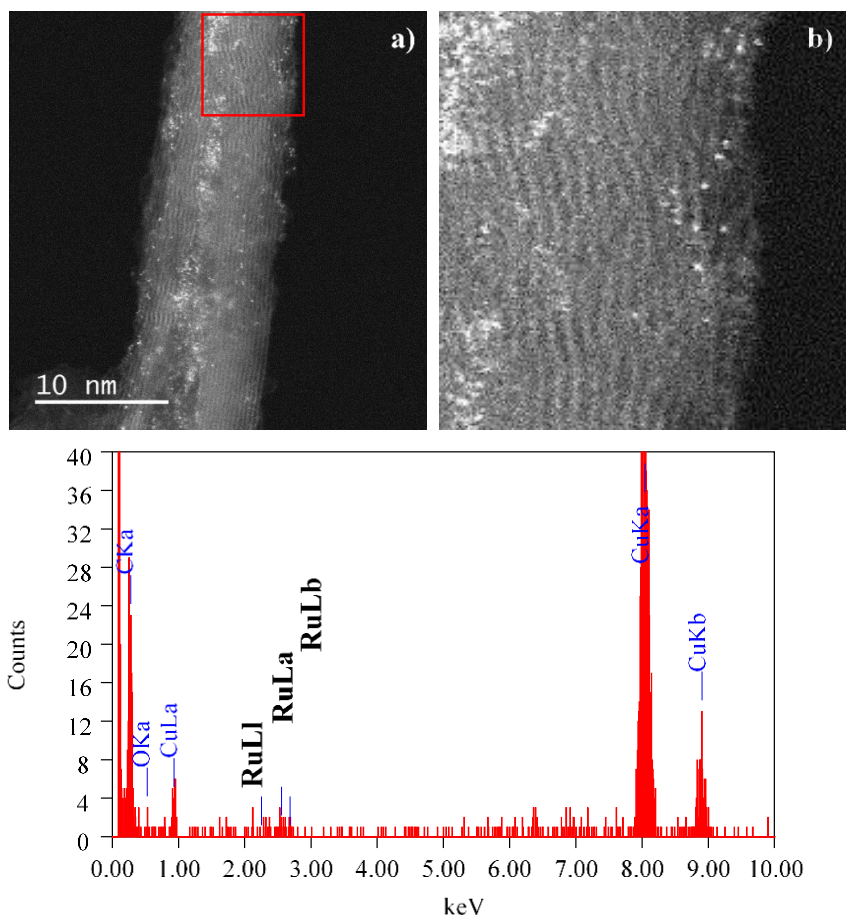


Figure 3.20. HAADF-STEM micrograph and EDX analysis of a) 0.4%Ru/O3h-CNT-1000; and b) zoomed zone highlighted on red, magnification 3.6 times

To quantify the metal loading we performed inductively coupled plasma optical emission spectrometry (ICP-OES). The **Ru/O3h-CNT-1000** sample prepared with a theoretical 0.4 wt.% Ru yielded a value of 0.12 wt%. This lower metal loading could be related with a low density of reactive sites. It can be explained by the phenomenon of rearrangement of carbon vacancies at high temperatures, conducting to the reconstruction of the graphitic structure.<sup>109,110,111</sup> Numerous studies have shown that with the increase of temperature of annealing, the structural ordering improves and a reduction in the overall defect concentration occurs. When lower temperatures are used, the resultant concentration of

<sup>107</sup> X. Guo, et al. *International Journal of Hydrogen Energy* **2018**, 43, 4880-4892.

<sup>108</sup> P. Liu, et al. *Physical Chemistry Chemical Physics* **2020**, 22, 9322-9329.

<sup>109</sup> J. T. H. Tsai, et al. *Journal of Experimental Nanoscience* **2009**, 4, 87-93.

<sup>110</sup> J. Chen, et al. *Carbon* **2007**, 45, 274-280.

<sup>111</sup> R. Andrews, et al. *Carbon* **2001**, 39, 1681-1687.



reactive defects should increase. We show in Table 3.6 the results obtained using **O3h-CNT-T** heat-treated at different temperatures. An optimal value was found at 400 °C where the amount of ruthenium reached was 1.6 wt%. For this reason, all our further investigation will set 400 °C as activation temperature for the supports.

*Table 3.6. Ruthenium content varying temperature of activation determined by ICP-OES.*

Sample	T° annealing (°C)	Ru loading (wt. %)
0.4% Ru/O3h-CNT-1000	1000	0.12
2.0% Ru/O3h-CNT-1000	1000	0.31
2.0% Ru/O3h-CNT-600	600	1.06
2.0% Ru/O3h-CNT-400	400	1.60
1.0% Ru/O3h-CNT-400	400	0.95
0.4% Ru/O3h-CNT-400	400	0.37

An evidence of saturation of the defect reactive sites is the change of color of the reaction media. In the cases of theoretical deposition 0.4 (**0.4%Ru/O3h-CNT-400**) and 1.0 wt% Ru (**1.0%Ru/O3h-CNT-400**), the pentane solution turned from yellow to colorless in a matter of minutes (Figure 3.21). In the case of higher metallic loading, the solution goes from intense yellow to pale yellow indicating no total deposition of the metal. Trying to get a general insight of the deposition process we have analyzed this supernatant by GC-MS. Before the analysis the liquid was filtrated with PTFE filter in order to remove any traces of solid. The analysis showed mostly the presence of COT in the solution (identification NIST library 97 % accuracy) and very low concentration of COD. This result suggests that under reaction conditions, COT is preferentially decoordinated from the complex. In this context, there are some examples in the literature dealing with ligand displacement in  $[\text{Ru}(\text{COD})(\text{COT})]$ ,<sup>112,113</sup> and it was generally accepted that COT ligand is more labile than COD. However, other studies report that reactions with alkyl phosphites, alkylphosphonites, and alkylphosphinites cause selective displacement of 1,5-COD.<sup>114</sup>

<sup>112</sup> P. Pertici, et al. *Inorganica Chimica Acta* **1988**, 149, 235-239.

<sup>113</sup> G. Deganello, et al. *Journal of Organometallic Chemistry* **1977**, 135, 215-219.

<sup>114</sup> M. Hirano, et al. *Organometallics* **2003**, 22, 2378-2386.



Figure 3.21. Change of color before and after deposition.

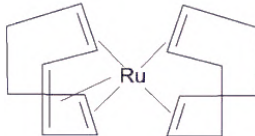
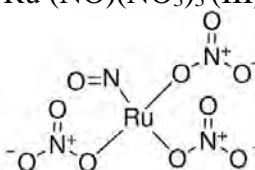
We studied the effect of the solvent and the ruthenium precursor in the synthesis by using  $[\text{Ru}(\text{COD})(\text{COT})]$  in ethanol and ruthenium nitrosyl nitrate (III)  $[\text{Ru}(\text{NO})(\text{NO}_3)_3]$ , in ethanol and water. The metal content decreased when ethanol is used (Table 3.7) with the organometallic precursor that might be related with ethanol reactivity on the reactive sites or with solubility limitations. For  $[\text{Ru}(\text{NO})(\text{NO}_3)_3]$ , we achieved a third of the amount of ruthenium (Table 3.7) than the previous conditions. As evidence of the poor Ru inclusion, the supernatant after the impregnation maintained a reddish tone belonging to  $[\text{Ru}(\text{NO})(\text{NO}_3)_3]$ . It is worth noting that commercially available  $[\text{Ru}(\text{NO})(\text{NO}_3)_3]$  is diluted in nitric acid, thus the protons present in the mixture could passivate the active sites generating H-terminated carbons hence decreasing the Ru adsorption. It has been reported for palladium that the saturation of dangling surface bonds of a defect (with H or OH) is expected to decrease the dispersion of supported Pd species by means of a decreasing number of active sites on the carbon surface.<sup>115</sup> The two samples prepared from  $\text{Ru}(\text{NO})(\text{NO}_3)_3$  were analyzed by HAADF-STEM. The micrographs in Figure 3.22 show the characteristic aspect of metallic atomic dispersion with bright dots along with some clusters with average size of 0.47 nm of diameter. According to the literature, this value would fit with DFT calculations predicting stable *in-line* formation of  $\text{Ru}_3$  conglomerates over  $sp^2$  carbon layer, having a  $\text{Ru}_1\text{-Ru}_3$  distance of 5.68 Å,<sup>116,117</sup> which is in a good agreement with the measured value in Figure 3.22d. To study the thermal stability of the prepared supported SA we subjected one sample to different reduction temperatures.

<sup>115</sup> I. Efremenko, et al. *Journal of Catalysis* **2003**, 214, 53-67.

<sup>116</sup> I. Czekaj, et al. *The Journal of Physical Chemistry C* **2013**, 117, 26588-26597.

<sup>117</sup> W. Zhang, et al. *The Journal of Physical Chemistry B* **2004**, 108, 2140-2147.

Table 3.7. Metal loading using different solvents determined by ICP-OES.

Sample	Precursor	Solvent	wt. %
2.0%Ru/O3h-CNT-400	[Ru (COD)(COT)] (0)	Pentane	1.60
2.0%Ru/O3h-CNT400		Ethanol	1.01
2.0%Ru/O3h-CNT400	Ru (NO)(NO <sub>3</sub> ) <sub>3</sub> (III)	Ethanol	0.38
2.0%Ru/O3h-CNT400		Water	0.32

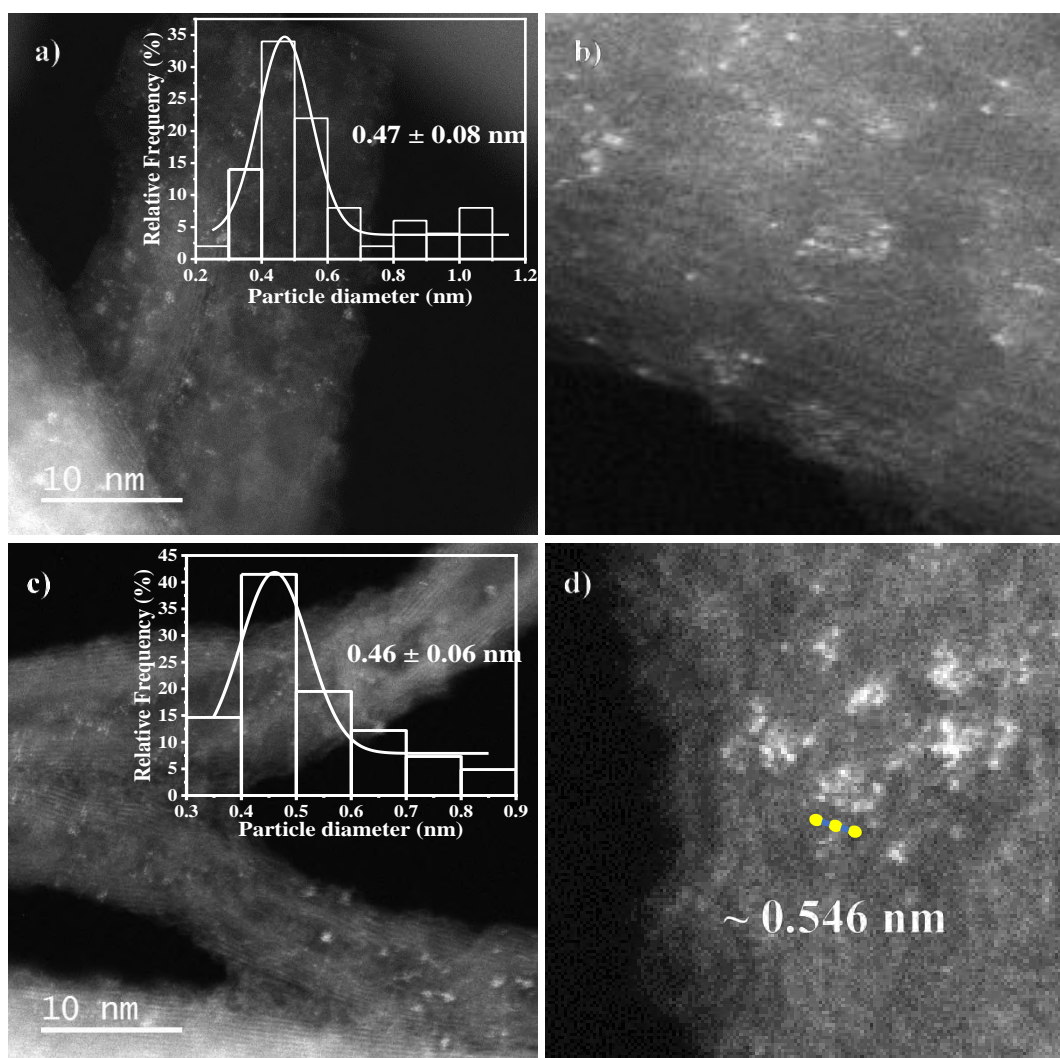
Figure 3.22. Histograms and HAADF-STEM micrographs of Ru/O3h-CNT-400 prepared with Ru(NO)(NO<sub>3</sub>)<sub>2</sub> in: a), b) ethanol and c), d) water.

Figure 3.23 shows conventional TEM images, revealing that when the **0.4%Ru/O<sub>3h</sub>-CNT-400** sample was treated either at 80, 150 or 300 °C during one hour under 80/20 Ar/H<sub>2</sub> flow, no formation of Ru<sub>NP</sub> was observed. Trying to demonstrate the role of the active site/defects in the metal anchoring process, we prepared a sample removing step II, that is, without support activation by controlled thermal removal of carboxylic groups (sample named **Ru/O<sub>3h</sub>-CNT**). Oxidized carbon nanotubes were impregnated with a theoretical 2 wt% of Ru, achieving full adhesion of the metal, as confirmed by ICP analysis. This is not surprising since it has been reported that generally -OH and -COOH surface groups act as ligand upon deprotonation and/or hydrolysis for the direct immobilization of the complexes *via* coordination to the metal center.<sup>118</sup> Machado *et al.* assessed the reactivity of surface carboxylic groups with [Ru(COD)(COT)]. They found that after some hours a ligand exchange take place to form [Ru(COD)(COO)] derivatives.<sup>119</sup>

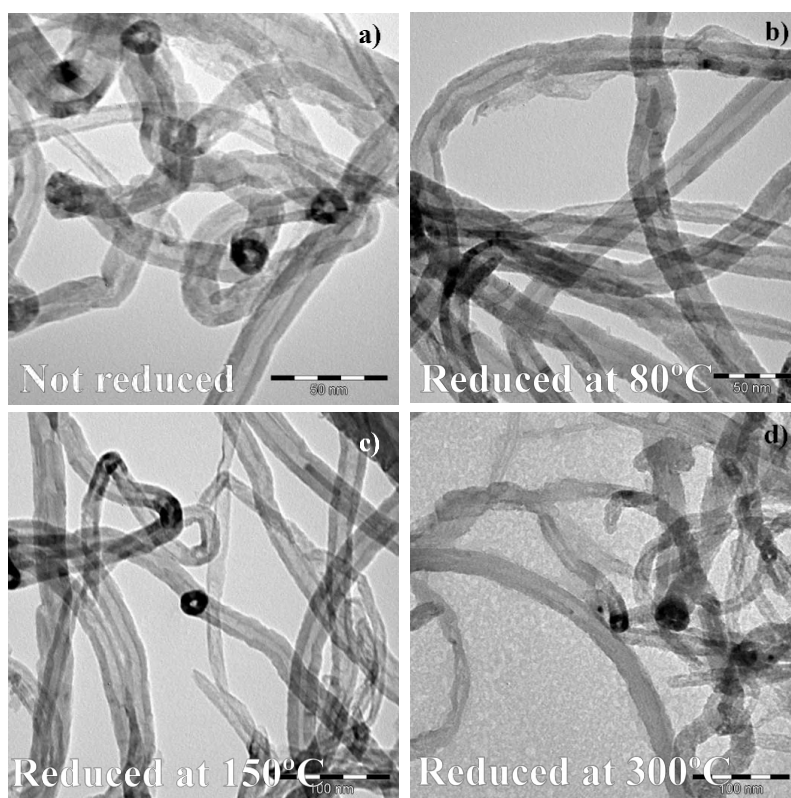


Figure 3.23. TEM micrographs of sample 0.4%Ru/O<sub>3h</sub>-CNT400 a) fresh, b) reduced at 80 °C, c) reduced at 150 °C; and d) reduced at 300 °C. Reduction with 80/20 Ar/H<sub>2</sub> during one hour.

<sup>118</sup> M. R. Axet, et al. *Coordination Chemistry Reviews* **2016**, 308, 236-345.

<sup>119</sup> B. F. Machado, et al. *Journal of Catalysis* **2014**, 309, 185-198.

The TPD-MS profiles of the supported catalysts provide valuable information on ruthenium grafting. The analyses performed on the two supports **O3h-CNT** and **O3h-CNT-400** are shown on Figure 3.24c,d.

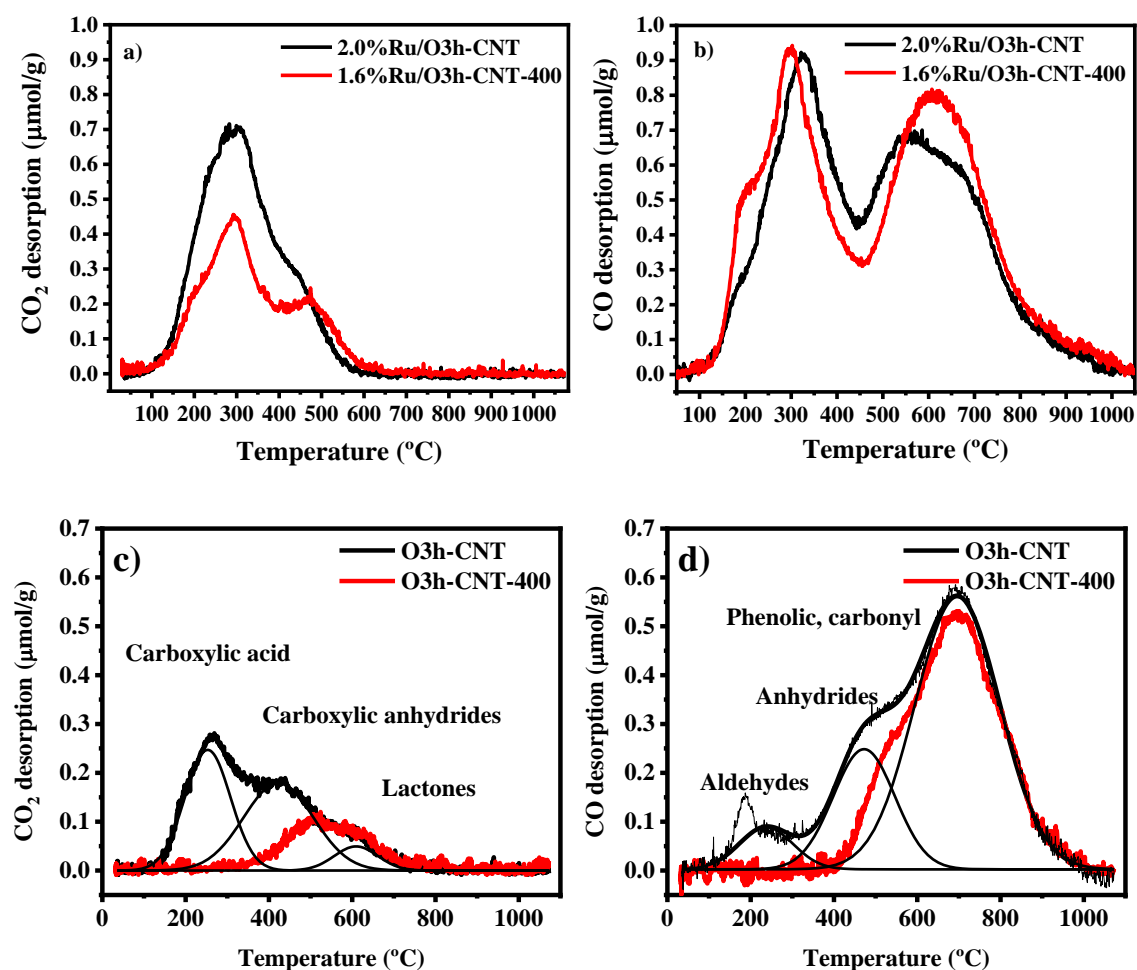


Figure 3.24. TPD-MS profiles of the carbon-supported ruthenium samples, a)  $\text{CO}_2$  evolution, and b) CO evolution and oxidized, and heated support, c)  $\text{CO}_2$  evolution, and d) CO evolution

This can be explained by the well-known ability of ruthenium to catalyze ring-opening polymerization of lactones and thus generating less stable surface groups.<sup>120</sup> Besides, we can see in both samples with Ru that the  $\text{CO}_2$ -evolving groups belonging to the remaining lactones (600 °C) decompose at lower temperatures. On the other hand, the CO evolution profiles developed new important peaks between 200 and 300 °C along with an increase in the intensity of the peak of carbonyl/quinone/epoxy at 600-700 °C. Ruthenium deposition induces the formation of new  $\text{CO}_2$  and CO releasing groups, either on

<sup>120</sup> R. R. Gowda, et al. *Journal of Molecular Catalysis A: Chemical* **2009**, 301, 84-92.



**Ru/O3h-CNT** and **Ru/O3h-CNT-400** (Figure 3.24a,b), as evidenced by the different decomposition temperatures and the larger amount of gases quantified compared with the oxidized support (Table 3.8).

Table 3.8. Quantification of temperature programmed desorption (TPD) profiles.

Sample	Total CO <sub>2</sub> (μmol/g)	Total CO (μmol/g)
Supports		
O3h-CNT	965	2637
O3h-CNT-400	331	1801
Catalysts		
2.0%Ru/O3h-CNT	1892	4444
1.6%Ru/O3h-CNT-400	1240	4699

The peak at low temperature can be assigned to the decomposition of labile surface epoxy groups.<sup>121</sup> The formation of such groups has been investigated by theoretical calculations for Ru<sub>13</sub>/graphene catalysts.<sup>119</sup> The new epoxy surface functional groups arises from the reaction of the oxidized Ru cluster (due to air exposure of the samples) and the graphene surface (Figure 3.25).

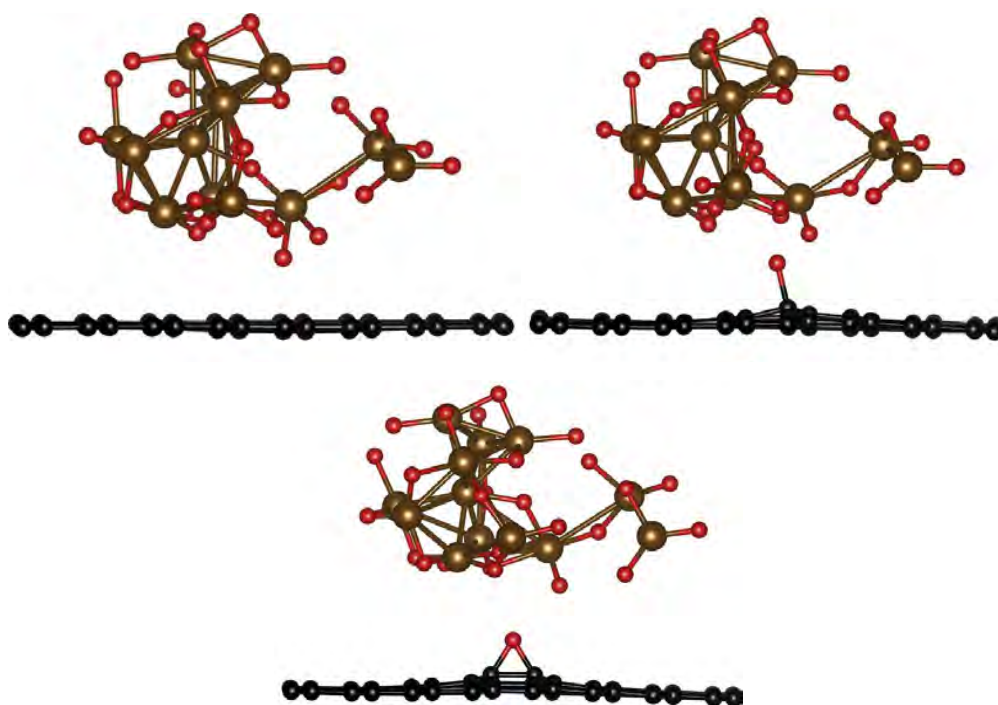


Figure 3.25. Geometries of Ru<sub>13</sub>O<sub>30</sub> + 1O atom on graphene. Top panel shows the initial state, in the middle lies the transition state geometry while the bottom panel shows the final state with the epoxy group. C atoms are in black, O in red, H in with white and Ru in red.

<sup>121</sup> M. P. Araújo, et al. *RSC Advances* **2017**, 7, 14290-14301.



In STEM, homogeneous deposition was observed on **Ru/O3h-CNT** that may correspond to the  $[\text{Ru}(\text{COD})(\text{COT})]$  precursor anchored on the external surface of CNT by acetato ligands (Figure 3.26a,b). However, when the sample was heat-treated at 300 °C 20/80  $\text{H}_2/\text{Ar}$ ,  $\text{Ru}_{\text{NP}}$  of size diameter of 1.03 nm appeared over the entire surface of the support, unlike previous thermal tests, indicating that the anchoring over vacancies delivers higher stability than using surface  $-\text{COOH}$  groups. For metals such as gold, the calculated binding energy of  $\text{Au}_{\text{SA}}$  to a defect site is 6-18 times (i.e., 3.02-9.56 eV) higher than that on a defect-free carbon surface (0.45 eV). In other words, it is evident that once Au atom is trapped on a defect site on the carbon surface, it is thermodynamically more stable.<sup>122</sup>

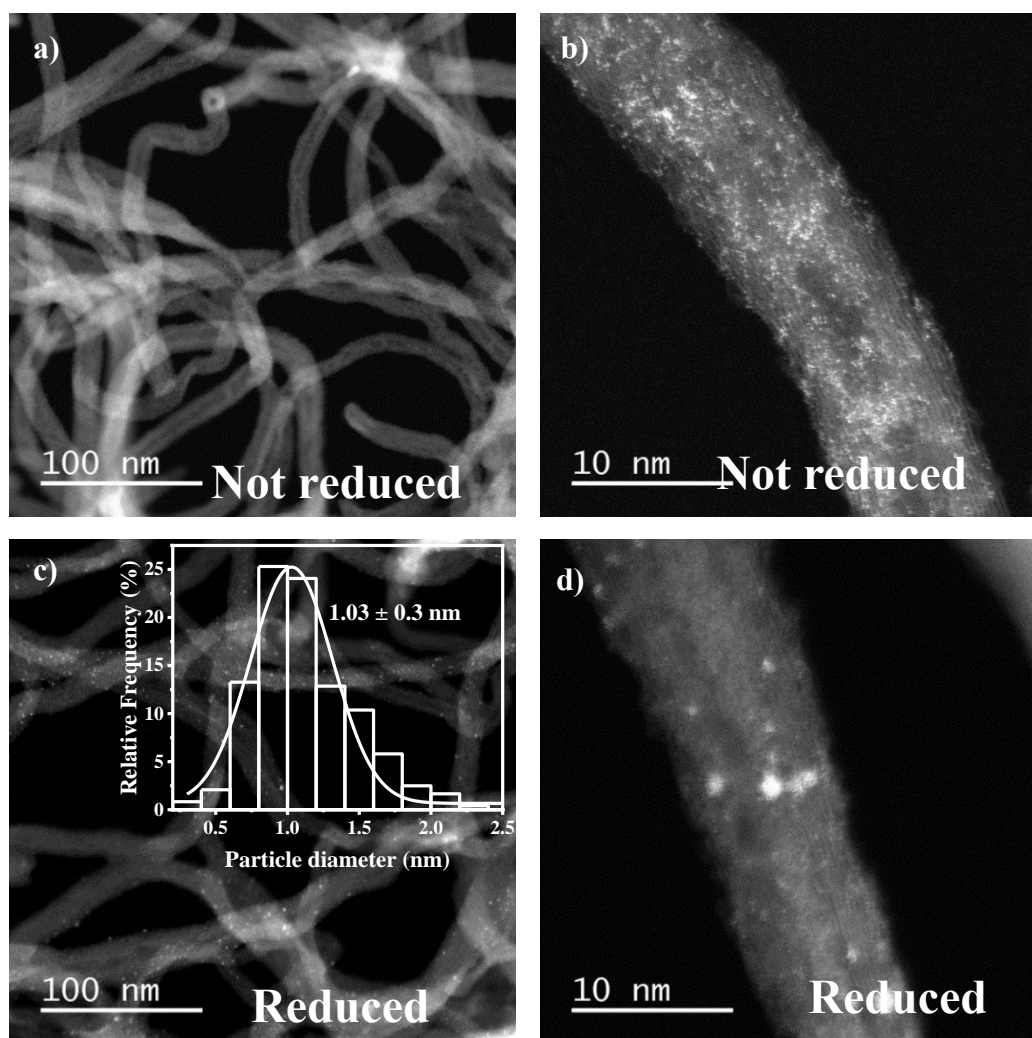
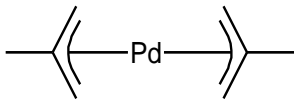
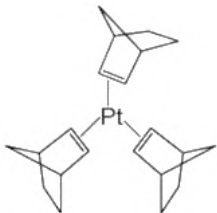
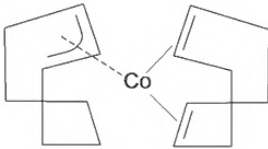
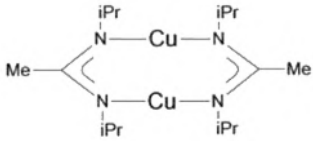
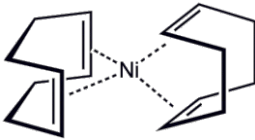
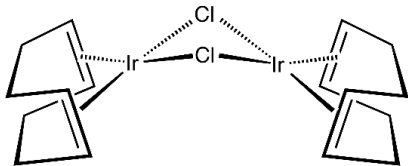


Figure 3.26. HAADF-STEM micrographs sample **0.4%Ru/O3h-CNT** without support activation a) and b) before reduction; and c) and d) after reduction at 300 °C.

<sup>122</sup> L. Wu, et al. *npj Computational Materials* **2020**, 6, 23.

To enlarge the scope of the deposited metals, we prepared samples **1.0%M/O3h-CNT-400** from six other organometallic precursors. The detail of each precursor and obtained metallic yield is presented on Table 3.9.

Table 3.9. Metal loading using different metal precursors determined by ICP-OES.

Sample	Metallic precursor	wt. %
	Bis(2-methylallyl) Palladium (II)	
1.0%Pd/O3h-CNT-400		0.98
	Tris(norbornene) Platinum (0)	
1.0%Pt/O3h-CNT-400		1.26
	(1,5-cyclooctadiene) (cyclooctadienyl) Cobalt (I)	
1.0%Co/O3h-CNT-400		1.21
	(N,N'-diisopropylacetamidinate) Copper (I)	
1.0%Cu/O3h-CNT-400		0.68
	Bis(η <sup>4</sup> -1,5-cyclooctadiene) Nickel (0)	
1.0%Ni/O3h-CNT-400		1.09
	Chloro-(1,5-cyclooctadiene) Iridium (I) dimer	
1.0%Ir/O3h-CNT-400		1.48

The preparation protocol followed was the same as for Ru. HAADF-STEM micrographs displayed in Figure 3.27 show similar appearance as for Ru samples although the discernment of the Cu or Ni atoms was more difficult due to poor contrast because their lower Z ( $^{44}\text{Ru} > ^{28}\text{Ni}$  and  $^{29}\text{Cu}$ ).

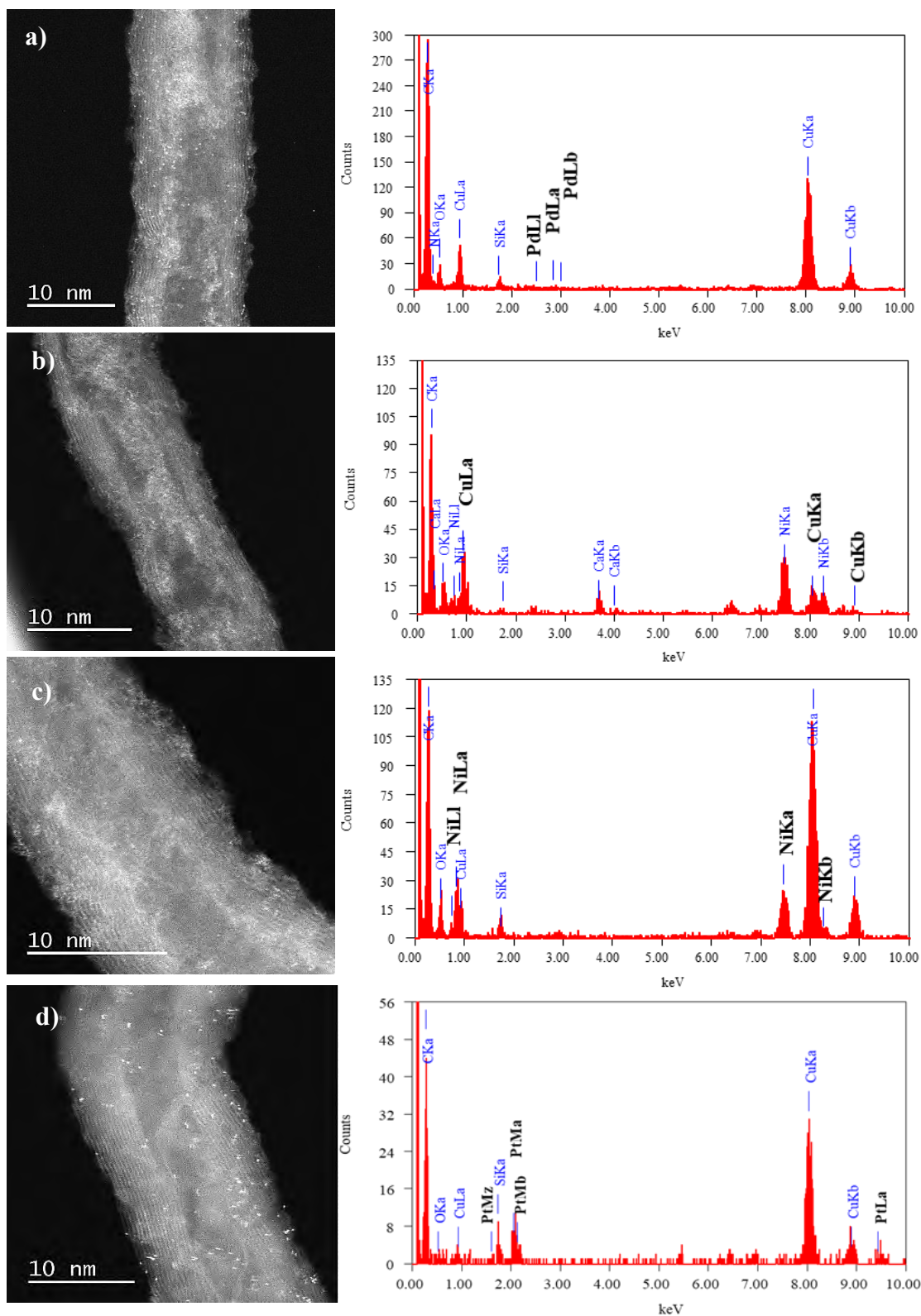


Figure 3.27. HAADF-STEM micrographs of a) 1.0%Pd/O3h-CNT400; b) 1.0%Cu/O3h-CNT400; c) 1.0%Ni/O3h-CNT400; and d) 1.0%Pt/O3h-CNT400 together with respective EDX analyses.

The EDX signals have low intensity due to the high dispersion of the metal. It is worth mentioning that to facilitate the identification of Cu species, the interference signals that usually come from the grid were eliminated by dispersing the sample on a nickel grid.

Finally, we extend the experiments to other carbon supports and prepare SAC using a fibrous carbon material (FM), small carbon nanofibers (sCNF) and carbon black (CB, Vulcan XC-72). As mentioned before, the supports were prepared and purified in our laboratory following the protocol described in Ref. <sup>123</sup>, with the exception of CB, obtained from CABOT Corp. The samples present different metallic loadings, which cannot be related with any textural properties including BET surface area, pore volume, inter-defect distance ( $L_d$ ) nor average stacking heights parallel to the fiber axis ( $L_c$ ), which is a measure of surface reactivity (Table 3.10). Anyhow, a high density of SA was obtained, accompanied with few clusters Figure 3.28.

Table 3.10. Ruthenium content varying type of support determined by ICP-OES.

Sample	Ru content (wt. %)	$S_{\text{BET}}$ (m <sup>2</sup> /g)	Pore Volume (cm <sup>3</sup> /g)	$L_d$	$L_c$
2.0% Ru/ O3h-CNT-400	1.60	220	1.2	11.9	4.57
2.0% Ru/ O3h-FM-400	1.41	215	0.4	10.1	6.71
1.5%Ru/O3h-sCNF-400	1.33	296	1.0	11.4	4.64
1.5%Ru/ O3h-CB-400	0.70	262 <sup>124</sup>	0.3	7.9	-

BET, Pore volume,  $L_c$ ,  $L_d$  obtained from ref. 13

### 3.5 Mixture of single atoms and nanoparticles

For decades benchmark catalysts such as Pd/C, Ru/C, Pt/C have been used at the industrial level assuming they contain nanoparticles on carbon but, recent research has shown that even these commercial catalysts unconsciously contain supported single atoms.<sup>125</sup> These results make us wonder if the so-far "unseen" atoms, may play a role in the catalytic performances (see Chapter 4).

<sup>123</sup> R. C. Contreras, et al. *Journal of Catalysis* **2019**, 372, 226-244.

<sup>124</sup> Y. Holade, et al. *Physical Chemistry Chemical Physics* **2014**, 16, 25609-25620.

<sup>125</sup> U. Petek, et al. *Catalysts* **2019**, 9, 134.



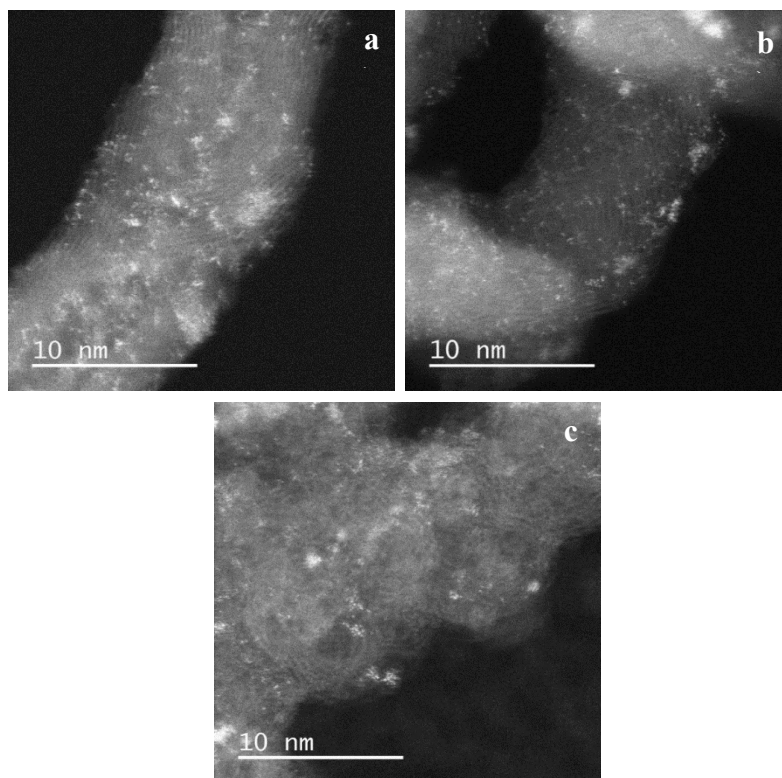


Figure 3.28. HAADF-STEM micrographs of: a) 2.0% Ru/O3h-FM-400; b) 1.5% Ru/O3h-sCNF-400; and c) 1.5% Ru/O3h-CB-400.

In a recent report, researchers detect a synergistic contribution from Ru nanoparticles in a system containing Ru<sub>SA</sub>, but surprisingly, they did not seek for the role and influence of each species on the catalytic activity.<sup>126</sup> Additionally, some articles have been published recently dealing with “two-component catalysts”, highlighting the synergistic effect between atomically dispersed species and nanosized cluster/particles.<sup>127,128,129</sup> The improved performances have been explained in different ways. For instance, Tiwari *et al.*, relate the positive effect of having both Pt<sub>SA</sub> and Pt nanoclusters onto graphitic tubes for the hydrogen evolution reaction in acidic solutions. A synergistic conductivity-enhancement effect between the Pt<sub>SA</sub> and the Pt nanoclusters has been proposed.<sup>130</sup> On the other hand, He and co-workers indicate a metal-metal charge transfer from Ru particles to Co<sub>SA</sub>.<sup>131</sup>

<sup>126</sup> B. Lu, et al. *Nature communications* **2019**, *10*, 631-631.

<sup>127</sup> G. Lan, et al. *ACS Applied Nano Materials* **2020**, *3*, 3004-3010.

<sup>128</sup> J. Kang, et al. *Materials* **2020**, *13*, 1513.

<sup>129</sup> W. Xi, et al. *Nature Communications* **2020**, *11*, 1919.

<sup>130</sup> J. N. Tiwari, et al. *Nature Energy* **2018**, *3*, 773-782.

<sup>131</sup> T. He, et al. *ACS Applied Materials & Interfaces* **2019**, *11*, 46912-46919.

One technique to achieve two-component catalysts is the “top-down” approach where atoms can be released from nanoparticles by "re-dispersion" under specific reaction conditions.<sup>132</sup> For example, Pd-NPs@ZIF-8 nanocomposites were heated at 900 °C under an inert atmosphere for 3 h, after which the Pd<sub>NP</sub> disappeared to give thermally stable Pd<sub>SA</sub>.<sup>133</sup> Thus, great changes in the electron structures of metal clusters are created by giving more metallic availability.<sup>134,135</sup> However, sometimes the process occurs without a rational control, and the size of the resultant species cannot be tuned, which can be detrimental to catalyst performances. Thus, dramatic differences in rate and selectivity on active sites of differing Rh nuclearity have been observed.<sup>136</sup> Alternatively, the “bottom-up” approach allows growing clusters from individual atoms by aggregation, creating nanomaterials in a clear and manageable manner, such as with atomic layer deposition.<sup>137</sup> The disadvantage of the latter method lies in its low practicality due to limitations in equipment and scale-up. That is why we present here a simple procedure that does not require sophisticated equipment to prepare catalysts containing simultaneously controlled amounts of single atoms and nanoclusters.

We discovered that by repeating the impregnation step we were able to produce a heterogeneous material composed of SA and NP/clusters. Furthermore, we realized that by controlling the number of impregnations cycles it was possible to tune the ratio of SA and clusters. More specifically, the following procedure has been followed:

**Step III: Metal deposition.** The solid obtained in step **II** was transferred to a Schlenk tube under argon avoiding contact with oxygen. Immediately, the solid is impregnated with 30 mL of pentane metal-containing solution transferred *via* canula. The concentration of the solution will correspond to the desire amount of metallic precursor to get a loading (*e.g.* 1.4 wt.% Pd, (bis(2-methylallyl)Pd)) divided X times (2, 3 or 4 parts), depending on the wished SA/NP ratio (smaller values of SA/NP ratio will require higher number of impregnations). The mixture was stirred one hour at room temperature under argon atmosphere. Afterwards, the solid is allowed to precipitate to remove the supernatant then washed 3 times with pure pentane and dried under vacuum overnight.

---

<sup>132</sup> A. K. Datye *Nature Nanotechnology* **2019**, *14*, 817-818.

<sup>133</sup> S. Wei, et al. *Nature Nanotechnology* **2018**, *13*, 856-861.

<sup>134</sup> Y.-G. Wang, et al. *Nature Communications* **2015**, *6*, 6511.

<sup>135</sup> A. Aitbekova, et al. *Chinese Journal of Catalysis* **2020**, *41*, 998-1005.

<sup>136</sup> C. Asokan, et al. *ACS Catalysis* **2020**, *10*, 5217-5222.

<sup>137</sup> D. Xu, et al. *ACS Applied Materials & Interfaces* **2019**, *11*, 29858-29867.



**Step IV: Elimination of ligands.** The previous solid was heated at 5 °C/min, up to 80 °C for one hour, at a flow rate of 80/20 Ar/H<sub>2</sub>. After, the sample is managed as step **III**. The number of times that step **III** is performed until to reach the given total metal loading will modify the SA/NP ratio. Finally, the samples were stored in air and room temperature. For two, three and four cycles, the samples were labeled **0.70%x2 Pd/O3h-CNT-400**, **0.46%x3 Pd/O3h-CNT-400** and **0.35% x4 Pd/O3h-CNT-400**, respectively. The procedure is summarized in Figure 3.29. After each impregnation, the real metallic content was measured by ICP-OES. Table 3.11 display the values obtained after each cycle of precursor addition.

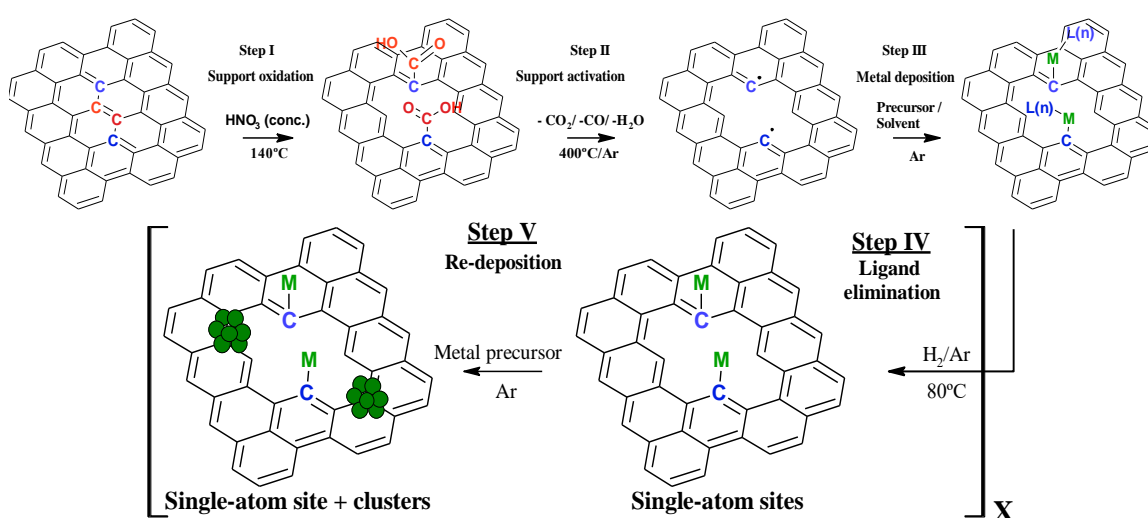


Figure 3.29. Production of catalysts with controlled SA/NP ratio.

Table 3.11. Metallic loading of Pd/O-CNT samples with different number of impregnation cycles determined by ICP-OES.

Sample	Metallic loading after n° impregnation cycle (wt.%)				Ratio SA/NP <sup>a)</sup>
	1	2	3	4	
1.40%x1 Pd/O3h-CNT-400	<b>1.33</b>				200
0.70%x2 Pd/O3h -CNT-400	0.74	<b>1.43</b>			65
0.46%x3 Pd/O3h -CNT-400	0.62	0.95	<b>1.37</b>		45
0.35%x4 Pd/O3h-CNT-400	0.38	0.68	0.93	<b>1.29</b>	15

a) From HR-TEM, by manual count on Image J software. SA/NP ratio calculated considering the total number of atoms and particles counted in at least 20 images per sample.

When analyzing the data, a linear correlation was obtained between nominal and actual metallic content (Figure 3.30). The variability of each cycle was low, indicated by the low deviation. These results suggest good efficiency and reproducibility of the method.

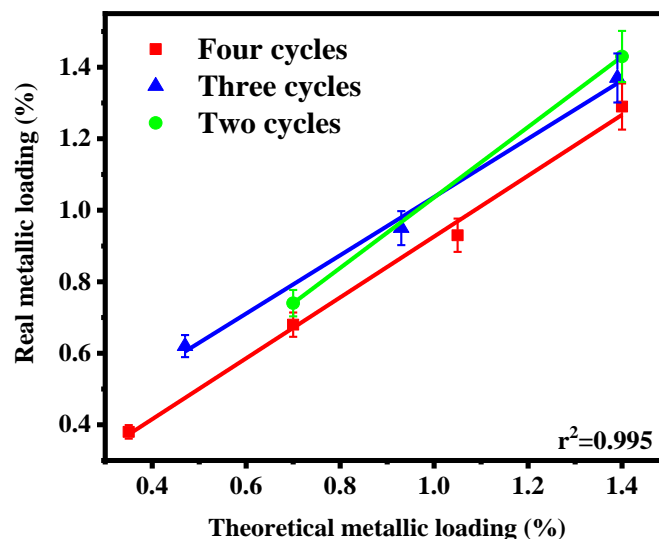


Figure 3.30. Linear correlation between theoretical and real metallic loading after 2, 3, and 4 impregnation cycles.

Figure 3.31 shows HAADF-STEM images of **1.40% Pd/O3h-CNT-400** prepared by this process, for which the SA/NP ratio is controlled between 200/1 (one deposition cycle of 1.40% Pd) and 10/1 (four deposition cycles of 0.35% Pd). Furthermore, with the repetition of the process, the size of the clusters begins to grow due to the coalescence effect going from 0.50 nm to 1.1 nm.

We also characterized these samples by XPS, to prove the chemical and compositional properties of the resultant materials. The electronic state of Pd was studied. Figure 3.32 shows a typical Pd 3d spectrum with characteristic doublet peaks corresponding to Pd 3d<sub>5/2</sub> and Pd 3d<sub>3/2</sub>.

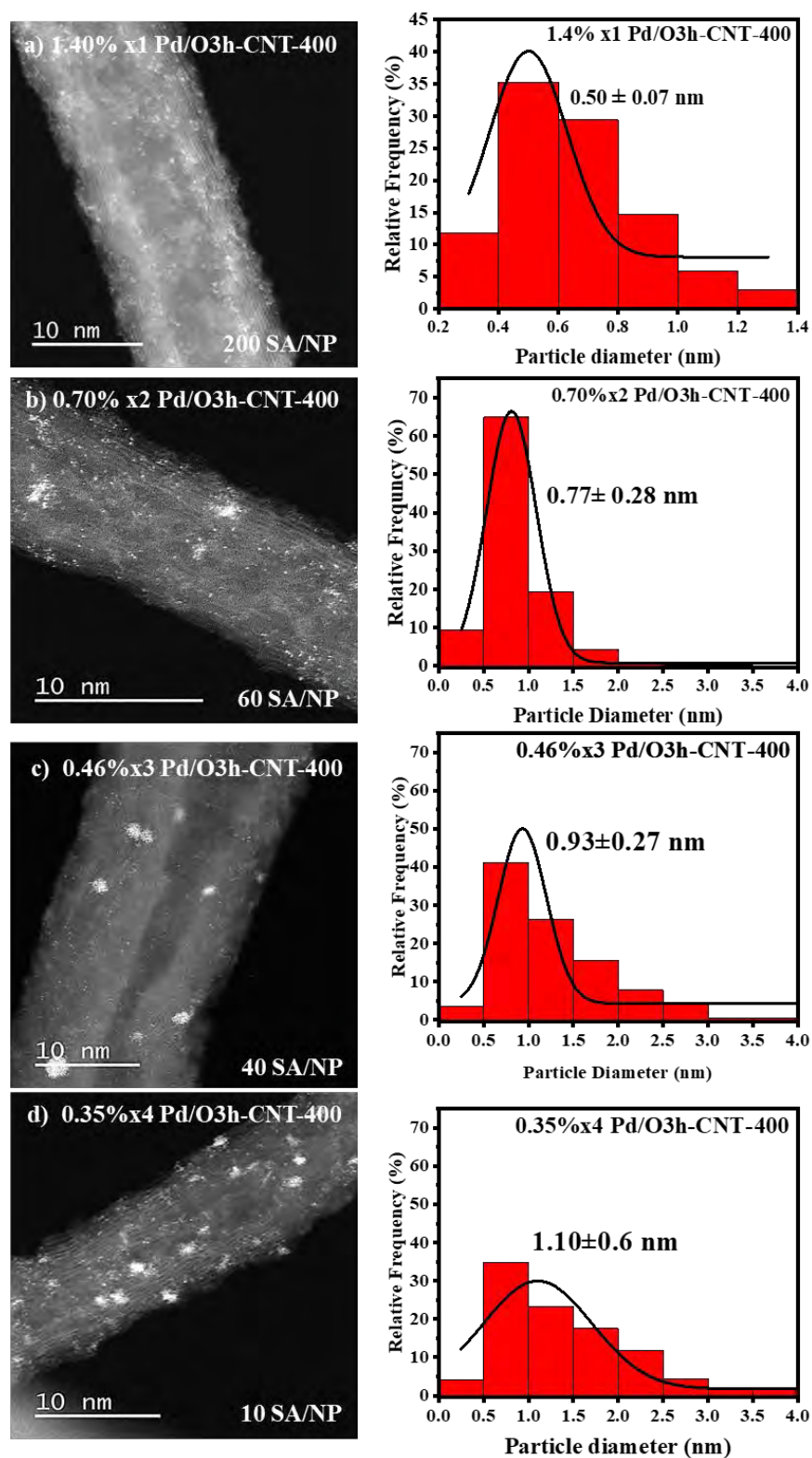


Figure 3.31. HAADF-STEM micrographs mixtures of SA and NP at different ratio in a) 0.70% x2 Pd/O3h-CNT-400; b) 0.46% x3 Pd/O3h-CNT-400; and c) 0.35% x4 Pd/O3h-CNT-400 catalysts.

Making a comparison with the reference values of bulk Pd at core level of Pd<sup>0</sup> 3d<sub>5/2</sub> (335.10 eV),<sup>138</sup> we can see that 1.4%Pd<sub>SA</sub>/O3h-CNT-400, presents a shift towards higher binding energies (335.58 eV), which has been broadly related to phenomena of charge transfer from the metal to the support, leaving electronically deficient Pd<sub>SA</sub>.<sup>139,140</sup>

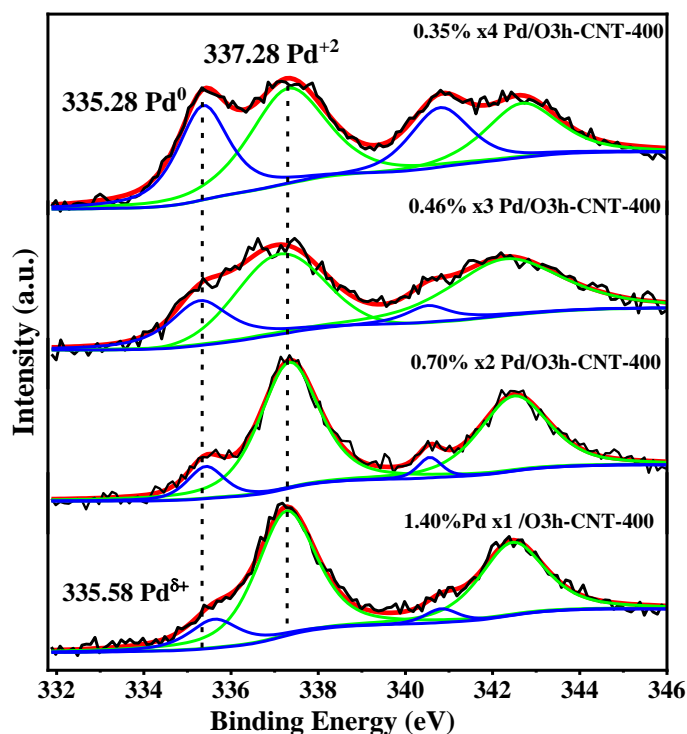


Figure 3.32. XPS spectra of Pd 3d (from bottom to top): 1.4%Pd<sub>x1</sub>/O3h-CNT-400, 0.70% x2 Pd/O3h-CNT-400, 0.46% x3 Pd/O3h-CNT-400 and 0.35% x4 Pd/O3h-CNT-400.

As the concentration of cluster/NP increases, the metallic palladium signal increases (Table 3.12) and shifts towards lower binding energy (335.28 eV), which is in good agreement with bulk Pd<sup>0</sup>.<sup>141</sup> This upshift for SA species has been observed for other elements such as Pt.<sup>142</sup>

<sup>138</sup> J. F. Moulder, et al. In: Perkin-Elmer Corp., Physical Electronics Division. Minnessota, United States (1992), pp. 118-119.

<sup>139</sup> W. Xiang, et al. *Journal of Materials Chemistry A* **2018**, 6, 23366-23377.

<sup>140</sup> J. Xi, et al. *Applied Catalysis B: Environmental* **2018**, 225, 291-297.

<sup>141</sup> A. L. Dantas Ramos, et al. *Applied Catalysis A: General* **2004**, 277, 71-81.

<sup>142</sup> Q. Liu, et al. *Catalysis Science & Technology* **2019**, 9, 4821-4834.

Table 3.12. XPS Pd 3d and O 1s peak deconvolution and relative content of species.

Sample	Atomic percentage (%)					
	Pd <sup>0</sup>	Pd <sup>+δ</sup>	Pd <sup>+δ</sup> /Pd <sup>0</sup>	C=O	C-O	H <sub>2</sub> O
1.40% x1 Pd/O3h-CNT-400	14.20	85.79	6.06	41.10	39.16	19.74
0.70% x2 Pd/O3h-CNT-400	15.25	84.75	5.55	43.00	33.14	23.86
0.46% x3 Pd/O3h-CNT-400	22.00	78.00	3.55	43.36	33.32	23.32
0.35% x4 Pd/O3h-CNT-400	41.75	58.25	1.39	40.13	33.21	26.67

The ratio between these two peaks is 13/87 and 41/59 for **0.70%x2 Pd/O3h-CNT-400** and **0.35%x4 Pd/O3h-CNT-400** samples, respectively. These data, in association with the STEM-HAADF observations, confirm that the proportion of SA is much higher in the sample with two cycles than the one with four. The spectrum of O 1s (Figure 3.33) did not evolve considerably from the second impregnation onwards, which suggests that the subsequent insertion of Pd happens on the sites created during the first deposition (these acting as seeds), and does not occur on the remaining oxygen groups.

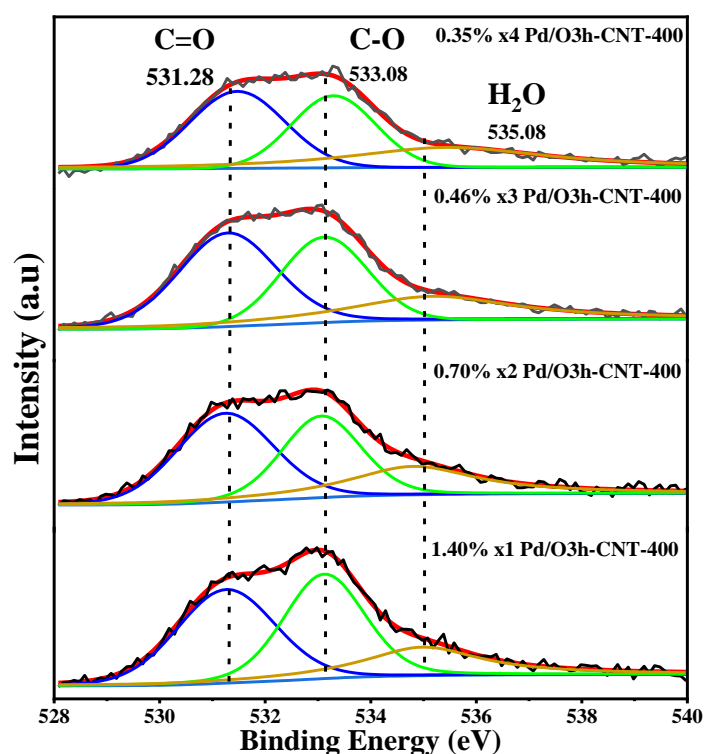


Figure 3.33. XPS spectra of O 1s (from bottom to top): 1.40%Pd x1/O3h-CNT-400, 0.70% x2 Pd/O3h-CNT-400, 0.46% x3 Pd/ O3h-CNT-400 and 0.35% x4 Pd/ O3h-CNT-400.

### 3.6 Conclusion

In summary, the preparation of SAC has been investigated through the reaction of a metallic precursor in the presence of a defective carbon support and the resulting materials have been characterized. We have evidenced the introduction of defects by a functionalization-defunctionalization process over a carbon support, thanks to magnetic techniques such EPR and SQUID. We have proved the importance of this process in the successful anchoring of stable metallic atoms. The temperature of activation as well as the choice of the precursor and solvent affect the final metallic loading. This method is reproducible and applicable to different metals (Ru, Pd, Pt, Ni, Co, Cu, and Ir were investigated) and supports (CNT, CNF, FM, and CB were used). Then, we have demonstrated in the case of Pd that it was possible to control the SA/NP ratio between 200 and 10 by repetition of impregnation cycles. Significant charge transfer from palladium to CNT was evidenced by XPS, which can be of importance when evaluating catalytic activity. This strategy allows engineering the minimal catalytic ensemble that we envision to produce in order to study a possible cooperative catalytic effect between SA and NP in Pd/C supported catalysts, which is the subject of the next chapter.

### 3.7 Experimental section

#### 3.6.1 Catalysts preparation

**Step I: Support oxidation.** 5.0 g of CNT prepared and purified as described in ref.123, were placed in a round bottom flask with 50 mL of HNO<sub>3</sub> 65% and refluxed at 140 °C for 1, 3 or 5 h. The acidic solution was filtered and the solid washed with distilled water. The solid was dried in an oven at 80 °C overnight to produce functionalized CNT **O1h-CNT**, **O3h-CNT**, and **O5h-CNT**.

**Step II: Support activation.** 1.0 g of **OXh-CNT** was placed in an alumina crucible and inserted into a quartz tube in a horizontal furnace. The support was heated under argon at 5 °C/min up to 400 °C during 1 hour (600 and 1000 °C were also used for comparison). After the heating program the samples were allowed to cool down on argon and finally kept under an inert atmosphere to perform further experiments. The obtained product was labelled as **OXh-CNT-400**.

**Step III: Metal deposition.** The solid obtained at **step II** was transferred to a Schlenk tube under argon avoiding contact with oxygen. Separately, a desire amount of a solution



containing the metallic precursor was prepared under inert atmosphere (for example: 0.4%; 12.5 mg of [Ru(COD)(COT)] was dissolved in 30 mL of degassed pentane). Immediately, the yellow solution was mixed with the support under argon by transferring the liquid *via* cannula and let to react during one hour at room temperature under argon atmosphere. Afterwards, the solid was allowed to precipitate to remove the supernatant, then washed 3 times with pure pentane, and finally dried under vacuum overnight.

**Step IV: Elimination of ligands.** The prepared carbon material containing the metal was heated at 5 °C/min, up to 80 °C for one hour, at a flow rate of 80/20 Ar/H<sub>2</sub>. After this treatment the sample was stored in air.

### 3.6.2 Catalysts Characterization

The high-resolution analyses were conducted using a transmission-corrected field emission electron microscope, probe coupled to an energy-dispersive x-ray spectrometer (EDX) and an energy loss spectrometer (EELS) JEOL JEM-ARM200F Cold FEG operating at 200 kV with a point resolution of > 1.9 Å.

Thermogravimetric analyses were performed in a Mettler Toledo TGA2 device with a heating rate of 5°C/min and constant flow of N<sub>2</sub> 20 mL/min.

Temperature-programmed desorption analysis were obtained with a fully automated AMI-200 Catalyst Characterization Instrument (Altamira Instruments), equipped with a thermal conductivity detector and a quadrupole mass spectrometer (Dymaxion 200 amu, Ametek) and the sample was heated to 1100 °C using a constant flow rate of helium (25 cm<sup>3</sup>/min, STP).

The Raman measurements have been recorded with a Raman Horiba Jobin Yvon Labram HR 800 spectrometer in backscattering geometry using an optical objective 100 (NA 0.9). The wavelength of the incident laser was 532 nm and its power was set to 1 mW.

XPS was performed using a Thermo Scientific K-alpha apparatus (hν (Al Kα) = 1486.6 eV); and the XPSpeak 4.1 software was used to perform curve fitting and to calculate the atomic concentrations.

NMR experiments were recorded on Bruker Avance 400 III HD spectrometer operating at magnetic fields of 9.4 T. Samples were packed into 2.5 mm zirconia rotors under argon inside a glove box. The rotors were spun at 10 kHz (ν<sub>r</sub>) at 295 K. <sup>13</sup>C Hahn-echo were

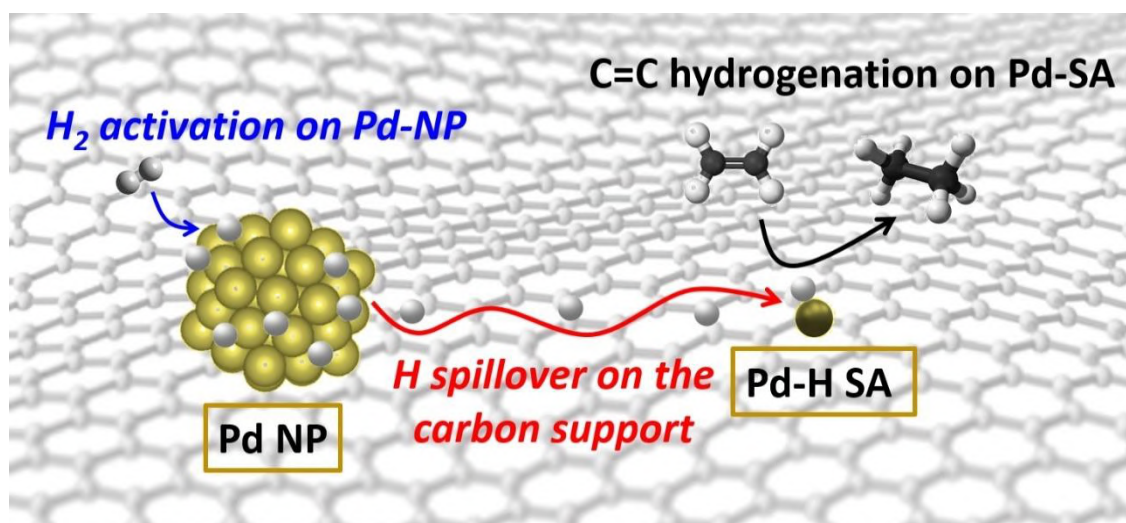
synchronized with the spinning rate and performed with a recycle delay of 30 s. Chemical shifts were referenced to liquid TMS.

We have measured the magnetic properties of our samples with a superconducting quantum interference device-vibrating sample (SQUID-VSM) magnetometer MPMS5. The magnetization loop was measured between -10 and 10 kOe at  $T = 300$  K after cooling the sample from 27 °C (300 K) to -268 °C (5 K) under a constant applied magnetic field  $H_{\text{cool}} = 50$  kOe.

EPR data were recorded using an Eleksys E 500 Bruker spectrometer, operating at a microwave frequency of approximately 9.5 GHz. All spectra were recorded using a microwave power of 10 mW across a sweep width of 1500 G (centered at 3100 G) with a modulation amplitude of 2 G. Experiments were carried out at 10 K using a liquid helium cryostat.



## Chapter 4. Hydrogenation of alkenes with single atom catalysts





## 4. Hydrogenation of alkenes with single atom catalysts

### 4.1. Introduction

The hydrogenation of alkenes is among the important technological reactions catalyzed by supported metals, finding application in the pharmaceutical, agrochemical, refining, and commodity chemical industries. As the catalyst active phase is often made of noble metals, expensive and for the most part identified as critical elements, a logical step is to optimize their dispersion on the support.<sup>1</sup> The highest dispersion that can be achieved corresponds to supported isolated metal atoms. Supported SA have coexisted with metal NP for a long time,<sup>2</sup> and may have played significant roles in many catalytic processes, but they have rarely been recognized as active sites. Today, aided by recent advances in synthesis methodologies, characterization techniques and computational modelling, single-atom catalysis has decidedly become the most active new frontier in heterogeneous catalysis.<sup>3</sup> Single atoms exhibit distinctive performances from the ones of NP for a wide variety of chemical reactions, and industrial applications employing them already exist.<sup>4</sup> The absence of atomic ensemble effects, and the charge transfer to or from the support, that strongly modifies the electronic structure of the metal atom in SA catalysts, significantly affect the adsorption, and definitively induce a different reactivity compared to metallic NP.<sup>5</sup> Current studies conducted on SA focus mainly on distinguishing them from NP and the possibility of synergy between these two species have been rarely explored.<sup>6,7</sup> Interestingly, it was recently proposed that a synergy may operate between Pd<sub>SA</sub> and Pd<sub>NP</sub> during ketone/aldehyde hydrogenation on Pd/TiO<sub>2</sub> catalysts.<sup>7</sup> In this reaction, Pd<sub>SA</sub> contributes for the C=O activation while Pd<sub>NP</sub> allow the easy dissociation of H<sub>2</sub> (Figure 4.1).

---

<sup>1</sup> W. S. Lamme, et al. *Journal of Catalysis* **2019**, 375, 448-455.

<sup>2</sup> U. Petek, et al. *Catalysts* **2019**, 9, 134.

<sup>3</sup> A. Wang, et al. *Nature Reviews Chemistry* **2018**, 2, 65-81.

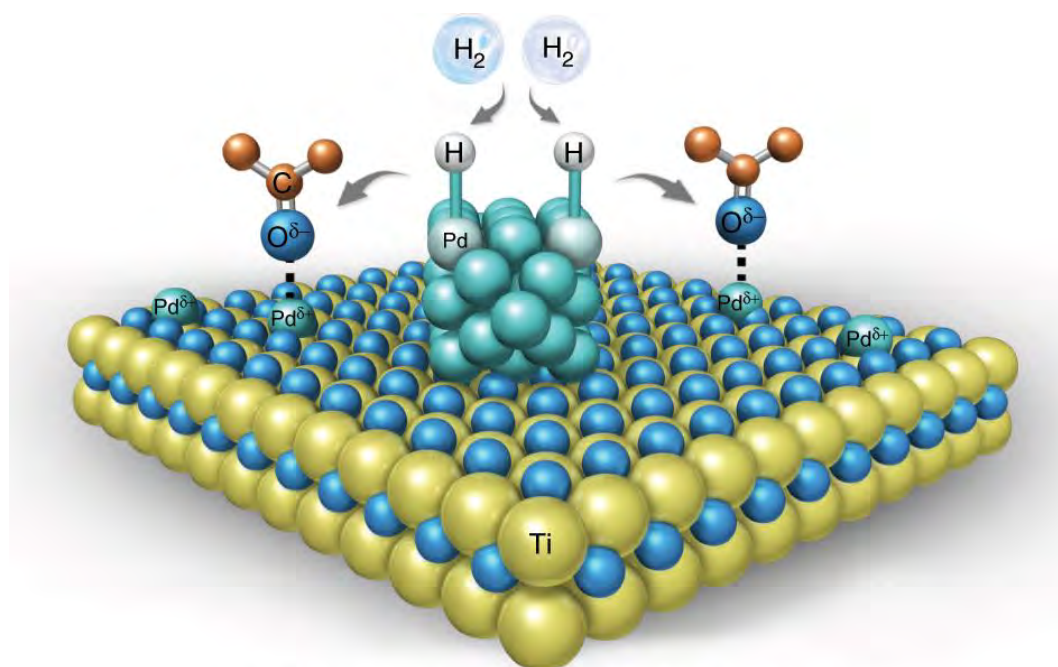
<sup>4</sup> G. Malta, et al. *Science* **2017**, 355, 1399.

<sup>5</sup> L. Liu, et al. *Chemical Reviews* **2018a**, 118, 4981-5079.

<sup>6</sup> J. N. Tiwari, et al. *Advanced Energy Materials* **2019**, 9, 1900931.

<sup>7</sup> L. Kuai, et al. *Nature Communications* **2020**, 11, 48.





$\text{Pd}^{\delta+}$ : single-atom Pd sites for C=O activation

Pd: Pd nanoparticles sites for  $\text{H}_2$  dissociation

Figure 4.1. The  $\text{Pd}_{\text{SA+NP}}/\text{TiO}_2$  integrates both  $\text{Pd}_{\text{SA}}$  and  $\text{Pd}_{\text{NP}}$  sites on  $\text{TiO}_2$  surface, in which the  $\text{Pd}_{\text{SA}}$  sites undertake the activation task of C=O group while  $\text{Pd}_{\text{NP}}$  sites boost the dissociation of  $\text{H}_2$ . The H atoms migrate to the C=O group bounded  $\text{Pd}_{\text{SA}}$  sites to complete hydrogenation. From ref. [7].

Palladium on carbon is a very common catalyst for alkene hydrogenation.<sup>8</sup> Hydrogenations with  $\text{Pd}_{\text{SA}}$  have been already reported<sup>3,9</sup> but the metal-support interaction in such catalysts often results in an ionic/electron-deficient state of the metallic atoms that prevents an efficient  $\text{H}_2$  activation compared to metallic surfaces<sup>7,9,10</sup> and limits their application to specific selective hydrogenation reactions.<sup>11,12</sup> Although a direct  $\text{H}_2$  activation has been reported for Pd/Cu single-atom alloy,<sup>11</sup> on  $\text{Pd}_{\text{SA}}$ ,  $\text{H}_2$  activation is performed thanks to support-assisted molecular hydrogen heterolytic dissociation.<sup>13,14</sup> Given that  $\text{H}_2$  dissociation is often the rate-limiting step in these reactions, efficient strategies toward engineering the minimal catalytic ensemble that can activate  $\text{H}_2$  would represent a substantial progress in pursuit of highly efficient Pd/C hydrogenation catalysts.

<sup>8</sup> S. Nishimura, *Handbook of Heterogeneous Catalytic Hydrogenation for Organic Synthesis*; Wiley-Interscience: New York, 2001

<sup>9</sup> C. Rivera-Cárcamo, et al. *ChemCatChem* **2018**, *10*, 5058-5091.

<sup>10</sup> A. Granja-DelRío, et al. *The Journal of Physical Chemistry C* **2017**, *121*, 10843-10850.

<sup>11</sup> G. Kyriakou, et al. *Science* **2012**, *335*, 1209.

<sup>12</sup> L. Zhang, et al. *Chemical Reviews* **2020**, *120*, 683-733.

<sup>13</sup> W. Liu, et al. *Angewandte Chemie International Edition* **2018b**, *57*, 7071-7075.

<sup>14</sup> H. Yan, et al. *Journal of Catalysis* **2018**, *366*, 70-79.

In this chapter, through a combined experimental-theoretical study (theoretical calculations performed in collaboration with the Laboratoire de Physique et Chimie des Nano-Objets (LPCNO)), we show that for alkene (myrcene, squalene, farnesene) hydrogenation (performed in collaboration with the Laboratoire de Génie des Procédés Catalytiques (LGPC) in Lyon a cooperative catalysis takes place between carbon-supported  $\text{Pd}_{\text{SA}}$  and  $\text{Pd}_{\text{NP}}$ . First,  $\text{Pd}_{\text{NP}}$  dissociate  $\text{H}_2$  easily, and subsequent hydrogen spillover provides  $\text{Pd-H}$  species on  $\text{Pd}_{\text{SA}}$  ( $\text{H-Pd}_{\text{SA}}$ ). The  $\text{H-Pd}_{\text{SA}}$  are much more active than  $\text{H-Pd}_{\text{NP}}$  for the hydrogenation and isomerization of  $\text{C}=\text{C}$  double bonds. Thanks to the control of the SA/NP ratio on the support, which has been achieved in this work, the rational design of highly active catalysts becomes possible.

#### 4.2. Hydrogenation and isomerization of alkenes

As a model substrate  $\beta$ -myrcene, an acyclic polyunsaturated monoterpene with highly reactive 1,3-diene moiety, and an isolated tri-substituted  $\text{C}=\text{C}$  bond, was chosen (Figure 4.2). The hydrogenation of this important molecule has been studied over different homogeneous<sup>15</sup> or heterogeneous<sup>16</sup> catalysts. The complete hydrogenation to 2,6-dimethyloctane usually requires long reaction times (and 3 equivalents of  $\text{H}_2$ ), resulting in a low average Site Time Yield (STY).

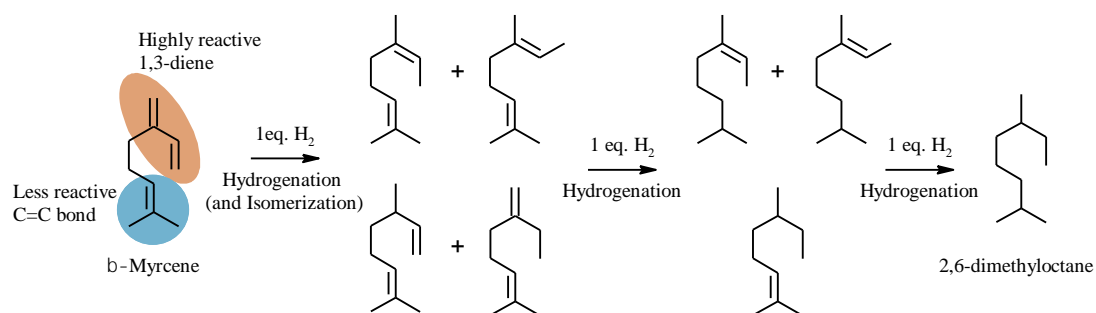


Figure 4.2.  $\beta$ -Myrcene hydrogenation reaction.

We recently reported<sup>17</sup> that a structure/activity correlation exists in  $\text{Pd/C}$  catalysts for myrcene hydrogenation, which integrates the metal dispersion, and the concentration of oxygen surface groups and defects on the support (see Figure 4.3). If the introduction of the dispersion values in this correlation and its impact on activity is not surprising, the influence of the percentage of oxygen and of defects on the carbon support was not clarified, and required further studies. The elucidation of the exact role of the percentage of oxygen and of defects on the carbon support on the catalytic activity was the main goal of my work.

<sup>15</sup> M. G. Speziali, et al. *Journal of Molecular Catalysis A: Chemical* **2005**, 239, 10-14.

<sup>16</sup> M. Guerrero, et al. *Journal of Materials Chemistry A* **2013**, 1, 1441-1449.

<sup>17</sup> R. C. Contreras, et al. *Journal of Catalysis* **2019**, 372, 226-244.

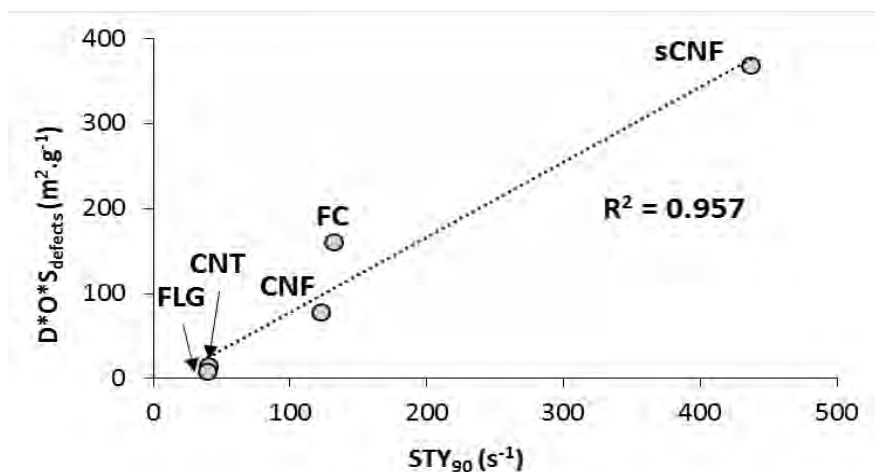


Figure 4.3. Correlations between dispersion combined to non-basal plane surfaces and oxygen content of the catalyst (from XPS) and mean apparent Site Time Yield – STY (calculated at 90% of conversion) for Pd/CNT, Pd/FLG, Pd/FC, Pd/CNF and Pd/sCNF catalysts. Ref 17 (CNT: carbon nanotubes; FLG: few layer graphene; FC: fibrous carbon; CNF: carbon nanofibers; and sCNF: small diameter carbon nanofibers).

We decided to test Pd/CNT on this reaction considering the relatively high amounts of oxygen surface groups on CNT supports,<sup>17</sup> and compared it with two commercial Pd catalysts supported on alumina and activated carbon (see Table 4.1 section 4.3). The reaction was performed at 120 °C and under 20 bar. The pressure and temperature monitoring of the calibrated gas reserve provides the hydrogen consumption rate, and thus the apparent and instantaneous activity of the catalysts expressed in moles of H<sub>2</sub> consumed per mole of Pd and per second, and being equivalent to an instantaneous Site Time Yield (“STY” in the following).

The instantaneous STY is determined by the local slope of the H<sub>2</sub> reserve consumption curve as following, where  $n_{Pd}$  is the quantity of Pd determined by ICP:

$$STY = \frac{\Delta n_{H_2}}{\Delta t \times n_{Pd}} \quad (mol_{H_2}/mol_{Pd}/s)$$

STY is qualified of apparent because (i) it addresses the overall consumption of H<sub>2</sub> through multiple reactions and (ii) depending on the catalyst and the reaction progress, possible external and internal mass transfer resistances are likely. Indeed, the reactivity of the first C=C is very high (terminal and conjugated C=C) and the first moments of the reaction are physically limited. Hopefully, this is not true for the whole range of reaction course. For robust and chemically consistent catalysts comparison, STY at 66% and 83% of reaction progress will be considered, *i.e.* when 2.0 and 2.5 equivalents of H<sub>2</sub> per  $\beta$ -myrcene are consumed respectively.

More details about the characterization of possible internal and external mass transfer limitations throughout the reaction progress are given in the experimental section 4.7.

The catalytic activity of Pd/CNT and Pd/C were similar and these two catalysts were significantly more active than Pd/Al<sub>2</sub>O<sub>3</sub> (Figure 4.4). Since the three catalysts present different Pd<sub>NP</sub> size (Figure 4.6 a,c,e), in order to have a fair comparison with commercial catalysts, a STY\* could be also used integrating the metal dispersion. A similar tendency was observed, and again higher STY\* were obtained on the two carbon-supported catalysts (Figure 4.5).

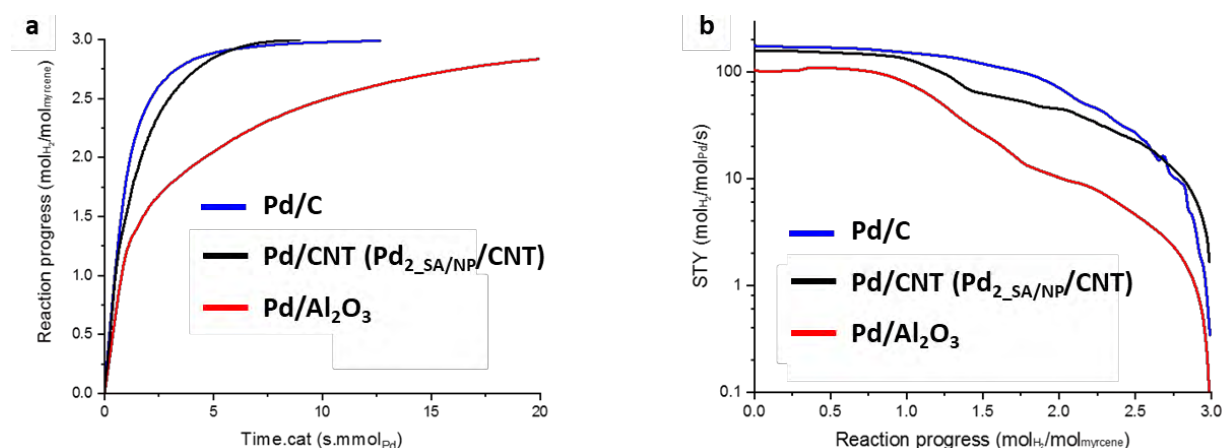


Figure 4.4. Catalytic results on Pd/Al<sub>2</sub>O<sub>3</sub>, Pd/C and Pd/CNT. Myrcene hydrogenation reaction. The reaction was carried out over supported Pd catalysts.  $P_{H_2}$  = 20 bar -  $T$  = 120 °C - myrcene 1 M (80 mL) - solvent heptane - 4 mg Pd a) Reaction progress as a function of time.cat. b) STY as a function of reaction progress.

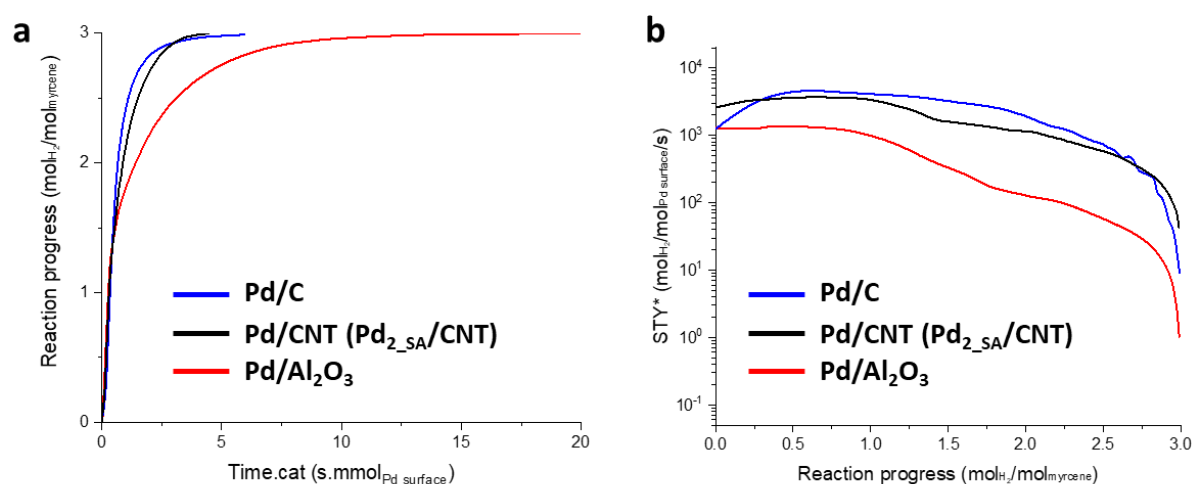


Figure 4.5. Catalytic results on Pd/Al<sub>2</sub>O<sub>3</sub>, Pd/C and Pd<sub>2-SA</sub>/NP/CNT as a function of surface Pd. β-myrcene hydrogenation reaction. The reaction was carried out over supported Pd catalysts.  $P_{H_2}$  = 20 bar -  $T$  = 120 °C - myrcene 1 M (80 mL) - solvent heptane - 200 mg cat. a) Reaction progress as a function of time.cat\*. b) STY\* as a function of reaction progress.

Analysis of these three catalysts by TEM and STEM-HAADF before and after reaction showed no very significant change in mean particle size after catalysis (Figure 4.6).

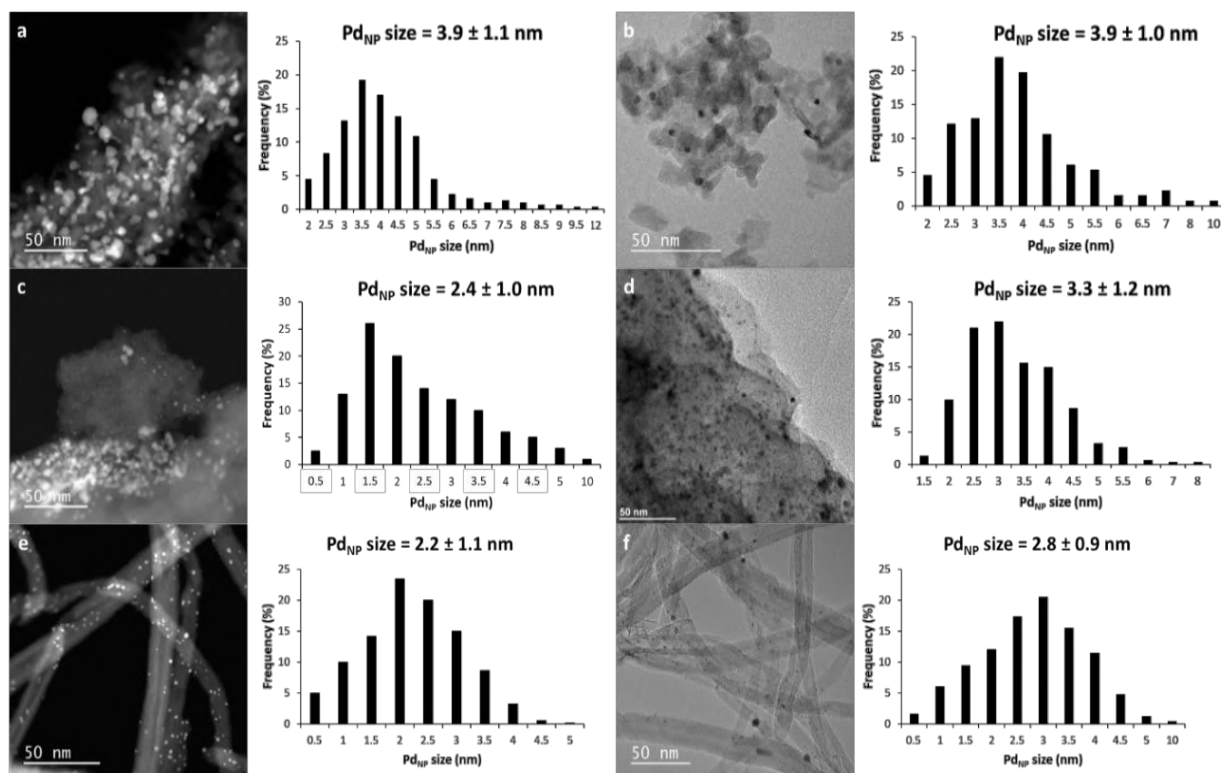


Figure 4.6. STEM-HAADF and TEM micrographs, and histograms of PdNP sizes of: a) fresh Pd/Al<sub>2</sub>O<sub>3</sub>; b) Pd/Al<sub>2</sub>O<sub>3</sub> after  $\beta$ -myrcene hydrogenation; c) fresh Pd/C; d) Pd/C after  $\beta$ -myrcene hydrogenation; e) fresh Pd/CNT; and f) Pd/CNT after  $\beta$ -myrcene hydrogenation. Scale bar = 50 nm

The major difference observed between these catalysts was the presence of Pd<sub>SA</sub> on Pd/CNT and Pd/AC (Figure 4.7a-c). It is worth noting that the probable presence of atomically dispersed Pd species on reduced Pd/CNT catalysts has been recently discussed by De Jong and coworkers,<sup>18</sup> and that the presence of Pd<sub>SA</sub> on commercial Pd/AC catalysts have been already reported.<sup>2</sup> A ratio SA/NP = 2 was measured from STEM-HAADF micrographs in the Pd/CNT catalyst (see Table 4.1 section 4.3). This catalyst (Figure 4.7c) will be named Pd<sub>2</sub><sub>SA/NP</sub>/CNT from now on. We independently checked that the SA/NP ratio of Pd<sub>2</sub><sub>SA/NP</sub>/CNT does not change significantly after catalysis.

<sup>18</sup> W. S. Lamme, et al. *Journal of Catalysis* **2019**, 375, 448-455.



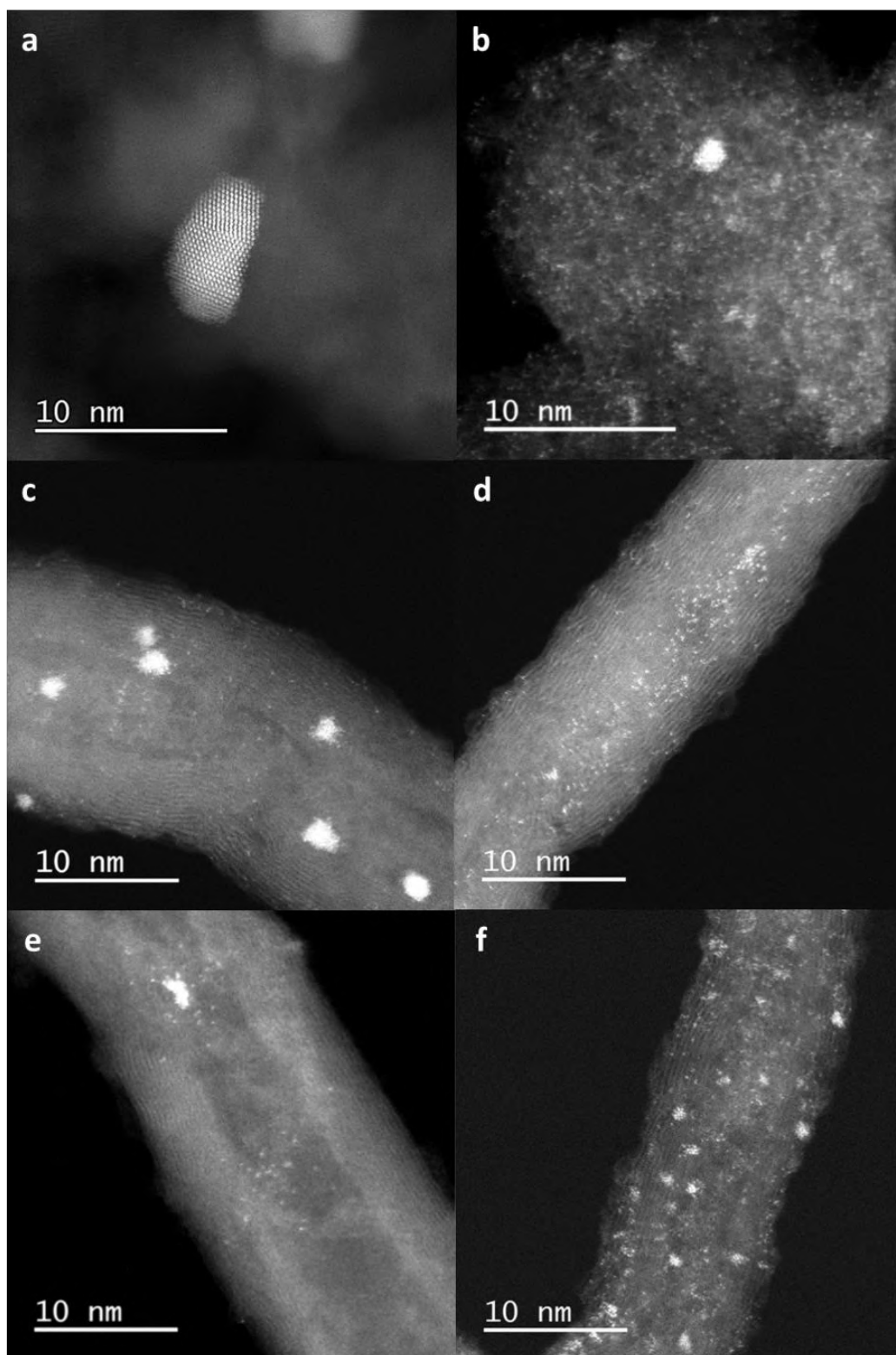


Figure 4.7. STEM-HAADF characterization. STEM-HAADF micrographs of: a)  $\text{Pd}/\text{Al}_2\text{O}_3$ ; b)  $\text{Pd}/\text{C}$ ; c)  $\text{Pd}_2\text{_{SA/NP/CNT}}$ ; d)  $\text{Pd}_{\text{SA/CNT}}$ ; e)  $\text{Pd}_2\text{_{SA/NP/CNT}_{HT}}$ ; and f)  $\text{Pd}_{10\text{_{SA/NP/CNT}}}$  catalysts. Scale bar = 10 nm.



Additionally, a sample prepared with mixtures of Pd<sub>SA</sub> and Pd<sub>NP</sub> was also obtained on few layers graphene (FLG). This latter catalyst was also tested for the hydrogenation of two other terpenes of industrial interest such as squalene or  $\beta$ -farnesene (Figure 4.8a) and again, this catalyst showed better activity compared to Pd/Al<sub>2</sub>O<sub>3</sub> (Figure 4.8b).

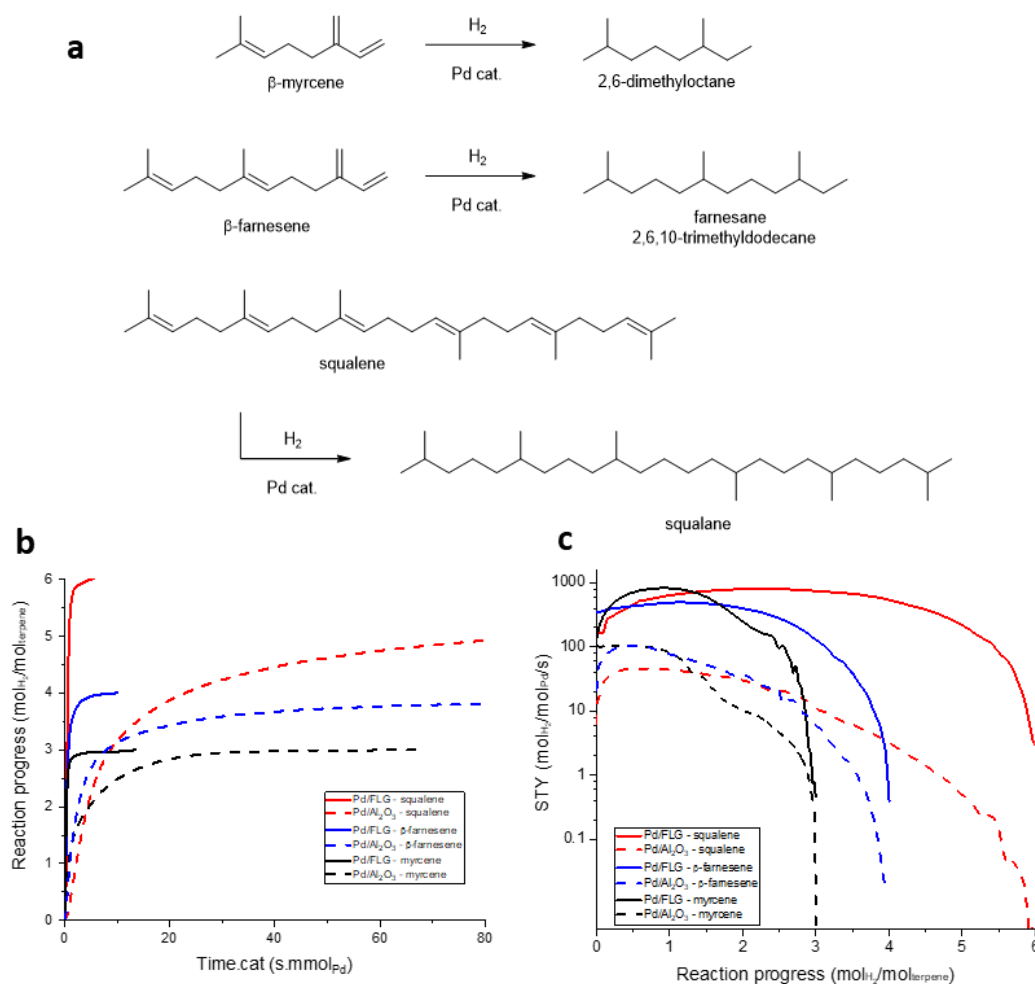


Figure 4.8. Comparison of the catalytic performances of Pd/Al<sub>2</sub>O<sub>3</sub> and Pd/FLG for the total hydrogenation of myrcene, farnesene and squalene. Hydrogenation reactions carried out over supported Pd catalysts. P<sub>H<sub>2</sub></sub> = 20 bar - T = 120 °C - substrate 1 M (80 mL) – solvent heptane – 280 mg catalyst.

For this catalyst also, the mean  $\text{Pd}_{\text{NP}}$  size and SA/NP ratio ( $\approx 10$  in this case) does not change significantly after catalysis (Figure 4.9). From these findings, we assumed that the presence of single atoms should be considered to rationalize the observed differences of reactivity. As discussed in the previous chapter, the existence of  $\text{Pd}_{\text{SA}}$  on carbon supports can be attributed to the presence of specific anchoring sites such as structural defects, which are necessary for their stabilization.<sup>9,19</sup> From the reaction profiles of Figures 4.3a,b, we can see that the reaction starts rapidly for all the samples, then for  $\text{Pd}/\text{Al}_2\text{O}_3$  it slows down, while a high rate is maintained for the catalysts supported on carbon.

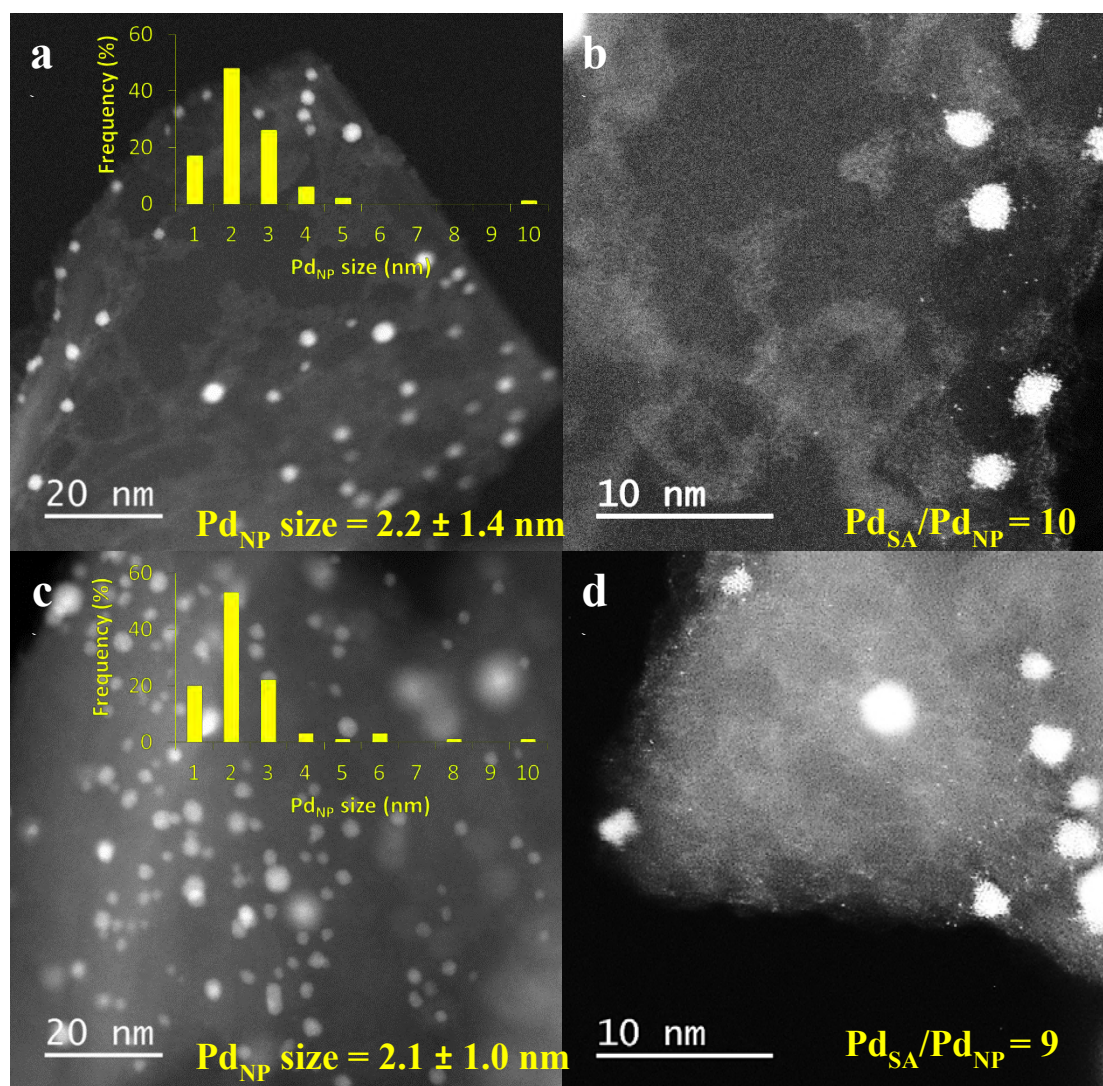


Figure 4.9. STEM-HAADF micrographs, particle size distribution and  $\text{Pd}_{\text{SA}}/\text{Pd}_{\text{NP}}$  ratio for the Pd/FLG catalyst: a) and b) before catalysis; and c) and d) after myrcene hydrogenation.

<sup>19</sup> I. C. Gerber, et al. *Chemical Reviews* **2020**, 120, 1250-1349.

We propose that this rate decrease for Pd/Al<sub>2</sub>O<sub>3</sub> catalyst can be associated to the difficult hydrogenation of the internal double bonds of myrcene.<sup>20</sup> On the other hand, the stable activity of carbon-supported catalysts might be explained in terms of the possible involvement of acidic sites in the isomerization of the relatively crowded double bond to an easier to reduce one. The potential of acidic sites on the isomerization of alkenes has been early reported.<sup>21</sup> In our case, two types of acidic sites may coexist on the carbon-supported catalysts. The first one corresponds to carboxylic acid groups (Bronsted acids) arising from the acid functionalization of the carbon material, which withstand the heat treatments carried out during catalyst preparation (see *Chapter 3*). The second type of acidic sites consists in the Pd<sub>SA</sub>. DFT calculations performed in LPCNO on a Pd<sub>SA</sub>/graphene single vacancy model show a charge transfer from Pd-4d to C-2p of -0.37 e<sup>-</sup> (Figure 4.10). Thus, a Pd<sub>SA</sub> would act as Lewis acid due to its electronic deficiency.

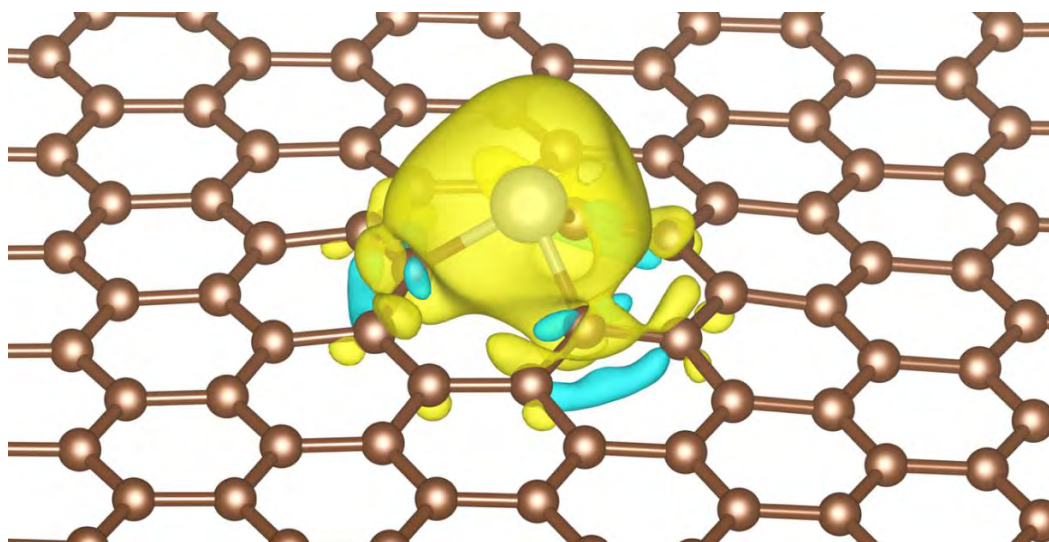


Figure 4.10. Isosurface plot of the electronic density differences for negative (in cyan) and positive (in yellow) isovalue of 0.002 e<sup>-</sup>/Å. The charge transfer from Pd<sub>SA</sub> 4d orbitals to the defective (single vacancy in graphene) support is estimated to be 0.37 e<sup>-</sup>.

To prove this hypothesis, we have studied independently the H<sub>2</sub>-assisted isomerization of 1-octene (Figure 4.11) on oxidized CNT (O-CNT, containing significant amounts of surface -COOH groups), Pd<sub>2-SA</sub>/NP/CNT, Pd/Al<sub>2</sub>O<sub>3</sub> and a fourth sample named Pd<sub>SA</sub>/CNT containing exclusively SA (Figure 4.7d).

<sup>20</sup> E. Bogel-Lukasik, et al. *Green Chemistry* **2009**, 11, 1847-1856.

<sup>21</sup> H. N. Dunning *Industrial & Engineering Chemistry* **1953**, 45, 551-564.

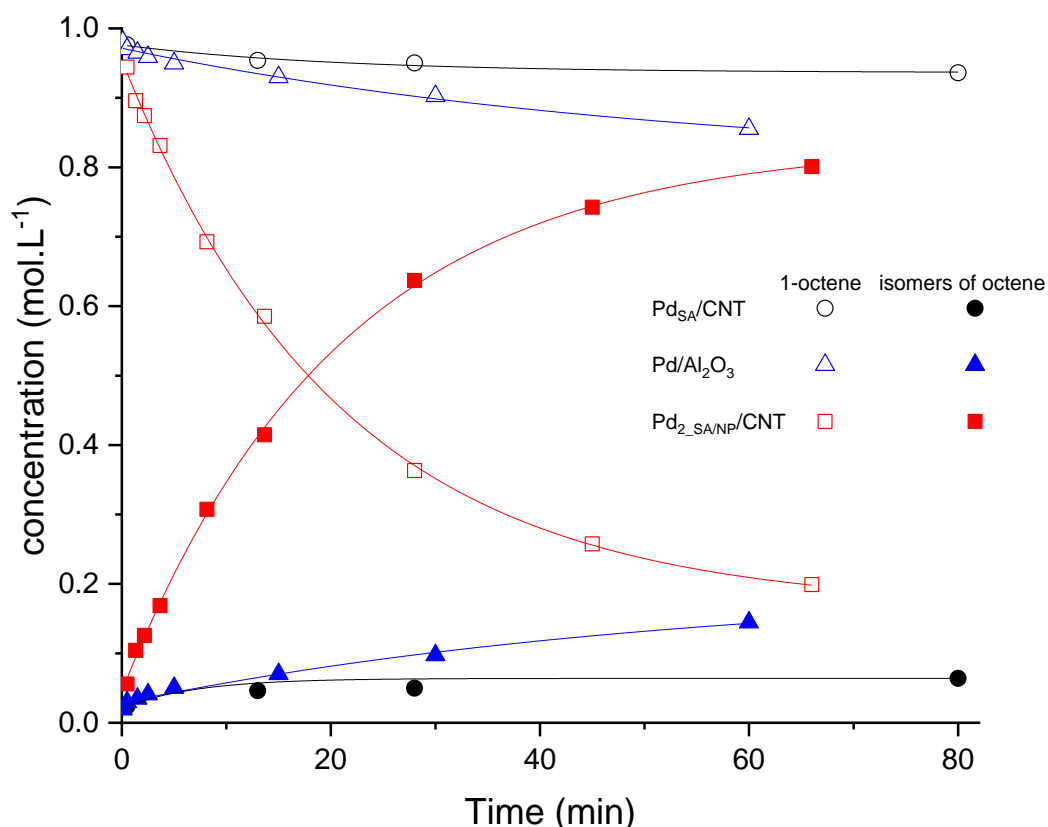


Figure 4.11. Evolution of the composition of the solution during 1-octene hydrogenation as the function of time and catalysts Pd<sub>SA</sub>/CNT, Pd/Al<sub>2</sub>O<sub>3</sub> and Pd<sub>2SA</sub>/NP/CNT. Reaction conditions: 1-octene (1M) in heptane, Pd 0.4 mg (60 ppm), reflux (98 °C), H<sub>2</sub> 1 atm. In the case of the O-CNT catalyst no measurable activity was obtained.

O-CNT and the Pd<sub>SA</sub>/CNT catalysts are almost inactive for isomerization, and the Pd<sub>2SA</sub>/NP/CNT clearly outperforms the Pd/Al<sub>2</sub>O<sub>3</sub> catalyst. Temperature programmed desorption experiments performed on both the CNT support and the Pd<sub>2SA</sub>/NP/CNT catalyst (Figure 4.12) do not establish the presence of significant amounts of carboxylic groups after Pd deposition, these groups acting as anchoring sites for the metal.<sup>22</sup> Thus, the presence of acidic sites that would assist the isomerization cannot explain the observed differences in reactivity. To gain further insight on the mechanistic pathway, DFT calculations were performed in LPCNO on Pd<sub>SA</sub> and Pd<sub>NP</sub> supported on graphene as model support.

<sup>22</sup> B. F. Machado, et al. *Journal of Catalysis* **2014**, 309, 185-198.

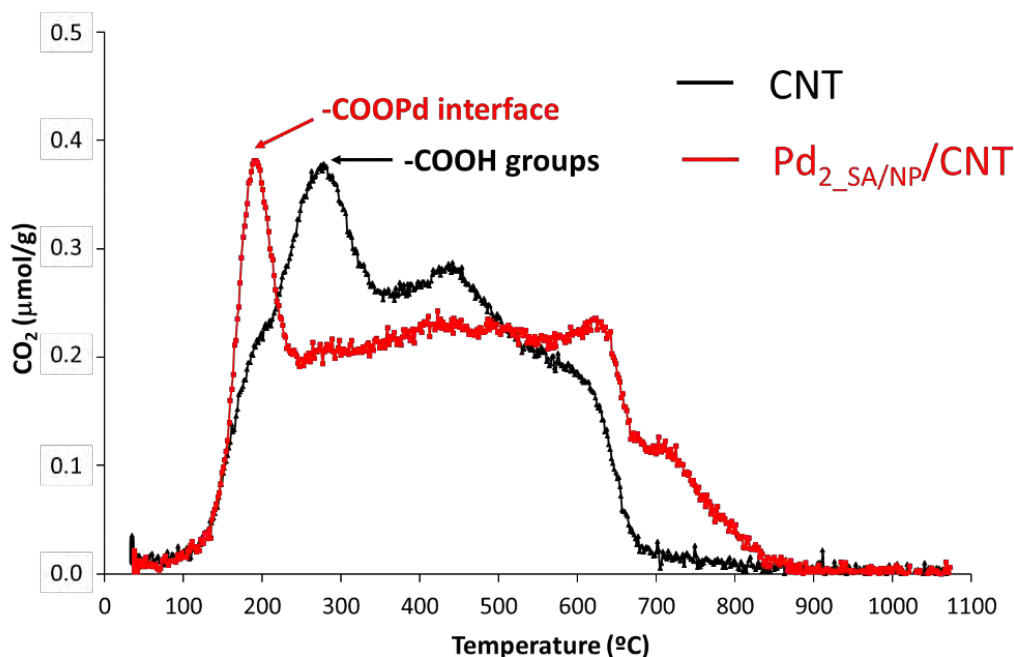


Figure 4.12.  $\text{CO}_2$  TPD profiles of the CNT support and the  $\text{Pd}_{2\text{SA/NP/CNT}}$  catalyst showing the disappearance of most of the surface carboxylic groups after catalyst preparation, and the appearance of a Pd-OOC- interface.

### 4.3. Mechanistic insights from DFT calculations

To study the isomerization and hydrogenation reactions, 2-butene instead of myrcene was used as a model substrate (for simplifying computational calculations). Starting with the isomerization, we considered the trapping of a  $\text{Pd}_{\text{SA}}$  in a mono-vacancy, which is strongly exothermic, with an adsorption energy of roughly 100 kcal/mol. On  $\text{Pd}_{\text{SA}}$ , both, isomerization and the hydrogenation reactions begin with the exothermic  $\pi$ -coordination of 2-butene to Pd (by -24.6 kcal/mol) (**1**). From **1**, the isomerization (Figure 4.13, black line) occurs *via* the formation of a  $\pi$ -allyl hydride intermediate as observed with homogeneous catalysts,<sup>23</sup> which requires to pass a high energy demanding transition state (36.4 kcal/mol) corresponding to the abstraction of one hydrogen atom from a methyl group. This leads to the formation of an unstable allyl intermediate (**2**), by +34.4 kcal/mol with respect to **1**. Then, the H atom is transferred with almost no barrier with respect to **2** (2.8 kcal/mol) to the carbon atom in alpha position of the methyl group, leading to the endothermic formation of but-1-ene (+4.8 kcal/mol with respect to **1**).

<sup>23</sup> *Hydrocarbon Chemistry*. In, edited by G. A. Olah, *et al.*: John Wiley & Sons, Inc. (2003).



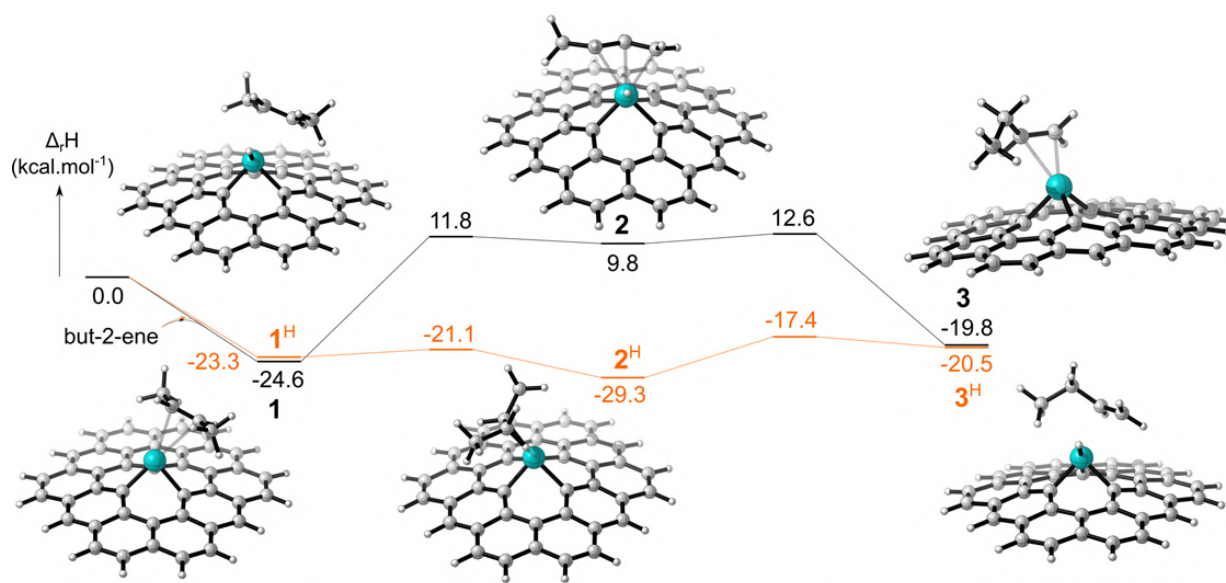


Figure 4.13. DFT mechanistic study of reaction mechanisms of isomerization of 2-butene mediated by  $\text{Pd}_{\text{SA}}$  and  $\text{H-Pd}_{\text{SA}}$  (in orange).

From **1**, the hydrogenation of the but-2-ene (Figure 4.14, black line) occurs through the Horiuti-Polanyi mechanism:<sup>24</sup> (i) alkene and  $\text{H}_2$  coordination to Pd, (ii)  $\text{H}_2$  dissociation, (iii) hydrogen transfer to one of the alkene methine carbon with formation of a  $\sigma$ -bond between Pd and the second C-methine, and finally (iv) reductive elimination of the free alkane. In our case, the coordination of the 2-butene (**1**) and of a  $\text{H}_2$  molecule (**4**) to the  $\text{Pd}_{\text{SA}}$  is exothermic. These initial steps are followed by an endothermic (+21.6 kcal/mol with respect to **4**) and kinetically demanding (activation barrier = +24.5 kcal/mol) H-H activation (**5**). This reaction exhibits a lower barrier than the isomerization reaction, by 9.9 kcal/mol. From **5**, the reaction continues by the transfer of one of the hydrogen atoms to one of the methine carbon atoms. The energy barrier of this last step is only +8.1 kcal/mol with respect to **5** but +29.7 kcal/mol with respect to **4**. This transfer induces the formation of a 2-butyl complex  $\sigma$ -coordinated to the Pd center (**6**), located at -11.7 kcal/mol with respect to the entrance channel. The subsequent reductive elimination occurs *via* an accessible transition state (+4.1 kcal/mol with respect to **6**) and leads to the exothermic formation of butane (-42.1 kcal/mol with respect to the separated reactants). In summary, the hydrogenation of the 2-butene into butane is preferred both from a kinetic and thermodynamic point of view over the isomerization to 1-butene.

<sup>24</sup> I. Horiuti, et al. *Transactions of the Faraday Society* **1934**, 30, 1164-1172.



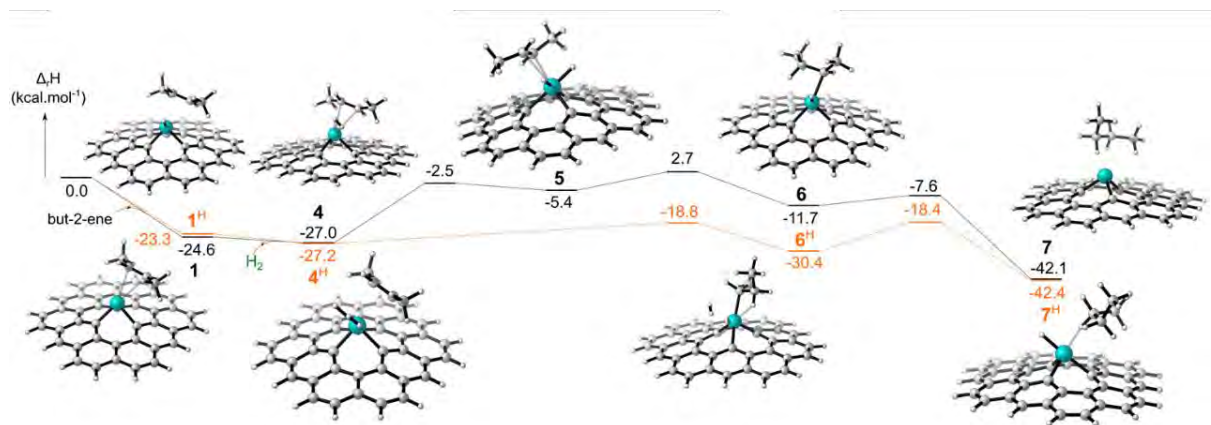


Figure 4.14. DFT mechanistic study of reaction mechanisms of hydrogenation of 2-butene mediated by  $\text{Pd}_{\text{SA}}$  and  $\text{H-Pd}_{\text{SA}}$  (in orange).

However, according to the high barriers, a poor catalytic activity is expected in both cases, as experimentally observed for hydrogenation using single Pd atoms.<sup>25,26</sup> For comparison, an activation energy of 18 kcal/mol has been reported for the hydrogenation of 2-butene on a  $\text{Pd}_9/\text{CNT}$  catalyst.<sup>27</sup> In this context we also verified that the  $\text{Pd}_{\text{SA}}/\text{CNT}$  catalyst shows a very low activity for  $\beta$ -myrcene hydrogenation (see Figure 4.21 in the section 4.3 *Control of the single atoms/nanoparticles ratio*).

At this point, it is interesting to note that a completely different potential energy landscape is obtained if the catalyst is a hydrogenated SA or Pd hydride ( $\text{H-Pd}_{\text{SA}}$ , orange lines on Figures 4.13 and 4.14). A plausible scenario for the formation of this active site is: (i) a nearly barrierless activation of  $\text{H}_2$  on  $\text{Pd}_{\text{NP}}$  ( $< 2$  kcal/mol on  $\text{Pd}_{13}$  supported on defective graphene monolayer), and (ii) hydrogen spillover. The latter phenomenon has been widely theoretically studied in the context of hydrogen storage and catalysis.<sup>28,29,30</sup> The entire spillover mechanism remains not fully understood, especially since some energy barriers remain high to be accessible at room temperature, but should correspond to a multi-step process after the dissociative adsorption of  $\text{H}_2$  on  $\text{Pd}_{\text{NP}}$ . The H-migration from the NP to the carbon support is supposedly the first step with large energy barrier to overcome and usually this step is not thermodynamically favorable for non-defective carbon supports. For instance a 60 kcal/mol energy barrier has been reported in the case of a Pt cluster on pristine graphene model, the final step being 35 kcal/mol above

<sup>25</sup> H. Gentsch, et al. *Zeitschrift für Physikalische Chemie* **1972**, 82, 49-57.

<sup>26</sup> M. D. Rossell, et al. *Catalysis Science & Technology* **2016**, 6, 4081-4085.

<sup>27</sup> V. D'Anna, et al. *Physical Chemistry Chemical Physics* **2010**, 12, 1323-1330.

<sup>28</sup> Y. Lin, et al. *Physical Review B* **2008**, 78, 041402.

<sup>29</sup> V. A. Borodin, et al. *Physical Review B* **2011**, 84, 075486.

<sup>30</sup> D. S. Pyle, et al. *International Journal of Hydrogen Energy* **2016**, 41, 19098-19113.

the initial one,<sup>31</sup> but when the graphene support is already hydrogenated the energy barrier is decreased and the thermodynamics become favorable.<sup>32</sup> However, it remains obscure how the support can be initially hydrogenated. Then H-diffusion on the carbon support occurs, with a relatively high energy barrier associated to a nearest-neighbor hopping process ( $> 20$  kcal/mol on pristine carbon support)<sup>19,30</sup> It has also been proposed that the presence of oxygenated functional groups on the carbon support can facilitate the diffusion.<sup>33</sup> H-clustering could also play a role by disturbing the  $sp^2$  network around the H-adsorption site, decreasing significantly the energy barrier.<sup>34</sup>

As we can see on Figure 4.13 (orange line), the coordination of 2-butene over H-Pd<sub>SA</sub> (**1<sup>H</sup>**) remains exothermic, -23.3 kcal/mol with respect to the separated reactants. However, in this case the isomerization reaction takes place through a so-called metal hydride addition–elimination mechanism, strongly preferred for monohydrides. Thus, the isomerization proceeds *via* an initial hydrogen transfer to one of the –CH= carbons, followed by the dehydrogenation of the methyl group at  $\alpha$  position with respect to the second methine carbon. This reaction is kinetically accessible with two low activation barriers (3.5 and 11.9 kcal/mol, respectively). However, even if the formation of the 2-butyl intermediate (**2<sup>H</sup>**) is exothermic with respect to **1<sup>H</sup>** by -6.0 kcal/mol, that of the 1-butene product (**3<sup>H</sup>**) remains endothermic by +2.8 kcal/mol.

Concerning the hydrogenation (Figure 4.14, orange line), the coordination of H<sub>2</sub> is followed by the transfer of the hydrogen atom to one of the methine carbons without H<sub>2</sub> dissociation. The corresponding activation barrier (8.4 kcal/mol above **4<sup>H</sup>**) corresponds to an easily kinetically accessible process. In the same way, the formation of the alkyl intermediate is found to be exergonic with respect to **4<sup>H</sup>** (-3.2 kcal/mol with respect to **4<sup>H</sup>**). The last step corresponds to the heterolytic splitting of H<sub>2</sub> leading to the regeneration of the H-Pd<sub>SA</sub> and the butane product (**7<sup>H</sup>**). The formation of butane is an exothermic process, by 25.2 kcal/mol with respect to **4<sup>H</sup>** (-42.4 kcal/mol with respect to the separated reactant). The corresponding activation barrier for this step is 12 kcal/mol. Therefore, this last step is the rate-determining step of an overall facile and exergonic reaction.

In order to confirm the key role of H-spillover in the cooperative catalysis between Pd<sub>SA</sub> and Pd<sub>NP</sub>, a Pd<sub>2\_SA/NP</sub>/CNT<sub>HT</sub> catalyst (Figure 4.15) was prepared on CNT<sub>HT</sub>, from which the oxygen

<sup>31</sup> G. M. Psogianakis, et al. *The Journal of Physical Chemistry C* **2009b**, *113*, 14908-14915.

<sup>32</sup> A. K. Singh, et al. *ACS Nano* **2009**, *3*, 1657-1662.

<sup>33</sup> G. M. Psogianakis, et al. *Journal of the American Chemical Society* **2009a**, *131*, 15133-15135.

<sup>34</sup> Y. Ferro, et al. *Chemical Physics Letters* **2003**, *368*, 609-615.

surface groups have been removed by thermal annealing at 1000 °C,<sup>17</sup> which should prevent H-spillover. Although this catalyst contains also a mixture of Pd<sub>SA</sub> and Pd<sub>NP</sub> (SA/NP  $\approx$  2), with mean particle size similar to the Pd<sub>2\_SA/NP</sub>/CNT catalyst (Figure 4.15) it shows a significantly reduced activity for myrcene hydrogenation (Figure 4.16), which is quite similar to the one of the Pd/Al<sub>2</sub>O<sub>3</sub> catalyst that contains only Pd<sub>NP</sub>.

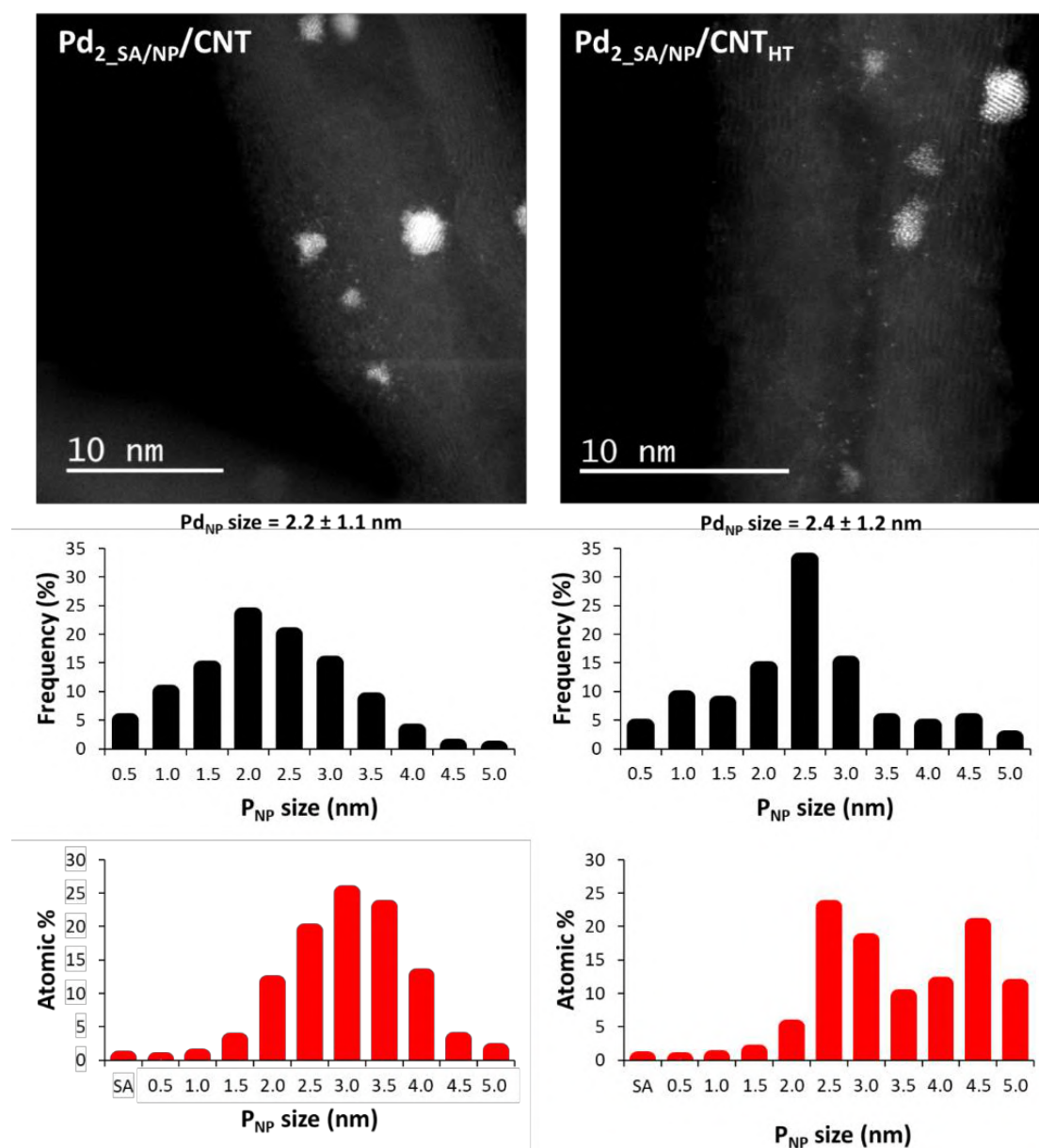


Figure 4.15. STEM-HAADF micrographs of Pd<sub>2\_SA/NP</sub>/CNT and Pd<sub>2\_SA/NP</sub>/CNT<sub>HT</sub> catalysts and related particle size distribution based on total particles and on total atoms (see section 4.3 for details of calculations).

It is also worth mentioning that the two catalysts  $\text{Pd}_{2\_SA/NP}/\text{CNT}$  and  $\text{Pd}_{2\_SA/NP}/\text{CNT}_{\text{HT}}$  present a similar amount of Pd clusters ( $\text{Pd}_{\text{NP}} < 1 \text{ nm}$ ), so that the observed high activity measured for the  $\text{Pd}_{2\_SA/NP}/\text{CNT}$  catalyst cannot be only related to the presence of Pd clusters (Figure 4.15), even if it has been reported that noble metal clusters are often more active than nanoparticles.<sup>35,36,37,38</sup>

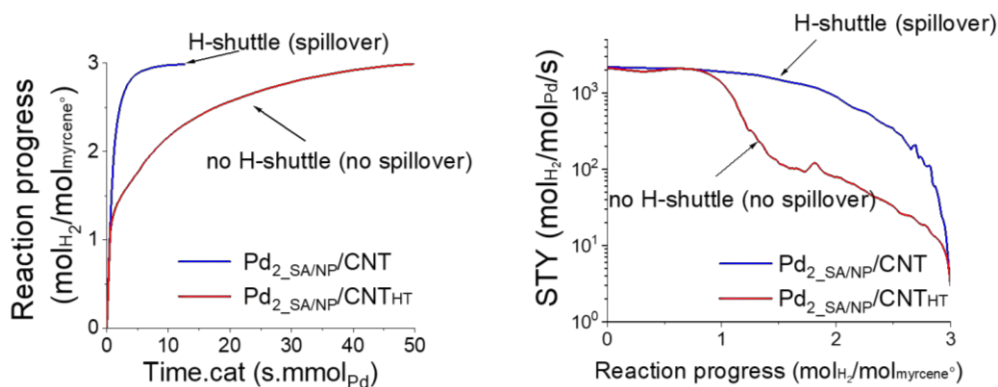


Figure 4.16.  $\beta$ -myrcene hydrogenation reactions carried out over  $\text{Pd}_{2\_SA/NP}/\text{CNT}$  and  $\text{Pd}_{2\_SA/NP}/\text{CNT}_{\text{HT}}$  catalysts.  $P_{\text{H}_2} = 20 \text{ bar}$  -  $T = 120 \text{ }^\circ\text{C}$  -  $\beta$ -myrcene  $1 \text{ M}$  ( $80 \text{ mL}$ ) – solvent heptane -  $200 \text{ mg cat}$ .

The hydrogen spillover was experimentally probed for these two CNT-supported catalysts. As the spilled-over hydrogen migrates and readily reacts with the yellow  $\text{WO}_3$  oxide to form dark blue  $\text{H}_x\text{WO}_3$ <sup>39,40,41</sup> we used the  $\text{WO}_3$  tungsten oxide to diagnose the activation of  $\text{H}_2$  on these two catalysts. As shown in the photographs of Figure 4.17, the pure  $\text{WO}_3$  did not change color after hydrogen treatment. When mixed with the  $\text{Pd}_{2\_SA/NP}/\text{CNT}_{\text{HT}}$  catalyst, no significant change in color after the hydrogen treatment was observed. While this Pd catalyst should activate hydrogen, the absence of surface oxygen groups on the support does not allow extended hydrogen spillover. In contrast, when  $\text{WO}_3$  was mixed with the  $\text{Pd}_{2\_SA/NP}/\text{CNT}$  catalyst this resulted in the darkest color of the tungsten species after hydrogen treatment at  $20 \text{ }^\circ\text{C}$  for  $3 \text{ min}$ , demonstrating that hydrogen dissociation and extended spillover occurred on this catalyst. We infer that the significant spillover should be attributed to the presence of oxygenated surface groups on the carbon support. These latter experiments confirm that the presence of oxygen surface groups is necessary for the cooperative catalysis to proceed *via* H-spillover.

<sup>35</sup> A. A. Herzing, et al. *Science* **2008**, 321, 1331.

<sup>36</sup> Y. Lei, et al. *Science* **2010**, 328, 224-228.

<sup>37</sup> A. Corma, et al. *Nature Chemistry* **2013**, 5, 775-781.

<sup>38</sup> T. Imaoka, et al. *Nature Communications* **2017**, 8, 688.

<sup>39</sup> S. Khoobiar *The Journal of Physical Chemistry* **1964**, 68, 411-412.

<sup>40</sup> C. Wang, et al. *Journal of the American Chemical Society* **2019**, 141, 8482-8488.

<sup>41</sup> Y. Xi, et al. *The Journal of Physical Chemistry C* **2014**, 118, 494-501.

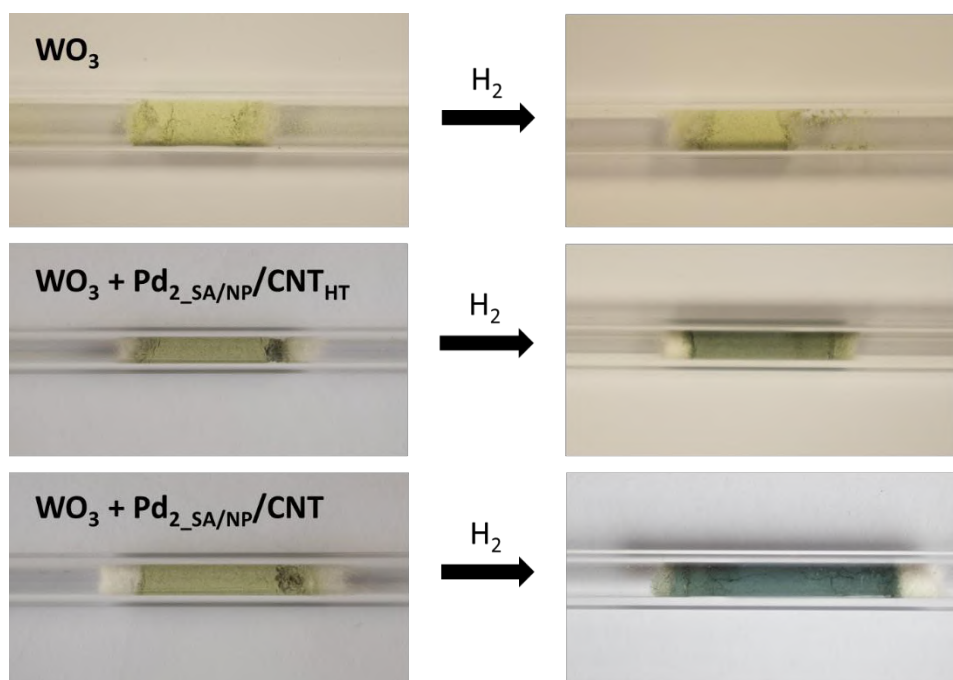


Figure 4.17. Photographs of samples made with 500 mg of  $\text{WO}_3$  mixed or not with 5 mg of catalyst before (left) and after (right) treatment with  $\text{H}_2$  (100 mL/min) at 20 °C for 3 min.

The hydrogen spillover was also investigated by DFT in LPCNO to propose a complete pathway for the formation of  $\text{H-Pd}_{\text{SA}}$  species through the migration of H atoms initially adsorbed on H-saturated  $\text{Pd}_{\text{NP}}$ . As we can see on Figure 4.18, the overall reaction is kinetically accessible and thermodynamically favorable. Our starting geometry is a H-saturated  $\text{Pd}_{\text{NP}}$  deposited on a defective di-vacancy with an oxygen atom in its vicinity. From this starting configuration the first H migration from the  $\text{Pd}_{\text{NP}}$  to the closest C atom in front of the ether group is thermodynamically favorable (-38 kcal/mol), with a reasonable energy cost (activation barrier = 10.2 kcal/mol). Then a second H can easily migrate (the energy barrier is less than 2 kcal/mol) to the same carbon atom leading to the formation of a  $-\text{CH}_2$  group. Mind that the presence of an oxygen atom, in the vicinity of a stabilizing defect on the carbon support favors the thermodynamics, when it is not usually the case for pristine support.<sup>42</sup> Then we have evaluated the migration of one H from the  $-\text{CH}_2$  group to a neighbor C carbon atom, still involved in the di-vacancy ring. This step, with an energy barrier of 29.7 kcal/mol, is the rate-determining step of the proposed profile. Then a second hopping process can proceed with a lower activation barrier (24.2 kcal/mol) to yield almost a single H atom adsorbed on the non-defective part of the carbon support. The adsorption of an extra  $\text{H}_2$  molecule on  $\text{Pd}_{\text{NP}}$  ensures

<sup>42</sup> M. Blanco-Rey, et al. *The Journal of Physical Chemistry C* **2016**, 120, 17357-17364.



the overall stability of the H-migration process. Then H-diffusion can occur with an energy barrier of around 24 kcal/mol, in line with previous works, or can be significantly decreased to less than 9 kcal/mol, when the H atom is surrounded by other H atoms, 6 in the present case. Finally, the formation of the H-Pd<sub>SA</sub> product takes place through a barrierless H transfer to Pd<sub>SA</sub> with a largely favorable stabilization energy of *ca.* -60.5 kcal/mol.

Thus, the correlation that we have recently reported between the activity of Pd/C catalysts for  $\beta$ -myrcene hydrogenation and their structure,<sup>17</sup> which integrates the dispersion of the metal, and the quantity of oxygen groups and defects on the support, arises from a cooperative catalysis between Pd<sub>SA</sub> and Pd<sub>NP</sub> that involves H-spillover. It is certainly necessary to have highly dispersed Pd<sub>NP</sub> on the support to activate H<sub>2</sub>, but a high concentration of surface defects and oxygenated surface groups are also necessary on the carbon support, which favors the stabilization of Pd<sub>SA</sub> and H-spillover, respectively. The resulting H-Pd<sub>SA</sub> are highly active for alkene hydrogenation/isomerization.

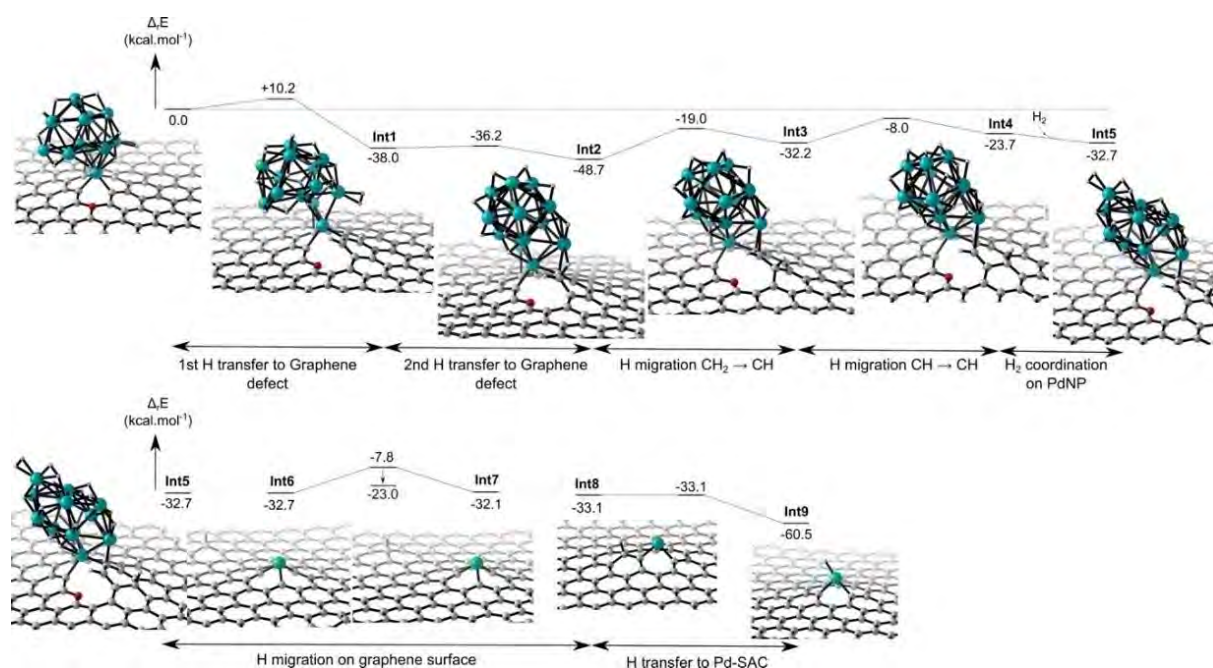


Figure 4.18. DFT mechanistic study. Spillover mechanism corresponding to the migration of H adsorbed on Pd<sub>NP</sub> leading to the formation of H-Pd<sub>SA</sub> species.



#### 4.4. Control of the single atom/nanoparticle ratio

From the above results, it becomes obvious that an optimized heterogeneous catalyst with an ultra-rational use of precious metals (often in short supply) could pass by an accurate control of the SA/NP ratio. With this in mind, we have tested samples with an engineered SA/NP ratio (for a similar Pd loading of 1.2 % w/w), in order to prove the influence of this parameter on the catalytic performance. Those samples were prepared with the previously presented protocol (*Chapter 3, Section 3.5 Mixture single atoms and nanoparticles*) and the samples have been re-labeled as Pd<sub>X</sub><sub>SA/NP</sub>/CNT, where X refers to the SA/NP ratio. Table 4.1 summarizes Pd loading, Pd<sub>NP</sub> size, Pd dispersion, SA/NP ratio and atomic percentage of SA of all samples used in this study.

Table 4.1. Pd loading, particle size, dispersion and SA/NP ratio.

Catalyst	Pd loading (%)	NP size from TEM (nm) <sup>a)</sup>	Pd dispersion (%) <sup>c)</sup>	SA/NP ratio <sup>d)</sup>	At. % SA
Pd/Al <sub>2</sub> O <sub>3</sub>	5	3.9 ± 1.1	31	n.d. <sup>e)</sup>	n.d. <sup>e)</sup>
Pd/C	5	2.4 ± 1.0	46	n.d. <sup>e)</sup>	n.d. <sup>e)</sup>
Pd/CNT					
also named Pd <sub>2</sub> <sub>SA/NP</sub> /CNT	2	2.2 ± 1.1	49	2	n.d. <sup>e)</sup>
Pd <sub>2</sub> <sub>SA/NP</sub> /CNT <sub>HT</sub>	1.6	2.2 ± 1.1	49	2	1.5
Pd <sub>SA</sub> /CNT	0.1	-	-	no NP	n.d. <sup>e)</sup>
Pd <sub>1000</sub> <sub>SA/NP</sub> /CNT	0.1	1 ± 0.5 <sup>b)</sup>	-	1000	n.d. <sup>e)</sup>
Pd <sub>200</sub> <sub>SA/NP</sub> /CNT	1.2	0.5 ± 0.1	-	200	94
Pd <sub>60</sub> <sub>SA/NP</sub> /CNT	1.2	0.8 ± 0.3	-	60	48
Pd <sub>40</sub> <sub>SA/NP</sub> /CNT	1.2	0.9 ± 0.3	-	40	21
Pd <sub>10</sub> <sub>SA/NP</sub> /CNT	1.2	1.1 ± 0.6	-	10	14
Pd/FLG	1.9	2.6 ± 1.6	43	10	n.d. <sup>e)</sup>

a) Calculated over 300 NP from STEM-HAADF micrographs  
b) Calculated over 20 NP from STEM-HAADF micrographs  
c) Metal dispersion was evaluated from a universal mathematical relation between the mean relative size of metallic crystallites and their dispersion <sup>1</sup>.  
d) SA/NP ratio in number calculated over 500 elements from STEM-HAADF micrographs.  
e) Not determined

In detail, the quantification of the percentage of single atoms was calculated with:

$$\text{Atomic percentage SA} = \frac{n \text{ Pd SA}}{n \text{ total atoms of Pd (SA+NP)}} \times 100\% \quad (4.3)$$

Where the number of atoms on each spherical nanoparticle was calculated with:

$$\text{Atoms per spherical NP} = \frac{\pi D^3 \rho N_A}{6 M_w} \quad (4.4)$$

D being the particle diameter measured by STEM,  $\rho$  the bulk metal density,  $N_A$  the Avogadro number, and  $M_w$  the molecular weight assuming that all the Pd is accessible.<sup>43</sup> The variation on this value along with SA/NP ratio gives an idea about how the palladium species evolve from one sample to another, and confirms that the method of preparation can effectively control single atom availability.

HRTEM images show that for the four 1.2% Pd/CNT samples prepared by this process (in grey on Table 4.1), the SA/NP ratio is controlled between 200/1 (a single deposition cycle of 1.2% Pd) to 10/1 (four deposition cycles of 0.3% Pd). The particle size distribution based on total particle number and on total atom number is given on Figure 4.19.

As transmission electron microscopy only informs us thanks to a very local analysis of the samples (poor statistic value), we also characterize these four samples by XPS, (*Chapter 3, Section 3.5. Mixture of single atoms and nanoparticles*) which constitutes a more general probe of the whole samples. The binding energy at 335.3 eV is in agreement with the value reported in the literature for metallic palladium.<sup>44</sup> For the sample Pd<sub>200\_SA/NP</sub>/CNT, this binding energy is slightly upshifted presumably due to charge transfer between the very small particles present on this sample and the support or to particle size-dependent shift.<sup>45,46</sup> The binding energy at 337.3 eV can be attributed to surface oxides and/or to electron-deficient palladium species (Pd<sup>δ+</sup>) such as SA or small clusters in strong interaction with the support.<sup>47,48,49</sup>

The Pd<sup>δ+</sup>/Pd<sup>0</sup> ratio for the four samples are shown on Table 4.2 as well as the fraction of SA in the same samples determined from STEM.

---

<sup>43</sup> Y. Lu, et al. *Journal of Catalysis* **2019**, 378, 121-130.

<sup>44</sup> A. L. Dantas Ramos, et al. *Applied Catalysis A: General* **2004**, 277, 71-81.

<sup>45</sup> A. Fritsch, et al. *Surface Science* **1985**, 162, 742-746.

<sup>46</sup> I. Aruna, et al. *Journal of Applied Physics* **2008**, 104, 064308.

<sup>47</sup> R. G. Rao, et al. *Nature Communications* **2017**, 8, 340.

<sup>48</sup> W. Xiang, et al. *Journal of Materials Chemistry A* **2018**, 6, 23366-23377.

<sup>49</sup> J. Xi, et al. *Applied Catalysis B: Environmental* **2018**, 225, 291-297.

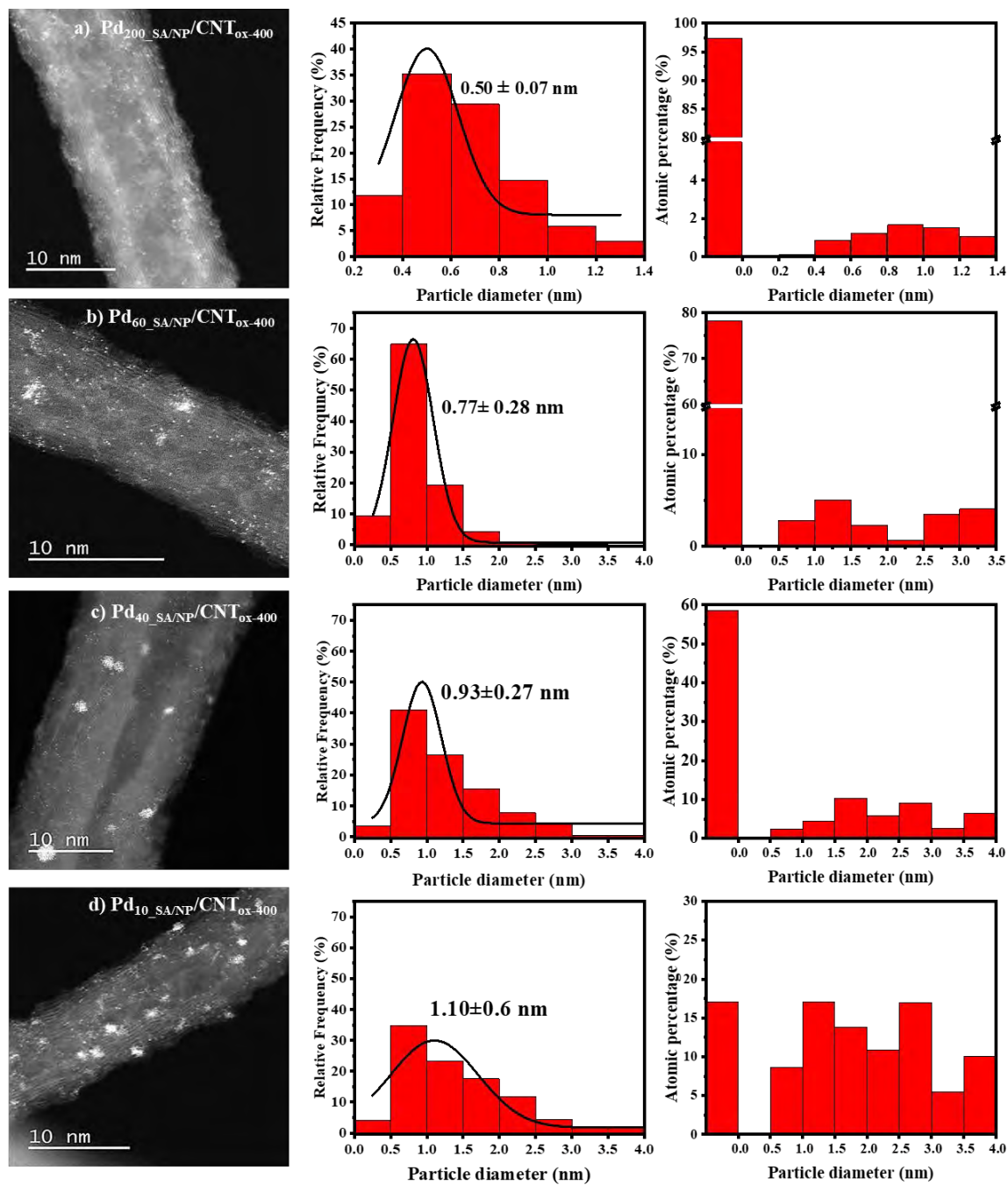


Figure 4.19. Mixtures of SA and NP at different ratio in 1.4% Pd/CNT catalysts.

Table 4.2. Fraction of SA in the same samples determined from STEM and ratio  $Pd^0/Pd^{\delta+}$  determined by XPS.

Sample	STEM fraction of SA	XPS atomic percentage (%)		
		$Pd^0$	$Pd^{\delta+}$	$Pd^{\delta+}/Pd^0$
$Pd_{200\_SA/NP/CNT}$	0.97	14.21	85.79	6.06
$Pd_{60\_SA/NP/CNT}$	0.78	15.25	84.75	5.55
$Pd_{40\_SA/NP/CNT}$	0.58	22.00	78.00	3.55
$Pd_{10\_SA/NP/CNT}$	0.17	41.75	58.25	1.39

A good correlation was found between the results obtained with these two techniques (Figure 4.20, Table 4.2). These data, in association with the STEM-HAADF observations, confirm that the proportion of  $Pd_{SA}$  is much higher in the sample  $Pd_{200\_SA/NP/CNT}$  than in  $Pd_{10\_SA/NP/CNT}$ . Thus, this strategy allows engineering the minimal catalytic ensemble that will activate  $H_2$  for the cooperative catalysis to operate.

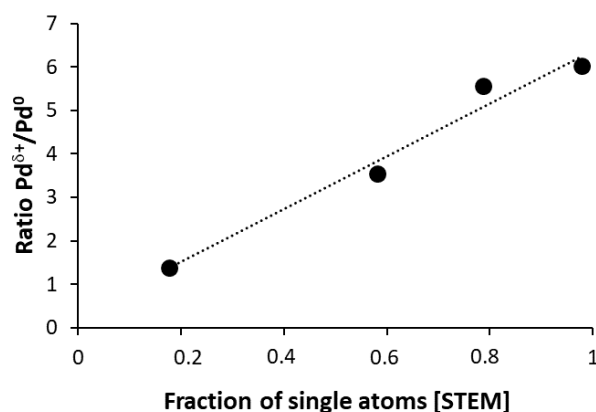


Figure 4.20. Correlation between the ratio  $Pd^0/Pd^{\delta+}$  determined by XPS and the fraction of SA in the same samples determined from STEM.

For  $\beta$ -myrcene hydrogenation at 120 °C, regarding the catalysts tested, the optimum SA/NP ratio was found at 10/1 (Figure 4.21). This optimal ratio offers the best control for the balance between  $H_2$  activation on  $Pd_{NP}$ , the H-spillover, and H- $Pd_{SA}$  catalyzed  $\beta$ -myrcene hydrogenation rates. The activity of the  $Pd_{10\_SA/NP/CNT}$  (Figure 4.7f) outperformed the one of the  $Pd_{2\_SA/NP/CNT}$  catalyst. At a reaction progress of 2, the STY with  $Pd_{200\_SA/NP/CNT}$ ,  $Pd_{2\_SA/NP/CNT}$ , and  $Pd_{10\_SA/NP/CNT}$  are 10, 44 and 272  $s^{-1}$ , respectively (Figure 4.21b).

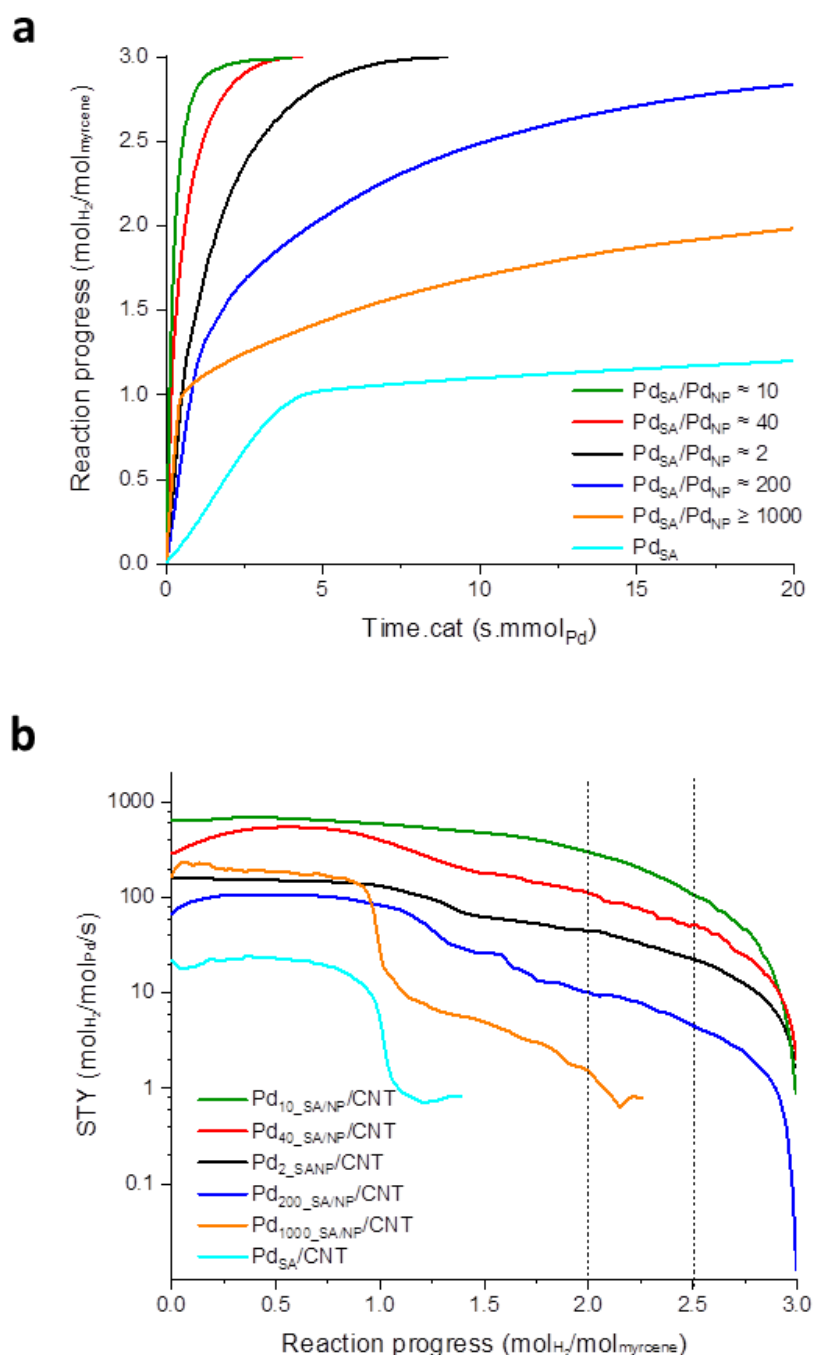


Figure 4.21. Catalytic results for myrcene hydrogenation at different SA/NP ratio. a) Reaction progress as a function of time catalyst. b) STY as a function of reaction progress.

Once again, it is interesting to note that for this sample series, for which the surface chemistry of the support is the same, it is not the sample that presents the higher proportion of palladium clusters that is the more active. Thus, the sample  $\text{Pd}_{60\_SA/NP}/\text{CNT}$  present a similar proportion of  $\text{Pd}_{\text{NP}} < 1$  nm based on total atoms than the sample  $\text{Pd}_{10\_SA/NP}/\text{CNT}$  (Figure 4.19) but is

significantly less active (Figure 4.21). Similarly, the sample Pd<sub>200\_SA/NP</sub>/CNT, which presents a significant amount of clusters of different atomicity, is the less active of the series.

Finally, at a reaction progress of 2, there is a 44-fold increase of STY between the Pd<sub>10\_SA/NP</sub>/CNT catalyst and Pd<sub>2\_SA/NP</sub>/CNT<sub>HT</sub> (a catalyst containing NP with no possibility of hydrogen spillover, see Figure 4.16) and 195-fold increase with Pd<sub>1000\_SA/NP</sub>/CNT (a catalyst containing almost exclusively SA). The evolution of STY with SA/NP ratio remains nearly the same for the reaction progress of 2.5 (Figure 4.22). This fact further confirms the consistency of these results.

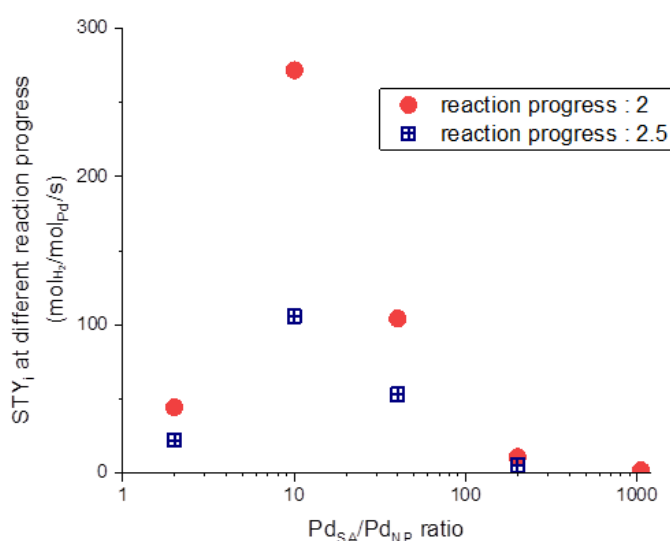


Figure 4.22. STY at a reaction progress of 2 and 2.5 as a function of SA/NP ratio. Catalysts nomenclature is Pd<sub>X\_SA/NP</sub>/CNT where X refers to the SA/NP ratio.

#### 4.5. Catalyst stability

Instead of running successive recyclability batch experiments catalyst stability was investigated in LGPC through a dedicated continuous reactor operation. When a single typical batch experiment allows us to reach a moderate turn-over number (TON) of 6200 mol<sub>H2</sub>/mol<sub>Pd</sub>, the chosen continuous testing mode leads to TON values as high as 600 000 mol<sub>H2</sub>/mol<sub>Pd</sub>. This represents a more intensive and powerful way to test catalyst stability.<sup>50</sup> The continuous experiments were run with the Pd<sub>2\_SA/NP</sub>/CNT catalyst coated on metallic open-cell solid foam cylinders. It is first worth mentioning that the coating process, performed at 300 °C under a

<sup>50</sup> S. L. Scott *ACS Catalysis* **2018**, 8, 8597-8599.



nitrogen flow did not significantly modify the particle size distribution and the SA/NP ratio of the catalyst (Figure 4.23a-f), pointing its good thermal stability.

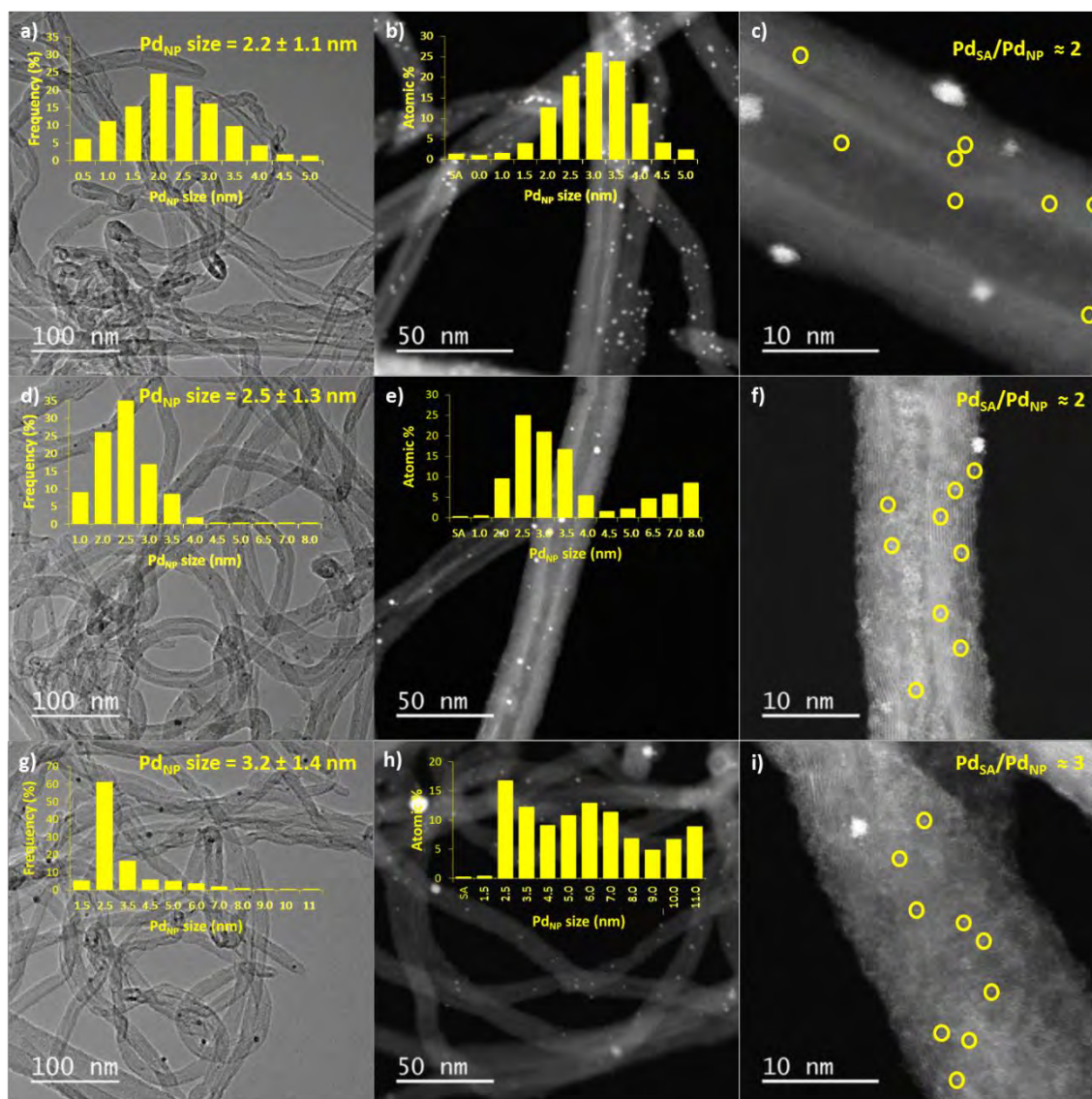


Figure 4.23. TEM and STEM micrographs and particle size distribution based on total particles and on total atoms for: a) to c) Pd<sub>2-SA/NP</sub>/CNT; d) to f) Pd<sub>2-SA/NP</sub>/CNT coated on metallic open-cell solid foam cylinders before catalysis; and g) to i) Pd<sub>2-SA/NP</sub>/CNT coated on metallic open-cell solid foam cylinders after catalysis.

Such internals in milli-channels are ideal candidates to promote such powdered catalysts in a continuous reactor. The particularly confined hydrodynamics lead to interesting heat and mass transfer performances as well as a small pressure drop due to the wide-open structure of open-

cell solid foams<sup>51,52,53</sup>. Figure 24a presents the obtained evolution of the mean STY against the Turn Over Number (TON). As already mentioned, this mean STY cannot be compared to the instantaneous one followed in batch through H<sub>2</sub> consumption. Here it is calculated from a mass balance regarding outlet flow composition between  $\beta$ -myrcene, mono, di, and tri hydrogenated products.

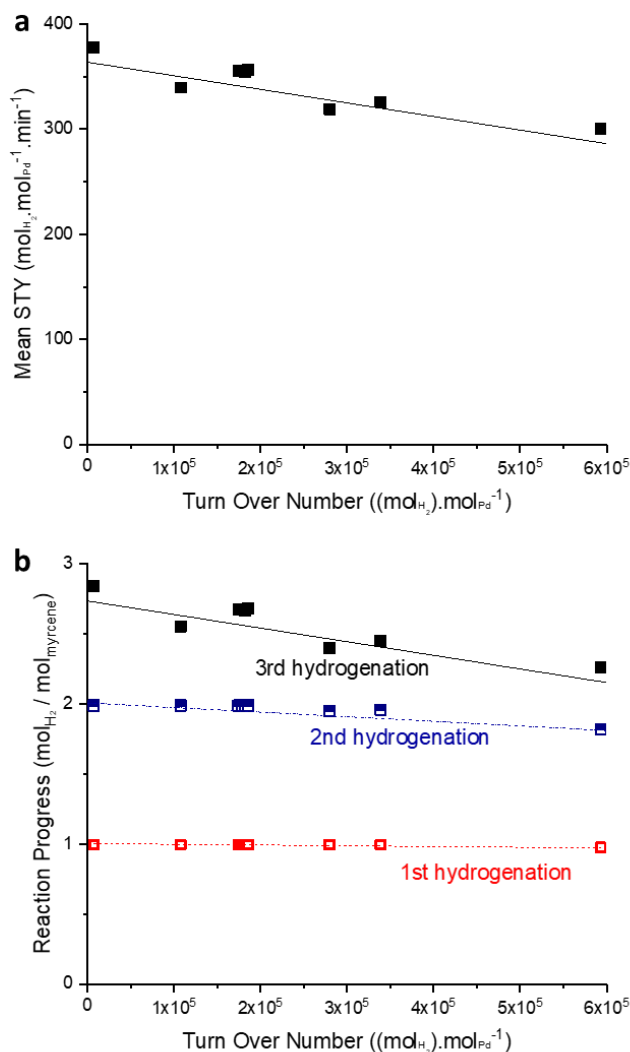


Figure 4.24 Catalyst stability testing in continuous mode using coated foam objects with Pd<sub>2</sub><sub>SA</sub>/NP/CNT catalyst (20 bar; 120 °C; 100 mg of catalyst; Q<sub>L</sub> = 2 mL/min; Q<sub>G</sub> = 2 NL/min, pure H<sub>2</sub>; Myrcene 1M in heptane). a) Mean STY as a function of Turn Over Number. b) Reaction progress versus Turn Over Number.

<sup>51</sup> J.-N. Tourvieille, et al. *Chemical Engineering Journal* **2015**, 267, 332-346.

<sup>52</sup> M. Serres, et al. *Chemical Engineering Science* **2018**, 190, 149-163.

<sup>53</sup> A. Avril, et al. *Reaction Chemistry & Engineering* **2017**, 2, 180-188.

Depending on this distribution, the evolution of the corresponding reaction progress can be determined and is presented on Figure 4.24b. First, it is noticeable that a very high TON of 600 000 mol<sub>H<sub>2</sub></sub>/mol<sub>Pd</sub> is obtained, which is equivalent up to 100 recycling in batch mode with our typical conditions. Such a high TON is obtained because of the relatively low amount of Pd involved in the experiment (2 mg) together with a relatively long time on stream (> 35 hours). Moreover, this indicates quite remarkable catalyst stability at all. The mean STY decreases quite regularly from 380 to 320 mol<sub>H<sub>2</sub></sub>/mol<sub>Pd</sub>/min at the final TON value of 600 000 mol<sub>H<sub>2</sub></sub>/mol<sub>Pd</sub>, which represent a loss of apparent activity of 15%. The corresponding evolution of the outflow composition indicates that the reaction progress decreases also with decreasing contributions of the second and third hydrogenation, while the first one remains constant. As in the batch experiments, this behavior for the first hydrogenation is explained by the gas-liquid external mass transfer limitation that hinder the intrinsic catalyst activity. For the slower second and third successive hydrogenations, the deactivation was logically more noticeable.

The coated catalyst was qualitatively examined by STEM-HAADF before and after this stability experiment (Figure 4.23). After the test the SA/NP ratio changes from  $\approx 2$  to  $\approx 3$  and the mean Pd<sub>NP</sub> size increased from 2.5 to 3.2 nm. The slight deactivation could thus be structural but could also be explained by the strong adsorption of impurities from the natural starting material ( $\beta$ -myrcene). Although they could not be detected in the charge by GC because of their too low concentration, these impurities could continuously be absorbed on the catalyst, resulting in a gradual decrease in activity at high TON numbers. Studies are in due course to recover and characterize these adsorbed impurities.

Overall, the catalysts developed in this study appear resistant to sintering due to the stabilization of the SA by the functionalized carbon support and can undergo very long TON either in batch or continuous mode. Nonetheless in the chosen reaction, the catalysts appear sensible to a charge impurity and purification steps may be required to reach very high TON with a more stable activity over time. This fact was only detectable with the continuous mode operation because of its easier operability and ability to reach a very high TON. Moreover, in addition to efficient catalyst stability testing, the continuous mode operation appears very promising for the compact intensified and secure operation of this reaction.

## 4.6. Conclusion

In this chapter, we have reported that a cooperative catalysis operates between carbon-supported Pd<sub>SA</sub> and Pd<sub>NP</sub> for alkene hydrogenation and isomerization, which involved: i) dihydrogen activation on Pd<sub>NP</sub>, ii) H-spillover on the support, and iii) the catalytic reaction on H-P<sub>SA</sub> species. This discovery provides a rational explanation for the structure/activity correlation that exists in Pd/C catalysts for myrcene hydrogenation.<sup>17</sup> While such a cooperative effect may occur in many Pd/C catalysts, it has never been recognized or exploited to improve catalytic performances in industrial catalysts. While this finding alone is important, major advances in heterogeneous catalysis can be achieved only if the SA/NP ratio can be controlled. Indeed, the control of this ratio, a major achievement of this work, allows tuning the catalyst performances. For  $\beta$ -myrcene hydrogenation, STY variations of several orders of magnitude were measured as a function of the value of this ratio. Finally, other types of cooperative catalysis than the one reported herein can be envisioned, such as bifunctional catalysis with a single metal: metallic NP ensuring one function, and SA of the same element presenting an altered electronic density ensuring a second function. This has been recently proposed for the hydrogenation of aldehydes and ketones on Pd/TiO<sub>2</sub> catalysts,<sup>7</sup> on which the electrodefficient Pd<sub>SA</sub> contribute to the activation of the carbonyl group, while Pd<sub>NP</sub> allow the dissociation of H<sub>2</sub>. It is our hope that this work paves the way for new chemical reactivity involving a rational use of the active metallic phase.

## 4.7. Experimental part

### 4.7.1. Palladium catalyst synthesis

A wet impregnation method was used to prepare the palladium catalysts supported on carbon nanomaterials. The desired amount of palladium(II) nitrate dihydrate Pd(NO<sub>3</sub>)<sub>2</sub>·2H<sub>2</sub>O (Sigma-Aldrich) was added to acetone (100 mL) containing 1 g of carbon nanomaterial (O-CNT or O-FLG), so as to introduce 2 %w/w of metal phase. The solution was sonicated at room temperature for 1 h and magnetically stirred overnight. The solution was then filtered and washed with acetone. The resulting solid was dried in an oven at 120 °C overnight. Finally, the Pd/CNT (Pd<sub>2-SA/NP</sub>/CNT) catalyst was reduced in a horizontal tube oven under a nitrogen and hydrogen flow (20 vol% H<sub>2</sub>) at 300 °C for 2 h (25 °C to 300 °C at 10 °C/min). The same

procedure was followed for the preparation of the 1.6% Pd/CNT<sub>HT</sub> (Pd<sub>2\_SA/NP</sub>/CNT<sub>HT</sub>) catalyst by using the CNT<sub>HT</sub> support.

For Pd<sub>SA</sub> synthesis (0.1% Pd<sub>SA</sub>/CNT), the wet impregnation method was also used. The desired amount of palladium(II) nitrate dihydrate Pd(NO<sub>3</sub>)<sub>2</sub>·2H<sub>2</sub>O was added to an acetone solution (100 mL) containing 1 g of CNT<sub>ox</sub>, so as to introduce 0.1 % w/w of metal phase. The solution was sonicated at room temperature for 6 h using a ultrasonic finger. The solution was then filtered and washed with acetone. The resulting solid was dried in an oven at 120 °C overnight. Finally, the catalyst was reduced in a horizontal tube oven under a nitrogen and hydrogen flow (20 vol% H<sub>2</sub>) at 300 °C for 2 h (25 °C to 300 °C at 10 °C/min).

For **Pd<sub>X\_SA/NP</sub>/CNT** catalysts we use the procedure described in *Chapter 3., Section 3.5 Mixture of single atoms and nanoparticles* synthesis where X refers to SA/NP ratio, a recently patented process was used.<sup>54</sup>

Finally, a 0.1%Pd<sub>1000\_SA/NP</sub>/CNT catalyst with a SA/NP ratio > 1000 was also prepared by the wet impregnation method. The desired amount of palladium(II) nitrate dihydrate [Pd(NO<sub>3</sub>)<sub>2</sub>·2H<sub>2</sub>O] was added to an acetone solution (100 mL) containing 1 g of O-CNT, so as to introduce 0.1 % w/w of metal phase. The solution was sonicated at room temperature for 1 h. Then, NaBH<sub>4</sub> (0.1 g) was added at room temperature, and let to react for 1 h to complete catalyst reduction. The solution was then filtered and washed with water and then acetone. The resulting solid was dried in an oven at 120 °C overnight.

For comparison purpose in myrcene hydrogenation we also used a commercial 5%Pd/activated carbon catalyst and a 5%Pd/Al<sub>2</sub>O<sub>3</sub> catalyst.

The palladium content in the products was measured by inductively coupled plasma optical emission spectroscopy (ICP-OES) performed at the LCC with a Thermo Scientific ICAP 6300 instrument. Elemental analyses of C, H were carried out on a PERKIN ELMER 2400 serie II elemental analyzer. TEM and HR-TEM analyses were performed at the “Centre de microcaracterisation Raimond Castaing, UMS 3623, Toulouse” by using a JEOL JEM 1011 CX-T electron microscope operating at 100 kV with a point resolution of 4.5 Å and a JEOL JEM 1400 electron microscope operating at 120 kV. The high-resolution analyses were conducted by using a JEOL JEM 2100F equipped with a field emission gun (FEG) operating at 200 kV with a point resolution of 2.3 Å and a JEOL JEM-ARM200F Cold FEG operating at

<sup>54</sup> P. Serp, et al. *FR1910044* **2019**.

200 kV with a point resolution of  $> 1.9 \text{ \AA}$ . The particle size distribution was determined through a manual measurement of enlarged micrographs from different areas of the TEM grid (at least 300 particles). The size distribution reported as Pd atomic percentage (based on total atoms) in each size range were obtained by calculating the number of atoms (N) in each nanoparticle assuming a spherical shape using an equation described in Ref. 55. The SA/NP ratio (a number ratio) was measured from the STEM-HAADF analyses of at least 500 elements.

The samples were analyzed by X-ray photoelectron spectroscopy (XPS) using a VG Escalab MKII spectrophotometer operating with a non-monochromatized Mg K source (1253.6 eV). A SQuID magnetometer MPMS5 was used to investigate the magnetic properties. The M(H) loop was measured at  $T = 300 \text{ K}$  after cooling the sample from 300 K to 2 K under a constant applied magnetic field  $H_{\text{cool}} = 50 \text{ kOe}$ . The M(H) loops were measured between -50 and 50 kOe. EPR data were recorded using an Elecsys E 500 Bruker spectrometer, operating at a microwave frequency of approximately 9.5 GHz. All spectra were recorded using a microwave power of 20 mW across a sweep width of 150 mT (centered at 310 mT) with a modulation amplitude of 0.5 mT. Experiments were carried out at 110 K using a liquid nitrogen cryostat.

#### 4.7.2. DFT periodic calculations (LPCNO, Dr. Iann Gerber, Dr. Iker del Rosal and Prof. Romuald Poteau)

Calculations using periodic boundary conditions were performed using the Vienna ab initio simulation package VASP,<sup>56,57,58,59</sup> which employs the full-potential projector augmented waves (PAW) framework.<sup>60,61</sup> Exchange-correlation effects were approximated using the PBE functional and applied in spin-polarized calculations.<sup>62</sup> A kinetic energy cutoff of 400 eV was found to be sufficient to achieve a total energy convergence within several meV, considering k-point sampling, *i.e.* with a (3x3x1)  $\Gamma$ -centered grid in conjunction with a 0.05 eV-width Gaussian smearing. All atoms were fully relaxed in order to have forces smaller than 0.005 eV/ $\text{\AA}^{-1}$ , and the Nudged Elastic Band method was used to estimate minimum energy paths of

---

<sup>55</sup> C.-T. Kuo, et al. *ACS Catalysis* **2019**, 9, 11030-11041.

<sup>56</sup> G. Kresse, et al. *Physical Review B* **1993**, 47, 558-561.

<sup>57</sup> G. Kresse, et al. *Physical Review B* **1994**, 49, 14251-14269.

<sup>58</sup> G. Kresse, et al. *Physical Review B* **1996a**, 54, 11169-11186.

<sup>59</sup> G. Kresse, et al. *Computational Materials Science* **1996b**, 6, 15-50.

<sup>60</sup> P. E. Blöchl *Physical Review B* **1994**, 50, 17953-17979.

<sup>61</sup> G. Kresse, et al. *Physical Review B* **1999**, 59, 1758-1775.

<sup>62</sup> J. P. Perdew, et al. *Physical Review Letters* **1996**, 77, 3865-3868.



transitions, as implemented by Henkelman et al.,<sup>63,64</sup> using 3 intermediates images and force criteria of 0.05 eV/Å<sup>-1</sup> to control the convergence. We have modeled the carbon support by a single graphene layer presenting a vacancy in (7x7) supercell, which can be either filled by a single Pd atom (Pd<sub>SA</sub>-model) or served as an anchorage point for a fully hydrogenated Pd<sub>13</sub>H<sub>20</sub> aggregate (Pd<sub>NP</sub>-model). We recall that a sufficient vacuum height of 16 Å was used to limit spurious interaction between repeated images in the z-direction due to periodic boundary conditions.

#### 4.7.3. DFT Gaussian calculations (LPCNO, Dr. Iann Gerber, Dr. Iker del Rosal and Prof. Romuald Poteau)

Calculations were carried out using the Gaussian09 package<sup>65</sup> at the DFT level by means of the hybrid density functional B3PW91.<sup>66,67</sup> For the Pd atom, the Stuttgart-Dresden pseudopotentials<sup>68</sup> were used in combination with their associated basis sets<sup>69</sup> augmented by a set of polarization functions (f-orbital polarization exponents of 1.472).<sup>70</sup> For the C and H atoms, a double-zeta 6-31G basis set<sup>71,72,73,74,75,76,77</sup> augmented by a polarization function were used. The different intermediates and transition states were simulated with dispersion corrected functional. More precisely, dispersion corrections were treated with the D3 version of Grimme's dispersion with Becke-Johnson damping.<sup>78</sup> The nature of the optimized stationary point, minimum or transition state, has been verified by means of analytical frequency calculations at 298.15 K and 1 atm. The geometry optimizations have been achieved without any geometrical constraints. IRC calculations were carried out to confirm the connectivity between reactant(s), transition state and product(s). Energy data in kcal/mol are reported in the gas phase.

<sup>63</sup> G. Henkelman, et al. *The Journal of Chemical Physics* **2000a**, *113*, 9901-9904.

<sup>64</sup> G. Henkelman, et al. *The Journal of Chemical Physics* **2000b**, *113*, 9978-9985.

<sup>65</sup> Gaussian09 revision D.01. M. J. Frisch, et al. Gaussian, Inc., Wallingford CT, 2013.

<sup>66</sup> J. P. Perdew, et al. *Physical Review B* **1992**, *46*, 6671-6687.

<sup>67</sup> A. D. Becke *The Journal of Chemical Physics* **1993**, *98*, 5648-5652.

<sup>68</sup> D. Andrae *Diplomarbeit* **1989**, *10.18419/opus-1359*.

<sup>69</sup> D. Andrae, et al. *Theoretica chimica acta* **1990**, *77*, 123-141.

<sup>70</sup> A. W. Ehlers, et al. *Chemical Physics Letters* **1993**, *208*, 111-114.

<sup>71</sup> R. Ditchfield, et al. *The Journal of Chemical Physics* **1971**, *54*, 724-728.

<sup>72</sup> W. J. Hehre, et al. *The Journal of Chemical Physics* **1972**, *56*, 2257-2261.

<sup>73</sup> P. C. Hariharan, et al. *Theoretica chimica acta* **1973**, *28*, 213-222.

<sup>74</sup> P. C. Hariharan, et al. *Molecular Physics* **1974**, *27*, 209-214.

<sup>75</sup> M. M. Francl, et al. *The Journal of Chemical Physics* **1982**, *77*, 3654-3665.

<sup>76</sup> T. Clark, et al. *Journal of Computational Chemistry* **1983**, *4*, 294-301.

<sup>77</sup> M. J. Frisch, et al. *The Journal of Chemical Physics* **1984**, *80*, 3265-3269.

<sup>78</sup> S. Grimme, et al. *Journal of Computational Chemistry* **2011**, *32*, 1456-1465.

#### 4.7.4. Catalytic experiments (LGPC, Dr. Boris Guicheret, Dr. Laurent Vanoye, Dr. Alain Favre-Régouillon, Prof. Claude de Bellefon and Dr. Régis Philippe)

##### 4.7.4.1. *$\beta$ -myrcene hydrogenation*

Myrcene catalytic hydrogenation has been carried out in a stirred tank reactor of 200 mL from Top Industrie. This reactor is equipped with 4 baffles and a gas inducing Rushton turbine having 6 straight blades to provide an efficient G-L-S contacting. The catalytic tests were operated at 1200 rpm and 120 °C with 200 mg of catalyst powder (except for Pd/C and Pd/Al<sub>2</sub>O<sub>3</sub> catalysts where 80 mg of catalyst has been used because of their Pd loading of 5 wt.%) under pure H<sub>2</sub> atmosphere at a constant pressure of 20 bar. The liquid phase consists in 80 mL of a 1M  $\beta$ -myrcene (Sigma-Aldrich, 98% purity, corresponding to 3M of C=C double bond) solution in n-heptane (Sigma-Aldrich, 99%) containing a known trace of n-tetradecane as internal standard for final GC-FID analysis (DB17 column). In this configuration, the reactor is operated in batch mode for the liquid and solid phases and in semi-batch mode for the gas because hydrogen was constantly fed *via* a pressure regulator and supplied by a calibrated reserve. The pressure and temperature monitoring of this reserve provides the hydrogen consumption rate, and thus the apparent and instantaneous activity of the catalysts expressed in moles of H<sub>2</sub> consumed per mole of Pd and per second, and being equivalent to an instantaneous Site Time Yield.

The instantaneous STY is determined with the local slope of the H<sub>2</sub> reserve consumption curve as following, where  $n_{Pd}$  is the quantity of Pd determined by ICP:

$$STY = \frac{\Delta n_{H_2}}{\Delta t \times n_{Pd}} \quad (mol_{H_2}/mol_{Pd}/s) \quad (4.1)$$

STY is qualified of apparent because (i) it addresses the overall consumption of H<sub>2</sub> through multiple reactions and (ii) depending on the catalyst and the reaction progress, possible external and internal mass transfer resistances are likely. Indeed, the reactivity of the first C=C is very high (terminal and conjugated C=C) and the first moments of the reaction are physically limited. Hopefully, this is not true for the whole range of reaction course. For robust and chemically consistent catalysts comparison, STY at 66% and 83% of reaction progress are thus considered, *i.e.* when 2.0 and 2.5 equivalents of H<sub>2</sub> per  $\beta$ -myrcene are consumed respectively.

For hydrogenation and isomerization reactions, we have also used normalized time (time.cat), a standardized notation that is convenient and usual in catalysis to compare catalysts with different loadings of the active phase. The quantity of Pd was determined by ICP. For

comparison with commercial catalysts (Figure 4.4), a  $\text{time.cat}^*$  could be also used where  $n_{\text{Pd}}$  is replaced by  $S_{\text{Pd}}$ , the quantity of surface Pd determined from metal dispersion.

To ensure a reproducible and precise initial time for the tests, heating of the reactor was first done with 1 bar of  $\text{N}_2$ , then agitation was stopped and the  $\text{N}_2$  atmosphere was replaced by 20 bar of  $\text{H}_2$  and agitation turned on again, defining the initial time for the experiment. No side-reactions like Diels-Alder or oligomerization are encountered in the experimental domain investigated for this substrate. Thus, no selectivity issue has to be considered. The good matching between the evolution of  $\text{H}_2$  consumption profiles and of liquid substrate compositions has been checked (not shown here) and validates the experimental approach for reaction progress monitoring.

#### 4.7.4.2. *Squalene and $\beta$ -farnesene hydrogenation*

The comparison between  $\beta$ -myrcene,  $\beta$ -farnesene and squalene hydrogenations has been carried out in the same experimental rig following the same procedure with identical experimental conditions excepting a slightly increased catalyst mass (280 mg instead of 200 mg). To illustrate the extension of the concept to other carbon supports, here FLG was chosen and compared to  $\text{Al}_2\text{O}_3$ . Squalene has been purchased from Sigma-Aldrich and  $\beta$ -farnesene has been synthesized and purified accordingly to ref. 79.

#### 4.7.4.3. *Catalyst stability testing under continuous reactor operation*

Catalyst stability has been investigated through a dedicated continuous reactor operation with coated metallic open-cell solid foams (Hollomet Foamet 800  $\mu\text{m}$ ). Stainless steel foam cylinders were precisely cut through EDM (Electrical Discharge Machining) to obtain cylindrical objects with a diameter of 4.3 mm and a length of 5 cm. 8 foam pieces were homogeneously coated with 12.5 mg of the  $\text{Pd}_{2\text{SA/NP/CNT}}$  catalyst (following the detailed procedure described elsewhere)<sup>80</sup> and inserted into a home-made millimeter-scale tubular reactor (40 cm long, 4.4 mm I. D.) to provide a reactor volume of 6 mL with a total catalyst amount of 100 mg. Figure 4.25 shows a photo of the foam coated in the tubular reactor. The continuous experiments were performed at 120 °C and 20 bar applying a gas flowrate of 2 NL/min of pure  $\text{H}_2$  and a liquid flow rate of 2 mL/min of a 1M solution of myrcene in heptane corresponding to a liquid space velocity of 106.4 molmyrcene/molPd/min. Analysis by GC-FID (method and apparatus are identical to the one described in the previous  $\beta$ -myrcene hydrogenation section) at the reactor outlet allow to verify the mass balance and to determine

<sup>79</sup> P. Baeckström, et al. *Synthetic Communications* **1990**, 20, 423-429.

<sup>80</sup> F. Simescu-Lazar, et al. *Applied Catalysis A: General* **2015**, 508, 45-51.

the liquid flow composition. The corresponding mean Site Time Yield and Reaction progress are then calculated. It is noteworthy that this mean STY and the instantaneous STY used in the batch experiment are different and cannot be compared directly.



Figure 4.25. Photo of the metallic foam coated in the tubular reactor for catalyst stability study under continuous reactor operation.

#### 4.7.4.4. $H_2$ -assisted isomerization of 1-octene

Isomerization of alkenes was assessed using a dedicated experience. 1-octene was used as a molecular probe (Figure 4.26). The different isomers and by-product that could be obtained during the isomerization of 1-octene by Pd catalysts is shown below:

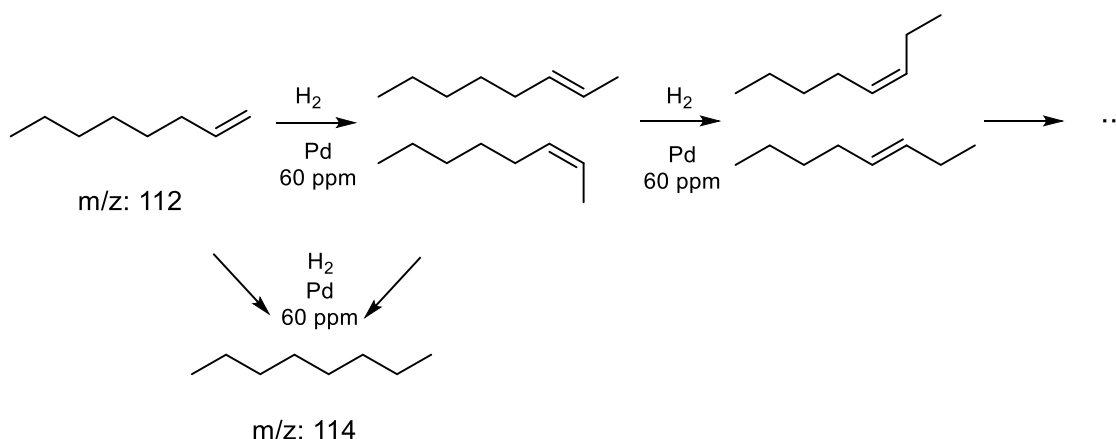


Figure 4.26.  $H_2$ -assisted isomerization of 1-octene.

60 mL of a solution of 1-octene (Sigma Aldrich, 99%) in heptane (1 M) was added in a 100 mL round bottom flask and then heat at reflux under  $H_2$  atmosphere. A sample was taken for ex-

*situ* analysis and then catalyst was added in one portion. The mass of the catalyst was adjusted in order to have 3.75  $\mu\text{mol}$  of Pd (0.4 mg, 60 ppm). Samples were taken as the function of time and were analyzed using GC-FID analysis.

The concentration of isomers of 1-octene and octane could be easily followed by GC as shown on Figure 4.27.

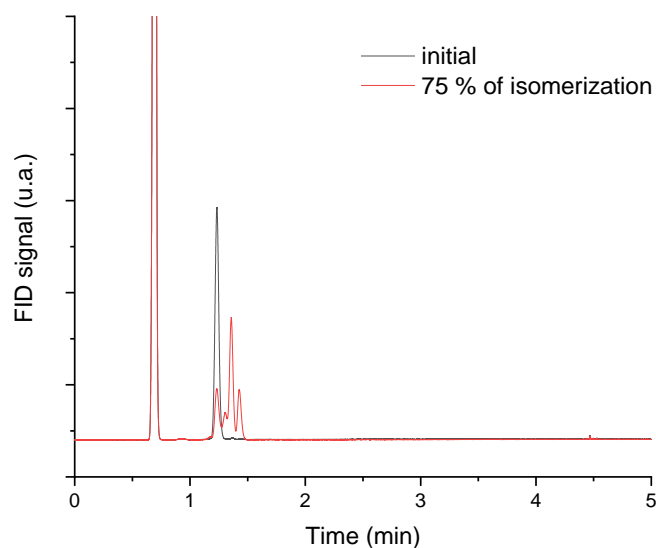


Figure 4.27 GC-FID of the reaction mixture.

The absence of hydrogenation product (*i.e.* *n*-octane) was assessed by comparison with pure octane and by GC-MS analysis (see chromatogram below). Under those conditions, no hydrogenation product (*i.e.* *n*-octane) could be identified in the reaction mixture. This was confirmed by comparison with pure octane and by GC-MS analysis in SIM mode (see chromatogram, Figure 4.28).

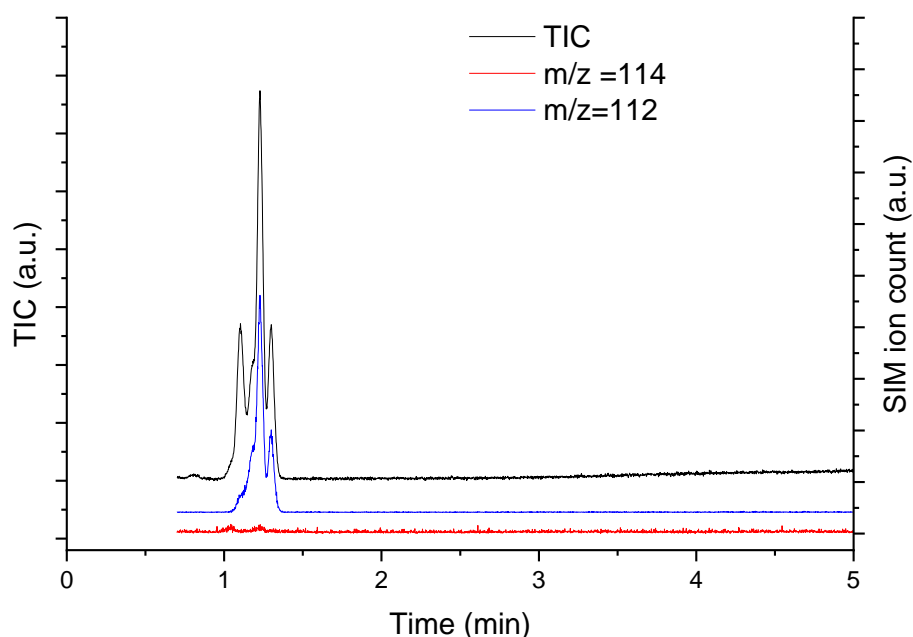


Figure 4.28 GC-MS chromatogram TIC and SIM ion count of a sample at 75 % of isomerization. Reaction conditions: 1 M 1-octene in heptane (1 M), reflux (98 °C), H<sub>2</sub> 1 atm.

#### 4.7.4.5. Tests to assess hydrogen spillover

To check for the H-spillover, we used WO<sub>3</sub> to diagnose the activation of H<sub>2</sub> in the various catalysts, because the spilled-over hydrogen migrates and readily reacts with the yellow WO<sub>3</sub> to form dark blue H<sub>x</sub>WO<sub>3</sub>.<sup>39</sup> Samples made with 500 g of WO<sub>3</sub> were mixed or not with 5 mg of catalyst and treated with H<sub>2</sub> (100 mL/min) at 20 °C for 3 min.

#### 4.7.4.6. Assessment of the impact of mass transfer for myrcene hydrogenation

Mass transfer limitations have been evaluated using common chemical engineering approaches regarding the limiting reagent H<sub>2</sub>. The physical properties of the different phases involved in the reaction are listed in the following Table 4.3. Gas and liquid properties are given for 20 bar and 120 °C.



Table 4.3. Physical properties of the different phases at 120 °C and 20 bar.

Phase	Name	Symbol	Value	Units
Liquid	Viscosity <sup>a</sup>	$\mu_L$	$1.71 \times 10^{-4}$	Pa.s
	Density	$\rho_L$	703	kg/m <sup>3</sup>
	Surface tension <sup>a</sup>	$\sigma_L$	$1 \times 10^{-2}$	N/m
	H <sub>2</sub> diffusivity <sup>a</sup>	$D_{m,H_2}$	$1.99 \times 10^{-9}$	m <sup>2</sup> /s
	H <sub>2</sub> solubility <sup>b</sup>	$C^*_{H_2}$	187	mol/m <sup>3</sup> <sub>L</sub>
Gas	Viscosity <sup>a</sup>	$\mu_G$	$1.07 \times 10^{-5}$	Pa.s
	Density	$\rho_G$	1.22	kg/m <sup>3</sup>
CNT support	Skeleton density <sup>c</sup>	$\rho_s$	1900	kg/m <sup>3</sup> <sub>skeleton</sub>
	Pore volume <sup>d</sup>	$V_{pore}$	2.5	mL/g
	Dry particle density <sup>d</sup>	$\rho_P$	600	kg/m <sup>3</sup> <sub>particle</sub>
	Wetted particle density	$\rho_P$	1080	kg/m <sup>3</sup> <sub>particle</sub>
	Internal porosity <sup>e</sup>	$\beta_P$	70%	m <sup>3</sup> <sub>void</sub> /m <sup>3</sup> <sub>particle</sub>
	Tortuosity <sup>f</sup>	$\tau$	$\approx 1$	-
	Mean Particle (agglomerate) diameter <sup>d</sup>	$d_P$	1-2	$\mu m$
$\gamma$ -Al <sub>2</sub> O <sub>3</sub> support	Skeleton density	$\rho_s$	3650	kg/m <sup>3</sup> <sub>skeleton</sub>
	Dry particle density	$\rho_P$	1460	kg/m <sup>3</sup> <sub>particle</sub>
	Wetted particle density	$\rho_P$	1880	kg/m <sup>3</sup> <sub>particle</sub>
	Internal porosity	$\beta_P$	60%	m <sup>3</sup> <sub>void</sub> /m <sup>3</sup> <sub>particle</sub>
	Tortuosity	$\tau$	$\approx 3$	-
	Mean Particle diameter	$d_P$	25	$\mu m$
Activated Carbon support	Skeleton density <sup>c</sup>	$\rho_s$	1900	kg/m <sup>3</sup> <sub>skeleton</sub>
	Dry particle density	$\rho_P$	760	kg/m <sup>3</sup> <sub>particle</sub>
	Wetted particle density	$\rho_P$	1180	kg/m <sup>3</sup> <sub>particle</sub>
	Internal porosity	$\beta_P$	60%	m <sup>3</sup> <sub>void</sub> /m <sup>3</sup> <sub>particle</sub>
	Tortuosity	$\tau$	$\approx 3$	-
	Mean Particle diameter	$d_P$	10	$\mu m$

a) Estimated using correlations found in [81].

b) Thermodynamic calculations with PPR78 group contribution using PROSIM software for a flash equilibrium at constant P & T.

c) Commonly taken equal to the graphite density.

d) See for example [82,83] for such typical orders of magnitudes.

e) Calculated from skeleton density and pore volume.

f) See [84] for a discussion about mass transfer inside nanotubes bundles.

#### 4.7.4.7. G-L external mass transfer

To evaluate the efficiency of the reactor set up to transfer hydrogen in the liquid phase, the mass transfer coefficient ( $k_{LaGL}$ ) of the reactor has been measured experimentally with a classical physical absorption technique<sup>85,86</sup> following the H<sub>2</sub> consumption in the regulated and calibrated gas tank. Identical conditions to the experimental ones have been used but without any catalyst (1200 rpm, 80mL of 1M myrcene solution in heptane, 120 °C, constant  $P_{H_2} = 20$  bar). The H<sub>2</sub> consumption profile of the reserve allowed adjusting and recovering 2 parameters of the system

<sup>81</sup> R. C. Reid, et al. In *The Properties of Gases and Liquids*: McGraw-Hill Inc. New York (1987).

<sup>82</sup> E. Lam, et al. *ACS Catalysis* **2014**, 4, 3393-3410.

<sup>83</sup> S. Jin, et al. *Australian Journal of Chemistry* **2010**, 63, 131-134.

<sup>84</sup> P. W. A. M. Wenmakers, et al. *Journal of Materials Chemistry* **2008**, 18, 2426-2436.

<sup>85</sup> R. V. Chaudhari, et al. *The Canadian Journal of Chemical Engineering* **1987**, 65, 744-751.

<sup>86</sup> E. Dietrich, et al. *Chemical Engineering Science* **1992**, 47, 3597-3604.

mass balance (eq. 4.5-4.7): the mass transfer coefficient  $k_L a_{GL}$  and the final saturation concentration of  $H_2$  in the solution (solubility)  $C_{H_2}^*$ .

$$dn_{H_2}^L(t) = -dn_{H_2}^{Res}(t) = -dp^{res}(t) \frac{V_{res}}{RT_{res}} \quad (4.5)$$

$$k_L a_{GL} V_R (C_{H_2}^* - C_{H_2}^L(t)) = \frac{dn_{H_2}^L(t)}{dt} = V_L \frac{dC_{H_2}^L(t)}{dt} \quad (4.6)$$

$$-dp^{res}(t) = \frac{RT_{res}}{V_{res}} C_{H_2}^* V_L \left( 1 - \exp\left(-\frac{k_L a_{GL}}{\varepsilon_L} t\right) \right) \quad (4.7)$$

In these equations,  $dn_{H_2}^L(t)$  is the variation of the quantity of dissolved  $H_2$  in the liquid phase between  $t_0$  and  $t$  (mol);  $dn_{H_2}^{Res}(t)$  is the corresponding variation of  $H_2$  in the calibrated reserve (mol);  $dp^{res}(t)$  is the corresponding pressure variation in the reserve (Pa);  $V_{res}$  is the volume of the reserve ( $m^3$ );  $T_{res}$  is the temperature of the reserve (K);  $V_L$  is the liquid volume inside the reactor ( $m^3$ );  $\varepsilon_L$  is the liquid fraction inside the reactor ( $m^3_L/m^3_R$ );  $C_{H_2}^*$  is the solubility of  $H_2$  in the liquid mixture ( $mol/m^3$ );  $k_L a_{GL}$  is the G-L mass transfer coefficient ( $s^{-1}$ ) with  $a_{GL}$  the specific surface area for G-L mass transfer ( $m^2_{GL}/m^3_{Reactor}$ ).

$k_L a_{GL}$  and  $C_{H_2}^*$  were estimated as  $0.2 s^{-1}$  and  $190 mol_{H_2}/m^3_L$  respectively. The  $k_L a_{GL}$  appears typical of well-equipped laboratory stirred tank reactor (for  $H_2$ ). The experimental solubility is in agreement with the one calculated with the PPR78 thermodynamic model ( $187 mol/m^3_L$ ).

Based on these mass transfer measurements, a theoretical maximum  $H_2$  consumption,  $F_{H_2}^{max,GL}$  (in  $mol_{H_2}/s$ ) can be defined for each experiment (4.8). This consumption can be linked to the corresponding theoretical apparent reaction rate,  $\overline{r_{p,app}^{max}}$  (4.9), or to the corresponding theoretical Site Time Yield,  $STY^{max}$  (4.10), both in full G-L mass transfer regime:

$$F_{H_2}^{max,GL} = k_L a_{GL} V_R C_{H_2}^* \quad (4.8)$$

$$\overline{r_{p,app}^{max,GL}} = \frac{F_{H_2}^{max,GL}}{V_{cata}} = \frac{k_L a_{GL} V_R C_{H_2}^*}{V_{cata}} \quad (4.9)$$

$$STY^{max,GL} = \frac{F_{H_2}^{max,GL}}{n_{Pd}} = \frac{k_L a_{GL} V_R C_{H_2}^*}{n_{Pd}} \quad (4.10)$$

Independently, following the instantaneous consumption curves of  $H_2$ , experimental instantaneous apparent reaction rates or STY can be determined at any reaction progress. These latter can be compared to the corresponding theoretical ones to appreciate a fraction of external G-L mass transfer limitation,  $f_{ex}^{GL}$  (4.11), on the measurements and is analogous of the L-S

external mass transfer one because no reaction occurs inside the liquid, only on the catalyst surfaces.

$$f_{ex}^{GL} = \frac{STY}{STY^{max,GL}} = \frac{\overline{r_{p,app}}}{\overline{r_{p,app}^{max}}} \quad (4.11)$$

The relationship between the instantaneous STY and the instantaneous apparent reaction rate  $\overline{r_p}$ , (per volume of wetted catalyst) is recalled in (4.12):

$$\overline{r_p} = \frac{STY \times \rho_P \times wt.\%Pd}{M_{Pd}} \quad (4.12)$$

Table 4.4 presents this determination for most of the catalysts of the study at three different reaction progresses: 0.5 mol<sub>H2</sub>/mol<sub>myrcene</sub>, 2.0 mol<sub>H2</sub>/mol<sub>myrcene</sub> and 2.5 mol<sub>H2</sub>/mol<sub>myrcene</sub>.

Table 4.4. Appraisal of G-L mass transfer limitations.

Catalyst	n <sub>Pd</sub> (μmol)	STY <sup>max</sup> (mol <sub>H2</sub> /s/mol <sub>Pd</sub> )	STY <sub>0.5</sub> (mol <sub>H2</sub> /s/mol <sub>Pd</sub> )	f <sub>ex,0.5</sub> <sup>GL</sup> (-)	E (-)	STY <sub>2.0</sub> (mol <sub>H2</sub> /s/mol <sub>Pd</sub> )	f <sub>ex,2.0</sub> <sup>GL</sup> (-)	STY <sub>2.5</sub> (mol <sub>H2</sub> /s/mol <sub>Pd</sub> )	f <sub>ex,2.5</sub> <sup>GL</sup> (-)
Pd/Al <sub>2</sub> O <sub>3</sub>	37.6	199	109	55%	1.0	10.2	5%	4.6	2%
Pd/C	36.5	205	168	82%	1.0	72	35%	26	13%
Pd/CNT also named Pd <sub>2_SA/NP</sub> /CNT	38.3	195	144	74%	1.0	44	23%	22	11%
Pd <sub>1000_SA/NP</sub> /CNT	1.9	3979	184	5%	1.0	1.4	0.04%	N.A.	N.A.
Pd <sub>200_SA/NP</sub> /CNT	25.0	299	104	35%	1.0	10.4	3%	4.5	2%
Pd <sub>40_SA/NP</sub> /CNT	25.8	290	544	187%	1.9	104	19%	50	9%
Pd <sub>10_SA/NP</sub> /CNT	24.2	308	672	218%	2.2	272	40%	106	16%

First of all, it is noticeable that the STY<sup>max</sup> reached different values depending on the different amounts of Pd in each experiment. The f<sub>ex,0.5</sub><sup>GL</sup>, for most of the catalysts (*except the Pd<sub>1000\_SA/NP</sub>/CNT catalyst which contains a very low amount of metal*) is revealed to be high indicating a strong G-L mass transfer impact on the STY<sub>0.5</sub> measurements and the impossibility to discuss robustly these STY<sub>0.5</sub>. This is indicated in the main text of the article. Interestingly, the 2 more active catalysts present a higher STY<sub>0.5</sub> compared to the theoretical STY<sup>max</sup>. This is a phenomenon already observed and explained in stirred tank reactors with very active fine slurry catalyst particles.<sup>87,88</sup> The approach detailed in ref. 87 is very close to an enhancement factor, E (-), for mass transfer G-L reactive absorption already well established.<sup>89</sup> In the present work, this situation is encountered. Thus, the first points at a reaction progress of 0.5 are used

<sup>87</sup> Z. Junmei, et al. *Chemical Engineering Journal* **2006**, 120, 149-156.

<sup>88</sup> S. Karve, et al. *Chemical Engineering Science* **1990**, 45, 587-594.

<sup>89</sup> K. B. B. G. F. Froment. In *Chemie Ingenieur Technik*: John Wiley & Sons, . New York (**1990**).

to estimate an experimental E factor as shown in the 6<sup>th</sup> column of the table. The values are equal to 1 when  $f_{ex,0.5}^{GL} < 100\%$  and equal to the value of  $f_{ex,0.5}^{GL}$  when  $> 100\%$ . The values obtained here for the two more active catalysts are consistent with those reported in ref. 87. For the other reaction progress, accordingly to these measurements, the  $F_{H_2}^{max,GL}$  (and  $STY^{max}$ ) takes into account this factor accordingly to (4.12):

$$F_{H_2}^{max,GL} = E k_L a_{GL} V_R C_{H_2}^* \quad (4.12)$$

For reaction progresses of 2.0 and 2.5 mol<sub>H2</sub>/mol<sub>myrcene</sub>, the impact of G-L mass transfer on the STY is drastically decreased as shown in the Table and a satisfactory comparison of the observed STY can be drawn on a chemical basis. The Pd<sub>10SA\_NP</sub>/CNT, which is the most active one, is the only catalyst that may still present a possible partial G-L mass transfer hindrance of its intrinsic performance. This partial leveling is a signature of its very high intrinsic activity and does not change the conclusions made in this article. In a quantitative point of view, one can just expect an increase of the observed differences between this catalyst and the other ones.

#### 4.7.4.8. L-S external mass transfer

In G-L-S slurry reactors, L-S external mass transfer is often less limiting than the G-L one. To verify this common assumption, the classical external mass transfer fraction,  $f_{ex}^{LS}$  (defined in 4.13) has been used for reaction progresses of 0.5, 2.0 and 2.5 mol<sub>H2</sub>/mol<sub>myrcene</sub>.

$$f_{ex}^{LS} = \frac{\overline{r}_P L}{k_S C_{H_2}^*} = \frac{STY}{STY^{max,LS}} \quad \text{with} \quad STY^{max,LS} = \frac{M_{Pd} k_S C_{H_2}^*}{\rho_{Pwt.\%Pd} L} \quad (4.13)$$

L is the characteristic length of the catalyst ( $d_p/6$  for spherical particles) and  $k_S$  is the L-S mass transfer coefficient. It has been estimated using the correlation of Armenante and Kirwan.<sup>90</sup> The different results are presented in Table 4.5. At a reaction progress of 0.5 mol<sub>H2</sub>/mol<sub>myrcene</sub>, only Pd/Al<sub>2</sub>O<sub>3</sub> and Pd/C present a L-S mass transfer limitation. All the CNT catalysts appear free of external L-S mass transfer limitation.

<sup>90</sup> P. M. Armenante, et al. *Chemical Engineering Science* **1989**, 44, 2781-2796.

Table 4.5. Appraisal of L-S external mass transfer limitations.

Catalyst	$STY^{max,LS}$ (mol <sub>H2</sub> /s/mol <sub>Pd</sub> )	$STY_{0.5}$ (mol <sub>H2</sub> /s/mol <sub>Pd</sub> )	$f_{ex,0.5}^{LS}$ (-)	$STY_{2.0}$ (mol <sub>H2</sub> /s/mol <sub>Pd</sub> )	$f_{ex,2.0}^{LS}$ (-)	$STY_{2.5}$ (mol <sub>H2</sub> /s/mol <sub>Pd</sub> )	$f_{ex,2.5}^{LS}$ (-)
Pd/Al <sub>2</sub> O <sub>3</sub>	137	109	79%	10.2	7.5%	4.6	3.4%
Pd/C	541	168	31%	72	13.3%	26	4.8%
Pd/CNT							
<b>also named</b> Pd <sub>2_SA/NP</sub> /CNT	31 486	144	0.5%	44	0.1%	22	0.07%
Pd <sub>1000_SA/NP</sub> /CNT	642 309	184	0.03%	1.4	0.0002 %	0.7	0.0001%
Pd <sub>200_SA/NP</sub> /CNT	48 294	104	0.2%	10.4	0.02%	4.5	0.01%
Pd <sub>40_SA/NP</sub> /CNT	46 884	544	1.2%	104	0.2%	50	0.1%
Pd <sub>10_SA/NP</sub> /CNT	49 791	672	1.4%	272	0.6%	106	0.2%

At reaction progress of 2.0 and 2.5 mol/mol, no L-S mass transfer limitation remains at all for all the catalysts (except slightly for the Pd/C) and STY comparisons are consistent and chemically robust.

#### 4.7.4.9. Internal mass transfer

To evaluate a possible internal mass transfer limitation, the classical Weisz-Prater criterion  $\varphi'$ <sup>89</sup> has been evaluated. When the criterion is inferior to 1 a surface efficiency of 1 is stated. When it is superior to 1, a surface efficiency is approximated as  $1/\varphi'$ . The Table 4.6 presents the results and equations (4.14) to (4.16), the formula used for.

$$\varphi' = \frac{\bar{r}_p L^2}{D_{eff} C_{H_2, su}} \quad (4.14)$$

$$D_{eff} = \frac{\beta_P}{\tau} D_{m, H_2} \quad (4.15)$$

$$\text{For } \varphi' > 1: \eta_{su} \approx \frac{1}{\varphi'} \text{ and for } \varphi' < 1: \eta_{su} \approx 1 \quad (4.16)$$

All the CNT catalysts at reaction progress 2.0 and 2.5 mol<sub>H2</sub>/mol<sub>myrcene</sub> are free of internal limitations. This remains true for the reference Pd/Al<sub>2</sub>O<sub>3</sub> and Pd/C at the reaction progress of 2.5 mol<sub>H2</sub>/mol<sub>myrcene</sub>. For these catalysts, an intermediate regime with little mass transfer resistance may be present at a reaction progress of 2.0 mol<sub>H2</sub>/mol<sub>myrcene</sub> because  $1 < \varphi' < 3$ . This is due to the bigger size of the catalyst particles.

Table 4.6. Appraisal of possible internal mass transfer limitations.

Catalyst	$Deff$ (m <sup>2</sup> /s)	$STY_{2.0}$ (mol <sub>H2</sub> /s/ mol <sub>Pd</sub> )	$\phi'$ (-)	$\eta_{su}$ (-)	$STY_{2.5}$ (mol <sub>H2</sub> /s/ mol <sub>Pd</sub> )	$\phi'$ (-)	$\eta_{su}$ (-)
Pd/Al <sub>2</sub> O <sub>3</sub>	4.0x10 <sup>-10</sup>	10.2	2.10	≈0.5	4.6	0.95	≈1
Pd/C	4.0x10 <sup>-10</sup>	72	1.44	≈0.7	26	0.52	≈1
Pd/CNT							
also named	1.4x10 <sup>-9</sup>	44	0.004	1	22	-	1
Pd <sub>2_SA/NP</sub> /CNT							
Pd <sub>1000_SA/NP</sub> /CNT	1.4x10 <sup>-9</sup>	1.4	1x10 <sup>-5</sup>	1	0.7	-	1
Pd <sub>200_SA/NP</sub> /CNT	1.4x10 <sup>-9</sup>	10.4	6x10 <sup>-4</sup>	1	4.5	-	1
Pd <sub>40_SA/NP</sub> /CNT	1.4x10 <sup>-9</sup>	104	6x10 <sup>-3</sup>	1	50	-	1
Pd <sub>10_SA/NP</sub> /CNT	1.4x10 <sup>-9</sup>	272	0.015	1	106	-	1

#### 4.7.4.10. Global conclusion on mass transfer limitations

Due to the high reactivity of the terminal alkene and the conjugated double bond of myrcene, the first hydrogenation is very fast and the overall hydrogenation of this study is subject to external mass transfer limitations (either G-L, L-S or both) at low reaction progress (typically < 1.0 mol<sub>H2</sub>/mol<sub>myrcene</sub>). For the usual reference hydrogenation catalysts (Pd/Al<sub>2</sub>O<sub>3</sub> and Pd/C), at higher reaction progress, (2 or 2.5 mol<sub>H2</sub>/mol<sub>myrcene</sub>), most of the experimental instantaneous STY measurements are free of external or internal limitations. Only the most active catalysts (Pd<sub>40\_SA/NP</sub>/CNT and Pd<sub>10\_SA/NP</sub>/CNT) can be subject to a little G-L limitation that may hinder slightly their true performance.

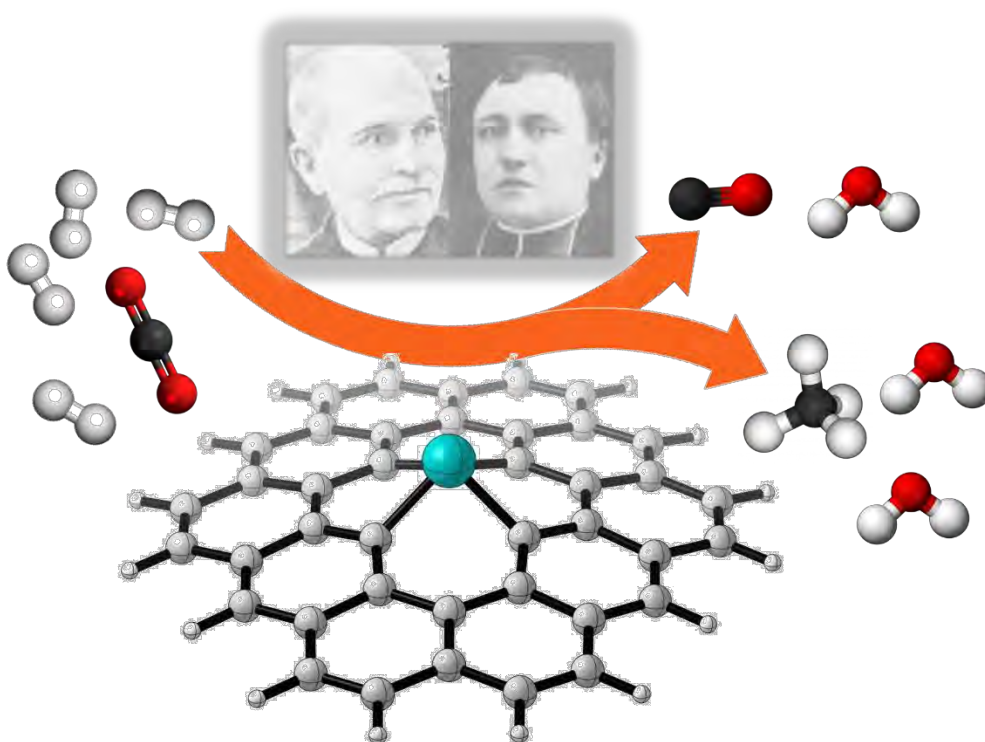
Regarding internal mass transfer limitations, only Pd/Al<sub>2</sub>O<sub>3</sub> and Pd/C may be subject to a little hindrance of their true kinetics at a reaction progress of 2.0 mol<sub>H2</sub>/mol<sub>myrcene</sub>. This latter tends to disappear at a reaction progress of 2.5 mol<sub>H2</sub>/mol<sub>myrcene</sub>.

Overall, comparison of instantaneous STY of this study is allowed and consistent for reaction progresses higher than 2.0. The conclusions drawn in our work can be linked with chemical phenomena.





## Chapter 5. Hydrogenation of carbon dioxide over SA catalysts





## 5. Hydrogenation of carbon dioxide over SA catalysts

### 5.1. Introduction

Atmospheric CO<sub>2</sub> is the main source of carbon for life on earth. It is produced by aerobic organisms and as a result of decay process of organic materials and fermentation. Also, since the industrial revolution, is released due to the use of fossil fuels and its concentration rise in the atmosphere has been related to global warming and ocean acidification. Nonetheless, during decades CO<sub>2</sub> has been used, as refrigerant, food additive or even as a solvent. Even more, in recent years CO<sub>2</sub> has been considered as a source of energy either by its direct reduction into hydrocarbons or by its use in the production of hydrogen.<sup>1</sup> Thus, CO<sub>2</sub> could be no longer considered as an undesirable waste to be reused, but as a driving force for the sustainable future of the chemical industry. In that context, much attention has been paid to CO<sub>2</sub> electro-, photo- or thermocatalytic hydrogenation to various value-added products, such as CO, acetaldehyde, formic acid, methanol, methane, or lower olefins.<sup>2</sup> CO<sub>2</sub> like water is well known to be very stable ( $\Delta G_f^\circ = -396 \text{ kJ.mol}^{-1}$ ). From the energetic point of view, the reduction of CO<sub>2</sub> will require an amount of energy that depends on the downward steps of the carbon oxidation state, from +IV in CO<sub>2</sub> to the value in the target product. Although most hydrogenation reactions are exothermic as shown in Table 5.1 (although no for reverse water gas shift - RWGS reaction), the low energetic level of CO<sub>2</sub> leads to severe limitations of the thermodynamic equilibrium, and some of them are strongly endergonic as for formic acid or formaldehyde formation.<sup>3</sup> According to thermodynamic calculations, CO<sub>2</sub> tends to convert to molecules with high carbon numbers at low temperature and high pressure.<sup>3</sup> However, these reactions are probably limited by kinetics. Thus, designing highly efficient catalysts is critical because CO<sub>2</sub> hydrogenation involves a complex reaction network, which is restricted by thermodynamics and kinetics.

In heterogeneous catalysis, metal-support interactions (MSI), including electronic MSI,<sup>4</sup> can significantly influence the course of the reactions, making MSI modulation one of the few tools able to enhance catalytic performances in terms of activity, selectivity but also stability.<sup>5</sup> In general, the efficiency of MSI tuning rapidly decayed with increasing NP size,<sup>6</sup> and for a single

---

<sup>1</sup> M. Aresta, et al. *Chemical Reviews* **2014**, *114*, 1709-1742.

<sup>2</sup> L. Wang, et al. *Chemical Society Reviews* **2019b**, *48*, 5310-5349.

<sup>3</sup> C. Jia, et al. *Journal of Energy Chemistry* **2016**, *25*, 1027-1037.

<sup>4</sup> C. T. Campbell *Nature Chemistry* **2012**, *4*, 597-598.

<sup>5</sup> T. W. van Deelen, et al. *Nature Catalysis* **2019**, *2*, 955-970.

<sup>6</sup> L. Liu, et al. *Chemical Reviews* **2018**, *118*, 4981-5079.

metal and a given support high electronic MSI are expected for SA catalysts.<sup>7</sup> Unlike for NP, there is a large spatial variation in the bond and coordination environment of SA on the support surface due to support heterogeneities. This can significantly affect catalyst performances.<sup>8</sup>

Table 5.1. Thermodynamics of CO<sub>2</sub> hydrogenation reactions.

Reaction	$\Delta H_{298}$ (kJ.mol <sup>-1</sup> )	$\Delta G_{298}$ (kJ.mol <sup>-1</sup> )	$K^{\ominus}_{298}$
CO <sub>2</sub> + 4 H <sub>2</sub> $\leftrightarrow$ CH <sub>4</sub> + 2 H <sub>2</sub> O	-164.8	-113.5	$7.79 \times 10^{19}$
CO <sub>2</sub> + 3 H <sub>2</sub> $\leftrightarrow$ CH <sub>3</sub> OH + H <sub>2</sub> O	-49.5	3.5	$2.45 \times 10^{-1}$
CO <sub>2</sub> + 3 H <sub>2</sub> $\leftrightarrow$ ½ CH <sub>3</sub> OCH <sub>3</sub> + ¾ H <sub>2</sub> O	-61.3	-4.9	7.15
½ CO <sub>2</sub> + 3 H <sub>2</sub> $\leftrightarrow$ ½ CH <sub>2</sub> CH <sub>2</sub> + 2 H <sub>2</sub> O	-64.0	-28.7	$1.07 \times 10^5$
CO <sub>2</sub> + 3 H <sub>2</sub> $\leftrightarrow$ ½ CH <sub>3</sub> CH <sub>2</sub> OH + ¾ H <sub>2</sub> O	-86.7	-32.4	$4.70 \times 10^5$
CO <sub>2</sub> + 2 H <sub>2</sub> $\leftrightarrow$ HCHO + H <sub>2</sub> O	35.7	55.9	$1.63 \times 10^{-10}$
2 CO <sub>2</sub> + 4 H <sub>2</sub> $\leftrightarrow$ CH <sub>3</sub> COOH + 2 H <sub>2</sub> O	-64.8	-21.6	$6.11 \times 10^3$
CO <sub>2</sub> + H <sub>2</sub> $\leftrightarrow$ CO + H <sub>2</sub> O	41.2	28.6	$9.67 \times 10^{-6}$
CO <sub>2</sub> + H <sub>2</sub> $\leftrightarrow$ HCOOH	14.9	43.5	$2.43 \times 10^{-8}$

The use of atomically dispersed metal for CO<sub>2</sub> hydrogenation has recently been the subject of several studies (Table 5.2), and high selectivity towards a single product are most of the time reached on low loading catalysts (metal loading < 1 % w/w). It is worth to notice that thermal reduction of CO<sub>2</sub> has been mainly studied over SA supported on reducible oxides, such TiO<sub>2</sub>, CeO<sub>2</sub>, In<sub>2</sub>O<sub>3</sub> and ZnO<sub>2</sub> and just few reports have been published on carbon-based SAC. The general trend observed is that CO is produced with isolated SA due to the fact that they bind CO weaker than metallic NP, and CH<sub>4</sub> production occurs at NP surface. This means that SA and NP composed of the same metal on the same support can exhibit unique selectivity in a parallel reaction pathway: RWGSR preferentially occurs at SA, while methanation at NP. However, a noticeable exception can be observed in the case of RuSA/CeO<sub>2</sub> catalysts,<sup>13,14</sup> for which two different research groups reported totally different selectivity.

<sup>7</sup> P. Hu, et al. *Angewandte Chemie International Edition* **2014**, 53, 3418-3421.

<sup>8</sup> Z. Kou, et al. *Nanoscale Horizons* **2020**, 5, 757-764.

Table 5.2. Catalytic hydrogenation of CO<sub>2</sub> on supported SA catalysts.

Catalyst	Reaction conditions	Conversion (%)	Selectivity (%)	Ref.
1.8% Co <sub>SA</sub> /SiO <sub>2</sub>	6 L·g <sub>cat</sub> <sup>-1</sup> hr <sup>-1</sup> ; 10 bar; CO:H <sub>2</sub> = 1:4; 400 °C	7	95 (CO)	<sup>9</sup>
10% Ni <sub>SA</sub> /MgO	30 bar (72% H <sub>2</sub> , 18% CO <sub>2</sub> , 10% Ar for balance); 300 °C	< 3	100 (CO)	<sup>10</sup>
0.1% Ni <sub>SA</sub> /N-C <sup>a)</sup>	27 L·g <sub>cat</sub> <sup>-1</sup> hr <sup>-1</sup> ; 1 bar; CO:H <sub>2</sub> = 1:4 (He as inert); 500 °C	14.5	96 (CO)	<sup>11</sup>
0.1% Ru <sub>SA</sub> /Al <sub>2</sub> O <sub>3</sub> <sup>b)</sup>	1 bar (15% H <sub>2</sub> , 5% CO <sub>2</sub> , He for balance); 350 °C	3	84 (CO)	<sup>12</sup>
0.5% Ru <sub>SA</sub> /CeO <sub>2</sub>	1 bar; CO:H <sub>2</sub> = 1:4 (N <sub>2</sub> as inert); 260 °C	< 5	98 (CO)	<sup>13</sup>
0.89% Ru <sub>SA</sub> /CeO <sub>2</sub>	4.8 L g <sub>cat</sub> <sup>-1</sup> hr <sup>-1</sup> ; 1 bar; CO:H <sub>2</sub> = 1:4 (He as inert); 260 °C	28	100 (CH <sub>4</sub> )	<sup>14</sup>
0.01% Ru/FeO <sub>x</sub>	1.2 L·g <sub>cat</sub> <sup>-1</sup> hr <sup>-1</sup> ; 1 bar; CO:H <sub>2</sub> = 1:1; 260 °C	4	100 (CO)	<sup>15</sup>
0.6% Ru <sub>SA</sub> /h-BN <sup>c)</sup>	GHSV = 18 000 h <sup>-1</sup> ; 10 bar; CO:H <sub>2</sub> = 1:4; 350 °C	29	93.5 (CH <sub>4</sub> )	<sup>16</sup>
0.4% Ru <sub>SA</sub> /LDH <sup>d)</sup>	1.0 M NaHCO <sub>3</sub> ; 20 bar; CO:H <sub>2</sub> = 1:1; 100 °C	-	100 (formate)	<sup>17</sup>
0.5% Rh <sub>SA</sub> /TiO <sub>2</sub> (60% SA)	1 bar; CO:H <sub>2</sub> = 1:4 (N <sub>2</sub> as inert); 200 °C	-	35 (CO)	<sup>18</sup>
0.2% Rh <sub>SA</sub> /TiO <sub>2</sub>	1 bar; CO:H <sub>2</sub> = 1:1 (He as inert); 200 °C		86 (CO)	
0.5% Pd <sub>SA</sub> /Al <sub>2</sub> O <sub>3</sub>	1 bar (15% H <sub>2</sub> , 5% CO <sub>2</sub> , He for balance); 400 °C	18	67 (CO)	<sup>19</sup>
1% Pd <sub>SA</sub> /CNT	1 bar (15% H <sub>2</sub> , 5% CO <sub>2</sub> , He for balance); 350 °C	inactive	-	
0.1% Pd <sub>SA</sub> /Fe <sub>3</sub> O <sub>4</sub>	60 L g <sub>cat</sub> <sup>-1</sup> h <sup>-1</sup> ; 1 bar; CO:H <sub>2</sub> = 1:4; 300 °C	0.2	100 (ethanol)	<sup>20</sup>
0.2% Re <sub>SA</sub> /CeO <sub>2</sub> <sup>e)</sup>	in 1,4-dioxane; 10 bar CO <sub>2</sub> – 50 bar H <sub>2</sub> ; 150 °C	-	95 (CO)	<sup>21</sup>
0.7% Ir <sub>SA</sub> /CeO <sub>2</sub>	10 bar (76% H <sub>2</sub> , 19% CO <sub>2</sub> , Ar for balance); 300 °C	2.9	>99 (CO)	<sup>22</sup>
0.1% Ir <sub>SA</sub> /TiO <sub>2</sub>	1 bar (45% H <sub>2</sub> , 45% CO <sub>2</sub> , He for balance); 350 °C	2	100 (CO)	<sup>23</sup>
1.25% Ir <sub>SA</sub> /AP-POP <sup>f)</sup>	1.0 mol/L aqueous triethylamine, 30 bar H <sub>2</sub> , 30 bar CO <sub>2</sub> , 120 °C	-	100 (formate)	<sup>24</sup>
0.05% Pt <sub>SA</sub> /CeO <sub>2</sub>	48 L g <sub>cat</sub> <sup>-1</sup> hr <sup>-1</sup> ; 1 bar (62.5% vol. H <sub>2</sub> , 5% vol. CO <sub>2</sub> , N <sub>2</sub> for balance); 340 °C	57	100 (CO)	<sup>25</sup>
0.2% Pt/MoS <sub>2</sub>	in DMF; 32 bar; CO <sub>2</sub> :H <sub>2</sub> = 1:3; 210 °C	-	93 (methanol)	<sup>26</sup>

<sup>a)</sup> Nitrogen-doped carbon. <sup>b)</sup> The catalyst is not stable and Ru NP are progressively formed leading to increased methane production. <sup>c)</sup> h-BN = porous hexagonal boron nitride. <sup>d)</sup> LDH = layered double hydroxide. <sup>e)</sup> A 1% Re/CeO<sub>2</sub> containing mixture of clusters and SA produces selectively methanol. <sup>f)</sup> AP-POP = porous organic polymer with aminopyridine functionalities.

<sup>9</sup> J. D. Jimenez, et al. *ChemCatChem* **2020**, *12*, 846-854.

<sup>10</sup> M.-M. Millet, et al. *Journal of the American Chemical Society* **2019**, *141*, 2451-2461.

<sup>11</sup> H. Chen, et al. *Journal of Materials Chemistry A* **2020**, *8*, 2364-2368.

<sup>12</sup> J. H. Kwak, et al. *ACS Catalysis* **2013a**, *3*, 2449-2455.

<sup>13</sup> A. Aitbekova, et al. *Journal of the American Chemical Society* **2018**, *140*, 13736-13745.

<sup>14</sup> Y. Guo, et al. *ACS Catalysis* **2018**, *8*, 6203-6215.

<sup>15</sup> D. Zhang, et al. *Chinese Journal of Catalysis* **2018**, *39*, 157-166.

<sup>16</sup> M. Fan, et al. *ACS Catalysis* **2019**, *9*, 10077-10086.

<sup>17</sup> K. Mori, et al. *ACS Catalysis* **2017**, *7*, 3147-3151.

<sup>18</sup> J. C. Matsubu, et al. *Journal of the American Chemical Society* **2015**, *137*, 3076-3084.

<sup>19</sup> J. H. Kwak, et al. *ACS Catalysis* **2013b**, *3*, 2094-2100.

<sup>20</sup> F. J. Caparrós, et al. *ChemCatChem* **2018**, *10*, 2365-2369.

<sup>21</sup> K. W. Ting, et al. *ACS Catalysis* **2019**, *9*, 3685-3693.

<sup>22</sup> S. Li, et al. *Angewandte Chemie International Edition* **2017**, *56*, 10761-10765.

<sup>23</sup> X. Chen, et al. *ACS Catalysis* **2017**, *7*, 4613-4620.

<sup>24</sup> X. Shao, et al. *Chem* **2019**, *5*, 693-705.

<sup>25</sup> Y. Wang, et al. *ACS Applied Energy Materials* **2018**, *1*, 6781-6789.

<sup>26</sup> H. Li, et al. *Nature Nanotechnology* **2018a**, *13*, 411-417.



On Ru<sub>SA</sub>/CeO<sub>2</sub> catalysts prepared by Ru redispersion from Ru NP supported on CeO<sub>2</sub>, the Ru-O shell showed a coordination number of 5.5, and this catalyst selectively produced CO at 260 °C.<sup>13</sup> On Ru<sub>SA</sub>/CeO<sub>2</sub> catalysts prepared on nanowires containing significant amount of oxygen vacancies, the Ru-O shell showed a coordination number of 4.5, and this catalyst selectively produced CH<sub>4</sub> at 260 °C.<sup>14</sup> These results highlight the importance of the coordination environment of SA and the presence of oxygen vacancies on reducible supports, which can actively participate to the reaction.<sup>27</sup> As far as activity is concerned, the study of Zhang *et al.* who compared a Ru<sub>SA</sub>/CeO<sub>2</sub> catalyst with Ru<sub>NP</sub>/CeO<sub>2</sub> (Ru NP size = 1.2 and 4 nm) showed that these three catalyst are very selective for methane ( $S_{CH_4} \approx 100\%$ ) and the activity order is Ru<sub>NP</sub>-1.2nm/CeO<sub>2</sub> > Ru<sub>SA</sub>/CeO<sub>2</sub> > Ru<sub>NP</sub>-4nm/CeO<sub>2</sub>. Finally, the stability of SA under reaction conditions can also be an issue. This parameter was evaluated for Ni<sub>SA</sub>/MgO,<sup>10</sup> Pt<sub>SA</sub>/CeO<sub>2</sub>,<sup>25</sup> Ru<sub>SA</sub>/CeO<sub>2</sub>,<sup>13</sup> Ru<sub>SA</sub>/TiO<sub>2</sub><sup>13</sup> and Ru<sub>SA</sub>/Al<sub>2</sub>O<sub>3</sub><sup>12,13</sup> catalysts. If nickel and platinum catalysts show good stability under CO<sub>2</sub> hydrogenation conditions, ruthenium catalysts are prone to deactivation whatever the support used. It is therefore needed to tune binding strength between SA and supports because a suitable interaction is required to not only prevent SA agglomeration into NP, but also to perform high catalytic activity and selectivity. Typically, the fully occupied bonding orbitals correspond to the stability between the SA and the support, while the free electrons near Fermi level caused by the unsaturated coordination can be responsible for the catalytic activity.<sup>28</sup> In that context, the use of vacancy containing support should offer interesting perspectives.<sup>29</sup>

In this chapter we tested in the CO<sub>2</sub> reduction reaction a series of SA catalysts (Ru, Pt, Pd, Ni, Co and Cu) supported on carbon nanotubes prepared by stabilization of metal SA on vacancies in the surface of CNT.

---

<sup>27</sup> D. C. Upham, et al. *Catalysis Science & Technology* **2015**, 5, 1783-1791.

<sup>28</sup> Y. Wang, et al. *Progress in Natural Science: Materials International* **2019a**, 29, 256-264.

<sup>29</sup> G. S. Parkinson *Catalysis Letters* **2019**, 149, 1137-1146.

## 5.2. Results and discussion

First, 1% $M_{SA}/CNT_{OX-400}$  ( $M=Pt, Ru, Pd, Ni, Co$  and  $Cu$ ) were tested in the hydrogenation of carbon dioxide. The characterization of these catalysts is reported in *Chapter 3* (See *Section 3.4 Synthesis of supported single atom catalysts (SAC)*), and the presence single metallic atoms dispersed all over the surface of CNT was evidenced. The  $CO_2$  hydrogenation was conducted under methanation conditions ( $CO_2/H_2 = 1/4$ ) in single fixed-bed reactor configuration under 6.1 bar, at either 260, 300 or 340 °C, and with a GHSV of 16500 mL/h·g. Under such conditions, the  $CO_2$  conversion does not exceed 10 %, and we are thus comparing catalysts far away from the thermodynamic equilibrium. The apparent and instantaneous activity of the catalysts is expressed in moles of  $CO_2$  consumed per mole of metal and per hour, being equivalent to an instantaneous Site Time Yield (“STY” in the following). It is worth noting that two reactions,  $CO_2$  methanation and RWGS, run simultaneously under the present conditions, and the selectivity could depend strongly on the nature of the dispersed metallic phase, metal crystallite size, metallic loading, temperature or additives.

The main results of  $CO_2$  reduction with 1% $M_{SA}/CNT_{OX-400}$  catalysts are summarized on Figure 5.1 and Table 5.3.

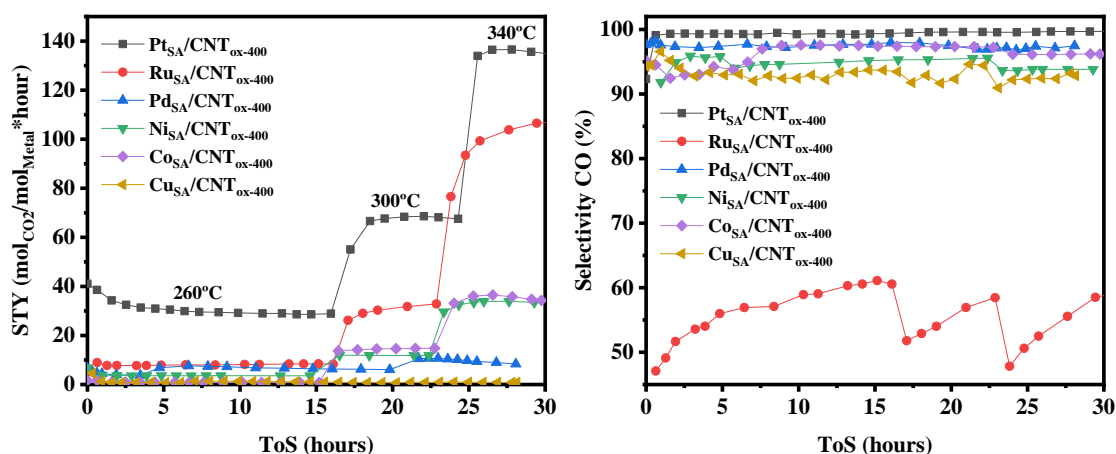


Figure 5.1. STY and selectivity of 1% $M_{SA}/CNT_{ox-400}$  at 260 °C, 300 °C and 340 °C.

The reaction profiles show the evolution of STY with time on stream (ToS) at different temperatures. All samples were active in  $CO_2$  reduction and as expected, an increase of the STY with temperature was observed. The apparent activation energies ranged between 21 and 86 kJ/mol. Overall, catalytic activity was observed to be the greatest for platinum and the poorest

for Cu. According to the activity values, metals can be ordered from more active to less active, in the following order  $\text{Pt} > \text{Ru} > \text{Ni} \sim \text{Co} > \text{Pd} > \text{Cu}$ . As we can see, the impact of the nature of the metal phase plays a role in the general catalytic performance. For all the metals, the main product was CO with a selectivity between 92-99% excluding for Ru, which produced methane in ~43%. Interestingly in this sample, as can be seen in figure 5.1b, the production of methane is favored with each increase in temperature, however the production to CO increase after a few hours of reaction.

Table 5.3. Catalytic performances of the produced catalysts on  $\text{CO}_2$  hydrogenation.

Catalyst	ICP wt%	T (°C)	$\text{CO}_2$ conversion (%) <sup>a)</sup>	STY ( $\text{mol}_{\text{CO}_2}/\text{mol}_{\text{M.h}}$ ) <sup>a)</sup>	CO sel. (%) <sup>a)</sup>	$\text{CH}_4$ sel. (%) <sup>a)</sup>	$E_a$ (kJ/mol)
$\text{Pt}_{\text{SA}}/\text{CNT}_{\text{ox-400}}$	0.68	260	0.92	29.81	99.31	0.68	50.86
		300	2.05	66.00	99.57	0.43	
		340	4.14	133.35	99.72	0.28	
$\text{Ru}_{\text{SA}}/\text{CNT}_{\text{ox-400}}$	0.95	260	0.68	8.07	56.84	43.16	86.69
		300	2.5	30.00	54.8	45.18	
		340	8.70	103.90	57.1	42.86	
$\text{Pd}_{\text{SA}}/\text{CNT}_{\text{ox-400}}$	0.98	260	0.34	4.20	98.95	1.05	21.12
		300	0.55	6.76	97.59	2.41	
		340	0.81	9.89	97.11	8.88	
$\text{Ni}_{\text{SA}}/\text{CNT}_{\text{ox-400}}$	1.09	260	0.60	3.65	94.80	5.19	75.04
		300	1.96	11.87	95.04	4.96	
		340	5.51	33.30	93.75	6.25	
$\text{Co}_{\text{SA}}/\text{CNT}_{\text{ox-400}}$	1.27	260	0.19	0.99	93.50	6.50	28.15
		300	2.29	11.93	97.39	2.61	
		340	6.74	35.09	96.16	3.84	
$\text{Cu}_{\text{SA}}/\text{CNT}_{\text{ox-400}}$	1.21	260	0.14	0.82	94.55	5.45	76.17
		300	0.18	1.08	92.75	7.25	
		340	0.15	0.91	92.82	7.18	

a) Average value

In fact, noble metals such as Pd, Pt or Ru, are generally preferred for higher value products such as alcohols<sup>21</sup> or to be used as promoter in Ni-catalyzed CO<sub>2</sub> methanation<sup>30</sup> or Co-catalyzed CO<sub>2</sub>-Fischer-Tropsch synthesis.<sup>31</sup> Surprisingly, Pd shows a poor conversion (0.8 % at 340 °C). Some reports inform about the performance of 0.01%Pd<sub>SA</sub>/TiO<sub>2</sub> in RWGS with 100 % yield to CO at 400 °C. These results indicate that an atomically, or near-atomically dispersed Pd catalyst would not be able to homolytically activate H<sub>2</sub> to form the formate intermediate; instead, Pd<sub>1</sub> was capable to activate dihydrogen heterolytically to yield carboxyl intermediate, explaining the selectivity toward CO.<sup>32</sup>

Nickel and cobalt had a similar STY but the last had a bit higher selectivity to CO (93 and 96 %, respectively). Actually, Ni has been widely used for CO<sub>2</sub> hydrogenation specially for methanation. Contrarily to the present study, Ni<sub>SA</sub> supported on silica allows > 70 % conversion of CO<sub>2</sub> at 20 bar and 300 °C producing exclusively CH<sub>4</sub>, pointing out to the importance of the support.<sup>33</sup> On the other hand, our results with Co are in good agreement with recently published reports on Co/γ-Mo<sub>2</sub>N nanocluster catalyst, with an average of four Co atoms in each Co cluster, exhibiting selectivity > 98 % to CO.<sup>34</sup> Cu/oxide has been one of the most extensively studied metal catalysts for the RWGS reaction.<sup>35</sup> Here, the SA sample showed the lowest activity among all the other active phases tested. To date, there are no other reports using copper single atoms for thermocatalytic CO<sub>2</sub> reduction. According to DFT calculations, the adsorption energy of the CO<sub>2</sub> molecule over Cu<sub>SA</sub>/g-C<sub>3</sub>N<sub>4</sub> was found to be 0.17 eV, lower compared to Fe (0.4 eV) and Ni (0.21 eV).<sup>36</sup> Additionally, the activation energies of the CO<sub>2</sub> hydrogenation to formic acid on M<sub>SA</sub>/g-C<sub>3</sub>N<sub>4</sub> was found to be 0.22, 0.6 and 0.7 eV for Fe<sub>SA</sub>/g-C<sub>3</sub>N<sub>4</sub>, Co<sub>SA</sub>/g-C<sub>3</sub>N<sub>4</sub> and Cu<sub>SA</sub>/g-C<sub>3</sub>N<sub>4</sub>, respectively. Another investigation predicts that the activation barrier of the rate-limiting step of the RWGS reaction on Cu<sub>SA</sub>@Mo<sub>2</sub>C is higher than for Cu<sub>4</sub>@Mo<sub>2</sub>C, therefore the latter would be more effective for this reaction.<sup>37</sup> Nonetheless, many groups have presented theoretical studies on the potential of this metal in electrochemical reduction of CO<sub>2</sub> to formic acid or methanol.<sup>38,39,40</sup>

<sup>30</sup> S. Kikkawa, et al. *The Journal of Physical Chemistry C* **2019**, 123, 23446-23454.

<sup>31</sup> D. Chakrabarti, et al. *Industrial & Engineering Chemistry Research* **2015**, 54, 1189-1196.

<sup>32</sup> N. C. Nelson, et al. *Angewandte Chemie International Edition* **2020**, doi:10.1002/anie.202007576.

<sup>33</sup> W. L. Vrijburg, et al. *Journal of Catalysis* **2020**, 382, 358-371.

<sup>34</sup> S. Yao, et al. *ACS Catalysis* **2019**, 9, 9087-9097.

<sup>35</sup> D. L. Jurković, et al. *Chemical Engineering & Technology* **2017**, 40, 973-980.

<sup>36</sup> K. Homlamai, et al. *Applied Surface Science* **2020**, 499, 143928.

<sup>37</sup> H. J. Jing, et al. *Journal of Physical Chemistry C* **2019**, 123, 1235-1251.

<sup>38</sup> J. Zhao, et al. *Journal of Physical Chemistry C* **2018**, 122, 19712-19721.

<sup>39</sup> D. N. Sredojevic, et al. *ChemistrySelect* **2018**, 3, 2631-2637.

<sup>40</sup> Z. L. Zhao, et al. *Journal of Physical Chemistry C* **2019**, 123, 4380-4387.

In terms of stability, the catalysts were analyzed before and after catalysis. HRTEM micrographs (*Chapter 3, Figure 3.27*) prove the existence of single atom species before reaction. After 30 h on stream at 6.1 bar of pressure, the formation of particles was evidenced for all the samples (*Figure 5.2*). This result is not surprising knowing that even under softer reductive conditions, clusters are formed after one hour at 1 bar of  $H_2/N_2$  and 300 °C for  $Rh_{SA}/TiO_2$  or 400 °C for  $Ni_{SA}/hydroxyapatite$ .<sup>41,42</sup> The sintering of SA is a key factor to overcome for such applications, reason why it is critically important to seek for methods to improve their durability.

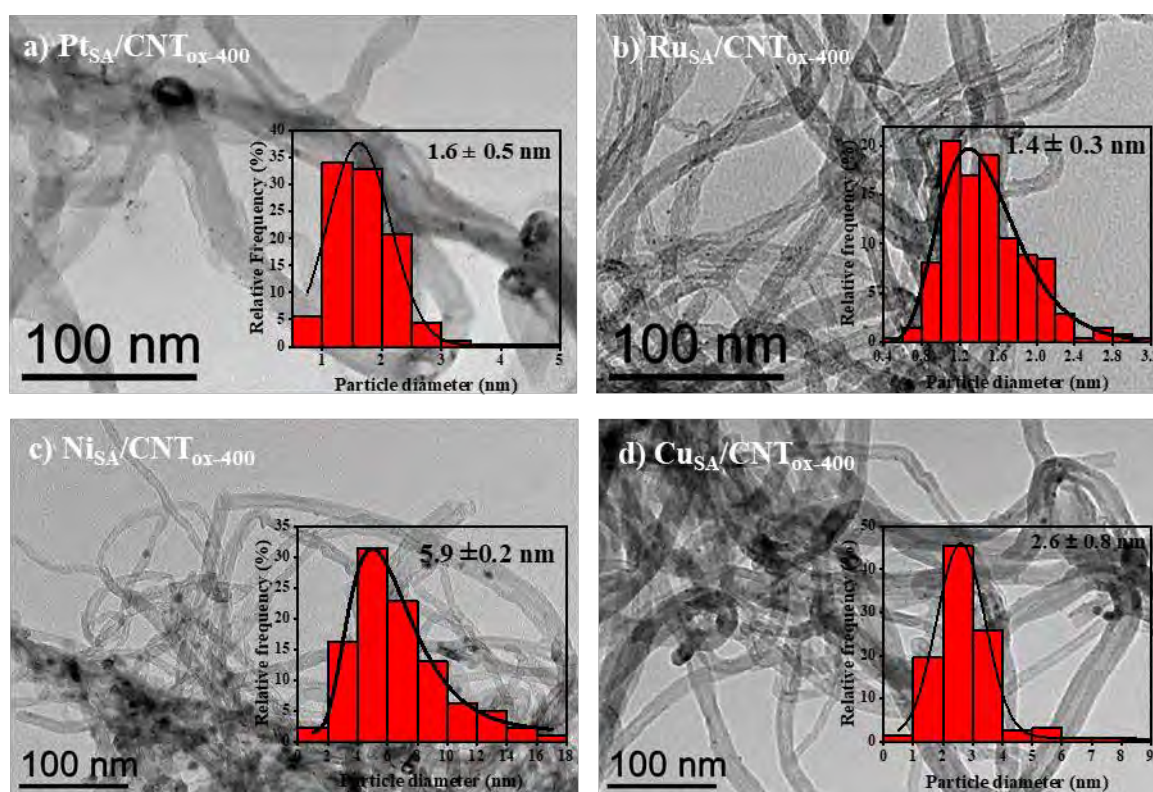


*Figure 5.2. TEM micrographs 1% $M_{SA}/CNT_{ox-400}$  catalysts after catalysis. a) Pt, b) Ru, c) Ni and d) Cu.*

The action of alkali promoters in heterogeneous catalysis has been broadly reviewed,<sup>43,44,45</sup> and it was shown that they can contribute to: i) increase the selectivity or specificity; ii) increase the activity; and more importantly iii) prolong the effective lifetime of the catalyst.<sup>46</sup> Their

<sup>41</sup> Y. Tang, et al. *Nature Communications* **2019**, *10*, 4488.

<sup>42</sup> M. Akri, et al. *Catalysts* **2020**, *10*, 630.

<sup>43</sup> M. Zhu, et al. *Transactions of Tianjin University* **2020**, *26*, 172-187.

<sup>44</sup> J. R. Morse, et al. *Journal of CO2 Utilization* **2020**, *35*, 38-46.

<sup>45</sup> F. Meshkani, et al. *International Journal of Green Energy* **2018**, *15*, 28-36.

<sup>46</sup> H. C. Wu, et al. *Catalysis Science & Technology* **2015**, *5*, 4154-4163.

modes of action includes: i) intrinsic catalytic effect of the alkali; ii) creation of basic sites; iii) neutralization of acidic centers; iv) modification of the electronic properties of the catalyst surface by charge transfer from alkali metal to transition metal, which brings about a higher electron density on the transition metal; v) reduction of the volatility of the active component through compound formation; and vi) prevention of phase transformations. For CO<sub>2</sub> methanation, various studies have shown that alkali addition to Ni or Ru catalysts supported on oxides contributes to an improvement of the catalytic performances.<sup>47</sup> This was attributed to the enhancement of the CO<sub>2</sub> adsorption and activation thanks to surface basicity of the supports or to modification of the local electron density on the metal. In the case of SA catalysis, it has been shown that the addition of alkali to Pt<sup>48</sup> or Au<sup>49</sup> SA has a beneficial influence on their performances for the water-gas shift reaction thanks to SA stabilization through nearby Na-O<sub>x</sub> moieties. Therefore, we decided to treat the prepared M<sub>SA</sub>/CNT<sub>ox-400</sub> with NaOH. With a simple aqueous impregnation, we introduce 2 equivalents of Na per mol of metal. We performed XPS analyses avoiding air exposure on sample Ru<sub>SA-Na</sub>/CNT<sub>ox-400</sub> (Figure 5.3).

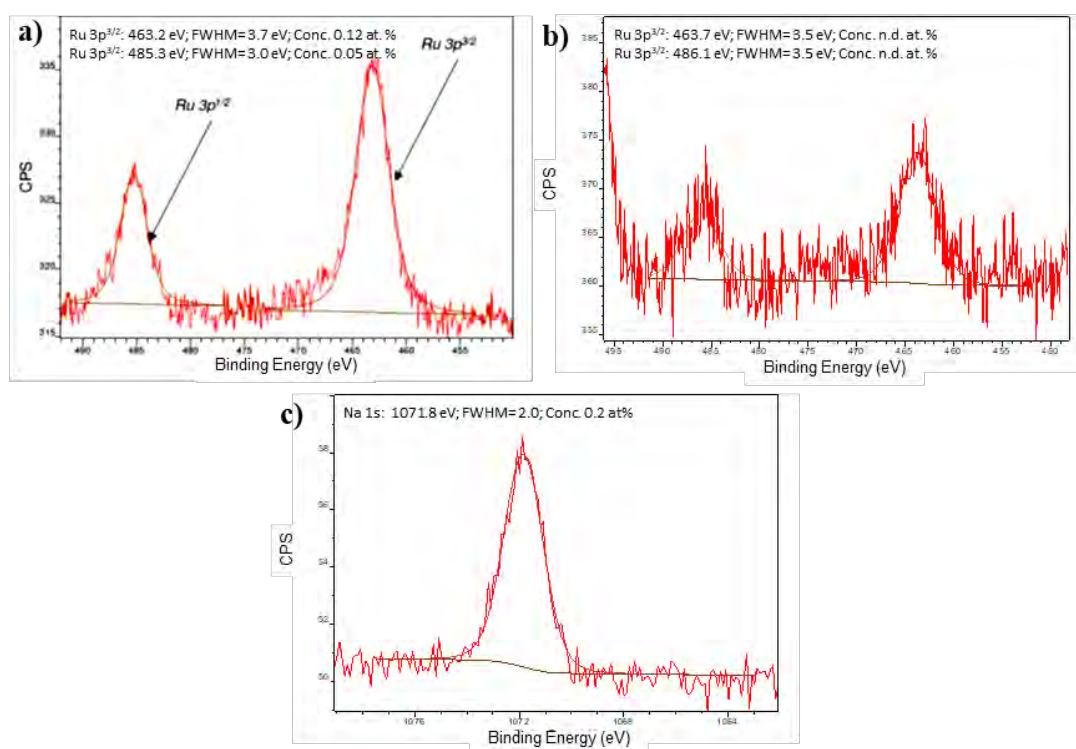


Figure 5.3. a) Ru 3p XPS spectra of Ru<sub>SA</sub>/CNT<sub>ox-400</sub> b) Ru 3p XPS spectra of Ru<sub>SA-Na</sub>/CNT<sub>ox-400</sub> c) Na 1s XPS spectra of Ru<sub>SA-Na</sub>/CNT<sub>ox-400</sub>.

<sup>47</sup> A. Petala, et al. *Applied Catalysis B: Environmental* **2018**, 224, 919-927.

<sup>48</sup> M. Yang, et al. *Journal of the American Chemical Society* **2015**, 137, 3470-3473.

<sup>49</sup> M. Yang, et al. *Science* **2014**, 346, 1498.



The signal of Na 1s was easily identified at 1071.8 eV, confirming the effective introduction of Na in the sample. Ru 3p binding energy were at 463.7 and 486.1 eV compared to 463.2 and 485.3 eV for Ru<sub>SA</sub>/CNT<sub>ox-400</sub>. The electronic state of Ru indicates an electron-deficient character after Na impregnation. This points to the absence of charge transfer from Na to Ru. This result is not surprising if we consider the work functions of Na, Ru and C, which should favor a charge transfer from Na to the carbon support. It is important to indicate that the further treatment with NaOH did not change either the metallic loading or the nature of the active phase. No nanoparticles were found after impregnation, ensuring the permanence of SA species on the support (Figure 5.4).

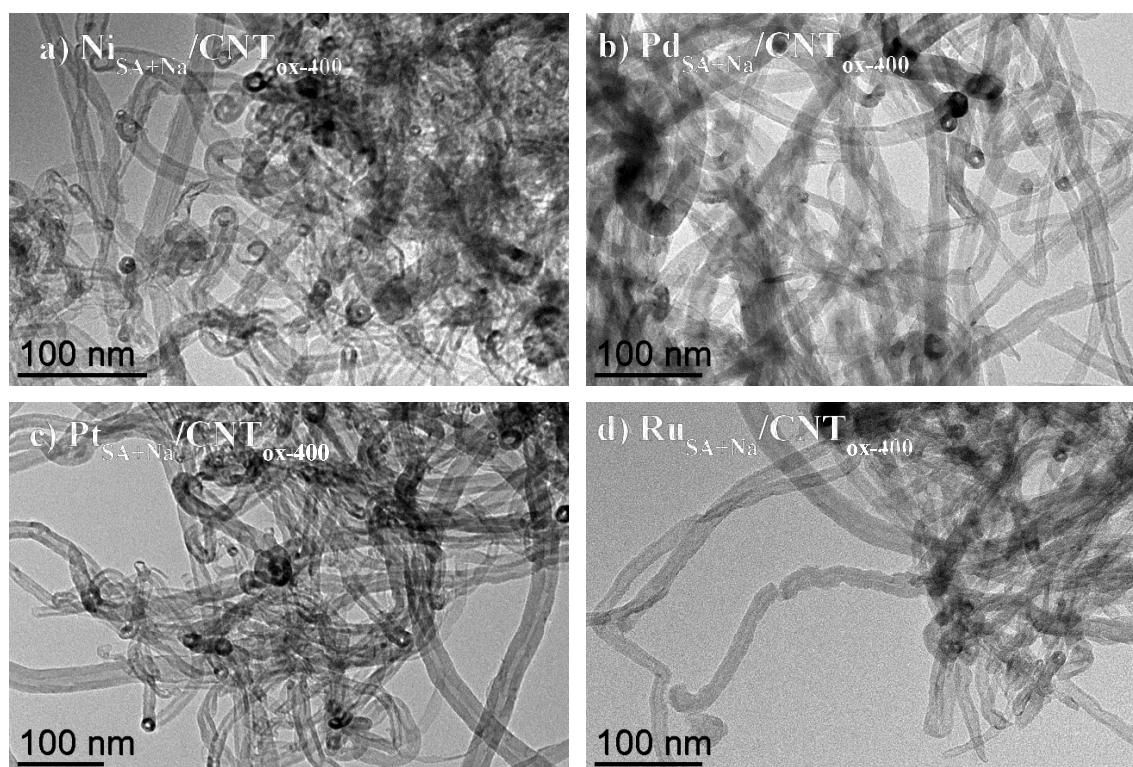


Figure 5.4. TEM micrographs 1% $M_{SA+Na}/CNT_{ox-400}$  catalysts before catalysis. a) Ni, b) Pd, c) Pt and d) Ru.

We noticed that the addition of Na as promoter had a very positive impact on the STY, for all samples (Table 5.4). Contrarily to Pt-Na/ZrO<sub>2</sub> catalyst,<sup>50</sup> sodium doping on Pt catalyst increased the overall catalysts activity dramatically. Changes can be seen comparing Pt<sub>SA</sub>/CNT<sub>ox-400</sub> and Pt<sub>SA-Na</sub>/CNT<sub>ox-400</sub> where in average, STY increased 8 times regardless the temperature. The stability of the catalyst is also very good (Figure 5.5).

<sup>50</sup> M. Martinelli, et al. *International Journal of Hydrogen Energy* **2020**, 45, 18490-18501.

Table 5.4. Catalytic performances of the 1% $M_{SA-Na}/CNT_{ox-400}$  catalysts on  $CO_2$  hydrogenation.

Catalyst	T (°C)	CO <sub>2</sub> conversion (%) <sup>a)</sup>	STY (mol <sub>CO2</sub> /mol <sub>M</sub> .h) <sup>a)</sup>	CO sel. (%) <sup>a)</sup>	CH <sub>4</sub> sel. (%) <sup>a)</sup>	E <sub>a</sub> (kJ/mol)
Pt <sub>SA-Na</sub> /CNT <sub>ox-400</sub>	260	7.6	246.0	99.8	0.2	46.7
	300	21.4	688.4	99.9	0.1	
	340	30.1	970.5	99.9	0.1	
Ru <sub>SA-Na</sub> /CNT <sub>ox-400</sub>	260	1.6	20.0	85.5	14.5	85.6
	300	7.9	97.1	85.9	14.0	
	340	20.7	252.3	80.3	19.7	
Pd <sub>SA-Na</sub> /CNT <sub>ox-400</sub>	260	1.5	18.5	98.7	1.3	40.5
	300	2.9	35.2	99.6	0.4	
	340	5.5	66.5	99.7	0.3	
Ni <sub>SA-Na</sub> /CNT <sub>ox-400</sub>	260	1.2	7.3	94.6	5.4	65.4
	300	3.5	22.0	93.7	6.3	
	340	8.1	50.7	95.5	4.5	
Co <sub>SA-Na</sub> /CNT <sub>ox-400</sub>	260	0.1	0.8	90.5	9.5	90.3
	300	0.6	3.3	96.7	3.3	
	340	2.4	12.6	98.2	1.8	
Cu <sub>SA-Na</sub> /CNT <sub>ox-400</sub>	260	0.4	2.3	97.5	2.5	n.d. <sup>b)</sup>
	300	0.6	3.8	97.1	2.9	
	340	0.4	2.6	97.5	2.5	
a)	Average value					
b)	Could not be accurately determined due to low conversion obtained					

The Ru<sub>SA-Na</sub>/CNT<sub>ox-400</sub> catalyst performed also very well in terms of STY compared to published performances of Ru/C catalysts containing metallic NP.<sup>51</sup> Thus, a 0.5%Ru/CNF catalyst (CNF = carbon nanofibers, Ru<sub>NP</sub> = 1.6 nm) has a STY of 1080 mol $_{CO_2}$ /mol $_{Ru}$ .h at 400 °C<sup>52</sup> compared to 247 mol $_{CO_2}$ /mol $_{Ru}$ .h for the 1%Ru<sub>SA-Na</sub>/CNT<sub>ox-400</sub> catalyst at 340 °C, and a 3%Ru/CB catalyst (Ru<sub>NP</sub> = 1.25 nm) has a STY of 7 mol $_{CO_2}$ /mol $_{Ru}$ .h at 240 °C, compared to 20 mol $_{CO_2}$ /mol $_{Ru}$ .h for the 1%Ru<sub>SA-Na</sub>/CNT<sub>ox-400</sub> catalyst at 260 °C. Additionally, Ru selectivity to CO improved significantly from 56 % to 86 % after doping.

<sup>51</sup> L. Roldán, et al. *ChemCatChem* **2015**, 7, 1347-1356.

<sup>52</sup> V. Jiménez, et al. *Applied Catalysis A: General* **2010**, 390, 35-44.

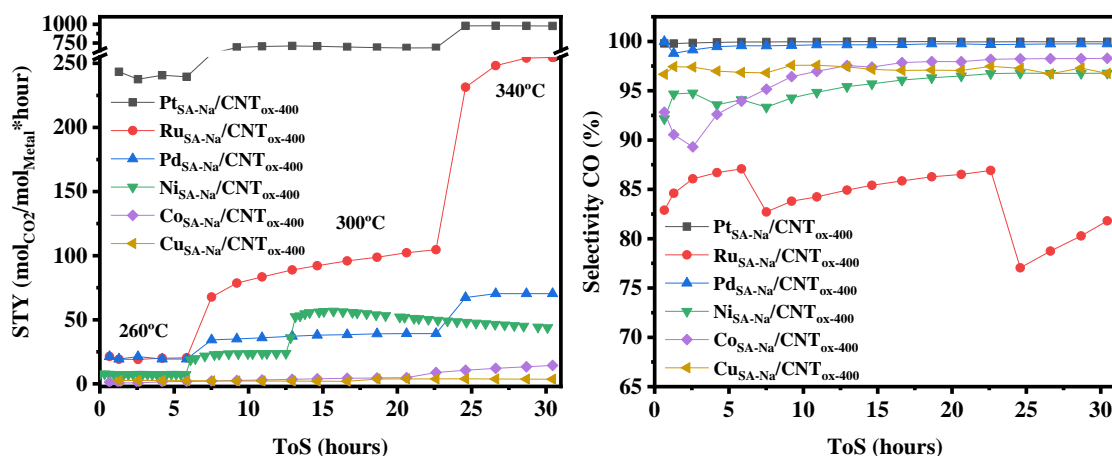


Figure 5.5. STY and selectivity of 1% $M_{SA-Na}/CNT_{ox-400}$  at 260 °C, 300 °C and 340 °C.

In the case of nickel, despite the STY increase upon Na addition, the stability of the catalyst is not optimal since after some hours on stream at 340 °C the STY of the  $Ni_{SA-Na}/CNT_{ox-400}$  catalyst reached the one of  $Ni_{SA}/CNT_{ox-400}$ . The catalyst deactivation may be due to the formation of Ni NP (mean size =  $5.5 \pm 2.5$  nm, see Figure 5.6e) during the reaction as shown by TEM observations of the catalyst after reaction. Stability issues have been already reported for  $Ni_{NP}$  supported on CNT.<sup>53</sup> Structural changes also occur in other samples such as 1% $Ru_{SA-Na}/CNT_{ox-400}$  catalyst since the presence of Ru clusters after reaction was detected by TEM observations (mean size =  $1.1 \pm 0.3$  nm, see Figure 5.6d). It is however worth noting that the size of these NP is lower than in the case of the 1% $Ru_{SA}/CNT_{ox-400}$  catalyst (mean size =  $1.4 \pm 0.3$  nm, see Figure 5.6c), pointing to a better stabilization for the Na-doped sample. For Pt, Ru and Ni catalysts, the small variations of activation energies between the promoted and unpromoted catalysts (Figure 5.7) imply that the presence of sodium does not change either the reaction mechanism or the rate limiting step, in accordance with published results on alkali promoted Ni catalysts.<sup>47,54</sup> This was not the case for the Co and Pd catalysts, for which a large increase of the activation energies was observed.

<sup>53</sup> Y. Feng, et al. *Integrated Ferroelectrics* **2014**, 151, 116-125.

<sup>54</sup> T. K. Campbell, et al. *Applied Catalysis* **1989**, 50, 189-197.



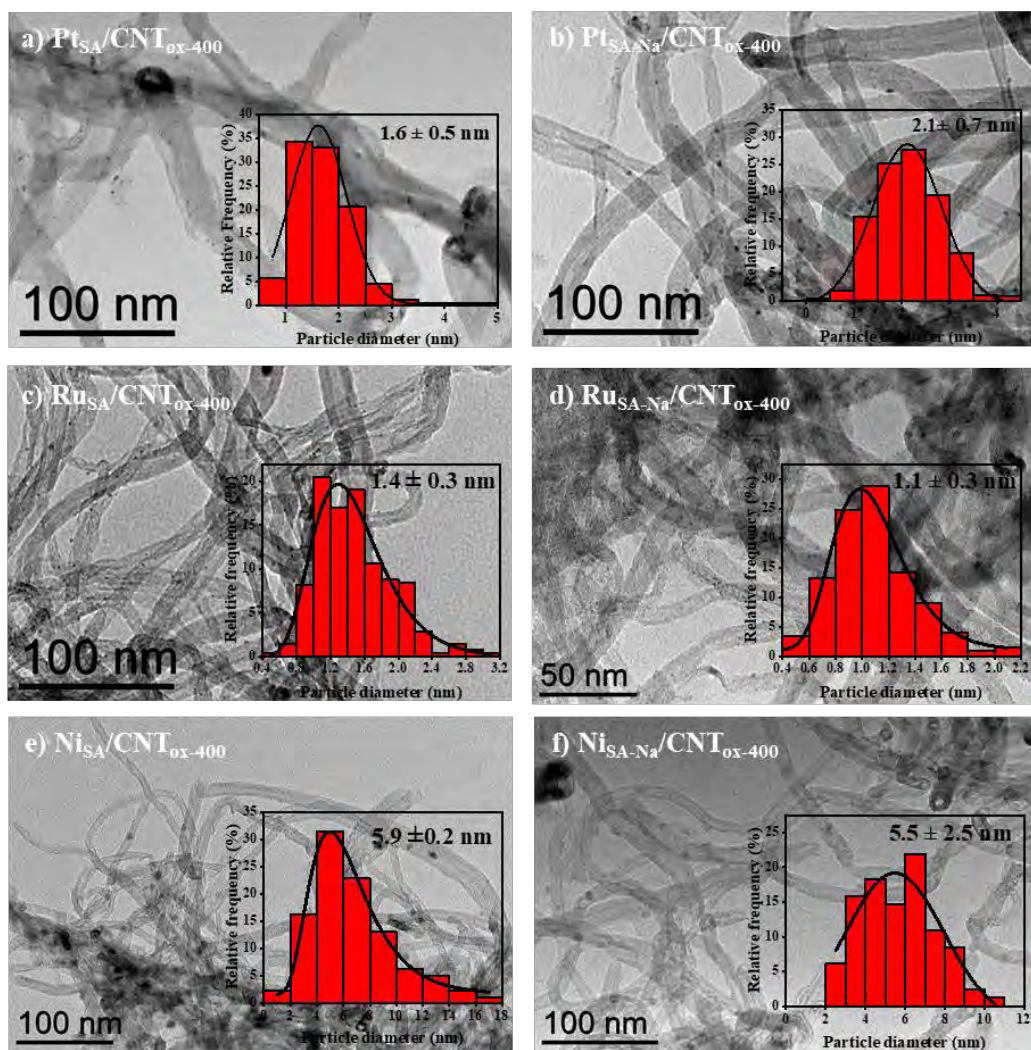


Figure 5.6. TEM micrograph of Ru, Pt and Ni after catalysis.

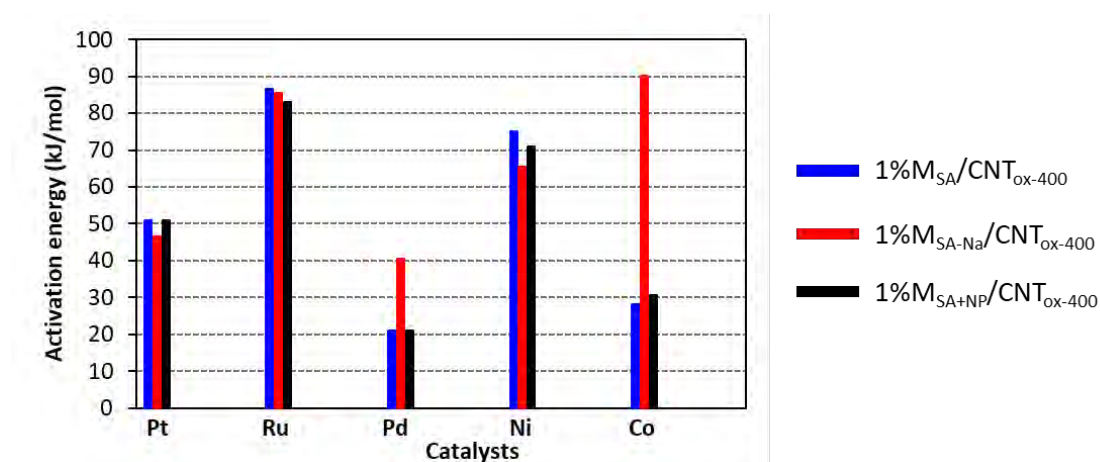


Figure 5.7. Apparent activation measured for  $\text{CO}_2$  hydrogenation with the  $1\%M_{\text{SA}}/\text{CNT}_{\text{ox-400}}$ ,  $1\%M_{\text{SA-Na}}/\text{CNT}_{\text{ox-400}}$  and  $1\%M_{\text{SA+NP}}/\text{CNT}_{\text{ox-400}}$  catalyst series.

Finally, in order to evaluate the cooperative effect between nanoparticles and single atoms, we have tested a series of 1% $M_{SA+NP}/CNT_{ox-400}$  catalysts prepared using the method previously described (*Chapter 3, Section 3.5 Mixture of single atoms and nanoparticles*). As a brief reminder, the impregnation of the metal is done in two stages allowing the growth of clusters/nanoparticles but keeping the SA sites available. The results of STY and selectivity of 1% $M_{SA+NP}/CNT$  catalysts at 260 °C, 300 °C and 340 °C are displayed in Table 5.5 and Figure 5.8

Table 5.5. Catalytic performances of the 1% $M_{SA+NP}/CNT_{ox-400}$  catalysts on  $CO_2$  hydrogenation.

Catalyst	ICP wt%	T (°C)	CO <sub>2</sub> conversion (%) <sup>a)</sup>	STY (mol <sub>CO2</sub> /m ol <sub>M</sub> .h) <sup>a)</sup>	CO sel. (%) <sup>a)</sup>	CH <sub>4</sub> sel. (%) <sup>a)</sup>	E <sub>a</sub> (kJ/m ol)
Pt <sub>SA</sub> +NP/CNT <sub>ox-400</sub>	0.86	260	1.09	27.80	98.30	1.70	50.86
		300	2.06	52.55	99.82	0.18	
		340	4.26	108.15	99.72	0.28	
Ru <sub>SA</sub> +NP/CNT <sub>ox-400</sub>	0.99	260	0.74	8.48	46.93	53.07	83.11
		300	2.76	31.64	53.66	46.34	
		340	8.62	98.74	51.65	48.35	
Pd <sub>SA</sub> +NP/CNT <sub>ox-400</sub>	0.92	260	0.39	4.99	98.42	1.58	21.12
		300	0.50	6.53	97.76	2.24	
		340	0.66	8.54	97.75	2.25	
Ni <sub>SA</sub> +NP/CNT <sub>ox-400</sub>	1.01	260	0.66	4.33	91.93	8.07	71.03
		300	2.24	14.64	89.73	10.27	
		340	5.35	34.92	89.22	10.78	
Co <sub>SA</sub> +NP/CNT <sub>ox-400</sub>	1.24	260	1.59	8.48	87.62	12.38	30.59
		300	2.56	13.63	93.01	6.99	
		360	4.09	21.80	94.48	5.52	
a)	Average value						

Comparing 1% $M_{SA+NP}/CNT_{ox-400}$  versus 1% $M_{SA}/CNT_{ox-400}$ , there was no significant change in terms of activity. In general, the values of STY varied a few units but instead selectivity slightly decrease favoring the formation of  $CH_4$  in the case of Ru, Ni and Co. Indeed, this is not surprising since studies indicate that NP are more active for  $CH_4$  production, and that

improvement of  $\text{CH}_4$  production are obtained with the increase of particle size.<sup>55,56</sup> Again, platinum presented the higher activity although after 10 hours at 300 °C, the STY went from 55 to 50  $\text{mol}_{\text{CO}_2}/\text{mol}_{\text{Pt}}\cdot\text{h}$ . Contrarily, Ru was stable in all the range of temperature. From our previous studies we have proven the existence of a cooperative effect between SA and NP on liquid phase so it may proceed differently for this specific gas phase reaction. Still, the  $\text{CO}_2$  reduction mechanisms differ between systems, and the precise reaction pathways are still being investigated on both single atoms and nanoclusters.

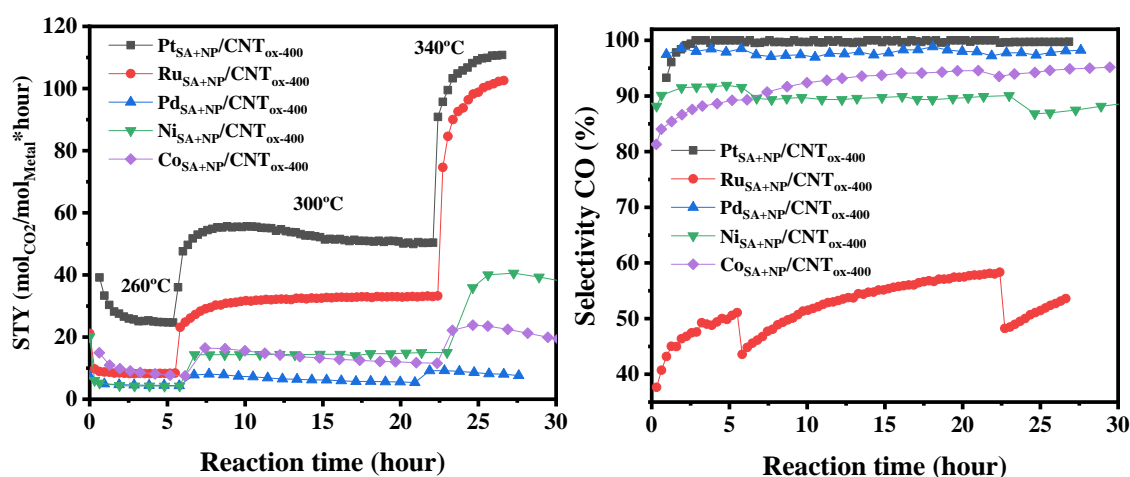


Figure 5.8. STY and selectivity of 1% $M_{\text{SA+NP}}/\text{CNT}$  at 260 °C, 300 °C and 340 °C.

### 5.3. Conclusion

We have reported a versatile and scalable approach to stabilize metallic single atoms on CNT. Preliminary catalytic experiments have shown that these catalysts exhibit distinct performances for the hydrogenation of  $\text{CO}_2$  under methanation conditions. Pt and Ru catalysts were much more active than the ones prepared with other metals (Co, Ni, Pd, Cu). The sodium doping of the catalysts led to a significant increase in catalytic activity; however further studies are necessary to elucidate its specific role in these catalytic systems. Although the stability of the catalysts is reasonable (tested for 30 hours), it is still necessary to resort with stronger MSI, that can withstand the harsh operational conditions to avoid the formation of nanoparticles over the CNT. When nanoparticles/clusters were present along with SA, a different selectivity was evidenced. Surprisingly, the use of nickel, a metal well identified for its good methanation performances leads systematically to RWGS reaction and the selective production of CO. For the ruthenium catalysts, moderate CO selectivity was obtained, which can be increased by the

<sup>55</sup> S. Navarro-Jaén, et al. *Applied Surface Science* **2019**, 483, 750-761.

<sup>56</sup> E. Marconi, et al. *Catalysts* **2019**, 9, 375.



addition of alkali dopants. The different ability of single atoms and nanoclusters to dissociate hydrogen may also contribute to the selectivity differences. These results open perspectives for the design of single atom catalysts on carbon for the RWGS reaction, and on the possibility to run CO<sub>2</sub>-Fischer-Trosch synthesis (FTS)<sup>57,58</sup> by combining a SA-based catalyst for the RWGS reaction that will transform CO<sub>2</sub> into CO with a more conventional Co-based FTS catalysts to *in fine* produce carbon-neutral fuels. Encouraging first results have already been obtained in the group as part of Amel Ghogia's thesis, and these studies will continue as part of Canio Scarfiello's thesis in collaboration with the LPCNO and the school of Mines of Albi.

## 5.4. Experimental part

### 5.4.1. Catalysts preparation

**Preparation of 1%  $M_{SA}/CNT_{ox-400}$ :** The catalysts were prepared by a 4-step synthesis method, comprising functionalization of the support, creation of defects, deposition of the metal and removal of organic ligand as described in *Chapter 3*. (for further information refer to *Chapter 3, Section 3.4. Preparation of carbon-based SA*).

**Preparation of 1%  $M_{SA-Na}/CNT_{ox-400}$ :** A desired amount of 1%  $M_{SA}/CNT_{ox-400}$  was treated with a proper volume of NaOH aqueous solution in order to obtain a ratio 1:2 Metal/Na. The mixture was sonicated during 15 min and magnetically stirred overnight at room temperature. The solid was filtrated using a PTFE membrane and washed until pH~6.5. The samples ( $M_{SA-Na}/CNT_{ox-400}$ ) were dried overnight at 80 °C.

**Preparation of 1%  $M_{SA+NP}/CNT_{ox-400}$ :** A desired amount of precursor to obtain 0.5wt.% is dissolved in 30 mL of pentane and mixed with 1g of previously activated  $CNT_{ox-400}$  during one hour under an Ar atmosphere. Afterwards, the solid is precipitated, filtrated and washed three times to remove the possible non reacted precursor. This powder is dried one night under vacuum, and is used to remake the impregnation process (0.5%  $M_{SA}/CNT_{ox-400}$ ). The totality of the previous product is heated at 80 °C during one hour under a mixture of 20/80 H<sub>2</sub>/Ar flow, and again after that time is mixed with 30 mL pentane solution of another 0.5wt.% of metallic precursor for finally obtaining 1wt.% of metal. After one hour of reaction the solid is precipitated, filtrated and washed three times to remove the possible non reacted precursor. Finally, the catalyst (0.5+0.5%  $M_{SA+NP}/CNT_{ox-400}$ ) was dried overnight and stored in air.

---

<sup>57</sup> Y. H. Choi, et al. *Applied Catalysis B: Environmental* **2017**, 202, 605-610.

<sup>58</sup> W. Li, et al. *RSC Advances* **2018b**, 8, 7651-7669.

#### 5.4.2. Catalysts characterization

TEM and HRTEM analyses were performed at the “Centre de microcaractérisation Raimond Castaing, UMS 3623, Toulouse”. Low resolution TEM was performed by using a JEOL JEM 1011 CX-T electron microscope operating at 100 kV with a point resolution of 4.5 Å, and a JEOL JEM 1400 electron microscope operating at 120 kv. The high-resolution analyses were conducted using a JEOL JEM 2100F equipped with a Field Emission Gun (FEG) operating at 200 kV with a point resolution of 2.3 Å and a JEOL JEM-ARM200F Cold FEG operating at 200 kV with a point resolution of > 1.9 Å. The approximation of the particles mean size was made through a manual analysis of enlarged micrographs by measuring at least 200 particles on a given grid. Other TEM micrographs were acquired with a JEOL 2100F S/TEM microscope equipped with a FEG operating at 200 kV, a spherical aberration probe corrector and a GATAN Tridiem energy filter. The resolutions attained are 2 Å and 1.1 Å under parallel TEM mode and scanning STEM modes, respectively.

#### 5.4.3. Catalytic tests

The catalytic tests of CO<sub>2</sub> hydrogenation were performed using a continuous flow stainless steel fixed bed reactor (height = 300 mm, *e.d.* = 9.52 mm, *i.d.* = 7.9 mm) under a total pressure of 6.1 bar. 200 mg of catalyst with a particle size in the 100-200 µm range were mixed with 1800 mg of SiC (Alfa Aesar). Before the catalytic test, the catalyst was reduced in situ at 400 °C for 4 h under a 1/4 mixture of N<sub>2</sub>/H<sub>2</sub>, at atmospheric pressure. Then, experiments were performed at a constant GHSV (Gas Hourly Space Velocity) of 16 500 mL/h.g. Catalytic tests were performed under a N<sub>2</sub>/H<sub>2</sub>/CO<sub>2</sub> gas mixture of 1/4/1 at 260, 300 and 340 °C and 6.1 bar. The composition of the reactant/product mixture was analyzed using an on-line gas chromatograph (500 Clarius) equipped with two TCD: one with argon as gas vector to quantify H<sub>2</sub>, CH<sub>4</sub>, and CO, and another with helium to quantify CO<sub>2</sub>. The GC is equipped with two Shincarbon columns (1/8, 2.0 mm, 80/100), and recorded the formation of methane and conversion of H<sub>2</sub> and CO<sub>2</sub> every 8 min.

The different response coefficients determined from the GC calibration allowed us to calculate the molar fractions (X) of the different molecules considered during the methanation reaction, as follows:

$$X_A = \left( \frac{\text{Area of A signal}}{\text{Area of N}_2 \text{ signal}} \times N_2 \text{ flow} \right) \times \frac{1}{k_A}$$

With a = CO<sub>2</sub>, CH<sub>4</sub>, H<sub>2</sub>, CO and k = response coefficient. The conversion rates of the reagents were then calculated as follows:

$$CO_2 \text{ conversion (\%)} = \left( 1 - \frac{X_{CO_2}}{X_{CO_2} + X_{CH_4} + X_{CO}} \right) \times 100\%$$

$$H_2 \text{ conversion (\%)} = \left( 1 - \frac{H_2 \text{ Output flow}}{H_2 \text{ Input flow}} \right) \times 100\%$$

With H<sub>2</sub> output flow = dry flow output x X<sub>H<sub>2</sub></sub>.

$$\text{Dry flow output} = \left( \frac{CO_2 \text{ input flow}}{X_{CO_2} + X_{CH_4} + X_{CO}} \right)$$

$$CH_4 \text{ yield (\%)} = \left( \frac{CH_4 \text{ output flow}}{CO_2 \text{ input flow}} \right) \times 100\%$$

CH<sub>4</sub> output flow = dry flow output x X<sub>CH<sub>4</sub></sub>.

CO Yield (%) = % CO<sub>2</sub> conversion – CH<sub>4</sub> Yield (%)

$$CH_4 \text{ selectivity (\%)} = \left( \frac{CH_4 \text{ yield (\%)}}{\%CO_2 \text{ conversion}} \right) \times 100\%$$

$$CO \text{ selectivity (\%)} = \left( \frac{CO \text{ yield (\%)}}{\%CO_2 \text{ conversion}} \right) \times 100\%$$

We expressed the percentage of CO<sub>2</sub> consumed by unit of time and by mole of metal, which corresponds to the STY

## General conclusions and perspectives

In this thesis, we have focused on the preparation, characterization and evaluation of the catalytic properties in hydrogenation reactions of carbon-supported SA catalysts.

First, we have prepared catalysts with very high metal content (up to 20%) consisting on covalent assemblies of Ru and fullerenes. These Ru@C<sub>60</sub> nano-architectures were synthesized by decomposition of [Ru(COD)(COT)] in the presence of C<sub>60</sub> using an organometallic approach. The influence of the solvent and the Ru/C<sub>60</sub> ratio on the nature of the metallic species were investigated. It was found that the use of pure toluene allows the exclusive production of Ru<sub>SA</sub>-fullerene structures regardless of the Ru/C<sub>60</sub> ratio (1/1, 5/1, 10/1, 20/1). As soon as small amounts of a second solvent (dichloromethane or methanol) is introduced, the morphology of the structure changes, with the suspicion of the formation of clusters in/on the polymeric structure. STEM-HAADF micrographs and EDX mapping suggested a core-shell distribution when a mixture T50%D50% was used in the synthesis. The use of methanol allows further metal deposition in the inner structure of the fulleride, achieving homogeneous metal distribution. We demonstrate that catalysis can be used as a method for identifying (or confirming the results from WAXS and EXAFS) the type of metal species in the final product. For nitrobenzene hydrogenation, when SA were present, after 5 hours of reaction a maximum of 40% of nitrobenzene conversion was obtained, instead when clusters were suspected activity increases dramatically reaching 99% in 3 hours. This behavior was rationalized thanks to DFT calculations that show that electrodefficient Ru<sub>SA</sub> (and few atom aggregates) are not efficient to activate H<sub>2</sub>, compared to larger clusters. Besides, for the hydrogenation of tetra-substituted 2,3-dimethyl-2-butene, due the high steric hindrance induced by the small C<sub>60</sub>-C<sub>60</sub> distance, the hydrogenation is not possible on Ru<sub>SA</sub>. On large clusters, for instance Ru<sub>13</sub>H<sub>18</sub>, the hydrogenation reaction is thermodynamically favorable, and we experimentally evidence that the catalysts containing clusters are very efficient for this difficult hydrogenation reaction.

Second, we discovered a straightforward and efficient method to produce stable low loading SAC (~1%) on carbon materials. This method involves the creation of defects on the support to anchor metallic atoms. The entire process comprises four stages: i) creating carboxylic groups on the support by nitric acid oxidation (step I); ii) decomposing these groups under an inert atmosphere to produce carbon vacancies, CO<sub>2</sub> and some water (step II); iii) depositing the metal on this defective support (step III); and iv) the removal of organic ligands possibly remaining

on the surface of the catalysts. Factors such, as the time of oxidation and activation temperature were found to be of paramount importance to achieve a high density of defects. The defective CNT support was characterized by EPR and VSM techniques, indicating the presence of paramagnetic species related to spin-polarized localized electronic states. Although the exact nature (vacancies or edges) of the localized electronic states created by the thermochemical process is not known, these defects efficiently stabilized metallic Ru<sub>SA</sub>. The deposition of the active phase was carried out by a simple impregnation of the defective support with a solution of the desired precursor. Besides Ru/CNT, this method was successfully used with six different metals (Pd, Pt, Co, Ni, Cu, Ir) and three other supports (CNF, FM, CB). A combination of organometallic precursors with labile ligands and non protic solvents yield higher metallic loading. Furthermore, we have proven that it was possible to control the SA/NP ratio by repetition of the impregnation step. We showed that for a given metal loading (1.4% in the case of Pd), it was possible to produce four different samples containing a SA/NP ratio of 200/1, 60/1, 40/1 and 10/1 by varying the number of impregnation cycles. Weight percentage values determined by ICP-OES after each impregnation, demonstrate the linearity and reproducibility of this approach. XPS data have shown a shift in the Pd<sup>0</sup> signal from Pd<sub>200\_SA/NP/CNT<sub>ox-400</sub></sub> to Pd<sub>10\_SA/NP/CNT<sub>ox-400</sub></sub>, indicating a particle size-dependency pointing to a charge transfer between the metallic clusters and the support. The previous findings combined with STEM-HAADF imaging prove the evolution of the metallic dispersion along the series.

In chapter 4, through a combined experimental-theoretical study, we provide an explanation of the influence of metal dispersion and the concentration of oxygen surface groups and defects on the support of Pd/C catalysts for  $\beta$ -myrcene hydrogenation. Highly dispersed Pd<sub>NP</sub> are necessary to activate H<sub>2</sub>. A high concentration of surface defects on the carbon support is necessary to stabilize Pd<sub>SA</sub>. A high concentration of oxygenated surface groups is also necessary on the carbon support to allow hydrogen spillover. DFT calculations using 1-butene as a probe molecule, demonstrate that such combination allows a cooperative catalysis between Pd<sub>NP</sub> and Pd<sub>SA</sub> involving the formation of Pd<sub>SA</sub>-H species, which are much more active than Pd<sub>NP</sub>-H for hydrogenation but also isomerization. In addition, we have assessed the previously prepared Pd series on myrcene hydrogenation, and activity variations of several orders of magnitude were measured as a function of the value of SA/NP ratio. Surprisingly, the sample that presents the best performance (Pd<sub>10\_SA/NP/CNT<sub>ox-400</sub></sub>) was not the one that contained the higher proportion of palladium clusters. This result indicates that a moderate number of clusters with an average diameter of 1.1 nm in combination with only 0.25% of the total Pd atoms as SA are the optimal

conditions to carry out the hydrogenation of myrcene. The control of this ratio allows the development of a new generation of highly active catalysts integrating the ultra-rational use of precious metals.

Finally, in the last chapter we presented the preliminary results of the application of the prepared SAC on the hydrogenation of carbon dioxide. In agreement with the literature, SA species produce selectively CO as a product under methanation conditions. Pt and Ru were by far the most active metals at 340 °C and 6.1bar of pressure. As anticipated, an increase in the temperature causes an increase in the activity due to the endothermic nature of the RWGS reaction. Unfortunately, after 30 hours on stream, a significant part of the atoms agglomerated, giving rise to the appearance of nanoparticles warning about the need to implement mechanisms to enhance the fixation of these species. Thus, the addition of 2 equivalents of Na per mol of metal, not only played a role on the stability (smaller particle size after catalysis) but also in terms of activity boosting the performance of all catalysts.

The work described in this doctoral thesis provides inspiration and perspectives for future research such as:

- The identification of the nature of the created defects stills need to be performed. In-situ measurements such time-resolved operando EPR spectroscopy would help to gain insight about these reactive species. Another approach could be the synthesis of molecular models (carbene molecular models) containing well-defined edge-like defects; and the study of their chemical reactivity towards selected organometallic compounds.
- Grafting other species different from transition metal atoms on the defective supports such coordination complexes in a manner to binding homogeneous catalysts or even ligands or other molecules for different applications than catalysis such gas sensors, biosensors or polymer functionalization could be envisaged.
- Enlarging the scope of the method to other supports and metals can be investigated. Nitrogen- or sulfur-doped carbon supports represents interesting choices as starting materials for the SA deposition. There is a vast bibliography referring to the excellent stability of M-N-C moieties. S-doped carbons would also be interesting due to their affinity and strong interaction with precious metals, which could contribute to improve SA stabilization.



- The concept of cooperative catalysis between SA and NP can be extended to plenty other reactions involving hydrogen (or hydrogen spillover), such as nitrogen fixation, Fischer-Trosch, etc.
- Preliminary results obtained in the hydrogenation of CO<sub>2</sub> encourage pursuing further investigation with platinum for example to perform CO<sub>2</sub>-FTS. In such a reaction, the role of the Pt<sub>SA</sub> catalyst would be to transform CO<sub>2</sub> to CO *via* the RWGS reaction but also to assist the reduction of a conventional Co-based FTS catalyst to improve its performances.

## **Chapter 6. Résumé de Thèse**



## 6. Résumé

### 6.1. Catalyseurs à base d'atomes métalliques isolés sur matériaux carboné

Depuis le début du siècle, les catalyseurs à base d'atomes métalliques isolés (SAC pour single atom catalysts) ont suscité un grand intérêt pour la recherche, et de nombreuses revues ont déjà été consacrées à ce sujet.<sup>1,2,3</sup> Les développements récents des techniques de caractérisation, des outils de modélisation et les progrès de la chimie de coordination de surface ont permis des avancées significatives dans ce domaine. Il est plausible que les SAC opèrent dans de nombreuses réactions catalytiques; cependant, dans le passé, le manque d'outils de caractérisation puissants tels que la microscopie électronique à transmission avec correction d'aberration n'a pas permis leur identification.<sup>4</sup>

L'utilisation de SAC est particulièrement intéressante car elle maximise l'utilisation des métaux précieux; mais il faut bien entendu aussi qu'ils atteignent des performances optimales en termes de stabilité, d'activité et de sélectivité. La Figure 6.1 montre que différents types de catalyseurs hétérogènes peuvent répondre à la définition de SAC: i) un catalyseur à un seul atome de métal supporté ne contenant que des atomes uniques isolés noyés sur un support, dans cette recherche nous appellerons SAC ce type de catalyseur; ii) des atomes isolés incorporés dans l'ossature d'un matériau (comme dans une zéolite, des MOF (Metal Organic Frameworks) ou des tamis moléculaires de phosphate d'aluminium (ALPO)); et iii) un catalyseur homogène supporté ou un catalyseur hétérogène à site isolé<sup>5</sup> contenant un complexe de coordination (pouvant contenir un ou plusieurs atomes métalliques) ancré sur un support.

La préparation d'un SAC nécessite des sites spécifiques sur le support qui feront office de pièges pour les atomes métalliques. Dans le domaine des matériaux carbonés, une surface de carbone  $sp^2$  parfaite ne semble pas adaptée pour obtenir un SAC stable. En effet, la plupart du temps, l'énergie d'adsorption des adatoms métalliques sur des matériaux de type graphitique sans défaut<sup>6</sup> sont inférieures aux énergies de liaison métal-métal dans la nanoparticule (NP) supportée;<sup>7</sup> par conséquent, la formation de NP métallique est favorisée par rapport au SAC. La présence de défauts dans le matériau carboné, tels que des lacunes, augmentera

<sup>1</sup> C. Rivera-Cárcamo, et al. *ChemCatChem* **2018**, *10*, 5058-5091.

<sup>2</sup> A. Wang, et al. *Nature Reviews Chemistry* **2018c**, *2*, 65-81.

<sup>3</sup> M. Li, et al. *Advanced Materials* **2020b**, *32*, 2001848.

<sup>4</sup> J. C. Matsubu, et al. *Journal of the American Chemical Society* **2015**, *137*, 3076-3084.

<sup>5</sup> J. Liu *Acs Catalysis* **2017b**, *7*, 34-59.

<sup>6</sup> X. Liu, et al. *Crystals* **2013**, *3*, 79-111.

<sup>7</sup> C. T. Campbell *Accounts of Chemical Research* **2013**, *46*, 1712-1719.

considérablement l'énergie d'adsorption des adatoms métalliques.<sup>8</sup> La création de défauts est donc une étape clé dans la préparation de SAC.

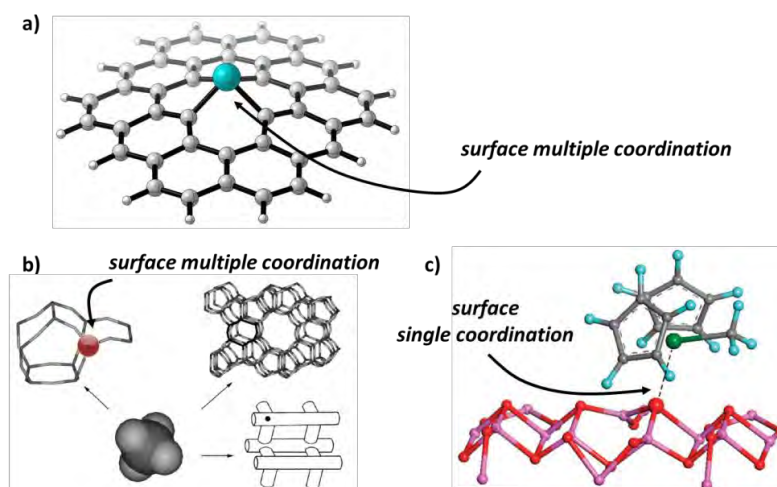


Figure 6.1. Illustrations schématiques de: a) un seul atome de Pd supporté sur un support carboné (SAC), l'atome de Pd est situé dans une lacune de carbone; (b) un atome d'Al site isolé incorporé dans le cadre d'un site T, d'un cycle de zéolite et d'un système de canaux de zéolite ; et (c) d'un catalyseur homogène supporté, coordination de zirconocénium oxo-ponté sur un site de surface d'alumine  $\mu^3$ -O.

L'utilisation de matériaux  $sp^{2+\delta}$  présentant une surface courbe permet des énergies de liaison significativement plus élevées, en particulier avec les fullerènes, permettant la production de fullerides métalliques (métallofullerène), dans lesquels des atomes métalliques isolés sont liés au  $C_{60}$ .<sup>9</sup> L'incorporation d'hétéroéléments tels que l'oxygène, l'azote, le bore,<sup>10</sup> le soufre<sup>11</sup> ou le phosphore<sup>12</sup> dans le réseau graphitique peut également potentiellement améliorer l'adsorption d'un seul atome de métallique, c'est pourquoi l'utilisation de matériaux dopés a été particulièrement étudiée.

Enfin, il est important de noter que dans les SAC, l'interaction électronique métal-support est d'une importance fondamentale pour établir des corrélations entre les propriétés électroniques des sites catalytiques et l'activité catalytique.<sup>13</sup> Dans ce contexte, la possibilité de régler les propriétés électroniques des matériaux carbonés par dopage est particulièrement intéressante.

<sup>8</sup> A. V. Krashennnikov, et al. *Physical Review Letters* **2009**, 102, 126807.

<sup>9</sup> F. Leng, et al. *Rsc Advances* **2016**, 6, 69135-69148.

<sup>10</sup> M. N. Groves, et al. *Journal of Physical Chemistry C* **2012**, 116, 10548-10556.

<sup>11</sup> D. Higgins, et al. *Advanced Functional Materials* **2014**, 24, 4325-4336.

<sup>12</sup> L. Feng, et al. *Science of The Total Environment* **2020**, 698, 134239.

<sup>13</sup> P. Hu, et al. *Angewandte Chemie-International Edition* **2014a**, 53, 3418-3421.

Ce travail de recherche se concentre sur la préparation de catalyseurs à site unique supportés sur des matériaux carbonés et leur applicabilité aux réactions d'hydrogénation.

## 6.2. Catalyseurs à base d'atomes métalliques isolés à fort chargement en métal

Comme examiné dans la section bibliographique, des recherches approfondies sont actuellement consacrées à la synthèse reproductible des SA.<sup>14,15</sup> Ceci est dû aux propriétés physico-chimiques spécifiques de ces espèces par rapport au métal massif mais aussi aux particules nanométriques,<sup>16</sup> qui ouvrent la voie à des applications dans de nombreux domaines tels que les technologies quantiques, les capteurs, l'énergie, l'environnement, la biologie ou la catalyse.<sup>17,18</sup> Au cours des dernières années, différentes stratégies de dispersion d'atomes métalliques isolés sur supports ont vu le jour.<sup>19</sup>

Le fullerène C<sub>60</sub> est un élément de base intéressant pour stabiliser les atomes métalliques uniques ou des NP. En effet, le haut degré de symétrie, la forte tendance à la polymérisation de cette molécule, et ses géométries de coordination en font un candidat idéal pour la construction de nanostructures bien définies.<sup>20</sup> Dans les fullerides de métaux de transition, en fonction de la quantité de métal, la structure obtenue pourrait être polymérique avec un arrangement en forme de chaîne -(M<sub>1</sub>@C<sub>60</sub>)<sub>n</sub>- des SA du métal, ou avec une coordination bidimensionnelle ou tridimensionnelle.<sup>21,22</sup> Des nanostructures sphériques contenant des SA de palladium,<sup>23,24</sup> et plus récemment de ruthénium<sup>25</sup> ont été produites. Pour le Pd, il a été proposé que la synthèse de fullerides de Pd puisse produire des structures polymériques contenant des atomes de Pd isolés avec une stoechiométrie entre Pd<sub>1</sub>C<sub>60</sub> et Pd<sub>4,9</sub>C<sub>60</sub>.<sup>26</sup>

D'après un précédent travail de notre groupe, des résultats intéressants ont été obtenus dans le cas du ruthénium.<sup>27</sup> Il apparaît difficile de produire des NP métalliques de fulleride, probablement lié au fait qu'une fois le produit cinétique de la réaction formé (les structures polymériques sphériques contenant des SA), le métal supplémentaire se dépose sur la surface

<sup>14</sup> J. Calvo Fuentes, et al. In *Encyclopedia of Nanotechnology*, edited by B. Bhushan: Springer Netherlands. Dordrecht (2014), pp. 1-15.

<sup>15</sup> C. Rivera-Cárcamo, et al. *ChemCatChem* **2018**, 10, 5058-5091.

<sup>16</sup> X.-F. Yang, et al. *Accounts of Chemical Research* **2013**, 46, 1740-1748.

<sup>17</sup> A. Mathew, et al. *Particle & Particle Systems Characterization* **2014**, 31, 1017-1053.

<sup>18</sup> X. Yuan, et al. *Particle & Particle Systems Characterization* **2015**, 32, 613-629.

<sup>19</sup> H. Zhang, et al. *Advanced Energy Materials* **2018**, 8, 1701343.

<sup>20</sup> E.-Y. Zhang, et al. *Current Opinion in Colloid & Interface Science* **2009**, 14, 148-156.

<sup>21</sup> J. Goclon, et al. *RSC Advances* **2017**, 7, 2202-2210.

<sup>22</sup> A. L. Balch, et al. *Chemical Reviews* **2016**, 116, 3812-3882.

<sup>23</sup> H. Nagashima, et al. *Journal of the Chemical Society, Chemical Communications* **1992**, 377-379.

<sup>24</sup> A. V. Talyzin, et al. *Carbon* **2007**, 45, 2564-2569.

<sup>25</sup> F. Leng, et al. *RSC Advances* **2016b**, 6, 69135-69148.

<sup>26</sup> A. S. Lobach, et al. *Russian Chemical Bulletin* **1996**, 45, 464-465.



externe des sphères car il ne peut pas diffuser dans leur porosité se traduisant par une structure cœur-coquille. Ainsi, l'objectif des travaux décrits dans ce chapitre était de produire des hétéro-structures  $\text{Ru}@C_{60}$  à forte charge de ruthénium en évitant la morphologie cœur-coquille en utilisant des mélanges de solvants lors de la synthèse pour favoriser le dépôt de ruthénium dans la porosité du matériaux  $-(\text{Ru}_1@C_{60})_n$  de manière à obtenir des fullerides de NP métalliques  $-(\text{Ru}_n@C_{60})_n$ . Ainsi, nous rapportons la synthèse d'auto-assemblage simple de particules subnanométriques de Ru et de  $\text{Ru}_{SA}$  avec le  $C_{60}$ .

Les hétéro-structures  $\text{Ru}@C_{60}$  ont été synthétisées en décomposant  $[\text{Ru}(\text{COD})(\text{COT})]$  en présence de  $C_{60}$ , en faisant varier le rapport  $\text{Ru}/C_{60}$ , sous  $\text{H}_2$  (3 bar) en utilisant du dichlorométhane (D), du toluène (T) et/ou du méthanol (M) comme solvants. Les conditions de réaction pour chaque échantillon, la charge métallique résultante et la taille des  $\text{Ru}_{NP}$  sont résumées dans Tableau 6.1.

Tableau 6.1. Chargement et granulométrie moyenne des échantillons  $\text{Ru}@C_{60}$ .

Entrée	Echantillon	Solvant	T (°C)	Ru loading (%) <sup>a</sup>	Ru NP size (nm)
1	D- $\text{Ru}_1@C_{60}$ 1/1 <sup>27</sup>	$\text{CH}_2\text{Cl}_2$	25	10.6 (12.3)	n. d. <sup>b</sup>
2	D- $\text{Ru}@C_{60}$ 2/1 <sup>27</sup>	$\text{CH}_2\text{Cl}_2$	25	16.7 (21.9)	$1.2 \pm 0.1$
3	D- $\text{Ru}@C_{60}$ 5/1 <sup>27</sup>	$\text{CH}_2\text{Cl}_2$	25	35.6 (41.2)	$1.3 \pm 0.1$
4	T- $\text{Ru}_1@C_{60}$ 1/1 <sup>27</sup>	Toluene	25	9.1 (12.3)	n. d.
5	T- $\text{Ru}@C_{60}$ 5/1	Toluene	25	11.0 (41.2)	n. d.
6	T- $\text{Ru}@C_{60}$ 10/1	Toluene	25	16.6 (58.3)	n. d.
7	T- $\text{Ru}@C_{60}$ 20/1	Toluene	25	20.0 (73.7)	n. d.
8	T- $\text{Ru}@C_{60}$ 40/1	Toluene	25	19.2 (84.8)	n. d.
9	T- $\text{Ru}@C_{60}$ 20/1	Toluene	50	19.6 (73.7)	n. d.
10	T- $\text{Ru}@C_{60}$ 20/1	Toluene	100	20.5 (73.7)	n. d.
11	$\text{T}_{95}\text{D}_5$ - $\text{Ru}@C_{60}$ 20/1	Toluene (95%)/ $\text{CH}_2\text{Cl}_2$ (5%)	25	24.4 (73.7)	n. d.
12	$\text{T}_{75}\text{D}_{25}$ - $\text{Ru}@C_{60}$ 20/1	Toluene (75%)/ $\text{CH}_2\text{Cl}_2$ (25%)	25	35.8 (73.7)	n. d.
13	$\text{T}_{50}\text{D}_{50}$ - $\text{Ru}@C_{60}$ 20/1	Toluene (50%)/ $\text{CH}_2\text{Cl}_2$ (50%)	25	36.0 (73.7)	suspected
14	$\text{T}_{95}\text{M}_5$ - $\text{Ru}@C_{60}$ 20/1	Toluene (95%)/ MeOH (5%)	25	34.7 (73.7)	suspected
15	$\text{T}_{75}\text{M}_{25}$ - $\text{Ru}@C_{60}$ 20/1	Toluene (75%)/ MeOH (25%)	25	41.6 (73.7)	suspected
16	$\text{T}_{50}\text{M}_{50}$ - $\text{Ru}@C_{60}$ 20/1	Toluene (50%)/ MeOH (5 %)	25	47.1 (73.7)	suspected

a) À partir d'analyses ICP. La valeur entre parenthèses est la charge de Ru visée compte tenu de la quantité initiale de précurseur métallique utilisée dans la synthèse. b) n. ré. = non détecté

Des nanostructures de forme indéfinie ont été produites en utilisant du toluène pur (entrée 4, Tableau 6.1, T- $\text{Ru}_1@C_{60}$ ).<sup>27</sup> Cela indique l'influence prononcée du solvant sur la forme des structures produites (comparer avec des sphères bien définies produites dans du  $\text{CH}_2\text{Cl}_2$ ).

Néanmoins, quel que soit le rapport Ru/C<sub>60</sub>, aucune nanoparticule n'a été détectée dans des matériaux synthétisés dans du toluène pur (Figure 6.2). Nous avons proposé que ces structures constituent le produit cinétique de la réaction et ne contiennent que des atomes isolés de Ru. Dans Ru<sub>1</sub>@C<sub>60</sub> les atomes de Ru sont reliés au C<sub>60</sub> avec une coordination  $\eta^2$ - $\eta^6$  (mesures EXAFS) comme précédemment rapporté par notre groupe pour des structures similaires produites dans le dichlorométhane.<sup>27</sup> L'existence du plateau à des rapports Ru/C<sub>60</sub> plus élevés et même à des températures de synthèse élevées est liée à la formation rapide d'un complexe stable, le [(1,5-cyclooctadiène)(toluène)Ru(0)], en solution par la réaction du solvant avec le précurseur du ruthénium. La formation de ce produit a été confirmée par <sup>1</sup>H-RMN, et ce complexe a été isolé à partir des filtrats jaunes obtenus à l'issue des réactions. Afin de limiter la formation de [Ru(COD)(toluène)] et d'augmenter la charge en Ru, nous avons étudié l'utilisation de mélanges de solvants avec du toluène. Deux solvants ont été étudiés, le CH<sub>2</sub>Cl<sub>2</sub> (entrées 11-13, Tableau 6.1) et le méthanol (entrées 14-16, Tableau 6.1), qui peuvent agir comme des solvants de coordination des atomes de Ru pour limiter la formation du complexe de Ru stable avec le toluène.<sup>27,28</sup>

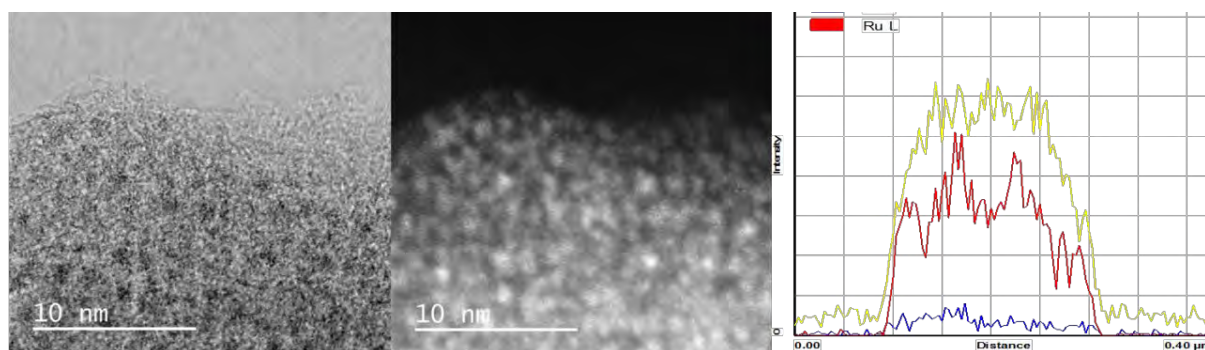


Figure 6.2. a) STEM; b) micrographie HAADF; et c) cartographie EDX de T-Ru@C<sub>60</sub> 20/1.

L'utilisation de mélanges toluène/CH<sub>2</sub>Cl<sub>2</sub> (50/50) permet d'augmenter la charge en Ru (pour un rapport Ru/C<sub>60</sub> = 20) de 20 à 36%. Le Ru atteint 34,7% en poids pour un mélange toluène/méthanol (95/5), et 47.1% en poids pour un mélange toluène/méthanol (50/50). À ce chargement élevé, l'identification des espèces métalliques n'était pas possible à partir d'une analyse microscopique. Les spectres Raman (532 nm) de T-Ru@C<sub>60</sub> à différents rapports Ru/C<sub>60</sub> sont présentés sur la Figure 6.3. La gamme spectrale se concentre principalement sur le

<sup>27</sup> M. Bown, et al. *J Am Chem Soc* **1990**, 112, 2442-2443.

<sup>28</sup> M. Kawai, et al. *Acta Crystallographica Section C* **2002**, 58, m581-m582.

mode de pincement pentagonal Ag(2). On sait que l'énergie du mode Ag(2) ( $1460\text{ cm}^{-1}$  pour le  $\text{C}_{60}$  pur) est sensible au transfert de charge dans les fullerides de métaux de transition.<sup>29</sup> En effet, un fort déplacement et un élargissement sont observés dans ce signal distinctif avec la teneur en ruthénium comme illustré dans Figure 6.2. Des calculs DFT indiquent qu'un transfert de charge évolue de  $0.62\text{e}/\text{Ru}$  sur  $\text{Ru}_{\text{SA}}$  à  $0.11\text{e}/\text{Ru}$  dans le cas du cluster  $\text{Ru}_{13}$  vers les unités  $\text{C}_{60}$ .

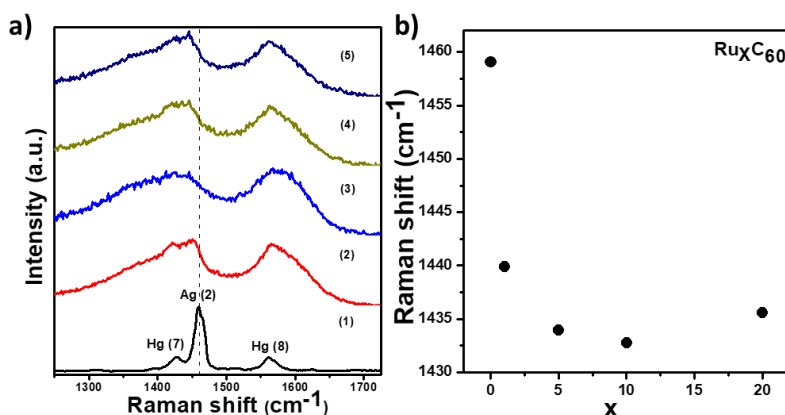


Figure 6.3. a) Spectres Raman de (1)  $\text{C}_{60}$ , (2)  $\text{T-Ru@C}_{60}$  1/1, (3)  $\text{T-Ru@C}_{60}$  5/1, (4)  $\text{T-Ru@C}_{60}$  10/1 et (5)  $\text{T-Ru@C}_{60}$  20/1; et b) le décalage Raman par rapport à la composition de Ru dans  $\text{C}_{60}$  illustre l'élargissement et le décalage vers le bas du pic Ag(2) par rapport à l'augmentation de la teneur en Ru.

Des analyses WAXS ont été réalisées afin de mettre en évidence la présence éventuelle d'amas de Ru métalliques dans les hétéro-structures  $\text{Ru@C}_{60}$ . Seul l'échantillon  $\text{T}_{50}\text{D}_{50}\text{-Ru@C}_{60}$ , a montré une forte contribution observée à  $0.267\text{ nm}$  en très bon accord avec la longueur de liaison métallique Ru-Ru ( $0.265\text{ nm}$ ); confirmant la présence d'amas de Ru dans cet échantillon montrant une structure cœur-coquille. Nous avons également analysé les échantillons préparés dans du toluène pur à différents rapports Ru/ $\text{C}_{60}$ . Comme prévu, pour tous les rapports, il était impossible de détecter une distance Ru-Ru métallique mais une contribution dans la gamme  $0.20\text{-}0.23\text{ nm}$  pouvait également être systématiquement détectée, indiquant fortement une liaison Ru-C. En accompagnant ces résultats avec un profil PDF simulé, il est intéressant de noter qu'aucune contribution à  $0.270\text{ nm}$  peut être observé pour les atomes isolés ( $\text{Ru}_1$ ) et les petits clusters avec un nombre limité de liaisons métalliques Ru-Ru ( $\text{Ru}_2$ ,  $\text{Ru}_4$ ) suggérant l'inefficacité de l'analyse WAXS pour la détection des espèces subnanométriques de ruthénium.

<sup>29</sup> S. J. Chase, et al. *Physical Review B* **1992**, 46, 7873-7877.

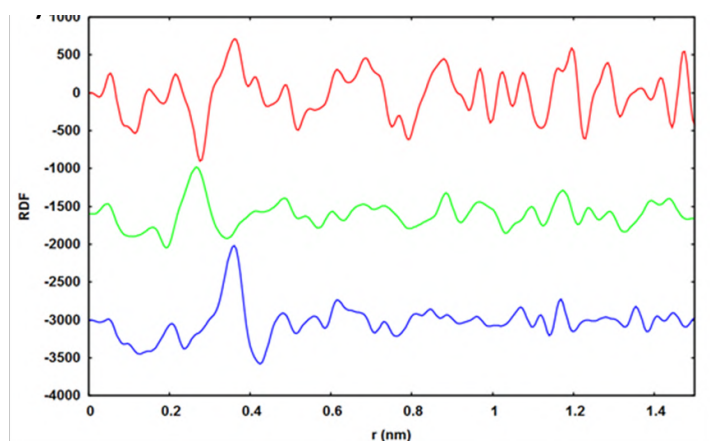


Figure 6.4. a) Diffractogrammes WAXS des échantillons  $T_{95}D_5\text{-Ru@C}_{60}$ ,  $T_{95}M_5\text{-Ru@C}_{60}$  et  $T\text{-Ru@C}_{60}$  ( $\text{Ru/C}_{60} = 20/1$ ).

Des analyses EXAFS ont également été effectuées sur les séries d'échantillons préparées dans du toluène pur à différents rapports  $\text{Ru/C}_{60}$  et sur l'échantillon  $T_{95}M_5\text{-Ru@C}_{60}$ . Les nombres de coordination  $\text{Ru-C}$  sont proches de 8 pour tous les échantillons (cohérent avec la coordination  $\eta^2\text{-}\eta^6$ ). Pour l'échantillon  $T_{95}M_5\text{-Ru@C}_{60}$ , l'ajustement s'est amélioré en ajoutant une deuxième couche  $\text{Ru-Ru}$  avec un nombre de coordination de 2,7 suggérant la présence de clusters dans cet échantillon.

Les observations STEM-HAADF et les analyses WAXS et EXAFS n'étant pas déterminantes quant à la présence ou non de particules subnanométriques de  $\text{Ru}$  dans tous les échantillons obtenus avec un mélange de solvants, nous avons décidé d'utiliser la catalyse pour sonder leur présence. En effet, dans les réactions d'hydrogénation, les  $\text{Ru}_{\text{SA}}$  déficients en électrons devraient être moins efficaces que les  $\text{Ru}_{\text{NP}}$ /clusters pour la chimisorption dissociative de l'hydrogène, qui est souvent l'étape limitant la vitesse.<sup>30</sup> Nous avons choisi comme première réaction sonde l'hydrogénation du nitrobenzène en aniline (AN), car les  $\text{Ru}_{\text{NP}}$  sont connues pour être actives pour cette réaction.<sup>31,32</sup> La réaction a été étudiée à 30 bar  $\text{H}_2$  et 80 °C dans l'éthanol avec une concentration en  $\text{Ru}$  de 0.025 mmol. Pour tous les échantillons préparés dans le toluène pur (rapport  $\text{Ru/C}_{60}$  1/1 à 20/1), pour lesquels seuls des  $\text{Ru}_{\text{SA}}$  sont présents, la conversion du NB est faible par rapport à ceux préparés dans les mélanges toluène/méthanol (Tableau 6.2).

<sup>30</sup> M. D. Rossell, et al. *Catalysis Science & Technology* **2016**, 6, 4081-4085.

<sup>31</sup> F. Leng, et al. *ACS Catalysis* **2016a**, 6, 6018-6024.

<sup>32</sup> M. R. Axet, et al. *ACS Applied Nano Materials* **2018**, 1, 5885-5894.

Tableau 6.2 Résultats de l'hydrogénation du nitrobenzène dans l'éthanol avec différents catalyseurs Ru@C<sub>60</sub>.

Ru/C <sub>60</sub>	Groupe nitro		Sélectivité [%] <sup>a</sup>				
	STY (h <sup>-1</sup> ) <sup>b</sup>	Temps (h) <sup>c</sup>	AN	AN-Et	CA	CA-Et	PHA
T-Ru@C <sub>60</sub> 1/1	14.5	2.3	82.4	8.5	7.1	2.0	-
T-Ru@C <sub>60</sub> 5/1	15.0	2.2	85.3	4.6	-	-	10.1
T-Ru@C <sub>60</sub> 10/1	13.4	2.5	78.4	6.4	5.5	3.6	2.9
T-Ru@C <sub>60</sub> 20/1	12.5	3.0 <sup>d</sup>	86.7	5.4	3.1	-	4.9
T <sub>95</sub> M <sub>5</sub> -Ru@C <sub>60</sub> 20/1	49.9	0.64	100.0	-	-	-	-
T <sub>75</sub> M <sub>25</sub> -Ru@C <sub>60</sub> 20/1	107.36	0.34	83.5	-	-	2.9	13.6
T <sub>50</sub> M <sub>50</sub> -Ru@C <sub>60</sub> 20/1	135.5	0.30	79.9	-	0.4	-	19.0
T <sub>75</sub> D <sub>25</sub> -Ru@C <sub>60</sub> 20/1	12.6	2.5	75.9	14.3	-	-	8.8
T <sub>50</sub> D <sub>50</sub> -Ru@C <sub>60</sub> 20/1	18.2	2.6	66.6	30.8	-	-	2.6

Conditions de réaction: 0,025 mmol Ru, 500 mg (4,06 mmol) de nitrobenzène, 200 mg (1,1 mmol) de dodécane (étalon interne), 30 bar H<sub>2</sub>, 80 °C, 30 mL EtOH. a) déterminé par GC-FID en utilisant la technique de l'étalon interne à  $\approx 20\%$  de conversion. b) STY (mol<sub>NBconverti</sub>/mol<sub>Ru</sub>.t) calculé à  $\approx 20\%$  de conversion. c) Temps pour atteindre 20% de conversion. d) Temps pour atteindre 16% de conversion, qui est le maximum obtenu avec cet échantillon.

Pour ces dernières séries, l'augmentation d'activité est déjà observable pour l'échantillon T<sub>95</sub>M<sub>5</sub>-Ru@C<sub>60</sub>, pour lequel la présence de clusters Ru a été suggérée à partir des analyses EXAFS. De plus, le TOF élevé obtenu en hydrogénation du NB par rapport aux études précédentes,<sup>33,34</sup> nous a incité à évaluer l'activité catalytique de l'échantillon T<sub>50</sub>M<sub>50</sub>-Ru@C<sub>60</sub> dans la difficile hydrogénation de l'oléfine tétra-substituée 2,3-diméthyl-2-butène. A 50 ° C et sous 20 bars de H<sub>2</sub>, la réaction est terminée en 2 h. Le « Site Time Yield » (STY) calculé à 20% de conversion de 470 h<sup>-1</sup> est, à notre connaissance, le plus élevé jamais rapporté pour des NP métalliques supportées. Enfin, nous avons effectué une série de calculs DFT pour proposer le mécanisme de l'hydrogénation des oléfines tétra-substituées. Fait intéressant, en raison de l'encombrement stérique élevé induit par la petite distance C<sub>60</sub>-C<sub>60</sub>, l'hydrogénation n'est pas possible sur les Ru<sub>SA</sub> car le substrat ne peut pas s'adsorber Sur Ru<sub>13</sub>H<sub>18</sub>, la réaction d'hydrogénation apparaît thermodynamiquement favorable, avec une énergie d'activation de seulement 11 kcal/mol.

<sup>33</sup> J. Wu, et al. *Small Methods* **2020**, *4*, 1900540.

<sup>34</sup> F. Leng, et al. *ACS Catalysis* **2016a**, *6*, 6018-6024.

### 6.3. Catalyseurs à base d'atomes métalliques isolés à faible chargement en métal

Comme nous l'avons vu dans le chapitre précédent, une production efficace de SAC repose sur la capacité à produire de fortes interactions métal-support. Cela nous amène à réfléchir sur la nécessité de trouver des sites susceptibles d'être utilisés comme pièges pour stabiliser des atomes métalliques isolés. Sur des supports carbonés, pendant des décennies, les scientifiques ont utilisé des faisceaux à haute énergie (ions ou électrons) en utilisant des équipements sophistiqués tels que des microscopes à effet tunnel/à force atomique pour produire des lacunes induites par l'irradiation.<sup>35</sup> Ces techniques possèdent un degré élevé de contrôle, étant capables d'éliminer le carbone même atome par atome pour former de la mono-lacune à la multi-lacune. Néanmoins, l'utilisation de tels protocoles n'est pas appropriée pour la préparation de catalyseurs. En 1996, Menéndez *et coll.*<sup>36</sup> ont proposé que le traitement thermique sous atmosphère d'azote permet d'éliminer les groupes oxygène de surface (provenant des traitements d'oxydation) sous forme de CO<sub>2</sub> (principalement à des températures basses) et de CO (principalement à des températures plus élevées), laissant des atomes de carbone insaturés (également appelés sites défectueux). Nous avons proposé d'utiliser cette approche pour créer des supports de carbone défectueux pour greffer ultérieurement des atomes métalliques isolés dans de tels défauts pour obtenir des catalyseurs mono-atomes stables. Nous avons développé une procédure en quatre étapes présentées sur la

Figure 6.5. L'étape I) correspond à l'oxydation du support graphitique par d'acide nitrique à 140°C, l'étape II) correspond à l'activation du support par traitement thermique à 400°C sous atmosphère inerte. L'étape III) correspond au dépôt métallique par imprégnation humide et l'étape IV) à l'élimination des ligands rémanents à 80°C sous H<sub>2</sub>.

---

<sup>35</sup> A. V. Krashennnikov, et al. *Journal of Vacuum Science & Technology B: Microelectronics and Nanometer Structures Processing, Measurement, and Phenomena* **2002**, 20, 728-733.

<sup>36</sup> J. A. Menéndez, et al. *Langmuir* **1997**, 13, 3414-3421.



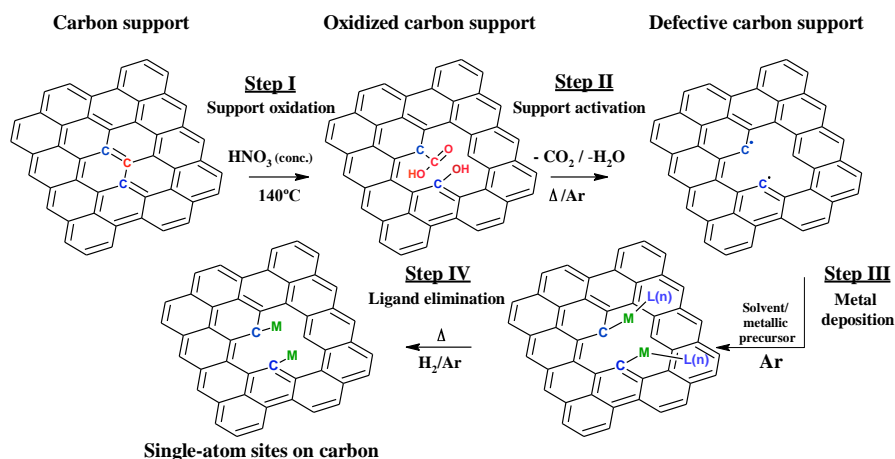


Figure 6.5. Procédure de synthèse de catalyseurs mono-atomes sur matériaux carbonés.

Les résultats obtenus à partir de nanotubes de carbone (CNT) indiquent que les meilleures conditions pour créer des défauts sont à  $400^\circ\text{C}$  (D-CNT). En effet, à des températures plus élevées, un phénomène de réarrangement des lacunes a lieu, conduisant à la reconstruction de la structure graphitique.<sup>37</sup> De nombreuses études ont montré qu'avec l'augmentation de la température de recuit, l'ordre structurel s'améliore et une réduction de la concentration globale des défauts se produit. La formation et la décomposition des groupes oxygénés de surface ont été suivies par analyse TPD ; prouvant que le chauffage à  $400^\circ\text{C}$  est efficace pour éliminer les groupes acides carboxylique (Figure 6.6a).

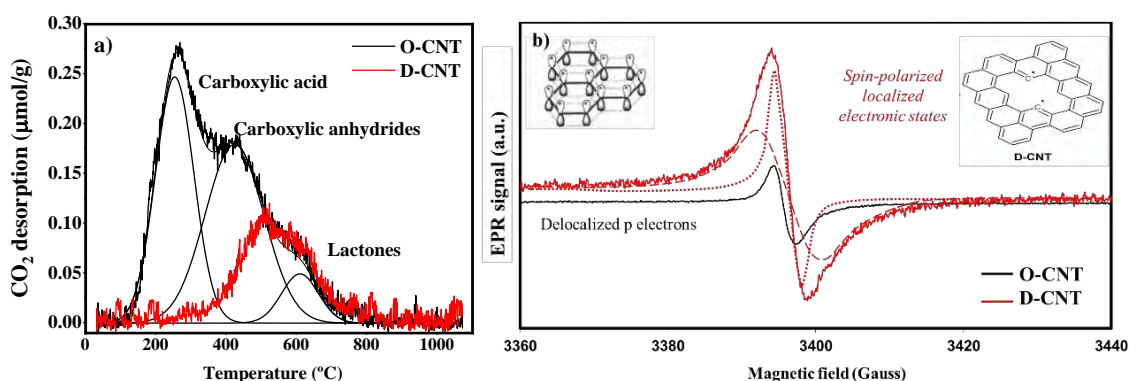


Figure 6.6. a) Profils TPD de désorption du  $\text{CO}_2$  des CNT oxydés et activés ; et b) signal RPE des CNT oxydés et activés.

L'identification des sites defectueux après l'étape II a été réalisée par la combinaison d'analyses  $\text{C}^{13}$ -NMR, SQUID et RPE. Les résultats indiquent la présence d'états électroniques

<sup>37</sup> J. T. H. Tsai, et al. *Journal of Experimental Nanoscience* **2009**, 4, 87-93.

paramagnétiques polarisés en spin fortement liés aux électrons non appariés tels que des lacunes ou des sites de type arêtes non saturés (Figure 6.6b).<sup>38</sup> Suite aux étapes III et IV, nous avons utilisé différents précurseurs et différents solvants pour incorporer des espèces métalliques dans le support défectueux. La Figure 6.7 montre des images HRTEM d'atomes isolés de Cu, Pt, Pd, Ni et Ru supportés sur D-CNT. La quantité maximale de métal déposé était de 1.6% en poids déterminée par analyse ICP et la portée de la procédure a été testée en utilisant d'autres supports tels que le graphène multi-feuillets, des nanofibres de carbone et du noir de carbone pour obtenir des résultats similaires.

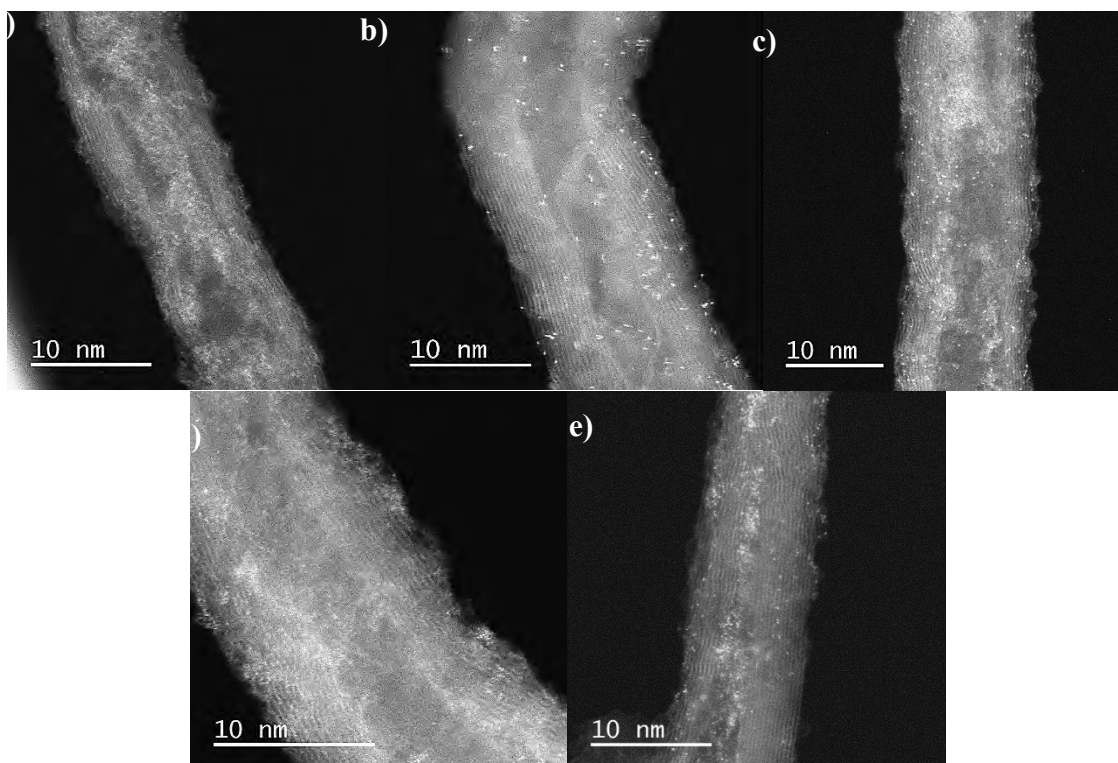


Figure 6.7. Micrographies HAADF-STEM de : a) 1,0% Cu/D-CNT; b) 1,0% de Pt/D-CNT; c) 1,0% de Pd/D-CNT; d) 1,0% Ni/D-CNT ; et e) 1,0% Ru/D-CNT.

Nous avons également découvert que, de manière très simple, en répétant les étapes III et IV pour une quantité donnée de métal, il était possible de moduler le rapport SA/NP. Nous avons préparé une série de 4 catalyseurs à 1.4% de palladium en faisant varier le nombre d'imprégnations de 1 à 4. Dans chaque cas, la quantité totale de précurseur utilisée pour atteindre le pourcentage de métal visé a été divisée en 1, 2, 3, et 4.

<sup>38</sup> O. V. Yazyev *Reports on Progress in Physics* **2010**, 73, 056501.

Tel que présenté dans Tableau 6.3, après chaque imprégnation, les résultats ICP indiquent que l'ajout de métal est assez linéaire après chaque cycle.

*Tableau 6.3. Chargement métallique des échantillons de Pd/D-CNT avec un nombre différent de cycles d'imprégnation déterminé par ICP-OES.*

Echantillon	Pd% après chaque cycle				SA/NP <sup>a)</sup>
	1	2	3	4	
1.40% x1 Pd/D-CNT	<b>1.33</b>				200
0.70% x2 Pd/D-CNT	0.74	<b>1.43</b>			65
0.46% x3 Pd/D-CNT	0.62	0.95	<b>1.37</b>		45
0.35% x4 Pd/D-CNT	0.38	0.68	0.93	<b>1.29</b>	15

a) Par HR-TEM, par comptage manuel sur le logiciel Image J. Rapport SA/NP calculé en tenant compte du nombre total d'atomes et de particules comptés dans au moins 20 images par échantillon

Nous avons réussi à faire varier le rapport SA/NP (qui a été déterminé par comptage direct des SA et NP dans les images HAADF-TEM) de 200 à 10 (Figure 6.8). De plus, avec la répétition du processus, la taille des NP/clusters commence à croître en raison de l'effet de coalescence allant de 0.50 nm à 1.1 nm. Nous avons également caractérisé ces échantillons par XPS, pour sonder les propriétés chimiques et de composition des matériaux résultants. À mesure que la concentration de cluster/NP augmente, le signal du palladium métallique augmente et se déplace vers une énergie de liaison inférieure (335.28 eV), ce qui est en bon accord avec le Pd<sup>0</sup> massif.<sup>39</sup> Néanmoins, lorsque les agrégats sont plus petits, le signal est légèrement décalé vers des énergies de liaison supérieures du fait du fort transfert d'électrons du Pd vers le support dans le cas des clusters les plus petits.

Cette stratégie permet donc de concevoir l'ensemble catalytique minimal que nous envisageons de produire afin d'étudier un éventuel effet catalytique coopératif entre SA et NP dans des catalyseurs supportés par Pd/C en hydrogénation, ce qui fait l'objet de la section suivante.

<sup>39</sup> A. L. Dantas Ramos, et al. *Applied Catalysis A: General* **2004**, 277, 71-81.

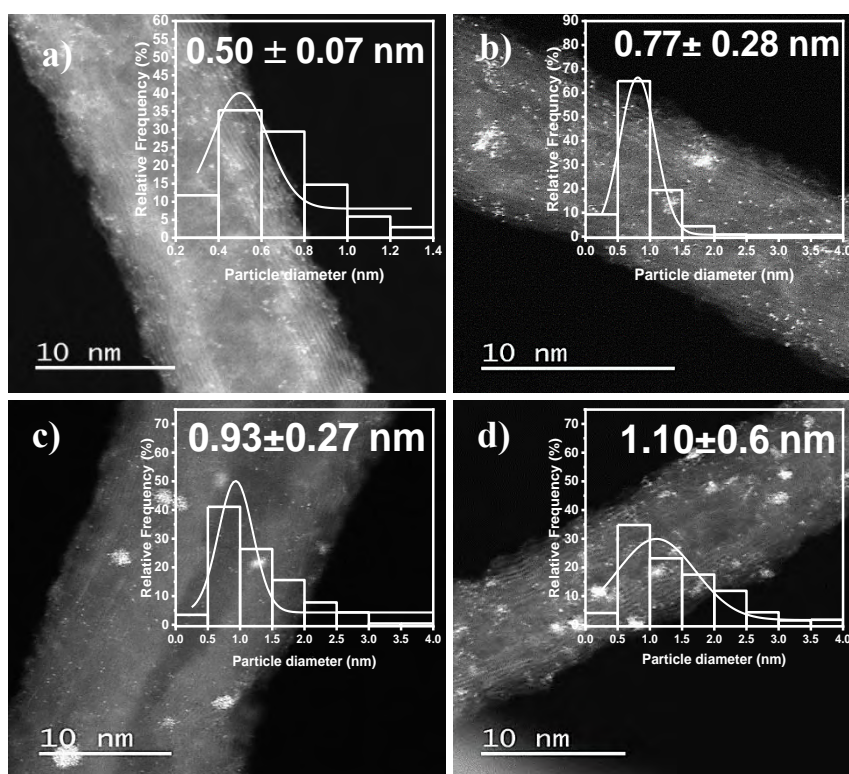


Figure 6.8. Micrographies HAADF-STEM des mélanges de SA et de NP à des rapports différents dans : a) 1.4%Pd/D-CNT ; b) 0.70% x2Pd/D-CNT; c) 0.46%x3Pd/D-CNT; et c) 0.35%x4Pd/D-CNT.

#### 6.4. Hydrogénation d'alcènes sur des catalyseurs à atomes métalliques isolés

L'hydrogénation des alcènes fait partie des réactions technologiques importantes catalysées par les métaux supportés, trouvant une application dans les industries pharmaceutique, agrochimique, du raffinage et des produits chimiques de base. Les atomes isolés présentent des performances distinctes de celles des NP pour une grande variété de réactions chimiques, et des applications industrielles les employant existent déjà.<sup>40</sup> Les études actuelles menées sur les SA visent principalement à les distinguer des NP et la possibilité de synergie entre ces deux espèces a rarement été explorée.<sup>41</sup>

Dans le domaine de l'hydrogénations, des Pd<sub>SA</sub> ont déjà été utilisés,<sup>42</sup> mais l'interaction métal-support dans de tels catalyseurs entraîne souvent un état ionique/électron-déficient des atomes métalliques qui empêche une activation efficace du dihydrogène par rapport aux surfaces métalliques,<sup>43</sup> ce qui limite leur application à des réactions d'hydrogénation sélective

<sup>40</sup> G. Malta, et al. *Science* **2017**, 355, 1399.

<sup>41</sup> J. N. Tiwari, et al. *Advanced Energy Materials* **2019**, 9, 1900931.

<sup>42</sup> C. Rivera-Cárcamo, et al. *ChemCatChem* **2018**, 10, 5058-5091.

<sup>43</sup> A. Granja-DelRío, et al. *The Journal of Physical Chemistry C* **2017**, 121, 10843-10850.

spécifiques.<sup>44</sup> Étant donné que la dissociation de H<sub>2</sub> est souvent l'étape limitant la vitesse dans ces réactions, des stratégies efficaces pour concevoir l'ensemble catalytique minimal qui peut activer H<sub>2</sub> représenteraient un progrès substantiel dans la recherche de catalyseurs d'hydrogénation Pd/C hautement efficaces. Dans ce contexte, nous avons étudié l'hydrogénation de différents alcènes (myrcène, squalène, farnésène) sur différents catalyseurs au palladium (y compris des échantillons commerciaux Pd/Al<sub>2</sub>O<sub>3</sub> et Pd/C) et nous avons corrélié leur activité catalytique à la structure des catalyseurs.

Dans un premier temps, nous avons choisi le  $\beta$ -myrcène comme substrat modèle en raison de la variété des doubles liaisons qu'il possède. Un groupement 1,3-diène hautement réactif (facile à hydrogéner) et une liaison C=C trisubstituée isolée (difficile à hydrogéner). Il est important de noter que l'hydrogénation complète en 2,6-diméthyl-octane nécessite généralement de longs temps de réaction et peut être associée à l'étape intermédiaire d'isomérisation de la double liaison la moins réactive pour produire une liaison C=C plus facile à hydrogéner (Figure 6.9).

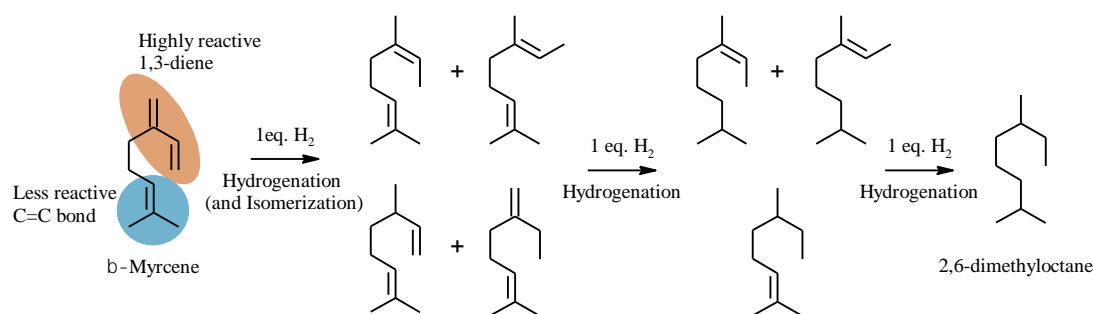


Figure 6.9. Réaction d'hydrogénation du  $\beta$ -myrcène.

L'activité catalytique du Pd/CNT et du Pd/C sont similaires et ces catalyseurs sont nettement plus actifs que le Pd/Al<sub>2</sub>O<sub>3</sub> (Figure 6.10). La différence majeure observée entre ces catalyseurs était la présence de Pd<sub>SA</sub> sur Pd/CNT et Pd/AC. À partir de ces résultats, nous avons supposé que la présence d'atomes isolés devrait être considérée pour rationaliser les différences de réactivité observées. Néanmoins, après plusieurs mesures expérimentales, nous avons prouvé que les Pd<sub>SA</sub> eux-mêmes ne sont responsables ni de l'hydrogénation ni de l'isomérisation, mais le catalyseur le plus actif est celui qui possède à la fois des SA et des NP. Pour mieux comprendre le mécanisme réactionnel, des calculs DFT ont été effectués au Laboratoire de physique et chimie des nano-objets sur les sites Pd<sub>SA</sub> et Pd<sub>NP</sub> supportés sur du graphène comme

<sup>44</sup> G. Kyriakou, et al. *Science* **2012**, 335, 1209.



support de modèle. Pour étudier les réactions d'isomérisation et d'hydrogénation et pour simplifier les calculs, le 2 butène au lieu du myrcène a été utilisé comme substrat modèle. Du fait des barrières énergétiques élevées obtenues, une faible activité catalytique est attendue, comme observé expérimentalement pour l'hydrogénation à l'aide de  $\text{Pd}_{\text{SA}}$  ( $\text{Pd}_{\text{SA}}$ , lignes noires sur *Figure 6.11* et *Figure 6.12*).<sup>45</sup>

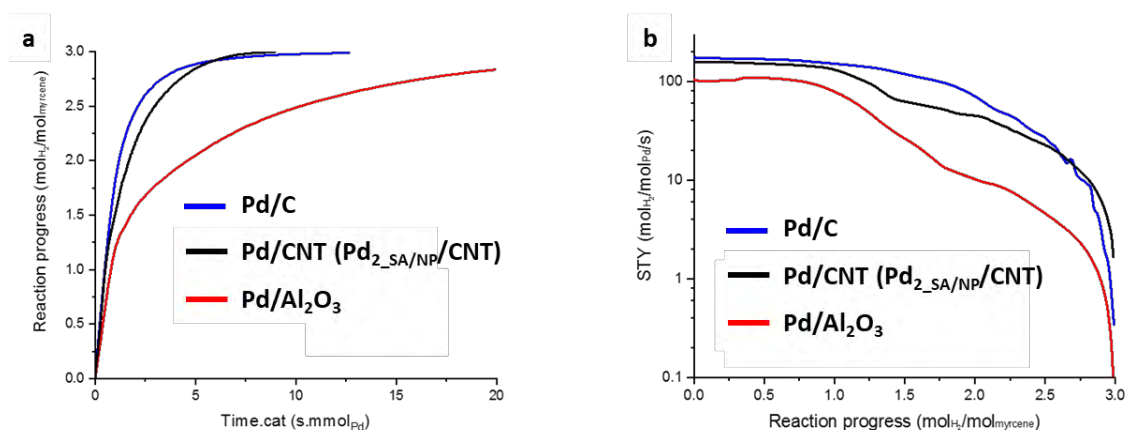


*Figure 6.10. Résultats catalytiques sur Pd/ $\text{Al}_2\text{O}_3$ , Pd/C et Pd/CNT. Réaction d'hydrogénation du myrcène. La réaction a été effectuée sur des catalyseurs Pd supportés.  $\text{PH}_2 = 20 \text{ bar}$  -  $T = 120^\circ \text{C}$  - myrcène 1 M (80 mL) - solvant heptane - 4 mg Pd a) Progression de la réaction en fonction du temps cat. b) STY en fonction de la progression de la réaction.*

Fait intéressant, un paysage énergétique potentiel complètement différent est obtenu si le catalyseur est un hydruure de  $\text{Pd}_{\text{SA}}$  ( $\text{H-Pd}_{\text{SA}}$ , lignes oranges sur *Figure 6.11* et *Figure 6.12*). Un scénario plausible pour la formation de ce site actif est: a) une activation presque sans barrière de  $\text{H}_2$  sur  $\text{Pd}_{\text{NP}}$  ( $< 2 \text{ kcal/mol}$  sur  $\text{Pd}_{13}$  supporté sur graphène), et b) du *spillover* d'hydrogène. Le *spillover* d'hydrogène a également été étudié en utilisant comme géométrie une  $\text{Pd}_{\text{NP}}$  saturée en H déposée sur une di-lacune avec un atome d'oxygène à son voisinage. La réaction globale est cinétiquement accessible et thermodynamiquement favorable, c'est pourquoi nous avons en outre effectué un test expérimental confirmant l'existence d'un H-spillover dans nos systèmes.

<sup>45</sup> H. Gentsch, et al. *Zeitschrift für Physikalische Chemie* **1972**, 82, 49-57.



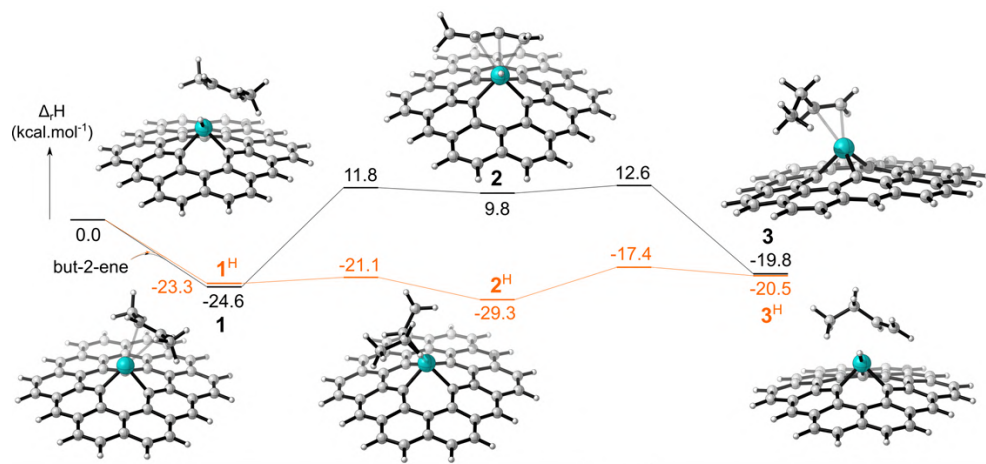


Figure 6.11. Etude DFT des mécanismes de réaction de l'isomérisation du 2-butène sur  $\text{Pd}_{\text{SA}}$  (en noir) et  $\text{H-Pd}_{\text{SA}}$  (en orange).

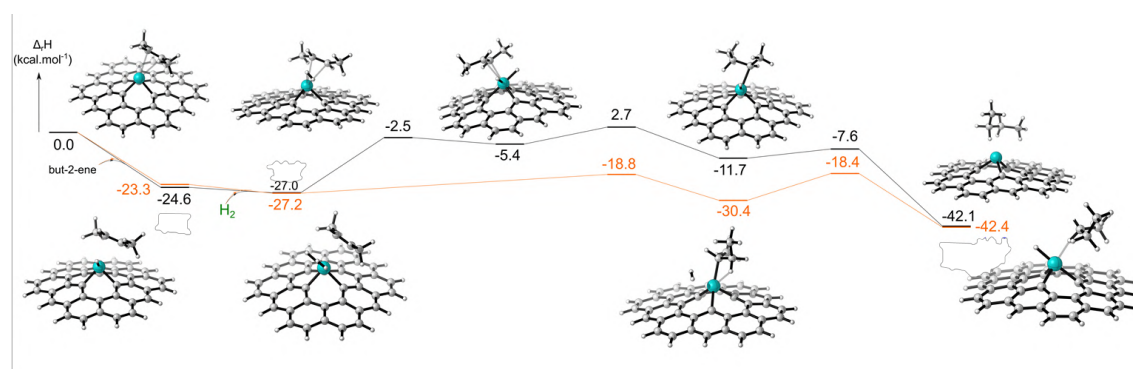


Figure 6.12. Etude DFT des mécanismes de réaction d'hydrogénation du 2-butène sur  $\text{Pd}_{\text{SA}}$  (en noir) et  $\text{H-Pd}_{\text{SA}}$  (en orange).

Ainsi, la corrélation que nous avons rapportée entre l'activité des catalyseurs  $\text{Pd/C}$  pour l'hydrogénation du  $\beta$ -myrcène et leur structure,<sup>46</sup> qui intègre la dispersion du métal, et la quantité de groupes oxygénés et de défauts sur le support, résulte d'une catalyse coopérative entre  $\text{Pd}_{\text{SA}}$  et  $\text{Pd}_{\text{NP}}$  qui implique le H-spillover. Il est certes nécessaire d'avoir des  $\text{Pd}_{\text{NP}}$  très dispersées sur le support pour activer  $\text{H}_2$ , mais une forte concentration de défauts de surface et de groupes de surface oxygénés est également nécessaire sur le support carboné, qui favorise la stabilisation des  $\text{Pd}_{\text{SA}}$  et le H-spillover, respectivement. Les  $\text{H-Pd}_{\text{SA}}$  résultants sont très actifs pour l'hydrogénation et l'isomérisation d'alcènes.

A partir des résultats ci-dessus, il devient évident qu'un catalyseur hétérogène optimisé avec une utilisation ultra-rationnelle de métaux précieux (souvent en pénurie) pourrait passer par un

<sup>46</sup> R. C. Contreras, et al. *Journal of Catalysis* **2019**, 372, 226-244.

contrôle précis du rapport SA/NP. Dans cette optique, nous avons testé différents catalyseurs présentant des rapports SA/NP différents (pour une charge en Pd similaire de 1.4% p/p), afin de prouver l'influence de ce paramètre sur les performances catalytiques. Comme prévu, chaque échantillon ayant un rapport SA/NP différent présentait une activité catalytique différente, comme illustré sur Figure 6.13. Plus important encore, nous avons trouvé que la valeur optimale pour l'hydrogénation du myrcène était de 10.

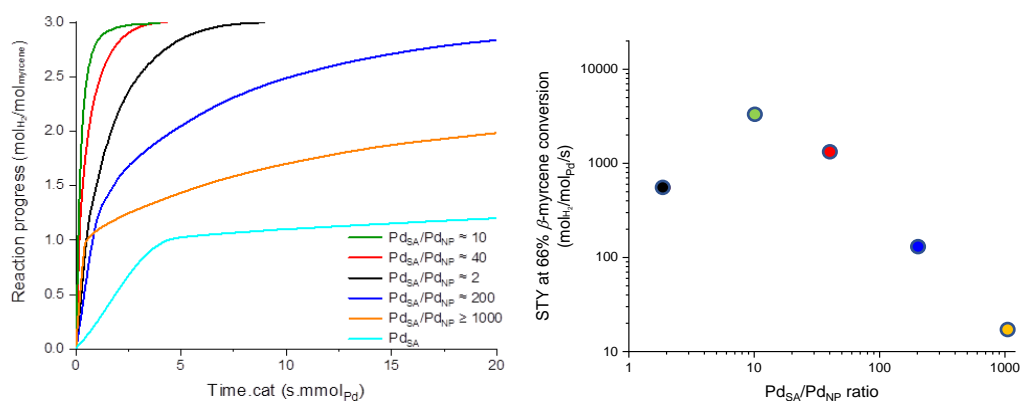


Figure 6.13. Catalytic results for myrcene hydrogenation at different SA/NP ratio. a) Reaction progress as a function of time catalyst

### 6.5. Hydrogénation du dioxyde de carbone sur des catalyseurs à atomes isolés

Pendant des décennies, le CO<sub>2</sub> a été utilisé comme réfrigérant, additif alimentaire ou même comme solvant. Ces dernières années, le CO<sub>2</sub> a été considéré comme une source d'énergie par sa réduction directe en hydrocarbures.<sup>47</sup> Dans ce contexte, une grande attention a été accordée à l'hydrogénation électro-, photo- ou thermo-catalytique du CO<sub>2</sub> en divers produits à valeur ajoutée, tels que le CO, l'acétaldéhyde, l'acide formique, le méthanol, le méthane ou les oléfines inférieures.<sup>48</sup> Selon des calculs thermodynamiques, le CO<sub>2</sub> a tendance à se convertir en molécules à grand nombre de carbone à basse température et haute pression. Cependant, ces réactions sont probablement limitées par la cinétique. Ainsi, la conception de catalyseurs hautement efficaces est essentielle car l'hydrogénation du CO<sub>2</sub> implique un réseau de réactions complexes, qui est limité par la thermodynamique et la cinétique. Dans cette section, nous présentons les résultats de la réduction du CO<sub>2</sub> sur une série de SAC (Ru, Pt, Pd, Ni, Co et Cu) supportés sur des nanotubes de carbone.

<sup>47</sup> M. Aresta, et al. *Chemical Reviews* **2014**, 114, 1709-1742.

<sup>48</sup> L. Wang, et al. *Chemical Society Reviews* **2019b**, 48, 5310-5349.

L'hydrogénation du  $\text{CO}_2$  a été conduite dans des conditions de méthanation ( $\text{CO}_2/\text{H}_2 = 1/4$ ) dans une configuration de réacteur à lit fixe sous 6.1 bar, à 260, 300 ou 340°C, et avec une GHSV de 16500 mL/h.g. Les principaux résultats de la réduction du  $\text{CO}_2$  avec des catalyseurs 1% $\text{M}_{\text{SA}}/\text{D-CNT}$  sont résumés sur le Tableau 6.4 et la Figure 6.14, où les profils de réaction montrent l'évolution du STY avec le temps en service (ToS) à différentes températures.

Tableau 6.4. Performances catalytiques des catalyseurs série 1%  $\text{M}_{\text{SA}}/\text{D-CNT}$  sur l'hydrogénation au  $\text{CO}_2$ .

Catalyseurs	ICP wt%	T (°C)	$\text{CO}_2$ conversion (%) <sup>a)</sup>	STY ( $\text{mol}_{\text{CO}_2}/\text{mol}_{\text{M.h}}^{\text{a)}$ )	CO sel. (%) <sup>a)</sup>	$\text{CH}_4$ sel. (%) <sup>a)</sup>	$E_a$ (kJ/ mol)
$\text{Pt}_{\text{SA}}/\text{D-CNT}$	0.68	260	0.92	29.81	99.31	0.68	50.86
		300	2.05	66.00	99.57	0.43	
		340	4.14	133.35	99.72	0.28	
$\text{Ru}_{\text{SA}}/\text{D-CNT}$	0.95	260	0.68	8.07	56.84	43.16	86.69
		300	2.5	30.00	54.8	45.18	
		340	8.70	103.90	57.1	42.86	
$\text{Pd}_{\text{SA}}/\text{D-CNT}$	0.98	260	0.34	4.20	98.95	1.05	21.12
		300	0.55	6.76	97.59	2.41	
		340	0.81	9.89	97.11	8.88	
$\text{Ni}_{\text{SA}}/\text{D-CNT}$	1.09	260	0.60	3.65	94.80	5.19	75.04
		300	1.96	11.87	95.04	4.96	
		340	5.51	33.30	93.75	6.25	
$\text{Co}_{\text{SA}}/\text{D-CNT}$	1.27	260	0.19	0.99	93.50	6.50	28.15
		300	2.29	11.93	97.39	2.61	
		340	6.74	35.09	96.16	3.84	
$\text{Cu}_{\text{SA}}/\text{D-CNT}$	1.21	260	0.14	0.82	94.55	5.45	76.17
		300	0.18	1.08	92.75	7.25	
		340	0.15	0.91	92.82	7.18	

a) Valeur moyenne

Tous les échantillons étaient actifs pour la réduction du  $\text{CO}_2$  et comme prévu, une augmentation du STY avec la température a été observée. Selon les valeurs d'activité, les métaux peuvent être classés du plus actif au moins actif, dans l'ordre suivant :  $\text{Pt} > \text{Ru} > \text{Ni} \sim \text{Co} > \text{Pd} > \text{Cu}$ . Comme on peut le voir, l'impact de la nature de la phase métallique joue un rôle sur les performances catalytiques générales. Pour tous les métaux, le produit principal était le CO avec une sélectivité comprise entre 92 et 99%, à l'exclusion du Ru qui produisait du méthane à ~ 43%. Ces résultats suggère qu'un catalyseur au Pd atomiquement ou presque atomiquement dispersé ne serait pas capable d'activer de manière homolytique  $\text{H}_2$  (pour former l'intermédiaire formiate conduisant

*in fine* au méthane) ; au lieu de cela le Pd<sub>SA</sub> était capable d'activer le dihydrogène de manière hétérolytique pour produire un intermédiaire carboxyle, expliquant la sélectivité envers le CO.<sup>49</sup>

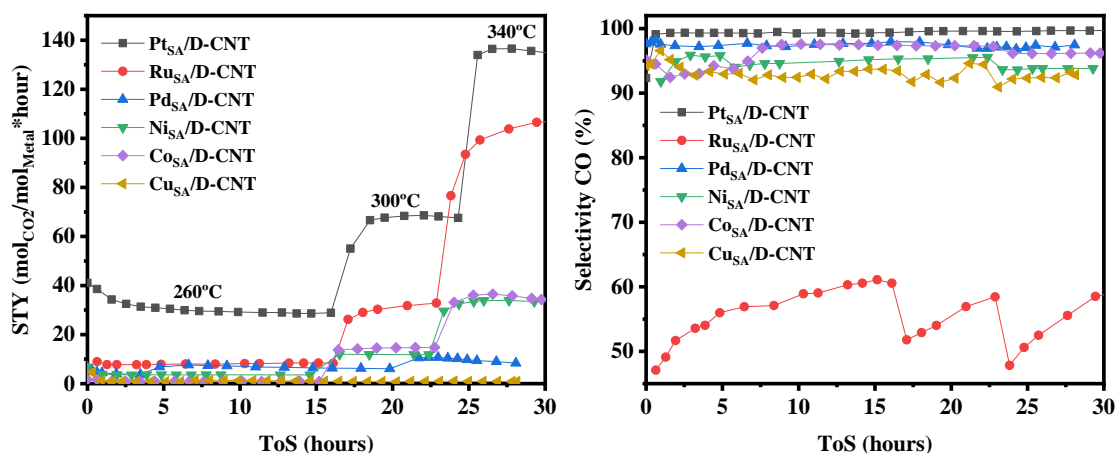


Figure 6.14. STY et sélectivité de 1% M<sub>SA</sub>/D-CNT à 260 °C, 300 °C et 340 °C.

Après 30 h de fonctionnement à 6.1 bars de pression, la formation de particules a été mise en évidence pour tous les échantillons (Figure 6.15). Ce résultat n'est pas surprenant sachant que même dans des conditions réductrices plus douces, des amas se forment après une heure à 1 bar de H<sub>2</sub>/N<sub>2</sub> et 300°C pour Rh<sub>SA</sub>/TiO<sub>2</sub> ou 400°C pour Ni<sub>SA</sub>/hydroxyapatite.<sup>50,51</sup> Le frittage de SA est un facteur clé à surmonter pour de telles applications, raison pour laquelle il est d'une importance cruciale de rechercher des méthodes pour améliorer leur durabilité.

L'action de promoteurs alcalins en catalyse hétérogène a été largement étudiée,<sup>52</sup> et il a été démontré qu'ils peuvent contribuer à : a) augmenter la sélectivité; b) augmenter l'activité; et surtout c) prolonger la durée de vie du catalyseur.

<sup>49</sup> N. C. Nelson, et al. *Angewandte Chemie International Edition* **2020**, doi:10.1002/anie.202007576.

<sup>50</sup> Y. Tang, et al. *Nature Communications* **2019**, *10*, 4488.

<sup>51</sup> M. Akri, et al. *Catalysts* **2020**, *10*, 630.

<sup>52</sup> M. Zhu, et al. *Transactions of Tianjin University* **2020**, *26*, 172-187.

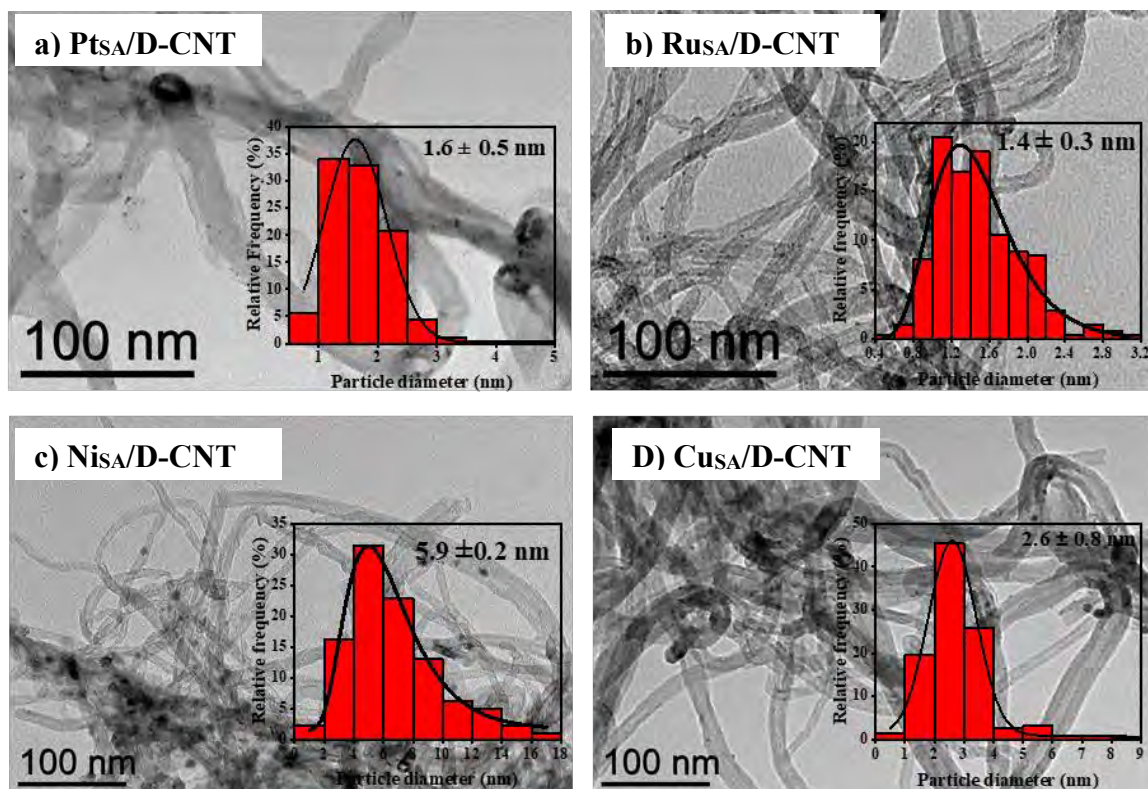


Figure 6.15. Micrographes MET de catalyseurs 1% $M_{SA}/CNT_{ox-400}$  après catalyse : a) Pt, b) Ru, c) Ni et d) Cu.

Par conséquent, nous avons décidé de traiter les  $M_{SA}/D-CNT$  avec NaOH. Avec une simple imprégnation aqueuse, on introduit 2 équivalents de Na par mole de métal. L'ajout de Na comme promoteur a eu un impact très positif sur le STY, pour tous les échantillons (Tableau 6.5).

Pour les catalyseurs Pt, Ru et Ni, les faibles variations d'énergies d'activation entre les catalyseurs dopés et non dopés impliquent que la présence de sodium ne modifie ni le mécanisme de réaction ni l'étape limitant la vitesse, conformément aux résultats publiés sur des catalyseurs au Ni à promotion alcaline.<sup>53</sup> Ce n'était pas le cas pour les catalyseurs Co et Pd, pour lesquels une forte augmentation des énergies d'activation a été observée.

<sup>53</sup> T. K. Campbell, et al. *Applied Catalysis* **1989**, 50, 189-197.

Tableau 6.5. Performances catalytiques des catalyseurs 1%  $M_{SA-Na}/D-CNT$  pour l'hydrogénation du  $CO_2$ .

Catalyseur	T (°C)	CO <sub>2</sub> conversion (%) <sup>a)</sup>	STY (mol <sub>CO2</sub> /mol <sub>M.h</sub> ) <sup>a)</sup>	CO sel. (%) <sup>a)</sup>	CH <sub>4</sub> sel. (%) <sup>a)</sup>	E <sub>a</sub> (kJ/mol)
Pt <sub>SA-Na</sub> /D-CNT	260	7.6	246.0	99.8	0.2	46.7
	300	21.4	688.4	99.9	0.1	
	340	30.1	970.5	99.9	0.1	
Ru <sub>SA-Na</sub> /D-CNT	260	1.6	20.0	85.5	14.5	85.6
	300	7.9	97.1	85.9	14.0	
	340	20.7	252.3	80.3	19.7	
Pd <sub>SA-Na</sub> /D-CNT	260	1.5	18.5	98.7	1.3	40.5
	300	2.9	35.2	99.6	0.4	
	340	5.5	66.5	99.7	0.3	
Ni <sub>SA-Na</sub> /D-CNT	260	1.2	7.3	94.6	5.4	65.4
	300	3.5	22.0	93.7	6.3	
	340	8.1	50.7	95.5	4.5	
Co <sub>SA-Na</sub> /D-CNT	260	0.1	0.8	90.5	9.5	90.3
	300	0.6	3.3	96.7	3.3	
	340	2.4	12.6	98.2	1.8	
Cu <sub>SA-Na</sub> /D-CNT	260	0.4	2.3	97.5	2.5	n.d. <sup>b)</sup>
	300	0.6	3.8	97.1	2.9	
	340	0.4	2.6	97.5	2.5	

a) Valeur Moyenne b) Impossible de déterminer avec précision en raison de la faible conversion obtenue